HYBRID NANOMATERIALS

HYBRID NANOMATERIALS

SYNTHESIS, CHARACTERIZATION, AND APPLICATIONS

Edited by

Bhanu P. S. Chauhan

WILEY

A JOHN WILEY & SONS, INC., PUBLICATION

For general information on our other products and services or for technical support, please contact our Customer Care Department within the United States at (800) 762-2974, outside the United States at (317) 572-3993 or fax (317) 572-4002.

Wiley also publishes its books in a variety of electronic formats. Some content that appears in print may not be available in electronic formats. For more information about Wiley products, visit our web site at www.wiley.com.

Om Sat Guru

in fond memory of my parents

and to my life lines bholu, doujal, and shati

CONTENTS

vii

PREFACE

Research concepts in the area of nanoscale sciences are providing a common meeting platform for chemists, physicists, biologists, and engineers. The interdisciplinary nature of the nanoscale science has made it imperative to collect knowledge and present it in a form that all disciplines can understand and use. This need is very acute in the area of hybrid nanomaterials because such materials are unique conjugates of organic/inorganic structures and have found applications and appeal in various fields.

The term hybrid in a simplistic manner means fusion, union, or combination of the features, into one monolithic identity to exploit the advantages of combined features and to negate the disadvantages of the individual components. In chemical materials terminology, this will mean the fusion of properties at the molecular level, which will produce a hybrid material possessing advantageous features of each constituent while at the same time not inheriting the disadvantageous features of the individual component. In other words, the creation of hybrid materials leads to fusion of the desired properties with the elimination of undesired behavior providing an appealing property profile for such materials. It is because of this potential that hybrid materials can find applications in diverse fields even though their original components might not have been considered for those applications.

The aim of this book is to present cutting edge discoveries and their future applications as seen by the discoverers themselves. The coverage of this volume can be divided into three broad categories of nanohybrids: (1) the hybrids generated by the fusion of organic/inorganic components for new materials design; (2) hybrids generated by fusion of heterogeneous/homogeneous catalysts at nanoscale for new catalytic applications, and (3) hybrids arising due to fusion of hard and soft materials designed to explore novel materials applications. The book is targeted to appeal to researchers, professionals, industrial practitioners, as well as graduate and postdoctoral associates in the fields of chemistry, biochemistry, physics, and materials science. This book will also serve the need of the general scientific community to know the most recent developments pertaining to the synthesis, characterizations, and applications of hybrid nanomaterials.

The editor gratefully acknowledges the contributions of all the authors, who have put a great deal of energy and hard work to summarize their discoveries and those of others in the field. Without their insight, ingenuity, inquisitiveness, and

encouragement this work would not be possible. Thanks are due to all reviewers as well, who volunteered their time and wisdom to review the manuscripts. I would also like to thank Anita Lekhwani (Wiley) for her infectious enthusiasm and help. Last but not least, I would like to thank my family for allowing me to undertake this task and helping me to bring it to fruition.

BHANU P. S. CHAUHAN

CONTRIBUTORS

Hanying Bai, Department of Chemistry and Biochemistry, City University of New York–Hunter College, 695 Park Avenue, New York, New York 10065, USA

Matthias Ballauff, Soft Matter and Functional Materials, Helmholtz-Zentrum Berlin für Materialien und Energie GmbH, Berlin, Germany

Mrinmoyee Basu, Department of Chemistry, Indian Institute of Technology, Kharagpur-721302, India

Bhanu P. S. Chauhan, Engineered Nanomaterials Laboratory, Department of Chemistry, William Paterson University, Wayne, New Jersey 07470, USA

Moni Chauhan, Queensborough Community College of City University of New York, New York, New York 11364, USA

Venkat Reddy Chintareddy, Department of Chemistry, 1311 Gilman Hall, Iowa State University, Ames, Iowa 50011, USA

Jack F. Douglas, Nanostructured Materials, Polymers Division, National Institute of Standards and Technology, 100 Bureau Drive, Gaithersburg, Maryland 20899, USA

Manas K. Haldar, Department of Pharmaceutical Sciences, North Dakota State University, 1401 Albrecht Boulevard, Fargo, North Dakota 58108, USA

Narayan S. Hosmane, Department of Chemistry and Biochemistry, The Michael Faraday Laboratories, Northern Illinois University, DeKalb, Illinois 60115, USA

Chin Ming Hui, Center for Engineered Polymeric Materials, Department of Chemistry, College of Staten Island, City University of New York, 2800 Victory Boulevard, Staten Island, New York 10314, USA

Mannepalli Lakshmi Kantam, Inorganic and Physical Chemistry Division, Indian Institute of Chemical Technology, Hyderabad 500007, Andhra Pradesh, India

Alamgir Karim, Department of Polymer Engineering, University of Akron, Akron, Ohio 44224, USA

Prerna Kaur, Department of Chemistry and Biochemistry, City University of New York Hunter College, 695 Park Avenue, New York, New York 10065, USA

Yusuke Kawakami, School of Materials Science, Japan Advanced Institute of Science and Technology (JAIST), 1-1 Asahidai, Nomi, Ishikawa 923-1292, Japan

Michal Kruk, Center for Engineered Polymeric Materials, Department of Chemistry, College of Staten Island, City University of New York, 2800 Victory Boulevard, Staten Island, New York 10314 and Graduate Center, City University of New York, 365 Fifth Avenue, New York, New York 10016, USA

Silvia H. De Paoli Lacerda, Nanostructured Materials, Polymers Division, National Institute of Standards and Technology, 100 Bureau Drive, Gaithersburg, Maryland 20899, USA

Yan Lu, Soft Matter and Functional Materials, Helmholtz-Zentrum Berlin für Materialien und Energie GmbH, Berlin, Germany

John A. Maguire, Department of Chemistry, Southern Methodist University, Dallas, Texas 75275, USA

Sanku Mallik, Department of Pharmaceutical Sciences, North Dakota State University, 1401 Albrecht Boulevard, Fargo, North Dakota 58108, USA

Hiroshi Matsui, Department of Chemistry and Biochemistry, City University of New York Hunter College, 695 Park Avenue, New York, New York 10065, USA

Ahmad Mehdi, Institut Charles Gerhardt Montpellier, UMR 5253 CNRS, Chimie Moléculaire et Organisation du Solide, CC 1701, Université Montpellier II, Place E. Bataillon, 34095 Montpellier Cedex 5, France

Tarasankar Pal, Department of Chemistry, Indian Institute of Technology, Kharagpur-721302, India

Jitendra S. Rathore, Engineered Nanomaterials Laboratory, Department of Chemistry, William Paterson University, 300 Pompton Road, Wayne, New Jersey 07470, USA

Michael D. Scott, Department of Pharmaceutical Sciences, North Dakota State University, 1401 Albrecht Boulevard, Fargo, North Dakota 58108, USA

Marc Walters, Department of Chemistry, New York University, 100 Washington Square East, New York, New York 10003, USA

Koh Cheng Yan, Institute of Chemical and Engineering Sciences, No. 1 Pesek Road, Jurong Island, Singapore 627833

Zhu Yinghuai, Institute of Chemical and Engineering Sciences, No. 1 Pesek Road, Jurong Island, Singapore 627833

◼◼◼◼ CHAPTER 1

Hybrids from Polymer Colloids and Metallic Nanoparticles: A Novel Type of "Green" Catalyst

YAN LU and MATTHIAS BALLAUFF

Soft Matter and Functional Materials, Helmholtz-Zentrum Berlin für Materialien und Energie GmbH, Berlin, Germany

Metallic nanoparticles have interesting perspectives in the application of catalysis as they exhibit unusual chemical and physical properties differing from the bulk material. However, for all practical applications, metallic nanoparticles must be stabilized in solution in order to prevent aggregation. Here we have reviewed our recent studies on metallic nanoparticles encapsulated in spherical polyelectrolyte brushes (SPBs) and thermosensitive core–shell microgels, respectively. SPB particles consist of a poly(styrene) (PS) core onto which long chains of polyelectrolyte brushes are densely grafted by a grafting-from technique. In the case of thermosensitive microgels, the core consists of PS whereas the network consists of poly(N-isopropylacrylamide) (PNIPA) crosslinked by N,N'-methylenebisacrylamide (BIS). Both polymeric particles present as excellent carrier systems for applications in catalysis. More importantly, the composite systems of metallic nanoparticles and polymeric carrier particles allow us to do "green chemistry," that is, low temperature, easy removal of the catalyst and low leaching of heavy metal into the product. The chemical reactions can be conducted in a very efficient way. In addition, in the case of using microgels as the carrier system, the reactivity of composite particles can be adjusted by the volume transition within the thermosensitive networks. Hence, this chapter gives clear indications on how carrier systems for metallic nanoparticles should be designed to adjust their catalytic activity.

1.1. INTRODUCTION

Metal nanoparticles have attracted a lot of attention, because they may exhibit unusual chemical and physical properties differing strongly from the bulk material,[1–3] which are due to three major factors: high surface-to-volume ratio, quantum size effect, and electrodynamic interactions.[4] Metallic nanoparticles have interesting perspectives in the applications as catalysts,[5–8] sensors,[9] and electronics. However, the high specific surface area of the metal nanoparticles often leads to the common tendency of agglomeration, and usually requires their immobilization in mesoscopic carriers to prevent precipitation. Using suitable polymeric systems, such as microgels,[10–12] dendrimers,[13–16] and block copolymer micelles[17–19] as carriers or "nanoreactors," metal nanoparticles can be immobilized and handled in an easier fashion. Metallic nanoparticles immobilized in such systems can then be used for catalysis in various media.[20] Moreover, the concept of green chemistry has become a top priority item for catalysis industry, that is, low temperature, easy removal of the catalyst and low leaching of heavy metal into the product.[21, 22] This requires a carrier system that should allow separation (e.g., via filtration), have long-term stability, be easy to handle, and prevent the metallic nanoparticles from coagulating. Moreover, no stabilizing agent that may alter or block the surface of the nanoparticles should be used. The carrier systems should also be sufficiently stable during recycling of the catalyst.

In this chapter, we review recent work on two special types of polymeric carrier systems, namely, the spherical polyelectrolyte brushes (SPBs) and thermosensitive core–shell microgels, which have been used successfully for the immobilization of metal nanoparticles. Figure 1.1a gives a schematic representation of the SPB particles: Long linear polyelectrolyte chains are grafted densely to a colloidal core particle.[23, 24] The term brush implies that the grafting of the chains is sufficiently
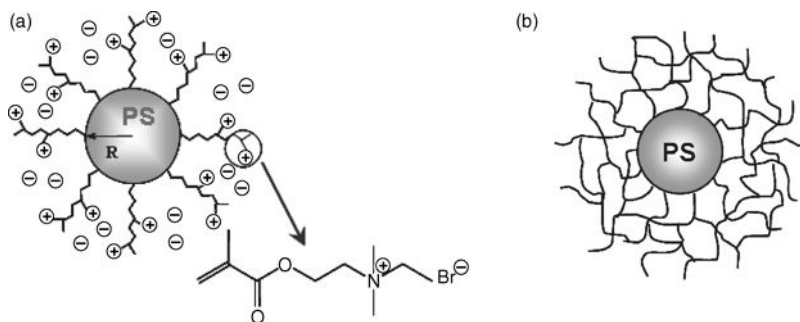
Figure 1.1. (a) Structure of the spherical polyelectrolyte brushes having cationic polyelectrolyte chains on their surface. The core consists of poly(styrene) and has diameters of approximately 100 nm. The chains are densely grafted to the surface of these cores by a grafting-from technique ("photoemulsion polymerization," cf. Ref. 24). (b) The core–shell microgel particles shown in a schematic fashion: The core consists of poly(styrene) (PS) whereas the network consists of poly(N-isopropylacrylamide) (PNIPA) crosslinked by N,N'-methylenebisacrylamide (BIS).

dense; that is, the linear dimensions of the polyelectrolyte chains are much larger than the average distance between two neighboring chains on the surface. These positively charged polyelectrolyte chains form a dense layer on the surface of the core particles and can bind metal ions. Reduction leads to metallic nanoparticles. Figure 1.1b depicts core–shell microgels that consist of a solid core of polystyrene and a shell of crosslinked poly(N-isopropylacrylamide) (PNIPA).[25] The metal ions are localized within the network because of complexation between the metal ions and the nitrogen atoms of PNIPA. Reduction of these ions leads to nearly monodisperse metallic nanoparticles that are only formed within the polymer layer.

The focus of this chapter is the use of both the spherical polyelectrolyte brushes and microgel particles as carrier systems for novel metal nanoparticles, which can be used for catalysis in aqueous media, that is, under very mild conditions.[26–30] Thus, the composite systems of metallic nanoparticles and polymeric carrier particles allows us to do "green chemistry"[31] and conduct chemical reactions in a very efficient way. This approach can open new possibilities for catalytic application of metal composite particles in different reactions and represents a typical example of "mesotechnology":[32] Nanoscopic objects with catalytic properties are judiciously combined with polymeric carriers to serve for a given, well-defined purpose.

1.2. SPHERICAL POLYELECTROLYTE BRUSH BASED METALLIC NANOPARTICLES

Often, nanoparticles are stabilized by alkyl chains attached through thiol bonds to the surface of the metal.[33, 34] However, the strong interaction of the thiol group with the surface of the nanoparticles may profoundly alter the catalytic properties of the metal. The same problem may occur when immobilizing nanoparticles on solid substrates.

Recently, we reported that the SPBs are excellent carriers for various metal nanoparticles. In particular, we demonstrated that the composites of metal nano-particles and SPBs are very stable. This fact can be understood when considering the synthesis of the composites in detail:[28] Figure 1.2 shows the synthesis of Au nanoparticles (NPs) on a cationic SPB. The $AuCl_4^-$ ions are introduced as counter-ions of the brush layer and all metal ions not firmly bound in this layer are flushed away by ultrafiltration. Hence, only the reduction of these immobilized $AuCl_4^-$ ions will lead to well-defined Au NPs. All stages of nanoparticle formation within the brush layer can be followed easily by dynamic light scattering (DLS), which determines the hydrodynamic radius (R_H) of the particles. Since the radius R of the core particles is exactly known, the thickness L of the surface layer can be obtained by $L = R_H - R$ throughout all stages of the synthesis of the particles. We found that even low concentrations of $AuCl_4^-$ ions lead to a considerable shrinking of the polyelectrolyte layer on the surface of the core particles from 71 to 59 nm. This shrinking of the surface layer is due to partial crosslinking of the polyelectrolyte chains by the $AuCl_4^-$ ions.

The $AuCl_4^-$ ions are partially complexed by the polyelectrolyte chains. In this way the $AuCl_4^-$ ions create a densely crosslinked mesh of polyelectrolyte chains. Thus, the local concentration of $AuCl_4^-$ ions is therefore enlarged considerably.
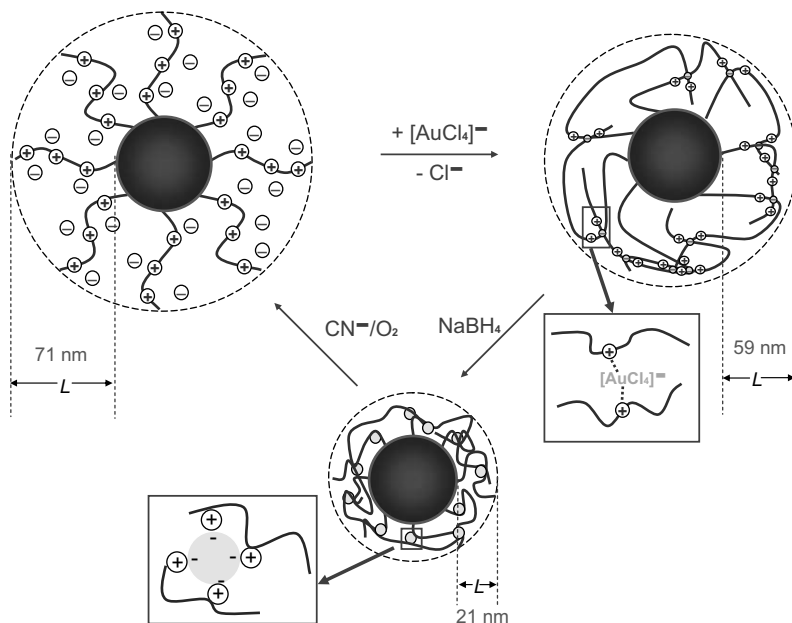
Figure 1.2. Schematic representation of the generation of Au NPs and their dissolution with CN^-/O_2: In the first step Cl^- ions are exchanged against $AuCl_4^-$ ions. The excess of $AuCl_4^-$ ions is removed subsequently by ultrafiltration. Replacing Cl^- ions by $AuCl_4^-$ ions leads to a decrease of the layer thickness L from 71 nm to 59 nm. In next step, Au NPs are generated by reduction of the confined $AuCl_4^-$ counterions by $NaBH_4$. Here L decreased to only 21 nm. In last step, Au NPs are dissolved by complexation with CN^-/O_2. The original thickness of the surface layer is recovered in this step. (See Ref. 28.)

In the next step the reducing agent $NaBH_4$ is added, which results in a collapse of the surface layer to a thickness of 21 nm. The micrographs of the resulting composite particles obtained by cryo-TEM are shown in Figure 1.3. It demonstrates that small Au NPs have been formed in this step.

   A possible reason for the decrease of the hydrodynamic radius may be sought in a degradation of the polyelectrolyte layers by cleavage or other side reactions. However, this explanation can easily be refuted by dissolution of the Au NPs upon addition of NaCN in the presence of O_2. This process leads to $L = 69$ nm, which is identical to the starting value of 71 nm within the limits of error. Hence, the polyelectrolyte chains of the brush layer are condensed by the Au NPs as shown schematically in Figure 1.2. After the dissolution of the Au NPs the chains stretch again and assume their previous conformation. Hence, the Au NPs formed by reduction within the brush layer lead to an additional crosslinking of the polyelec-trolyte chains that extend far beyond the crosslinking effect of the $AuCl_4^-$ ions. This attractive interaction could be related to the negative charge of the Au NPs. Thus, the Au NPs crosslink the polyelectrolyte chains by ionic interaction.

   The advantages of generating metallic nanoparticles using this method are obvious: Because of the confinement of the counterions, nanoparticles are only
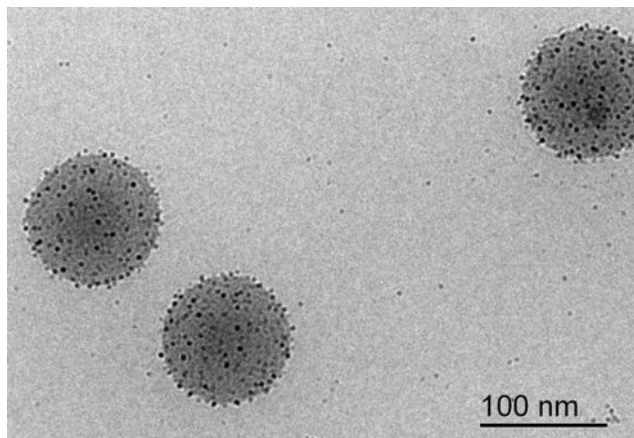
Figure 1.3. Cryo-TEM images of Au NP–SPB composite particles. The Au NPs are visible as black dots attached near the surface. (Reproduced from Ref. 28.)

generated within the polyelectrolyte layer. Stabilization of the nanoparticles against aggregation is effected by the colloidal carrier particles. Because the metal nanoparticles carry no group stabilizing their surface, they exhibit a high catalytic activity. Thus, these systems can be used for catalysis of various chemical reactions that proceed in aqueous solution or in two-phase systems. In the following we review the main applications established so far.

1.2.1. SPB Based Au, Pt, and Pd Nanoparticles for Catalysis in Two-Phase Systems

In 1912, Paul Sabatier received the Nobel Prize for chemistry for his investigations into the use of finely divided metals in hydrogenation reactions. Since then, heterogeneous catalysis in organic chemistry has been developed extensively. During our research, we examined the hydrogenation of butyraldehyde to 1-butanol catalyzed by platinum nanoparticles supported on SPB particles. All reactions were carried out in aqueous solution at 40 °C and 70 bar hydrogen pressure. Product extraction was accomplished using a second (organic) liquid phase.[27] The reactant and product concentrations (butyraldehyde and 1-butanol) were monitored by gas chromatography (GC). Excellent recyclability was observed concerning the catalytic performance and the product extraction, as shown in Figure 1.4. The catalyst system was used for 10 reactions, and the products extracted with ether after each reaction. It was found that the efficiency of the catalyst remains unaltered in nine consecutive reactions. The catalyst was stable against aggregation during the reactions and the workup procedure. Moreover, our previous work showed that platinum and palladium nanoparticles prepared by the same method can be used as catalysts for the degradation of 4-nitrophenol using $NaBH_4$. It is interesting to note that palladium was more effective than platinum, but their catalytic activities were in the same magnitude when normalized to the surface of metal particles.[35] However, the hydrogenation
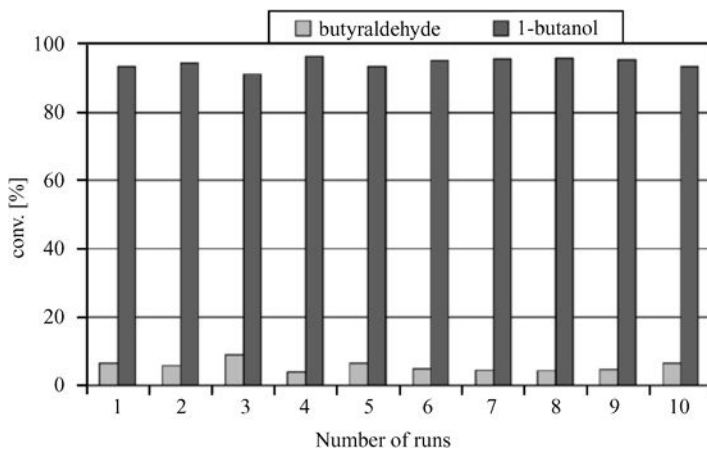
Figure 1.4. Stability and reuse of the Pt/SPB composite catalyst (hydrogenation of butyr-aldehyde). The same catalyst was used for 10 runs. After each run products were extracted by ether (3 times with 3 mL) and fresh substrate was added. (See Ref. 27.)

activities of palladium nanoparticles were orders of magnitude smaller than those observed for the platinum system.

1.2.2. Pd-Nanoparticles Immobilized on SPBs for the Heck and Suzuki Coupling

The palladium-catalyzed Heck[36, 37] and Suzuki[38, 39] reactions (cobalt nanospheres are also able to catalyze these reactions[40]) between aryl halides and alkenes or boronic acids are well-established tools for C=C bond formation in organic synthesis, respectively.[41, 42] Such reactions are traditionally catalyzed using many different kinds of phosphine-based palladium catalysts and phosphine-free palladium catalysts such as $Pd(PPh_3)_4$, $Pd(Oac)_2$, $[(n^3-C_3H_5)PdCl]_2$, and $Pd_2(dba)_3C_6H_6$.[43] Recently, there have been many reports on the use of palladium nanoparticles as catalysts.[44, 45] A convenient route for cross-coupling reactions involves reusable palladium nanoparticles that promote these reactions in organic solvents or in water.[46, 47] However, the handling of the nanoparticles may impose problems during workup unless the particles are immobilized on suitable carriers. Recently, we reported that Pd nanoparticles immobilized in cationic spherical polyelectrolyte brushes (SPBs) present a composite system that can be used as an efficient catalyst for the Heck and Suzuki coupling reactions, as shown in Figure 1.5.[48] Figure 1.6 shows the typical test reactions for the Suzuki- and Heck-type cross-coupling reactions using palladium nanoparticles as catalyst. We demonstrate that both reactions can be carried out under mild conditions and low temperatures (Suzuki reaction: 50 °C; Heck reaction: 70 °C). Pd loadings of 0.09 mol% (Suzuki) and 0.029 mol% (Heck) were used. For the Suzuki reaction the boronic acid gave rise to homocoupling products in 14% yield under the above-mentioned mild reaction conditions. Hetero-coupling was observed for bromides (conversions of 80–90%) and iodides (around
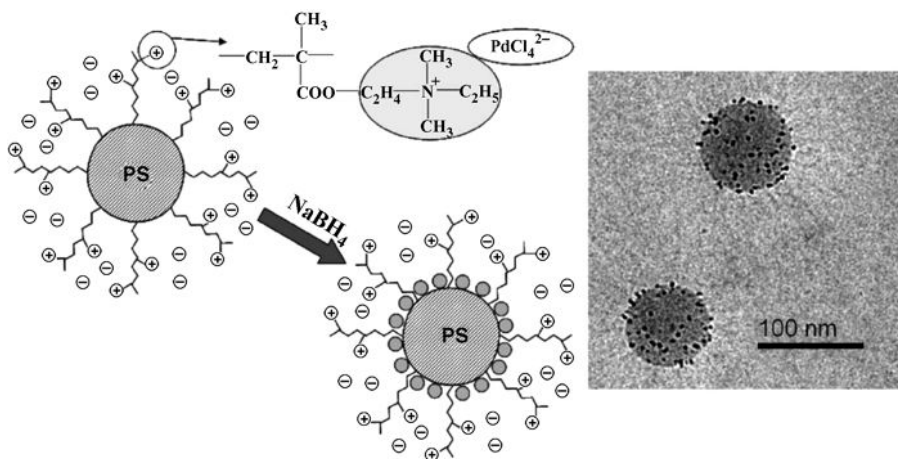
Figure 1.5. Synthesis of the spherical polyelectrolyte (left) and cryo-TEM of Pd@SPB (right) used for coupling reactions. Long chains of poly[(2-methylpropenyloxyethyl) trimethylammonium chloride] were grafted onto polystyrene cores of approximately 100 nm diameter. $PdCl_4^{2-}$ ions were introduced as counterions and reduction by $NaBH_4$ in aqueous solution led to Pd nanoparticles with diameters of 2.6 ± 0.5 nm immobilized on the surface of the carrier particles. (See Ref. 48.)

70%). However, chlorides resulted in low yields (ca. 6%). Additionaly, substituents in the ortho and meta positions resulted in lower yields (due to steric hindrance) than para-substituted arenes. Selected results are listed in Table 1.1.

The Heck-type reaction (see Figure 1.6 and Table 1.2) using palladium nanoparticles as a catalyst was investigated using eight different aryl halides. With a
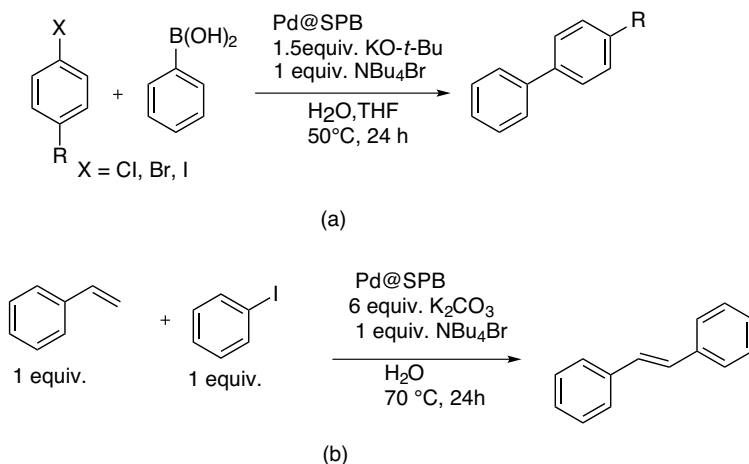
Figure 1.6. Test reaction for (a) Suzuki-type and (b) Heck-type cross-coupling using palladium nanoparticles stabilized in SPB particles as a catalyst.

TABLE 1.1. Suzuki-Type Cross-coupling Using Palladium Nanoparticles Stabilized in SPB Particles as Catalyst[a]

Halide	Product	GC Conversion	Homocoupling
		83%	4%
		79%	5%
		15%	6%
		22%	1%
		50%	1%
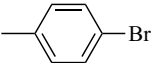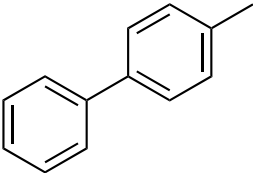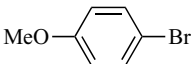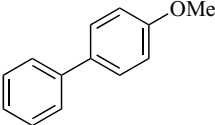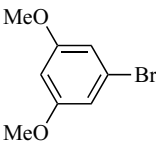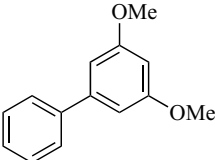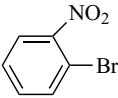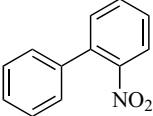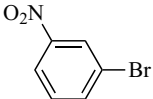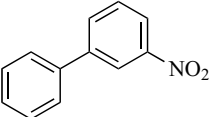
[a] Yields were determined by GC; hcp = homocoupling product (biphenyl).[48]

catalyst loading of 0.029 mol% Pd a variety of aryl iodides showed almost complete conversion, whereas aryl bromides were unreactive under the conditions employed. Under such mild conditions in water it is not possible to expand the scope of the Heck reaction to bromides or chlorides.

The reproducibility was found to be very good for palladium nanoparticles as catalyst of both Suzuki- and Heck-type reactions. In four runs the products were removed by ether and new starting materials were added to the water phase. We found that Pd@SPB could be used repeatedly without loss of activity. After these four

TABLE 1.2. Heck Reaction Promoted by Pd@SPB in Aqueous Media[a]

Iodide	Product	GC Conversion
		97%
		98%
		96%
		98%
		96%
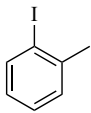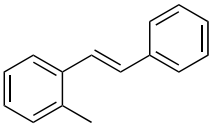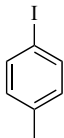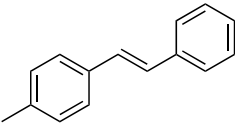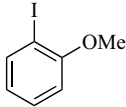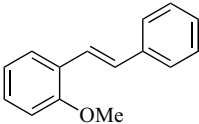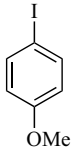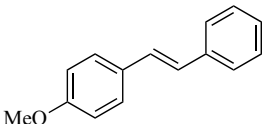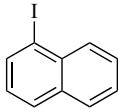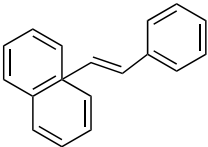
[a] One mL of catalyst solution leads to a loading of 0.029 mol% Pd; the catalytic reactions were carried out at 70 °C for 24 h.[48]

cycles the nanoparticles were filtered off and investigated by cryo-TEM in order to detect possible changes in the number and morphology of the nanoparticles. We found that the nanoparticles are still embedded in the SPB support. Hence, the present Pd@SPB catalyst system could easily be recycled and reused. The excellent reproducibility can be explained by the robustness of the catalyst system during catalysis and workup.

1.2.3. SPB-Based Nanoalloys of Noble Metals

Recently, we developed a method for the immobilization of Au–Pt nanoparticles into spherical polyelectrolyte brushes.[30] Figure 1.7 a shows the method of synthesis employed here: First, $AuCl_4^-$ ions are immobilized as counterions within the surface layer of cationic polyelectrolyte chains. Because we know the total number of charges on the surface of the core particles, the number of $AuCl_4^-$ ions can be adjusted precisely in order to replace only a certain fraction of the Cl^- counterions. After ultrafiltration, $PtCl_6^{2-}$ ions are introduced in the same manner. Any excess of metal ions is flushed away by ultrafiltration. Finally, reduction by $NaBH_4$ leads to Au–Pt alloy nanoparticles of a given composition. Figure 1.7b displays the HR-TEM of $Au_{73}Pt_{27}$. The crystal lattice is observed throughout the entire particle. Moreover, electron diffraction (inset of Figure 1.7b) demonstrates the crystalline state of the nanoparticles. Wide-angle X-ray scattering (WAXS) studies demonstrated that these alloys present solid solutions; that is, the particles consist of a random mixture of both types of metal atoms. Therefore, the lattice constants measured for the alloys vary continuously between the values found for the pure metals (Vegard-type[49]).

The catalytic oxidation of alcohols to aldehydes has been applied to investigate the catalytic activity of these Au–Pt alloy particles. All reactions were carried out at room temperature using aerobic conditions. Notably, no phase transfer catalyst is needed for this reaction and the reaction conditions are very mild. GC revealed that no by-product is obtained under these conditions. We find full conversion within the limits of error. Hence, water is the only product formed by this reaction (besides the aldehyde or ketone). We find that systems containing pure Au nanoparticles are much less stable than the alloy particles. Substrates containing phenyl groups lead to considerable leaching of gold and even coagulation. This may result from the strong interaction of Au with the phenyl groups, as determined by Miyamura et al.[50]
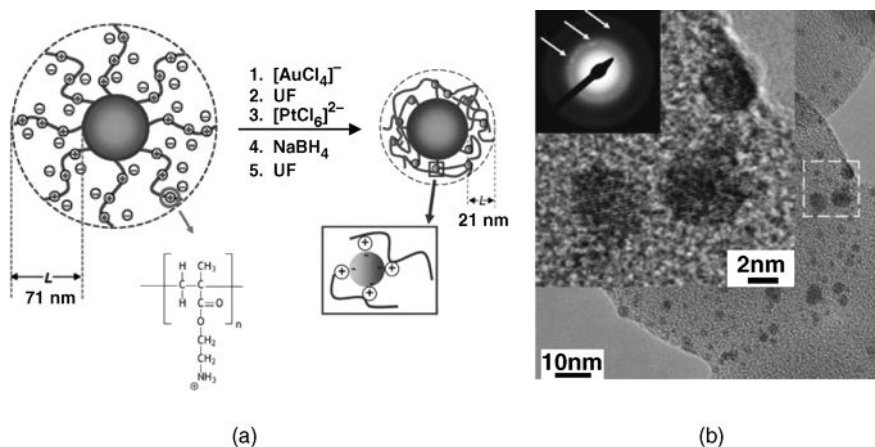
Figure 1.7. SPBs used as carriers for bimetallic Au–Pt NPs (left), with an HR-TEM image of $Au_{73}Pt_{27}$ alloy particles embedded in SPB (lattice imaging) and the diffractogram in the insets (right). (See Ref. 30.)

However, alloy nanoparticles turned out to be fully stable under the same conditions. This finding is corroborated by an analysis of the composite particles before and after catalysis by cryogenic TEM. No change or leaching of the nanoparticles is observed. Moreover, repeated use of the composite particles as catalysts did not lead to a noticeable decrease of catalytic activity. Hence, spherical polyelectrolyte brushes present a system that allows us to generate and to utilize alloy nanoparticles that exhibit properties widely differing from the properties of the respective bulk alloys.

Faceted, well-defined Pt single nanocrystals (NCs) with a typical size of 2–3 nm can be obtained by partial dissolution of nanoalloys of Pt and Au as shown in Figure 1.8.[51] The dealloying of the Au–Pt nanoalloy proceeded surprisingly smoothly. The colloidal stability of the composite particles was not lost during the reaction with the cyanide ions, and coagulation of the NPs on the surface of the carrier particles was not observed during this process. The structure of the Pt NPs was analyzed by combining high-angle annular dark-field scanning TEM (HAADF-STEM) and HR-TEM with electron diffraction (ED) and WAXS. A low-magnification HAADF-STEM micrograph of the PS spheres on the supporting holey carbon film is shown in Figure 1.9a, and Figure 1.9b (from the same area at higher magnification) shows the uniform distribution of the Pt NPs on the PS spheres. In order to avoid any disturbance of this analysis by the core particles, only NPs sitting on the periphery of the carrier spheres were analyzed by HR-TEM (Figure 1.9c–f). The HR-TEM shows that the Pt NPs contain no grain boundaries and are single crystals. In several cases, the facets can be indexed because the NCs are aligned by chance; in Figure 1.9e, f, the electron diffraction shows directly the hexagonal symmetry of the cubic crystal.

The catalytic reduction of 4-nitrophenol to 4-aminophenol has been used for the analysis of the catalytic activity of the Pt NPs. The Pt NCs exhibit a high catalytic activity and turnover numbers as high as 1580 ± 50, which is among the highest turnover numbers measured for this reaction.[26, 35, 52] Hence, the composite particles consisting of the SPBs and the Pt NCs present a system with high colloidal stability that may be used for catalysis in an aqueous environment.

The composite particles of metal nanoparticles and spherical polyelectrolytes present robust systems that can be employed in catalysis.[53] More importantly, such metal nanoparticles can be used as effective catalysts in a "green" fashion,[54] that is, low temperature, easy removal of the catalyst, and low leaching of heavy metal into the product.

1.3. MICROGEL-BASED METALLIC NANOPARTICLES

Microgels may have several important advantages over other systems, namely, stability, ease of synthesis, good control over particle size, and easy functionalization for stimulus-responsive behavior (e.g., change in volume in response to a change in pH, ionic strength, or temperature).[55] It is clear that this kind of materials holds great promise for nanotechnology.[56] Moreover, microgel-stabilized metal nanoparticles are kind of "quasi-homogeneous" nanoparticle catalysts, which have advantages of
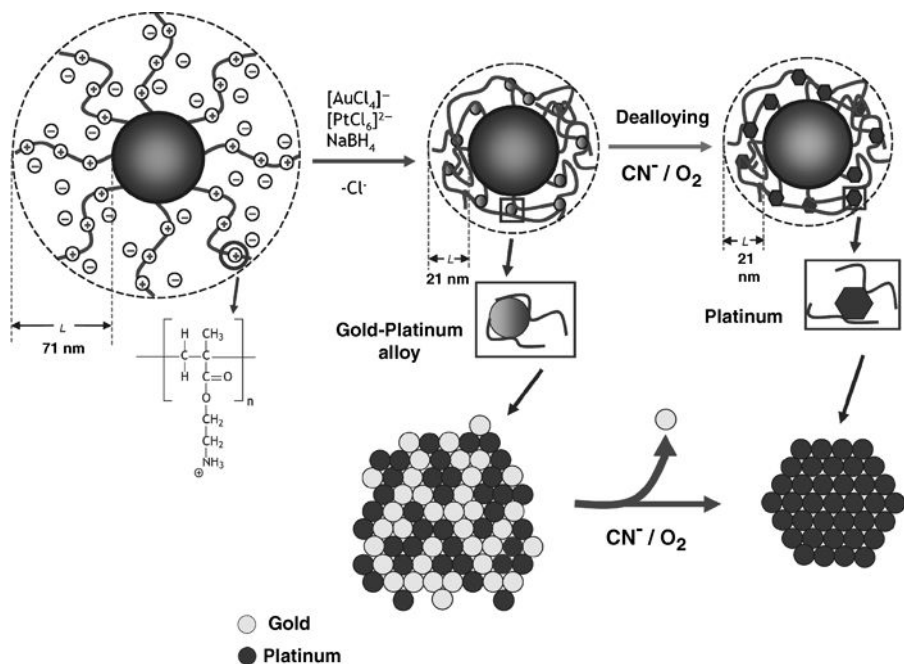
Figure 1.8. Synthesis scheme of Pt NCs by dealloying of an Au–Pt nanoalloy. The carrier particles are SPBs that consist of a solid PS core ($R_h = 50$ nm) onto which cationic polyelectrolyte chains of 2-aminoethylmethacrylate (2-AEMH) are attached. In a first step, the chloride counterions were exchanged against $AuCl_4^-$ ions; in a second step the rest of Cl^- ions were exchanged against $PtCl_4^{2-}$ ions. Bimetallic $Au_{45}Pt_{55}$ nanoalloy particles were generated by reduction of the mixture of these ions by $NaBH_4$. The composition of the resulting nanoalloy can be adjusted by the ratio of the metal ions in the brush layer. In the final step, cyanide ions and oxygen were used to leach out the Au atoms from the nanoalloy under very mild conditions. This procedure leads to faceted Pt NCs with a few nanometers in diameter embedded in the surface layer of polyelectrolyte chains. (See Ref. 51.)

both homogeneous and heterogeneous catalysts, such as high activity and easy separation for reuse.[31]

Most of these systems are poly(N-isopropylacrylamide) or related copolymers.[57] In aqueous media, PNIPA exhibits a lower critical solution temperature (LCST) at about 32 °C, which is close to the physiological temperature.[58–60] Below the LCST, the polymer chains are soluble in water due to formation of hydrogen bonds between the water molecules and the amide side chains. When the temperature increases, the polymer undergoes a volume phase transition. Water is expelled from the microgel interior, thus causing a drastic decrease in volume above the LCST of the polymer. Antonietti et al.[61, 62] were the first to employ microgels as "exotemplates" for the preparation of metal nanoparticles. Recently, Kumacheva and co-workers[63] introduced polymer microgels as carrier systems for nanoparticles. They showed that semiconductors, metal, and magnetic NPs with
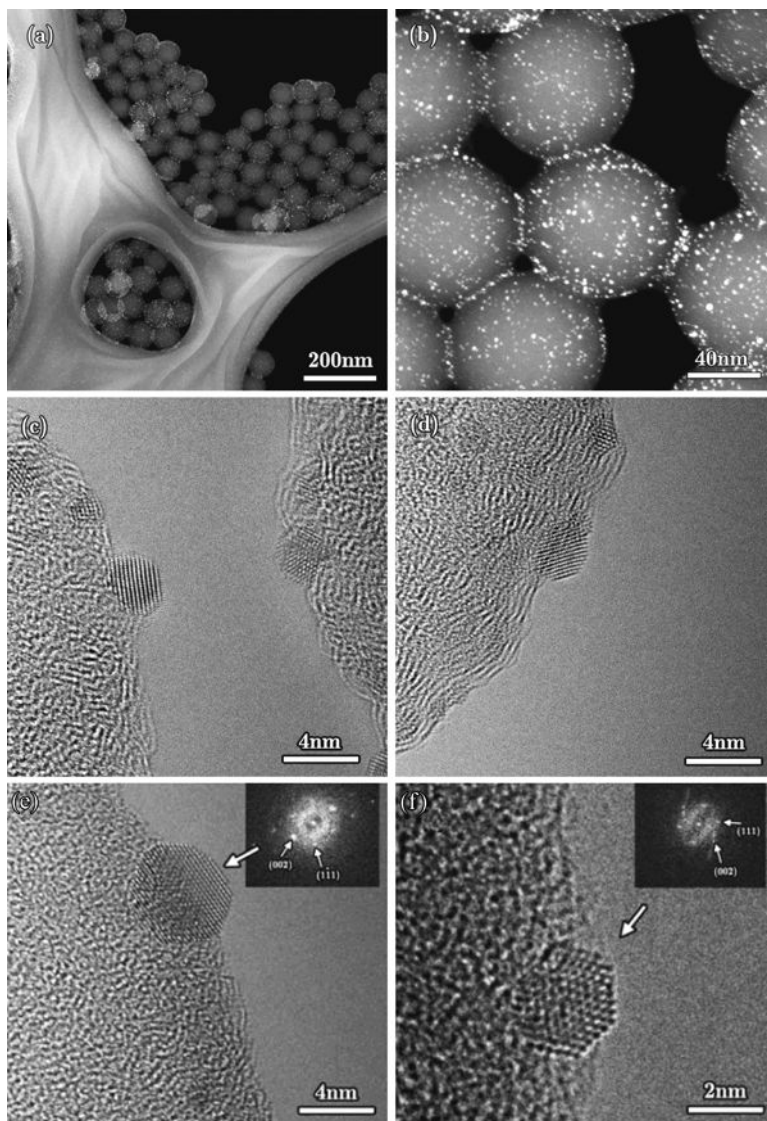
Figure 1.9. (a, b) HAADF-STEM micrographs of the Pt NPs (bright spots) embedded and uniformly dispersed on a surface layer of the spherical polyelectrolyte. (c) HR-TEM micrograph of nanoparticles on the surface of two adjacent carrier particles. (d) HR-TEM micrograph of several NCs. (e, f) HR-TEM micrographs of two different Pt single NCs of sizes 4.6 and 2.8 nm, respectively, showing well-defined facets. All micrographs were acquired at 300 keV. (Insets) The Fourier transforms of the images. (See Ref. 51.)

predetermined size, polydispersity, and optical and magnetic properties can successfully be synthesized using polymer microgels as a template, which will have promising applications in catalysis, biolabeling, and chemical and biological separation. Pich et al.[64] have used temperature-sensitive polyvinylcaprolactam-based microgels as containers for the deposition of catalytic active silver nanoparticles. Biffis and Sperotto[65] have studied the application of microgel–stabilized metal nanoclusters as catalysts for different reactions and confirmed the enhanced catalytic activity of Pd nanoclusters in Heck reaction of activated aryl bromides, which was attributed to the smaller size of the metal nanoclusters.

Recently, we have successfully used thermosensitive core–shell microgel particles as a template for the deposition of metal nanoparticles (Ag, Au, Pd, Pt, and Rh).[25, 31, 66, 67] These microgel particles consist of a PS core onto which a shell of PNIPA has been affixed in a seeded emulsion polymerization.[68, 69, 70] The synthesis of metallic nanoparticles in the presence of microgel particles was performed at room temperature via the addition of $NaBH_4$, and could be followed optically by the color change of the suspension. The immobilization of metal nanoparticles may be due to the strong localization of the metalate ions within the network, which is probably caused by a complexation of the metalate ions by the nitrogen atoms of the PNIPA.[71, 72] Both negatively charged and positively charged microgel particles can be used as the template. Their charges are introduced by the anionic initiator ($K_2S_2O_8$) and cationic initiator (V50), respectively, and not by anionic or cationic comonomers. Figures 1.10 and 1.11 display the cryo-TEM images of different metal nanoparticles embedded in microgel particles with negative charge and positive charge, respectivley. From cryo-TEM images, the dark spherical area indicates the PS core, whereas the light corona around the dark core represents the PNIPA shell of the particles. The metal nanoparticles are seen as small black dots. It is evident that most of the metal nanoparticles are homogeneously immobilized inside the PNIPA networks affixed to the surface of the core particles. The analysis revealed that the size of metal nanoparticles is different. This may be due to the difference of the complexation of the metal ions with the functional groups of the microgels. Furthermore, Figures 1.10 and 1.11 show another important point: All particles have a well-defined distance to their neighboring particles. This is due to the electrostatic repulsion that originates from the charges affixed to the core particles. These charges keep the entire suspension stable even above the volume transition where the steric repulsion between the particles breaks down. This point will become important further below when considering the catalytic activity of the composite particles above the volume transition.[69]

Moreover, investigations by DLS measurements of composite particles indicated that the original thermosensitive properties of the PNIPA network are not suppressed by the incorporation of metal particles into the network. The metal nanoparticles do not alter the volume transition within the network. Such a microgel system can work as an "active carrier" for the metal nanoparticles that allows us to modulate the catalytic activity of nanoparticles by a thermodynamic transition that takes place within the carrier system.[25, 26, 73] The principle is shown in Figure 1.12: Metallic nanoparticles embedded in such a network are fully accessible by the reactants at low
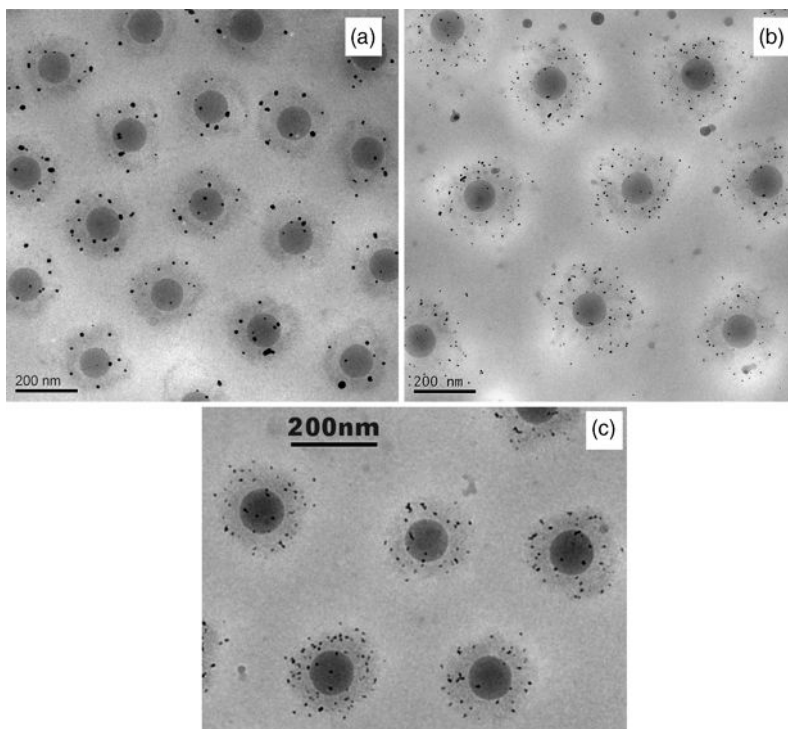
Figure 1.10. Cryo-TEM images of negatively charged microgel particles embedded with different metal nanoparticles: (a) with Ag (d: 8.5 ± 1.5 nm), (b) with Au (d: 2.0 ± 0.5 nm), and (c) with Pd (d: 3.8 ± 0.6 nm) nanoparticles. (See Ref. 25.)

temperature. Above the transition, however, the marked shrinking of the network should be followed by a reduction in the diffusion of the reactants within the network. Thus, the rate of reactions catalyzed by the nanoparticles should also be reduced. In this way, the network could act as a "nanoreactor" that can be opened or closed to a certain extent.

1.3.1. Catalytic Activity for Reduction of 4-Nitrophenol

The catalytic activity of microgel-based metal nanoparticles was investigated by monitoring photometrically the reduction of 4-nitrophenol by an excess of NaBH$_4$.[74, 75] We assumed that reduction rates were independent of the concentration of NaBH$_4$ because it was in excess compared to 4-nitrophenol. Moreover, the apparent rate constant, k_{app}, was found to be proportional to the surface S of the metal nanoparticles present in the system:[35, 67]

$$ -\frac{dc_t}{dt} = k_{app}c_t = k_1 S c_t $$
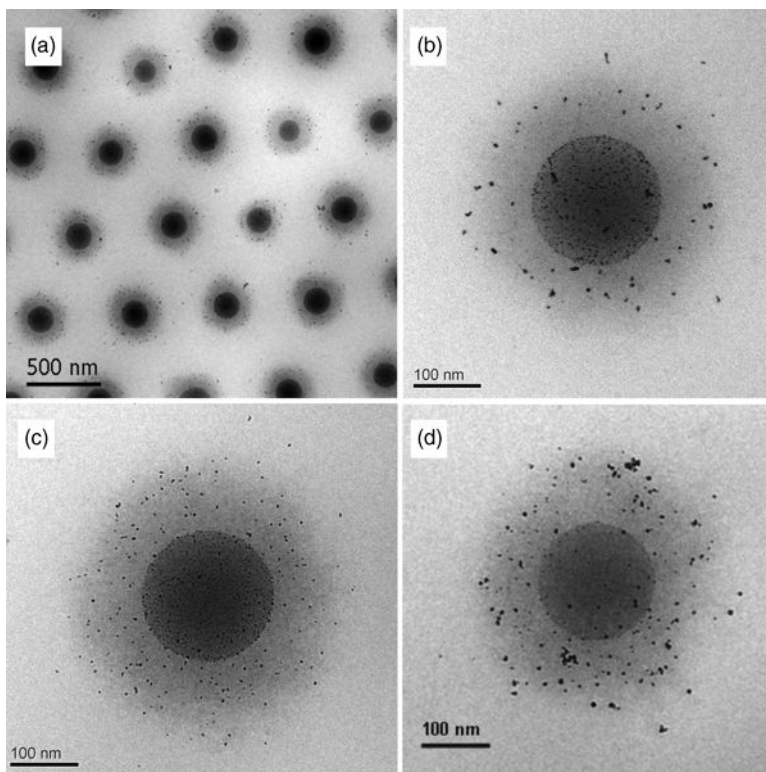
Figure 1.11. Cryo-TEM images of (a,b) Au (*d*: 4.8 ± 1.2 nm), (c) Pt (*d*: 2.8 ± 1.3 nm), and (d) Rh (*d*: 4.5 ± 1.5 nm) nanocomposite particles embedded in positively charged microgel particles, respectively. (See Ref. 31.)
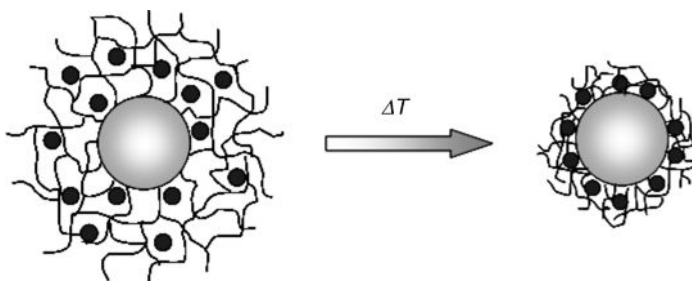
Figure 1.12. Schematic representation of composite particles consisting of thermosensitive core–shell particles in which metallic nanoparticles are embedded. The composite particles are suspended in water, which swells the thermosensitive network attached to the surface of the core particles. In this state the reagents can diffuse freely to the nanoparticles, which act as catalysts. At higher temperatures ($T > 32\,^\circ$C) the network shrinks and the catalytic activity of the nanoparticles is strongly diminished.

where c_t is the concentration of 4-nitrophenol at time t and k_1 is the rate constant normalized to S, the surface area normalized to the unit volume of the system. Figure 1.13 gives a typical curve for the influence of the temperature on the rate constant k_{app} of the catalytic reaction, which does not follow a typical Arrhenius-type dependence on temperature. When the reaction temperature is low, the PNIPA network is swollen. In this case, metal nanoparticles, which have been embedded in the network, can be accessed by the reactants of the catalytic reduction. So the rate constant k_{app} will exhibit a linear relation of ln k_{app} with T^{-1}. However, when the temperature increases further, the PNIPA network shrinks markedly, which is followed by reduction in the diffusion of reactants within the network. This in turn will lower the rate of reaction catalyzed by the metal nanoparticles. It is obvious that the increase of k_{app} by the rise of temperature is overcompensated by the diffusional barrier. Hence, the reaction rate must reach its minimum at the transition temperature. If the increase of temperature continues, the PNIPA network will not shrink any more and the density within the network stays constant. Now the strong increase of k_{app} with T will be predominant and the reaction rate will rise again. This demonstrates that the volume transition within a thermosensitive network can be used as a switch: Figure 1.13 shows that the catalytic activity of the metallic nanoparticles can be tuned down by more than one order of magnitude. In the case of the SPB-based metallic system, that is, the SPB-30-Pd9, the rate constant k_{app} is fully described by a conventional Arrhenius expression. Therefore, the S-curve seen in the Arrhenius plot in Figure 1.13 must solely be due to the diffusional barrier for the reactants if the
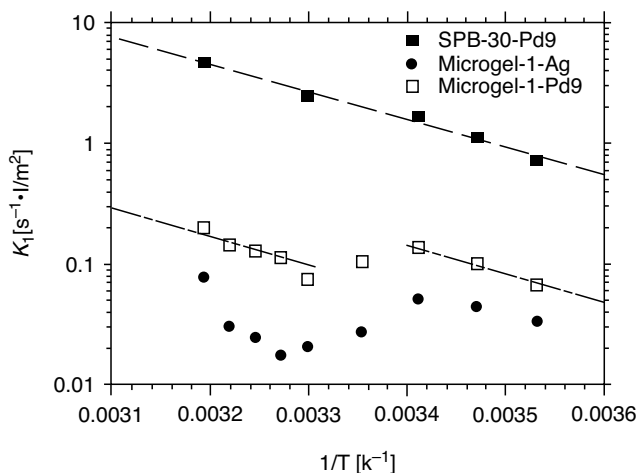
Figure 1.13. Dependence of the rate constant k_1 on the temperature T for different systems: Arrhenius plot of k_1 measured in the presence of the composite particles SPB-30-Pd9 (filled squares; system 1; [Pd composites]: 0.00063 g/L). In the case of the Microgel-1-Pd9 system (open squares; system 2; [Pd composites]: 0.00128 g/L), we obtained an S-curve, which is similar to that of silver nanoparticles (filled circles; data taken from Ref. 66; [Ag composites]: 0.0063 g/L). The concentrations of the reactants were as follows: [4-nitrophenol]: 0.1 mmol/L; [NaBH$_4$]: 10 mmol/L. (See Ref. 26.)

network is shrinking with increasing temperature. This phenomenon has also been proved by other groups for thermosensitive polymer-based metal nanoparticles.[76, 77] Li et al.[78] have observed a similar behavior for the hydrogenation of a hydrophobic alkene.

1.3.2. Catalytic Activity for Oxidation of Alcohol

The polarity of the gel also changes with the volume phase transition of the microgel from hydrophilic to hydrophobic. As shown in Figure 1.14, at low temperatures ($T < 32\ °C$) the network is swollen in water, and hydrophilic. Above the volume transition ($T > 32\ °C$), the network becomes hydrophobic and can thus accumulate hydrophobic reactants. From this point of view, the catalytic activity of metal–microgel composite particles at high temperatures will be affected both by the volume transition of the microgel (as shown in Figure 1.12) and by the change of polarity of the microgel (as shown in Figure 1.14). Oxidation reaction of alcohols to the corresponding aldehydes or ketones[79–82] has been used to investigate the catalytic behavior of microgel-based metal nanoparticles at different temperatures. It is worth noting that the reaction conditions are very mild and no phase transfer catalyst is needed. Microgel-based metal nanocomposites can efficiently catalyze the aerobic oxidation of benzyl alcohol at room temperature, which demonstrates that composite
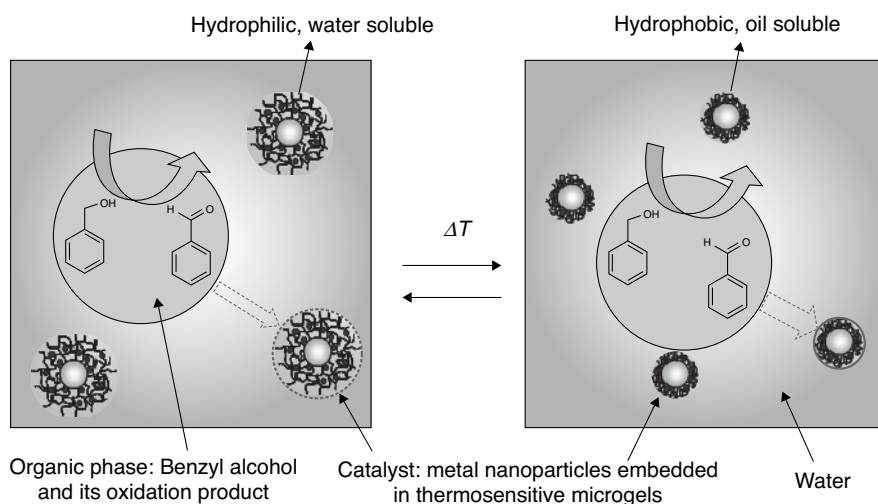
Figure 1.14. Schematic presentation of catalytic oxidation of benzyl alcohol in the presence of metal nanoparticles immobilized in thermosensitive core–shell microgels at different temperatures. At lower temperatures ($T < 32\ °C$), the microgel network is hydrophilic and swollen in water, while at high temperatures ($T > 32\ °C$), the network shrinks and becomes hydrophobic. Thus, microgel particles embedding the metal catalyst will move to the oil phase, which will be favorable for the uptake of hydrophobic benzyl alcohol into the metal–micorgel composite. Therefore, the catalytic activity of the metal–microgel composites will be affected by both the volume transition and the polarity change of the microgel. (See Ref. 31.)

microgels represent robust catalysts. No by-products have been detected by GC after the reaction and water is the only product formed besides the aldehyde.

Figure 1.15 shows the influence of temperature on the catalytic activity in an Arrhenius plot of the turnover frequency (TOFs). These data can now be compared to data obtained for the reduction of 4-nitrophenol with an excess of $NaBH_4$ in presence of the metal nano-composite particles. From Figure 1.15 a nonlinear relation between ln(TOF) and $1/T$ can be seen. The TOFs increase more than exponentially when increasing the temperature. Only in the immediate vicinity of the LCST is a significantly smaller TOF monitored.

In principle, there are two factors that will influence the catalytic activity: First, the collapsed PNIPA layer presents a steric barrier for benzyl alcohol molecules to diffuse from bulk aqueous dispersion to the surface of Au nanoparticles, causing the reaction to slow down, as shown in Figure 1.12. Second, with the increase of temperature, water-soluble hydrophilic PNIPA networks will become oil-soluble and hydrophobic, which will be favorable for the diffusion of hydrophobic benzyl alcohol onto the Au nanoparticle surface (as shown in Figure 1.14). Thus, the catalytic activity of Au composite particles should increase with increasing temperature. Figure 1.15 demonstrates that the second effect prevails in most of the temperature range; the TOF value observed at 40 °C is much higher than the value from conventional Arrhenius kinetics. This is different from the behavior that we found for the reduction reaction of 4-nitrophenol. The results demonstrate that the catalytic activity of oxidation reaction of benzyl alcohol is more sensitive to the change of polarity than the diffusional barrier brought about by the volume transition of a crosslinked PNIPA network. It should be noted that the selectivity of the reaction is lower when the reaction temperature is higher than 30 °C. Under these conditions benzoic acid was detected as a by-product by GC, which is in accord with the phenomenon found by Hutchings and co-workers[79] and Biffis et al.[82]
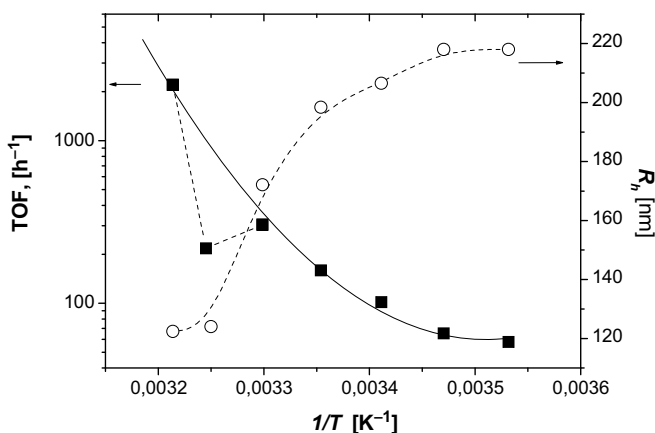
Figure 1.15. TOF versus $1/T$ for the oxidation of benzyl alcohol in the presence of microgel–Au nanocomposite particles (1 atm air, 1 mmol K_2CO_3, [microgel–Au] = 3.68 × 10^{-5} mol/L). The broken lines are guide lines for the reader. (See Ref. 31.)

CONCLUSION

Here we have reviewed our recent studies on metallic nanoparticles encapsulated in spherical polyelectrolyte brushes and thermosensitive core–shell microgels, respectively. Both polymeric particles present excellent carrier systems for applications in catalysis. The composite systems of metallic nanoparticles and polymeric carrier particles allow us to do "green chemistry" and conduct chemical reactions in a very efficient way. Moreover, in the case of using microgels as the carrier system, the reactivity of composite particles can be adjusted by the volume transition within the thermosensitive networks. Hence, the present chapter gives clear indications on how carrier systems for metallic nanoparticles should be designed to adjust their catalytic activity.

ACKNOWLEDGMENT

REFERENCES

1. Burda, C.; Chen, X.; Narayanan, R.; El-Sayed, M. A. *Chem. Rev.*, **2005**, *105*, 1025.
2. Ferrando, R.; Jellinek, J.; Johnston, R. L. *Chem Rev.*, **2008**, *108*, 845.
3. Pool, R. *Science*, **1990**, *248*, 1186.
4. Ghosh, S. K.; Pal, T. *Chem. Rev.*, **2007**, *107*, 4797.
5. Ahmadi, T. S.; Wang, Z. L.; Green, T. C.; Henglein, A.; El-Sayed, M. A. *Science*, **1996**, *272*, 1924.
6. Campbell, C. T.; Parker, S. C.; Starr, D. E. *Science*, **2002**, *298*, 811.
7. Chauhan, B. P. S.; Rathore, J. S.; Chauhan, M.; Krawicz, A. *J. Am. Chem. Soc.*, **2003**, *125*, 2876.
8. Chauhan, B. P. S.; Rathore, J.S.; Bandoo, T. *J. Am. Chem. Soc.*, **2004**, *126*, 1493.
9. Tokareva, I.; Minko, S.; Fendler, J. H.; Hutter, E. *J. Am. Chem. Soc.*, **2004**, *126*, 15950.
10. Wong, J. E.; Gaharwar, A. K.; Müller-Schulte, D.; Bahadur, D.; Richtering W. J. *Colloid Interf. Sci.*, **2008**, *324*, 47.
11. Pich, A.; Hain, J.; Lu, Y.; Boyko, V.; Prots, Y.; Adler H.-J. *Macromolecules*, **2005**, *38*, 6610.
12. Biffis, A.; Orlandi, N.; Corain, B. *Adv. Mater.*, **2003**, *15*, 1551.
13. Scott, R. W. J.; Wilson, O. M.; Crooks, R. M. *J. Phys. Chem. B*, **2005**, *109*, 692.
14. Hawker, C. J.; Frechét, J. M. J. *J. Am. Chem. Soc.*, **1990**, *112*, 7638.
15. Balogh, L.; Tomalia, D. A. *J. Am. Chem. Soc.*, **1998**, *120*, 7355.
16. Peng, X.; Pan, Q.; Rempel, G. L. *Chem. Soc. Rev.*, **2008**, *37*, 1619.
17. Xu, H.; Xu, J.; Zhu, Y.; Liu, H.; Liu, S. *Macromolecules*, **2006**, *39*, 8451.

18. Förster, S.; Antonietti, M. *Adv. Mater.*, **1998**, *10*, 195.

19. Pachón, L. D.; Rothenberg, G. *Appl. Organometal. Chem.*, **2008**, *22*, 288.

20. Astruc, D., Ed. *Nanoparticles and Catalysis*. Wiley-VCH, Weinheim, Germany, 2008.

21. Anastas P. T.; Kirchhoff, M. M. *Acc. Chem. Res.*, **2002**, *35*, 686.

22. Hashmi, A. S. K.; Hutchings, G. J. *Angew. Chem. Int. Ed.*, **2006**, *45*, 7896.

23. Ballauff, M. *Prog. Polym. Sci.*, **2007**, *32*, 1135.

24. Guo, X.; Weiss, A.; Ballauff, M. *Macromolecules*, **1999**, *32*, 6043.

25. Ballauff, M.; Lu, Y. *Polymer*, **2007**, *48*, 1815–1823.

26. Mei, Y.; Lu, Y.; Polzer, F.; Ballauff, M.; Drechsler, M. *Chem. Mater.*, **2007**, *19*, 1062.

27. Sharma, G.; Mei, Y.; Lu, Y.; Ballauff, M.; Irrgang, T.; Proch, S.; Kempe, R. *J. Catal.*, **2007**, *246*, 10.

28. Schrinner, M.; Polzer, F.; Mei, Y.; Lu, Y.; Haupt, B.; Ballauff, M.; Göldel, A.; Drechsler, M.; Preussner, J.; Glatzel, U. *Macromol. Chem. Phys.*, **2007**, *208*, 1542.

29. Malysheva, Y. B.; Gushchin, A. V.; Mei, Y.; Lu, Y.; Ballauff, M.; Proch, S.; Kempe, R. *Eur. J. Inorg. Chem.*, **2008**, *3*, 379.

30. Schrinner, M.; Proch, S.; Mei, Y.; Kempe, R.; Miyajima, N.; Ballauff, M. *Adv. Mater.*, **2008**, *20*, 1928.

31. Lu, Y.; Proch, S.; Schrinner, M.; Drechsler, M.; Kempe, R.; Ballauff, M. *J. Mater. Chem.*, **2009**, *19*, 3955.

32. Antonietti, M.; Ozin, G. A. *Chem. Eur. J.*, **2004**, *10*, 28.

33. Astruc, D.; Lu, F.; Aranzaes, R. *Angew. Chem. Int. Ed.*, **2005**, *44*, 7852.

34. Brust, M.; Walker, M.; Bethell, D.; Schiffrin, D. J.; Wyman, R. *J. Chem. Soc. Chem. Commun.*, **1994**, 801.

35. Mei, Y.; Sharma, G.; Lu, Y.; Drechsler, M.; Irrgang, T.; Kempe, R.; Ballauff, M. *Langmuir*, **2005**, *21*, 12229.

36. Heck, R. F.; Nolley, J. P. *J. Org. Chem.*, **1972**, *37*, 2320.

37. Heck, R. F. *Acc. Chem. Res.*, **1979**, *12*, 146.

38. Miyaura, N.; Suzuki, A. *Chem. Rev.*, **1995**, *95*, 2457.

39. Beletskaya, I. P.; Cheprakov, A. V. *Chem. Rev.*, **2000**, *100*, 3009.

40. Zhou, P.; Li, Y.; Sun, P.; Zhou, J.; Bao, J. *Chem. Commun.*, **2007**, 1418.

41. Phan, N. T. S.; Van Der Sluys, M.; Jones, C. W. *Adv. Synth. Catal.*, **2006**, *348*, 609.

42. Astruc, D. *Inorg. Chem.*, **2007**, *46*, 1884.

43. Suzuki, A., In: *Metal-Catalyzed Cross-Coupling Reactions*; Diederich, F.; Stang, P. J.; Eds. VCH, Weinheim, Germany, 1998; p. 49.

44. Li, Y.; Boone, E.; El-Sayed, M. A. *Langmuir*, **2002**, *18*, 4921.

45. Moreno-Manas, M.; Pleixats, R.; Villarroya, S. *Organometallics*, **2001**, *20*(22), 4524.

46. Reetz, M. T.; Breinbauer, R.; Wanninger, K. *Tetrahedron*, **1996**, *37*, 4499.

47. Klingelhofer, S.; Heitz, W.; Greiner, A.; Oestreich, S.; Fçrster, S.; Antonietti, M. *J. Am. Chem. Soc.*, **1997**, *119*, 10116.

48. Proch, S.; Mei, Y.; Rivera Villanueva, J. M.; Lu, Y.; Karpov, A.; Ballauff, M.; Kempe, R. *Adv. Synth. Catal.*, **2008**, *350*, 493.

49. Bond, G. C. *Platinum Met. Rev.*, **2007**, *51*, 63.

50. Miyamura, H.; Matsubara, R.; Miyazaki, Y.; Kobayashi, S. *Angew. Chem. Int. Ed.*, **2007**, *46*, 4151.

51. Schrinner, M.; Ballauff, M.; Talmon, Y.; Kauffmann, Y.; Thun, J.; Möller, M.; Breu, J. *Science*, **2009**, *323*, 617.

52. Lu, Y.; Mei, Y.; Schrinner, M.; Ballauff, M.; Möller, M.; Breu, J. *J. Phys. Chem. C*, **2007**, *111*, 7676.

53. Lu, Y.; Wittemann, A.; Ballauff, M. *Macromol. Rapid Commun.*, **2009**, *30*, 806.

54. Anastas, P. T.; Kirchhoff, M. M. *Acc. Chem. Res.*, **2002**, *35*, 686.

55. Zhang, J.; Xu, S.; Kumacheva, E. *Adv. Mater.*, **2005**, *17*, 2336.

56. Nayak, S.; Lyon, L. A. *Angew. Chem. Int. Ed. Engl.*, **2005**, *44*, 7686.

57. Pelton, R. *Adv. Colloid Interface Sci.*, **2000**, *85*, 1.

58. Schild, H. G. *Prog. Polym. Sci.*, **1992**, *17*, 163.

59. Wu, C.; Wang, X. *Phys. Rev. Lett.*, **1998**, *80*, 4092.

60. Hellweg, T.; Dewhurst, C. D.; Eimer, W.; Kratz, K. *Langmuir*, **2004**, *20*, 4330.

61. Antonietti, M.; Groehn, F.; Hartmann, J.; Bronstein, L. *Angew. Chem. Int. Ed.*, **1997**, *36*, 2080.

62. Whilton, N.T.; Berton, B.; Bronstein, L.; Henze, H.; Antonietti, M. *Adv. Mater.*, **1999**, *11*, 1014.

63. Zhang, J.; Xu, S.; Kumacheva, E. *J. Am. Chem. Soc.*, **2004**, *126*, 7908.

64. Pich, A.; Karak, A.; Lu, Y.; Ghosh, A.; Adler, H. J. P. *Macromol. Rapid Commun.*, **2006**, *27*, 344.

65. Biffis, A.; Sperotto, E. *Langmuir*, **2003**, *19*, 9548.

66. Lu, Y.; Mei, Y.; Drechsler, M.; Ballauff, M. *Angew. Chem. Int. Ed.*, **2006**, *45*, 813.

67. Lu, Y.; Mei, Y.; Drechsler, M.; Ballauff, M. *J. Phys. Chem. B*, **2006**, *110*, 3930.

68. Dingenouts, N.; Norhausen, Ch.; Ballauff, M. *Macromolecules*, **1998**, *31*, 8912.

69. Crassous, J.; Drechsler, Y.; Talmon, Y.; Ballauff, M. *Langmuir*, **2006**, *22*, 2403.

70. Lu, Y.; Wittemann, A.; Drechsler, M.; Ballauff, M. *Macromol. Rapid Commun.*, **2006**, *27*, 1137.

71. Frattini, A.; Pellegri, N.; Nicastro, D.; de Sanctis, O. *Mater. Chem. Phys.*, **2005**, *94*, 148.

72. Das, M.; Mordoukhovski, L.; Kumacheva, E. *Adv. Mater.*, **2008**, *20*, 2371.

73. Lu, Y.; Yu, M.; Drechsler, M.; Ballauff, M. *Macromol. Symp.*, **2007**, *254*, 94.

74. Pradhan, N.; Pal, A.; Pal, T. *Colloids Surf. A*, **2002**, *196*, 247.

75. Lu, Y.; Spyra, P.; Mei, Y.; Ballauff, M.; Pich, A. *Macromol. Chem. Phys.*, **2007**, *208*, 254.

76. Hain, J.; Schrinner, M.; Lu, Y.; Pich, A. *Small*, **2008**, *4*(11), **2016**.

77. Wang, Y.; Wei, G.; Wen, F.; Zhang, X.; Zhang, W.; Shi, L. *J. Mol. Catal. A: Chem.*, **2008**, *280*, 1.

78. Li, D.; Dunlap, J. R.; Zhao, B. *Langmuir*, **2008**, *24*, 5911.

79. Enache, D. I.; Edwards, J. K.; Landon, P.; Solsona-Espriu, B.; Carley, A. F.; Herzing, A. A.; Watanabe, M.; Kiely, C. J.; Knight, D. W.; Hutchings, G. J. *Science*, **2006**, *311*, 362.

80. Uozumi, Y.; Nakao, R. *Angew. Chem. Int. Ed.*, **2003**, *42*, 194.

81. Biffis, A.; Minati, L. *J. Catal.*, **2005**, *236*, 405.

82. Biffis, A.; Cunial, S.; Spontoni, P.; Prati, L. *J. Catal.*, **2007**, *251*, 1.

Metal and Metal Oxide Nanostructure on Resin Support

MRINMOYEE BASU and TARASANKAR PAL

Department of Chemistry, Indian Institute of Technology, Kharagpur, India

Metal and metal oxides in their nanoregime have become the elegant choice for their multifaceted applications in the wide material world. It has already been documented that the sizes of these nanostructured materials govern the structure–property relationship of the nanomaterials. However, it is now pertinent to mention that shapes also affect the behavior of the nanomaterials at times. It is a fact that, generally, a nanomaterial becomes progressively active and unstable as the size goes to smaller and smaller dimension. Thus, the materials in question become so active that sometimes it becomes difficult to manipulate them in practice. Now indifferent and inactive support has been conceived for the manipulation of nanomaterials to carry the proper essence of the nanostructures. Organically engineered inactive support for the inorganic nanostructured materials has been fabricated where commercial resin has been shown to give some promise. Electrostatic field force (EFF) of the charged resin matrix and in some cases physical encapsulation of the material in a polymeric network is able to carry the essence and message of the nanostructured material. The chapter reviews some elegant and updated applications of the supported nanostructure materials mainly for catalysis and spectroscopic applications.

2.1. INTRODUCTION

Nanoscience is even now in the "discovery phase." New materials are being synthesized (using any means available) on nanoscales (hundreds of milligrams or less) for scavenging specific physical properties. Nanoparticle synthesis is

currently an area of scientific research, due to its wide variety of potential applications in biomedical, optical, magnetic, and electronic fields. Nanotechnology, on the other hand, deals with deliverables. In the 9th century in Mesopotamia, nanoparticles were used for generating glittering effect on the surface of the ceramic materials and glasses. Michel Faraday provided the first description, in scientific terms, of the optical properties of nanometer-scale gold in his classic 1857 paper.[1] Nanoparticles have great scientific interest as they are effectively a bridge between bulk materials and atomic or molecular structures. A microscopic particle having size at least 1–100 nm is called a nanoparticle. This critical size is strongly related to the exponential increase in the number of surface atoms as the size decreases and delineates a smaller set of nanoparticles (typically with diameters less than 20–30 nm). These smaller nanoparticles have a size-dependent crystallinity that gives them properties drastically different from the bulk material.[2] The interest in nanoscale materials stems from the fact that new properties are acquired at this length scale and, equally important, that these properties change with their size or shape.[3, 4] The change in the properties at this length scale is not a result of scaling factors but it depends on the material. Nanoparticles present possible high catalytic activity or reactivity. All of these are due to the high surface-to-volume ratio, which can make the particles very reactive.[5, 6] From the literature we come to know that, in general, nanoparticles can easily be prepared following two main methods: One is a top–down method that is the physical method and another is the bottom–up approach, which is a chemical method.[7] In the chemical method metal salts are reduced by suitable reducing agents and in the physical method there are some physical techniques that are used for the synthesis of nanoparticles from the bulk such as sonolysis, radiolysis, and laser irradiation.[8] In this framework, the physical method yields nanoparticles having a wide size distribution with comparatively larger size with inconsistent catalytic activity.[9] Generally, nanoparticles are prepared by the bottom–up technique as metal sol. Metallic nanoparticles are very unstable due to their high surface-to-volume ratio. In most of the cases of application of the prepared nanoparticles aggregation of colloidal metallic nanoparticles leads to a significant loss of catalytic activity. So stabilization of the nanoparticles is an important factor during the evolution/synthesis of nanoparticles.

Nanoparticles may be stabilized following a few protocols that include (i) electrostatic stabilization, (ii) steric stabilization, (iii) elctrosteric stabilization, and (iv) stabilization by ligand, surfactant, or polymer.[7]

Metal nanoparticles are unique materials with interesting physical and chemical properties.[10, 11] These properties suggest enormous potential applications for metal nanoparticles as adsorbents, biological stains, elements of novel nanoscale optical, electronic, and magnetic devices, and especially novel high-efficiency chemical catalysts.[12–16] These distinct properties may be attributed to the quantum confinement phenomena derived from the change in the density and effective bandgap of the electronic energy level as well as a high ratio of surface to bulk atoms.[5] Therefore, many of these proposed applications will require well dispersed nanoparticles. A metal nanoparticle, whether it is in a dispersion or isolated, bears a Fermi level in between the valence and conduction bands. Therefore, the Fermi level is located in

the bandgap region.[17] The probability of the occupation of an energy level is based on the Fermi function. A measure of the energy of the least tightly held electrons within a solid is named for Enrico Fermi, the physicist who first proposed it. It is important in determining the electrical and thermal properties of solids.[18] The value of the Fermi level at absolute zero (-273.15 °C) is called the Fermi energy and is a constant for each solid.[19] The Fermi level changes as the solid is warmed and as electrons are added to or withdrawn from the solid. It is normally said that in semiconductors the Fermi level is half-way between the valence and the conduction band.[20–22] It is worth mentioning that a nucleophile shifts the Fermi level toward the conduction band in a metal nanoparticle. Thus, a nucleophile makes a metal nanoparticle prone to oxidation. Even polymers and ligands can cause a shift of the Fermi level and they must have a bearing on the property of metal nanoparticles. This can easily be demonstrated when coinage metal nanoparticles (Cu, Ag, and Au) are considered, as they have rich plasmon absorption in the visible range.

Among all the metal/polymer composites, silver composites are found to have important applications in material technologies like optical materials,[22] catalytic systems, antibacterial materials, chemical nanosensors, and surface-enhanced Raman scattering (SERS).[23, 24] Gold, being noble, finds application in the biomedical field.[25]

Interestingly, variation of nanoparticle size and shape has strong control over the catalytic activity of the desired catalyst nanoparticle.[26] For application in optoelectronics and electronics, there must be a strong control over particle size and the particles uniform distribution. Unfortunately, the problem of agglomeration often exists when these metal nanoparticles are used during practical operations.[27–29] To overcome this problem of agglomeration, catalytic nanoparticles have been immobilized on supports[30] (e.g., carbon, metal oxides, and zeolites) or stabilized by capping with ligands ranging from small organic molecules to large polymers, which also facilitates catalyst recycling. Sometimes nanoparticles are prepared in various micellar media, which may be cationic, anionic, or neutral. However, supported metal nanoparticles highly dispersed in a host material are mainly desired for practical applications. Various submicrospheres, mesoporous silica (such as MCM-41, MCM-48, and SBA-15), and porous AAO films are suitable supports for nanoparticles.[31–34] However, the synthesis of metal nanoparticles well dispersed in porous AAO films has been well explored recently. Porous AAO film has a huge pore density (108–1013 pores/cm^2).[35, 36] Porous membranes are attractive supports for catalysts due to several reasons. Recently, novel systems such as dendrimers, block copolymer nanospheres, and crosslinked lyotropic liquid crystals are employed to encapsulate metal nanoparticles.[37–39] Carbon nanotubes (CNTs) have been used as ideal nanotemplates or space confined nanoreactors for making one-dimensional (1D) nanowires in the past decade.[40–42] Their fascinating structures including well-defined 1D morphology, small diameters, and hollow interior cavities make it possible to govern and direct the growth of nanowires.[43] Carbon nanotubes have high chemical stability, a high length-to-diameter ratio, strong mechanical strength, high activated surface area, and high conductivity and are attractive materials in energy storage devices, such as pseudocapacitors, fuel cells, and secondary batteries.

Recently, integrating CNTs into functional architectures and composites has been an active research field.[44–47]

For low temperatures and applications in an aqueous environment, polymers, dendrimers, microgels, and colloids have been used as carrier systems.[48–57] There are few reports for the synthesis of well-defined gold nanoparticles, which can be generated in spherical polyelectrolyte brushes.[58] The advantages of this method of generating composite particles of a colloidal carrier and metal nanoparticles are at hand. These spherical polyelectrolyte brushes are synthesized by photoemulsion polymerization by which polyelectrolyte chains are grafted from the surface of colloidal poly(styrene) particles.[59–62] There are reports of successive synthesis of Pt, Ag, and Au nanoparticles in brushes which are also applied in various catalytic reactions.[63, 64] Thus, it is very clear that the support for the metal nanoparticles must be inert and act as a good carrier.[65–67]

But there are few reports on the synthesis of metal and metal oxide nanoparticles on solid polystyrene matrix (resin). Recovery of the prepared nanoparticles from the resin support or exploitation of the resin matrix as the preparative template is also an important factor. To offer stability to the nanoparticles, to fabricate a required nanostructure, and to recover the prepared nanoparticle whenever needed, synthesis of metal and metal oxide nanostructure on resin support has recently been looked into. The nucleation and growth of metal and metal oxide nanoparticles generally follow fast kinetics. To tailor the size and shape—a problem indeed—is solved by judicious exploitation of ligand, polymer, and surfactant molecules. All of these have been exploited as stabilizers because of the coordinatively unsaturated surface structures. These stabilizer molecules act as capping agent. Sometimes these capping agents pose a difficulty not only for characterizations of the particles but also because they deactivate the surface. As a result, catalysis and spectroscopic studies involving metal and metal oxide particles become complicated. To eradicate the complication, functionalized polystyrene resin moieties rejuvenate the stabilization, catalytic function, and spectroscopic application of metal and metal oxide nanoparticles in a straightforward way.

2.2. ION EXCHANGE RESIN

Ion exchange resin or ion exchange polymer is a matrix normally insoluble and in the form of small beads having diameters of 0.5–1.0 mm, fabricated from organic substrates. The material has highly developed structure of pores on the surface and the framework contains some active sites.[68] There are many different types of ion exchange resins that are fabricated to selectively prefer one or several different types of ions. Active sites of ion exchange resins are generally charged with different ions; for example, cation exchange resins are charged with H^+ or Na^+ and anion exchange resins are charged with Cl^- or OH^-. The trapping of ions takes place only with simultaneous releasing of other ions; thus, the process is called ion exchange.[69] These exchanges take place without any physical alteration to the ion exchange

material. Generally, ion exchange resins are widely used in different separation, purification, and decontamination processes. The most common examples are water softening and water purification. In many cases, ion exchange resins were introduced in such processes as a more flexible alternative to the use of natural or artificial zeolites. Synthetic ion exchange materials based on coal and phenolic resins were first introduced for industrial purposes during the 1930s. A few years later, resins consisting of polystyrene with sulfonate groups to form cation exchangers or amine groups to form anion exchangers were developed. These two kinds of resin are still the most commonly used resins today.[70] The affinity of sulfonic acid resins for cations varies with the ionic size and charge of the cation. Generally, the affinity is greatest for large ions with high valency.

Keeping this background in mind and being provoked by the selective exchangeability of various cations on the resin surface, there are various methods developed for the synthesis of metal and metal oxide nanoparticles on the resin. Generally, in the solution phase with very short interparticle distances, the van der Waals forces will attract two metallic particles to each other. These forces vary inversely as the sixth power of the distance between their surfaces. In the absence of any repulsive forces opposed to the van der Waals forces, the colloidal metal particles will aggregate. Consequently, the use of a stabilizing agent able to induce a repulsive force opposed to the van der Waals forces is necessary to provide stable nanoparticles in solution. In the present context, when metal ions are exchanged on the resin and after the synthesis of nanoparticles there is no need for stabilization of the prepared nanoparticles as the distance between each two nanoparticles is quite higher than that of the van der Waals distance. Another major factor is that the nanoparticle prepared on a resin surface loses its mobility due to the presence of the solid support. So, from the literature, we know that resin is being explored as a new and revolutionary material in the synthesis of metal and metal oxide nanoparticles.

The major advantages of the process are its simplicity and its ability to control the purity and homogeneity of the final material on a molecular level.

2.3. STRUCTURES OF ION EXCHANGE RESINS

A widely used cation exchange resin is that obtained by the copolymerization of styrene and a small proportion of divinylbenzene , followed by sulfonation (Scheme 2.1). We may define a cation exchange resin as a high molecular weight crosslinked polymer containing sulfonic, carboxylic, and phenolic groups as an integral part of the resin and equivalent amount of cations.
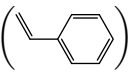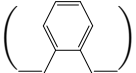
An anion exchange resin is a polymer containing amine (quaternary ammonium) groups as an integral part of the polymer lattice and an equivalent amount of anions such as chloride, hydroxide, and sulfate ions.
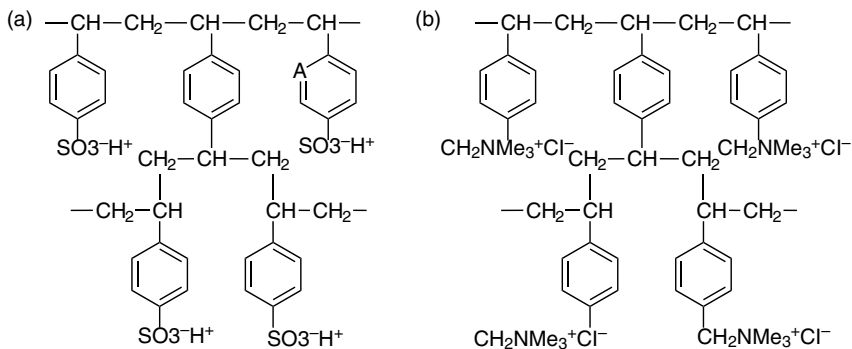
Scheme 2.1. Structures of ion exchange resin: (a) cation and (b) anion.

2.4. SYNTHESIS OF METAL NANOPARTICLES ON A RESIN SURFACE

Dispersions of metallic nanoparticles can be obtained by two main methods: (i) mechanic subdivision of metallic aggregates (physical method) or (ii) nucleation and growth of metallic atoms (chemical method). The physical method yields dispersions where the particle size distribution is very broad. Traditional colloids are typically larger (>10 nm) and not reproducibly prepared, giving irreproducible catalytic activity.[71] Chemical methods such as the reduction of metal salts is the most convenient way to control the size of the particles. Today, the key goal in the metal colloid area is the development of reproducible nanoparticle (or modern nanocluster) syntheses in opposition to traditional colloids. As previously reported, nanoclusters should be or have at least (i) specific size (1–10 nm), (ii) well-defined surface composition, (iii) reproducible synthesis and properties, and (iv) be isolable and redissolvable ("bottleable").[72]

The reduction of metal salts in solution is the most widely used method to generate colloidal suspensions of metals. In fact, this method is generally very simple to put into operation. A wide range of reducing agents have been used to obtain colloidal materials—such as hydrogen, carbon monoxide, hydrides, or other salts such as sodium borohydride or sodium citrate, or even oxidable solvents such as alcohols and ascorbic acid.[73–80] Surfactants are generally used as stabilizers of aqueous colloidal suspensions of metal nanoparticles. Several authors applied the reduction of metal salts to the preparation of colloidal suspensions of metal in organic media.[81] $NaBH_4$ reduction is used to obtain Au, Ag, Pt, Pd, or Cu nanoparticles stabilized by dendrimers (polyamidoamine or PAMAM).[82–87] From the literature we know that Möller and Antonietti described the preparation of Au, Pd, Ag, or Rh nanoparticles stabilized by block copolymers such as polystyrene-*b*-polyvinylpyridine, polystyrene-*b*-poly-*m*-vinyltriphenylphosphine, or poly(ethylene oxide)-polyethyleneimine. Several polymer-stabilized systems have high thermal stability and can be used under drastic conditions.[88–94] Other than simple chemical reduction, there are many methods that have been successfully developed for the synthesis of metal

nanoparticles including thermal, photochemical, and sonochemical decomposition, photolysis or radiolysis, ultrasonic reduction, and reduction by electrochemical methods.[95–99] But as scientists are eager to prepare nanoparticles having a narrow size distribution and good morphology, methods must be reproducible. Synthesis of metal nanoparticles on a resin surface having a charge on it can serve all theses purpose satisfactorily. There are a few reports on the synthesis of mono- and bimetallic nanoparticles on a resin surface and in some cases isolation of the nanoparticles form the resin surface becomes easy. Synthesis of silver nano- particles on the cationic as well as anionic exchange resin surface is easily achieved following a simple complexation protocol. Similarly, Ni, Au, and various bimetallic nanoparticles have successfully been obtained on a resin surface. A layer-by-layer deposition technique in some cases helps the formation of core–shell bimetallic structures.

2.5. MONOMETALLIC NANOPARTICLES ON CATION EXCHANGE RESIN

The literature describes the synthesis of monometallic nanoparticles on a resin surface being carried out by taking metal ion solution or some cationic metal complex ion. First, charged cation exchange resins are immobilized with the cationic metallic solution or with the cationic complex solution. Then the metal ion charged resin beads are reduced using various reducing agents.

2.5.1. Silver Nanoparticles

According to Nath et al.[100] for the synthesis of silver nanoparticles on a resin surface, first Ag(I) was taken as the silver amine complex and then the complex was immobilized on the charged cation exchange resins. After that, the resin beads were heated for the formation of Ag_2O on the resin surface and then treated with sodium borohydride solution for the reduction process (Scheme 2.2).
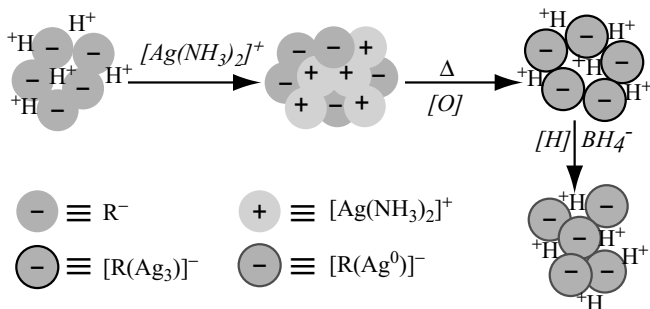
Scheme 2.2. Schematic representation for the synthesis of silver nanoparticles on the cation exchange resin.

The mechanism for the synthesis of silver nanoparticles on a resin surface is as follows:

$$Ag^+ + 2NH_3 \rightarrow \left[Ag(NH_3)_2\right]^+$$

$$R^- H^+ + \left[Ag(NH_3)_2\right]^+ \rightarrow \left[R - Ag(NH_3)_2\right] + H^+$$

$$\left[R - Ag(NH_3)_2\right] \xrightarrow[[O]]{\Delta} [R(Ag_2O)]^- H^+ + 2NH_3$$

$$[R(Ag_2O)]^- H^+ \xrightarrow{[H]} \left[R(Ag^2)\right]^- H^+$$
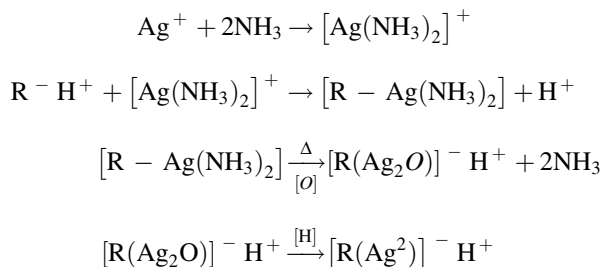
2.5.2. Nickel Nanoparticles

According to Sarkar et al.,[101] Ni nanoparticles (Figure 2.1) can easily be synthesized on a resin surface and the prepared nanoparticle can also be striped off the resin surface (Scheme 2.3). For the synthesis of Ni(0) nanoparticles on a resin surface, NiCl$_2$ solution (25 mL of 0.05 M) was taken as the precursor of Ni(II), and first this was allowed to exchange with the H$^+$ ion of the cation exchange resin in portions, that is, in small aliquots (5 mL), for complete immobilization. After each step, the colorless supernatant indicates the ready exchange of Ni^{2+} with H$^+$. A gradual change in color of the resin beads from pale yellow to Kelly green substantiates the completion of the binding process of Ni^{2+}. The Ni^{2+}-immobilized resin beads were further washed with plenty of water to drain out the liberated HCl and unexchanged NiCl$_2$. Then ice-cold aqueous solution of borohydride was introduced into the wet resin beads under aerobic conditions, which results in the reduction of Ni^{2+} to Ni(0)
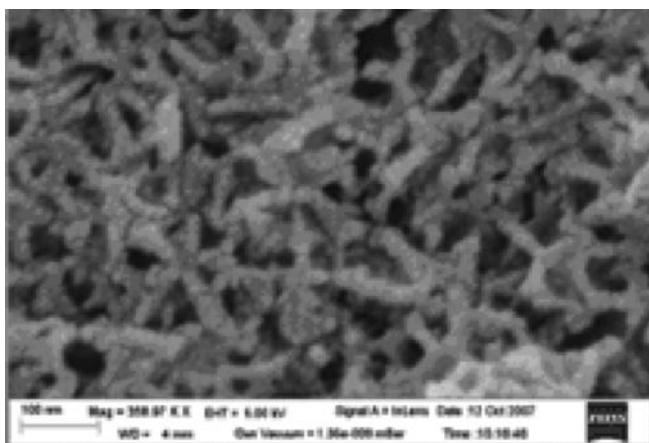
Figure 2.1. SEM image of Ni nanoparticle.
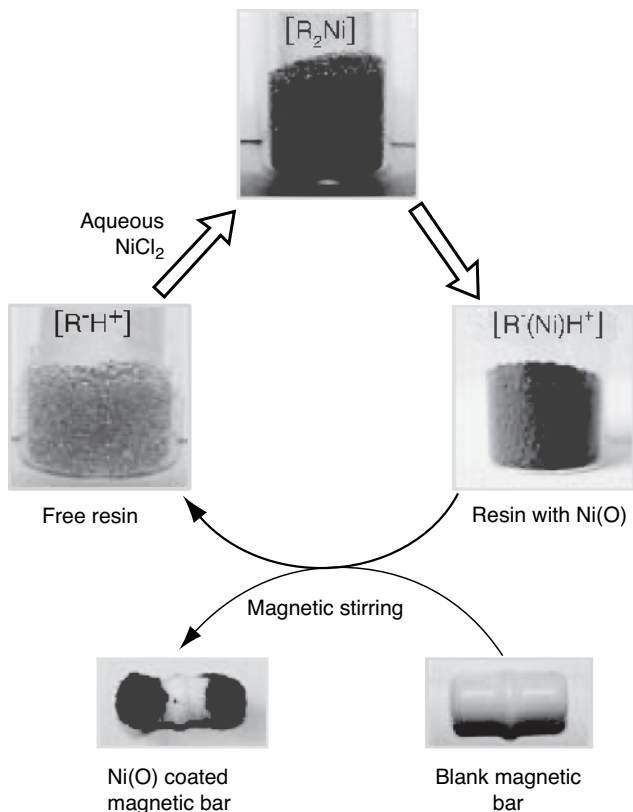
Scheme 2.3. Schematic representation of the synthesis of Ni nanoparticles on the resin surface and also isolation of the nanoparticles from the resin surface.

and their subsequent deposition on the polystyrene beads. After completion of the reduction process, the black nickel-coated beads, $[R(Ni)]^- H^+$, were washed thoroughly with water and dried under vacuum.

To strip out the prepared magnetic nanoparticles from the resin surface, the as-prepared Ni(0)-coated dried beads were then put into CH_3CN and stirred magnetically for ∼1 h. The key strategy for the protocol described here is the introduction of a PTFE-coated magnetic bar. This leads to the trouble-free and efficient separation of the magnetic nanoparticles from the resin matrix onto the bar, leaving separated the metal-free resin beads. Finally, the product was isolated from the bar mechanically, washed several times with water and ethanol, and dried in vacuum. Ni nanoparticles were obtained in batches as long as the resin beads remained loaded with Ni(0). However, the quantity of Ni(0) nanoparticles successively decreased in amount. The exposed resin beads were repetitively used for the gram level synthesis of Ni nanoparticles.

2.6. MONOMETALLIC NANOPARTICLES ON ANION EXCHANGE RESIN

2.6.1. Silver Nanoparticles

From the report of Jana et al.,[102] resin-bound silver nanocomposites (Figure 2.2) were synthesized by a two-step procedure, making the Ag as a negatively charged complex. At first, a few drops of dilute HCl (1 M) solution were added to the stirred freshly prepared aqueous solution of silver nitrate for the preparation of $AgCl_2$, which was washed thoroughly for the removal of HNO_3. The silver precursor $[AgCl_2]^-$ complex was prepared by dissolving 0.3 g of solid AgCl in concentrated HCl solution and placing the mixture in an ultrasonic bath for dissolution. Next, the silver precursor ions were allowed to exchange with Cl^- ions of the neat chloride form of anion exchange resin beads (R^+Cl^-) and the mixture was kept overnight. The resin beads, on which silver precursor ions were immobilized, were washed several times with water to drain out the liberated HCl and unexchanged $[AgCl_2]^-$ and then reduced with a freshly prepared ice-cold aqueous solution of sodium borohydride.

The reduction of the attached silver precursor ions leads to silver nuclei and nanoparticle deposition onto the polystyrene beads (Scheme 2.4). The as-prepared shining reddish-black, silver-coated beads, $[R(Ag)^0]^+Cl,^-$ were washed thoroughly with distilled water and dried at room temperature under vacuum. The mechanism of the above synthetic procedure is represented well.

2.6.2. Gold Nanoparticles

According to Praharaj et al.,[103] the immobilization of gold nanoparticles (Figure 2.3) in anion exchange resin and their quantitative retrieval by means of a cationic

50 nm
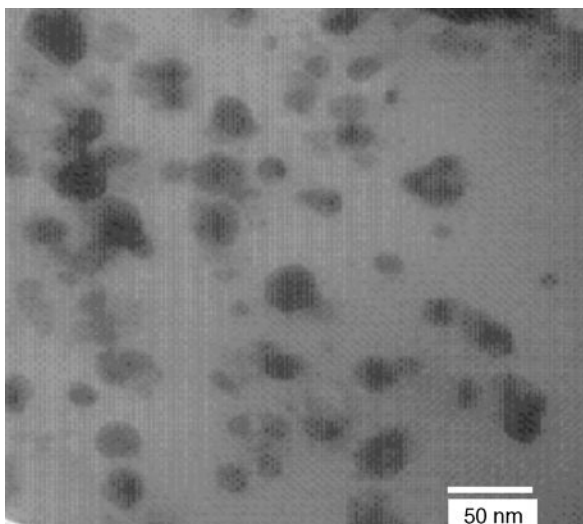
Figure 2.2. TEM image of the silver nanoparticle.
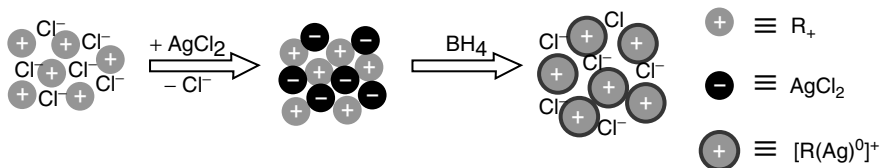
Scheme 2.4. Schematic representation of the synthesis of silver nanoparticles on anion exchange resin.

surfactant, cetylpyridinium chloride, have been studied (Scheme 2.5). First, gold nanoparticles were prepared by the well-known Frens method. A 50 mL aqueous solution of $HAuCl_4$ (0.25 mmol dm-3) was heated to boiling, and trisodium citrate (650 µL, 1% by weight) was added to it with continuous stirring. Within 25 s of boiling, the solution turned faint blue. After 70 s, the blue color suddenly changed to red, indicating formation of gold nanoparticles. For completion of the reaction, the reaction mixture was then boiled for 30 min. Finally, the formed gold colloid showed an intense absorption band with a maximum at 531 nm. This gold solution is now ready to exchange on anion exchange resin. For the activation of the anion exchange resin, 5 g of resin was first treated with NaCl (2 mol/dm^3) solution for 2 h. The excess NaCl was removed by washing with water, and finally the resin became activated in the chloride form. Then 15 mL of 0.25 mmol/dm^3 gold was immobilized in an anion exchange resin column (10 cm length and 1.5 cm diameter) loaded with 5 g of the resin, and the flow rate of the citrate-capped Au solution was 2 mL/min. A gradual change in color of the resin bead from yellow to black substantiates the binding process. The resin in the column was further washed with plenty of water to
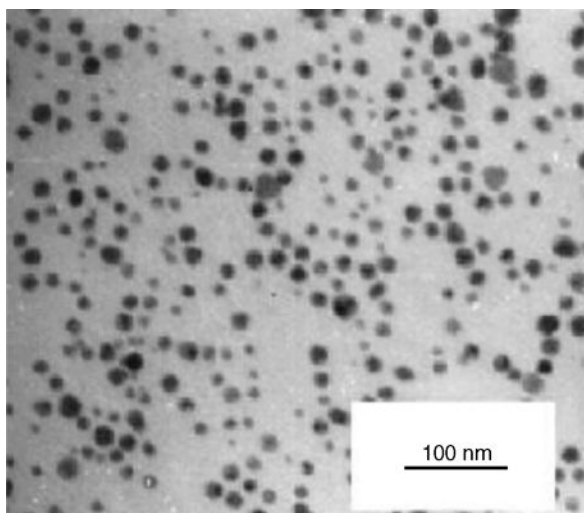
Figure 2.3. TEM image of gold nanoparticle.
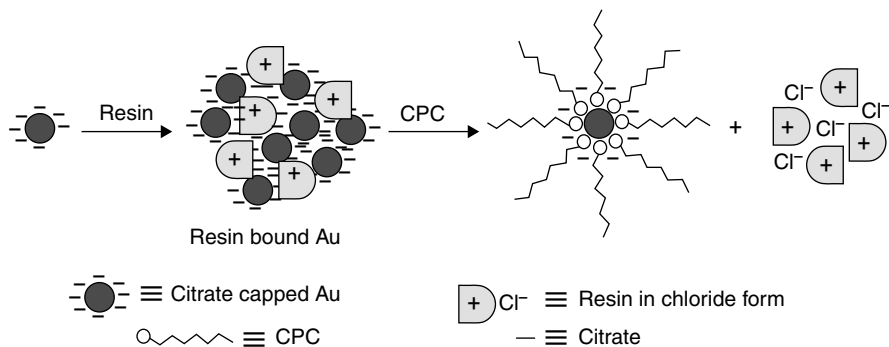
Scheme 2.5. Schematic representation of the immobilization of anionic charge gold nanoparticles on the resin and also extraction of gold nanoparticles as cationic charge.

remove unbound gold nanoparticles between the beads. For the recovery of the metallic nanoparticles from the resin beads, the resin-bound gold NPs were transferred to a beaker and 30 mL of aqueous CPC (50 mmol/dm^3) was added in portions of 5 mL at the respective stages. The solution above the resin became pink instantaneously and showed an absorption maximum at 533 nm, indicating the regeneration of gold NPs. Finally, free resin beads were set free, ready for another exchange process. So, from this experiment, versatility of the resin was also confirmed: resins are not only used as a growth controlling agent or stabilizers and can act as such agents so that we can successfully change the surface charge of the metal nanoparticle.

2.7. APPLICATION OF METAL NANOPARTICLES SYNTHESIZED ON RESIN MATRIX

Nanosized metal and semiconductor particles possess unique electronic, optical, and catalytic properties that are obviously different from bulk macrocrystallites. In particular, fabrication of metal-coated polymer particles is currently an attractive area of investigation because of their applications in the fields of surface enhanced Raman scattering and catalysis or their potential uses in optoelectronic devices and ultrasensitive chemical and biological sensors. Gold nanoparticles, in particular, are interesting because bulk gold is frequently an inactive catalyst due to its filled d orbitals, whereas supported gold nanoparticles readily catalyze CO oxidation, olefin hydrogenation, and several other reactions.[104–108]

2.8. CATALYSIS

A catalyst must be a nanoscale material and catalysis is a nanoscale phenomenon. During the 20th century, chemists made considerable achievements in

heterogeneous catalysis, whereas homogeneous catalysis progressed after the Second World War (hydroformylation) and especially since the early 1970s (hydrogenation).[109] Heterogeneous catalysis that benefits from easy removal of catalyst materials and possible use of high temperatures suffered for a long time from lack of selectivity and understanding of the mechanistic aspects that are indispensable for parameter improvements.[110, 111] Homogeneous catalysis is very efficient and selective and is used in a few industrial processes, but it suffers from the difficulty of removal of the catalyst from the reaction media, its recyclabilty, and limited thermal stability. Metal catalysts immobilized on supports can easily be separated from the reaction mixture for reuse, while homogeneous catalysts with uniform active species structure that gives high activity and selectivity are difficult to recover. The use of unprotected, bare nanoparticles as homogeneous and heterogeneous catalysts, respectively, is extensively described in the literature. In particular, supported metal particles are traditionally applied in industrial catalysis for many purposes. The catalytic behavior of bare particles on supports has been studied as a function of size and shape in a huge number of papers in the course of the last few decades. The study of gold nanoparticles (Au NPs) has attracted much attention because of their fascinating size-related electronic, optical, magnetic, and catalytic properties and many applications in biology and catalysis.[112–118] The discovery in the 1980s that supported nanoparticles of gold could act as catalysts for reactions at low temperatures has to be one of the most fascinating recent observations in chemistry, because before this observation most researchers considered that gold was an unreactive metal. Because gold is such a stable element in the presence of air, it is really surprising that it can be a highly effective oxidation catalyst.[119] In the 1980s, there were two significant observations that completely changed this perception and highlighted the special attributes of gold as a heterogeneous catalyst: (i) the discovery that supported Au catalysts are very active for low-temperature CO oxidation; and (ii) the prediction that Au would be the best catalyst for ethyne hydrochlorination. Silver catalysts have become increasingly important in the oxidation of olefins for the synthesis of industrially interesting products such as epoxides and aldehyde.[120–122]

Transition metal clusters stabilized by polymers offer an ideal platform to study the size dependence of catalysis because surface passivation by polymers allows reactants to access the cluster surface for catalysis and the cluster size can be synthetically controlled.[123–125] Au nanoparticles (Au NPs) deposited on reducible metal oxides, such as TiO_2, Fe_2O_3, and Co_3O_4, show a high degree of activity for CO oxidation because the support or gold–support interface can activate the O_2 molecules.[126–128] In a series of publications, Tsukuda and co-workers have demonstrated that poly(N-vinyl-2-pyrrolidone) (PVP)-stabilized gold clusters in water can catalyze a variety of aerobic oxidations under mild conditions: the homocoupling of aryl-boronic acids, H_2O_2 formation from ammonium formate, and the oxidation of alcohols.[129–134] The catalytic activities of the platinum clusters supported on the chelate resin–metal complexes are examined during the hydrogenation of olefins and diene, as affected by the metal ions complexed with the chelate resin and by the surface area of the support.[135] On the other hand, bimetallic catalysts have become

the subject of intensive efforts both in academia and industry, the special properties of which are derived from an electronic ligand effect and a structural ensemble effect. These bimetallic alloy powders have provided the first example of Cu-based catalysts with high activity, selectivity, and stability against air for the selective hydration of acrylonitrile to acrylamide while Cu catalysts used for the hydration are usually air sensitive.[136]

2.8.1. Catalytic Reduction Reaction

Anthranilic acid is a commercially important intermediate for the synthesis of different dyes, perfumes, and medicinal substances such as anticancer agents.[137] Up to now, several groups have devoted their efforts to synthesize it. In 1957, Lesiak and Schittek synthesized anthranilic acid from o-nitroethylbenzene.[138] Jan Bakke et al.[139] prepared it from o-nitrotoluene. With the help of the Ullman reaction, Cook also synthesized it. Srinivasan, in 1957, described the synthesis of anthranilic acid from Shikimic acid-5-phosphate and L-glutamine.[140] Jana et al.[102] explored for the first time a facile approach for the catalytic reduction of o-nitrobenzoic acid (o-NBA) to anthranilic acid (o-aminobenzoic acid) over a resin-bound silver nanocomposite as catalyst in the presence of sodium borohydride.

According to Jana et al.,[102] the catalytic reaction was carried out in a standard quartz cuvette of 1 cm path length, 2.5 mg of solid catalyst was taken along with an aqueous solution of o-NBA (0.1 mM), and the volume of the solution was made up to 2 mL with water. Next, 0.2 mL of 0.1 M aqueous $NaBH_4$ solution was added to the reaction mixture, and time-dependent absorption spectra were recorded using a UV–visible spectrophotometer at 27 ± 2 °C.

Anthranilic acid has been synthesized by catalytic reduction of o-NBA over resin-bound silver nanocomposites, and the progress of the catalytic reaction was studied spectrophotometrically. Figure 2.4 shows typical UV–visible absorption spectra for the successive reduction of o-NBA by the catalyst particles. An aqueous solution of o-NBA shows a distinct spectral profile with an absorption maximum at 267 nm as shown by trace a (Figure 2.4). Upon the addition of a freshly prepared ice-cold aqueous solution of $NaBH_4$ to this solution, there was no shift of the λ_{max} value at all; only a slight decrease in the absorbance value was noted, and the peak position remained unaltered for a couple of days in the absence of any catalyst particle. After the addition and proper mixing of 2.5 mg of the resin-bound silver nanocomposite in the reaction mixture, it was observed that the peak at 267 nm gradually red-shifted and finally moved to 307 nm as shown by trace f (Figure 2.4). Thus, progress of the reaction is visualized from the red shifting of the peak from 267 to 307 nm and is due to the continuous increase in concentration of anthranilic acid.

2.8.2. Reduction of 4-Nitrophenol

Jana et al.[141] have successfully synthesized Ag nanoparticles on the anion exchange resin surface and exploited those nanoparticles as a solid phase catalyst for the
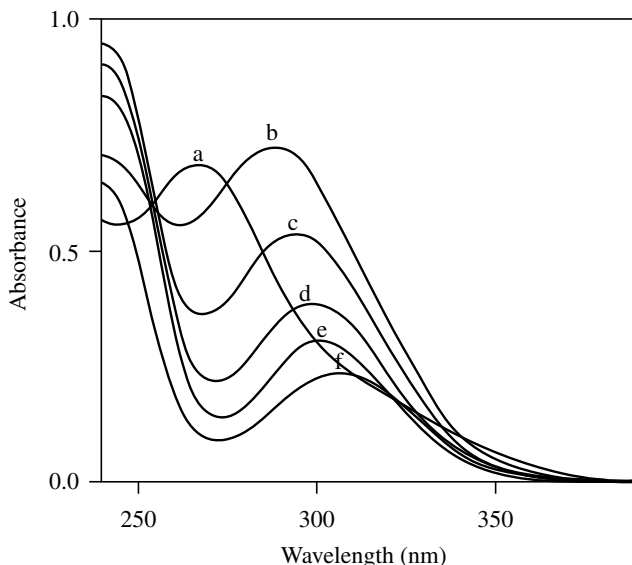
Figure 2.4. UV–visible spectra of (a) *o*-NBA and (b–f) successive reduction of *o*-NBA catalyzed by Ag nanoparticle.

reduction of 4-nitrophenol in the presence of sodium borohydride. In a typical reaction, 0.0015 g solid catalyst was taken along with an aqueous solution of 4-nitrophenol (0.1 mM) in a 1 cm quartz cuvette and the volume of the solution was made up to 3 mL. Next, 0.3 mL of 0.1 M aqueous NaBH$_4$ solution was added to the reaction mixture and time-dependent absorption spectra were recorded in the UV–visible spectrophotometer at 28–30 °C.

An aqueous solution of 4-nitrophenol has a maximum absorption (λ_{max}) at 317 nm, as shown by trace a in Figure 2.5. It has been observed that, after immediate addition of freshly prepared ice-cold aqueous solution of NaBH$_4$, the peak due to 4-NP was red shifted from 317 to 400 nm. This peak was due to the formation of 4-nitrophenolate ions in alkaline conditions caused by the addition of NaBH$_4$. In the absence of any catalyst, the thermodynamically favorable reduction of 4-NP (E^o for 4-NP/4-AP $= -0.76$ V and H$_3$BO$_3$/BH$_4^-$ $= -1.33$ V versus NHE) was not observed and the peak due to 4-nitrophenolate ions at 400 nm remains unaltered even for a couple of days. Addition and proper mixing of 0.0015 g of resin-bound silver nanocomposites to the reaction mixture caused a gradual fading and ultimate bleaching of the yellow color of the solution. This was due to the steady exchange of nitrophenolate ions with the chloride ions present in the catalyst. The reduction could be visualized as the disappearance of the peak at 400 nm with the concomitant appearance of a new peak at 295 nm (traces b–e, Figure 2.5), which substantiates the formation of 4-aminophenol.[142, 143]

According to Praharaj et al.,[103] the resin-bound gold nanoparticles (R-Au) have been used successfully as a solid-phase catalyst for the reduction of 4-nitrophenol by
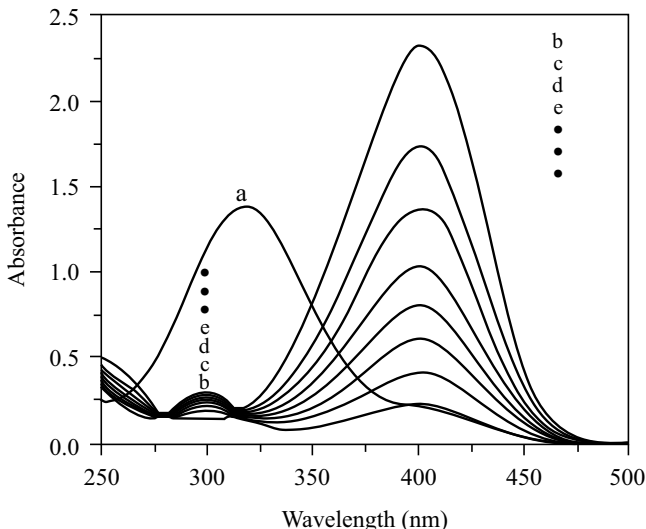
Figure 2.5. UV–visible spectra for (a) 4-NP and (b–e) successive reduction of 4-NP catalyzed by silver nanoparticle-coated resin beads.

sodium borohydride (Scheme 2.6). At the end of the reaction, the solid matrix remains activated and separated from the product. The recycling of catalyst particles after the quantitative reduction of 4-nitrophenol and the recovery of gold nanoparticles with unaffected particle morphology from the resin-bound gold nanoparticle entity have been reported.

To study the catalytic activity of the resin-bound gold nanoparticles, the reduction of 4-nitrophenol with sodium borohydride was chosen as a model reaction. An aqueous solution of 4-nitrophenol shows a distinct spectral profile with an absorption maximum at 317 nm. Now addition of sodium borohydride solution results in the shifting of the peak position to 403 nm (Figure 2.6). This peak was due to the formation of 4-nitrophenolate ions in alkaline conditions caused by the addition of $NaBH_4$. The BH_4^- under the experimental conditions (devoid of catalyst) is incapable of reducing 4-nitrophenol to the corresponding amino compound. Hence, the resin-bound gold entity has been employed as a catalyst for the effective reduction to occur.

2.9. SURFACE ENHANCED RAMAN SCATTERING (SERS)

Over the past decades, surface enhanced Raman scattering (SERS) has became a valuable spectroscopic technique as a powerful surface diagnostic tool. In 1974 Fleischmann, Hendra, and McQuillan performed the first measurement of a surface Raman spectrum from pyridine adsorbed on an electrochemically roughened silver electrode.[144] It has been explained that some vibrational bands of pyridine are selectively enhanced a million times. This increases the sensitivity of

Scheme 2.6. Schematic representation of reduction of 4-NP by the as-synthesized Au nanoparticles.

Figure 2.6. Absorption spectra of the successive adsorption of 4-nitrophenolate ions on the resin-bound gold at an interval of 10 min.

detection of pyridine. Similarly, other analytes may also be detected using silver substrates. Recently, substrates made with transitional metals have been used and have proved to be as efficient as silver substrates in selected cases. The mechanism of enhancement of vibrational peaks is explained on the basis of chemical effect (CE) and electromagnetic (EM) effect relating to the enhancement criterion.

2.9.1. SERS by Ag Nanoparticles

Silver has proved to be the best suited material to fabricate a substrate for surface enhanced Raman scattering (SERS) studies. This is due to the frequency-dependent behavior of its complex dielectric constant, giving rise to intense surface plasmon absorption in the visible wavelength region.[145–147] In this regard, the silver-coated resin beads have been employed as solid phase SERS substrate, whereas crystal violet (CV) was used as a Raman probe, because of the giant Raman cross-sections of the molecules.[148, 149] In Figure 2.7, the surface enhanced Raman scattering spectra are shown where the probe is adsorbed on the surface of the silver-coated resin beads. The HR-SEM image shows the rough surface morphology of the particles. A giant enhancement of the Raman signals of the probe indicates the interaction of it on the rough surface of silver-coated resin beads. The enhancement of the Raman signals of the probe is attributed not only to the rough surface morphology but also to the induced electrostatic interaction. The dye, crystal violet, is adsorbed on the silver shell, due to the electrostatic attraction between the $[R(Ag^0)]^-$ species and CV^+ species. The absence of any SERS out of the probe CV with bulk metallic silver ball Ag(0) (purchased from Aldrich) under the same experimental conditions substantiates the fact.
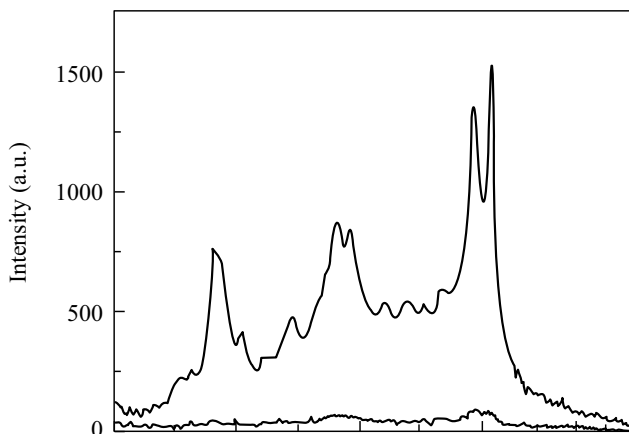
Figure 2.7. Raman spectra of Crystal Violet adsorbed on (a) free resin bead and (b) silver-coated resin bead.
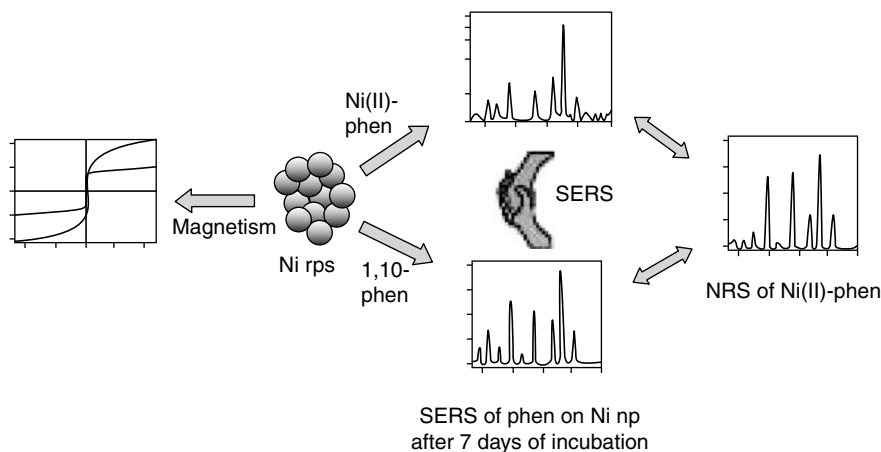
Scheme 2.7. Schematic representation of manifold application of Ni nanoparticles and the investigated SERS phenomena.

2.9.2. SERS by Ni Nanoparticles

A practical virtue of the transition metal nanoparticle, Ni, was expressed from the rich and high-quality vibrational information of a chelating ligand, 1,10-phenanthroline (phen), onto the magnetically separated metal particles.[101] Thus, surface enhanced Raman scattering (SERS) has emerged exclusively from the time-dependent surface complexation of the chemically adhered probe molecule. Finally, the kinetic effect has bestowed Ni(II)-phen chelate, which later on demonstrates unique SERS activity on fcc Ni nanocrystals (Scheme 2.7). The results provide a benchmark illustration of the value of transition metals for aiding interpretation of the vibrational signature of the adsorbate attainable from SERS studies.

2.10. BIMETALLIC NANOPARTICLES ON A RESIN SURFACE

It is always easier to synthesize monometallic nanoparticles. The synthesis of bimetallic core–shell particles always follows a thermodynamic criterion. Looking at the standard reduction potential value, one can easily synthesize Au@Ag bimetallic particles (E). The reverse, Ag@Au synthesis, is difficult to achieve because of thermodynamic considerations. Easily, one would expect to obtain a hollow core-shell structure that means Ag(0) is easily oxidized by Au(III).[150] However, one can achieve success only through the exploitation of a specialized capping agent,[151] which can control the kinetics of the normal oxidation process.

$$Ag(0) + Au(III) \rightarrow Ag(I) + Au(0)$$
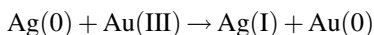
It may not be possible to always find a molecule like β-CD. The simplest solution lies with the application of functionalized resin matrices.

Inorganic nanoshell-coated organic polystyrene beads with well-defined nanostructures are attractive because of their applications in the fields of SERS, catalysis, biochemistry, and chemical sensors. The core–shell type composite materials are in the frontier of advanced research, in which the shell component determines the surface properties and the core component indirectly induces the other properties of the system. Bimetallic nanoshells on functionalized polystyrene beads have been fabricated through a layer-by-layer deposition pathway involving the electrostatic interaction of the polystyrene moiety.

2.10.1. Pd@Au, Cu@Ag, Au@Pd, Pt@Pd, and Au@Ag Bimetallic Nanoparticles

According to Praharaj et al.,[152] the bimetallic coating on functionalized anion exchange resin beads was fabricated by using a synthetic strategy as shown in Scheme 2.8 in a stepwise pathway. For the synthesis of gold–palladium-coated resin beads, 1 g of the anion exchange resin, SERALITE-SRA-400 (in chloride form), was treated with 5 mL of 10^{-2} M $HAuCl_4$ and stirred on a magnetic stirrer for complete exchange of Cl^- ions with $AuCl_4^-$ ions. Within 2 h, the solution above the beads became colorless, indicating the immobilization of the $AuCl_4^-$ ions onto the resin. Afterward, the resin-bound $AuCl_4^-$ moiety, $[R^-AuCl_4]$, was washed with distilled water, dried, and finally reduced by a freshly prepared $NaBH_4$ solution. The product was a gold-nanoshell-coated resin bead, $[R(Au^0)]^+Cl.^-$ A total of 5 mL of a 10^{-2} M aqueous solution of H_2PdCl_4 was added to the preformed $[R(Au^0)]^+Cl,^-$ and the mixture was stirred again on the magnetic stirrer. The solution above the bead became colorless within 2–3 h, indicating the ready exchange of $PdCl_4^{2-}$ with the Cl^- of $[R(Au^0)]^+Cl^-$. The addition of freshly prepared $NaBH_4$ results in a black gold–palladium-coated bead, $[R(Au^0)(Pd^0)]^+Cl.^-$ Anionic precursor $AuCl_4^-$ was exchanged with the Cl^- ion of the resin (R^+Cl^-) through an ion exchange
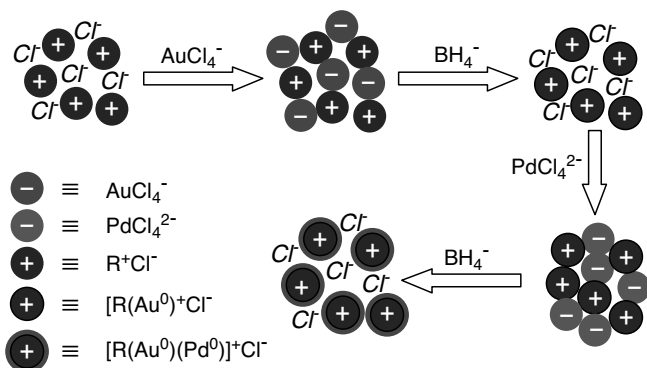
Scheme 2.8. Schematic representation for layer-by-layer bimetallic nanoparticle formation.

mechanism and initiated the synthesis. The anion exchange resin has a positive functional group, $-N(CH_3)_3{}^+$, which can bind $AuCl_4{}^-$ electrostatically to form $[R^-AuCl_4]$. Now upon subsequent reduction, the resin-bound gold chloride moiety was converted to gold-coated resin beads, $[R(Au^0)]^+Cl^-$. To maintain the electroneutrality of the matrix, the Cl^- remained bonded to the positive entity $[R(Au^0)]^+$, which was authenticated from EDX analysis. Now the addition of a $PdCl_4{}^{2-}$ solution to $[R(Au^0)]^+Cl^-$ followed by reduction leads to the formation of a palladium nanoshell on the gold-coated resin beads, represented as $[R(Au^0)(Pd^0)]^+Cl^-$. The following reactions are involved during the synthesis of the particles. The exchange of $PdCl_4{}^{2-}$ was authenticated by adding dilute HCl to the $[R(Au^0)]_2{}^{2+}PdCl_4{}^{2-}$ beads. The colorless HCl solution above the resin bead turned yellow, showing the characteristic absorption band of H_2PdCl_4 at 398 nm. The layer-by-layer deposition of metals on a functionalized cation exchange resin was done by employing the same synthetic protocol. Cationic complexes $[Ag(NH_3)_2]^+$ and $[Cu(NH_3)_4]^{2+}$ were used as silver and copper precursors, respectively, for the fabrication of $[R(Ag^0)(Cu^0)]^-H^+$ particles. The sulfonate functionality $(-SO_3{}^-)$ of the cation exchange resin leads to electrostatic attachment of the cationic precursors. In the case of core–shell bimetallic nanoparticle synthesis, the more noble metal usually forms the core and the less noble one forms the shell. In contrast, the construction of an inverted structure is not easy because the less noble metal is solubilized by a redox reaction upon the addition of more noble metal ions.

The above synthetic strategy leads to easy generation of $[R(Ag^0)(Cu^0)]^-H^+$ and $[R(Au^0)(Pd^0)]^+Cl^-$ nanocomposites with their inverted structures. The order of deposition of the bimetallic shells on the polystyrene beads can be altered by the successive immobilization of their corresponding precursors. Matrixes such as $[R(Pd^0)(Pt^0)]^+Cl^-$ and $[R(Ag^0)(Au^0)]^+Cl^-$ were also synthesized from their corresponding metal chloride precursors. The layer-by-layer deposition technique has been widely used to fabricate core–shell particles because of its convenience to tailor the thickness and composition of the shells. The thickness can be controlled by varying the number of cycles of operation: immobilization and subsequent reduction. In this way, we can deposit more than two metals on any kind of charged polystyrene bead.

2.11. METAL OXIDE NANOPARTICLES

Metal oxide nanoparticles have been widely exploited for use in many different areas, such as photography, catalysis, biological labeling, photonics, optoelectronics, information storage, surface enhanced Raman scattering, and formulation of magnetic ferrofluids.[153–157] The intrinsic properties of a metal oxide nanoparticle are mainly determined by its size, shape, composition, crystallinity, and structure.[158, 159] In principle, one could control any one of these parameters to fine-tune the properties of these nanoparticles. Over the past few decades, the synthesis of inorganic hierarchical nano/microstructures with well-defined morphologies has attracted considerable attention. The structural characteristics of these materials

endow them with a wide range of potential applications.[160] In particular, monodisperse hierarchical nanomicrospheres, which are self-assemblies from building blocks including nanoparticles, nanorods, and nanosheets, are of great interest for scientists because of their novel physical and chemical properties.[161–163] In recent years, many methods have been used to prepare complex hierarchical nanomicrospheres, including hydrothermal methods, wet chemical methods, thermal reduction and the oxidation process, oriented aggregation, self-assembly of building blocks, template-assisted synthesis, and template-free synthesis.[164–168] The use of transition metal oxides as electrode materials for next generation rechargeable lithium ion batteries with both high energy and high power densities has been widely studied because of their high theoretical capacity, high safety, environmental benignity, and low cost. One of the challenging issues in using them for high performance lithium ion batteries is to tackle their poor electronic conductivities. Furthermore, nanoparticles of various shapes have specific faces. Choudary et al.[169] reported that MgO hexagonal crystals exposing the most {100} planes were more active than nanocrystalline samples.

2.12. SYNTHESIS OF METAL OXIDE NANOPARTICLES ON A RESIN SUPPORT

There are various methods developed during the last few years for the successful synthesis of hierarchical metal oxide nanostructure both in solution phase and in solid matrix. Recently, various morphologies of metal oxide materials have been fabricated including nanoparticles, nanoboxes, nanocubes, nanoflowers, nanopetals, nanobundles, nanowires, nanovesicles, nanodisks, and micrometer-scale hierarchical tubular structures. In fact, many methodologies in synthesizing metal oxide nanomaterials have been very well explored and include solventless and solution thermolysis of single-source precursors, sacrificial templating methods, solution phase reactions, the hydrothermal or solvothermal method, ultrasonic and microwave irradiation, template-assisted methods, micelles and microemulsions, electrodeposition, and chemical vapor deposition. Templating is commonly employed for the controlled production of materials with ordered structure having the desired properties. In the past, templates such as aluminum oxide, carbon nanotubes, polymer fibers, and egg-shell membranes have also been employed for the synthesis of metal nanoparticles. A group of scientists have now synthesized metal oxide nanoparticles using the support of the same metal ion.

Synthesis of metal oxide nanoparticles on a resin support is a growing field. In this synthetic protocol, the resin not only gives a standard support for the nucleation and growth of the nanoparticles but also has a clear command on the orientation of the nanoparticles because of the electrostatic field force of the resin. Various metal oxides have been synthesized on a resin surface employing different types of procedures; for example, Cu_2O nanoboxes can easily be synthesized on the resin surface upon reduction of the simple Cu(II) ion on the resin under alkaline conditions, whereas magnetic Fe_3O_4 can be successively prepared by aerial oxidation, alkaline

hydrolysis, and dehydration of $[Fe(bpy)_3]^{2+}$ on a resin surface giving a beautiful wafer structure. In the case of synthesis of a metal oxide nanostructure, a two-step reaction takes place: (i) hydration and (ii) dehydration. If we have control over either of these two steps, we can command the orientation of the growing nanostructure. The resin moiety serves this purpose effectively.

2.13. METAL OXIDE NANOPARTICLES ON AN CATION EXCHANGE RESIN

2.13.1. Synthesis of Cu₂O Nanocubes

According to Pande et al.,[170] Cu_2O nanocubes (Figure 2.8) can be synthesized by a two-step mechanism (Scheme 2.9). In the first step, we prepared the resin-bound Cu(II) composites. The water-soluble Cu(II) precursor, $CuSO_4$ (1 mL of 0.1 M), was allowed to exchange with the H^+ ion of the cation exchange resin (R^-H^+, 0.1 g suspended in 5 mL of water) and stored overnight. The resin beads, on which Cu(II) precursor ions were immobilized, were washed several times with water to drain out the liberated H_2SO_4 and unexchanged $CuSO_4$. The solid Cu(II)-bound resin beads in water remain stable for months. The Cu(II)-bound blue-colored beads were employed for the synthesis of Cu_2O nanoparticles in aqueous phase. In the second step, aqueous solutions of glucose (0.2 g in 5 mL water) and NaOH (250 μL of 1 M) were introduced in succession into a conical flask containing Cu(II)-coated wet resin beads. The pH of the solution was 10–11. The mixture was placed in a water bath (70 °C) for 6–7 min. Slowly, the Cu(II) ions get reduced to the Cu(I) state and enter the solution phase with a brilliant yellow color showing a $\lambda_{max} = 470$ nm. The yellow

Figure 2.8. TEM image of Cu₂O nanocubes.

Scheme 2.9. Schematic representation of the synthesis of Cu_2O nanoboxes on the resin surface and the subsequent extraction from the resin surface.

supernatant solution with Cu_2O (10^{-3} M) nanoparticles remained stable for 12 days, and in turn the resin beads turned iridescent sea-green color.

The green color is presumably due to the formation of a Cu(II)–gluconic acid complex, which remains adsorbed on the resin beads. Separation of the beads from the Cu_2O nanoparticle-containing solution and their subsequent glucose reduction produced a new batch of Cu_2O nanoparticles in solution. Cu_2O nanoparticles were obtained in batches as long as the resin beads remained loaded with Cu(II) ions. However, the number of Cu_2O nanoparticles produced successively decreased in subsequent batches. In the solution phase but in a nitrogen atmosphere, the Cu_2O nanoparticles remained unchanged for many months. The yellowish solution of Cu_2O nanoparticles was centrifuged and washed with distilled water and finally with absolute ethanol to obtain powdered Cu_2O nanoparticles. The product was dried under vacuum, which remained stable over 5 months. Gram level synthesis of Cu_2O nanoparticles was possible employing this synthetic protocol. The percentage yield of Cu_2O nanoparticles was 74.4%. Variable concentrations of glucose (0.1–0.4 g) and NaOH (0.04–0.06 M) were used for the formation of Cu_2O nanoparticles. Scheme 2.10 represents the mechanistic pathway for the formation of Cu_2O nanocubes.

2.13.2. CuO Nanoparticles

Pande et al.[171] successfully synthesized resin-bound spherical CuO nanocomposite (Figure 2.9) following a step-wise manner (Scheme 2.11). In the first step, 1 g fresh cation exchange resin bead (R^-H^+) was suspended in 5 mL of water and kept

Scheme 2.10. Schematic representation of the chemical reaction that occurs on the resin surface at the time of Cu_2O nanobox formation.

Figure 2.9. SEM and TEM images of CuO nanosphere on the resin.

overnight. Then it was thoroughly washed with distilled water and the resin beads were immersed in aqueous 5 mL of 0.1 M $CuSO_4$ solution and allowed to stand again for 12 h. The yellow-colored resin beads turned bluish green. The bluish green $CuSO_4$ immobilized resin beads were then washed thoroughly with distilled water at least 5 times to remove unexchanged $CuSO_4$ and the liberated H_2SO_4. In the second step, β-CD (0.04 g) and NaOH (1 mL 0.1 M) solutions were employed as reducing agents; CuO nanocomposites were produced upon warming the solution to a temperature of ~80–90 °C for ~15–20 min. During heating the resin beads turned black. The mixture was heated for 20 min with occasional stirring to ensure complete conversion of Cu^{2+} ions to CuO nanoparticles. The black beads were then washed thoroughly with distilled water at least 10 times to make the beads free from adsorbed NaOH and β-CD. Similarly, CuO nanocomposites were also obtained using the same quantity of α- or γ-CD from alkaline (NaOH) solution. To make the method cost effective β-CD has been employed.

2.13.3. TiO$_2$ Nanocrystals

According to Sinha et al.,[172] successive syntheses of TiO_2 nanocrystals were achieved on cation exchange resin. Cation exchange resin immobilized titanium peroxo- or titanic sulfate was irradiated by a 100 W bulb separately as in a screw
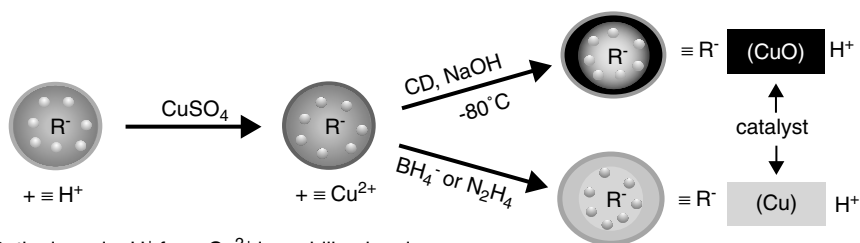
Scheme 2.11. Schematic representation of the synthesis of CuO nanoparticles on the resin surface.
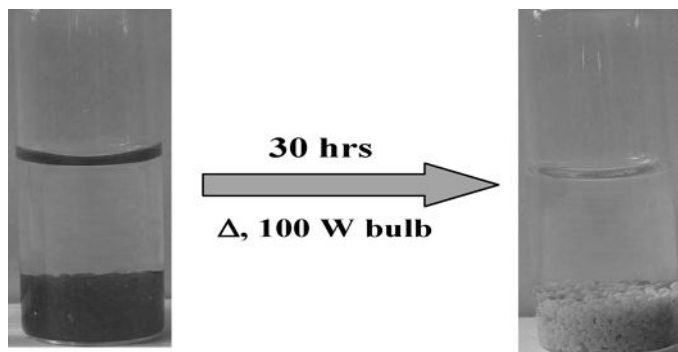
Scheme 2.12. Schematic representation of synthesis of TiO_2 nanostructure on resin.

capped closed reaction vessel in the presence and absence of organic base. The growth controlling organic base was pyridine or triethyl amine. The TiO_2 nanocrystals were also grown on a resin surface. Scheme 2.12 shows that the red color of the titanium peroxo complex immobilized cation exchange resin changed to white upon hydrothermolysis reaction. Hydrothermolysis gives rise to well-defined morphologies of TiO_2 nanocrystals on the resin surface.

The slow 1D growth of TiO_2 nanocrystals from the resin-bound precursor, $[Ti(O_2)(OH)(H_2O)_n]^+$ or Ti(IV), in the absence of any other coexisting ions has been reported. The 1D morphology of the nanocrystal formation takes place in the presence of coexisting ions and is also affected by the reaction rate regardless of the crystal phases.

A high reaction rate results in the production of nonoriented spherical particles with massive precipitates via homogeneous nucleation. In contrast, a relatively low reaction rate predominantly gives rise to heterogeneous nucleation and induces the formation of the highly oriented 1D growth.

However, hydrothermolysis of resin-bound chain-like $[Ti(O_2)(OH)(H_2O)_n]^+$ species promotes exclusively 1D growth along the c axis of the crystals due to ion–dipole interaction. This leads to the formation of petals (Figure 2.10) and rods (Figure 2.12).
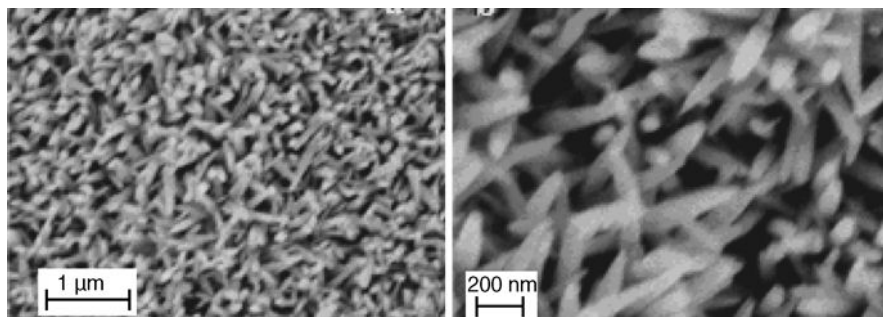
Figure 2.10. Formation of TiO_2 nanopetals on resin surface upon hydrothermolysis of resin-bound $[Ti(O_2)(OH)(H_2O)_n]^+$ in a closed reaction vessel in aqueous medium.
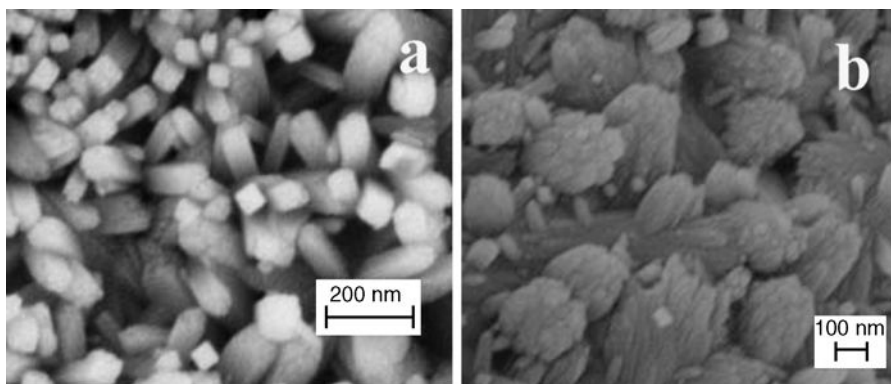
Figure 2.11. Formation of TiO_2 (a) nanopillar and (b) nanobundle on resin surface upon hydrothermolysis of resin-bound Ti(IV) in a closed reaction vessel in the presence and absence of organic base, respectively.

On the other hand, resin-bound Ti(IV) ions presumably attract similar Ti(IV) ionic species, which leaves sidewise growth generating pillars and bundles (Figure 2.11). It is very difficult to explain why the open end of the pillars is rectangular.

In the intermediate stage, some TiO_2 nanocrystals bound to the resin surface would bear positive charge, due to adsorption of $[Ti(O_2)(OH)(H_2O)_n]^+$ or Ti(IV) ions on the surface of the nanocrystals. The overall charge balance is maintained by the negative charge of the resin moiety. However, there still remain residual microscopic charges of TiO_2 nanocrystals. In order to avoid electrostatic repulsion of the residual charge, a structure is formed in which the charged parts can be located as far away as possible from each other.

2.13.4. Fe_3O_4 Nanowafers

According to Basu et al.,[173] porous Fe_3O_4 nanowafers (Figure 2.13) can be successfully prepared by following two reaction methods (Scheme 2.13). In these
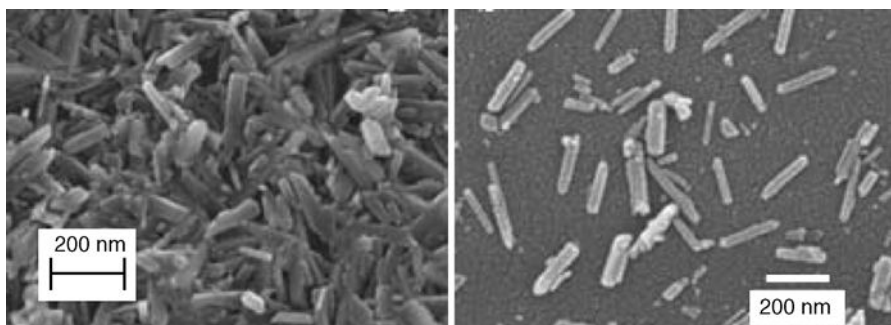
Figure 2.12. Formation of TiO_2 nanorods on resin surface upon hydrothermolysis of resin-bound $[Ti(O_2)(OH)(H_2O)_n]^+$ in a closed reaction vessel in the presence of organic bases.
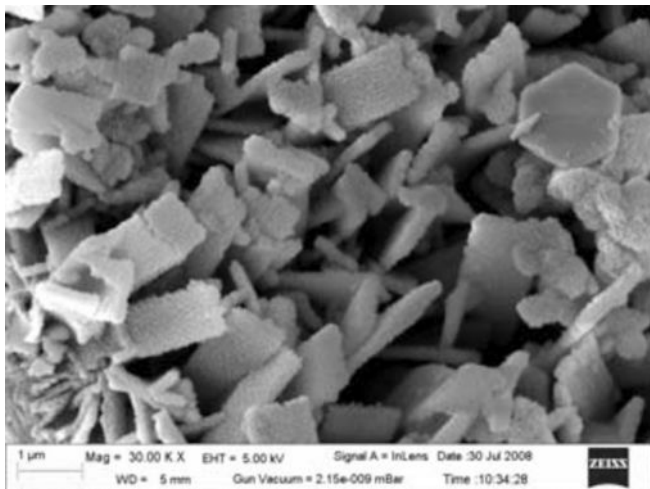
Figure 2.13. SEM image of the Fe_3O_4 nanowafer.

two procedures, the only one difference is that in one case complex formation takes place on the resin support and in the other case the formed complex was immobilized. But this difference in synthetic strategy makes a drastic change on the particle morphology: In method 1, large wafers were prepared, whereas in method 2 spherical wafers were formed. For the preparation of Fe_3O_4 nanostructure, 1 g of cation exchange resin was used in both methods. At first, cation exchange resins were incubated in 0.1 M HCl for 12 h to convert all the resin beads to the H^+ form. The
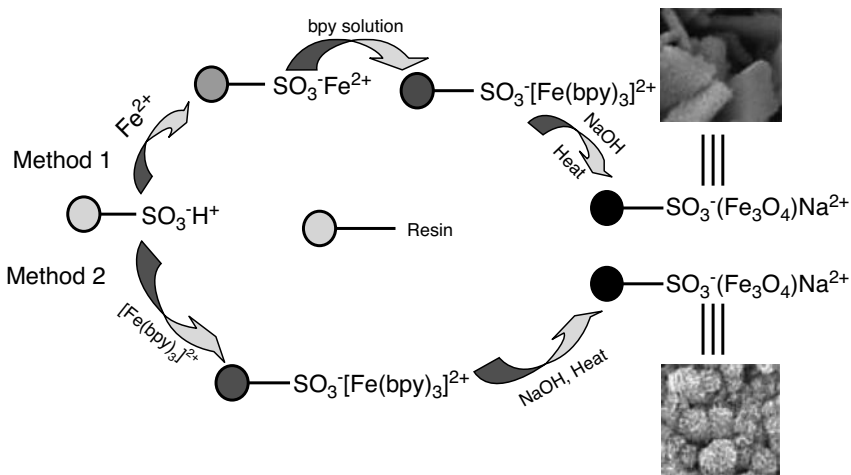
Scheme 2.13. Schematic representation of the formation of Fe_3O_4 nanowafers on the resin surface.

resin beads in the protonated form were washed thoroughly with double distilled water and were reserved for future use. Then 100 mL of 0.1 M NaOH, 100 mL of 0.1 M aqueous solution of ammonium ferrous sulfate, 100 mL of 0.1 M alcoholic solution of 2,2′-bipyridine, and 100 mL of 0.1 M $[Fe(bpy)_3]^{2+}$ were prepared separately.

Method 1. In this method, at first 10 mL of the 0.1 M Fe(II) solution, as ammonium ferrous sulfate, was added to 1 g washed resin beads. The mixture was magnetically stirred for uniform immobilization of Fe(II) ions onto the resin beads. After ∼15 min of stirring, 10 mL of fresh aliquot ammonium ferrous sulfate solution was added and stirred. This procedure was continued for the uptake of maximum amount of Fe(II) ion by the resin matrix, and the resin beads were thoroughly washed with water to remove the unexchanged Fe(II) solution. After that, 30 mL of 0.1 M aqueous alcoholic solution of 2,2′-bipyridine was added to the Fe(II) immobilized resin beads. The addition of 2,2′-bipyridine solution made the resin beads red in color, indicating the formation of the $[Fe(bpy)_3]^{2+}$ complex on the cation exchange resin surface. The red-colored resin beads were washed thoroughly with water and dried in air. Now 0.5 g of the dried resin beads were put into a 15 mL screw capped test tube. The screw capped test tube was partially filled with 5 mL of 0.1 M solution of NaOH and heated under a 100 W bulb at ∼100 °C for the modified hydrothermolysis (MHT) reaction. After 8 h of heat treatment, the red-colored beads became black (Scheme 2.14), bearing the nanowafers, which showed strong magnetic and porous characteristics.

Method 2. In the second method, the washed H^+ forms of the cation exchange resin beads were used and 10 mL of laboratory prepared aqueous $[Fe(bpy)_3]^{2+}$ solution was added and stirred for the immobilization. After complete exchange of the cationic complex with the resin matrix, the beads turned red. Then 0.5 g of the red-colored resin beads were placed in a screw capped test tube and 5 mL of 0.1 M solution of NaOH was added and heated, as was done for the method 1. Here also, the black-colored Fe_3O_4 magnetic nanocomposites were obtained.

0.1 M NaOH 8 hours

100 W bulb

R⁻[Fe(bpy)₃]²⁺   R⁻(Fe₃O₄)Na⁺
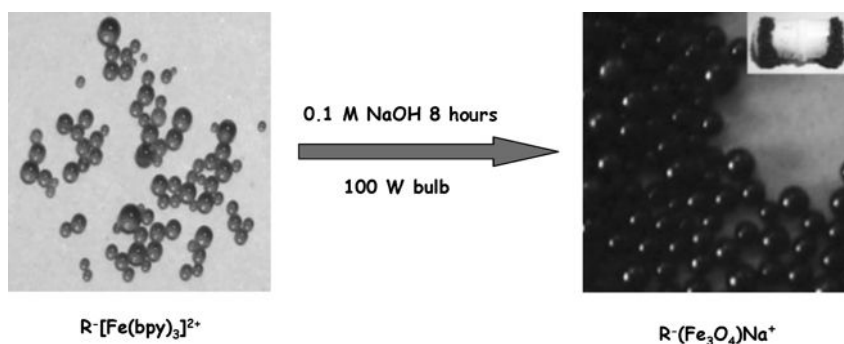
Scheme 2.14. Real-time images of the Fe_3O_4 formation and its magnetic nature.
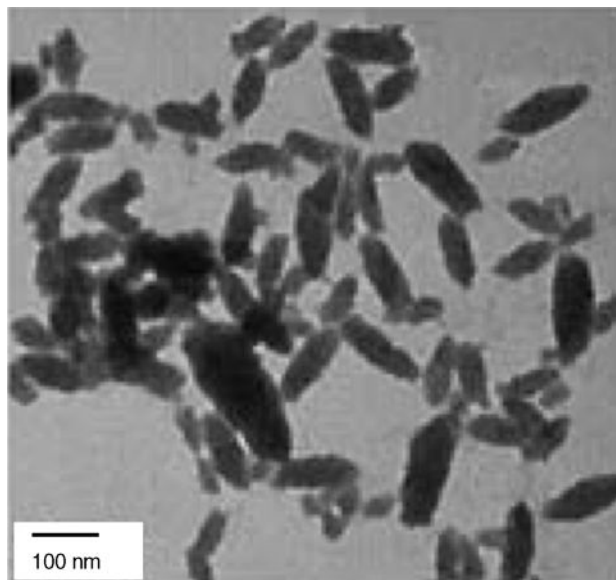
Figure 2.14. TEM image of MnO_2 nanorod.

2.14. METAL OXIDE NANOPARTICLES ON ANION EXCHANGE RESIN

2.14.1. MnO$_2$ Nanorods

Jana et al.[174] showed the synthetic strategy for the deposition of MnO_2 nanorods (Figure 2.14) on a resin surface exploiting an anion exchange resin. First, 0.5 g of the anion exchange resin, $[R^+Cl^-]$, was treated with 25 mL of 1 M aqueous $KMnO_4$ solution and the solution was stirred to complete the exchange of Cl^- ions with MnO_4^- ions. Within 1 h, the purple solution became colorless, indicating ready exchange of MnO_4^- with Cl^-. After that, the resin-bound permanganate moiety $[R^+MnO_4^-]$ was washed several times with distilled water and completely reduced photochemically (24 h, 40 W tungsten lamp, fluence $\sim$50 mJ/cm^2) while stirring in weakly alkaline conditions (0.1 M NaOH). Thus, the reaction of resin-bound precursor ions led to the deposition of MnO_2 nanoparticles on the resin surfaces (Scheme 2.15).
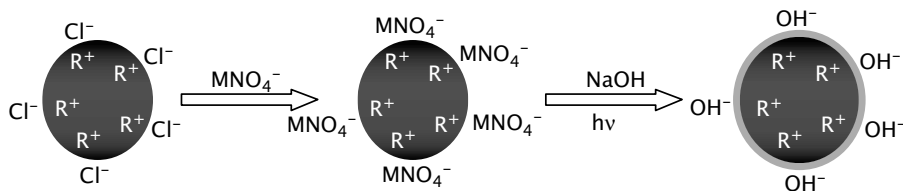
Scheme 2.15. Schematic representation of formation of MnO_2 nanorods on resin.

2.15. APPLICATION OF OXIDE NANOSTRUCTURE SYNTHESIZED ON A RESIN SURFACE

Metallic oxides having different shapes and sizes have received considerable attention because of their theoretical, technological applications in various organic reactions. Catalysts, for example, are mostly nanoscale particles, and catalysis is a nanoscale phenomenon. In the case of various reactions, separation of the catalyst from the reaction mixture is the main problem and loss of product occurs. Nanoparticles prepared on the resin can easily be applied as a heterogeneous catalyst for efficient recovery and recycling of the photocatalyst from liquid-phase reactions.

2.16. CATALYSIS

2.16.1. Mineralization of Dye

Mineralization is a process through which an organic compound is converted into nontoxic CO_2 and H_2O. This conversion may be of various types involving air, electromagnetic radiation, solar irradiation, and bacterial strains. The as-synthesized Fe_3O_4 nanowafer on a cation exchange resin support can show its potential applicability for the mineralization of dye molecules under UV light irradiation conditions.[173] To evaluate the photocatalytic activity of the Fe_3O_4 nanowafer, a potential pollutant RhB solution was used as a representative dye. The degradation of an aqueous solution of RhB was observed in the presence of UV light. Fe_3O_4 photocatalyst (0.01 g) was suspended in 20 mL of an RhB aqueous solution $(1 \times 10^{-5} \, M)$. Then, while stirring, the solution was exposed to UV irradiation $(\lambda_{max} = 365 \, nm)$ at room temperature. The temporal UV–visible spectral changes in the RhB aqueous solution during the photocatalytic degradation reactions are depicted (Figure 2.15) and the kinetics follow the pseudo-first-order reaction.
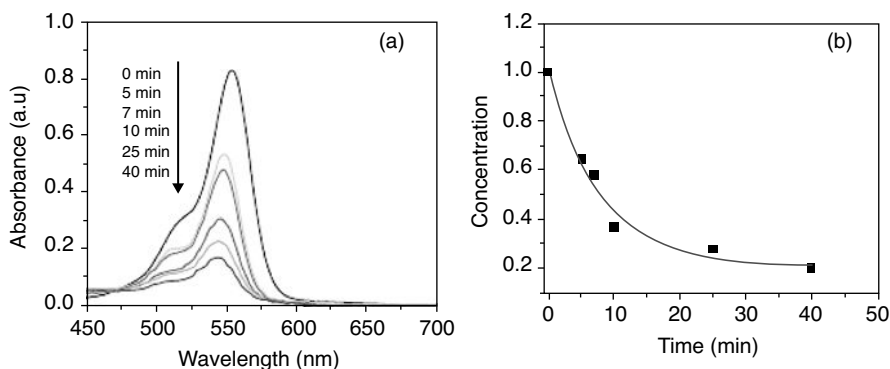
Figure 2.15. Gradual decrease in absorption maxima in of RhB dye catalyzed by Fe_3O_4 in UV light.

2.16.2. Clock Reaction

The "clock reaction," one of the most popular types of chemistry demonstrations, is widely available from innumerable experiments. During the progress of a clock reaction an initial induction period occurs before a significant concentration of one of the chemical species involved is produced. Clock reactions not only provide a crowd-pleasing, visually dramatic reversible color change, but also provide an engaging illustration of redox phenomena, reaction kinetics, and the principles of chemical titration. MB is a water-soluble cationic dye and has a basic dye skeleton of a thiazine group; it is used as an oxidation–reduction indicator in chemistry and biology.[175] It is easily reduced to the colorless hydrogenated molecule leucomethylene blue (LMB), which can, in turn, be oxidized back to its original form. The as-prepared stable Cu_2O nanocubes were applied for a clock reaction involving MB and hydrazine as a reducing agent in aqueous medium (Scheme 2.16).[170] The oxidized and reduced form of MB shows an intense absorption band in the region 200–700 nm.[176, 177] So, by measuring the changes in the specified ($\lambda_{max} = 664$ nm) absorbance maxima by a UV–visible spectrophotometer, the progress of the reaction can be monitored. In this catalytic procedure, an aqueous solution of MB was mixed with Cu_2O nanocubes and hydrazine under ambient conditions. Then the color bleaching of MB starts, and the absorbance of the solution is measured at an interval of 1 min. The pH of the reaction medium was in the alkaline (pH $\sim$ 8) range. With progress of the reaction, a steady decrease of the absorbance of the dye was noted, as shown in Figure 2.16. The blue color of the dye, MB, faded away, producing LMB, indicating the progress of the reduction reaction, and finally a colorless solution results and the kinetics follow the pseudo-first-order reaction.
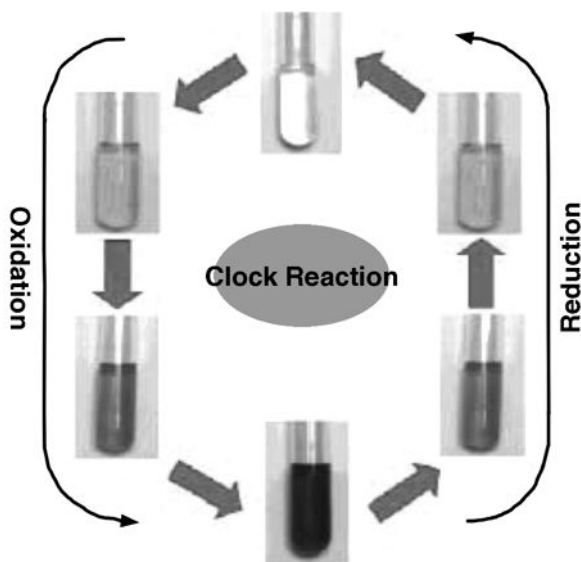
Scheme 2.16. Schematic representation of clock reaction.
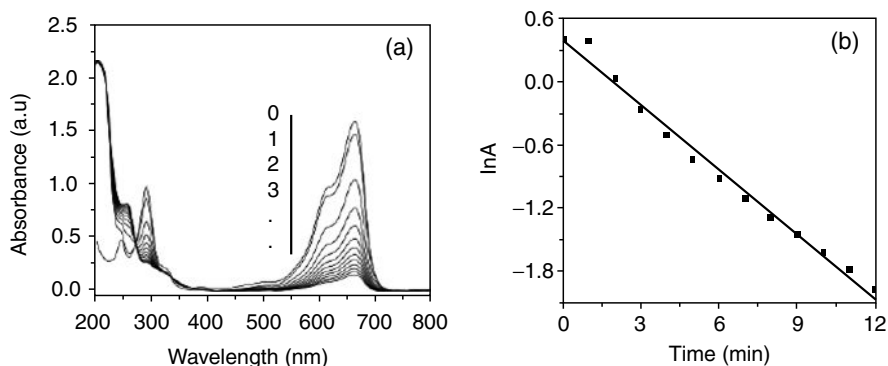
Figure 2.16. (a) Decrease in the UV–visible absorption maxima with continuous time scale from MB to LMB formation; (b) plot of ln A vs. T for the reduction process.

2.16.3. Oxidation Reaction

Resin immobilized, stable, spherical CuO nanoparticles prepared in the presence of cyclodextrins (CDs) and NaOH act as catalysts for liquid phase oxidation of various alcohols in air (Table 2.1).[171] A major interest of this process lies with the preparation of this catalytic material under mild conditions, reusability of the catalyst, and the green chemistry approach for liquid phase alcohol.

2.16.4. Hydrolysis Reaction

Hydrolysis of nitriles to amides (Table 2.2) in the presence of visible light in a weakly basic medium has been carried out to examine the catalytic activity of the MnO_2 nanorods synthesized on the anionic resin surface.[174] From the literature it is confirmed that the hydrolysis of nitriles to amides requires strongly acidic or alkaline conditions and sometimes may be quite drastic. In 1966, during oxidation of alcohols,

TABLE 2.1. A Series of Alcohols Oxidized by CuO Catalyst to Its Corresponding Aldehydes

Reactant	Product	Time (ca. h)	Yield (%)
CH_3-OH	H-CHO	4	95
CH_3-CH_2-OH	CH_3-CHO	4	90
CH_3-$(CH_2)_2$-OH	CH_3-CH_2-CHO	4.5	85
CH_3-$(CH_2)_3$-OH	CH_3-$(CH_2)_2$-CHO	4.5	74
CH_3-$(CH_2)_4$-OH	CH_3-$(CH_2)_3$-CHO	4.5	65
CH_3-$(CH_2)_5$-OH	CH_3-$(CH_2)_4$-CHO	5	20
CH_3-$(CH_2)_7$-OH		5	0
CH_3-$(CH_2)_9$-OH		5	0
C_6H_5-CH_2-OH	C_6H_5-CHO	5	90
P-CH_3O-C_6H_4-CH_2-OH	P-CH_3O-C_6H_4-CHO	4.5	74
P-NO_2-C_6H_4-CH_2-OH	P-NO_2-C_6H_4-CHO	4.5	80

TABLE 2.2. Hydrolysis of Nitriles by R(MnO$_2$)OH Particles at Room Temperature and Pressure

Substrates	Reaction Time (h)	Yield (%) of Corresponding Amide
Acetonitrile	7	71
Propionitrile	6	65
Acrylonitrile	6	82
Benzonitrile	6	74
Benzyl cyanide	10	50
Anthranilonitrile	7	61

Cook and colleagues observed that acetamide was produced under neutral conditions at room temperature, where commercial MnO$_2$ was used as a catalyst. But the reaction time was quite long (80 h) with a 40% yield. In our study, 50 mg of R(MnO$_2$)OH converts acetonitrile (CH$_3$CN) to acetamide (CH$_3$CONH$_2$) within 7 h under weakly basic conditions and gives good yield (71% from 10 mL of neat acetonitrile) without any side product. A wide variety of bases like pyridine, Et$_3$N, (EtOH)$_3$N, and Me$_2$NH were employed for hydrolysis under ambient conditions and they all serve the purpose well. The same reaction strategy happens to be quite successful for the hydrolysis of propionitrile (EtCN), benzonitrile (PhCN), acrylonitrile (H$_2$CCHCN), benzyl cyanide (PhCH$_2$CN), and 0.5 g of anthranilonitrile (Ph(NH$_2$)$^-$ CN); they all serve as good substrates.

2.17. USEFULNESS OF METAL AND METAL OXIDE NANOPARTICLES ON A RESIN MATRIX

Metal nanoparticles with very high positive standard reduction potential (E°) values are easily reduced. These metal particles are said to be noble and there remains a possibility of finding them even in their elemental stage in the Earth's crust. One such example is gold with an E° value of $+1.52$ V. So, the E° value is an index of nobility for metals in particular. The reduction of noble metal ions by the bottom–up approach thus becomes easy, which gives birth to metal nanoparticles if the stabilization of particles takes place at a proper nanostage. On the other hand, metals like Ni and Cu are difficult to reduce. This is a case where resin support can really help their reduction, which is otherwise difficult to achieve. This may be explained by diffusion resistance (DR) and charge transfer resistance (CTR).[178, 179] Again, Ag@Au bimetallic nanoparticle synthesis is easily done on a resin surface and in the absence of resin support this process becomes thermodynamically impossible and leads to Au@Ag bimetallic particles. Another unique feature of resin support has recently been discovered, where it offers a great stability to the synthesized metal and metal oxide nanoparticles when Ni and Fe$_3$O$_4$ are considered.

The main focus of the application of metal and metal oxide nanoparticles encompasses optoelectronic devices, sensor applications, and data storage. However, to a chemist it is the field of catalysis that has greatly been revolutionized by the

judicial application of metal and metal oxide nanoparticles. In this chapter, the size of the metal and metal oxide nanoparticles has been shown to be very important and can easily be controlled on a suitable resin surface. The shape tuning of metal and metal oxide nanoparticles has been authenticated with the advancement of commercially available characterization techniques. Thus, it has been shown that the surface energy of a particular shape of particles facilitates the catalytic pathways. So, shape-dependent catalysis becomes a new dimension in nanoparticle chemistry. Resin support becomes a fascinating solid material to make the catalyst cost effective, eco-friendly, and recyclable, where size and shape tuning become simple, straightforward, and trouble-free.

CONCLUSION

Metal nanoparticles have been shown to be important for catalysis, spectroscopy, optoelectronic devices, and magnetic data storage. Successful exploitation of metallic nanoparticles lies in the successful conjugation of their active surface structure. Thus, size and shape play a role in terms of variable surface energy. This becomes paradoxical when surface activity and stabilization are examined; both surface activity and particle stabilization need to be controlled. Thus, proper support becomes inevitably a unique choice, which simultaneously can promote surface activity and provide stabilization to the metallic nanoparticles for innumerable applications. Proper support stabilizes metal nanoparticles of different sizes and shapes but not at the cost of surface activity. At this time, only a few achievements are promising. In an analogous fashion, metal oxides, generally transition metal oxides, are robust and are the future material of choice for supports.

REFERENCES

1. Faraday, M. *Philos. Trans. R. Soc. London*, **1857**, *147*, 145.
2. Schmid, G.; Bäumle, M.; Geerkens, M.; Heim, I.; Osemann, C.; Sawitowski, T. *Chem. Soc. Rev.*, **1999**, *28*, 179.
3. Burda, C.; Chen, X.; Narayanan, R.; El-Sayed, M. A. *Chem. Rev.*, **2005**, *105*, 1025.
4. Hines, M. A.; Guyot-Sionnest, P. *J. Phys. Chem.*, **1996**, *100*, 486.
5. Alivisatos, A. P. *Science*, **1996**, *271*, 933.
6. Bruchez, M. Jr.; Moronne, M.; Gin, P.; Weiss, S.; Alivisatos, A. P. *Science*, **1998**, *281*, **2013**.
7. Roucoux, A.; Schulz, J.; Patin, H. *Chem. Rev.*, **2002**, *102*, 3757.
8. Willner, I.; Mandler, D. *J. Am. Chem. Soc.*, **1989**, *111*, 1330.
9. Finke, R. G. In: *Metal Nanoparticles: Synthesis, Characterization, and Applications*; Feldheim, D. L.; Foss, C. A., Jr.; Eds. Marcel Dekker, New York, 2002; Chapter 2, pp. 17–54.
10. Volokitin, Y.; Sinzig, J.; de Jong, L. J.; Schmid, G.; Vargaftik, M. N.; Moiseev, I. I. *Nature*, **1996**, *384*, 621.

11. Lewis, L. N. *Chem. Rev.*, **1993**, *93*, 2693.

12. Templeton, A. C.; Wuelfing, W. P.; Murray, R. W. *Acc. Chem. Res.*, **2000**, *33*, 27.

13. Schmid, G.; Bäumle, M.; Geerkens, M.; Heim, I.; Osemann, C.; Sawitowski, T. *Chem. Soc. Rev.*, **1999**, *28*, 179.

14. Rao, C. N. R.; Kulkarni, G. U.; Thomas, P. J.; Edwards, P. P. *Chem. Soc. Rev.*, **2000**, *29*, 27.

15. Jana, N. R.; Sau, T. K.; Pal, T. *J. Phys. Chem. B*, **1999**, *103*, 115

16. Guo, Y. G.; Hu, J. S.; Liang, H. P.; Wan, L. J.; Bai, C. L.; *Chem. Mater.*, **2003**, *15*, 4332.

17. Alivisatos, A. P. *J. Phys. Chem.*, **1996**, *100*, 13226.

18. Batlogg, B. Physical properties of high-Tc superconductors. *Physics Today*, **1991**, *44* (June) 44.

19. Masala, O.; Seshadri, R. *Annu. Rev. Mater. Sci.*, **2004**, *34*, 41.

20. Brown, W. F. Magnetic Materials. In: *Handbook of Chemistry and Physics*. Condon, E. U.; Odishaw, H.; Eds. McGraw-Hill, New York, 1958; Chapter 8.

21. Kittel, C. *Introduction to Solid State Physics*, 7th ed. Wiley, Hoboken, NJ, 1996.

22. Stepanov, A. L.; Popok, V. N.; Khaibullin, I. B.; Kreibig, U. *Nucl. Instrum. Methods Phys. Rev. B*, **2002**, *191*, 473.

23. Sowmitri, T.; Neha, K.; Noureddine, A.; Eric, H.; Joe, F.; Lenore, L. D. *J. Appl. Polym. Sci.*, **2006**, *5*, 2938.

24. Stephan, T. D.; Panittamat, K.; Pranut, P. *Colloids Surf. A*, **2006**, *289*, 105.

25. Daniel, M. C.; Astruc, D. *Chem. Rev.*, **2004**, *104*, 293–346.

26. Burda, C.; Chen, X.; Narayanan, R.; El-Sayed, M. A. *Chem. Rev.*, **2005**, *105*, 1025.

27. Aiken, J. D.; Finke, R. G.; *J. Mol. Catal. A: Chem.*, **1999**, *145*, 1.

28. Aiken, J. D.; Lin, Y.; Finke, R. G. *J. Mol. Catal. A: Chem.*, **1996**, *144*, 29.

29. Hirtzel, C. S.; Rajagopalan, R. *Collidal Phenomena: Advanced Topics*. Noyes, Saddle River, NJ, 1985; pp. 27–39 and 73–87.

30. Mohanraj, V. J.; Chen, Y. *Trop. J. Pharm. Res.*, **2006**, *5*, 561.

31. Pol, V. G.; Gedanken, A.; Calderon, M. *J. Chem. Mater.*, **2003**, *15*, 1111.

32. Wong, M. S.; Cha, J. N.; Choi, K. S.; Deming, T. J.; Stucky, G. D. *Nano Lett.*, **2002**, *2*, 583.

33. Kresge, C.; Leonowicz, M.; Roth, W.; Vartuliand, C.; Beck, J. *Nature*, **1992**, *359*, 710.

34. Zhao, D.; Feng, J.; Huo, Q.; Melosh, N.; Fredrickson, G. H.; Chmelka, B. F.; Stucky, G. D. *Science*, **1998**, *279*, 548.

35. Martin, C. R. *Science*, **1994**, *266*, 1961.

36. Miller, S. A.; Young, V. Y.; Martin, C. R. *J. Am. Chem. Soc.*, **2001**, *123*, 12335.

37. Crooks, R. M.; Zhao, M.; Sun, L.; Chechik, V.; Yeung, L. K. *Acc. Chem. Res.*, **2001**, *34*, 181.

38. Underhill, R. S.; Liu, G. *Chem. Mater.*, **2000**, *12*, 3633.

39. Ding, J. H.; Gin, D. L. *Chem. Mater.*, **2000**, *12*, 22.

40. Iijima, S. *Nature*, **1991**, *354*, 56.

41. Wildoer, J. W. G.; Venema, L. C.; Rinzler, A. G.; Smalley, R. E.; Dekker, C. *Nature*, **1998**, *391*, 59.

42. Odom, T. W.; Huang, J. L.; Kim, P.; Lieber, C. M. *Nature*, **1998**, *391*, 62.

43. Wang, Z.; Zhao, Z.; Qiu, J. *Chem. Mater.*, **2007**, *19*, 3364.

44. Charlier, J. C.; Lambin, P. *Phys. Rev. B*, **1998**, *57*, R15037.

45. Zhou, G.; Duan, W. H.; Gu, B. L. *Chem. Phys. Lett.*, **2001**, *333*, 344.

46. Hamada, N.; Sawada, S.; Oshiyama, A. *Phys. Rev. Lett.*, **1992**, *68*, 1579.

47. Saito, R.; Dresselhaus, G.; Dresselhaus, M. S. *Physical Properties of Carbon Nanotubes*. Imperial College Press: London, 1998.

48. Kimura, Y.; Abe, D.; Ohnori, T.; Mizutani, M.; Harada, M. *Colloids Surf. A.*, **2003**, *231*, 131.

49. Vincent, T.; Guibal, E. *Langmuir*, **2003**, *19*, 8475.

50. Adlim, M.; Abu Bakar, M.; Liew, K. Y.; Ismail, J. *J. Mol. Catal. A: Chem.*, **2004**, *212*, 141.

51. Esumi, K.; Isono, R.; Yoshimura, T. *Langmuir*, **2004**, *20*, 237.

52. Tsunoyama, H.; Sakurai, H.; Negishi, Y.; Tsukuda, T. *J. Am. Chem. Soc.*, **2005**, *127*, 9375.

53. Scott, R. W. J.; Wilson, O. M.; Crooks, R. M. *J. Phys. Chem. B*, **2005**, *109*, 692 7908.

54. Mayer, A. B. R.; Mark, J. E. *Colloid Polym. Sci.*, **1997**, *275*, 333.

55. Liang, Z.; Susha, A.; Caruso, F. *Chem. Mater.*, **2003**, *15*, 3176.

56. Bedford, R. B.; Singh, U. G.; Walton, R. I.; Williams, R. T.; Davis, S. A. *Chem. Mater.*, **2005**, *17*, 701.

57. Zhang, J.; Xu, S.; Kumacheva, E. *J. Am. Chem. Soc.*, **2004**, *126*, 7908.

58. Mei, Y.; Sharma, G.; Lu, Y.; Ballauff, M. *Langmuir*, **2005**, *21*, 12229.

59. Guo, X.; Weiss, A.; Ballauff, M. *Macromolecules*, **1999**, *32*, 6043.

60. Guo, X.; Ballauff, M. *Langmuir*, **2000**, *16*, 8719.

61. Mei, Y.; Wittemann, A.; Sharma, G.; Ballauff, M.; Koch, Th.; Gliemann, H.; Horbach, J.; Schimmel, Th. *Macromolecules*, **2003**, *36*, 3452.

62. Lu, Y.; Mei, Y.; Schrinner, M.; Ballauff, M.; Möller, M.W.; Breu, J. *J. Phys. Chem. C*, **2007**, *111*, 7676.

63. Plamper, F.A.; Walther, A.; Müller, A. H. E.; Ballauff, M. *Nano Lett.*, **2007**, *7*, 167.

64. Lu, Y.; Mei, Y.; Ballauff, M.; Drechsler, M. *J. Phys. Chem. B*, **2006**, *110*, 3930.

65. Ji, T.; Lirtsman, V. G.; Avny, Y.; Davidov, D. *Adv. Mater.*, **2001**,

66. Dong, A. G.; Wang, Y. J.; Tang, Y.; Ren, N.; Yang, W. L.; Gao, Z. *Chem.Commun.*, **2002**, 350.

67. Kidambi, S.; Dai, J.; Li, J.; Bruening, M. L. *J. Am. Chem. Soc.*, **2004**, *126*, 2658.

68. Harland, C. E. *Ion Exchange: Theory and Practice*. The Royal Society of Chemistry, Cambridge, UK, 1994.

69. Vogel, A. I. *Text Book of Quantitative Inorganic Analysis*. Longman, London, 1961; Chapter 9, pp. 702–723.

70. Helfferich, F. *Ion Exchange*. McGraw Hill, New York, 1962 (Bible of the subject).

71. Willner, I.; Mandler, D. *J. Am. Chem. Soc.*, **1989**, *111*, 1330.

72. Finke, R. G. In: *Metal Nanoparticles: Synthesis, Characterization and Applications*; Feldheim, D. L.; Foss, C. A., Jr.; Eds.; Marcel Dekker, New York, 2002; Chapter 2, pp. 17–54.

73. Caswell, K. K.; Bender, C. M.; Murphy, C. J. *Nano Lett.*, **2003**, *3*, 667.

74. Nath, S.; Ghosh, S. K.; Kundu, S.; Praharaj, S.; Panigrahi, S.; Pal, T. *J. Nanoparticle Res.*, **2006**, *8*, 111

75. Henglein, A. *J. Phys. Chem.*, **1993**, *97*, 5457.

76. Kundu, S.; Pal, A.; Ghosh, S. K.; Panigrahi, S.; Praharaj, S.; Pal, T.; *Inorg. Chem.*, **2004**, *43*, 5489.

77. Larpent, C.; Patin, H. *J. Mol. Catal.*, **1988**, *44*, 191.

78. Larpent, C.; Brisse-Le Menn, F.; Patin, H. *New J. Chem.*, **1991**, *15*, 361.

79. Tan, C. K.; Newberry, V.; Webb, T. R.; McAuliffe, C. A. *J. Chem. Soc. Dalton Trans.*, **1987**, 1299.

80. Kiwi, J.; Grätzel, M. *J. Am. Chem. Soc.*, **1979**, *101*, 7214.

81. Jana, S.; Pande, S.; Sinha, A. K.; Pal, T. *Inorg. Chem.*, **2008**, *47*, 5558.

82. Chechik, V.; Crooks, R. M. *J. Am. Chem. Soc.*, **2000**, *122*, 1243.

83. Zhao, M.; Crooks, R. M. *Adv. Mater.*, **1999**, *11*, 217.

84. Myers, V. S.; Frenkel, I. A.; Crooks, R. M. *Chem. Mater.*, **2009**, *21*, 4824.

85. Garcia, M. E.; Baker, L. A.; Crooks, R. M. *Anal. Chem.*, **1999**, *71*, 256.

86. Esumi, K.; Suzuki, A.; Yamahira, A.; Torigoe, K. *Langmuir*, **2000**, *16*, 2604.

87. Esumi, K.; Nakamura, R.; Suzuki, A.; Torigoe, K. *Langmuir*, **2000**, *16*, 7842.

88. Spatz, J. P.; Mössmer, S.; Möller, M. *Chem. Eur. J.*, **1996**, *2*, 1552.

89. Chernyshov, D. M.; Bronstein, L. M.; Börner, H.; Berton, B.; Antonietti, M. *Chem. Mater.*, **2000**, *12*, 114.

90. Antonietti, M.; Wenz, E.; Bronstein, L.; Seregina, M. *Adv. Mater.*, **1995**, *7*, 1000.

91. Seregina, M. V.; Bronstein, L. M.; Platonova, O. A.; Chernyshov, D. M.; Valetsky, P. M.; Hartmann, J.; Wenz, E.; Antonietti, M. *Chem. Mater.*, **1997**, *9*, 923.

92. Sidorov, S. N.; Bronstein, L. M.; Valetsky, P. M.; Hartmann, J.; Cölfen, H.; Schnablegger, H.; Antonietti, M. *J. Colloid Interface Sci.*, **1999**, *212*, 197.

93. Klingelhöfer, S.; Heitz, W.; Greiner, A.; Oestreich, S.; Förster, S.; Antonietti, M. *J. Am. Chem. Soc.*, **1997**, *119*, 10116.

94. Le Bars, J.; Specht, U.; Bradley, J. S.; Blackmond, D. G. *Langmuir*, **1999**, *15*, 7621.

95. Zhou, Y.; Wang, C. Y.; Zhu, Y. R.; Chen, Z. Y. *Chem. Mater.*, **1999**, *11*, 2310.

96. Niidome, Y.; Hori, A.; Santo, T.; Yamada, S. *Chem. Lett.*, **2000**, 310.

97. Nakamoto, M.; Yamamoto, M.; Fukusumi, M. *Chem. Commun.*, **2002**, 1622.

98. Henglein, A.; Meisel, D. *Langmuir*, **1998**, *14*, 7392.

99. Dawson, A.; Kamat, P. V. *J. Phys. Chem. B*, **2000**, *104*, 11842.

100. Nath, S.; Ghosh, S. K.; Kundu, S.; Praharaj, S.; Panigrahi, S.; Basu, S.; Pal, T. *Mater. Lett.*, **2005**, *59*, 3986.

101. Sarkar, S.; Pande, S.; Jana, S.; Sinha, A. K.; Pradhan, M.; Basu, M.; Saha, S.; Yusuf, S. M.; Pal, T. *J. Phys. Chem. C*, **2009**, *113*, 6022.

102. Jana, S.; Pande, S.; Panigrahi, S.; Praharaj, S.; Basu, S.; Pal, A.; Pal, T. *Langmuir*, **2006**, *22*, 7091.

103. Praharaj, S.; Nath, S.; Ghosh, S.K.; Kundu, S.; Pal, T. *Langmuir*, **2004**, *20*, 9889.

104. Daniel, M.; Astruc, D. *Chem. Rev.*, **2004**, *104*, 293.

105. Shan, J.; Tenhu, H. *Chem. Commun.*, **2007**, 4580.

106. Rosi, N. L.; Mirkin, C. A. *Chem. Rev.*, **2005**, *104*, 1547–1562.

107. Hutching, G. J. *Chem. Commun.*, **2008**, 1148.

108. Murray, C. B.; Kagan, C. R.; Bawendi, M. G. *Annu. Rev. Mater. Sci.*, **2000**, *30*, 545.

109. *Heterogeneous Catalysis: Principles and Applications*. Oxford Science Publications/ Clarendon Press, Oxford, UK, 1987.

110. Thomas, J. M.; Thomas, W. J. *Principle and Practice of Heterogeneous Catalysis*. Wiley-VCH, Weinheim, Germany, 1996.

111. Cornils, B; Herrmann, W. A.; Eds. *Applied Homogeneous Catalysis with Organometallic Compounds*. Wiley–VCH, Weinheim, Germany, 1996; Vols. 1 and 2.

112. Bond, G. C.; Sermon, P. A.; Webb, G.; Buchanan, D. A.; Wells, P. B. *J. Chem. Soc. Chem. Commun.*, **1973**, 444.

113. Haruta, M.; Kobayashi, T.; Sano, H.; Yamada, N. *Chem. Lett.*, **1987**, 405.

114. Stephen, A.; Hashmi, K.; Hutchings, G. J. *Angew. Chem. Int. Ed.*, **2006**, *45*, 7896.

115. Jain, P. K.; Lee, K. S.; El-Sayed, I. H.; El-Sayed, M. A. *J. Phys. Chem. B*, **2006**, *110*, 7238.

116. Huang, X.; El-Sayed, I. H.; Qian, W.; El-Sayed, M. A. *J. Am. Chem. Soc.*, **2006**, *128*, 2115.

117. Huang, X.; El-Sayed, I. H.; Qian, W.; El-Sayed, M. A. *Nano Lett.*, **2007**, *7*, 1591.

118. El-Sayed, I. H.; Huang, X.; El-Sayed, M. A. *Nano Lett.*, **2005**, *5*, 829–834.

119. Haruta, M. *Catal. Today*, **1997**, *36*, 153.

120. Haruta, M.; Date, M. *Appl. Catal. A*, **2001**, *222*, 427.

121. Haruta, M. *Cattech*, *2002*, *6*, 102.

122. Haruta, M. *Chem. Rec.*, **2003**, *3*, 75.

123. Tsunoyama, H.; Tsukuda, T. *J. Am. Chem. Soc.*, **2009**, *131*, 18216–18217.

124. Teranishi, T.; Miyake, M. *Chem. Mater.*, **1998**, *10*, 594.

125. Yonezawa, T.; Toshima, N. In: *Advanced Functional Molecules and Polymers*; Nalwa, H. S.; Ed. OPA, Amsterdam, 2001; Vol. 2, p. 65.

126. Haruta, M.; Yamada, N.; Kobayashi, T.; Iijima, S. *J. Catal.*, **1989**, *115*, 301.

127. Rogatis, L. D.; Cargnello, M.; Gombac, V.; Lorenzut, B.; Montini, T.; Fornasiero, P. *ChemSusChem*, **2010**, *3*, 24.

128. Liu, Y.; Tsunoyama, H.; Akita, T.; Tsukuda, T. *J. Phys. Chem. C*, **2009**, *113*, 13457.

129. Tsunoyama, H.; Sakurai, H.; Ichikuni, N.; Negishi, Y.; Tsukuda, T. *Langmuir*, **2004**, *20*, 11293.

130. Sakurai, H.; Tsunoyama, H.; Tsukuda, T. *J. Organomet. Chem.*, **2007**, *692*, 368.

131. Sakurai, H.; Tsunoyama, H.; Tsukuda, T. *Trans. MRS J.*, **2006**, *31*, 521.

132. Tsunoyama, H.; Sakurai, H.; Negishi, Y.; Tsukuda, T. *J. Am. Chem. Soc.*, **2005**, *127*, 9374.

133. Tsunoyama, H.; Sakurai, H.; Tsukuda, T. *Chem. Phys. Lett.*, **2006**, *429*, 528.

134. Tsunoyama, H.; Tsukuda, T.; Sakurai, H. *Chem. Lett.*, **2007**, *36*, 212.

135. Toshima, N.; Teranishi, T.; Asaauma, H.; Saito, Y. *J. Phys. Chem.*, **1992**, *96*, 3796.

136. Wang, Y.; Liu, H.; Toshima, N. *J. Phys. Chem.*, **1996**, *100*, 19533.

137. European Patent Office, Patent # RU2187496, 2002.

138. Lesiak, T.; Schittek, W. *Przemysl Chemiczny*, **1957**, *13*, 456.

139. Bakke, J.; Heikman, H.; Nystroem, G. *Acta Chem. Scand.*, **1972**, *26*, 355.

140. Srinivasan, P. R. *J. Am. Chem. Soc.*, **1959**, *81*, 1772.

141. Jana, S.; Ghosh, S. K.; Nath, S.; Pande, S.; Praharaj, S.; Panigrahi, S.; Basu, S.; Endo, T.; Pal, T. *Appl. Catal. A: General*, **2006**, *313*, 41.

142. Pradhan, N.; Pal, A.; Pal, T. *Colloids Surf. A: Physicochem. Eng. Aspects*, **2002**, *196*, 247.

143. Ghosh, S. K.; Mandal, M.; Kundu, S.; Nath, S.; Pal, T. *Appl. Catal. A: General*, **2004**, *268*, 61.

144. Fleischmann, M.; Hendra, P. J.; McQuillan, A. J. *Chem. Phys. Lett.*, **1974**, *26*, 163.

145. Siiman, O.; Lepp, A.; Kerker, M. *Chem. Phys. Lett.*, **1983**, *100*, 163.

146. Breen, M. L.; Ruhl, T.; Hellmann, G. P. *Macromol. Chem. Phys.*, **2001**, *202*, 3502.

147. Cho, K.; Choo, J.; Joo, S. *Spectrochim. Acta Part A*, **2005**, *61*, 1141.

148. Kneipp, K.; Wang, Y.; Kneipp, H.; Perelman, L.T.; Itzkan, I.; Dasari, R.; Feld, M. S. *Phys. Rev. Lett.*, **1997**, *78*, 1667.

149. Krug, J. T.; Wang, G. D.; Emory, S. R.; Nie, S. M. *J. Am. Chem. Soc.*, **1999**, *121*, 9208.

150. Sun, Y.; Mayers, B.; Xia, Y. *Adv. Mater.*, **2003**, *15*, 641–646.

151. Pande, S.; Ghosh, S. K.; Praharaj, S.; Panigrahi, S.; Basu, S.; Jana, S.; Pal, A.; Tsukuda, T.; Pal, T. *J. Phys. Chem. C*, **2007**, *111*, 10806.

152. Praharaj, S.; Nath, S.; Panigrahi, S.; Ghosh, S. K.; Basu, S.; Pande, S.; Jana, S.; Pal, T. *Inorg. Chem.*, **2006**, *45*, 1439.

153. El-Sayed, M. A. *Acc. Chem. Res.*, **2001**, *34*, 257.

154. Pileni, M. P. *Adv. Funct. Mater.*, **2001**, *11* 323.

155. Nie, S.; Emory, S. R. *Science*, **1997**, *275*, 1102.

156. Kamat, P. V. *J. Phys. Chem. B*, **2002**, *106*, 7729.

157. Maier, S. A.; Brongersma, M. L.; Kik, P. G.; Meltzer, S.; Requicha, A. A. G.; Atwater, H. A. *Adv. Mater.*, **2001**, *13*, 1501.

158. Jun, Y. W.; Choi, J. S.; Cheon, J. *Angew. Chem. Int. Ed.*, **2006**, *45*, 3414.

159. Park, J.; Joo, J.; Kwon, S. G.; Jang, Y.; Hyeon, T. *Angew. Chem. Int. Ed.*, **2007**, *46*, 4630.

160. Cao, A. M.; Hu, J. S.; Liang, H. P.; Wan, L. J. *Angew. Chem. Int. Ed.*, **2005**, *44*, 4391.

161. Yu, J. G.; Yu, J. C.; Zhang, L. Z.; Wang, X. C.; Wu, L. *Chem. Commun.*, **2004**, 2414.

162. Zheng, Y. H.; Cheng, Y.; Wang, Y. S.; Zhou, L. H.; Bao, F.; Jia, C. *J. Phys. Chem. B*, **2006**, *110*, 8284.

163. Cao, A. M.; Hu, J. S.; Liang, H. P.; Song, W. G.; Wan, L. J.; He, X. L.; Gao, X. G.; Xia, S. H. *J. Phys. Chem. B*, **2006**, *110*, 15858.

164. Freid, T.; Shemer, G.; Markovich, G. *Adv. Mater.*, **2001**, *13*, 1158.

165. Ding, Y.; Morber, J. R.; Snyder, R. L.; Wang. Z. L. *Adv. Funct. Mater.*, **2007**, *17*, 1172.

166. Zhang, J. T.; Liu, J. F.; Peng, Q.; Wang, X.; Li, Y. D. *Chem. Mater.*, **2006**, *18*, 867.

167. Jiang, P.; Zhou, J. J.; Fang, H. F.; Wang, C. Y.; Wang, Z. L.; Xie, S. S. *Adv. Funct. Mater.*, **2007**, *17*, 1303.

168. Caruso, F.; Caruso, R. A.; Mohwald, H. *Science*, **1998**, *282*, 1111.

169. Choudary, B. M.; Mulukutla, R. S.; Klabunde, K. J. *J. Am. Chem. Soc.*, **2003**, *125*, **2020**.

170. Pande, S.; Jana, S.; Basu, S.; Sinha, A. K.; Datta, A.; Pal, T. *J. Phys. Chem. C*, **2008**, *112*, 3619.

171. Pande, S.; Saha, A.; Jana, S.; Sarkar, S.; Basu, M.; Pradhan, M.; Sinha, A. K.; Saha, S.; Pal, A.; Pal, T. *Org. Lett.*, **2008**, *10*, 5179.

172. Sinha, A. K.; Jana, S.; Pande, S.; Sarkar, S.; Pradhan, M.; Basu, M.; Saha, S.; Pal, A.; Pal, T. *Cryst. Eng. Commun.*, **2009**, *11*, 1210.

173. Basu, M.; Sinha, A. K.; Sarkar, S.; Pradhan, M.; Yusuf, S. M.; Negishi, Y.; Pal, T. *Langmuir*, **2010**, *26*, 5836.

174. Jana, S.; Praharaj, S.; Panigrahi, S.; Basu, S.; Pande, S.; Chang, C. H.; Pal, T. *Org. Lett.*, **2007**, *9*, 2191.

175. Mills, A.; Wang, J. *J. Photochem. Photobiol. A Chem.*, **1999**, *127*, 123.

176. Pande, S.; Ghosh, S. K.; Nath, S.; Praharaj, S.; Jana, S.; Panigrahi, S.; Basu, S.; Pal, T. *J. Colloid Interface Sci.*, **2006**, *299*, 421.

177. Basu, S.; Panigrahi, S.; Praharaj, S.; Ghosh, S. K.; Pande, S.; Jana, S.; Pal, A.; Pal, T. *J. Phys. Chem. A*, **2007**, *111*, 578.

178. Hsiao, L.Y.; Duh, J. G. *J. Electrochem. Soc.*, **2005**, *152*, 105.

179. Yang, C.C.; Wan, C. C.; Wang, Y.Y. *J. Electrochem. Soc.*, **2006**, *153*, 27.

Pd-Nanoparticle Catalyzed Poly(hydro)siloxane Grafting: A Selective and Efficient Approach to Organic/Inorganic Hybrid Polymers

BHANU P. S. CHAUHAN and JITENDRA S. RATHORE

Engineered Nanomaterials Laboratory, Department of Chemistry, William Paterson University, Wayne, New Jersey, USA

MONI CHAUHAN

Queensborough Community College of City University of New York, New York, New York, USA

3.1. INTRODUCTION

Synthesis of hybrid polymeric materials can be a fruitful endeavor due to the potential of producing a new generation of polymers, which will have a crossbreed of property profiles not available in any of the parental components. Such chemical crossbreeding can be very exciting and of commercial importance, if two very dissimilar functionalities such as organic and inorganic functional groups are involved. The major goal and expectation of such a hybridization study will be to achieve a well-defined material, which will possess the advantageous features of the parent functionalities and minimize the undesirable properties of each of its constituents. Although the implementation of such an approach will not be an easy task, the results of such on endeavor will be very rewarding.

In the past few years, we have demonstrated that catalytic grafting of poly-methylhydrosiloxane (PMHS) is an attractive route for the synthesis of organic–inorganic hybrid polymers, which can avoid the complexities involved in direct polymerization reactions of functional monomers.[1–3] In this work, our goal is to achieve a crossbreed of inorganic/organic polymers by stitching individual inorganic and organic components together. We plan to use a silicon–oxygen bond containing

a backbone generally known as polysiloxane (as an inorganic/organometallic component) and tether organic functionality to this backbone via a variety of catalytic reactions. Our choice of material for grafting (stitching) studies is a polymer known as polymethylhydrosiloxane, which is commercially available and contains silicon–hydrogen bonds at each silicon atom except for the terminal silicon groups. This monomodal, well-defined polymer is also very well suited for NMR studies because of its solubility profile. Some of the attractive features of this polymer are its low cost, easy availability, presence of catalytically transformable silicon–hydrogen bonds, and its stability toward oxidation reactions in the presence of humidity and moisture.

Moreover, organic functionalization of a polymer chain can lead to improvement in the physical properties, such as thermal stability and mechanical strength of the resulting siloxanes (Figure 3.1). Appropriate substitution on the polysiloxane backbone can lead to diverse materials such as liquid crystals,[4–6] crosslinking agents,[7] conductive[8, 9] and electroluminescent polymers,[10] nonlinear optical materials,[11, 12] and bactericides.[13]
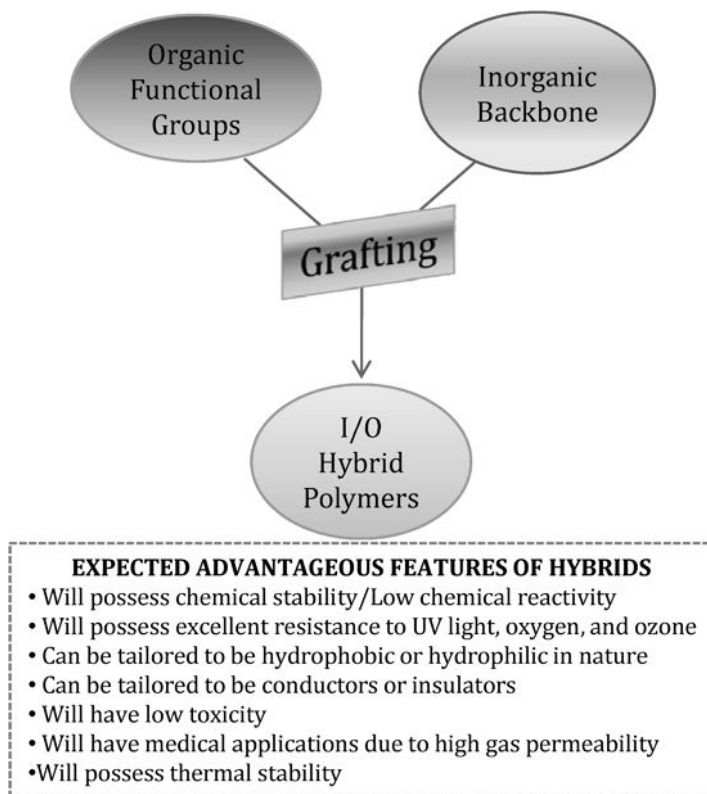
Figure 3.1. Conceptual representation of the grafting strategy.

We chose the polymer grafting (substitution) strategy because of the following appealing and advantageous features:

  (i) The grafting strategy does not require the synthesis of each and every functional monomer that one wants to polymerize to achieve a hybrid material.

  (ii) Since synthetic strategies for silicon containing organo functional monomers are very limited, the grafting of preformed silicon polymer can provide hybrid materials that will not be available via monomer polymerization routes.

 (iii) Selective tethering of a predefined silicon polymer will lead to a very well-defined hybrid material without compromising the property profile.

 (iv) In polymer grafting strategy, catalytic attachment of a functional group has to be investigated, which opens up the possibility of grafting or attaching the spectator groups via such functionality to the polymer backbone as required. This is a very desirable feature, because in monomer polymerization study, for each and every individual monomer exhaustive catalytic studies have to be carried out to find the best possible catalyst that will produce a well-defined hybrid material.

  (v) In polymer grafting strategy, the property profiling of the resulting polymer after tethering will easily be discernible in comparison to different polymers obtained via different monomer polymerization strategies.

 (vi) The polydispersity of the grafted polymers can remain constant if the tethering reactions are selective. On the other hand, polydispersity of hybrid materials achieved via polymerization of different monomers is expected to be different.

Polymer tailoring (macromolecular substitution) in the presence of catalysts is not without its own pitfalls, which can be summarized as follows:

  (i) The catalysts can lead to rearrangement of parent polymer or polysiloxane backbone, which will compromise the very purpose of the choice of the method as well as the desirable properties of the expected hybrid material.

  (ii) It is expected that as the tethering progresses the transformation of the attachment of organic functionality to adjacent silicon centers may become more difficult due to steric demand, which can compromise the expected property profile.

 (iii) The silicon oxygen polymer will have to contain catalytically functionalizable groups such as silicon–hydrogen bonds, which are also susceptible to partial crosslinking reactions,

 (iv) If the catalyst is not very effective side reactions such as oxidation of silicon–hydrogen bonds is also a strong possibility.

  (v) Since it is not easy to purify the mixture of polymers, particularly the silicon-based polymers, because of their propensity for oxidation reactions, the synthetic strategy will require quantitative transformations.

(vi) Finally, the preservation of the integrity of the backbone, selectivity of the attachment of organic functionality to the backbone, and the degree of grafting will be very important factors in defining the property profile of the resulting hybrid polymers. For example, inefficient tethering of organic functionalities will not produce true hybrid and property profiling of such a hybrid polymer may not represent the properties of a true hybridization resulting from the marriage of organic–inorganic functionalities.

3.2. SEARCH FOR THE RIGHT CATALYSTS

Ignoring the macromolecular substitution reactions, even for the monomeric transformation, designing a catalyst that could operate under mild reaction conditions with excellent activity, that has selectivity, and that has the attributes of recyclability is a very difficult task. No wonder that poor selectivity, limited activity, and nonrecyclability of the catalysts remain major shortcomings of most of the catalytic systems available for macromolecular substitutions of polymeric templates such as polysiloxanes. To address the problem of poor catalytic systems, our approach is to use metal nanoclusters as the catalyst because it is possible that the large surface area (i.e., presence of more active sites at the surface of such catalysts) may lead to higher activity and selectivity. These attributes, coupled with the opportunity to recycle such catalysts, make very compelling the case studies to explore new directions in macromolecular grafting studies. We initiated a systematic study to investigate if metal nanoparticles can be prepared and characterized independently, and subsequently can be used for macromolecular substitution reactions of a polymethylhydrosiloxane template. Recently, we and others have shown that metal nanoparticles can be used as catalysts for a number of catalytic transformations due to better activity, selectivity and reusability.[14–21]

The very first hurdle we and others have encountered in nanoparticle-based catalysis design is the deactivation of active sites on the cluster surface due to the presence of nanoparticle stabilizing agents used during the synthesis of the catalysts. These stabilizing ligands normally lead to deterioration in catalytic activity. By experimenting with various systems and also using a systematic design approach, we succeeded in preparing metal nanoparticles as isolable metallic powders, which were storable at room temperature for long periods without any compromise in their catalytic activity. We found that our nanoclusters were redispersible in solutions and yielded catalytically active metal nanoclusters even after multiple uses. Our approach for such a nanocatalyst is shown in Figure 3.2, which depicts utilization of metal nanoclusters as a redispersible and potent catalyst for macromolecular functionlization of PMHS.

3.3. POLYMETHYLHYDROSILOXANE SILAESTERIFICATION: A ONE-STEP ROUTE TO HYBRID POLYMERS

The increasing interest in environmentally amenable and biodegradable polymers has prompted us to investigate the new catalytic routes to polysilyl esters. The

**Stable, isolable, metal nanoclusters
redispersible in organic solvents**

Product

Substrates

**Catalytically active metal nanoclusters
dispersed in common organic solvents**
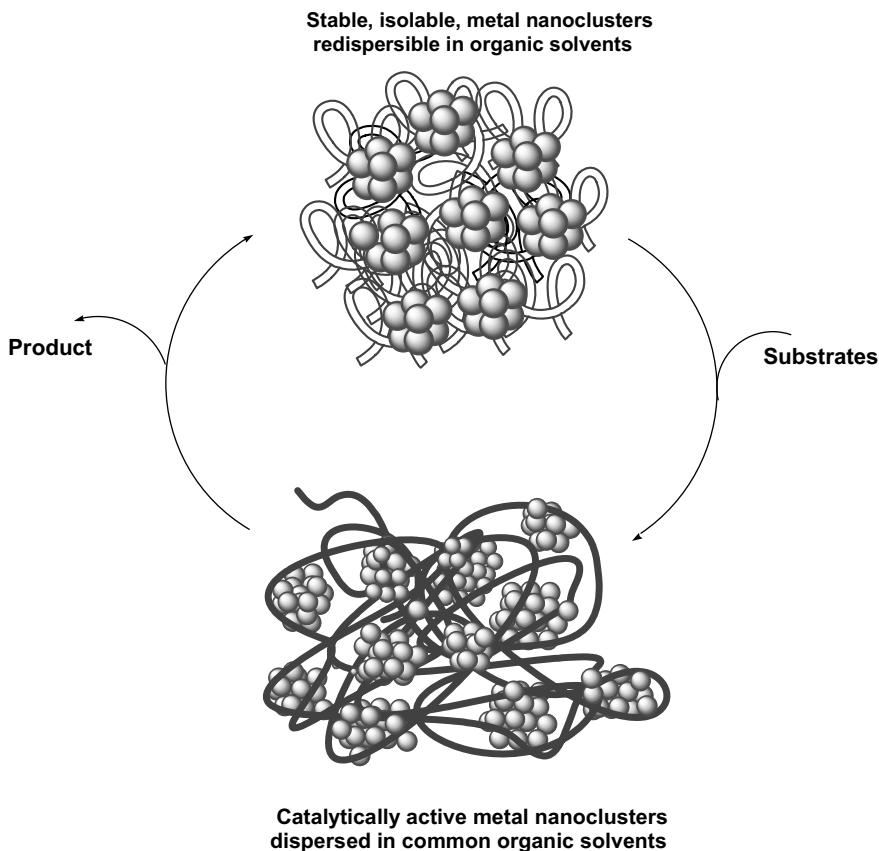
Figure 3.2. Pictorial representation of the mode of action of the nanoparticle catalysts used in our macromolecular functionalization studies.

biodegradable properties of polysilyl esters have received considerable attention in environmental and biomedical applications.[22–24] Moreover, polysilyl esters are utilized in the cotton textile industry to improve water repellency,[25, 26] as adhesion promoters, as protection agents in anionic polymerization,[27, 28] in photographic applications,[29, 30] as viscosity reducing agents,[31] and as a source of silicon dioxide.[32]

Direct processes are the most common synthetic routes available for the preparation of silyl esters.[33–35] A brief survey of the literature indicates that the conventional synthetic routes available for silaesterification reactions require harsh reaction conditions and most often are accompanied by side reactions.[33–39] For example, triethylacetoxysilane was prepared by the cleavage of acetic anhydride and triethylethoxysilane (Scheme 3.1).[37] The reaction involves nucleophilic attack of anhydride groups on the silicon center, resulting in the elimination of triethylacetoxysilane.

Another direct method reports the use of anhydrous sodium acetate and silicon tetrachloride to prepare acetoxy silanes (Scheme 3.2).[37] The main drawback of the

Triethylacetoxysilane
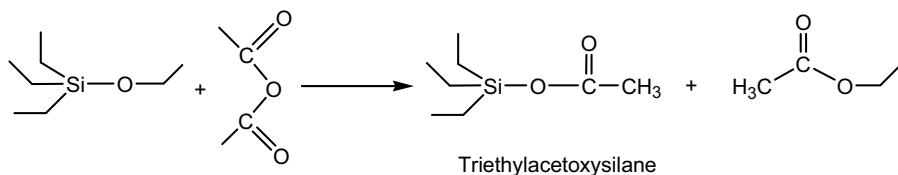
Scheme 3.1. Silyl ester synthesis by cleavage of acetic anhydride.

$SiCl_4$ + 4 CH_3COONa → ... + NaCl
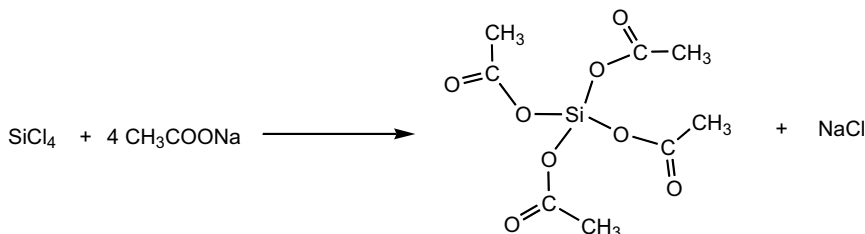
Scheme 3.2. Reaction of silicontetrachloride and sodium acetate to produce tetraacetoxysilane. (Adapted from Ref. 37.)

direct processes is the low yields of silyl esters (<50%). Furthermore, most of the direct processes yield a mixture of products due to unwanted side reactions, and the silyl esters were isolated via a multistep distillation process, making the direct process very tedious.

Anderson and co-workers reported a number of silver salt mediated one-step conversions for organosilicon halides, cyanides, sulfides, cyanides, and isothiocyanates to corresponding silyl esters.[38] Ag salts, such as AgOCOMe, AgS_2, and $AgOCOCF_3$, were made to react with organosilicon compounds {$Et_2SiClCl$, $(Et_3Si)_2S$, $Et_3Si(CN)$, $Me_2Si(NCO)$} to yield silyl esters (Scheme 3.3). Although the synthetic strategy was straightforward, the reaction required rugged conditions
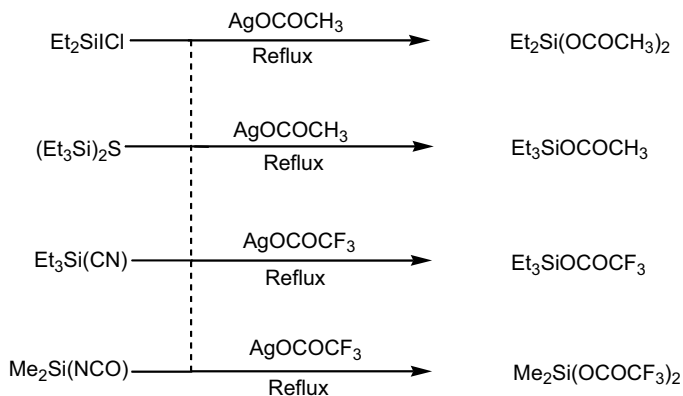
Scheme 3.3. Synthesis of acetoxysilanes using Ag salts. (Adapted from Ref. 23.)
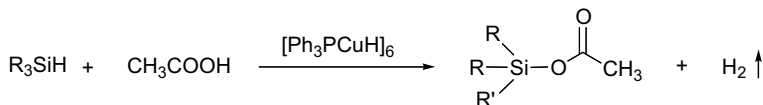
(1) R and R' = Ph; (2) R=Ph and R' = Me; (3) R=Me and R' = Ph; (4) R and R' = Et

Scheme 3.4. Catalytic silaesterification. (Reproduced from Ref. 39.)

(high temperature and pressure) and silyl esters were obtained after a tedious process of repeated distillations at low pressure. Moreover, the formation of compounds such as AgCN and Ag(NCO) during the reaction makes the process hazardous.

Although catalytic routes to silyl esters are rare, recently a few catalytic routes to silyl esters were reported.[1, 39] In one such report, $[Ph_3PCuH]_6$ was used as an efficient silaesterification catalyst: 0.4 mol% of catalyst was used in the presence of air with only tertiary silanes to yield a fair amount of corresponding silyl esters (Scheme 3.4).[39] The presence of air was reported to increase the rate of reaction; however, no mechanism for the effect was proposed. Same catalysts have also been reported to catalyze the reaction of H_2O with tertiary silanes to yield corresponding silanols. The reactivity of the silanes for silaesterification involving acetic acid was reported to decrease in the following order: $Ph_2MeSiH > Me_2PhSiH > Ph_3SiH > Et_3SiH$.

In another report, catalytic transsilylation of trimethylsilyl benzoate with a number of chlorosilanes was disclosed.[40] N,N-dimethylformamide (DMF) and sodium iodide were used as catalysts. Both DMF and sodium iodide were reported to catalyze with almost equal efficiency; however, the formation of insoluble sodium chloride and discoloration of solution made sodium iodide a less suitable catalyst. Then 1 mol% of DMF was used in THF as a solvent under reflux conditions for 24 h. The silyl ester was obtained in 77% yield after removal of trimethylsilyl chloride under reduced pressure. (See Scheme 3.5.)

Our strategy for the synthesis of polysilyl ester involves catalytic substitution of carboxylic acids (RCOOH) on the polymethylhydrosiloxane (PMHS) backbone.[1, 14] PMHS, as discussed earlier (Chapter 1), is a polymer with evenly spaced Si–H bonds with unique flexibility that can be substituted with functional groups in the presence of appropriate catalysts.

After examining the literature precedents, and their advantages and disadvantages, we decided to investigate the transition metal catalyzed routes to generate silyl esters. Since it is well established that Si–H bonds can be activated in the presence of metal, our choice of starting materials were Si–H bond containing silanes. Catalytic
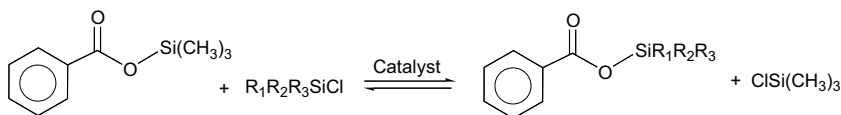
Scheme 3.5. Transsilylation reaction between trimethylsilyl benzoate and silychloride. (Reproduced from Ref. 40.)

efficiency of various metal complexes to produce silyl esters was investigated by using a commercially available monosiloxane 1,1,1,3,5,5,5-heptamethyltrisiloxane, [CH$_3$SiH(OSiMe$_3$)$_2$], a prototype of PMHS. The reactivity of this silane provided a direct route to examine the catalysis in details as well as the NMR signatures of the resulting products.[1] After screening of various metal complexes, Pd(OAc)$_2$ was found to be the catalyst of choice because of the ease of utilization as well as the ease of separation of the product. The present catalytic process was found to be quite general (Scheme 3.6). Thus, in the presence of catalytic amounts of Pd(OAc)$_2$, the substrate 1,1,1,3,5,5,5-heptamethyltrisiloxane reacted cleanly with a variety of acids under mild conditions to provide corresponding monosiloxy esters in good yields. With the exception of benzoic acid, which required 70°C, all acids were silylated at room temperature.

The reactions were monitored by ^{1}H and ^{29}Si NMR. Reaction completion is indicated by the disappearance of the 4.76 ppm signal in the ^{1}H NMR and -36.6 ppm signal in the ^{29}Si NMR showing consumption of the Si–H bonds. A new set of signals for the central silicon atoms appears in the ^{29}Si NMR spectrum in the range of -57 to -66 ppm. As expected, there are only small variations in ^{29}Si NMR shifts for OSiMe$_3$ in the products (δ 7 to 10 ppm) from the starting siloxane (δ 8.9 ppm). The [29]Si, ^{1}H, and ^{13}C signals were very similar and comparable with the peaks obtained in the case of corresponding polysilyl esters substantiating clean formation of polysilyl esters.

After establishing the reaction conditions and spectroscopic analysis of the products, the catalytic reaction of PMHS was examined with acetic acid in the

Scheme 3.6. A one-step catalytic route to silyl esters.
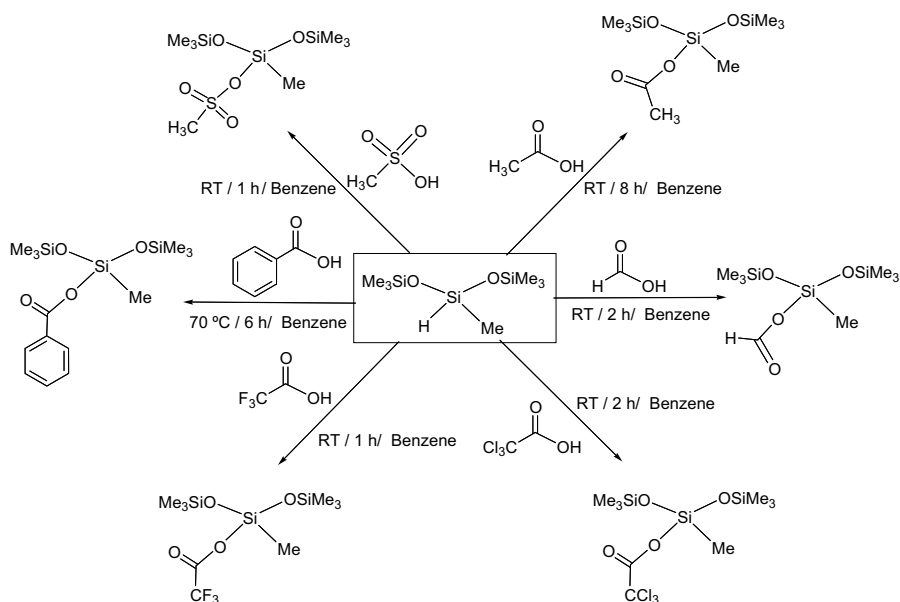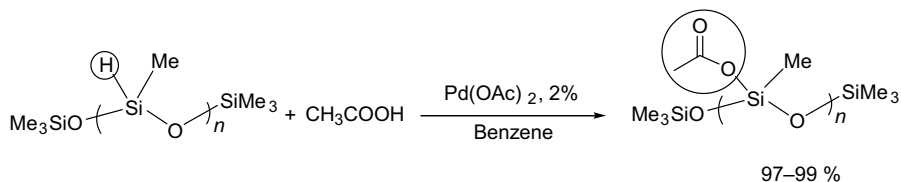
Scheme 3.7. A one-step catalytic route to polysilyl esters.

presence of $Pd(OAc)_2$ as catalyst (Scheme 3.7). Thus, in a 15 mL Schlenck tube, Pd $(OAc)_2$ (0.02 mmol) and acetic acid (0.060 mL, 1.00 mmol) were mixed in benzene (4.0 mL) and the Schlenk tube was degassed by three freeze–pump–thaw cycles. Upon addition of PMHS (0.06 mL, 1.0 mmol), to the reaction mixture, gas evolution (presumably H_2) was observed. The progress of the reaction was monitored by ^1H and ^{29}Si NMR spectra. The signal at -36.28 ppm (Si–H) in the ^{29}Si NMR disappeared, and a new signal appears at -58.6 ppm in ^{29}Si spectra, signifying an acetate-substituted silicon center. Stirring was stopped after 8 h. Black turbid solution turned colorless and catalyst precipitated out as black solid. The liquid was removed by syringe and was evaporated under vacuum to furnish pure polymethya-cetylsiloxane as a glue-like liquid.

The selectivity and ease of isolation of the product were the high points of this catalysis. This success opened a new door to attach the organic functionality to silicon via ester bond by using diverse functional groups on acid. We did extend this catalysis to a variety of acids. During the course of $Pd(OAc)_2$ catalyzed silaester-ification reactions, we made certain observations, which led us to explore the reactions in detail.[1] The main objectives of the study were to identify the real nature (homogeneous or heterogeneous) of the catalyst during the silaesterification reactions.

3.3.1. UV–Visible and TEM Studies

The following observations were made during the silaestrification of PMHS: (i) When PMHS was added to the reaction mixture containing catalytic amounts of $Pd(OAc)_2$, the color of the solution turned black accompanied by gas formation, presumably H_2. (ii) After the transformation was complete, a black precipitate was formed, and the solution became colorless. (iii) The black precipitate can be redispersed in the solution and was found to be catalytically active for silylester-ification reactions. On the basis of these observations, we decided to investigate the possibility that $Pd(OAc)_2$ was not the real catalyst but merely a precursor to other catalytically active species, which may be functioning as true catalysts.

To investigate our hypothesis, in a Schlenk tube, $Pd(OAc)_2$ (0.004 g, 0.02 mmol) and acetic acid (0.06 mL, 1.00 mmol) were dissolved in 4 mL of benzene, and the mixture was examined by UV–visible spectroscopy. A peak at 400 nm, which is indicative of $Pd(OAc)_2$, was observed (Figure 3.3). PMHS (0.06 mL, 1 mmol) was then added to the solution. The peak at 400 nm disappeared after 5 min of addition of PMHS. The final UV–visible spectra showed an unstructured, continuous absorption
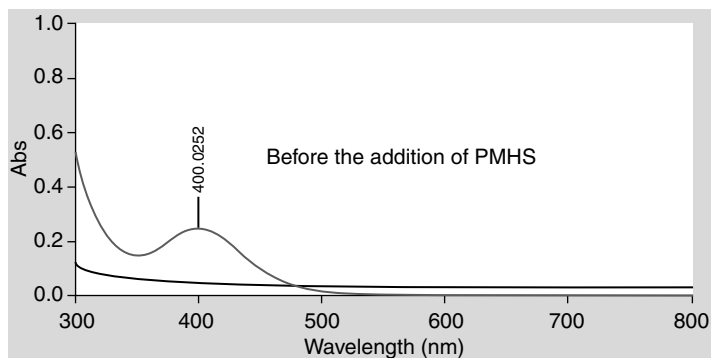
Figure 3.3. Reaction mixture analysis by UV–visible spectroscopy.

without any peaks in the visible range, which is typical of nanosized palladium particles.[41] This result is in accordance with our hypothesis that Pd(OAc)$_2$ was not the real catalytic species for these reactions, but acts as a catalyst precursor.

In order to gain further evidence for our hypothesis, during the course of the reaction (not after the catalysis was over) transmission electron microscopy (TEM) analysis of the reaction mixture was carried out to examine the presence of Pd nanoclusters in the solution. To carry out the TEM analysis, one drop from the reaction mixture was directly deposited on the formvar/carbon-coated grid and was analyzed by TEM. Indeed, the TEM graphs showed the presence of warm-like Pd nanoparticles, which we belive were due to their conjugation with the polysiloxane network (Figure 3.4a). Particle size analysis revealed particles in the size regime of 1–6 nm with standard deviation of 1.0 nm (Figure 3.4b). As is evident by the TEM images, polysiloxane matrix acts as a template for the stabilization of Pd nanoparticles. TEM characterization proved the presence of nanoclusters, but cannot prove the participation of nanoclusters during the catalysis. Thus, we decided to perform controlled poisoning experiments to unequivocally establish the colloidal nature of the catalyst during the silaesterification reactions.

3.3.2. Poisoning Experiment: Mercury Poisoning Test

Mercury (Hg) is a well-known poison for nanoclusters because of either amalgamation formation with the metal nanoparticles or physicoabsorbtion on the nanocluster surface.[42, 43] To test the poisoning with Hg during silaesterification reactions (Scheme 3.8), typically, in a Schlenk tube, Pd(OAc)$_2$ (0.004 g, 0.02 mmol) and acetic acid (0.06 mL, 1.0 mmol) are dissolved in 4 mL of benzene and the solution is examined by UV–visible spectroscopy. A peak at 400 nm suggestive of Pd(OAc)$_2$ is noted. PMHS (0.06 mL, 1.0 mmol, 33–35 Si–H units) was then added to the above solution.

The UV–visible band associated with Pd(OAc)$_2$ disappeared within 5 min of the addition of PMHS, which indicated conversion of Pd(OAc)$_2$ to Pd nanoparticles. The progress of the reaction was monitored by ^{1}H NMR spectroscopy, which showed

10–15% product. The yield of product was reported on the basis of ^{1}H NMR and the range of the product yield (10–15%) was provided after repeating the experiment twice. At this juncture, Hg was added to the reaction mixture. After 30 min, the black reaction mixture turned colorless and Hg was noticed sitting at the bottom of the Schlenk tube. The clear solution suggests the adsoption of the Pd nanoparticles on the Hg surface. No further transformation was recorded in the NMR spectra, even if the reaction mixture was stirred for 24 h. The above result strongly indicates that the catalytically active species were poisoned by Hg and were not effective for the above transformation. Moreover, the reaction mixture was analyzed by TEM, before and after the addition of Hg. TEM analysis manifested that Pd nanoparticles were present in the reaction mixture before the addition of the Hg (Figure 3.5a); however, after the addition of Hg, no such nanoparticles were observed (Figure 3.5b), suggesting poisoning by the Hg.

(a)

(b)
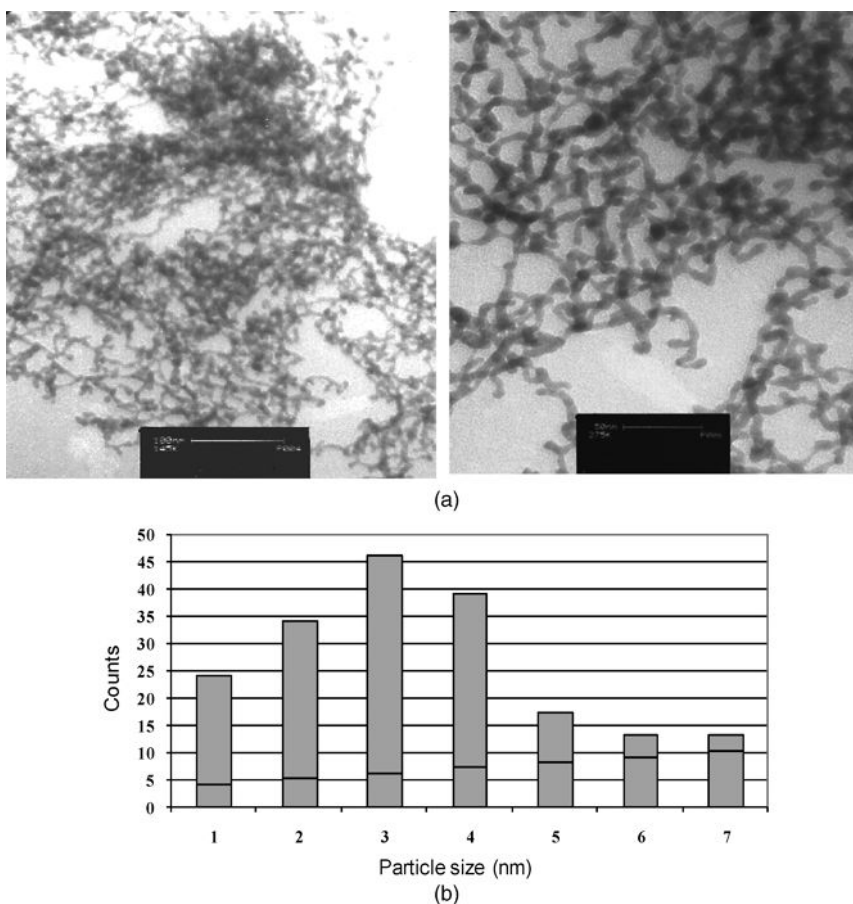
Figure 3.4. (a) TEM images of the reaction mixture during the silaesterification reactions. (b) Particle size plot showing size distribution of Pd nanoparticles.
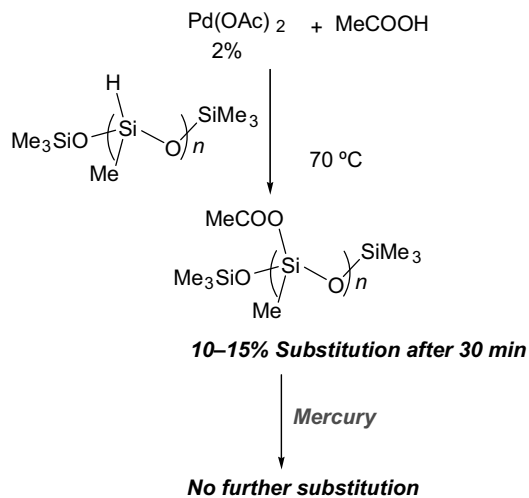
Scheme 3.8. Schematic representation of mercury poisoning experiment.
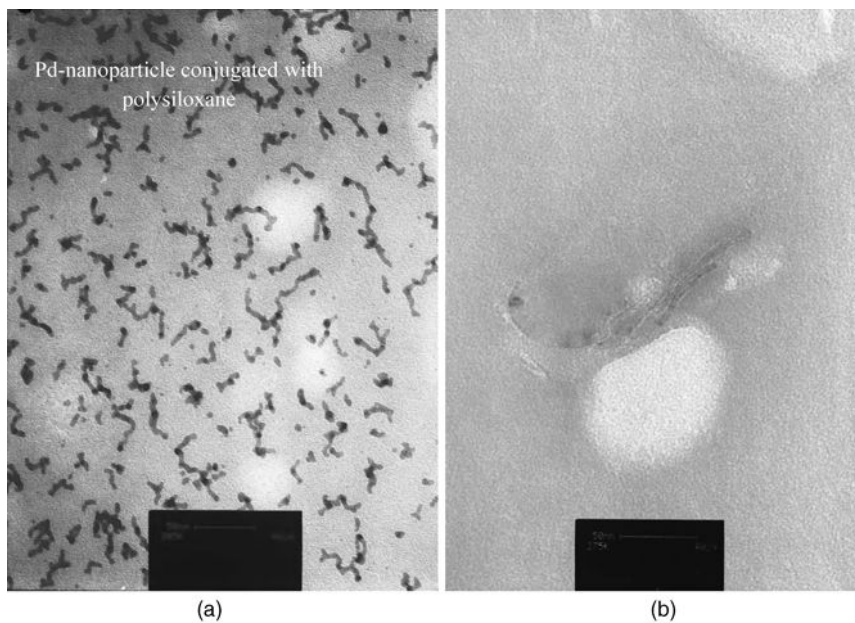
Figure 3.5. (a) TEM image of the reaction mixture without Hg. (b) TEM image of the reaction mixture after the addition of Hg.

3.3.3. Poisoning Experiment: Triphenylphosphine (TPP) Poisoning Test

Triphenylphosphine (TPP) forms a number of metal complexes with metals such as Pd and Pt via coodinating to the metal center. We decided to utilize this coordinating property of TPP to carry out a controlled poisoning experiment, in which TPP was used as the poisoning agent to passivate the catalytically active sites on the nanoclusters. To investigate the poisoning effect of TPP on Pd nanoparticles during silaesterification reactions, $Pd(OAc)_2$ (0.004 g, 0.02 mmol) and acetic acid (0.06 mL, 1.0 mmol) were dissolved in 4 mL of benzene. PMHS (0.06 mL, 1.00 mmol) was added to reaction mixture. The progress of the reaction was followed by ^1H NMR spectroscopy, which showed 15% conversion to product after 30 min (Scheme 3.9).

At this juncture, PPh_3 [0.016 g, 0.06 mmol, 3.0 equivalents w.r.t. $Pd(OAc)_2$] was added to the above solution. No further substitution took place under standard reaction conditions even after 24 h of stirring, suggesting the coordination of TPP to the metal cluster surface. To confirm the coordination of TPP, ^{31}P NMR experiments were performed on the reaction mixture, which showed a shift in the peaks from δ −4.25 to δ 28.81, indicative of TPP stabilized Pd nanoclusters.[44] No further study was conducted by varying the amounts of TPP w.r.t. $Pd(OAc)_2$.

3.3.4. Solid State Characterization of the Precipitate and Recyclability

As stated earlier, after the catalytic transformation was over, a black gummy precipitate was observed. This black solid was filtered and washed with excess of benzene. The solid was characterized by scanning electron microscopy (SEM), FT-IR spectroscopy, and solid state ^{29}Si NMR spectroscopy. Solid state ^{29}Si NMR spectra showed signals corresponding to Si–H (−36.15), Si–OCOR (−64.74), Si–OH
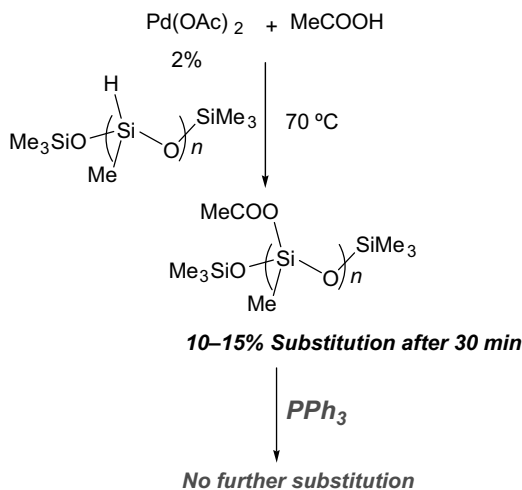
Scheme 3.9. Schematic representation of TPP poisoning experiment.
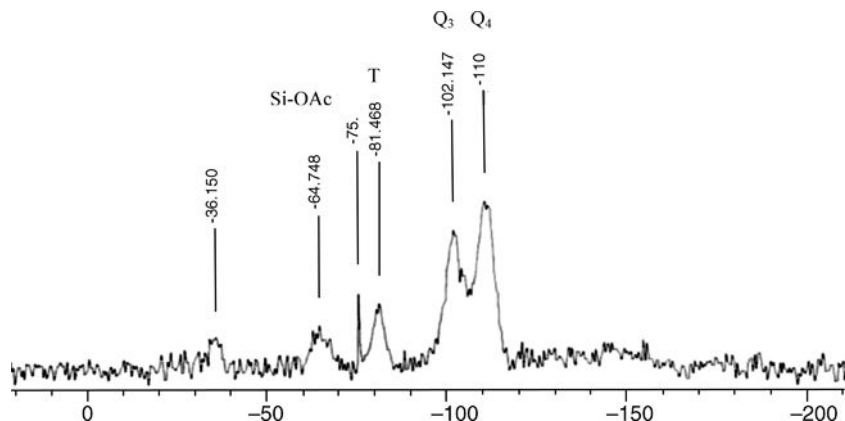
Figure 3.6. Solid state ^{29}Si NMR spectra of the precipitate.

(-81.46), and SiO_2 (-110.94) species (Figure 3.6), suggesting the solid to be a partially condensed polysiloxane network. In various batches of the reaction mixture, some variations in the intensity of these signals were observed but by and large the NMR spectra remained similar, indicating the presence of the same species.

Solid state FT-IR characterization of solid substantiated the presence of the aforementioned species. SEM analysis of this solid manifested spherical morphology of polysiloxane-conjugated Pd nanoclusters in the 40–50 nm size regime. Based on the above results, it can be concluded that the solid is a partially condensed polysiloxane network conjugated with Pd nanoclusters. Furthermore, the possibility of reusability of precipitated solid as catalyst was explored by injecting the substrate into the Schlenk tube with precipitated solid. After 30 min of stirring, the mixture became homogeneous. Multinuclear spectroscopy characterizations of the reaction mixture confirmed formation of polysilyl ester.

3.4. SYNTHESIS AND CHARACTERIZATION OF Pd–POLYSILOXANE NANOCONJUGATES AS STABLE ISOLABLE POWDERS

The wide range of properties of nanomaterials for biological and material applications emerge from controlled embedment of nanoparticles in designed and tunable polymer matrices.[45] Several biological templates like ferritin protein coat and viral protein cages, matrix assisted assemblies zeolite, polyimine, and organosilica are preformed cavities commonly used for the formation of metal nanoparticles.[46–48] But multigram syntheses of stable nanoclusters is a worthy challenge to target. One of our objectives is not only to develop the synthetic and repeatable route to stable nanoclusters, but also to be able to scale-up the process. Our approach is to utilize polymethylhydrosiloxane (PMHS) as stabilizing agent due to its dual property of acting as a "reducing" and a "stabilizing" agent. PMHS has been reported to produce hydrogen in the presence of certain metal complexes and this property could be used

to reduce the metal complexes into zero oxidation state.[49–53] PMHS stabilization of metal nanoclusters, however, is unprecedented, but our hypothesis is that the PMHS backbone[54] possesses certain properties that are unique to a single polymer and these properties can be exploited to generate isolable, stable, and catalytically active metal nanoclusters. Some of the unique and desirable properties and their consequences are summarized bellow:

(i) It is assumed that the unusual freedom of rotation around the Si–O–Si bonds of the PMHS backbone will allow for their wrapping around the metal cluster, which in turn may impart stability to the particles at the nanoscale.

(ii) The thermal stability of the polysiloxanes will provide thermal stability and facilitate the isolation of polysiloxane stabilized nanoclusters.

(iii) In our approach, since only weakly interacting Si–H bonds of polysiloxanes will act as stabilizing agents, it is our expectation that the major fraction of the generated nanoparticle surface will remain unpassivated or weakly passivated. Unlike the strong coordinating ligands, this type of stabilization will facilitate the interaction with substrates undergoing catalytic transformations. available to participate in catalytic reactions.

(iv) Solubility properties of PMHS will facilitate the dispersion of the nanoparticles, thus making such catalysts widely applicable.

(v) Finally, since polyhydrosiloxanes in the presence of metals and moisture can crosslink, this may allow the formation of templated heterogeneous catalysts in the form of powders, which will redisperse if exposed to proper solutions.

Keeping all these advantageous features of the polysiloxanes, reactions were carried out to generate Pd nanoclusters in the presence of PMHS. Under optimized reaction conditions, the synthesis of Pd nanoclusters was carried out in a 200 mL round bottom (RB) flask at room temperature. $Pd(OAc)_2$ (0.112 g, 0.5 mmol) was dissolved in 50 mL of toluene and PMHS (0.90 mL, 15.0 mmol) was added to this yellow solution. The color change from yellow to black was observed within 1 min of stirring with vigorous evolution of gas (H_2 presumably). Color change was monitored by UV–visible analysis of the reaction mixture. A featureless UV–visible spectra (Figure 3.7) indicated conversion of Pd(II) to Pd(0). After stirring the solution for 1 h, a black solid begins to precipitate out and the solution turned colorless after the next 3–4 h of stirring. At this juncture, black precipitate was filtered and washed with excess of toluene and the resulting solid was analyzed by various techniques. SEM characterization of the solid was carried out to investigate the morphology of the solid at the nanometer size scale. Spherical particles in the 40–50 nm size regime were found, as is evident by the SEM image (Figure 3.8). Energy dispersive spectroscopy (EDS) examination of the solid showed the solid material to be composed of 8.05 wt% palladium, 46.62 wt% silicon, 25.05 wt% carbon, and 20.25 wt% oxygen, respectively. Presence of the above species was confirmed with solid state ^{29}Si NMR
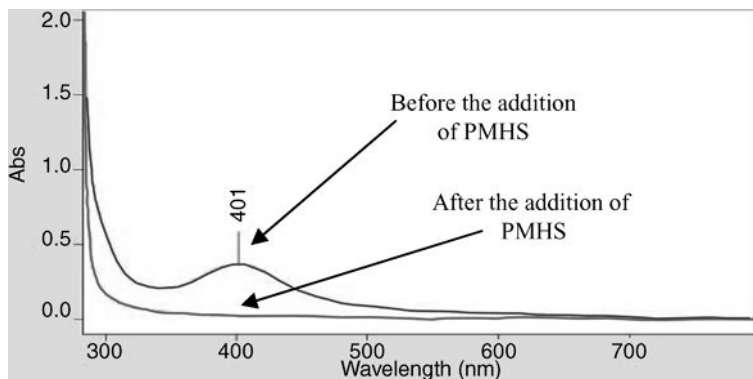
Figure 3.7. UV–visible characterization of Pd–polysiloxane nanoconjugates.

spectroscopy. Peaks at δ -36.15 (Si–H), -81.46 (T), -102.58 (Q$_3$), and 112.26 (Q$_4$) (ppm) in ^{29}Si NMR (see Figure 3.11) were found. FT-IR spectra also show characteristic signals associated with Si–H and Si–O–Si bonds {2162(m), 1021 (b), 900.77(s), 2964.86(m)}.

X-ray photoelectron spectroscopy (XPS) studies of the solid were also undertaken. XPS measurements of the solid showed Pd(3d$_{5/2}$) 335.9 eV and Pd(3d$_{3/2}$) 341.0, respectively, corresponding to palladium(0) species.[55–60] "Pd–polysiloxane" nano-composites obtained in the form of solid are air stable and can be stored at room temperature without any extra precautions for long periods of times.
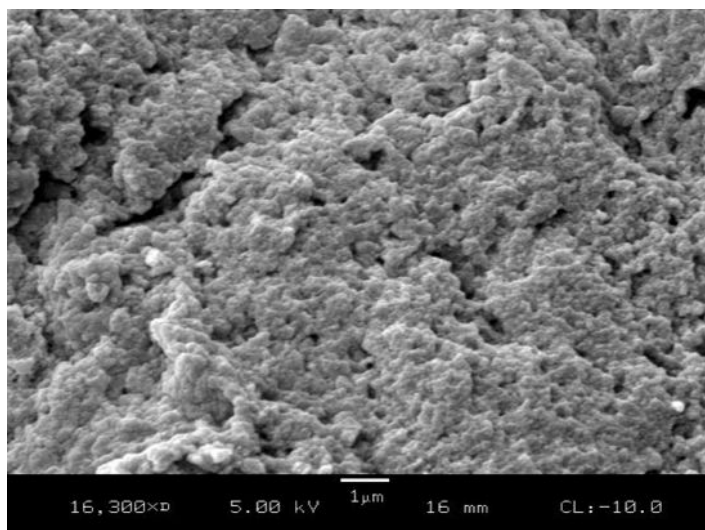
Figure 3.8. Representative SEM image of the polysiloxane conjugated Pd nanoclusters.

3.5. CATALYTIC APPLICATIONS OF POWDERED Pd NANOCLUSTERS: MACROMOLECULAR GRAFTING

3.5.1. Silaesterification of PMHS

The catalytic silaesterification activity of the isolable Pd nanoclusters was explored with 1,1,1,3,5,5,5-heptamethyltrisiloxane (HMTS) and PMHS as substrates. Substitution of both the substrates was performed under similar reaction conditions as used for Pd(OAc)$_2$. Indeed, the substitution of both the substrates proceeded with ease. A comparative study was performed with isolated Pd nanoclusters and Pd(OAc)$_2$ as catalyst and results are summarized in Table 3.1. As is clear from the table, comparable results of reactivity and selectivity were observed. Moreover, isolated Pd nanoclusters were reused for catalysis for three cycles without significantly losing the activity.

Based on the above results, we have proposed a classical Chalk–Harrod-like mechanism for the Pd nanocluster catalyzed reaction (Scheme 3.10).[14] The first step involves the reduction of Pd(OAc)$_2$ to zero-valent palladium nanoparticles followed by stabilization with a polysiloxane network. These particles followed the conventional pathway of oxidative-addition and reductive-elimination cycles to generate silyl esters. After the transformation was over, these palladium colloids precipitated out of the solution as a black solid supported on a polysiloxane network. The presence of the soluble polysiloxane matrix, which was not fully condensed in the form of silica, allows particle redispersion—thus allowing particles to be reused as catalyst.

3.5.2. Pd-Nanoparticle Catalyzed Alcoholysis of PMHS: Tailored Hybrid Polysiloxanes

In this part of the chapter, we investigate the tailoring of polymer template PMHS via a palladium nanoparticle catalyzed alcoholysis reaction.[15d] This investigation allowed us to attach various functionalities via an alcohol group. The major driving force for this research was availability and abundance of alcohol containing functionalities as well as its potential utility as a method of choice to produce the modern materials on an industrial scale. A representation of the strategy is shown in Figure 3.9.

The Pd nanoparticles were synthesized as described in the previous section. Catalytic efficiency of "Pd–polysiloxane nanoconjugates" was explored by using them as a catalyst for macromolecular grafting of PMHS with *tert*-butanol.[15d] In a

TABLE 3.1. Comparison of the Catalytic Activity Toward Silaesterification Reactions

Acids	Substrates	"Pd" Colloids	2% Pd(OAc)$_2$	Yields (%)
CH$_3$COOH	1a	RT, 5 h	RT, 8 h	95%
CH$_3$COOH	1b	70°C, 8 h	70°C, 12 h	95%
C$_6$H$_5$COOH	1a	70°C, 6 h	70°C, 6 h	95%
C$_6$H$_5$COOH	1b	70°C, 24 h	70°C, 24 h	90%
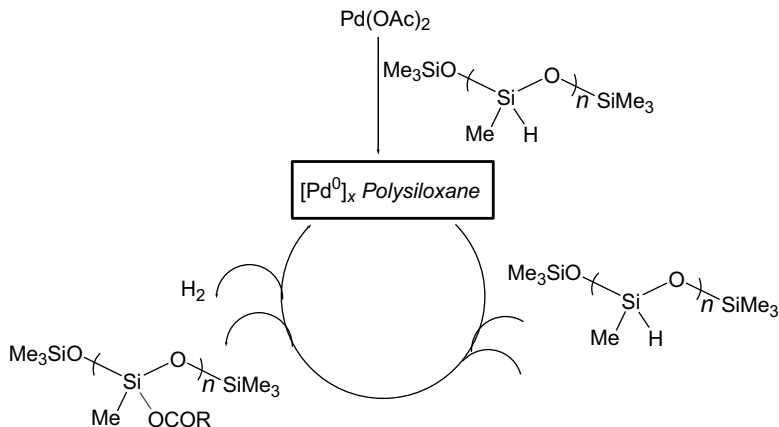
Scheme 3.10. Proposed reaction mechanism during silaesterification reaction.

typical alcoholysis experiment, Pd nanoparticles (0.01 g), were suspended in 4 mL of benzene at room temperature followed by addition of PMHS (0.12 mL, 2.0 mmol) and *tert*-butanol (0.19 mL, 2.0 mmol). The colorless reaction mixture gradually turned to a homogeneous black solution, indicating the generation of soluble nanoclusters. Evolution of gas (H_2 presumably) was also observed during the reaction. TEM study of the reaction mixture during the catalysis was undertaken. Indeed, the catalytic active Pd nanoclusters were present in the reaction mixture (Figure 3.10). A comparatively narrow distribution of particle size (2–6 nm) with an average particle size of 2.60 nm was observed with "Scion Image Software" assisted particle size analysis plot of TEM images. ^1H NMR examination of the reaction mixture after regular intervals shows gradual disappearance of Si–H signal (δ 4.85) and –OH signal (δ 2.09) associated with PMHS and *tert*-butanol, respectively.

Concomitant rise in the viscosity of the reaction mixture was also noticed. ^{13}C NMR spectroscopy manifested the appearance of a new peak at δ 69.83 (Me_3C–OSi) representative of a silane substituted tertiary carbon center of *tert*-butanol beside the peak at δ 68.02 (Me_3C–OH). After 34 h, the intensity of the silane substituted *tert*-carbon peak reached optimum level, while the unsubstituted carbon peak disappeared completely. ^{29}Si NMR spectra also corroborated complete transformation of Si–H
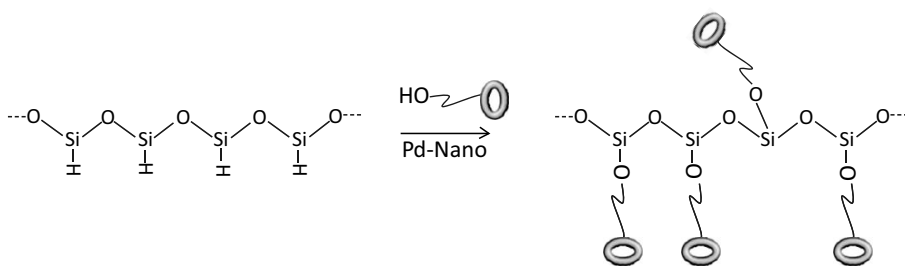
Figure 3.9. A representation of the Pd-nanoparticle catalyzed alcohol grafting strategy.
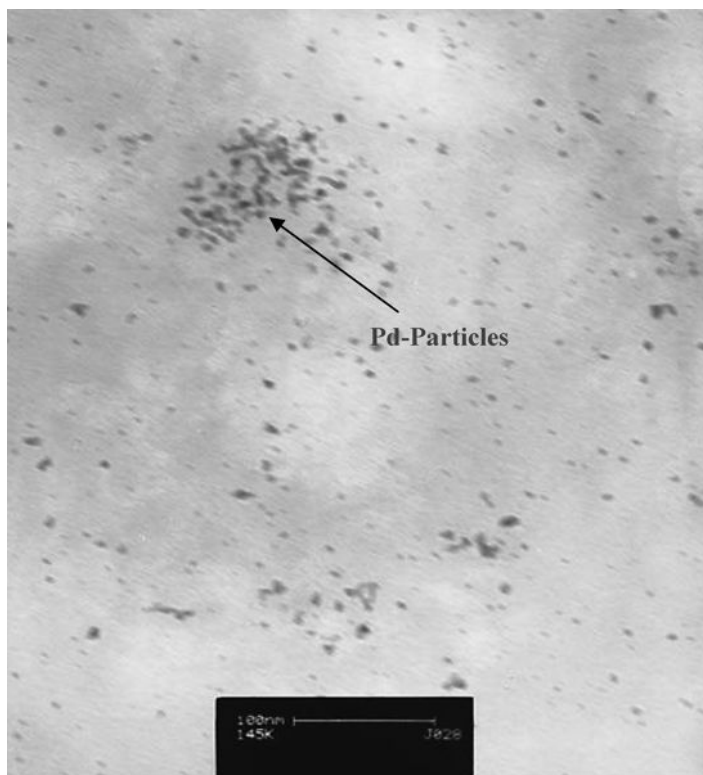
Figure 3.10. TEM image of the of the Pd nanoparticles obtained during the catalytic grafting.

bonds (δ −36.45) to *tert*-butoxy group (δ −54.78, Me$_3$C–OSi). After complete substitution, the reaction mixture was subjected to high-speed centrifugation (15 min), which led to the isolation of "Pd" nanoclusters at the bottom of the centrifuge tube. Filtration of the catalysts and subsequent evaporation of the solvent under reduced pressure yielded viscous *tert*-butoxy grafted polysiloxane.

In order to investigate the utility of this catalysis process, alcoholysis of PMHS was examined in the presence of a number of alcohols. The method was found to be applicable to primary, secondary, and tertiary alcohols and led to selective formation of corresponding polyalkoxysiloxanes (Table 3.2) in good yields. Macromolecular grafting of PMHS was equally successful with aromatic alcohols (Entries 5, 6, and 7; Table 3.2). Pd nanocluster catalyzed reactions with sterically bulky alcohols, such as benzhydrol, were comparatively slow but furnished desired product in good yields. Depending on the electronic and/or steric nature of the alcohols, highly viscous or solid products were recovered after the evaporation of solvent in each case.[15d]

Encouraged by these results, catalysis was further extended to reactions of functional alcohols. Grafting of PMHS with functional alcohols can offer a way to further modify the polymer backbone with functionalities, which are otherwise

TABLE 3.2. Pd Nanocluster Catalyzed Synthesis of Functional Polymethylalkoxysiloxanes

Entry	Alcohols	Reaction Conditions	Products	Yield (%)
1		34 h/70°C		90%
2		24 h/70°C		95%
3	CH_3CH_2OH	4 h/70°C		98%
4	$HO(CH_2)_9CH_3$	8 h/70°C		97%
5		24 h/70°C		95%
6		30 h/70°C		90%
7		35 h/70°C		80%
8		34 h/70°C		95%
9		28 h/70°C		95%
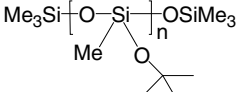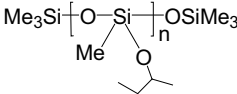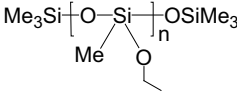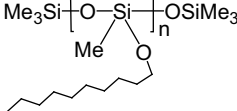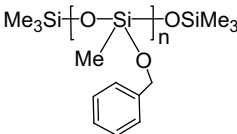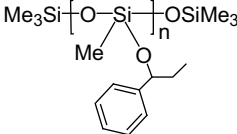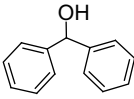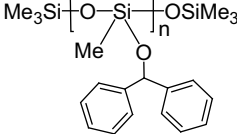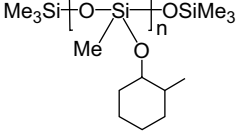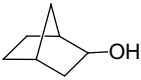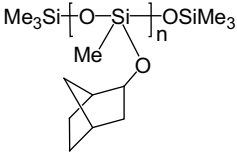
difficult to substitute directly to a polysiloxane chain. For instance, the attachment reactions of 3-*tert*-butoxycyclohexanol and hydroxypropylphthalimide can be cited as representative examples because these functionalities are rarely attached to polysiloxane backbones in a selective fashion. Examples of these two reactions are shown in Scheme 3.11.

Facile and selective reactions with 3-hydroxy-2-butanone, 4-methoxybenzyl alcohol, and 3-*tert*-butoxycyclohexanol were observed without any side reactions and yielded corresponding alkoxy polysiloxanes in excellent yields (Entries 1, 4, and 5; Table 3.3). Amino substituted polysiloxanes are desirable products due to their utility in various technological applications, but salt-free direct methods of their preparation are quite rare. To our surprise, the Pd-nanocluster alcoholysis reaction of PMHS with 2-(2-aminoethylamino)ethanol provided corresponding amino substituted polysiloxane (Entry 2, Table 3.3) in fair yields without undergoing degradation or rearrangement reactions. However, it should be pointed out that double the amount of solvent was used for alcoholysis of amine-functionalized alcohols, since the viscosity of the reaction mixture increased rapidly (as compared to nonamine functionalized alcohols) as reaction progressed. Similarly,
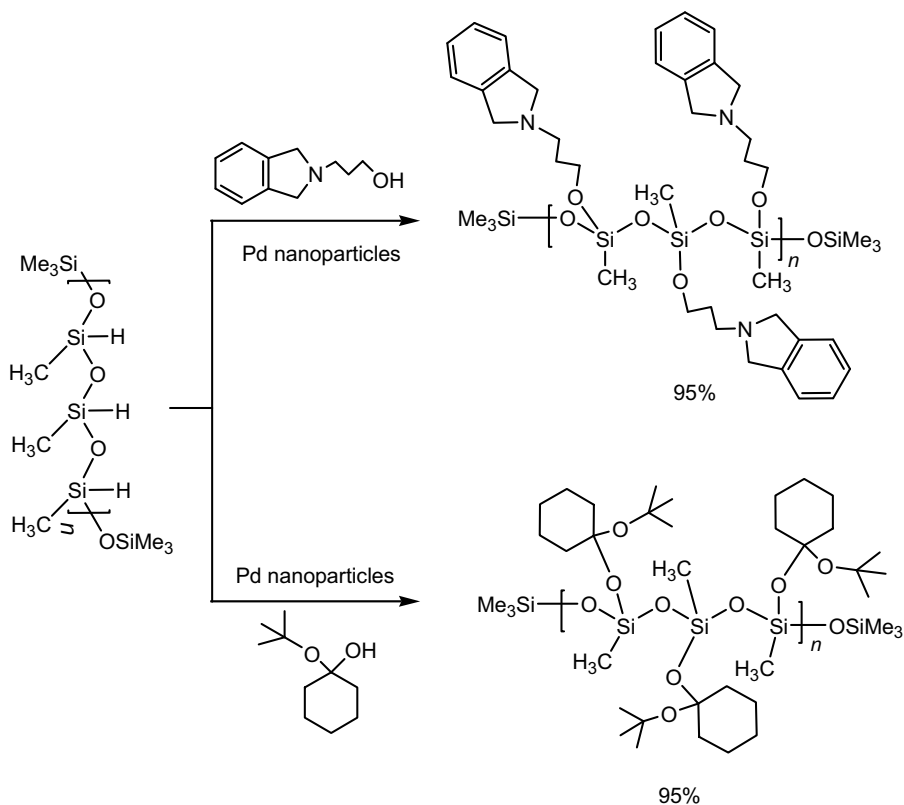
Scheme 3.11. Pd-nanoparticle catalyzed grafting of PMHS with functional alcohols.

TABLE 3.3. Pd-Nanocluster Catalyzed Synthesis of Functional Polymethylalkoxysiloxanes

Entry	Alcohols	Reaction Conditions	Product	Yield(%)
1		24 h/70°C		95%
2		24 h/70°C		98%
3		30 h/70°C		80%
4		30 h/70°C		95%
5		30 h/70°C		95%
6		30 h/70°C		95%
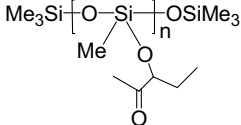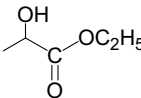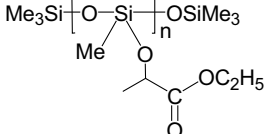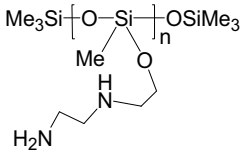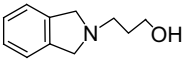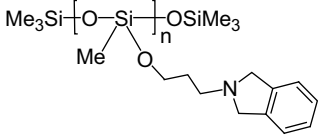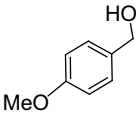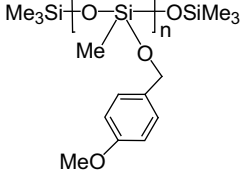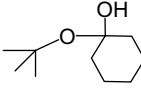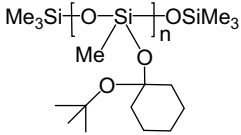
hydroxypropylphthalimide reacted with PMHS to produce aromatic amine substituted siloxane (Entry 3, Table 3.3) in excellent yield.

3.6. RECYCLABILITY STUDY

One of the major advantages of nanoparticle catalyzed reactions could be their pseudoheterogeneous properties by which the particles can be separated from the reaction mixtures. Based on our experience with other catalytic transformations,
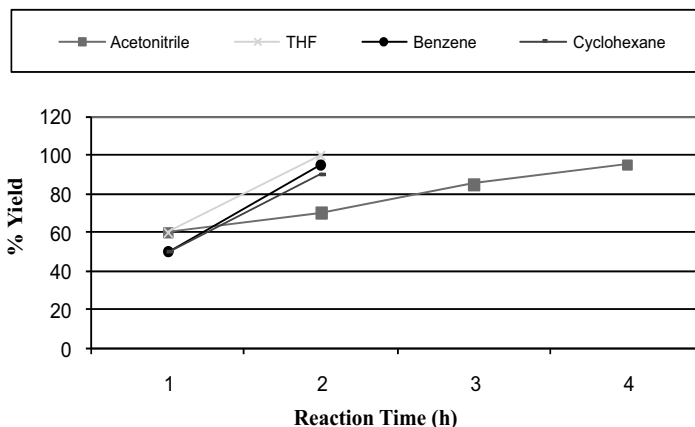
Figure 3.11. Plot of the reaction rates of PMHS grafting with ethanol in organic solvents.

where we were able to achieve facile and efficient separation of nanoclusters from the reaction mixture, we wanted to explore the possibility of reusability of catalyst in the present catalysis as well. Thus, the particles were separated as precipitate and this precipitate was washed with benzene (15 mL) and reused as catalyst for additional catalytic transformation. Almost identical activity and selectivity were observed, even after three recycling studies with the same batch of catalyst.

3.7. SOLVENT EFFECTS

A study of solvent effect on the catalytic efficiency of Pd–polysiloxane nanoconjugates was performed in common organic solvents. PMHS alcoholysis with ethanol was probed in four different solvents—that is, tetrahydrofuran (THF), benzene, cyclohexane, and acetonitrile—under identical reaction conditions. As is evident from the plot in Figure 3.11, Pd–polysiloxane nanoconjugates displayed almost similar catalytic activity in THF, benzene, and cyclohexane. The rate of PMHS alcoholysis is rather sluggish in acetonitrile as compared to other solvents. The slow rate of reaction in acetonitrile can be attributed to the ligand coordination imparted to the nanoclusters by the –CN functionality of acetonitrile (MeCN), making them less active for the catalytic transformation.

3.8. CATALYTIC STUDIES

3.8.1. Catalyst Poisoning Study: Mercury Poisoning Experiment

Mercury (Hg) is well known to poison the surface of metal nanoclusters, such as Ni, Pd, and Pt, either via forming an amalgam with the nanocluster or by physically adsorbing onto the cluster surface.[42,43] Hence, Hg can serve as a tool to probe the true
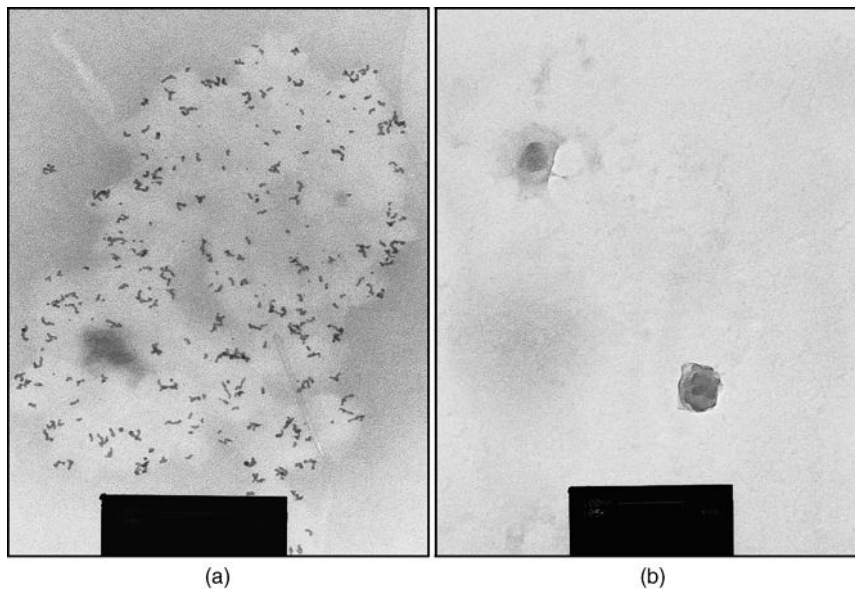
Figure 3.12. (a) TEM image without Hg. (b) TEM image with Hg.

nature of a catalyst during catalytic transformations. TEM and ^{1}H NMR spectroscopy were employed to study the effects of mercury during the functionalization reactions with ethanol. The reaction mixture was examined with TEM (Figure 3.12a) to establish the presence of "Pd–polysiloxane" nanoconjugates before the addition of mercury. After confirming the existence of Pd nanoclusters in the reaction mixture, Hg was added to the reaction mixture. ^{1}H NMR spectroscopy showed only 10–15% conversion to alcoholysis product. TEM examination (Figure 3.12b) of the grid prepared after 30 min of the addition of Hg demonstrated complete disappearance of Pd nanoparticles from the reaction mixture. A total of 15–20% expected product was formed after addition of Hg. If the stirring continued for a further 24 h, there was no increase in the product, indicating complete absence of catalytically active species.

3.8.2. Catalyst Poisoning Study: Thiol Poisoning Study

It has been suggested that the major part of the catalytic activity of the nanoparticles can arise from the kinks and defects present on the surface of the nanoparticles. By passivating these sites with strong coordinating ligands, it is possible to suppress the catalytic efficiency of the nanoparticles. Sulfur containing ligands such as thiols are known coordinating ligands, which can strongly bind to the metal nanoparticle surface and hence make them passive for catalytic applications.[61, 62]

In order to see the impact of the presence of thiol containing agents and to develop the proof of concept for this catalysis, a series of experiments were carried out to find the exact amount of dodecanethiol needed to fully passivate the surface of Pd particles during the reaction of PMHS with ethanol. DDT was chosen because of its
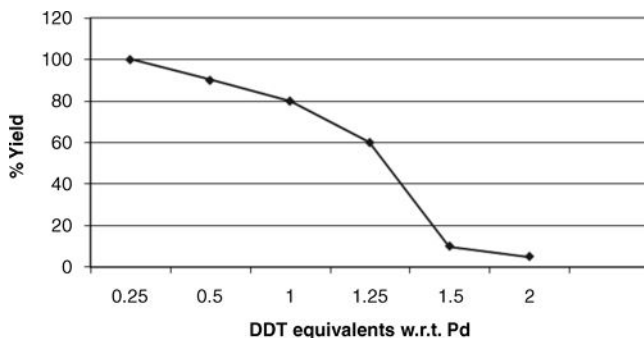
Figure 3.13. DDT poisoning study.

solubility properties. It was found that in the presence of 1.5 equivalent (with respect to Pd) of dodecanethiol (DDT), only 2–6% ethanol functionalization of PMHS took place even after 24 h of reaction under identical conditions, in which total conversion was achieved without DDT being present in the reaction mixture (see Figure 3.13).

3.9. REDISPERSION STUDY

Better catalytic efficiency of homogeneously dispersed nanoparticles than their heterogeneous counterpart prompted us to study the redispersion of Pd–polysiloxane nanoconjugates in common organic solvents. In a typical redispersion experiment, Pd–polysiloxane nanoconjugates (0.01 g) were suspended in 4 mL of benzene followed by stirring at 70°C for 30 min. No color change was observed during this period. EM (electron microscopy) analysis of the solution showed an absence of nanoparticles in solution. At this juncture, PMHS (0.12 mL, 2.0 mmol) was added to the above solution. The color of the solution gradually changes, yielding a homogeneous black solution after 30 min of the addition of PMHS. As is evident from the EM image, polysiloxane encapsulated Pd nanoclusters were present in the homogeneous black solution. The existence of polysiloxane encapsulated Pd nanoclusters demonstrates a unique approach for the homogenization of heterogeneous nanocatalyst in the presence of PMHS. To further investigate the redispersion phenomenon, a separate experiment was performed with polydimethysiloxane (PDMS) as the redispersion agent under identical conditions. EM assay of PDMS solution confirms no sign of nanoclusters, affirming the need for Si–H bonds for the homogenization (size reduction) process. Catalytic activity of the homogenized nanoclusters was investigated by adding *tert*-butanol to the solution containing homogeneously dispersed Pd nanoclusters. In situ EM characterization of the reaction mixture was performed after regular intervals to probe the active catalytic participation of Pd nanoclusters. EM studies of the mixture showed no visible change in the size and morphology of nanoclusters after the addition of alcohol. Catalytic transformation was also monitored with ^{1}H NMR spectroscopy, which showed complete conversion of Si–H bonds to Si–O–*tert*-butyl bonds after 34 h of reaction at 70°C. Complete

catalytic conversion substantiates the ligand-free and physical nature of polysiloxane interaction with "Pd" nanoclusters.

3.10. EXPERIMENTAL SECTION

3.10.1. General Information

All the experiments and manipulations were performed under a dry argon or nitrogen atmosphere using a standard Schlenk-tube technique. Solvents were purchased from EM Science (Merck) and distilled over sodium/benzophenone. PMHS (MW 2000, 32–33 Si–H units), 1,1,1,3,5,5,5-Heptamethyltrisiloxane and $Pd(OAc)_2$ were obtained from Aldrich and used as received. All alcohols used in this study were procured from Aldrich and were stored over molecular sieves prior to use. Acetic acid was received from J.T. Baker and dried over magnesium sulfate prior to use. Benzoic acid was purchased from Fluka and used without further drying. ^{1}H NMR and ^{13}C NMR spectra were recorded in $CDCl_3$ on Varian Unity NMR instruments (200 MHz). Varian Unity NMR instruments (300 MHz and 600 MHz) were used to carry out DP/MAS ^{29}Si NMR and liquid state ^{29}Si NMR spectroscopy experiments, respectively. Proton spectra were referenced internally to protonated solvent shifts. All the peaks in NMR spectra were reported in ppm. UV–visible spectra were recorded on a Varian Cary Model 50 UV Spectrophotometer. An Amray 1910 FE-scanning electron microscope (SEM) equipped with Thermo-Electron Noran-System-Six energy dispersive spectroscope (EDS) was used to conduct the morphological studies and the elemental analysis of polysiloxane-conjugated Pd nanoclusters. For SEM analysis, the solid sample was sprinkled on the carbon tab and coated before analysis. X-ray photoelectron spectroscopy (XPS) study of the catalyst was performed with an Omicron Nanotechnology XPS instrument equipped with Mg Kα X-ray source ($h\nu = 1253.6$ eV) and type EA125 analyzer with rest energy of 100.0 eV and EAC 2000 controller. A Philips CM 100-transmission electron microscope (TEM) was used to investigate the presence of Pd–polysiloxane nanoconjugates during the reaction. A few drops of the reaction mixture were taken out using a syringe and directly deposited on a carbon-formvar coated copper grid at room temperature. The solvent was allowed to evaporate from the grid under normal temperature and pressure for 1 h before the TEM examination of the grid. The particle size analysis of the Pd nanoclusters was carried out manually on the TEM images, using "Scion image" software. Around 100–150 particles were measured using the software on each TEM image before plotting the "Particle Size Analysis" plot.

3.10.2. Generation of Pd–Polysiloxane Nanoconjugates

$Pd(OAc)_2$ (0.112 g, 0.5 mmol) was dissolved in 50 mL of toluene in a 200 mL round-bottom flask at room temperature in open air. PMHS (0.90 mL, 15.00 mmol) was added to this solution. A color change from yellow to black was observed within 5 min of stirring with vigorous evolution of gas (H_2 presumably). A black solid was

observed after stirring the solution for 2–3 h, and the reaction mixture turned colorless. The stirring was stopped at this point, the reaction mixture was filtered under vacuum, and the black residue was collected after washing with an excess of toluene. The black solid obtained was characterized by CP/MAS ^{29}Si NMR spectroscopy, FT-IR spectroscopy, and scanning electron microscopy (SEM). ^{29}Si (DP/MAS NMR) δ −36.15 (Me–Si–H-containing silicons), −81.46 (Me–Si–OH), −102.58 (SiO$_2$), 112.26 (SiO$_2$). FT-IR spectra (KBr) 2162(m), 1021(b), 900.77(s), 2964.86 (m).

3.10.3. Silaesterification Reactions: Typical Procedure

Pd(OAc)$_2$ or Pd nanoclusters (0.010 g) and acetic acid (0.060 mL, 1.00 mm) were mixed in benzene (4.0 mL) and the Schlenk tube was degassed by three freeze–pump–thaw cycles. Upon addition of PMHS (0.06 mL, 1.0 mmol) to the reaction mixture, gas evolution (presumably H$_2$) was observed. The progress of the reaction was monitored by ^{1}H and ^{29}Si NMR spectra. The signal at −36.28 ppm (Si–H) in the ^{29}Si NMR disappeared, and a new signal appears at −58.6 ppm in ^{29}Si spectra, signifying an acetate-substituted silicon center. Stirring was stopped after 8 h. The black turbid solution turned colorless and catalyst precipitated out as a black solid. The liquid was removed by syringe and was evaporated under vacuum to furnish pure polymethyacetylsiloxane as a glue-like liquid.

3.10.4. Alcoholysis of PMHS: Typical Procedure

Pd–polysiloxane composite (0.010 g, 0.805 mg Pd^0), CH$_3$CH$_2$OH (2.0 mmol, 0.12 mL), and PMHS (2.0 mmol, 0.12 mL) were mixed together with 4 mL of benzene in a 50 mL Schlenk tube. Reaction mixture was stirred at 70°C for 2 h. Progress of the reaction was examined with ^{1}H and ^{29}Si NMR spectroscopy. Centrifugation of the reaction mixture yielded black solid (which can be further utilized as catalyst) and clear solution. Evaporation of the solvent from the clear solution yielded ethoxy-substituted polysiloxane in quantitative yields.

Poly(methyl-tert-butoxysiloxane) (Entry 1, Table 3.2). ^{1}H NMR (CDCl$_3$, 200 MHz) δ 0.48, 1.22(m), 1.52(m), ^{13}C NMR (CDCl$_3$, 200 MHz) δ −0.26, 32.45, 69.83, ^{29}Si NMR (CDCl$_3$, 600 MHz) −54.78 (broad, SiMe).

Poly{methyl(3-methylbutoxy)siloxane} (Entry 2, Table 3.2). ^{1}H NMR (CDCl$_3$, 200 MHz) δ 0.16, 1.08(m), 1.33(m), 1.45(m), 4.08(m), ^{13}C NMR (CDCl$_3$, 200 MHz) δ −1.23, 14.00, 20.32, 61.34, 66.73, ^{29}Si NMR (CDCl$_3$, 600 MHz) δ 57.61 (broad, SiMe).

Poly(methylethoxy)siloxane (Entry 3, Table 3.2). ^{1}H NMR (CDCl$_3$, 200 MHz) δ −0.04, 1.03(m), 3.48(m), ^{13}C NMR (CDCl$_3$, 200 MHz) δ −2.97, 19.52, 59.50, δ ^{29}Si NMR (CDCl$_3$, 600 MHz) δ 52.26 (broad, SiMe).

Poly(methyldecyloxy)siloxane (Entry 4, Table 3.2). ^{1}H NMR (CDCl$_3$, 200 MHz) δ 0.22, 0.88, 1.25(m), 1.41(m), 1.57(m), 3.47(m), 3.79(m), ^{13}C NMR (CDCl$_3$, 200 MHz) δ −3.99, 14.35, 23.06, 26.18, 29.75, 29.88, 29.99, 30.06, 32.30, 33.09, 62.80, ^{29}Si NMR (CDCl$_3$, 600 MHz) δ −56.46, 57.12 (broad, SiMe).

Poly(methylbenzyloxy)siloxane (Entry 5, Table 3.2). ^{1}H NMR (CDCl$_3$, 200 MHz) δ 0.17, 4.55, 7.16(m), 7.29(m), 7. 34(m), 7.38(m), ^{13}C NMR (CDCl$_3$, 200 MHz) δ −2.84, 67.04, 128, 128.36, 129.57, 135.03, ^{29}Si NMR (CDCl$_3$, 600 MHz) δ −56.81 (broad, SiMe).

Poly{methyl(1-phenyl-1-propanoxy)siloxane} (Entry 6, Table 3.2). ^{1}H NMR (CDCl$_3$, 200 MHz) δ 0.09, 0.82(t), 1.69(q), 4.43(t), 6.90(m), 7.16(m), 7.36(m), 7,68(m), ^{13}C NMR (CDCl$_3$, 200 MHz) δ 0.68, 9.90, 31.66, 75.67, 125.79, 127.18, 128.12, 144.47 ^{29}Si NMR (CDCl$_3$, 600 MHz) δ 52.26 (broad, SiMe).

Poly(methylbenzhydroxy)siloxane (Entry 7, Table 3.2). ^{1}H NMR (CDCl$_3$, 200 MHz) δ 0.14, 3.85, 6.85(m), 7.15(m), 7.24(m), 7.50(m), 7.64(m), ^{13}C NMR (CDCl$_3$, 200 MHz) δ 76.00, 126.53, 127.33, 128.25, 143.96, ^{29}Si NMR (CDCl$_3$, 600 MHz) δ −57.18, −54.03 (SiMe).

Poly{methyl(4-methylcyclohexanoxy)siloxane} (Entry 8, Table 3.2). ^{1}H NMR (CDCl$_3$, 200 MHz) δ 0.09, 0.76(m), 1.17(m), 1.62(m), 1.84(m), 3.39(m), 3.67 (m), ^{13}C NMR (CDCl$_3$, 200 MHz) δ −53.54 (broad, SiMe).

Poly(methylnorborneoxy)siloxane (Entry 9, Table 3.2). ^{1}H NMR (CDCl$_3$, 200 MHz) δ 0.12, 0.94(m), 1.35(m), 1.58(m), 2.15(m), 3.62(m), 3.89(m), ^{13}C NMR (CDCl$_3$, 200 MHz) δ −3.57, 24.28, 28.33, 34.49, 35.26, 42.37, 44.07, 74.63, ^{29}Si NMR (CDCl$_3$, 600 MHz) δ −59.11 (broad, SiMe).

Poly{methyl(2-butanone-3-oxy)siloxane} (Entry 1, Table 3.3). ^{1}H NMR (CDCl$_3$, 200 MHz) δ 0.09, 1.73(m), 2.07(m), 3.60(m), ^{13}C NMR (CDCl$_3$, 200 MHz) δ −4.13, 19.24, 25.47, 67.47, 210.13, ^{29}Si NMR (CDCl$_3$, 600 MHz) δ −57.94 (broad, SiMe).

Poly[{methyl(butyricacidethylester)-2-oxy}siloxane] (Entry 2, Table 3.3). ^{1}H NMR (CDCl$_3$, 200 MHz) δ 0.24, 0.93(m), 1.19(m), 3.39(m), 3.90, ^{13}C NMR (CDCl$_3$, 200 MHz) δ −3.37, 17.91, 18.09, 19.84, 35.01, 72.53, ^{29}Si NMR (CDCl$_3$, 600 MHz) δ −59.21 (broad, SiMe).

Poly[methyl-{2-(2-aminoethyl-amino)ethanoxy}siloxane] (Entry 3, Table 3.3). ^{1}H NMR (CDCl$_3$, 200 MHz) δ 0.006, 2.32(m), 2.53(m), 3.46(m), ^{13}C NMR (CDCl$_3$, 200 MHz) δ −3.32, 41.37, 51.94, 60.24, 78.17, ^{29}Si NMR (CDCl$_3$, 600 MHz) δ −58.30 (broad, SiMe).

Poly{methyl(phthalimide-3-propyloxy)siloxane} (Entry 4, Table 3.3). ^{1}H NMR (CDCl$_3$, 200 MHz) δ −0.33 (m), 1.46(m), 3.23(m), 6.75(m), 6.83(m), 6.95(m), ^{13}C NMR (CDCl$_3$, 200 MHz) δ −4.98, 0.98, 30.57, 34.69, 59.55, 122.21, 131.53, 133.14, 167.662 ^{29}Si NMR (CDCl$_3$, 600 MHz) δ −57.93 (broad, SiMe).

Poly{methyl(4-methoxybenzyloxy)siloxane} (Entry 5, Table 3.3). ^{1}H NMR (CDCl$_3$, 200 MHz) δ 0.14, 2.28, 4.45, 7.09(m), 7.11(m), 7.29(m), 7.38(m), ^{13}C NMR (CDCl$_3$, 200 MHz) δ −2.84, 22.26, 66.09, 128.22, 129.56, 130.22, 138.08, ^{29}Si NMR (CDCl$_3$, 600 MHz) δ −56.93 (broad, SiMe).

Poly{methyl(tert-butoxycyclohexanoxy)siloxane} (Entry 6, Table 3.3). ^{1}H NMR (CDCl$_3$, 200 MHz) δ 0.13, 0.72(m), 1.32(m), 1.63(m), 1.94(m), 3.25(m), 3.81 (m), −3.57(b), ^{13}C NMR (CDCl$_3$, 200 MHz) δ 20.65, 25.35, 27.31, 31.86, 33.52, 35.62, 47.81, 47.91, 65.26, 70.60, ^{29}Si NMR (CDCl$_3$, 600 MHz) δ −58.80 (broad, SiMe).

CONCLUSION

In conclusion, we have demonstrated the first example of Pd nanoparticles as a selective and recyclable catalyst for the alcoholysis of polyhydrosiloxane. Fair numbers of alcohols with diverse structures (primary, secondary, sterically bulky, and functionalized alcohols) were selectively and efficiently grafted onto the polysiloxane backbone without any side reactions and under moderate reaction conditions. Additionally, active participation of Pd nanoclusters during the catalytic transformations was established by "in situ" EM analysis and controlled poisoning experiments. Moreover, a new approach for the synthesis and stabilization of Pd nanoclusters as a stable isolable powder and their redispersion in common solvents was presented.

ACKNOWLEDGMENTS AND CREDITS

REFERENCES

1. Chauhan, M.; Chauhan, B. P. S. Boudjouk, P. *Org. Lett.*, **2000**, *2* (8), 1027.
2. Chauhan, B. P. S.; Ready, T. E.; Al-Badri, Z.; Boudjouk B. *Organometallics*, **2001**, *20*, 2725.

3. Chauhan, B. P. S.; Boudjouk, P. *Tetrahedron Lett.*, **2000**, *41*, 1127.

4. Gray, G. W.; Hawthorne, W. D.; Lacey, D.; White, M. S.; Semlyen, J. A. *Liq. Cryst.*, **1989**, *6*, 503.

5. Richard, H.; Mauzac, M.; Sigaud, G.; Achard, M. F., Hardouin, F. *Liq. Cryst.*, **1991**, *9*, 679.

6. Richard, H.; Mauzac, M.; Sigaud, G.; Achard, M. F., Hardouin, F. *Liq. Cryst.*, **1991**, *192*, 679.

7. Coqueret, X.; ElAchari, A.; Hajaiej, A.; Lablache-Combier, A.; Loucheux, C.; Randrianarisoa, L. *Makromol. Chem.*, **1991**, *192*, 1517.

8. Zhu, Z.; Einset, A. G.; Yang, C. Y.; Chen, W. X.; Wnek, G. E. *Macromolecules*, **1994**, *27*, 4076.

9. Bisberg, J.; Cumming, W. J.; Gaudiana, R. A.; Hutchinson, K. D.; Ingwall, R. T.; Kolb, E. S.; Mehta, P. G.; Minns, R. A.; Petersen, C. P. *Macromolecules*, **1995**, *28*, 386.

10. Belfield, K. D.; Chinna, C.; Najjar O. *Macromolecules*, **1998**, *31*, 2918.

11. Nohr, R. S.; McDonald, J. G. *J. Biomater. Sci. Polym. Ed.*, **1994**, *5*, 607.

12. Hazziza-Laskar, J.; Helarry, G.; Sauvet, G. *J. Appl. Polym. Sci.*, **1995**, *58*, 77.

13. Bratcher, M. S.; DeClue, M. S.; Grunnet-Jepsen, A.; Wright, D.; Smith, B. R.; Moerner, W. E.; Siegel, J. S. *J. Am. Chem. Soc.*, **1998**, *120*, 9680.

14. Chauhan, B. P. S.; Rathore, J. S.; Chauhan, M.; Alexandra, K. *J. Am. Chem. Soc.*, **2003**, *125*, 2876.

15. (a) Chauhan, B. P. S.; Sardar, R.; Latif, U.; Chauhan, M.and Lamoreaux, W. *Acta. Chim. Slov.*, **2005**, *52*, *361*. (b) Chauhan, B. P. S.and Rathore, J. S. *J. Am. Chem. Soc.*, **2005**, *127*, 5790. (c) Chauhan, B. P. S.; Rathore, J. S.; Bandoo T. *J. Am. Chem. Soc.*, **2004**, *126*, *1493;* (d) Chauhan, B. P. S.; Rathore, J. S.; Glloxhani, N. *Appl. Organomet. Chem.*, **2005**, *19* (4), 542.

16. Chung, M. K.; Schlaf, M. *J. Am. Chem. Soc.*, **2004**, *126*, 7386.

17. Chung, M. K.; Orlova, G.; Goddard, J. D.; Schlaf, M.; Harris, R.; Beveridge, T. J.; White, G.; Hallett, F. R. *J. Am. Chem. Soc.*, **2002**, *124*, 10508.

18. Reetz, M. T.; Westerann E. *Angew.Chem. Int. Ed.*, **2000**, *39*, 165.

19. Henglein, A. *Chem. Rev.*, **1989**, *89*, 1861.

20. Lewis, L. N. *Chem. Rev.*, **1993**, *93*, 2693.

21. Schmid, G.; Morun, B.; Malm, J. O. *Angew. Chem. Int. Ed. Engl.*, **1989**, *28*, 778.

22. Peppas, N. A.; Langer, R. *Science*, **1994**, *263*, 1715.

23. Langer, R. *Acc. Chem. Res.*, **1993**, *26*, 537.

24. Weinberg, J. M.; Gitto, S. P.; Wooley, K. L. *Macromolecules*, **1998**, *31*, 15.

25. Patrode, W. I.U.S. Patent 2,306,222, December 22, **1942**.

26. Barry, A. J.U.S. Patent 2,405,988, August 20, **1946**.

27. Mormann, W.; Schwabe, A.; Sikora, R. *Makromol. Chem.*, **1986**, *187*, 133.

28. (a) Morshima, Y.; Hashimoto, T.; Itoh, Y.; Kamachi, M.; Nozakura, S. *J. Polym. Sci. Polym. Chem. Ed.*, **1982**, *20*, 299. (b) Shirai, M.; Miwa, T.; Tsunooka, M. *Chem. Mater.*, **1995**, *7*, 642 and references therein.

29. Aoai, T. (Fuji Film Co. Ltd.) Eur. Pat. Appl. EP010599, January 9 1985; JP Appl. 83/117 769, June 29, 1983.

30. Greber, G.; Darms, R. Gen. Offen. DE 2206359 720907.

31. Kendrick, T. C.; Parbhoo, B.; White, J. W. In: *The Chemistry of Organic Silicon Compounds*. Patai, S., Rappoport, Z.; Eds. Wiley, Hoboken, NJ, 1989; Chapter 21.

32. Aizpurua, J. M.; Palomo, C.; Palomo, A. L. *Can. J. Chem.*, **1984**, *62*, 336.

33. Sauer, R. O.; Patnode, W. *J. Am. Chem. Soc.*, **1945**, *67*, 1548.

34. Friedel, C.; Crafts, J. M. *Am. J. Sci. Arts*, **1867**, *2*(43), 331.

35. Post, H. W.; Hofrichter, C. H. *J. Org. Chem.*, **1940**, *5*, 443.

36. Mbah, G. C.; Speier, J. L.; *J. Organomet. Chem.*, **1984**, *271*, 77.

37. Schuyten, H. A.; Weaver, J. W.; Reid, J. D. *J. Am. Chem. Soc.*, **1945**, *67*, 1548–1549.

38. Anderson, H.; Fischer, H. *J. Am. Chem. Soc.*, **1954**, 1296–1299.

39. Schubert, U.; Lorenz, C. *Inorg. Chem.*, **1997**, *36*, 1258–1259.

40. Weinberg, J. M.; Wooley, K. L. *J. Orgmet. Chem.*, **1997**, *542*, 235–240.

41. Creighton, J. A.; Eadon, D. G. *J. Chem. Soc. Faraday Trans.*, **1991**, *87*, 3881.

42. Anton, D. R.; Crabtree, R. H. *Organometallics*, **1983**, *2*, 855.

43. Whitesides, G. M.; Hackett, M.; Brainard, R. L.; Lavalleye, J-P. P. M.; Sowinski, A. F.; Izumi, A. N.; Moore, S. S.; Brown, D. W.; Staudt, E. M. *Organometallics*, **1985**, *4*, 1819.

44. Son, S. U.; Jang, Y.; Yoon, Y. K, Kang, E.; Hyeon, T. *Nano. Lett.*, **2004**, *4*, 1147–1151.

45. Vaia, R. A.; Maguire, J. F. *Chem. Mater.*, **2007**, *19*, 2736–2751.

46. Douglas, T.; Dickson, D. P. E.; Betteridge, S.; Charnock, J.; Garner, C. D.; Mann, S. *Science*, **1995**, *269*, 54.

47. Cowen, J. A.; Tsai, K. L.; Dye, J. L. *J. Appl. Phys.*, **1994**, *76*, 6567.

48. Rao, M. S.; Dubenko, I. S.; Roy, S.; Ali, N.; Dave, B. C. *J. Am. Chem. Soc.*, **2001**, *123*, 1511.

49. Keinan, E.; Greenspoon, N. *J. Org. Chem.*, **1983**, *48*, 3545–3548.

50. Lipowitz, J.; Bowman, S. A. *Aldrichimica Acta*, **1973**, *6*, 1.

51. Savers, R. O.; Scheiber, W. J.; Brewer, S. O. *J. Am. Chem. Soc.*, **1946**, *68*, 962.

52. Lipowitz, J.; Bowman, S. A. *J. Org. Chem.*, **1973**, *38*, 162.

53. Fritzsche, H.; Hasserodt, V.; Korte, E., *Chem. Ber.*, **1964**, *97*, 1988.

54. Mark, J. E. *Acc. Chem. Res.*, **2004**, *37*(12), 946–953.

55. Diaz-Ayala, R.; Arroyo, L.; Raptis, R.; Cabrera, C. R. *Langmuir*, **2004**, *20*(19), 8329–8335.

56. Hermans, S.; Wenkin, M.; Devillers, M. *J. Mol. Catal. A*, **1998**, *136*, 59.

57. Poole, R. T.; Kemeny, P. C.; Liesegang, J.; Jenkin, J. G.; Leckey, R. C. G. *J. Phys. F: Met. Phys.*, **1973**, *3*, L46.

58. Fleisch, T. H.; Zajac, G. W.; Schreiner, J. O.; Mains, G. J. *Appl. Surf. Sci.*, **1986**, *26*, 488.

59. Kumar, G.; Blackburn, J. R.; Albridge, R. G.; Moddeman, W. E.; Jones, M. M. *Inorg. Chem.*, **1972**, *11*, 296.

60. Tressaud, A.; Khairoun, S.; Touhara, H.; Watanabe, N. Z. *Anorg. Allg. Chem.*, **1986**, *540*, 291.

61. Dassenoy, F.; Philippot, K.; Ould Ely, T.; Amiens, C.; Lecante, P.; Snoeck, E.; Mosset, A.; Casanove, M. J.; Chaudret, B. *New J. Chem.*, **1998**, *22*, 703.

62. Chen, S.; Kimura, K. *J. Phys. Chem. B*, **2001**, *105*, 5397.

Design and Synthesis of Nanohybrid Systems Based on Silicon–Oxygen Bond

YUSUKE KAWAKAMI

School of Materials Science, Japan Advanced Institute of Science and Technology (JAIST), Ishikawa, Japan

4.1. INTRODUCTION

Properties of polymeric systems with high enough molecular weight strongly depend on the molecular weight distribution. Living anionic polymerization, established by M. Szwarc in 1956[1] has been utilized to control these factors in many carbon-based polymers. Stereochemical structure is another very important factor to control the polymer property. Such control has usually been achieved by enantioface-selective polymerization of unsaturated carbon–carbon bonds for carbon-based polymers, typically seen in stereospecific olefin polymerization.

Silicon-containing polymers in general,[2] especially poly(silsesquioxane),[3] poly (siloxane),[4] poly(carbosilane),[5] polysilazane,[2] and poly(silylene),[6] can be said to be organic–inorganic hybrid systems, and have practical importance as rubber, surface modifying agents, reinforcing agents, precursors of silicon carbide, and photo- and electroactive polymers, but they have been insufficiently studied in relation to their chemical structure, stereoregularity, molecular weight, and higher order structure. Properties of silicon-containing polymeric systems also depend very much on what kind of atoms, and how many such atoms are attached to the silicon atom in the molecular structure. Stereochemical aspects of silicon centers, as well as molecular weight of the polymers, are also very important to control their properties. One of the characteristic aspects of the bonding of silicon compounds is in the point that sp^2 or sp configuration is not well stabilized and sp^3 is the stablest configuration. The silicon–silicon double bond is not stable at room temperature,

and since the enantioface-selective polymerization is not applicable, optically active silicon compounds with sp^3 configuration must be used as the monomer to control the stereochemistry of the polymerization reaction. Since silicon compounds are nonnatural derivatives, optically active silicon compounds must be separated or synthesized to obtain monomers.

We have been interested in creating new polymeric systems of controlled structure and function by taking advantage of the reactivity and chemical structure of the silicon compounds. Formation of silicon–oxygen bond can be used to create a new system to convert oxyanion to carbanion, which can be used to synthesize multiblock copolymers from ring-opening monomer and vinyl monomer. Polysiloxanes are polymers with a flexible and hydrophobic nature, which can be used to design surface-modifying agent. The thermal properties of polysiloxane can be improved by the introduction of various rigid structures in the main chain. Silsesquioxane structure can create dynamic microvoids in polymeric systems, which can be used to design contact lens materials. Formation of silsesquioxanes with controlled structure of higher order is also interesting. In this chapter, design and synthesis of new structures of materials composed of silicon–oxygen bonds are mainly described, paying attention to the creation of new nanohybrid structure.

4.2. STEREOCHEMICAL ASPECT OF SILICON COMPOUNDS AND REACTION IN THE SYNTHESIS OF POLYMERS WITH SILICON–CARBON BONDS

The most common optically active starting silicon compound is (methyl)phenyl-naphthylmenthoxysilane, as shown in Figure 4.1.
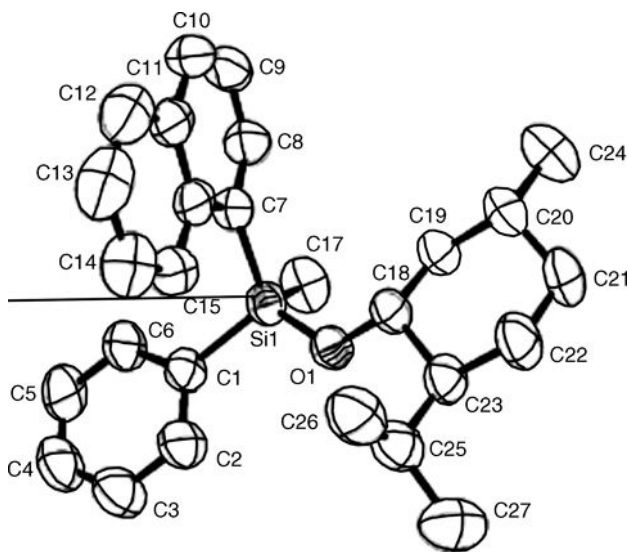
Figure 4.1. ORTEP structure of (*S*)-(methyl)naphthylphenylmenthoxysilane.

S, *R* configuration of chiral silicon center is determined by the absolute
configurations of chiral centers of menthol (*1S,2R,5S*) and (*1R,2S,5R*)
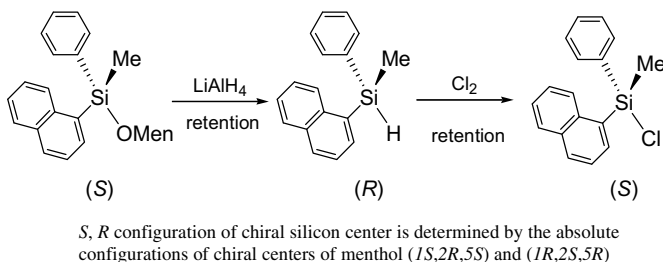
Scheme 4.1. Stereochemical aspect of the basic transformations of optically active silicon
compounds.

Some of the silicon compounds can be separated on chromatograph.[7] The stereo-
chemistry of reduction to (methyl)phenylnaphthylsilane and chlorination of silane
function were established to be a complete retention process as shown in Scheme 4.1.[8]

Nucleophilic substitution at halogen–silicon bonds are basically inversion pro-
cesses, but the stereochemistry strongly depends on the reaction conditions, as
discussed later.

Isotactic polycarbosilane was synthesized for the first time by polyaddition via the
hydrosilylation reaction. The starting optically active allylsilane was synthesized
from methylphenyldi[(−)-bornyloxy]silane, another optically pure starting material,
and allyllithium, followed by the reduction by lithium aluminum hydride to give a
colorless oil. $[\alpha]_D^{25} = -16.0$(c 0.50, pentane). The reaction scheme of the synthesis
of polymer is shown in Scheme 4.2, and the ^{1}H NMR spectrum of the polymer is
shown in Figure 4.2.[9]

In the spectrum, the SiCH_3 signal is split into three singlets at 0.120, 0.125, and
0.131 ppm according to the triad tacticity, which were assigned to the isotactic,
heterotactic, and syndiotactic triad, respectively. The calculated concentration of
each triad starting from the optically active monomer with 60.8% ee assuming
complete retention of Si stereochemistry in the reduction and in the polymerization
via hydrosilylation is S : H : I = 1.0 : 2.0 : 3.3 (0.16 : 0.32 : 0.52). The actual concen-
tration was 1.0 : 2.0 : 2.3 (0.19 : 0.37 : 0.44).

A scheme of ring-opening polymerization of an optically pure 1-methyl-1-
(naphthyl)-2,3-benzosilacyclobut-2-ene by various catalysts is shown in Scheme 4.3.
^{1}H NMR signal of the obtained product is shown in Figure 4.3.

The signals at −0.34, −0.40, and −0.48 ppm are reasonably assignable to
isotactic, heterotactic, and syndiotactic triad sequence, respectively. Ring-opening

optically active silane   isotactic poly(carbosilane)
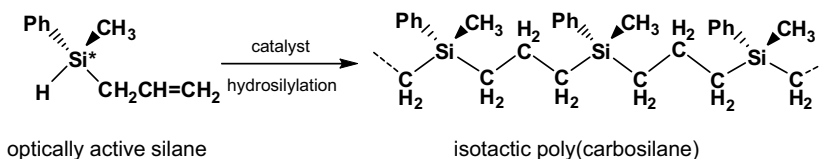
Scheme 4.2. Synthesis of optically active allylsilane and isotactic poly[(phenylmethylsily-
lene)trimethylene].
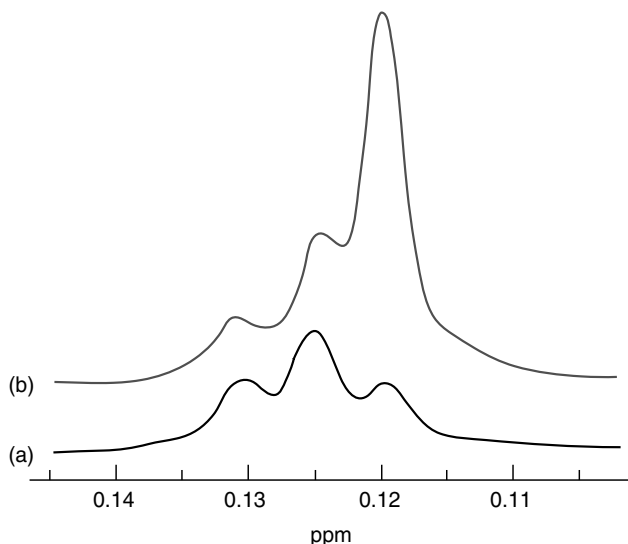
Figure 4.2. The 750 MHz ^{1}H NMR of SiCH$_3$ signal of isotactic poly[(phenylmethylsilylene) trimethylene].

polymerization with platinum-1,3-divinyl-1,1,3,3-tetramethyldisiloxane complex as catalyst (0.1 mol%) in the presence of triethylsilane gave a high polymer and 1-triethylsilyl-2-{methyl(naphthyl)silylmethyl}benzene, 1-{methyl(naphthyl)(2'-triethylsilylphenylmethyl)silyl}-2-{methyl(naphthyl)silylmethyl}-benzene, and 1-{methyl(naphthyl)-(2'-triethylsilylphenylmethyl)silyl}-2-[methyl(naphthyl)[2'-{methyl-(naphthyl)silylmethylphenyl}]silylmethyl]benzene, shown in Figure 4.4, in 54%, 18%, and 11% yield, respectively, whose enantiomer excess (ee) or optical purity (op) as higher than 99%, through regioselective ring-opening reaction, followed by the σ-bond metathesis process.[10] Not only the initiation reaction but also all the following propagation steps seem to proceed regio- and stereoselectively.

Optically active silyllithium derivatives will make it possible to synthesize silicon–carbon bonds in which asymmetry is introduced at both silicon and carbon centers, which cannot be achieved by the substitution reaction by a carbanion at the asymmetric silicon center. The disilane and silylstannane derivatives were obtained by the reaction of chlorosilane with silyllithium or stannyllithium as shown in Scheme 4.4.

The formation of silyllithium is a retention process. The optical purity was kept higher than 85% ee at −78°C even after 5 h.[11] Such optically active silyllithium can be used to synthesize various optically active oligosilanes. The reaction of (S)-chloro-,
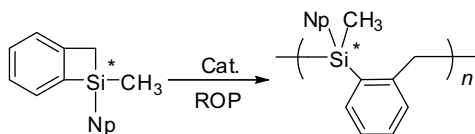
Scheme 4.3. Ring-opening polymerization of an optically active silacyclobutene derivative.
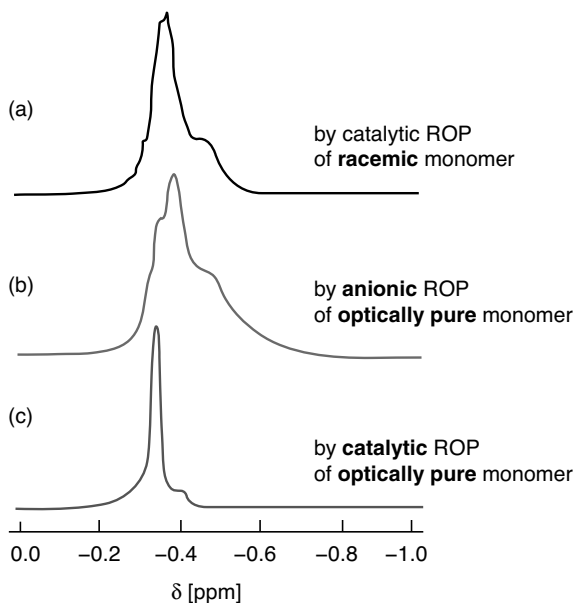
Figure 4.3. Stereoregularity of polymers obtained from 1-methyl-1-(naphthyl)-2,3-benzosilacyclobut-2-ene: (a) racemic, by Pt-1,3-divinyl-1,1,3,3-tetramethyldisiloxane, (b) optically pure, by BuLi, and (c) optically pure, by the Pt catalyst.

(S)-bromo-, and (R)-fluoro[methyl(naphthyl)phenyl]silane (>99% ee) with the optically active silyllithium gave almost quantitative yield of the expected disilane, 1-methyl(naphthyl)phenyl-2-dimethyl(4-methoxynaphthyl)disilane. Interestingly enough, the fluoride with opposite configuration to the chloride also gave the same (R) antipode of the disilane as the major product at room temperature, indicating retention of configuration at the chiral silicon center. Surprisingly, opposite (S) antipode was produced as 97% inverted product at −78°C in pentane.[12] The stereochemistry of fluorosilane very much depends on the reaction conditions.

4.3. SILACYCLOBUTANE AS "CARBANION PUMP" COMPONENT

In the living anionic polymerization, the formation of block copolymers by sequential monomer addition depends mainly on the nucleophilic reactivity of the living chain end. For instance, the highly nucleophilic polystyrene carbanion[13] can initiate
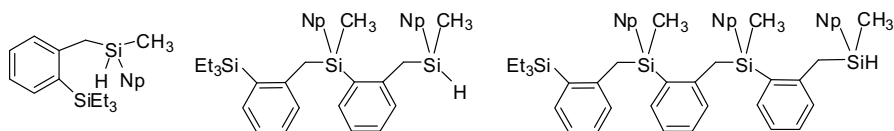
Figure 4.4. Low molecular weight products from 1-methyl-1-(naphthyl)-2,3-benzosilacyclobut-2-ene by the platinum catalyst in the presence of Et_3SiH.
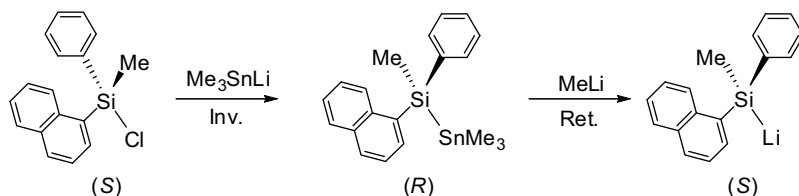
Scheme 4.4. Synthesis of optically active silyllithium from optically active chlorosilane.

the polymerization of ethylene oxide to form polystyrene-*block*-poly(ethylene oxide), whereas the comparatively less nucleophilic poly(ethylene oxide) oxyanion cannot initiate the polymerization of styrene. As a result, polystyrene–*block*-poly(ethylene oxide)–*block*-polystyrene triblock copolymers and poly(ethylene oxide)–polystyrene multiblock copolymers cannot be prepared[14] by sequential addition in the living anionic polymerization system. This has long been an obstacle in the unrestricted synthesis of tri- and multiblock copolymers from hydrocarbon and oxirane monomers.

We proposed the concept of a "carbanion pump," where a silacyclobutane having high ring distortional energy was used to convert an oxyanion into a carbanion, which can further initiate polymerization of styrene as shown in Scheme 4.5.

To improve the efficiency, 1,1-diphenylethylene was used to trap the initially formed carbanion from potassium *tert*-butoxide (BuOK) and dialkylsilacyclobutane. When a twofold excess of dimethylsilacyclobutane was added over 90 min, the carbanion pump efficiency reached almost 88%. Diphenylsilacyclobutane gave almost quantitative efficiency, which could be used to synthesize block copolymer from the propagating end of poly(ethylene oxide) to methyl methacrylate to give polymers with a narrow molecular weight distribution. Such a system was also used by other researchers successfully.[15]
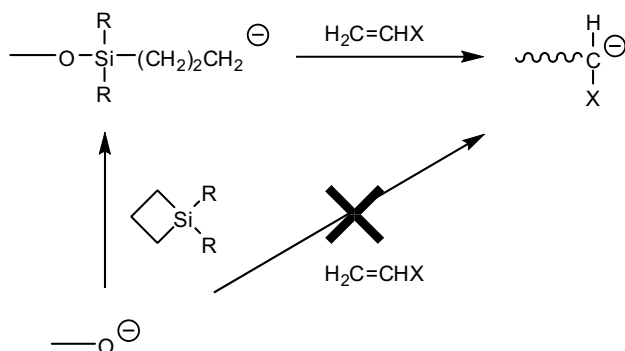
Scheme 4.5. Concept of carbanion pump to convert oxyanion into carbanion by the aid of ring opening of silacyclobutane ring by oxyanion through the formation of silicon–oxygen bond.

4.4. CATALYTIC CROSS-COUPLING POLYMERIZATION

Silarylene-disiloxane polymers, which exhibit a wide range of physical properties depending on their composition and structure, have received considerable academic and industrial interest for nearly 50 years.[16] One of the prominent properties of silarylene-disiloxane polymers is their excellent thermal stability. The typical methods employed for the synthesis of silarylene-siloxane polymers are the self-polycondensation of arylenedisilanols or the copolycondensation of arylenedisilanols with other bifunctional compounds.[17] We found that the easily accessible 1,4-bis(dimethylsilyl)benzene (*p*-BSB) could react with water in the presence of a catalytic amount of transition metal (Pd, Pt, Rh, etc.) compounds at room temperature to afford high molecular weight poly[(oxydimethylsilylene)(1,4-phenylene)(dimethylsilylene)] with the evolution of H_2 as the only by-product, as shown in Scheme 4.6.[18]

$Pd_2(dba)_3$ is an excellent catalyst to give a high molecular weight polymer ($M_n = 16,300$) at room temperature in a short time (2 h). We extended the reaction to the polymerization of *p*-BSB with other labile-hydrogen-containing compounds, such as ammonia, disilanol, aliphatic and aromatic diols, and dicarboxylic acids to prepare a series of silphenylene-containing polymers, including polycarbosilazane, polycarbosiloxanes, poly(silyl ether)s, and poly(silyl ester)s.

The $Pd_2(dba)_3$ was not a proper catalyst for the polymerization of *p*-BSB with aliphatic diols like ethylene glycol and 1,3-propanediol, and rather low molecular weight poly(silylether)s were obtained ($M_n = 1000$–3000). On the other hand, 10% Pd/C was an efficient catalyst to afford higher molecular weight ($M_n = 9400$ and 12,400, respectively) at an elevated temperature (50°C) in 3 h. Depending on the constitutional unit between silphenylenes being varied from –O– to –O(CH$_2$)$_2$O– and –O(CH$_2$)$_3$O–, the glass transition temperature (T_g) changed markedly from -19.1°C to -38.0°C and -43.7°C, respectively. On the other hand, introducing –OSi(Ph)$_2$O– and –O(*o*-C$_6$H$_4$)O– groups increased the T_g to -3.3°C and 2.7°C, respectively, indicating that incorporating aromatic groups in both side chain or main chain increased the barrier of the longitudinal motion of the polymer chains. In addition to a glass transition temperature, polymers from *p*-BSB with H_2O and NH_3 also exhibited a melting point T_m (123.5 and 92.5°C) and a crystallization temperature T_c (34.0 and 37.6°C). A well-developed spherulite texture was observed for polymer (X = –O–), and schlieren structure for polymer (X = –NH–) (Figure 4.5), indicating its very regular structure.
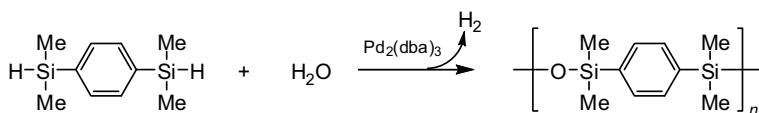
Scheme 4.6. Catalytic formation of poly(silphenylene-disiloxane).

(a)   (b)
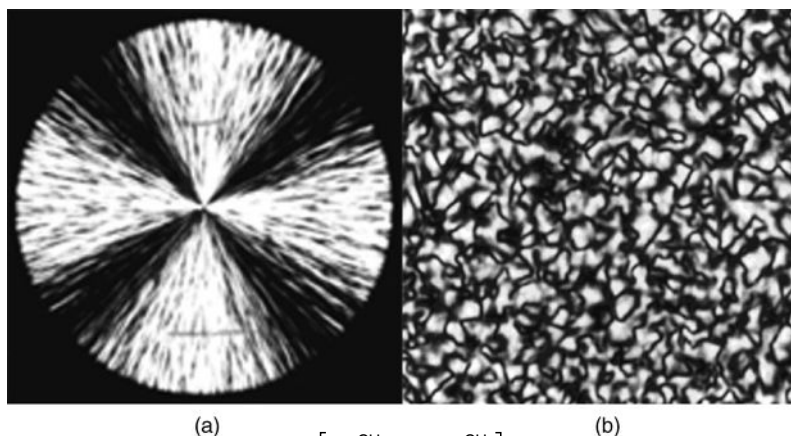
Figure 4.5. Crystalline textures of $\left[\begin{array}{c} \mathrm{CH_3} \\ \mathrm{X-Si-} \\ \mathrm{CH_3} \end{array} \mathrm{C_6H_4} \begin{array}{c} \mathrm{CH_3} \\ \mathrm{-Si-} \\ \mathrm{CH_3} \end{array}\right]_n$: (a) X = –O– and (b) X = –NH–.

The influence of the structure of X groups on the thermal stability of polymers was studied by thermogravimetric analysis (TGA) and the results are represented in Figure 4.6.

For further improvement of thermal properties of the polymer, some functional groups, such as vinyl, hydride, hydroxy, and epoxy groups, instead of a methyl group on the silylene unit were introduced into the polymer structure.[18e, 19] Tris(penta-fluorophenyl)borane $[B(C_6F_5)_3]$ was also found very effective for the formation of siloxane bond by cross-condensation between silane and silanol or alkoxysilane.[20] We used this catalyst to synthesize polysiloxanes with cage silsesquioxane in place of

Legend:
X	
——	-O-
– – –	-NH-
–·–	-OSi(Ph)$_2$O-
– –	-O(CH$_2$)$_2$O-
- - -	-O(CH$_2$)$_3$O-
–·–·–	-O(o-C$_6$H$_4$)O-
–··–··–	-OCO(CH$_2$)$_4$COO-
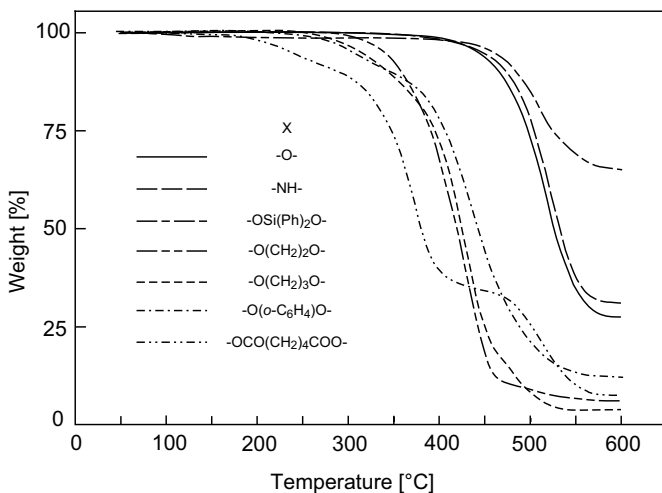
Figure 4.6. TGA curves of polymers at a heating rate of 5°C/min under nitrogen (50 mL/min).
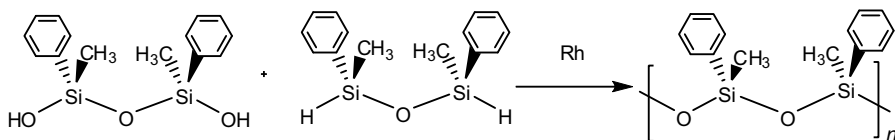
Scheme 4.7. Synthesis of stereoregular poly(methylphenylsiloxane) by cross-coupling.

the arylene group, in the main chain, to enhance the thermal property of the formed polymer as described later.

4.5. STEREOCHEMICAL CONTROL OF POLYSILOXANE

Cross-dehydrocoupling polymerization of 1,3-dimethyl-1,3-diphenyl-1,3-disiloxa-nediol with 1,3-dihydro-1,3-dimethyl-1,3-diphenyl-1,3-disiloxane in the presence of a catalyst gave poly(methylphenylsiloxane). This reaction was applied to the synthesis of stereoregular poly(methylphenylsiloxane) in the presence of rhodium catalyst as shown in Scheme 4.7.

Assignment of the triad signals of the polymer was made by ^{13}C NMR spectroscopy of *ipso* carbon of phenyl group ($S = 136.7$, $H = 136.9$, and $I = 137.1$ ppm), as shown in Figure 4.7.[21]

Although the reaction of optically pure (S,S)-1,3-dimethyl-1,3-diphenyl-1,3-disiloxanediol with 1,3-dihydro-1,3-dimethyl-1,3-diphenyl-1,3-disiloxane [(S,S):(S,R): (R,R)] = 84:16:0] gave a poly(methylphenylsiloxane) of rather low molecular weight, its triad tacticity was found to be rich in syndiotacticity ($S:H:I = 60:32:8$). Some racemization seems to have occurred for the silane derivative with this catalyst.

Stereochemistry in the reactions of silanols and methoxysilanes with methyl (naphthyl)phenylsilane in the presence of $B(C_6F_5)_3$ were studied as shown in Scheme 4.8.

The stereochemistry was proved as completely inversion and retention for the chiral silicon centers of the silane and methoxysilane, respectively, by the fact that the reaction of optically pure methylnaphthylphenylsilane with (R)-(methoxy)methyl
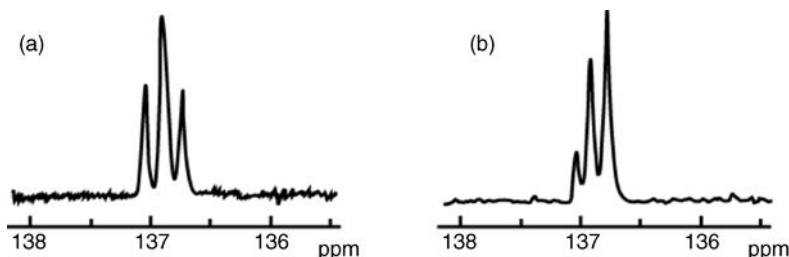
Figure 4.7. ^{13}C NMR spectra of poly(methylphenylsiloxane): (a) random and (b) syndiotactic rich.
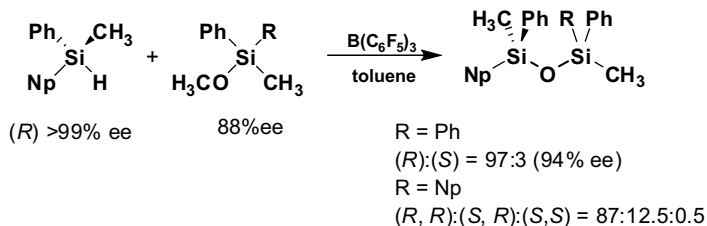
Scheme 4.8. Stereochemistry of siloxane bond formation from optically active methoxysilane and silane.

(naphthyl)phenylsilane (88 %ee) gave (R, R)-1,3-dimethyl-1,3-di(naphthyl)-1,3-diphenyldisiloxane [(R, R) : (R, S) : (S, S) = 87 : 12 : 0.5].

Unfortunately, application of this reaction to the actual synthesis of completely syndiotactic poly(methylphenylsiloxane) has not been successful, yet.[20]

4.6. POLYSILOXANE MACROMONOMERS AND GRAFT COPOLYMERS

Living polymerization created the idea of Macromer® (proposed by R. Milkovich, generic term is macromonomer) for synthesizing a graft copolymer of well-controlled structure[22]. We reported the synthesis of polydimethylsiloxane (PDMS) macromonomers.[23] Copolymerization of PDMS macromonomer having styrene as a terminal functional group ($M_n = 5300$) with methyl methacrylate in 20 : 80 weight ratio gave copolymers containing 21 wt% of PDMS.[23a] In the homogeneous system, the macromonomer shows a reactivity almost similar to that of low molecular weight compounds having the same polymerizable group to give a graft copolymer.

One of the most characteristic properties of polysiloxane graft copolymers is their surface activity. Since PDMS has a very low surface energy, it accumulates at the
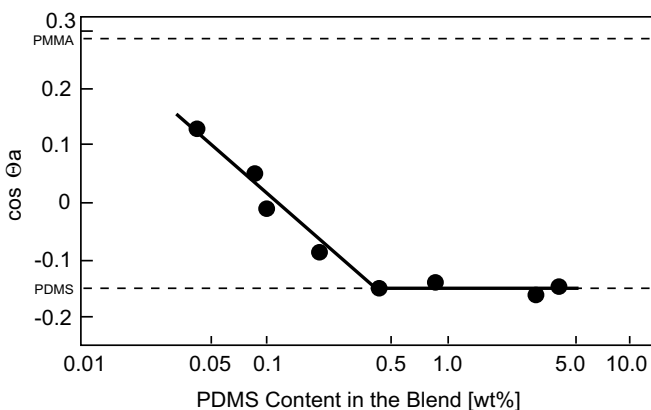
Figure 4.8. Change of the advancing contact angle against water in the blend of a PDMS graft copolymer in poly(methyl methacrylate).

surface of the film when mixed with another polymer. Such a surface accumulation can be used to modify the surface properties of the polymer blend. Addition of a small amount of PDMS-containing graft copolymer is quite effective in modifying the surface of a bulk polymer without damaging the good mechanical property of the base polymer. Only 0.3 wt% of the graft copolymer is enough to modify the surface of poly(methyl methacrylate) completely and render it similar to PDMS surface (Figure 4.8).[24]

4.7. SEGMENTAL MOBILITY AND INCOMPATIBILITY OF SILSESQUIOXANE OR SILICATE-SUBSTITUTED POLYMERS IN DESIGNING FUNCTIONAL POLYMERIC SYSTEMS: OXYGEN PERMEABLE CONTACT LENS MATERIAL

In the permeation of a gas through a condensed film, the gas molecules permeate through the dynamic gaps between polymer chains, less than 1–2 nm in size, determined by micro-Brownian motion and interaction with permeating molecules. The permeation of gases is treated by Fick's and Henry's laws[25]:

$$P = D \times S$$

Poly(dimethylsiloxane) has the highest permeability coefficient given by a large diffusion coefficient among industrial membrane materials, since it is composed of very flexible Si–O linkages and has large free volume. However, it also has the lowest O_2/N_2 permeation selectivity value for membrane polymers, that is, $P_{O_2}/P_{N_2} = 2$.

Moreover, it has only insufficient self-supporting characteristics. Polymers consisting of oligosilsesquioxane or silicate side chains, which contribute to permeation, and high glass transition temperature (T_g) main chain components, which give film-forming properties, should demonstrate well-balanced permeation properties. Properties of the polymers with polystyrene main chain (Figure 4.9) are listed in Table 4.1.

The polymers show only one significantly lowered T_g by the introduction of the siloxane linkages. PSn5 showed the highest permeability coefficient maintaining reasonable selectivity and self-supporting property. The permeability coefficient is mainly controlled by the diffusion coefficient. Each silicon atom in the side chain of these polymers gives not only different chemical shifts but independent T_1 as typically shown for PSi3 in Figure 4.10.

The spin-lattice relaxation time, T_1, of Si[1] must have strong correlation with the mobility of the side chain as a whole, and consequently with the gas permeability.

4.8. HOLOGRAPHIC SYSTEMS

Holographic polymer dispersed liquid crystal (HPDLC) systems have attracted much interest due to their unique switching property by an electric field to make them applicable to information displays, optical shutters, and information storage media.[26]
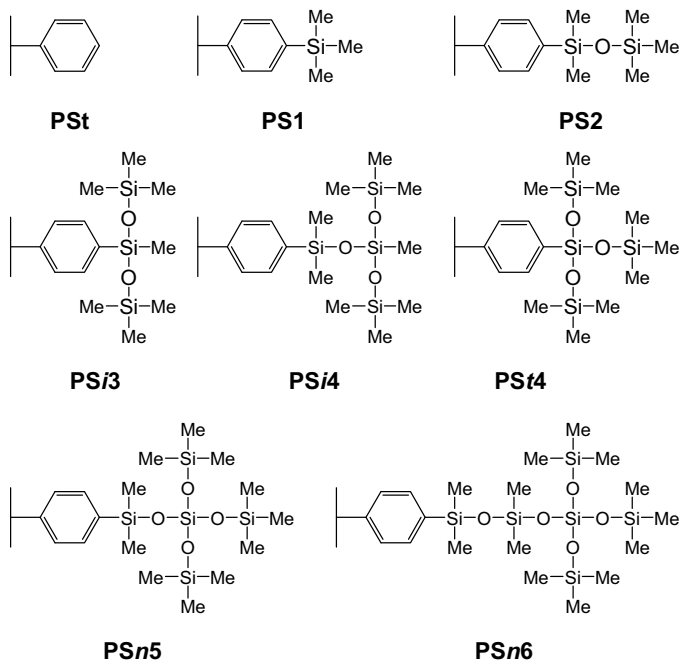
Figure 4.9. Structures of poly(*p*-oligosiloxanyl, oligosilsesquioxanylstyrene)s.

Photopolymerizable materials, typically multifunctional acrylates, have mostly been studied as materials for HPDLC because of their advantages of large refractive index modulation, low cost, and easy fabrication and modification.[27] However, these HPDLC materials still have significant drawbacks such as volume shrinkage, low reliability, and poor long-term stability.

TABLE 4.1. Properties of Poly(*p*-oligosiloxanyl, oligosilsesquioxanylstyrene)s

Polymer	$T_g(°C)$	$\Delta v(°C)^a$	$P_{O_2}^{\ b}$	α	$D_{O_2}^{\ c}$	$S_{O_2}^{\ d}$
PSt	373	31.25	1	5.5	1	2.2
PS1	409	13.23	14	3.4	—	—
PS2	309	9.97	40	3.0	18	2.2
PS*i*3	325	8.27	71	2.8	32	2.3
PS*i*4	364	2.33	74	2.8	35	2.1
PS*t*4	387	5.52	—	—	—	—
PS*n*5	314	5.21	110	2.6	49	2.2
PS*n*6	256	2.76	141	2.6	64	2.2

[a] Δv: half-amplitude width of the CH_3 signal in solid state ^{1}H NMR (90 MHz).
[b] 10^{-10} cm^3 (STP) cm/(cm$^2 \cdot$ s $\cdot$ cmHg).
[c] 10^{-7} cm^2/s.
[d] 10^{-3} cm^3 (STP)/(cm$^3 \cdot$ cmHg).
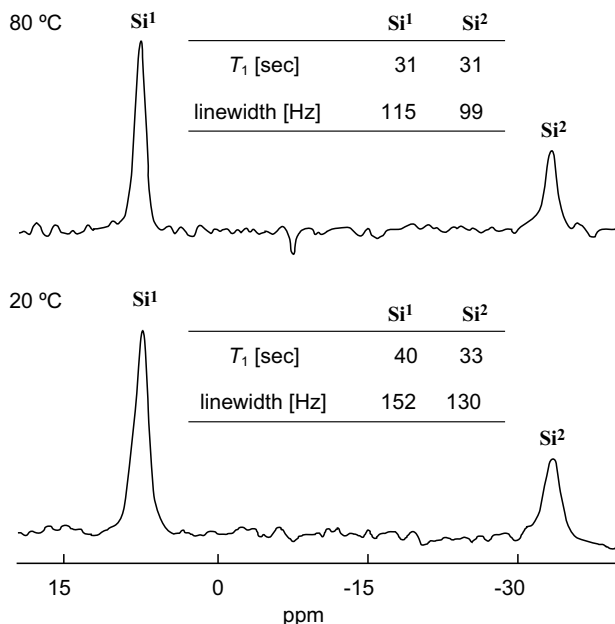
Figure 4.10. Change of T_1 of Si^1 and Si^2 of PSi3 estimated by 79.6 MHz ^{29}Si solid state NMR.

Since the performance of HPDLC is governed by the stability of precisely formed periodic polymer rich layers and LC rich layers created by the interference of two incident laser beams, control of the formation of the polymer matrix and phase separation of the LC are very important.[28] The principal role of multifunctional acrylate in grating formation is to make the LC phase separate by the formation of crosslinked polymer matrix. Control of the rate and density of crosslinking in the polymer matrix is one of the most important factors, which determines the size, distribution, and shape of phase-separated LC domains and accordingly the final morphology and performance. In order to obtain clear phase separation of the LC from the polymer matrix to homogeneous droplets, high crosslinking density, but not rapid crosslinking, is very important.

Until now optimization of the crosslinking process has mainly been pursued by controlling the average functionality of multifunctional acrylate by mixing dipentaerythritol pentaacrylate (DPEPA), trimethylolpropane triacrylate (TMPTA), and tri (propyleneglycol) diacrylate, or by diluting the system with monofunctional vinyl compound like 1-vinyl-2-pyrollidone (NVP).[29] Monofunctional NVP adjusts the initial polymerization rate and final conversion of acrylate functional groups by lowering the concentration of crosslinkable double bonds.[30]

Recently, we proposed the use of siloxane-containing compounds together with a multifunctional acrylate to improve the drawbacks of the HPDLC system in the grating formation with the intention to assist the efficient phase separation of monomer and LC components in a controlled manner by taking advantage of the highly incompatible nature of the siloxane component against polymer matrix and its

flexibility to ease the diffusion of the LC.[31] Volume shrinkage during polymerization was also intended to be suppressed through ring-opening polymerization of epoxide function.

Introduction of polyhedral oligosilsesquioxane structure also improved the performance of the formed grating.[32] Our new idea is to improve the property of gratings through importing the siloxane network formation in the polymer matrix, by not only lowering the contribution of initial rapid radical crosslinking of TMPTA and realizing complete conversion of double bonds, but also maintaining the desirable total crosslinking density assisted by hydrolysis-condensation crosslinking of the trialkoxysilyl group in the methacrylate component to control the phase separation of the LC from the polymer matrix.[33] Such crosslinking can be promoted by the proton species produced from the initiating system together with a radical species by photoreaction.[34] These systems should provide many advantages over traditional systems induced only by radical polymerization by improving: (i) the volume shrinkage by reducing the contribution of radical initial crosslinking by importing the siloxane network in whole polymer networks, (ii) the contrast of siloxane network formed by the hydrolysis of ω-methacryloxyalkyltrialkoxysilane against polymer matrix, and (iii) the stability of the final gratings via combination of the characteristics of siloxane gel and a rather loosely crosslinked radically polymerized system.[35]

Materials for recording solution are shown in Figure 4.11.

A combination of photosensitizer (PS) and photoinitiator (PI) having sensitivity to the visible wavelength of the Nd-YAG laser ($\lambda = 532$ nm) selected for this study are 3,3′-carbonylbis(7-diethylaminocoumarin) (KC, Kodak) and diphenyliodonium chexafluorophosphate (DPI, AVOCADO Research Chemicals Ltd.), respectively, which produce both cationic and radical species.[36] (See Figure 4.12.)

The ratio of polymer matrix components, a fast curing TMPTA and ω-methacryloxyalkyltrialkoxysilane, was changed from 80 : 10 to 10 : 80 wt% in the relative ratio with 10 wt% reactive diluent NVP. Recording solution was prepared by mixing the matrix components (65 wt%) and liquid crystal (35 wt%).

Gratings could not be formed with MM-TMS. Dramatic enhancing in the diffraction efficiency to about 86% (induction period of 144 s) was observed in the case of MM-TMOS, even with only 10 wt% TMPTA. Figure 4.13 shows the real-time diffraction efficiency of holographic gratings formed with various ω-methacryloxyalkyltrialkoxysilanes capable of radical photopolymerization and hydrolysis condensation.

When spacer was changed from methylene to propylene (MP-TMOS), the diffraction efficiency dropped to 72% with a longer induction period (576 s). By changing the trialkoxysilyl functional group from trimethoxy to triethoxy (MP-TMOS to MP-TEOS) with the same propylene spacer, not only the diffraction efficiency was decreased to 13%, but the induction period was also elongated to 693 s, which strongly suggested that the hydrolysis-condensation process of trialkoxysilane function is playing an essential role in grating formation.

Hydrophilic urethane and hydroxylpropylene groups were introduced in the spacer of the monomer structure. The highest diffraction efficiency of 75% and remarkably shorter induction period of 75 s were obtained for the grating formed
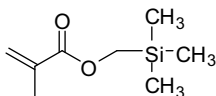
Methacryloxymethyltrimethylsilane (**MM-TMS**)
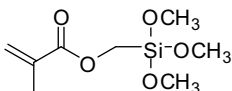
Methacryloxymethyltrimethoxysilane (**MM-TMOS**)
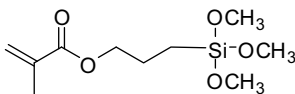
3-Methacryloxypropyltrimethoxysilane (**MP-TMOS**)
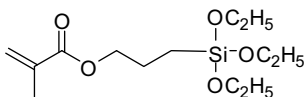
3-Methacryloxypropyltriethoxysilane (**MP-TEOS**)
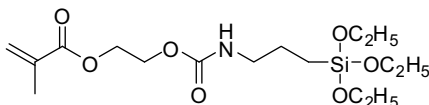
3-*N*-(2-methacryloxyethoxycarbonyl)aminopropyltriethoxysilane (**MU-TEOS**)
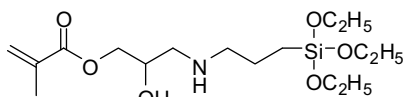
3-*N*-(3-methacryloxy-2-hydroxypropyl)aminopropyltriethoxysilane (**MH-TEOS**)

Figure 4.11. Materials for holographic recording used together with multifunctional acrylate.
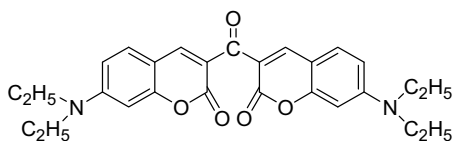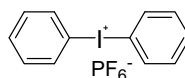
3,3'-Carbonylbis(7-diethylaminocoumarin)(KC)   Diphenyliodonium hexafluorophosphate(DPI)

Figure 4.12. Chemical structures of photosensitizer (PS) and photoinitiator (PI) for this study.
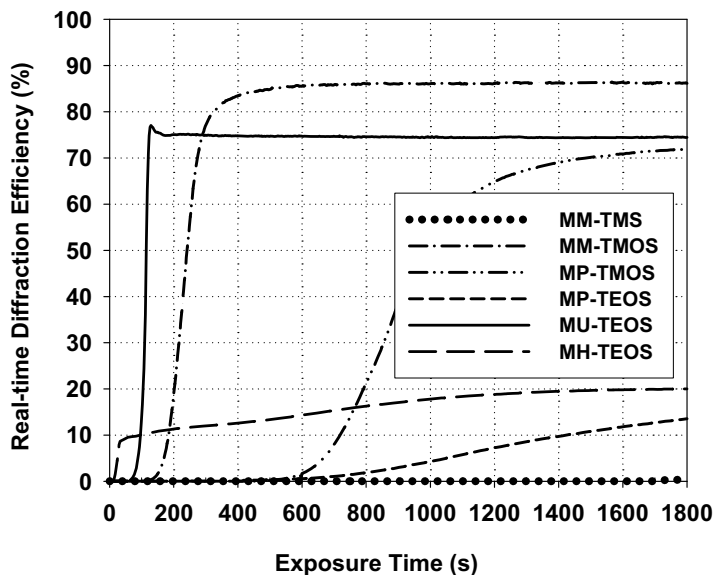
Figure 4.13. Real-time diffraction efficiency of the gratings formed with various ω-metha-cryloxyalkyltrialkoxysilanes in the recording solution with 65 wt% matrix compounds of TMPTA: ω-methacryloxyalkyltrialkoxysilane: NVP = 10 : 80 : 10 wt% and 35 wt% TL203, and KC-DPI (0.2 wt%–2 wt% to matrix compounds) with one beam intensity of 20 mW/cm^2.

with MU-TEOS having a urethane linkage in the spacer group. In addition, gratings formed with MH-TEOS having a hydroxylpropylene group in the spacer showed the shortest induction period of 18 s, although the diffraction efficiency was considerably low (20%).

Introduction of oligoethylene oxide component in the spacer further increased the diffraction efficiency of the grating. (See Scheme 4.9.)
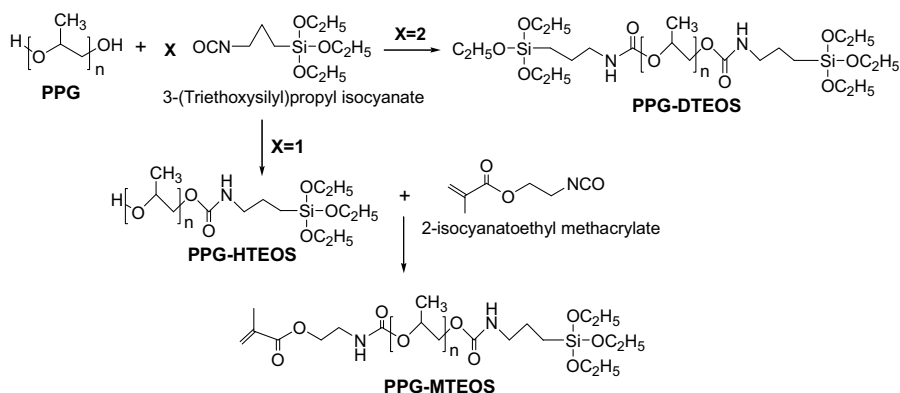
Scheme 4.9. Chemical structures of PPG derivatives functionalized with triethoxysilyl, hydroxyl, and methacrylate groups as polymer matrix components.
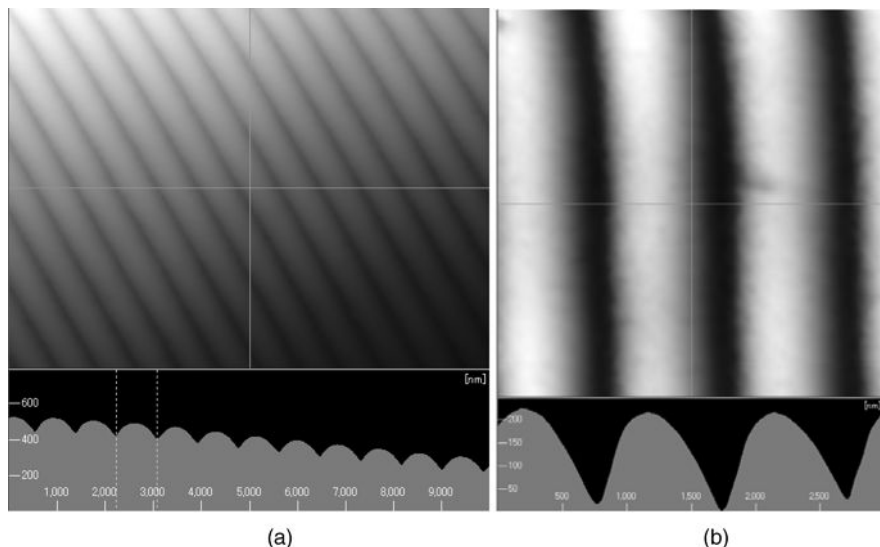
Figure 4.14. AFM surface topologies of the gratings formed with the formulation of 65 wt% polymer matrix compound in the ratio 20 : 10 : 50 : 20 in TMPTA : NVP : Mu-TEOS : PPG-DTEOS and 35 wt% of E7 in (a) 10 μm and (b) 3 μm scanning lengths.

Figure 4.14 shows the AFM surface topology of the gratings formed with the formulation with 65 wt% polymer matrix compound in the ratio 20 : 10 : 50 : 20 in TMPTA : NVP : Mu-TEOS : PPG-DTEOS and 35 wt% of commercial E7. Very regular and well-defined gratings were fabricated as shown in Figure 4.14a scanned in 10 μm lengths. The grating spacing was approximately 839.8 nm as shown in Figure 4.14b, which was in good agreement with the calculated spacing value of 965 nm the by Bragg's equation (grating spacing $\Lambda = \lambda/2 \sin \theta$, λ is 532 nm, the wavelength of laser light and θ is 16° of incident external half-angle in this experiment). Polymer matrix layers are shown as the sinusoidal pattern in profile of AFM topology since the LC layers were washed out by methanol from the positions of the valley parts in the sinusoidal pattern; thus, we may conclude that polymer matrix with PPG-DTEOS was exactly formed by photoreaction in high intensity regions and E7 was phaseseparated in low intensity regions of the interference pattern of the two laser beams.

4.9. POLYSILSESQUIOXANE WITH CONTROLLED STRUCTURE

Polysilsesquioxanes are a class of compounds having the emperical formula $[RSi(O)_{3/2}]_n$, in which three oxygen atoms and one alkyl or aryl group are attached to the silicon atom. These compounds are formed under various reaction conditions and can take various three-dimensional structures. They can be random, ladder, or even cage. Polyhedral oligomeric silsesquioxane (POSS) is usually abbreviated as T_n, in which n indicates the number of silicon atoms in the frame structure.

R-T$_8$
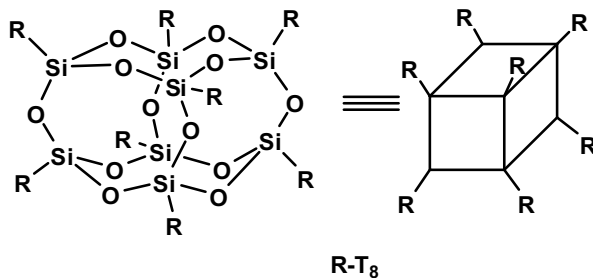
Figure 4.15. Framework of R-T$_8$ cage with R as the substituent on silicon atom.

Scott initially discovered completely condensed methyl-substituted oligomeric silsesquioxanes in 1946.[37] Later, Barry and co-workers showed the cubic or hexagonal prismatic shape of the completely condensed molecules.[38] The structure of T$_8$ is shown in Figure 4.15.

Brown and co-workers reported the formation of completely condensed cubic cage-structured octahedral octaphenylsilsesquioxane (Ph-T$_8$).[39] The other typical cage is decahedral decasilsesquioxane, T$_{10}$.

The cage can be completely and incompletely condensed structure.[3, 39–47] Over the past decade, completely and incompletely condensed POSS, obtained by hydrolysis and condensation of trifunctional alkyl- or arylsilane, have been used to enhance the physical properties, such as thermal stability, glass transition temperature, dielectric constant, oxidative resistance, and even the optoelectronic property of the POSS-based hybrid systems.[48a–k]

Meanwhile, Flory and co-workers showed that the 8-membered ring, cyclic octamethyltetrasiloxane, and the 10-membered ring, decamethylpentasiloxane, are thermodynamically the most stable rings, and exist mostly in the equilibrium mixture of cyclic oligomers and the linear polymer of dimethylsiloxane.[49] It should be noted that all-cis cyclic tetrasiloxanetetrol, namely, all-cis T$_4$-tetrol, or its alkali metal salt is actually often selectively formed under acidic or under basic condition.[50] Cyclic tetrasiloxane and pentasiloxane frames shown in Figure 4.16 might be key to construct the specific structures.

In the formation of cage or ladder structures of silsesquioxanes, the stereochemical structure around the silicon atom also seems important. When two all-cis-R-T$_4$-tetrols condense by forming a siloxane linkage, there are two arrangements, *facing* and *apart* for the two rings as illustrated in Scheme 4.10.

Imaginarily, the *facing* arrangement might give an R-T$_8$ cage by further intramolecular condensation. Contrary, the *apart* arrangement might lead to formation of the ladder structure by successive intermolecular condensation.

Cages including hexahedral T$_6$ and dodecahedral T$_{12}$ can be considered imaginarily to be formed through condensation of all-cis-T$_4$-tetrols and -T$_5$-pentaols of *facing* arrangement as one of the key steps in forming the siloxane linkage, as shown in Scheme 4.11. Kudo and co-workers reported the molecular orbital calculation of the formation energy of such cages assuming a similar reaction mechanism.[51]
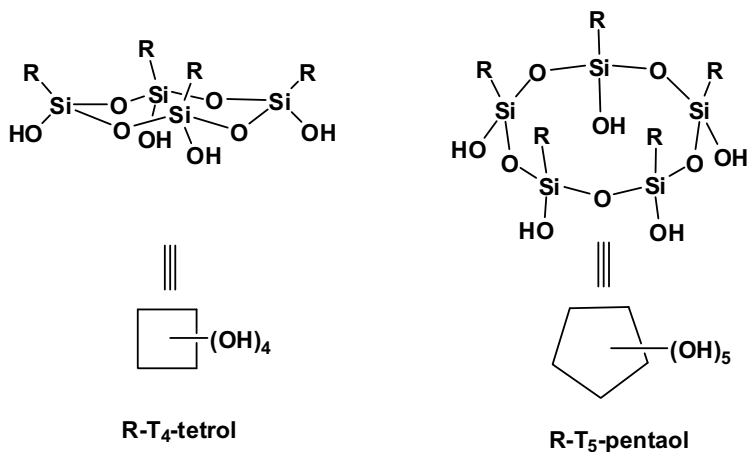
Figure 4.16. Cyclic all-cis-R-T_4-tetrol and R-T_5-pentaol.

Of course, this scheme is an imaginary one and does not express the real reaction mechanism. Nevertheless, the all-cis T_4-tetrol might be a possible key intermediate for the formation of various T_8.[39, 51, 52]

4.10. OCTAHEDRAL OCTASILSESQUIOXANE (T_8) FROM T_4-TETROL

When the all-cis-R-T_4-tetrol was treated with benzyltrimethylammonium hydroxide (BzTMAH), the T_8 cage was obtained as shown in Scheme 4.12.
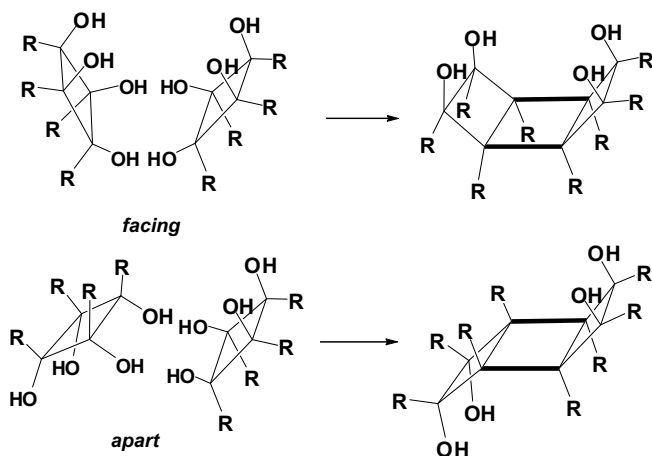
Scheme 4.10. Two possible *facing* and *apart* arrangements for the two all-cis-R-T_4-tetrols in forming a siloxane linkage (indicated by bold line).

Scheme 4.11. Imaginary schemes to give completely and incompletely condensed cage structures

Typical catalyst is BzTMAH or tetrabutylammonium fluoride (TBAF). The results under various reaction conditions are summarized in Table 4.2.[53]

It is interesting to comment that benzene is the best choice as the solvent to produce T_8 from T_4-tetrol as is the same with the direct synthesis of T_8 from phenyltri-(ethoxy)silane in the presence of BzTMAH. Tetrabutylammonium fluoride showed

Scheme 4.12. Formation of R-T_8 from all-cis-R-T_4-tetrol.

TABLE 4.2. Formation of Ph-T_8 from all-cis-Ph-T_4-tetrol (0.25 M) by Ammonium Catalysts

Catalyst	[Ph-T_4-tetrol]/ [Catalyst]	Temperature	Time (h)	Solvent	Yield (%)
				Acetone	1.5
				Methanol	Randomized
				Chloroform	16
BzTMAH	4.2 : 1	Reflux	2	Benzene	95
TBAF	100 : 1	Reflux	2	Benzene	82
	100 : 1	r.t.	72	Acetone[a]	85
	1.7 : 1		24	Acetone[b]	>95 (T_8 and T_{10})
	100 : 1		72	Methanol[a]	Mix[c]
	100 : 1		72	Chloroform[a]	61

[a] 0.14 M.
[b] 1.7 M Ref. 52.
[c] Mix: randomized with identifiable Ph-T_8.

higher reactivity than BzTMAH in benzene. Acetone is another choice to selectively obtain T_8, when TBAF is used as the catalyst. When a higher concentration of TBAF was used, a mixture of cages were formed[44a, 52]. Under such conditions, the kinetic rate of the formation and further scrambling and decomposition, described later, seems competitive. Solubility of the products in the solvent is another important factor to determine the products. The reaction with TBAF was applied to 4-methylphenyl-(4-CH_3Ph-), i-butyl-(i-Bu-), naphthyl-(Np-), and T_4-tetrol derivatives.

Isobutyl (2-methylpropyl) derivative gave a good yield of T_8 in various solvents. In the case of naphthyl-T_4-tetrol, the reaction was slower than in the case of the isobutyl derivative, and a higher concentration of the reagents and a longer reation time were applied.

4.11. SCRAMBLING OF THE COMPONENTS IN THE FORMATION OF T_8

The formation of T_8 from T_4-tetrol was originaly intended to synthesize unsymmetrical T_8 from the combination of two different T_4-tetrols. The interesting fact in the formation of T_8 from T_4-tetrols lies at the points where T_8 could also be obtained from the steroisomeric mixture of Ph-T_4-tetrol, and that scrambling of the component of T_4-tetrol in the produced T_8 had occurred. To study the situation, a mixture of Ph-T_4-tetrol and Ph-d_5-T_4-tetrol was treated under the same reaction conditions. The MALDI-TOF MS of the product shown in Figure 4.17 clearly indicates the random distribution of each component in the produced T_8.

Decomposition of T_4-tetrols and reassembling to T_8's simultaneously occur in the reaction system. This reaction can be applied to synthesize T_8 with mixed substituents in the cage.
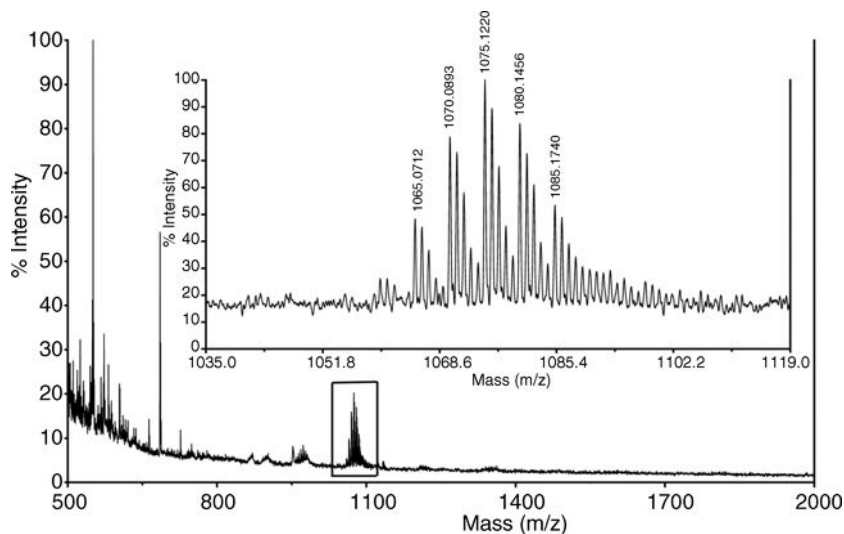
Figure 4.17. MALDI-TOF MS of the product Ph-T_8 from the mixture of Ph-T_4-tetrol and Ph-d_5-T_4-tetrol.

To widen the applicability of POSS derivatives, it is very important to introduce functional groups in the POSS structure. There are some cases where the T_4-tetrol cannot be isolated as pure tetrol, or neutralization of the alkali metal salt with acid gives a complex product mixture. A typical example is the 4-bromophenyl (4-BrPh) derivative.[54] The alkali metal salt of 4-BrPh-T_4-tetrol could be isolated as a solid crystalline material, but neutralization gave complex oligomeric condensed products. When the condensed product was treated with BzTMAH, 4-BrPh-T_8 was obtained as the pure crystalline material in reasonable yield (30%). Laine and co-workers reported the synthesis of 4-BrPh-T_8 by the bromination of Ph-T_8 and obtained a complex mixture of the product.[55] The brominated T_8 can be used in the synthesis of new POSS systems.

The amino group is one of the versatile functional groups to construct new structure by condensation or addition reactions. Introduction of a nitro group is the key step to introduce an amino group directly on the aromatic group. Olsson, Laine, and co-workers reported the nitration of Ph-T_8 by fuming nitric acid[56] and further functionalization and application of the product[5, 6b] but the extent and position of nitration was not controlled, and the multi- but incomplete functionalization of the phenyl ring often made it unclear how to correlate the property of the system with the structure. Recently, Zhang and co-workers reported an improved synthesis of octa-nitrated Ph-T_8, but the position of the nitration was not controlled. Nitration at the 2-, 3-, and 4-positions had occurred.[57] We also confirmed their result.

It is well known that the aryl-silicon bonds are susceptible to cleavage by electrophilic reagents. Deans and Eaborn reported that nitration of 1,4-bis(trimethyl-silyl)benzene by fumic nitric acid resulted in the substitution of one trimethylsilyl group by a nitro group.[58]
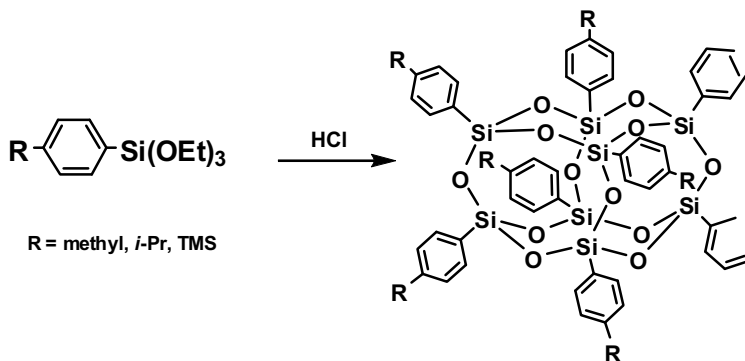
Scheme 4.13. Formation of 4-substituted-phenyl-T_8 under acidic conditions.

4-Methylphenyl-T_8 (4-tolyl-T_8), 4-(1-methylethyl)lphenyl-T_8 (4-i-PrPh-T_8), and (4-trimethylsilylphenyl)-T_8 (4-TMSPh-T_8) were obtained by direct acidic hydrolysis of (4-tolyl)triehoxysilane, (4-i-PrPh)triehoxysilane, and (4-TMSPh)triethoxysilane in the presence of hydrochloric acid as shown in Scheme 4.13.

Hydrolysis of (4-TMSPh)triethoxysilane in the presence of TBAF gave a mixture of 4-TMSPh-T_8, -T_{10}, and -T_{12} cages having T_{10} as the major fraction, as shown in Scheme 4.14.

These cages could easily be separated by selective crystallization. Such a rearrangement and scrambling of POSS cage structures is commonly observed[44a, 45b, 47c, 52].

4.12. NITRATION OF 4-SUBSTITUTED-Ph-OLIGOSILSESQUIOXANE (POSS)

First, nitration of 4-tolyloctasilsesquioxane was examined. Nitration by fumic acid at room temperature was not clean and gave various products. Nitration by copper(II) nitrate trihydrate (copper(II) nitrate/octasilsesquioxane = 1.2/0.125 mol/mol at room
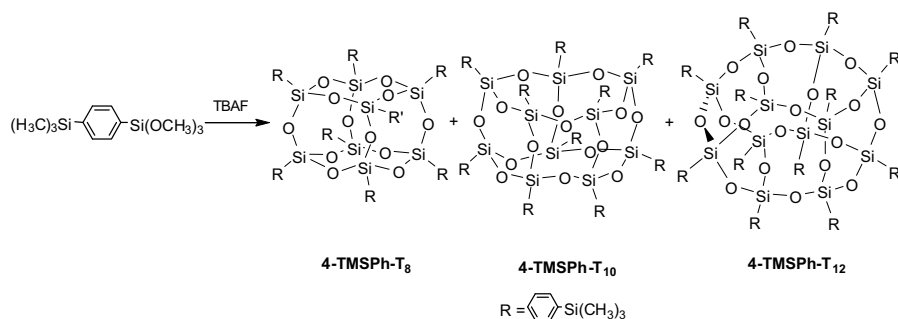
Scheme 4.14. Synthesis of 4-TMSPh-POSS cages in the presence of TBAF.

temperature) seemed clean but slow. When the starting material's peak in ^{1}H NMR has disappeared, three aromatic protons at 8.32, 7.87, and 7.45 ppm, and one CH_3Ph at 2.64 ppm appeared, which strongly supported the formation of a 4-methyl-3-nitrophenyl group. Nitration with fuming nitric acid at $-30°$C was also found to give a clean reaction product. ^{29}Si NMR showed only one peak at -79.4 ppm assignable to T^3 structure in the absence of T^1 (~-68 ppm) or T^2 (~-70 ppm) structure.

Nitration of 4-TMSPh-T_8 by fuming nitric acid was carried out. The reaction at $-30°$C gave almost pure completely nitrated products. Cleavage of Si–oxygen or Si–phenyl in silsesquioxane structure was not noticed. The reaction is shown in Scheme 4.15.[59]

4.13. INCOMPLETELY CONDENSED POSS: HEPTAPHENYLTRICYCLO [7.3.3.1^{5,11}]HEPTASILSESQUIOXANE-3,7,14-TRIOL (HEPTAPHENYLHEPTASILSESQUIOXANETRIOL: Ph-T$_7$-TRIOL) AND OCTAPHENYLTETRACYCLO[7.3.3.3^{3,7}]OCTASILSESQUIOXANE-5,11,14,17-TETROL (OCTAPHENYLOCTASILSESQUIOXANETETROL: Ph-T$_8$-TETROL)

When application to the synthesis of new cage-containing structure is considered, incompletely condensed systems, in which silanol functional groups are included,
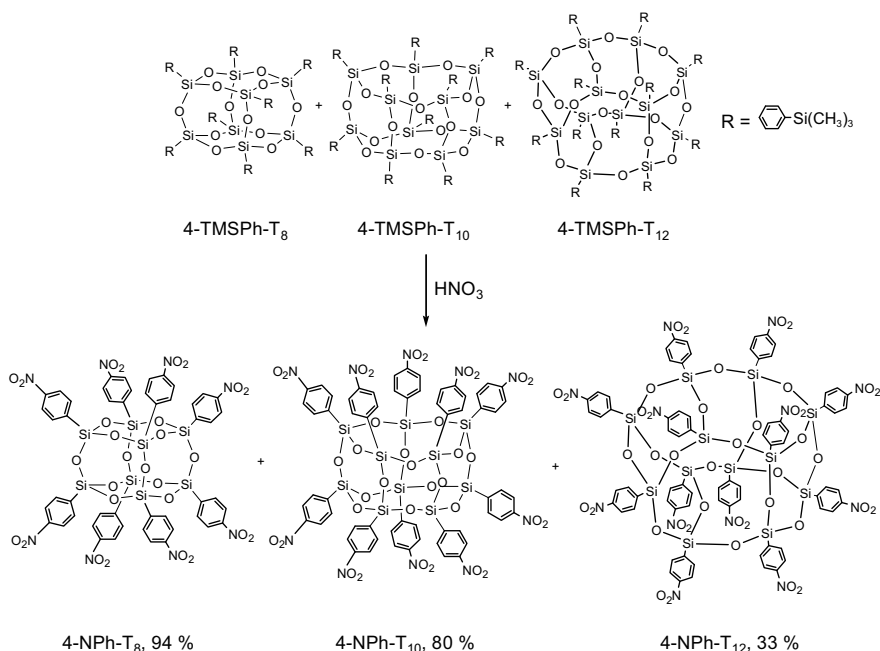
Scheme 4.15. Clean and complete nitration at 4-position of phenyl groups of 4-TMSPh-POSS cages (see also Scheme 4.14).
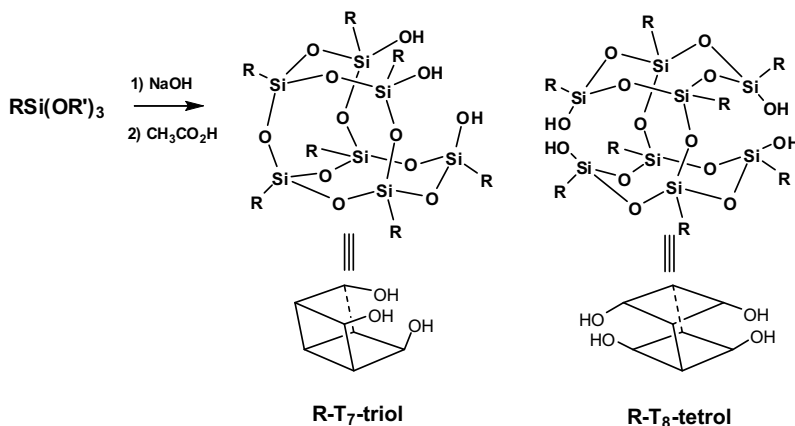
Scheme 4.16. Formation of incompletely condensed R-T$_7$-triol and R-T$_8$-tetrol cages.

can conveniently be used. A typical incompletely condensed cage is heptasilses-quioxanetriol (T$_7$-triol), which is usually used to synthesize a POSS-functionalized monomer like methacrylate.[43] Products seem to have been generated from multistep processes via many different intermediates.[3, 42b–h, 44, 46, 47b–c, 60] We paid attention to tetrafunctional octasilsesquioxanetetrol (T$_8$-tetrol)[47] possibly produced for aromatic substituents according to Scheme 4.16.

4.14. FORMATION OF Ph-T$_8$-TETROL

When phenyltri(methoxy)silane was reacted with water in the presence of sodium hydroxide (Si : Na : H$_2$O $= 1.0 : 1.0 : 1.0$) in i-propanol or i-butanol, all-cis-Ph-T$_4$-tetrol was formed. Meanwhile, when phenyltrimethoxysilane (0.24 mol) was treated with sodium hydroxide in the molar ratio of Si : sodium $= 2 : 1$ at the refluxing temperature of i-propanol (240 mL) for 4 h under nitrogen, a crystalline compound was formed.[47b–c] After 40 h of stirring, a product with 1379.47m/z (calculated 1379.24) and two ^{29}Si signals at -76.12 and -78.94 (O$_3$$Si$Ph) was obtained after trimethylsilyl (TMS) capping, which was determined as tetrakis (TMS)-Ph-T$_8$-tetrol (68.2% yield). Single crystal XRD analysis of the compound after neutralization confirmed the double-decker structure. The XRD structure is shown in Figure 4.18.

4.15. SCRAMBLING OF COMPONENTS IN THE FORMATION OF Ph-T$_8$-TETROL

The cleavage of completely condensed octaphenyloctasilsesquioxane (Ph-T$_8$) under strongly basic conditions was studied with the intention of obtaining Ph-T$_8$-tetrol.
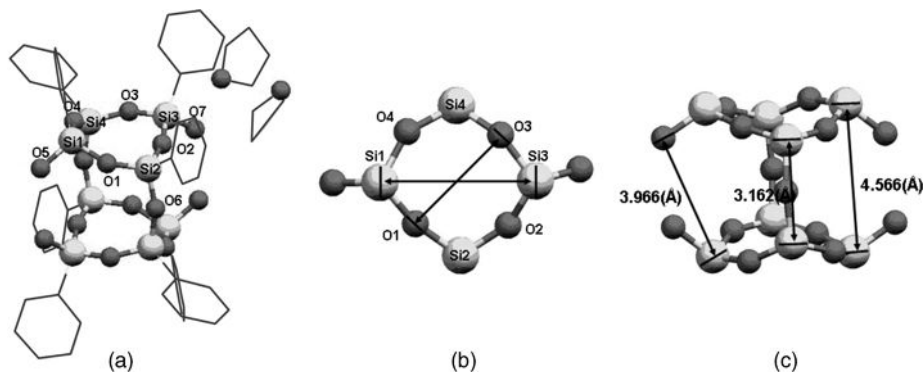
Figure 4.18. XRD structure of Ph-T$_8$-tetrol.

Apparent reaction paths are shown in Scheme 4.17.

When Ph-T$_8$ was hydrolyzed with water and sodium hydroxide (Ph-T$_8$: H$_2$O : NaOH = 1 : 2 : 4 in molar ratio) in i-propanol, Ph-T$_8$-tetrol was obtained in high yield, when the hydrolysis was carried out in refluxing i-propanol or at 90°C in i-butanol for 24 h. When the molar ratio of raw materials (Ph-T$_8$: H$_2$O : NaOH) was changed from 1 : 2 : 4 to 1 : 1 : 2, Ph-T$_7$-triol became the main product. When cohydrolysis of Ph-T$_8$ and Ph-d_5-T$_8$ was carried out, not only T$_8$-tetrol but also T$_7$-triol with mixed substituents were formed. Quantitative data of the distribution of deuterated substituents were obtained by MALDI-TOF MS, as shown in Table 4.3.
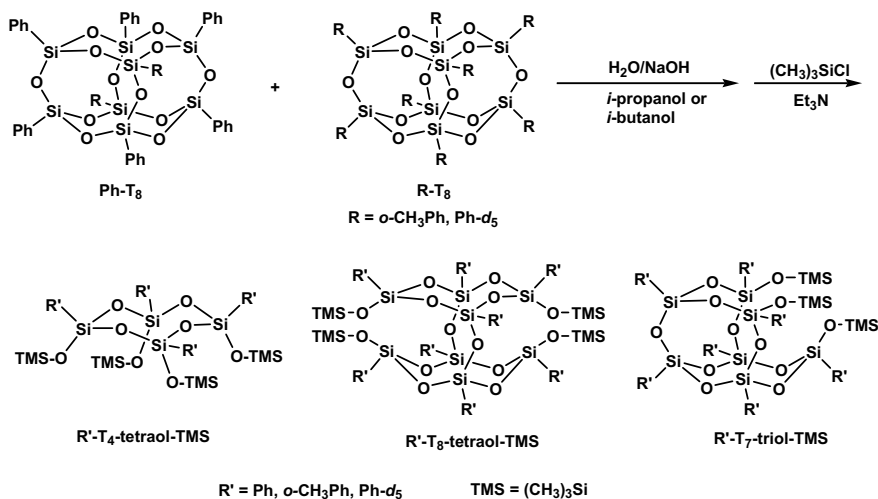
Scheme 4.17. Formation of incompletely condensed T$_7$-triol and T$_8$-tetrol cages via hydrolysis of the mixture of completely condensed T$_8$ cages followed by trimethylsilyl (TMS) capping.

TABLE 4.3. MALDI-TOF MS Data for R′-T$_7$-triol-TMS and R′-T$_8$-tetrol-TMS Obtained from Ph-T$_8$ and Ph-d_5-T$_8$ Cohydrolysis After TMS Capping

	Ph/Ph-d_5	Relative Intensity	[M + Na]$^+$ Found	[M + Na]$^+$ Calculated
R′-T$_7$-triol-TMS	6/1	25	1174.61	1174.21
	5/2	63	1180.15	1179.25
	4/3	100	1185.22	1184.28
	3/4	99	1189.26	1189.31
	2/5	64	1195.16	1194.34
	1/6	34	1199.09	1199.37
R′-T$_7$-triol-TMS	7/1	11	1384.50	1384.27
	6/2	21	1389.99	1389.30
	5/3	40	1394.82	1394.33
	4/4	45	1399.65	1399.36
	3/5	41	1403.99	1404.39
	2/6	26	1409.81	1409.42
	1/7	11	1415.48	1414.46

Deuterated substituents were distributed randomly in both R′-T$_7$-triol-TMS and R′-T$_8$-tetrol-TMS. The scrambling of substituents occurred even at room temperature for T$_4$, although not as extensively.

If the hydrolysis of Ph-T$_8$ is a simple decomposition process, the frameworks of Ph-T$_7$-triol-TMS and Ph-T$_8$-tetrol-TMS should consist of only one kind of the same substitutent, but this is not the case.

4.16. REACTIVITY OF FOUR SILANOL GROUPS OF Ph-T$_8$-TETROL

The reactivity of each silanol in Ph-T$_8$-tetrol seems quite similar, and selective functionalization was difficult. Treatment of Ph-T$_8$-tetrol with equimolar amount of dialkyldichlorosilane usually gave bis(dialkylsilyl)-substituted product, R,R′-B$_{10}$, as shown in Scheme 4.18.

By controlling the reaction conditions, the facing diol functions could be bridged to give capped product at only one side, R,R′-B$_9$-diol.
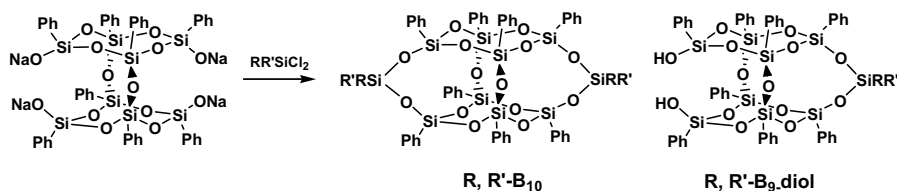
Scheme 4.18. Bridging of Ph-T$_8$-tetrol by dialkyldichlorosilane.

4.17. POLYMERS AND HIGHER ORDER STRUCTURE WITH CAGE POSS CORE

It is generally accepted that many of the properties of polysiloxanes are a consequence of the static and dynamic nature of the siloxane backbone.[61] Linear poly (dimethylsiloxane)s have been well known to show particular characteristics such as low glass transition temperature (T_g), thermostability, stability against oxidation originated from a strong and flexible main chain, physiological inertness, and hydrophobicity based mainly on the methyl side chain. However, low T_g and easy cleavage of Si–O–Si bonds under acidic or basic conditions or by thermal treatment often limits their applications.[62] Introduction of bulky and rigid moieties like phenylene, naphthylene, anthrylene, phenanthrylene, or adamantylene moieties in the main chain increases T_g and thermal stability of the polysiloxanes.[18c, 63] These polymers, especially poly(arylene-dimethylsiloxane)s, are good candidates for high-temperature elastomers.[62a, 64]

Although the introduction of bulky and rigid organic moieties improves some expected properties, it breaks the continuity of the Si–O–Si backbone in the polymer. If double-decker silsesquioxane consisting of only siloxane bonds was introduced into the polysiloxane backbone instead of an organic counterpart, the resulting polymer is expected to exhibit further higher T_g and better thermostability compared to the case with organic moieties, because of the stronger siloxane bonds. In addition, the 3D silsesquioxane part might introduce toughness and enhanced gas permeability to the polymer through loose packing, leaving some free volumes, and also reduce its dielectric constant because of the low polarity of cage silsesquioxane.[43b, 48a–c]

By selecting a suitable bridging group of Ph-T_8-tetrol, a functional group can be introduced to the cage POSS structure to produce R,R'-B_{10} with a polymerizable group. A typical functional group is SiH, namely, a silane functional group. Usually, hydrosilylation is the choice of the reaction to construct a polymer structure using hydrosilyl-bridged R,H-B_{10}.[65] We have been interested in achieving a higher order structure of polymers or silsesquioxanes by borane catalyzed siloxane bond formation.

4.18. SYNTHESIS OF SILANE-, SILANOL-FUNCTIONALIZED CAGE POSS

The synthetic route to i-B,OH-B_{10} is shown in Scheme 4.19.[66]

Hydrolysis of the product gave silanol. Existence of two doublets at 0.81 (CH_2) and another two doublets at 0.91 (CH_3)$_2$ ppm in ^{1}H strongly suggests the existence of isomers for i-B,OH-B_{10}. (See Figure 4.19.)

Isomers of i-B,OH-B_{10} were separated by fractional crystallization and column chromatography. ^{1}H, ^{29}Si, and MALDI-TOF MS and single crystal XRD definitely confirmed the structure of each isomer.

Other silane- or silanol-functionalized compounds were also synthesized similarly, as reported and as shown in Scheme 4.20.[43b, 67]
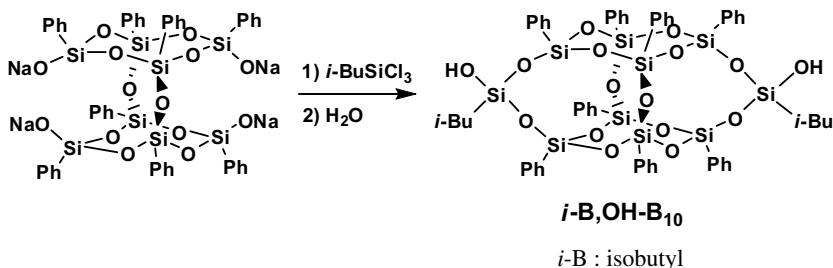
Scheme 4.19. Capping of T_8-tetrol tetra sodium salt with i-butyltrichlorosilane.

4.19. REACTIVITY OF SILANE AND SILANOL FUNCTIONS IN CAGE POSS STRUCTURE: SILOXANE BOND FORMATION IN THE PRESENCE OF TRIS(PENTAFLUOROPHENYL)BORANE

Condensation of a silane functional group with either silanol, alkoxysilane, or alcohol catalyzed by tris(pentafluorophenyl)borane (TFB) has proved useful to form siloxane linkages.[66, 68] A transition metal catalyst can be also used.[18a] The reaction catalyzed by TFB is considered to proceed by the activation of the silane functional group by TFB. (See Scheme 4.21.)

We noticed that the reactivity of the silane and silanol (alkoxysilane) components in the condensation was very much dependent on the steric environment of the silicon atom bearing the functional group. Reaction of M,H-B$_{10}$ with M,OH-B$_{10}$, or i-B,OH-B$_{10}$ also proceeded without any big problem. For example, M,H-B$_{10}$ (0.97 g, 10.9×10^{-4} mol) and an isomeric mixture of i-B,OH-B$_{10}$ (0.1 g, 1.8×10^{-4} mol), and TFB (0.0074 g, 1.5×10^{-5} mol, 2 mol%) were reacted in toluene (5 mL) at room temperature for 24 h. The resulting solution after filtration through a Florisil column was reduced in volume under vacuum and precipitated slowly via slow addition into methanol (40 mL) to obtain a white polymeric solid (0.98 g).

The reaction of triphenylsilanol with i-B,H-B$_{10}$ or i-B-T$_8$H did not proceed well. The reactions of i-B,H-B$_{10}$ with M,OH-B$_{10}$ or i-B,OH-B$_{10}$ did not give any polymers, even at 110°C with a long reaction time (72 h). Steric hindrance around the silane function in i-B,H-B$_{10}$ seems quite high in the presence of isobutyl substituent as shown in Scheme 4.22.
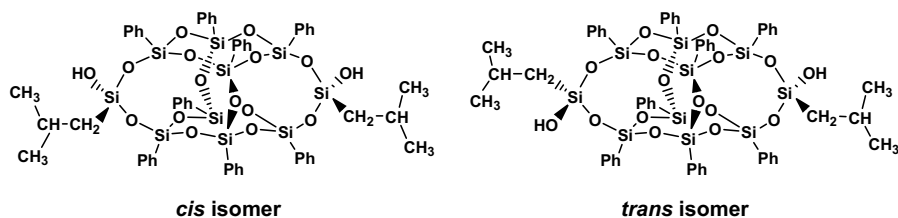
Figure 4.19. Cis and trans configuration of i-B,OH-B$_{10}$.
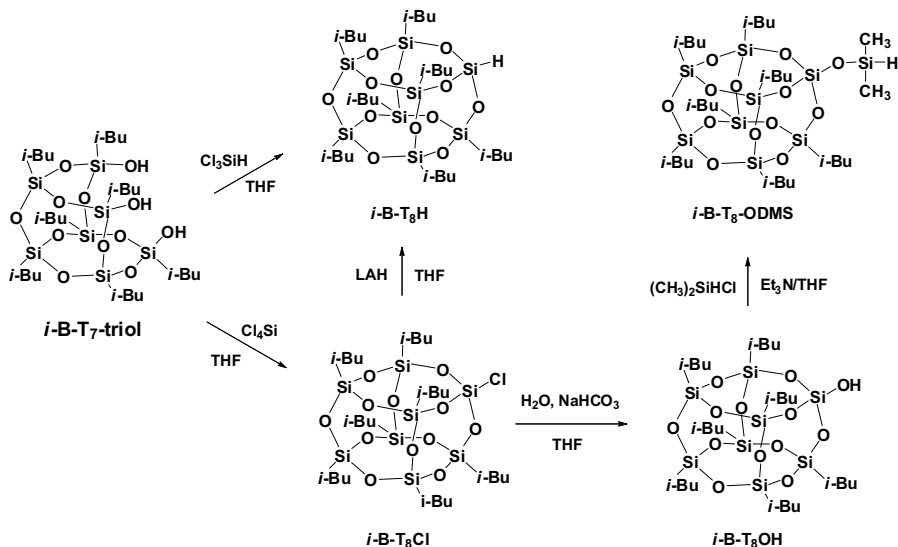
Scheme 4.20. Synthetic scheme of functional i-B-T$_8$ from i-B-T$_7$-triol.

The reactivity of the silane is improved in M,H-B$_{10}$ (D structure). Not surprisingly, if one more silicon atom is covalently introduced onto the T$_8$ framework structure, the reactivity of the produced i-B-T$_8$-ODMS (M structure) is very much improved compared with that of i-B-T$_8$H in which the hydrogen is attracted to the T-structured atom, as shown in Figure 4.20.

4.20. POLYMERS WITH CAGE POSS CORE IN THE MAIN CHAIN

Based on the above-mentioned results, polymers were synthesized using i-B,OH-B$_{10}$ and linear oligosiloxane. (See Scheme 4.23.)

The results of polymerization are summarized in Table 4.4.
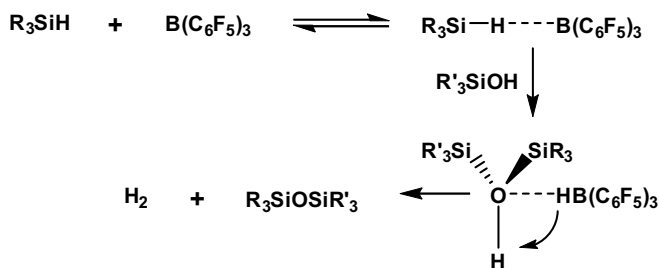
Scheme 4.21. Proposed reaction mechanism of the TFB-catalyzed dehydrogenative coupling reaction.
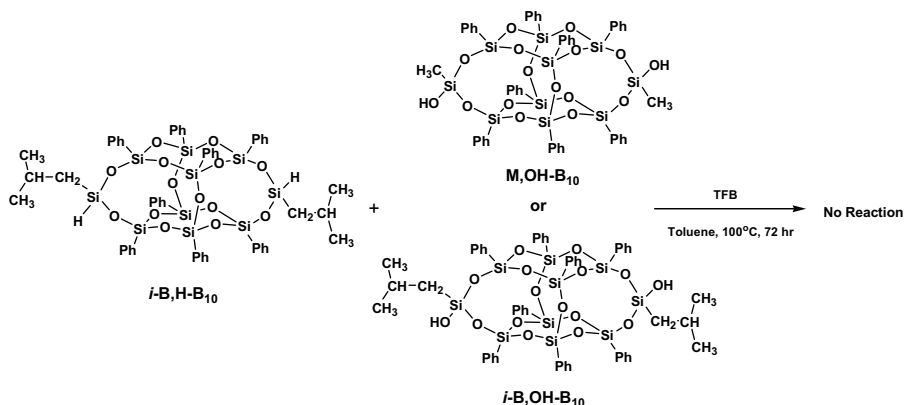
Scheme 4.22. Attempted polymerization of *i*-B,H-B$_{10}$ and *i*-B,OH-B$_{10}$ and M,OH-B$_{10}$.

Figure 4.21 shows the ^{29}Si NMR of polymers. The peak at around -55.95 ppm assigned to the T$_2$-structured silicon O$_2$*Si*(*i*-B)(OH) completely disappeared and a new signal at -67.27 ppm was observed as a T$_3$-structured silicon atom, which also confirms the condensation between the hydroxyl group of *i*-B,OH-B$_{10}$ and the hydrogen atom (HSi) of tetrasiloxane. Furthermore, two new signals at -21.18 ppm and -20.63 ppm in Figure 4.21 are assignable to the silicon chemical shifts of tetrasiloxane.

All the polymers exhibit good thermal stability above 450°C. The high thermal stabilities of these polysiloxane polymers arise due to the presence of the B$_{10}$ unit in the main chain. It can be seen that 5% weight loss temperature (T_{d5}) for the P$_{cis}$ and P$_{trans}$ are around 500°C in a nitrogen atmosphere while that of P$_{mix}$ is 450°C. The distinguishable low degradation temperature recorded for P$_{mix}$ compared to that of P$_{cis}$ and P$_{trans}$ might be due to the presence of the random cis and trans sequence of B$_{10}$ in the backbone. The residual weights at 760°C for P$_{cis}$, P$_{trans}$, and P$_{mix}$ are 77%, 79%, and 71%, respectively, in nitrogen. The residual weight at the same temperature analyzed in air was 53%, which was consistent with the complete removal of only organic moieties from the polymer structure via oxidation, namely, as SiO$_2$ (53%). Apparently, no cleavage of tetrasiloxane or cage component occurred. Accordingly,
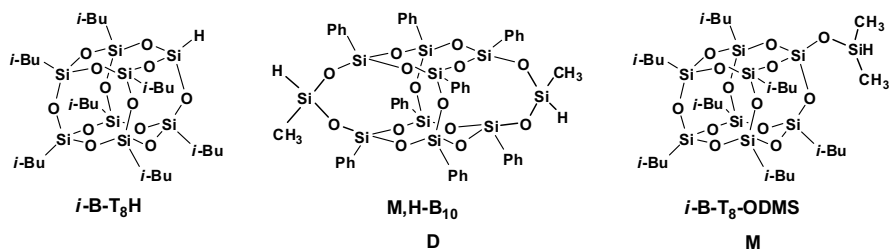
Figure 4.20. Structure of silane function in various POSS structures.
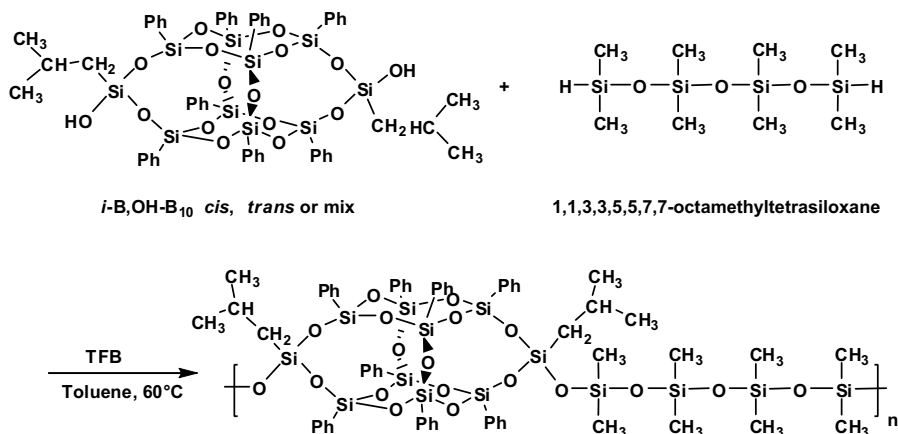
Scheme 4.23. Cross-dehydrocoupling polycondensation of *i*-B,OH-B$_{10}$ and 1,1,3,3,5,5,7,7-octamethyltetrasiloxane to obtain polymer P$_{cis}$, P$_{trans}$, and P$_{mix}$.

some of the organic moieties still remain at 760°C, while maintaining all the siloxane-connected main chain under a nitrogen atmosphere.

   Although polymers P$_{cis}$, P$_{trans}$, and P$_{mix}$ were made of a high content of double-decker silsesquioxane (82 wt%), they provide excellent film qualities with high transparency. Films with thickness of 50–85 μm were prepared. The optical transparency of polymer can be compared by the photograph of the silsesquioxane symbol taken through polymer as shown in Figure 4.22 for P$_{cis}$.

   Polymers were also synthesized from M,H-B$_{10}$ and M,OH-B$_{10}$ or *i*-B,OH-B$_{10}$ based on previously described data. Interestingly, the reactions proceeded at 90°C in 12 h. (See Scheme 4.24).

TABLE 4.4. Polymerization of *i*-B, OH-T$_8$-tetrol with Octamethyltetrasiloxane with 1:1 Feed Ratio Catalyzed by TFB at 60°C and Thermal Properties of the Formed Polymers

						Polymers			
						$T_{d5}{}^d$ (°C)		Residual (wt%)	
i-B, OH-B$_{10}$									
Structure	$T_m{}^a$ (°C)		$(M_w/M_n)^b$ × 10^{-3}	$T_g{}^a$ (°C)	$T_s{}^c$ (°C)	N$_2$	Air	N$_2$	Air
cis	304	**P**$_{cis}$	50/29	~30	~39	500	470	77	52
trans	357	**P**$_{trans}$	64/39	~35	~82	500	460	79	53
mix	295	**P**$_{mix}$	42/27	~34	~45	450	400	71	53

^{a} Determined by DSC (30°C/min).
^{b} By GPC with polystyrene standard.
^{c} By TMA (10°C/min).
^{d} A 5% weight loss by TGA (10°C/min).
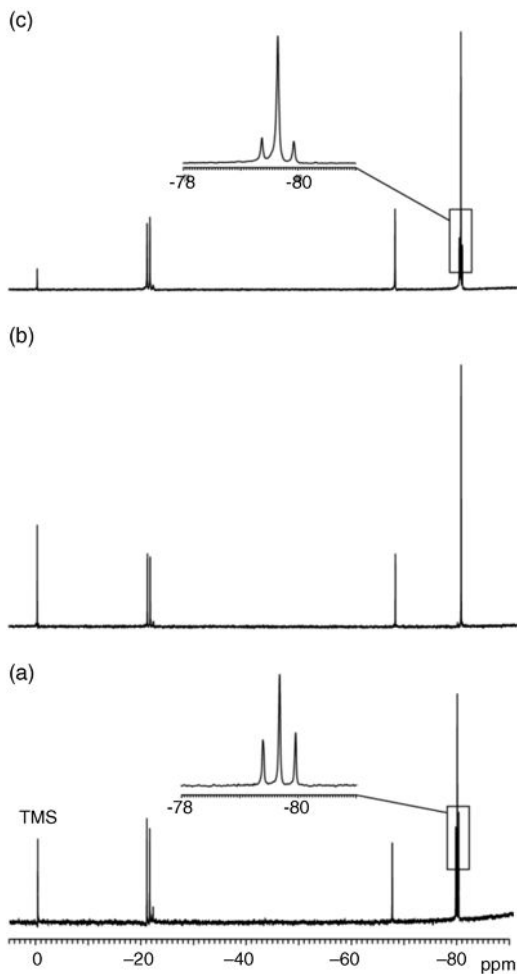
Figure 4.21. ^{29}Si NMR of polymer (a) P$_{cis}$, (b) P$_{trans}$, and (c) P$_{mix}$.
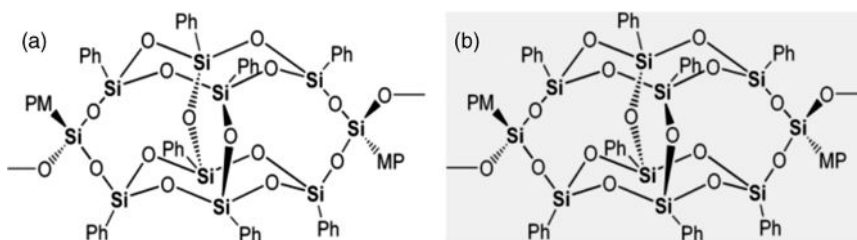
Figure 4.22. Photographs of silsesquioxane symbol on a white paper, taken (a) directly or (b) through a film of P$_{cis}$.
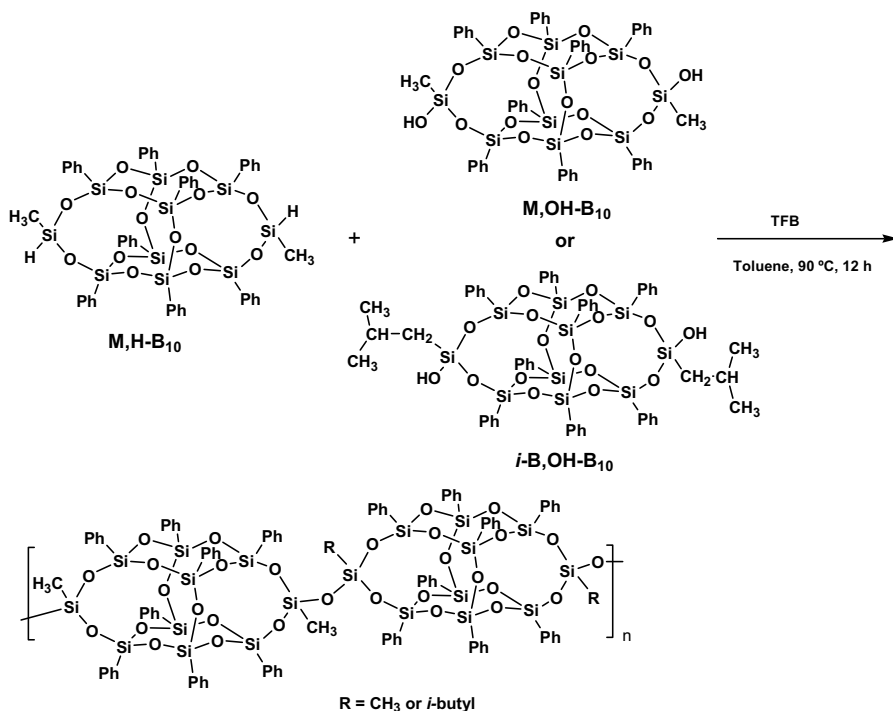
Scheme 4.24. Polymerization of M,H-B$_{10}$ with B$_{10}$ silanols.

Polymers with M_w by GPC—$M_w/M_n = 24000/9000$ and $M_w/M_n = 23000/9000$—were obtained from the combination of M,H-B$_{10}$ and M,OH-B$_{10}$ or i-B,OH-B$_{10}$

4.21. HIGHER ORDER POLYSILSESQUIOXANE STRUCTURE WITH POSS AS CONSTITUTIONAL UNITS

Although some interest has been shown in the construction of dendritic polysiloxane systems,[68h,i,69] research on the preparation of higher order silsesquioxane systems with cage oligosilsesquioxane (POSS) as constitutional units has been limited until now. Wada and co-workers reported on alkylene bridged higher order POSS as a model for a silica catalyst surface.[70] This was the first attempt to prepare the giant silsesquioxanes with dendritic structure, in which POSS was incorporated as cores and periphery. However, there have been almost no reports on the construction of higher order silsesquioxane systems composed of POSS with definite structure connected through the siloxane linkage, which allows enhanced thermal stability of the materials compared to those made of the alkylene linkages.

Dehydrogenative coupling reactions of POSS silanes with POSS silanols were carried out in the presence of TFB. The reaction scheme and the structure of the compounds are shown in Scheme 4.25.
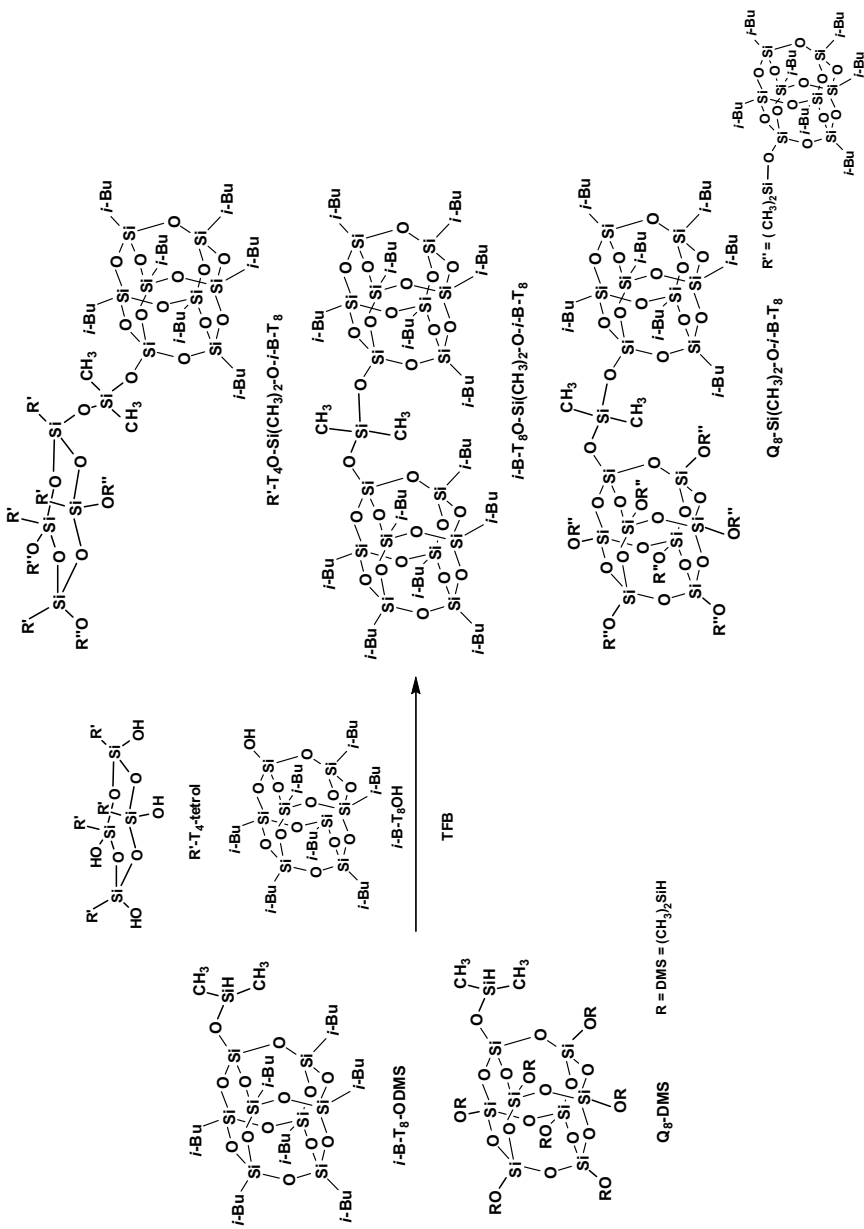
Scheme 4.25. Dehydrogenative coupling reaction of POSS silane with POSS silanol.
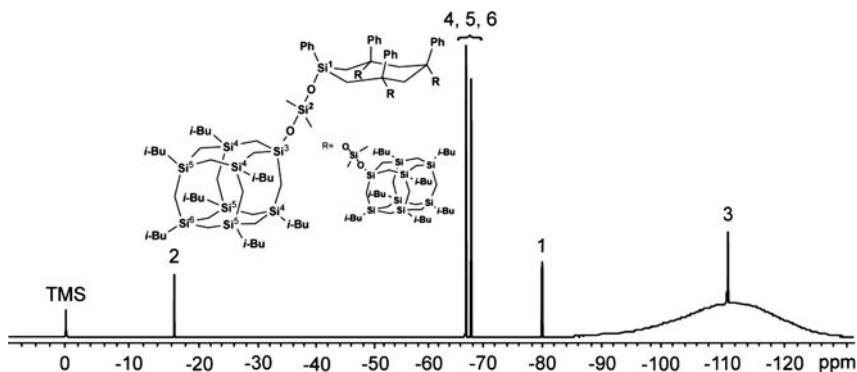
Figure 4.23. ^{29}Si NMR of the product from Ph-T$_4$-tetrol with i-B-T$_8$-ODMS.

The reaction of Ph-T$_4$-tetrol with i-B-T$_8$-ODMS was rather slow, when equimolar amounts of the reagents were used. Simple passage through a Florisil column was sufficient to obtain the completely substituted product by removing the incompletely reacted compounds with remaining silanol groups, or excess Ph-T$_4$-tetrol. ^{29}Si NMR signal of the product is shown in Figure 4.23. MALDI-TOF MS gave the value of 4135 for $[M + Na]^+$, for the calculated molecular weight based on the most abundant isotope, 4110. The compound was concluded to be the target compound.

To investigate further, the reaction of Q$_8$-DMS with i-B-T$_8$OH was performed at room temperature, or at 60°C. When fourteen equivalents of i-B-T$_8$OH were used, a product was obtained after passing through a long Florisil column to remove excess i-B-T$_8$OH, whose ^{29}Si NMR signal is shown in Figure 4.24.

Hydrosilane resonance (δ 4.7 in ^{1}H) completely disappeared, and a new siloxane methyl signal appeared at 0.2 ppm. ^{29}Si NMR indicates the presence of Q (-112 ppm), T (-70 ppm), and D (-18 ppm) type silicon atoms. The presence of D type Si signal also clearly indicates the formation of siloxane linkage between Q and
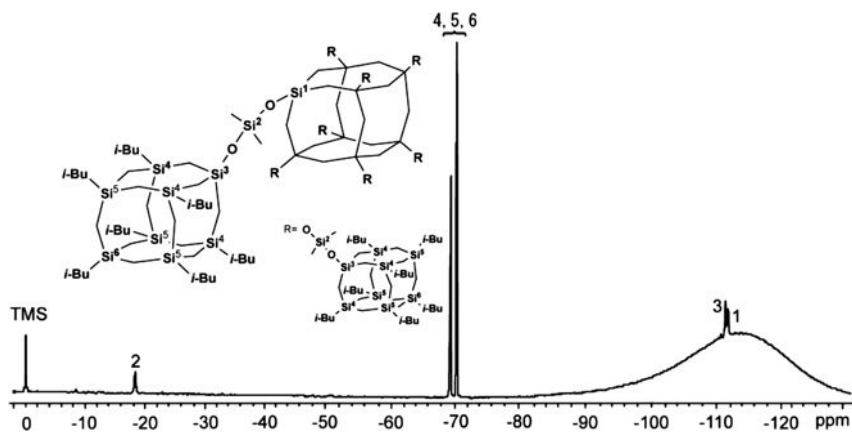
Figure 4.24. ^{29}Si NMR for the product from Q$_8$-DMS with i-B-T$_8$OH.

T_8 cages. The Q type signal was shifted to a higher field compared with its original position (-108 ppm), and the T type signal was also shifted from -100 ppm. Thus, the NMR signals qualitatively support the formation of desired product.

CONCLUSION

Synthesis, specific reactivity, and stereochemical aspects of silicon compounds were described. By taking advantage of such characteristics, new function was designed, stereoregularity of polysiloxane was controlled, and new polymeric systems and higher order polysilsesquioxane systems were constructed.

ACKNOWLEDGMENT

REFERENCES

1. (a) Szwarc, M. *Nature*, **1956**, *178*, 1168. (b) Szwarc, M.; Levy, M.; Milkovich, R. *J. Am. Chem. Soc.*, **1956**, *78*, 2656. (c) Szwarc, M.; Beylen, M. V. *Ionic Polymerization and Living Polymers*. Chapman & Hall, New York, 1993.

2. Jones, R. G.; Ando, W.; Chojnowski, J.; Eds. *Silicon Containing Polymers: The Science and Technology of Their Synthesis and Applications*. Kluwer Academic Publishers, Dordrecht, 2000.

3. (a) Baney, R. H.; Itoh, M.; Sakakibara, A.; Suzuki, T. *Chem. Rev.*, **1995**, *95*, 1409. (b) Harrison, P. G. *J. Organomet. Chem.*, **1997**, *542*, 141. (c) Clarson, S. J.; Fitzgerald, J. J.; Owen, M. J.; Smith, S. D. *Silicones and Silicone-Modified Materials*. ACS Symposium Series 729. American Chemical Society, Washington DC, 2000. (d) Chandrasekhar, V.; Boomishankar, R.; Nagendran, S. *Chem. Rev.*, **2004**, *104*, 5847. (e) Hanssen, R. W. J. M.; Van Santen, R. A.; Abbenhuis, H. C. L. *Eur. J. Inorg. Chem.*, **2004**, 675.

4. Smith, A. L. *The Analytical Chemistry of Silicones*. Wiley Interscience, Hoboken, NJ, 1991.

5. (a) Yajima, S.; Hayashi, J.; Omori, M. *Chem. Lett.*, **1975**, *4*, 931. (b) Yajima, S.; Okamura, K.; Hayashi, J. *Chem. Lett.*, **1975**, *4*, 1209.

6. Miller, R. D.; Michl, J. *Chem. Rev.*, **1989**, *89*, 1360.

7. Shinke, S.; Kawakami, Y. *Chromatographia*, **2001**, *53*, 140.

8. (a) Corriu, R. J. P.; Guerin, C.; Moreau, J. J. E. Dynamic stereochemistry at silicon. In: *The Chemistry of Organic Silicon Compounds*, Vol. 1. Patai, S.; Rappoport, Z., Eds. Wiley, *Chichester, UK*, 1989; Chapter 4, p. 305. (b) Brook, M. A. *Silicon in Organic, Organometallic, and Polymer Chemistry*. Part 1. Wiley, Hoboken, NJ, 2000; p. 115. (c) Sommer, L. H. *Stereochemistry, Mechanism and Silicon*. McGraw-Hill, New York, 1965.

9. (a) Kawakami, Y.; Takeyama, K.; Komuro, K.; Ooi, O. *Macromolecules*, **1998**, *31*, 551. (b) Kawakami, Y.; Takahashi, T.; Yada, Y.; Imae, I. *Polym. J.*, **1998**, *30*, 1001.

10. Uenishi, K.; Imae, I.; Shirakawa, E.; Kawakami, Y. *Macromolecules*, **2002**, *35*, 2455.

11. Omote, M.; Tokita, T.; Shimizu, Y.; Imae, I.; Shirakawa, E.; Kawakami, Y. *J. Organomet. Chem.*, **2000**, *611*, 20.

12. Suzuki, K.; Kawakami, Y. *Organometallics*, **2003**, *22*, 2367.

13. Sheikh, Md. R. K.; Imae, I.; Tharanikkarasu, K.; LeStrat, V. M.-J.; Kawakami, Y. *Polym. J.*, **2000**, *32*, 527. (b) Sheikh, Md. R. K.; Imae, I.; Tharanikkarasu, K.; Kawakami, Y. *Macromolecules*, **2001**, *34*, 4384. (c) Hyun, J.-Y.; Kawakami, Y. *Polym. J.*, **2004**, *36*, 865.

14. (a) Baer, M. *J. Polym. Sci. A2*, **1964**, 417. (b) Tsuruta, T. *Prog. Polym. Sci.*, **1972**, *3*, 1.

15. (a) Kloninger, C.; Rehahn, M. *Macromolecules*, **2004**, *37*, 1720. (b) Wang, H.; Winnik, M. A.; Manners, I. *Macromolecules*, **2007**, *40*, 3784. (c) Kloninger, C.; Knecht, D.; Rehahn, M. *Polymer*, **2004**, *45*, 8323. (d) Datta, U.; Rehahn, M. *Macromol. Rapid Commun.*, **2004**, *25*, 1615. (e) Bellas, V.; Rehahn, M. *Angew. Chem. Int. Ed.*, **2007**, *46*, 5082. (f) Kloninger, C.; Rehahn, M. *Macromol. Chem. Phys.*, **2007**, *208*, 833.

16. Dvornic, P. R.; Lenz, R. W. *High Temperature Siloxane Elastomers*. Hüthig & Wepf, Basel, 1990.

17. (a) Merker, R. L.; Scott, M. J. *J. Polym. Sci., Part A*, **1964**, *2*, 15. (b) Merker, R. L.; Scott, M. J.; Haberland, G. G. *J. Polym. Sci., Part A*, **1964**, *2*, 31.

18. (a) Li, Y.; Kawakami, Y. *Macromolecules*, **1999**, *32*, 3540. (b) Li, Y.; Kawakami, Y. *Macromolecules*, **1999**, *32*, 6871. (c) Li, Y.; Kawakami, Y. *Macromolecules*, **1999**, *32*, 8768. (d) Li, Y.; Seino, M.; Kawakami, Y. *Macromolecules*, **2000**, *33*, 5311. (e) Liu, Y.; Imae, I.; Makishima, A.; Kawakami, Y. *Sci. Tech. Adv. Mater.*, **2003**, *4*, 27.

19. Liu, Y.; Imae, I.; Kawakami, Y. *Polym. Int.*, **2004**, *53*, 1259.

20. Shinke, S.; Tsuchimoto, T.; Kawakami, Y. *Silicon Chemistry*, **2007**, *3*, 243.

21. Oishi, M.; Moon, J. Y.; Janvikul, W.; Kawakami, Y. *Polym. Int.*, **2001**, *50*, 135.

22. Schulz, G. O.; Milkovich, R. *J. Appl. Polym. Sci.*, **1982**, *27*, 4773.

23. (a) Kawakami, Y.; Miki, Y.; Tsuda, T.; Murthy, R. A. N.; Yamashita, Y.; *Polym. J.*, **1982**, *14*, 913. (b) Kawakami, Y.; Ajima, K.; Nomura, M.; Hishida, T.; Mori, A. *Polym. J.*, **1997**, *29*, 95.

24. (a) Kawakami, Y.; Murthy, R. A. N.; Yamashita, Y. *Polym. Bull.*, **1983**, *10*, 368. (b) Kawakami, Y.; Murthy, R. A. N.; Yamashita, Y. *Makromol. Chem.*, **1984**, *185*, 9. (c) Kawakami, Y.; Aoki, T.; Yamashita, Y. *Macromolecules*, **1985**, *18*, 580.

25. (a) Kammermeyer, S.-T. H. *Membranes in Separation Process*. Wiley, Hoboken, NJ, 1975. (b) Stern, S. A.In: *Membrane Separation Processes*. Meares, P.; Ed. Elsevier, New York, 1976. (c) Barrer, R. M. *Trans. Farad. Soc.*, **1939**, *35*, 628, (d) Barrer, R. M. *Trans. Farad. Soc.*, **1939**, *35*, 644.

26. (a) Meng, S.; Nanjundiah, K.; Kyu, T.; Natarajan, L. V.; Tondiglia, V. P.; Bunning, T. J. *Macromolecules*, **2004**, *37*, 3792–3798. (b) Meng, S.; Kyu, T.; Natarajan, L. V.; Tondiglia, V. P.; Sutherland, R. L.; Bunning, T. J. *Macromolecules*, **2005**, *38*, 4844. (c) Kyu, T.; Nwabunwa, D. *Macromolecules*, **2001**, *34*, 9168. (d) Pikas, D. J.; Kirkpatrick, S. M.; Tomlin, D. W.; Natarajan, L.; Tondiglia, V.; Bunning, T. J. *Appl. Phys. A*, **2002**, *74*, 767. (e) Sutherland, R. L. *J. Opt. Soc. Am. B*, **2002**, *19*, 2995. (f) Kato, K.; Hisaki, T.; Date, M. *Jpn. J. Appl. Phys.*, **1999**, *38*, 1466. (g) White, T. J.; Natarajan, L. V.; Tondiglia, V. P.; Bunning, T. J.; Guymon, C. A. *Macromolecules*, **2007**, *40*, 1112. (h) White, T. J.; Natarajan, L. V.; Tondiglia, V. P.; Lloyd, P. F.; Bunning, T. J.; Guymon, C. A. *Macromolecules*, **2007**, *40*,

1121. (i) Kato, K.; Hisaki, T.; Date, M. *Jpn. J. Appl. Phys.*, **1999**, *38*, 805. (j) Natarajan, L. V.; Brown, D. P.; Wofford, J. M.; Tondiglia, V. P.; Sutherland, R. L.; Lloyd, P. F.; Bunning, T. J. *Polymer*, **2006**, *47*, 4411.

27. (a) Choi, D. H.; Cho, M. J.; Yoon, H.; Yoon, H.; Kim, J. H.; Paek, S. H. *Opt. Mater.*, **2004**, *27*, 85. (b) Jazbinsek, M.; Olenik, I. D.; Zgonik, M.; Fontecchio, A. K.; Crawford, G. P. *J. Appl. Phys.*, **2001**, *90*, 3831. (c) Zhang, J.; Carlen, C. R.; Palmer, S.; Sponsler, M. B. *J. Am. Chem. Soc.*, **1994**, *116*, 7055. (d) Lucchetta, D. E.; Karapinar, R.; Manni, A.; Simoni, F. *J. Appl. Phys.*, **2002**, *91*, 6060. (e) Rosa, M. E. D.; Tondiglia, V. P.; Natarajan, L. V. *J. Appl. Phys. Sci.*, **1998**, *68*, 523. (f) Carretero, L.; Blaya, S.; Mallavia, R.; Madrigal, R. F.; Fimia, A. *J. Mod. Opt.*, **1998**, *45*, 2345. (g) Zhang, J.; Sponsler, M. B. *J. Am. Chem. Soc.*, **1992**, *114*, 1506.

28. (a) Date, M.; Takeuchi, Y.; Kato, K. *Jpn. J. Appl. Phys.*, **1999**, *32*, 3164. (b) Bunning, T. J.; Natarajan, L. V.; Tondiglia, V. P.; Sutherland, R. L.; Vezie, D. L.; Adams, W. W. *Polymer*, **1995**, *36*, 2699. (c) Natarajan, L. V.; Shepherd, C. K.; Brandelik, D. M.; Sutherland, R. L.; Chandra, S.; Tondiglia, V. P.; Tomlin, D.; Bunning, T. J. *Chem. Mater.*, **2003**, *15*, 2477. (d) Park, M. S.; Kim, B. K.; Kim, J. C. *Polymer*, **2003**, *44*, 1595. (e) Sutherland, R. L.; Natarajan, L. V.; Tondiglia, V. P.; Bunning, T. J. *Chem. Mater.*, **1993**, *5*, 1533. (f) Zhang, J.; Carlen, C. R.; Palmer, S.; Sponsler, M. B. *J. Am. Chem. Soc.*, **1994**, *116*, 7055. (g) Bunning, T. J.; Natarajan, L. V.; Tondiglia, V. P.; Sutherland, R. L. *Annu. Rev. Mater. Sci.* **2000**, *30*, 83.

29. (a) Liu, Y. J.; Zhang, B.; Jia, Y.; Xu, K. S. *Opt. Commun.*, **2003**, *218*, 27. (b) Sarkar, M. D.; Qi, J.; Crawford, G. P. *Polymer*, **2002**, *43*, 7335–7344. (c) Escuti, M. J.; Kossyrev, P.; Crawford, G. P. *Appl. Phys. Lett.*, **2000**, *77*, 4262. (d) Cairns, D. R.; Bowley, C. C.; Danworaphong, S.; Fontecchio, A. K.; Crawford, G. P.; Li, L.; Faris, S. M. *Appl. Phys. Lett.*, **2000**, *77*, 2677.

30. White, T. J.; Liechty, W. B.; Natarajan, L. V.; Tondiglia, V. P.; Bunning, T. J.; Guymon, C. A. *Polymer*, **2006**, *47*, 2289.

31. (a) Cho, Y. H.; Shin, C. W.; Kim, N.; Kim, B. K.; Kawakami, Y. *Chem. Mater.*, **2005**, *17*, 6263. (b) Cho, Y. H.; He, M.; Kim, B. K.; Kawakami, Y. *Sci. Technol. Adv. Mater.*, **2004**, *5*, 319. (c) Cho, Y. H.; Kawade, R.; Kubota, T.; Kawakami, Y. *Sci.Technol. Adv. Mater.*, **2005**, *6*, 435. (d) Cho, Y. H.; Kawakami, Y. *Appl. Phys. A.*, **2006**, *83*, 365. (e) Li, Z.; Cho, Y. H.; Kawakami, Y. *Polym. Int.*, **2007**, *56*, 666. (f) He, M.; Cho, Y. H.; Kim, N.; Kawakami, Y. *Design. Monom. Polym.*, **2005**, *8*, 473. (g) He, M.; Cho, Y. H.; Kawakami, Y.; *Polym. J.*, **2006**, *38*, 678.

32. Hoque, M. A.; Cho, Y. H.; Kawakami, Y. *React. Funct. Polym.*, **2007**, *67*, 1192.

33. Cho, Y. H.; Kawakami, Y. *Silicon Chemistry*, **2007**, *3*, 219.

34. (a) Gomurashvili, Z.; Crivello, J. V. *Macromolecules*, **2002**, *35*, 2962. (b) Gomurashvili, Z.; Crivello, J. V. *J. Polym. Sci., Part A: Polym. Chem.*, **2001**, *39*, 1187. (c) Crivello, J. V.; Jiang, F. *Chem. Mater.*, **2002**, *14*, 4858.

35. Cho, Y. H.; Suzuki, Go.; Kawakami, Y. *Polym. J.*, **2007**, *39*, 1157.

36. (a) Crivello, J. V.; Lam, J. H. W. *Macromolecules*, **1997**, *10*, 1307. (b) Crivello, J. V.; Lee, J. L. *J. Polym. Sci., Part A: Polym. Chem.*, **1989**, *27*, 3951. (c) Castellanos, F.; Fouassier, J. P.; Priou, C.; Cavezzan, J. *J. Appl. Polym. Sci.*, **1996**, *60*, 705.

37. Scott, D. W. *J. Am. Chem. Soc.*, **1946**, *68*, 356.

38. Barry, A. J.; Daud, W. H.; Domicone, J. J.; Gilkey, J. W. *J. Am. Chem. Soc.*, **1955**, *77*, 4248.

39. (a) Brown, J. F., Jr.; Vogt, L. H., Jr.; Katchman, A.; Eustance, J. W.; Kiser, K. M.; Krantz, K. W. *J. Am. Chem. Soc.*, **1960**, *82*, 6194. (b) Brown, J. F., Jr.; Vogt, L. H., Jr.; Prescott, P. I. *J. Am. Chem. Soc.*, **1964**, *86*, 1120. (c) Brown, J. F., Jr. *J. Am. Chem. Soc.*, **1965**, *87*, 4317.

40. Li, G.; Wang, L.; Ni, H.; Pittman, C. U., Jr. *J. Inorg. Organomet. Polym.*, **2002**, *11*, 123.

41. Pielichowski, K.; Njuguna, J.; Janowski, B.; Piechowski, J. *Avd. Polym. Sci.*, **2006**, *201*, 225.

42. (a) Feher, F. J.; Newman, D. A.; Walzer, J. F. *J. Am. Chem. Soc.*, **1989**, *111*, 1741. (b) Feher, F. J.; Budzichowski, T. A.; Weller, K. J. *J. Am. Chem. Soc.*, **1989**, *111*, 7288. (c) Feher, F. J.; Newman, D. A. *J. Am. Chem. Soc.*, **1990**, *112*, 1931. (d) Feher, F. J.; Budzichowski, T. A.; Blanski, R. L.; Weller, K. J.; Ziller, J. W. *Organnometallics*, **1991**, *10*, 2526. (e) Feher, F. J.; Schwab, J. J.; Soulivong, D.; Ziller, J. W. *Main Group Chemistry*, **1997**, *2*, 123. (f) Feher, F. J.; Soulivong, D.; Lewis, G. T. *J. Am. Chem. Soc.*, **1997**, *119*, 11323. (g) Feher, F. J.; Terroba, R.; Ziller, J. W. *Chem. Commun.*, **1999**, 2153. (h) Feher, F. J. Terroba, R.; Ziller, J. W. *Chem. Commun.*, **1999**, 2309.

43. (a) Haddad, T. S.; Lichtenhan, J. D. *Macromolecules*, **1996**, *29*, 7302. (b) Shockey, E. G.; Bolf, A. G.; Jones, P. F.; Schwab, J. J.; Chaffee, K. P.; Haddad, T. S.; Lichtenhan, J. D. *Appl. Organomet. Chem.*, **1999**, *13*, 311. (c) Lichtenhan, J. D.; Gilman, J. W.; Feher, F. J. US 5,484,867 A January 16, 1996. (d) Lichtenhan, J. D.; et al., WO 01/10871. (e) Lichtenhan, J. D.; Schwab, J. J.; An, Y-Z.; Reinerth, W.; Feher, F. J. US 2004/0068075 A1 April 8, 2004. (f) Lichtenhan, J. D.; Schwab, J. J.; An, Y.-Z.; Liu, Q.; Haddad, T. S. US 6,927,270 B2 August 9, 2005. (g) Lichtenhan, J. D.; Schwab, J. J.; An, Y-Z.; Reinerth, W.; Carr, M. J.; Terroba, R.; Liu, Q. US 6,972,312 B1 December 6, 2005. (h) Lichtenhan, J. D.; Hait, S. B.; Schwab, J. J.; Carr, M. J. US 2006/0263318 A1 November 23, 2006.

44. (a) Bassindale, A. R.; Liu, Z.; Mackinnon, I. A.; Taylor, P. G.; Yang, Y.; Light, M. E.; Horton, P. N.; Hursthouse, M. B.; *Dalton Trans.*, **2003**, 2945. (b) Bassindale, A. R.; Chen, H.; Liu, Z.; Mackinnon, I. A.; Parker, D. J.; Taylor, P. G.; Yang, Y.; Light, M. E.; Horton, P. N.; Hursthouse, M. B. *J. Organomet. Chem.*, **2004**, *689*, 3287.

45. (a) Unno, M.; Takada, K.; Matsumoto, M. *Chem. Lett.*, **1998**, *27*, 489. (b) Kawakami, Y.; Yamaguchi, K.; Yokozawa, T.; Serizawa, T.; Hasegawa, M.; Kabe, Y. *Chem. Lett.*, **2007**, *36*, 792.

46. (a) Kawakami, Y. *React. Funct. Polym.*, **2007**, *67*, 1137. (b) Pakjamsai, C.; Kawakami, Y. *Polym. J.*, **2004**, *36*, 455. (c) Pakjamsai, C.; Kobayashi, N.; Koyano, M.; Sasaki, S.; Kawakami, Y. *J. Polym. Sci. Part A: Polym. Chem.*, **2004**, *42*, 4587. (d) Pakjamsai, C.; Kawakami, Y. *Design. Monom. Polym.*, **2005**, *8*, 423.

47. (a) Yoshida, K.; Morimoto, Y.; Watanabe, K.; Ootake, N.; Inagaki, J.; Ohguma, K. Int. Pat. Appl. WO 03/24870 A1 Mar 27, 2003. (b) Lee, D. W.; Kawakami, Y. *Polym. J.*, **2007**, *39*, 230. (c) Li, Z.; Kawakami, Y. *Chem. Lett.*, **2008**, *37*, 804.

48. (a) Cheng, W.-D.; Xiang, K.-H.; Pandey, R.; Pernisz, U. C. *J. Phys. Chem. B.*, **2000**, *104*, 6737. (b) Xu, H.; Kuo, S.-W.; Lee, J.-S.; Chang, F.-C. *Macromolecules*, **2002**, *35*, 8788. (c) Huang, J.-C.; He, C.-B.; Xiao, Y.; Mya, K. Y.; Dai, J.; Siow, Y. P. *Polymer*, **2003**, *44*, 4491. (d) Pellice, S. A.; Fasce, D. P.; Williams, R. J. J. *J. Polym. Sci. Part B: Polym Phys.*, **2003**, *41*, 1451. (e) Imae, I.; Kawakami, Y.; *J. Mater. Chem.* **2005**, *15*, 4581. (f) Lo, M. Y.; Zhen, C.; Lauters, M.; Jabbour, G. E.; Sellinger, A. *J. Am. Chem. Soc.*, **2007**, *129*, 5808. (g) Iacono, S. T.; Vij, A.; Grabow, W.; Smith. D. W., Jr.; Mabry, J. M. *Chem. Commun.*, **2007**, 4992. (h) Létant, S. E.; Herberg, J.; Dinh, L. N.; Maxwell, R. S.; Simpson, R. L.; Saab, A. P. *Cat. Commun.*, **2007**, *8*, 2137. (i) Froehlich, J. D.; Young, R.; Nakamura, T.; Ohmori, Y.; Li, S.; Mochizuki, A. *Chem. Mater.*, **2007**, *19*, 4991. (j) Laine, R. M.; Roll, M.; Asuncion, M.; Sulaiman, S.; Popova, V.; Bartz, D.; Krug, D. J.; Mutin, P. H. *J. Sol-Gel. Sci. Technol.*, **2008**, *46*, 335. (k) Wahab, M. A.; Mya, K. Y.; He, C. *J. Polym. Sci. Part A: Polym. Chem.*, **2008**, *46*, 5887. (l) Anderson, S. E.; Baker, E. S.; Mitchell, C.; Haddad, T. S.; Bowers, M. T. *Chem. Mater.*, **2005**, *17*, 2537.

49. (a) Carmichael, J. B.; Kinsinger, J. *Can. J. Chem.*, **1964**, *42*, 1996. (b) Brown. J. F., Jr.; Slusarczuk, G. M. J. *J. Am. Chem. Soc.*, **1965**, *87*, 931. (c) Flory, P. J.; Semlyen, J. A. *J. Am. Chem. Soc.*, **1966**, *88*, 3209. (d) Suter, U. W.; Mutter, M.; Flory, P. J. *J. Am. Chem. Soc.*, **1976**, *98*, 5740.

50. Ito, R.; Kakihana, Y.; Kawakami, Y. *Chem. Lett.*, **2009**, *38*, 364.

51. (a) Kudo, T.; Machida, K. *J. Phys. Chem. A.*, **2005**, *109*, 5424. (b) Itoh, M., Ed. *Shiruseskiokisann Zairyo Kagaku to Oyo Tenkai*. CMC, Tokyo, 2007; pp. 22–36.

52. Zhi-hua, L.; Bassindale, A. R.; Taylor, P. G. *Chem. Res. Chainese U.*, **2004**, *20*, 433.

53. Tateyama, S.; Kakihana, Y.; Kawakami, Y. *J. Organomet. Chem.*, **2010**, *695*, 898.

54. Ronchi, M.; Pizzotti, M.; Biroli, A. O.; Macchi, P.; Lucenti, E.; Zucchi, C. *J. Organomet. Chem.*, **2007**, *692*, 1788.

55. (a) Laine, R. M.; Tamaki, R.; Choi, J.WO 02/100867 A1 December 19, 2002. (b) Brick, C. M.; Tamaki, R.; Kim, S.-G.; Asuncion, M. Z.; Roll, M.; Nemoto, T.; Ouchi, Y.; Chujo, Y.; Laine, R. M. *Macromolecules*, **2005**, *38*, 4655.

56. (a) Olsson, K.; Grönwall, C. *Arkiv. foer. Kemi.*, **1961**, *17*, 529. (b) Tamaki, R.; Tanaka, Y.; Asuncion, M. Z.; Choi, J.; Laine, R. M. *J. Am. Chem. Soc.*, **2001**, *123*, 12416.

57. Zhang, J.; Xu, R.-W.; Yu, D.-S. *J. Appl. Polym. Sci.*, **2007**, *103*, 1004.

58. Deans, F. B.; Eaborn, C. *J. Chem., Soc.*, **1957**, 498.

59. Miyazato, A.; Pakjamsai, C.; Kawakami, Y. *Dalton. Trans.*, **2010**, *13*, 3239.

60. (a) Mantz, R. A.; Jones, P. F.; Chaffee, K. P.; Lichtenhan, J. D.; Gilman, J. W. *Chem. Mater.*, **1996**, *8*, 1250. (b) Hasegawa, I.; Sakka, S.; Sugahara, Y.; Kuroda, K.; Kato, C. *J. Chem. Soc. Chem. Commun.*, **1989**, 208. (c) Pescarmona, P. P.; Van der Waal, J. C.; Maschmeyer, T. *Eur. J. Inorg. Chem.*, **2004**, 978.

61. Clarson, S. J.; Semlyen, J. A. *Siloxane Polymers*. Prentice Hall, Englewood Cliffs, NJ, 1993.

62. (a) Ziegler, J. M.; Fearon, F. W. G.; Eds. *Silicon-Based Polymer Science: A Comprehensive Resource*, Advances in Chemistry Series 224. American Chemical Society, Washington DC, 1990. (b) Brook, M. A. *Silicon in Organic, Organometallic, and Polymer Chemistry*. Wiley, Hoboken, NJ, 2000.

63. (a) Otomo, Y.; Nagase, Y.; Nemoto, N. *Polymer*, **2005**, *46*, 9714. (b) Sato, I.; Takeda, S.; Arai, Y.; Miwa, H.; Nagase, Y.; Nemoto, N. *Polym Bull.*, **2007**, *59*, 607. (c) Ito, H.; Akiyama, E.; Nagase, Y.; Yamamoto, A.; Fukui, S. *Polym J.*, **2006**, *38*, 109.

64. (a) Lewin, M.; Atlas, S. M.; Pearce, E. M. *Flame Retardant Polymeric Materials*. Plenum Press, New York, 1975. (b) Dvorinc, P. R.; Lenz, R. W. *High Temperature Siloxane Elastomers*. Huthig & Wepf, Basel, 1990.

65. (a) Aminuzzaman, M.; Watanabe, A.; Miyashita, T. *J. Photopolym. Sci. Technol.*, **2008**, *21*, 537. (b) Aminuzzaman, M.; Watanabe, A.; Miyashita, T. *J. Mater. Chem.*, **2008**, *18*, 5092.

66. Hoque, M. A.; Kakihana, Y.; Shinke, S.; Kawakami, Y. *Macromolecules*, **2009**, *42*, 3309.

67. Anderson, S. E.; Mitchell, C.; Haddad, T. S.; Vij, A.; Schwab, J. J.; Bowers, M. T. *Chem. Mater.*, **2006**, *18*, 1490.

68. (a) Blackwell, J. M.; Foster, K. L.; Beck, V. H.; Piers, W. E. *J. Org. Chem.*, **1999**, *64*, 4887. (b) Parks, D. J.; Piers, W. E. *J. Am. Chem. Soc.*, **1996**, *118*, 9440. (c) Harrison, D. J.; McDonald, R.; Rosenberg, L. *Organometallics*, **2005**, *24*, 1398. (d) Chojnowski, J.; Rubinsztajn, S.; Cella, J. A.; Fortuniak, W.; Cypryk, M.; Kurjata, J.; Kaźmierski, K. *Organometallics*, **2005**, *24*, 6077. (e) Rubinsztajn, S.; Cella, J. A. *Macromolecules*,

2005, *38*, 1061. (f) Chen, X.; Cui, Y.; Yin, G.; Liao, L. *J. Appl. Polym. Sci.*, **2007**, *106*, 1007. (g) Longuet, C.; Joly-Duhamel, C.; Ganachaud, F. *Macromol. Chem. Phys.*, **2007**, *208*, 1883. (h) Wu, S.; Hayakawa, T.; Kikuchi, R.; Grunzinger, S. J. Kakimoto, M.; Oikawa, H. *Macromolecules*, **2007**, *40*, 5698. (i) Thompson, D. B.; Brook, M. A. *J. Am. Chem. Soc.*, **2008**, *130*, 32. (j) Zhou, D.; Kawakami, Y. *Macromolecules*, **2005**, *38*, 6902.

69. Uchida, H.; Kabe, Y.; Yoshino, K.; Kawamata, A.; Tsumuraya, T.; Masamune, S. *J. Am. Chem. Soc.*, **1990**, *112*, 7077.

70. Wada, K.; Watanabe, N.; Yamada, K.; Kondo, T.; Mitsudo, T. *Chem. Commun.*, **2005**, 95.

Nanocrystalline Magnesium Oxide for Asymmetric Organic Reactions

MANNEPALLI LAKSHMI KANTAM

Inorganic and Physical Chemistry Division, Indian Institute of Chemical Technology, Hyderabad, India

VENKAT REDDY CHINTAREDDY

Department of Chemistry, Iowa State University, Ames, Iowa, USA

A tremendous increase in interest in the area of nano metal oxide catalysis has been seen over the last decade. The promising results of nano metal oxides in organic synthesis have been explained by their unique properties that change in the nanoregime including bandgaps, magnetic moments, specific heats, melting points, surface chemistry, and morphology/particle shape. Inorganic metal oxides, for example, nano magnesium oxide (nano-MgO), has a three-dimensional polyhedral structure, with a high surface concentration of hydroxyl groups on edge/corner and various exposed crystal planes, leading to an inherently high surface reactivity per unit area. In addition, nano-MgO possesses Lewis acid sites (Mg^{2+}), Lewis basic sites (O^{2-} and O^-), lattice bound and isolated Brønsted hydroxyls, and anionic and cationic vacancies. In this chapter, the use of nano-MgO as a catalyst in reactions such as asymmetric Henry, Michael, direct aldol, and epoxidations in the presence of suitable chiral ligands is discussed. The use of nano-MgO as a catalyst support in the asymmetric epoxidation of unfunctionalized olefins utilizing $Mn(acac)_n$-nano-MgO and $(1R,2R)$-($-$)-diaminocyclohexane as a chiral ligand, and the synthesis of chiral diols using a nano-MgO supported osmium catalyst in the presence of $(DHQD)_2PHAL$ is also presented. In order to achieve high enantioselectivities (ee's), the effects of solvent, temperature, and ligand have been investigated. Preliminary results of investigations on putative mechanistic pathways have been included in order to better understand the role of nano-MgO on selected asymmetric organic transformations.

5.1. INTRODUCTION

For the past two decades there has been tremendous demand for solid acid–base catalysts for the production of fine and specialty chemicals. The use of stoichiometric inorganic reagents, though decreasing, is still widespread, and there is pressure to develop new, environmentally benign methods. In many instances, homogeneous catalysis is a powerful process, but on an industrial scale the problems related to corrosion and plating out on the reactor wall, handling, recovery, and reuse of the catalyst represent major limitations.

However, the industry generally favors catalytic processes induced by heterogeneous catalysts over homogeneous catalysts in view of their ease of handling, simple workup, and regenerability. Heterogenization of homogeneous chiral catalysts presents a complex problem of conceptual transfer of molecular chemistry to surface metal–organic chemistry to realize a single-site catalyst with the retention of activity and high enantioselectivity.

Porous nanocrystalline inorganic oxides are of topical interest[1–4] because they exhibit different characteristics in bandgaps,[5, 6] magnetic moments,[2] specific heats,[7] melting points,[8, 9] surface chemistry,[10, 11] and morphology/particle shape.[12] Having variable properties depending on the size of the particles, the inorganic oxides present enormous opportunities in allied fields of chemical sciences.

Over the last two decades, Klabunde and co-workers have reported many uses of nanocrystalline MgO. These include efficient destructive chemisorbents for toxic gases, NO_2, SO_2, SO_3, and HCl as well as chlorinated and phosphorus containing compounds, dehydrohalogenation of chlorohydrocarbons, and chlorination of alkanes.[13–15]

Choudary, Kantam, and co-workers began their research in this area to probe further applications of nano-MgO in organic synthesis. They have demonstrated for the first time the transfer of molecular chemistry to surface metal–organic chemistry by fabricating a single-site catalyst for the successful introduction of asymmetric center in a prochiral substrate.[16] Nanomaterials are expected to have a well-defined shape and size, and recently, there have been a number of reports[17–31] on nanocrystalline magnesium oxide (nano-MgO) in many areas of chemistry (Figure 5.1).

Lakshmi Kantam and co-workers have demonstrated the other uses of nano-MgO as a catalyst in several organic transformations, such as the cyanosilylation of aldehydes and ketones,[17] the Baylis–Hillman,[18] Strecker,[19] and Wittig reactions,[20] and the synthesis of organic carbonates,[21] α-diazo-β-hydroxy esters,[22] and flavanones.[23] Nano-MgO is a promising support for many metal-assisted reactions: nanocrystalline magnesium oxide stabilized palladium-catalyzed Heck coupling-hydrogenation,[24] reduction of nitro compounds,[25] Heck and Sonogashira reactions,[26] nanocrystalline magnesium oxide stabilized molybdenum catalyzed aerobic oxidation of alcohols,[27] ruthenium nanoparticles stabilized on nanocrystalline magnesium oxide by ionic liquids for transfer hydrogenation,[28] ruthenium species stabilized on nanocrystalline magnesium oxide by basic ionic liquids for aerobic alcohol oxidation,[29] and achiral dihydroxylation of olefins by osmate.[30] Other uses of nano-MgO are in the synthesis of biodiesel,[31, 32] substituted 2-amino-2-chromenes,[33]
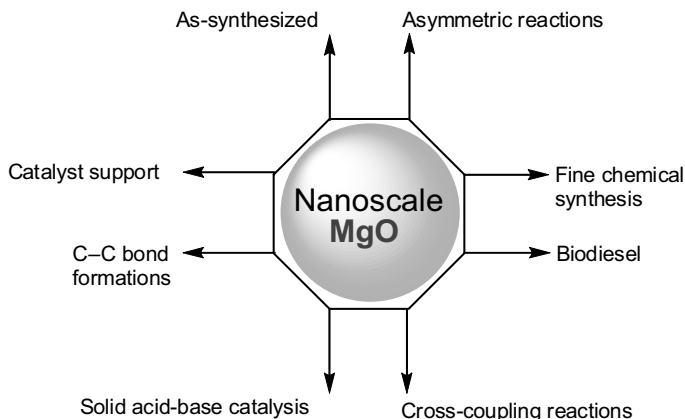
Figure 5.1. Representation of the multiple uses of nano-MgO in heterogeneous catalysis.

decomposition of ammonium perchlorate,[34] Claisen-Schmidt condensation,[35] and environmental remediation.[36]

5.2. STRUCTURAL PROPERTIES OF NANOCRYSTALLINE MgO CATALYSTS

The synthesis of nanocrystalline MgO is well established in the literature (see Section 5.3) and various types are now commercially available. Abbreviations and specific properties for various types of MgOs are listed in Table 5.1.

In general, most metal oxides possess very high lattice energies and melting points due to their high ionicity. In theory, very small crystals of material with high lattice energies should be stable and resistant toward melting, atom/ion migration, and subsequent crystal growth, even at elevated temperatures. Therefore, if synthetic techniques to produce nanocrystals of highly ionic metal oxides were available, it should be possible to isolate and store these ultrafine materials. Furthermore, these solids can exist with numerous surface sites with enhanced surface reactivity, such as crystal corners, edges, or ion vacancies (Figure 5.2).[12, 13, 37–40] Residual surface hydroxyl groups can also add to the rich surface chemistry exhibited by metal oxides such as MgO, CaO, SrO, BaO, Al_2O_3, TiO_2, Fe_2O_3, ZnO, and others, and this chemistry is generally attributable to Lewis acid, Lewis base, and Brønsted acid sites of varying coordination; that is, metal cations, oxide anions, and surface –OH groups, which can be isolated or lattice bound (Figure 5.3).

TABLE 5.1. Some Physical Properties of Different Crystallites of MgO

Entry	Catalyst	Abbreviation	Specific Surface Area (SSA)
1	Commercial MgO	CM-MgO	10–30 m^2/g
2	Conventionally prepared MgO	CP-MgO (NA-MgO)	130–250 m^2/g
3	Aerogel prepared MgO	AP-MgO (NAP-MgO)	300–590 m^2/g

AP-MgO

(a)

Total surface area = 47 nm^2
Total surface ions = 1065 ions
Length of edges = 48 nm
Edge ions = 228 ions
Percentage of edge ions = 21%

~4nm

CP-MgO

(b)

5nm

100nm

Total surface area = 5.5 x 10^4 nm^2
Total surface ions = 1.5 x 10^6 ions
Length of edges = 1230 nm
Edge ions = 5860 ions
Percentage of edge ions = 0.5%

CM-MgO

(c)

100 nm

100 nm

Total surface area = 6 x 10^4 nm^2
Total surface ions = 1.4 x 10^6 ions
Length of edges = 1200 nm
Edge ions = 5715 ions
Percentage of edge ions = 0.4%

Figure 5.2. (a) Model of a MgO nanocrystal of polyhedral shape (AP-MgO). (b) Model of a MgO hexagonal microcrystal (CP-MgO). (c) Model of a cubic-shaped microcrystal (CM-MgO). (Reproduced with permission from Ref. 13, Wiley-VCH Verlag GmbH.)

lattice bound -OH

isolated -OH

cation vacancy
(a neighboring oxygen may be
missing one
electron)

edge Lewis
acid site

anion vacancy
(may posess one
or two electrons)

associated
-OH groups

corner Lewis
base site
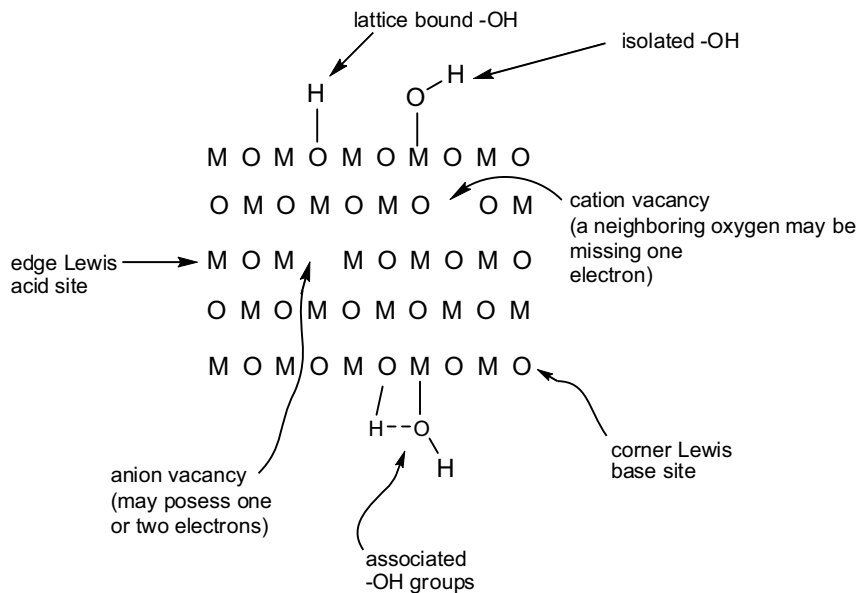
Figure 5.3. Illustration of reactive surface sites on highly ionic metal oxides. (Reproduced with permission from Ref. 13, Wiley-VCH Verlag GmbH.)

NAP-MgO has a three-dimensional polyhedral structures, with high surface concentrations of edge/corner and various exposed crystal planes (such as 002, 001, and 111), leading to inherently high surface reactivity per unit area. Additionally NAP-MgO has Lewis acid sites (Mg^{2+}), Lewis basic sites (O^{2-} and O^-), lattice bound and isolated Brønsted hydroxyls, and anionic and cationic vacancies (see Figure 5.2 and 5.3).[10, 11, 12, 41, 43, 45–47]

In this chapter, recent applications of nano-MgO either as a catalyst or as support for asymmetric organic reactions are described. The work described here mostly involves the use of commercial MgO, CM-MgO [specific surface area (SSA): $30\,m^2/g$], conventionally prepared MgO, CP-MgO (NA-MgO) (SSA: $250\,m^2/g$), aerogel prepared nano active plus MgO, AP-MgO (NAP-MgO) (SSA: $590\,m^2/g$).

5.3. PREPARATION OF THE DIFFERENT TYPES OF NANOCRYSTALLINE MgO CATALYSTS

5.3.1. Preparation of CP-MgO (NA-MgO)

Several grams of commercially available MgO was magnetically stirred under reflux in 500 mL of distilled water overnight.[10, 11, 19, 43] After cooling, the slurry was filtered, and the filter cake was dried in an oven at 120 °C. The dried powder was broken into pieces and heat treated to 500 °C under vacuum in a Pyrex reaction tube that fit into a cylindrical furnace. Heating took about 12 h, and the sample was maintained at 500 °C for several hours, usually overnight. The vacuum reached about 1×10^{-3} Torr.

5.3.2. Preparation of AP-MgO (NAP-MgO)

To a three-necked 2 L round bottom flask equipped with a mechanical stirrer, water cooled condensor, and argon inlet with a three-way stopcock was placed 300 mL of toluene.[10, 11, 19, 43] In another flask, 2.4 g (0.1 mol) of Mg turnings was allowed to react with 100 mL of CH_3OH under argon. The resultant 1 M solution of $Mg(OCH_3)_2$ was added dropwise to the toluene with vigorous stirring under argon. Subsequently, 4 mL (0.22 mol) of distilled water was added dropwise from a syringe over a 30 min period. This solution was stirred at room temperature under argon overnight. The resulting slightly milky solution (gel-like) was placed in an autoclave, slowly heated to 265 °C, and vented to give a $Mg(OH)_2$ aerogel.[11] After cooling, the slurry was filtered, and the filter cake was dried in an oven at 120 °C. The dried powder was broken into pieces and heat treated to 500 °C under vacuum in a Pyrex reaction tube that fit into a cylindrical furnace. Heating took about 12 h, and the sample was maintained at 500 °C for several hours, usually overnight.

5.3.3. Preparation of Sil-NAP-MgO

A mixture of 0.5 g of NAP-MgO and 0.3 g of methoxytrimethylsilane in 20 mL of toluene was refluxed for 7 h and the reaction mixture was allowed to cool and

centrifuged to obtain silylated NAP-MgO, which was washed several times with *n*-pentane.[19, 47]

5.4. ASYMMETRIC HENRY AND MICHAEL REACTIONS OF NITRO ALKANES

Carbon–carbon bond forming reactions are ubiquitous in synthetic organic chemistry and have generated increasing interest from both industrial and academic researchers over the last few decades. Nitroaldol and Michael reactions are two fundamental synthetic tools for the formation of C–C bonds.[48, 49] The nitro group of these products can undergo the Nef reaction,[50] reduction to an amino group, or nucleophilic displacement.[51] Asymmetric Henry (AH) reactions with impressive enantioselectivities (ee's) can be achieved using a dinuclear zinc-chiral semi-azacrown complex[52] or copper bisoxazoline complexes.[53] Asymmetric Michael (AM) reactions[54] with good to excellent ee's are accomplished using alkaloids, chiral crown ethers in the presence of bases, proline and proline-derived catalysts, diamines, natural proteins, aminoalcohols and binol derived complexes[55] in homogeneous media. In the area of heterogenized catalysts, chiral polymers provide moderate ee's in the AM reactions.[56, 57] A break-through, both in AM and AH catalytic reactions, is achieved with the introduction of in situ prepared heterobimetallic catalysts, composed of both Lewis acidic sites and Lewis/Brønsted basic sites.[58–63] Transition metal chiral complexes are single-site catalysts with a defined shape and stereochemistry, which induce, in general, higher enantioselectivity in asymmetric synthesis, by permitting unidirectional introduction of the reacting species on to a prochiral substrate in three-dimensional space to generate the asymmetric center. Conversely, heterogeneous catalysts are not as effective as transition metal chiral complexes due to steric restrictions and their multisite active sites resulting from assorted crystal structures with different shapes and sizes.

In the context of heterogeneous asymmetric catalysis, Choudary et al.[64] reported a recyclable heterogeneous nanocrystalline magnesium oxide catalyst for the AH and AM reactions to afford chiral nitro alcohols and Michael adducts in good to excellent yields and enantioselectivities (ee's) (Scheme 5.1).

Various magnesium oxide crystals CM-MgO, NA-MgO, and NAP-MgO have been screened for the catalytic activity in the achiral Henry reaction between benzaldehyde and nitromethane at room temperature. NAP-MgO and NA-MgO gave nitro alcohols in good yields, while CM-MgO afforded a mixture of an olefin (major) and nitroaldol product (Table 5.2).

5.4.1. Asymmetric Henry Reaction

For the chiral version of the Henry reaction, magnesium oxides of various surface areas (Table 5.3, entry 1) were screened in the presence of a number of chiral auxiliaries (Table 5.3). Among the MgO samples screened in the AH reaction, NAP-MgO was found to be superior to NA-MgO and CM-MgO in terms of yields
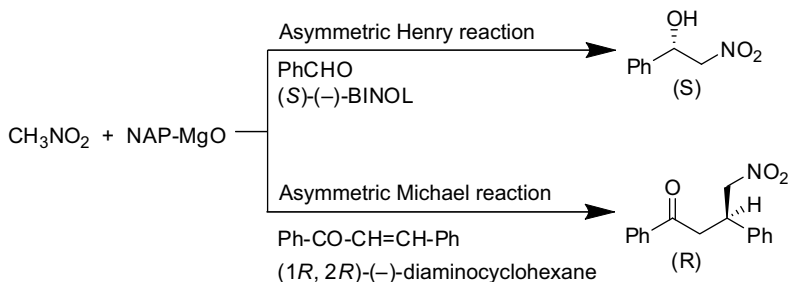
Scheme 5.1. Asymmetric Henry and Michael reactions catalyzed by nanocrystalline magnesium oxide (NAP-MgO).

and ee's. Using THF as the solvent and maintaining the reaction at the temperature $-78\,°C$ gave optimum ee's.

Generality of the reaction was extended to various aromatic, aliphatic, and cyclic aldehydes with nitromethane. When benzaldehyde is substituted at the 4-position with electron-withdrawing (EW) groups, higher ee's are observed than those bearing electron donating (ED) groups (Table 5.4, entries 4, 6–8). On the other hand, in the AH reaction using NAP-MgO, 2-substituted benzaldehydes with either of EW or ED groups exhibit a decrease of enantioselectivity when compared with the corresponding 4-substituted benzaldehydes, which may be ascribed to the steric hindrance of the unidirectional entry of reacting species (Table 5.4, entries 3, 5, 7, and 9).

NAP-MgO catalyzed the AH reaction of α-keto esters with nitromethane to β-nitro α-hydroxy esters, which are vital chiral intermediates with quaternary carbon centers, in higher ee's than that reported in the literature[64] using (S)-binol as a chiral auxiliary (Scheme 5.2).

5.4.2. Asymmetric Michael Reaction

Even though the three forms of magnesium oxide crystals catalyze the asymmetric Henry reaction, only NAP-MgO induces high enantioselectivity (Table 5.5). Spurred

TABLE 5.2. Achiral Henry Reaction Catalyzed by Different Crystallites of MgO Between Benzaldehyde and Nitromethane at $25\,°C^a$

Entry	Catalyst	Time (h)	Yield (%)[b]
1	NAP-MgO	6	95
2	NA-MgO	10	95
3	CM-MgO	18	20[c]
4	Sil-NAP-MgO	20	90
5	Sil-NA-MgO	30	90

[a] Conditions: benzaldehyde (1.0 mmol, 0.1 mL), nitromethane (5.0 mmol, 0.305 g), catalyst (0.125 g), dry THF (5 mL).
[b] Isolated yields.
[c] The by-product was a dehydrated Henry product (olefin).

TABLE 5.3. Asymmetric Henry Reaction Between Nitromethane and Benzaldehyde Catalyzed by NAP-MgO with Different Ligands at −78 °C

Entry	Ligand	Yield (%)[a]	ee (%)[b]
1	(S)-(−)-binol	95, 70,[c] 50,[d] 40,[e] 95,[f] 0[g]	90, 58,[c] 10,[d] 0,[e] 90[f]
2	Silylated (S)-(−)-binol	95	0
3	(S)-(−)-1,1′-binaphthyl-2,2′-diamine	90	30
4	(1R,2R)-(−)-1,2-diaminocyclohexane	90	40
5	(DHQD)₂PHAL	80	30
6	(L)-proline	No reaction	—
7	(+)-diethyl L-tartrate	90	20

Conditions: benzaldehyde (1.0 mmol), nitromethane (5.0 mmol), NAP-MgO (0.125 g), dry THF (5 mL), (S)-(−)-binol (0.040 g).

[a] Isolated yields.
[b] Absolute configurations were determined to be (S).
[c] With NA-MgO.
[d] With CM-MgO.
[e] With silylated NAP-MgO.
[f] Fifth cycle.
[g] Without catalyst. ee's were determined by HPLC.

by the success of the AH reactions, another important C–C bond forming reaction, the asymmetric Michael (AM) reaction between chalcone and nitromethane was studied, catalyzed by nano oxides. Using (S)-(−)-binol, no reaction was observed due to inadequate basicity.[64] To enhance the basicity, several chiral amines were evaluated in the asymmetric Michael reaction (Table 5.6). Among the MgO samples screened in the AM reaction of chalcone with nitromethane using (1R, 2R)-(−)-diaminocyclo-hexane (DAC) as a chiral auxiliary, the NAP-MgO was found to be superior to NA-MgO and CM-MgO in terms of yields and ee's. The ee's of the product are 90%, 46%, and 5% using NAP-MgO, NA-MgO, and assorted crystals of CM-MgO, respectively. In an attempt to optimize the AM reaction, the effects of solvent and temperature were studied. It was found that NAP-MgO and DAC as a chiral auxiliary in THF at −20 °C gave the highest yield and enantioselectivity. In general, chiral bidentate systems composed of primary and secondary amines afforded better ee's (Table 5.6, entries 1, 2, 3, 6, and 9), while chelation with tertiary amines, carboxylate, or hydroxyl groups displayed no ee's (Table 5.6, entries 4, 5, 7, and 8).

To broaden the scope of the AM reaction, NAP-MgO-DAC in THF was evaluated using various acyclic enones, nitromethane and 2-nitropropane. Chalcones gave good to excellent yields and ee's (Table 5.7, entries 1–7). Conversely, no reaction was observed using aliphatic enones.

It can be seen that the unsubstituted phenyls of chalcone gave the best ee. Substitution on either of phenyls of the chalcones and nature of substituents has a considerable impact on the stereochemistry of the products. Broad substrate scope and functional group tolerance has been reported (Table 5.7).

TABLE 5.4. Asymmetric Henry Reaction Catalyzed by NAP-MgO with Substituted Benzaldehydes and Nitromethane at $-78\,^\circ$C[64]

R-CHO + CH$_3$NO$_2$ $\xrightarrow[\substack{\text{(S)-(−)-binol} \\ -78\ \text{C}}]{\text{NAP-MgO}}$ OH / R$\overset{}{\underset{}{}}NO_2$

1   **2**   **3a-3l**

R = Ph : **1a**
R = 4-NO$_2$-C$_6$H$_4$: **1b**   R = 4-Me-C$_6$H$_4$: **1h**
R = 2-NO$_2$-C$_6$H$_4$: **1c**   R = 2-Me-C$_6$H$_4$: **1i**
R = 4-Cl-C$_6$H$_4$: **1d**   R = Cyclohexyl: **1j**
R = 2-Cl-C$_6$H$_4$: **1e**   R = t-Bu: **1k**
R = 4-OMe-C$_6$H$_4$: **1f**   R = n-Bu: **1l**
R = 2-OMe-C$_6$H$_4$: **1g**

Entry	Substrate	Time (h)	Product	Yield (%)[a]	ee (%)[b]
1	**1a**	12	**3a**	95	90
2	**1b**	18	**3b**	95	98
3	**1c**	15	**3c**	95	80
4	**1d**	16	**3d**	90	98
5	**1e**	15	**3e**	90	77
6	**1f**	20	**3f**	80	85
7	**1g**	20	**3g**	95	70
8	**1h**	15	**3h**	90	70
9	**1i**	15	**3i**	90	60
10	**1j**	18	**3j**	80	86
11	**1k**	18	**3k**	70	70
12	**1l**	15	**3l**	70	60

 Conditions: Aldehyde (1.0 mmol), nitromethane (5.0 mmol), NAP-MgO (0.125 g), dry THF (5.0 mL), (S)-(−)-binol (0.040 g).
[a] Isolated yields.
[b] Absolute configurations were determined to be (S).

5.4.3. Reaction Mechanism

To understand the relation between structure and reactivity in both AH and AM reactions, it is important to know the structure and nature of the reactive sites of NAP-MgO. NAP-MgO has a three-dimensional polyhedral structure, with high surface

R$\overset{O}{\underset{}{\|}}CO_2C_2H_5$ + CH$_3$NO$_2$ $\xrightarrow[\substack{\text{(S)-(−)-BINOL} \\ -78\ ^\circ\text{C}}]{\text{NAP-MgO}}$ R$\overset{OH}{\underset{NO_2}{}}CO_2C_2H_5$

4   **2**   **5a–5b**

R = CH$_3$: **4a**
R = C$_2$H$_5$: **4b**
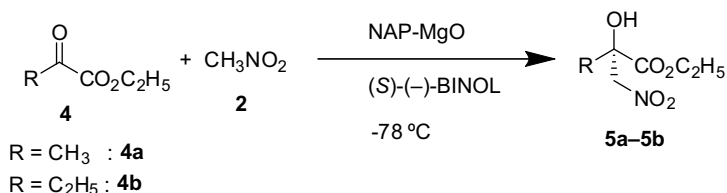
Scheme 5.2. Asymmetric Henry reaction of α-keto esters with nitromethane catalyzed by NAP-MgO at $-78\,^\circ$C.

TABLE 5.5. Asymmetric Henry Reaction between α-Keto Esters and Nitromethane Catalyzed by NAP-MgO at –78 °C

Entry	Substrate	Time (h)	Product	Yield (%)[a]	ee (%)[d]
1	**4a**	20	**5a**	75, 40[b], 30[c]	98, 0[c]
2	**4b**	24	**5b**	70	98

[a] Isolated yields.
[b] With NA-MgO.
[c] With CM-MgO.
[d] Absolute configurations were determined to be (S).

concentrations of edge/corner and various exposed crystal planes (such as 002, 001, 111), leading to an inherently high surface reactivity per unit area. Thus, NAP-MgO indeed displayed the highest activity compared to NA-MgO and CM-MgO. NAP-MgO also contains Lewis acid sites (Mg^{2+}), Lewis basic sites (O^{2-} and O^{-}), lattice bound and isolated Brønsted hydroxyls, and anionic and cationic vacancies.[1, 16, 41–47] Both Henry and Michael reactions are known to be driven by basic catalysts and, accordingly, the surface –OH and O^{2-} sites of these oxide crystals are expected to trigger these reactions. To examine the role of –OH, the silylated magnesium oxides, Sil-NA-MgO and Sil-NAP-MgO, devoid of free –OH groups were tested in the AH and AM reactions. It was found that the silylated MgO samples required longer reaction times than the corresponding MgO samples for both reactions and no enantioselectivity was observed. These results indicate that Brønsted hydroxyls are the sole contributors for the enantioselectivity and increase the activity of the catalyst in the AH and AM reactions, which are largely driven by Lewis basic O^{2-} and O^{-} sites. When silylated (S)-(−)-binol (Table 5.3, entry 2) was used in place of (S)-(−)-binol in the AH reaction catalyzed by NAP-MgO, no enantioselectivity was observed. Similarly, in the AM reaction, a bidentate system composed of at least

TABLE 5.6. Effect of Ligand on the AM Reaction Between Chalcone and Nitromethane Catalyzed by NAP-MgO at 25 °C

Entry	Ligand	Time (h)	Yield (%)[a]	ee (%)
1	(1R, 2R)-(−)-1,2-diaminocyclohexane (DAC)	8	95	90
2	(1R,2R)-(+)-1,2-diphenylethylenediamine	8	95	82
3	(1S,2R)-(+)-2-amino-1,2-diphenylethanol	12	90	60
4	(1R,2S)-(−)-N-methylephedrine	12	90	0
5	(+)-Diethyl L-tartrate	18	50	0
6	(S)-(−)-1,1′-binaphthyl-2,2′-diamine	12	90	60
7	(S)-(−)-binol	15	No reaction	—
8	(L)-proline	15	No reaction	—
9	(L)-proline methyl ester	12	90	80

Conditions: Chalcone (1.0 mmol, 0.208 g), nitromethane (5.0 mmol, 3.05 g), NAP-MgO (0.125 g), dry THF (5 mL); in all cases 25 mol% of ligand was used.
[a] Isolated yields.

TABLE 5.7. Asymmetric Michael Reaction between Nitroalkanes and Various Michael Donors Catalyzed by NAP-MgO at –20 °C Using (1R, 2R)-(−)-1,2-Diaminocyclohexane

6

2 : R = R^1 = H
2a : R = R^1 = CH$_3$

7a–7j

Ar^1 = Ar^2 = C$_6$H$_5$: **6a**

Ar^1 = C$_6$H$_5$; Ar^2 = 4-Cl-C$_6$H$_4$: **6b**

Ar^1 = C$_6$H$_5$; Ar^2 = 2-naphthyl : **6c**

Ar^1 = 4-Cl-C$_6$H$_4$; Ar^2 = C$_6$H$_5$: **6d**

Ar^1 = 4-Me-C$_6$H$_4$; Ar^2 = C$_6$H$_5$: **6e**

Ar^1 = C$_6$H$_5$; Ar^2 = 4-NO$_2$-C$_6$H$_4$: **6f**

Ar^1 = C$_6$H$_5$; Ar^2 = 4-Me-C$_6$H$_4$: **6g**

Ar^1 = CH$_3$; Ar^2 = C$_6$H$_5$: **6h**

Ar^1 = C$_6$H$_5$; Ar^2 = CH$_3$: **6i**

Entry	Michael Acceptor	Michael Donor	Time (h)	Product	Yield (%)[a]	ee (%)[b]
1	**6a**	**2**	12	**7a**	95, 70,[c] 30,[d] 95,[f] 0[g]	96, 48,[c] 5,[d] 0,[e] 96[f]
2	**6b**	**2**	15	**7b**	90	95
3	**6c**	**2**	18	**7c**	70	70
4	**6a**	**2a**	16	**7d**	95	82
5	**6d**	**2a**	24	**7e**	90	68
6	**6e**	**2a**	24	**7f**	84	66
7	**6f**	**2a**	20	**7g**	90	80
8	**6g**	**2a**	30	**7h**	74	63
9	**6h**	**2a**	72	**7i**	No reaction	—
10	**6i**	**2a**	72	**7j**	No reaction	—

[a] Isolated yields.
[b] Absolute configurations were found to be (R).
[c] With NA-MgO.
[d] With CM-MgO.
[e] With silylated NAP-MgO.
[f] Fifth cycle.
[g] Without catalyst.

one primary or secondary amine gave better ee's while a tertiary amine gave no enantioselectivity. These results indicate that the hydrogen bond interactions between the –OH or –NH groups of the chiral auxiliary and the –OH groups of the MgO are essential for enantioselectivity. Although both NAP-MgO and NA-MgO possess defined shapes and the same average concentrations of surface –OH groups, a possible rationale for the display of higher ee by the NAP-MgO is that the –OH groups are present on edge and corner sites, which are stretched in three-dimensional space, and are more isolated and accessible for the chiral ligand. NA-MgO possesses hindered –OH's situated on flat planes and in closer proximity with each other,[10] making proper alignment for chiral ligands more difficult.

Figure 5.4. XPS high resolution narrow scans for Mg 2p (a) NAP-MgO and (b) nitromethane treated NAP-MgO. (Reproduced, with permission from Ref. 64, American Chemical Society, Washington DC.)

The XPS spectrum of the CH_3NO_2 treated NAP-MgO for the Mg 2p peak exhibits two lines at 48.70 and 49.65 eV, which can be attributed to the magnesium atoms in NAP-MgO and O_2NH_2C-MgO,[65] respectively (Figure 5.4). An endotherm at 450 °C in the DTA-TGA-MS spectrum of the nitromethane treated NAP-MgO gives off a fragment ($m/z = 60$ amu) corresponding to $NO_2CH_2^{+\cdot}$, which further reiterates the formation of a surface moiety.[64] In the AH and AM reactions, O^{2-}/O^- of NAP-MgO abstracts an acidic proton of the nitromethane molecule, generating a carbanion, which is able to form a complex with an unsaturated Mg^+ site (Lewis acid type) of NAP-MgO. The AH and AM reactions proceed via dual activation of both substrates (nucleophiles and electrophiles) by the NAP-MgO. Thus, the Lewis base (O^{2-}/O^-) of the catalyst activates nitroalkanes and the Lewis acid moiety (Mg^{2+}/Mg^+) activates the carbonyls of aldehydes and enones (Scheme 5.3).

The activation of a carbonyl through a Lewis acid site has been reported in the achiral Henry reaction.[64] The activation of carbonyls through hydrogen bonding by Lewis acids is also known,[64] and similar acid–base dichotomy is well known in biological systems. The chiral auxiliaries[64] binol or DAC bound to NAP-MgO with proper alignment via hydrogen bonds directs the delivery of $^-CH_2NO_2$ stereoselectively to the Mg^+ (Lewis acid) activated carbonyl of an aldehyde or chalcones via oxygen coordination to afford the chiral nitro alcohols or Michael adduct (Scheme 5.3).

5.4.4. Catalyst Reusability

The NAP-MgO can be reused five times with consistent activity both in AH and AM reactions (Table 5.3, entry 1 and Table 5.7, entry 1) by heating to 250 °C for 1 h under
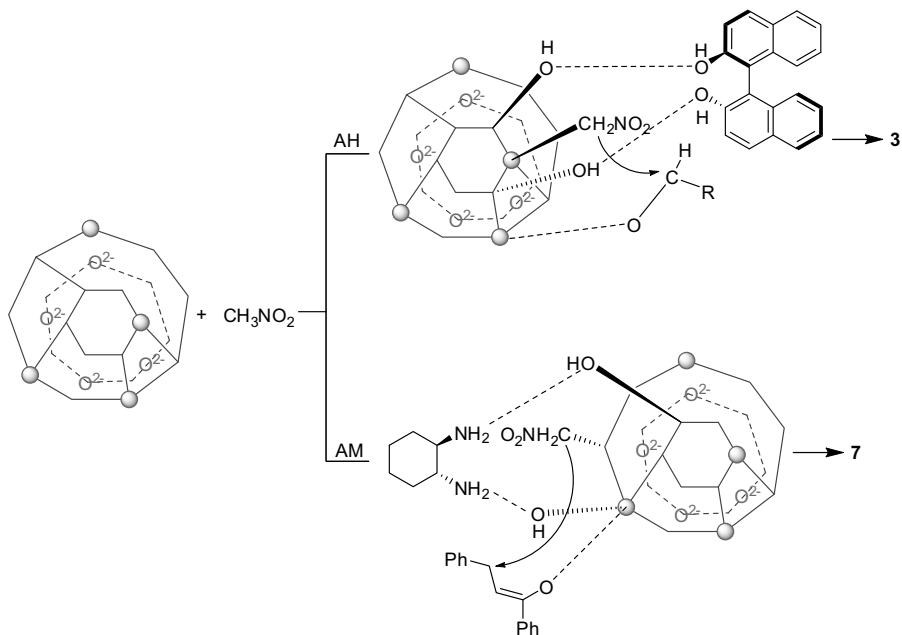
Scheme 5.3. Proposed mechanism for the asymmetric Henry and Michael reactions catalyzed by NAP-MgO. (Reproduced with permission from Ref. 64, American Chemical Society, Washington DC.)

a nitrogen atmosphere. The catalyst regenerated in this way gives comparable ee's to that of the homogeneous systems for the AH and AM reactions.

5.5. DIRECT ASYMMETRIC ALDOL REACTIONS

Aldol reactions are ubiquitous in synthetic organic chemistry to generate intermediates of antihypertensive drugs and calcium antagonists.[66–68] Chiral β-hydroxy carbonyl compounds can readily be converted to 1,3-*syn* and *anti*-diols and amino alcohols, which are the building blocks in many natural products such as antibiotics and pheromones and in many biologically active compounds.[67] Aldol products have successfully been converted to key synthetic intermediates of epithilone A and bryostatin 7.[68]

The direct aldol reaction, starting from an aldehyde and an unmodified ketone, is highly atom efficient,[69, 70] compared to processes that require preconversion of a ketone moiety to a more reactive species such as an enol silyl ether, enol methyl ether, or ketone silyl acetal, to generate the aldol donor (Mukaiyama aldol reaction).[71, 72]

Shibasaki and co-workers have reported the first catalytic asymmetric aldol reaction between aldehydes and unmodified ketones by using heterobimetallic multifunctional catalysts.[68, 73] Later, Trost and co-workers reported the direct

asymmetric aldol reactions with good to excellent enantioselectivities by using dinuclear transitional metal catalysts.[74–76] Barbas and co-workers[77] reported the direct asymmetric aldol reactions catalyzed by aldolase enzymes and antibodies. List, Barbas and co-workers have explored the asymmetric aldol reactions with excellent enantioselectivity by using *L*-proline[78, 79] and its structural analogs[80, 81] for α-branched aliphatic aldehydes. In the area of heterogenized catalysts, solid supported proline-terminated peptides and benzylpencillin derivatives in conjunction with proline grafted into mesoporous MCM-41 provide moderate ee's for the direct asymmetric aldol reaction.[82] L-Proline in ionic liquids and silica supported ionic liquids also provided moderate enantioselectivity.[83–85]

In this direction, Choudary et al.[86] reported the direct asymmetric aldol reaction of aldehydes and ketones to afford the optically active β-hydroxy carbonyl compounds in good yields and moderate ee's catalyzed by nanocrystalline magnesium oxide.

5.5.1. Catalyst Optimization

Various magnesium oxide crystals were initially screened in the achiral aldol reaction between *p*-nitrobenzaldehyde and acetone at room temperature, and NAP-MgO was found to be superior compared to CP-MgO and CM-MgO (Table 5.8). Based on the results of the achiral aldol reaction, the work was further extended to the direct asymmetric aldol reaction.

5.5.2. Ligand Optimization

Among the chiral auxiliaries tested, (1S, 2S)-(+)-1,2-diaminocyclohexane was found to give the highest yield and enantioselectivity (see Table 5.9) for the asymmetric aldol reaction between *p*-nitrobenzaldehyde and acetone catalyzed by NAP-MgO.

The use of the THF at –20 °C gave the optimum enantioselectivity compared to the other solvents. NAP-MgO was also tested in the direct asymmetric aldol reaction of various substituted aromatic aldehydes (Table 5.10). When benzaldehydes were substituted at the 4-position with electron-withdrawing (EW) groups or electron-donating (ED) groups, higher ee's were observed when compared with the corresponding 2-substituted benzaldehydes with either EW or ED groups, and may be ascribed to the steric hindrance for the unidirectional entry of the reacting species.

TABLE 5.8. Achiral Aldol Reaction Catalyzed by Different Crystallites of MgO Between *p*-Nitrobenzaldehyde and Acetone at Room Temperature[a]

Entry	Catalyst	Solvent	Time (h)	Conversion (%)
1	NAP-MgO	THF	24	75
2	CP-MgO	THF	36	10
3	CM-MgO	THF	36	0

[a] Conditions: catalyst (100 mg), *p*-nitrobenzaldehyde (1 mmol), acetone (13.7 mmol).

TABLE 5.9. Effect of Ligand on the Asymmetric Aldol Reaction Between
***p*-Nitrobenzaldehyde and Acetone Catalyzed by NAP-MgO at Room Temperature**[a]

Entry	Ligand	Yield (%)[b]	ee (%)[c]
1	(1*R*, 2*R*)-(+)-1,2-Diphenylethylenediamine	75	15
2	(1*R*, 2*R*)-(−)-1,2-Diaminocyclohexane	75	12
3	(1*S*, 2*S*)-(+)-1,2-Diphenylethylenediamine	75	16
4	(1*S*, 2*S*)-(+)-1,2-Diaminocyclohexane	75	25
5	(*S*)-(−)-1,1′-Binaphthyl-2,2′-diamine	75	0
6	(*R*)-(−)-1,1′-Binaphthyl-2,2′-diamine	75	0
7	(+)-Diethyl-L-tartrate	75	0
8	(*S*)-(−)-Binol	60	0
9	(*R*)-(−)-Binol	60	0
10	(−)-Diethyl-L-tartrate	75	0

[a] Conditions: *p*-nitrobenzaldehyde (1.0 mmol), acetone (13.7 mmol), NAP-MgO (0.100g), dry THF (2.0 mL), 24 h. In all cases 20 mol% of ligand was used.
[b] Isolated yields.
[c] The ee% was determined by HPLC analysis using a chiral column.

5.5.3. Catalyst Reusability

The NAP-MgO could be reused for four times with consistant activity by heating the catalyst to 250 °C for 1 h under nitrogen atmosphere.

5.6. ASYMMETRIC MICHAEL REACTION OF MALONATES

The catalytic asymmetric Michael (AM) reaction of malonates to enones, in which a new C–C bond is formed at the β-position of the enones, is an important organic transformation, since the resulting compounds are used in the synthesis of several natural products and drug molecules.[87–89] Many catalyst systems have been reported in recent years using a variety of metal catalysts with suitable chiral ligand combinations under homogeneous reaction conditions.

Kantam et al.[90] have investigated the use of a nano-MgO catalyst[1, 16, 41–47] for asymmetric Michael addition of malonates to cyclic and acylic enones in the presence of chiral auxiliary (1*R*,2*R*)-(+)-1,2-diphenyl-1,2-ethylenediamine (DPED) (Scheme 5.4).

5.6.1. Ligand Effect

Among the MgO samples screened in the asymmetric Michael addition of chalcone and dimethylmalonate using (1*R*, 2*R*)-(+)-1,2-diphenyl-1,2-ethylenediamine (DPED, see Figure 5.5) as a chiral auxiliary, NAP-MgO was found to be superior to NA-MgO and CM-MgO in terms of yields and ee's. In general, chiral bidentate systems composed of primary and secondary amines afforded better ee's, while chelation with –OH groups displayed no reaction and ee (Table 5.11).

TABLE 5.10. Direct Asymmetric Aldol Reaction of Aldehydes and Acetone with NAP-MgO[a]
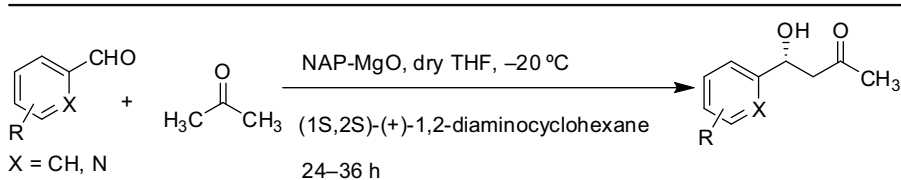
Entry	Aldehyde	Yield (%)[b]	ee (%)[c]	Entry	Aldehyde	Yield (%)[b]	ee (%)[c]
1	F-C6H4-CHO	70	60	6	3-NO2-C6H4-CHO	70	27
2	Cl-C6H4-CHO	65	48	7	2-Cl-C6H4-CHO	55	33
3	Br-C6H4-CHO	67	40	8	C6H5-CHO	60	23
4	NC-C6H4-CHO	60	40	9	H3C-C6H4-CHO	50	17
5	O2N-C6H4-CHO	75, 72,[d] 0[e]	53	10	pyridine-2-CHO	75	43

[a] All reactions were performed on 1 mmol substrate in 1.0 mL (13.7 mmol) acetone using 100 mg of NAP MgO.
[b] Isolated yield after column chromatography.
[c] The ee % was determined by HPLC analysis using a chiral column.
[d] Fifth cycle.
[e] Without catalyst.

5.6.2. Reaction Between Chalcone and Cyclic Enones with Malonates

The nature of the ester group of the malonate strongly influences the ee of the product. As the bulkiness of the ester group increases, the rate of reaction decreases (Table 5.12). It was observed that the rate of the reaction was slower with cyclic enones than with acyclic enones. Interestingly, as the ring size was increased, the rate of reaction decreased but with an increase in ee (Table 5.13). The ee was found to be higher with cyclic enones than with acyclic enones, which may be due to the rigidity of the cyclic systems (Tables 5.12 and 5.13).
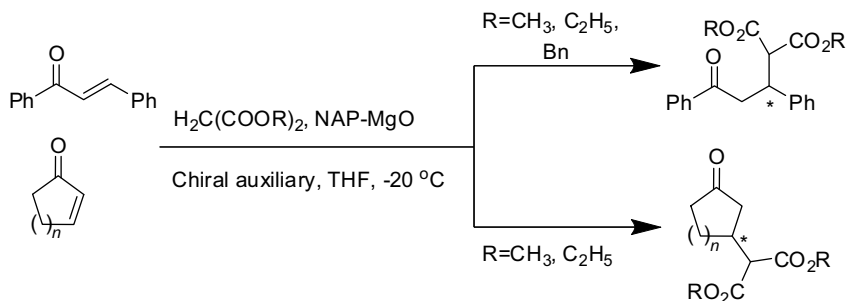
Scheme 5.4. Asymmetric Michael addition between malonates and enones catalyzed by NAP-MgO in the presence of a chiral auxiliary.
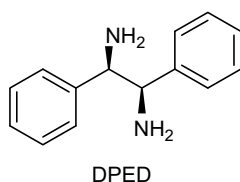
DPED

Figure 5.5. Ligand (1R, 2R)-(+)-1,2-diphenyl-1,2-ethylenediamine (DPED).

The Michael reaction is known to be driven by basic catalysts,[91] and accordingly, the surface OH and O^{2-} sites of these oxide crystals are expected to trigger the reaction. Although both NAP-MgO and NA-MgO possess defined shapes and the same average concentrations of surface OH groups, a possible rationale for the higher rate of reaction by NAP-MgO is the presence of more surface Mg^{2+} (Lewis acid) ions (20%).[47] The acid–base interactions of the Mg^{2+} ions (Lewis acid) of NAP-MgO and the basic chiral auxiliary may also influence the enantioselectivity.

TABLE 5.11. Effect of Ligand on the Asymmetric Michael Reaction Between Chalcone and Dimethyl Malonate Catalyzed by NAP-MgO at 25 °C

Entry	Ligand	Time (h)	Yield (%)[a]	ee (%)[b]
1	(1R, 2R)-(+)-1,2-diphenylethylenediamine	8, 14,[c] 24,[d] 12,[e] 8[f]	91, 64,[c] 30,[d] 60,[e] 89[f]	60, 42,[c]10,[d] 60,[e] 60[f]
2	L-Proline	15	No reaction	—

Reaction conditions: chalcone (1.0 mmol), dimethyl malonate (5.0 mmol), NAP-MgO (0.125 g), dry THF (5 mL). In all cases 25 mol% of ligand was used.
[a] Isolated yields.
[b] ee was determined by HPLC analysis.
[c] With NA-MgO.
[d] With CM-MgO.
[e] With silylated NAP-MgO.
[f] Fifth cycle.

TABLE 5.12. Asymmetric Michael Reaction Between Chalcone and Malonates Catalyzed by NAP-MgO in the Presence of a Chiral Auxiliary (DPED) at $-20\,°C$

Entry	R	Time (h)	Yield (%)[a]	ee (%)[b]
1	CH$_3$	12, 12[c]	93, 90[c]	82, 70[c]
2	C$_2$H$_5$	15	95	76
3	Bn	18	92	85

 Reaction conditions: chalcone (1.0 mmol), malonate (5.0 mmol), NAP-MgO (0.125 g), dry THF (5 mL). In all cases 25 mol% of DPED was used.
[a] Isolated yields.
[b] ee was determined by HPLC analysis.
[c] At 0 °C.

Heterogeneous catalysis is a surface phenomenon in which the crystal face plays a major role. NAP-MgO has a polyhedral shape with a three-dimensional structure with reactive ions on the surface. The crystal morphology and crystal shape induce the chirality in the reaction.

TABLE 5.13. Asymmetric Michael Reaction Between Various Cyclic Enones and Malonates Catalyzed by NAP-MgO in the Presence of a Chiral Auxiliary (DPED) at $-20\,°C$

Entry	n	R	Time (h)	Yield (%)[a]	ee (%)[b]
1	1	Me	12	94	84
2	1	Et	12	93	86
3	2	Me	16	95	90
4	2	Et	16	90	90
5	3	Me	24	96	94
6	3	Et	24	90	96

 Reaction conditions: enone (1.0 mmol), malonate (5.0 mmol), NAP-MgO (0.125 g), dry THF (5 mL). In all cases 25 mol% of DPED was used.
[a] Isolated yields.
[b] ee was determined by HPLC analysis.

5.6.3. Recyclability Protocol

The NAP-MgO could be reused for five cycles with consistent activity. After completion of the reaction, the recovered catalyst was thoroughly washed and activated by heating at 250 °C for 1 h under a nitrogen atmosphere. It was found that the crystal morphology of reused NAP-MgO was unchanged, as shown by XRD.

5.7. CLAISEN–SCHMIDT CONDENSATION-ASYMMETRIC EPOXIDATION REACTIONS

Asymmetric epoxidation (AE) of α,β-unsaturated ketones is an important organic transformation, since the resulting chiral epoxy ketones are versatile precursors to many natural products and drug molecules.[92] These epoxidation reactions can be achieved using various basic chiral auxiliaries such as polypeptides[93] under phase transfer conditions or in situ prepared chiral metal complexes, La/Yb/Zn-BINOL,[94, 95] magnesium tartrate,[96, 97] and zinc ephedrine[98] systems in homogeneous media. In the direction of heterogenization, polymer supported polypeptides[99] have been designed and synthesized by a simple process of anchoring and successfully used for the AE of α,β-unsaturated ketones. Choudary et al.[16] reported a recyclable bifunctional nano-MgO catalyst for the Claisen–Schmidt condensation (CSC) of the benzaldehydes with acetophenones to yield chalcones followed by AE to afford chiral epoxy ketones with moderate to good yields and impressive enantioselectivities (ee's) in a two-pot reaction (Scheme 5.5, Table 5.14, Method A).

5.7.1. Effect of Various MgO Catalysts

Various magnesium oxide crystals[6] [commercial MgO, CM-MgO (SSA: 30 m^2/g), conventionally prepared MgO, NA-MgO (SSA: 250 m^2/g), aerogel prepared MgO, NAP-MgO (SSA: 590 m^2/g)] were initially evaluated in the CSC and AE reactions separately in order to understand the relationship between structure and reactivity. All these MgO samples catalyzed both CSC of benzaldehyde with acetophenone to form chalcone quantitatively and selectively, and subsequent AE using (+)-diethyl tartrate (DET) as a chiral auxiliary to obtain a chiral epoxy ketone in good yield and impressive ee. The nanocrystalline MgO (NAP-MgO) was found to be more active than the NA-MgO and CM-MgO in the condensation and epoxidation reactions (Figure 5.6).
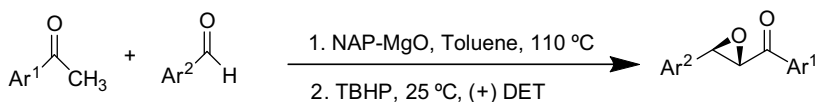
Scheme 5.5. Claisen–Schmidt condensation-asymmetric epoxidation catalyzed by nanocrystalline magnesium oxide.

TABLE 5.14. Synthesis of Chiral Epoxides Using Nanocrystalline Magnesium Oxide

Entry	Ar^1	Ar^2	Method	Yield (%)^a	e.e. (%)^b
1	Ph	Ph	A	70, 58,^{c} 30,^{d} 0,^{e}70,^{f} 0^g	90, 60,^{c} 0,^{d} 90^f
			B	60 (68),^{h}15,^{b} 0,^{c} 0,^{d} 60^f	82 (86), 0,^{c} 82^f
2	4-Me-C$_6$H$_4$	Ph	A	70	80
			B	58(60)	50(54)
3	4-Cl-C$_6$H$_4$	Ph	A	70	96
			B	40(58)	48(60)
4	4-MeO-C$_6$H$_4$	Ph	A	68	53
			B	56(59)	40(43)
5	Ph	4-Cl-C$_6$H$_4$	A	52	97
			B	40(46)	58(70)
6	Ph	4-Me-C$_6$H$_4$	A	62	69
			B	51(53)	39(42)
7	Ph	4-NO$_2$-C$_6$H$_4$	A	52	98
			B	48(60)	48(63)
8	2-C$_4$H$_3$S	Ph	A	68	71
			B	(50)	(48)
9	2-C$_4$H$_3$O	Ph	A	70	84
			B	(48)	(46)
10	C$_6$H$_5$	2-C$_5$H$_4$N	A	64	80
			B	(47)	(45)

^{a} Isolated yields.
^{b} Absolute configurations were determined to be (αR, βS). See Ref. 93.
^{c} With NA-MgO.
^{d} With CM-MgO.
^{e} With silylated AP-MgO.
^{f} Fifth cycle.
^{g} Without catalyst.
^{h} Values in parenthesis are after the addition of 4 Å molecular sieves. Method A: Direct AE; Method B: Tandem CSC–AE.

5.7.2. Scope of the Reaction

The ee of the product was shown to be 90%, 60% and 0% using NAP-MgO, NA-MgO, and CM-MgO, respectively (Table 5.14, entry 1). When either of the benzaldehydes or acetophenones are substituted with electron-withdrawing groups, higher ee's were obtained than those bearing electron-donating groups using NAP-MgO as catalyst (Table 5.14, entries 2–7). The CSC and AE with heteroaromatic compounds[100] was also carried out in the presence of NAP-MgO, which gave very good ee's (Table 5.14, entries 8–10). Identical activity was observed for five cycles in the CSC and epoxidation reactions (Table 5.14, entry 1).

These catalytic CSC reactions are very impressive when compared to the recently reported hydrotalcites and zeolites,[101–104] in terms of selectivity or conversions and far superior to the other systems using AlCl$_3$, BF$_3$, POCl$_3$, alumina, or Ba(OH)$_2$, which require greater than the stoichiometric quantities, are nonregenerable, and give poor selectivity of desired products.
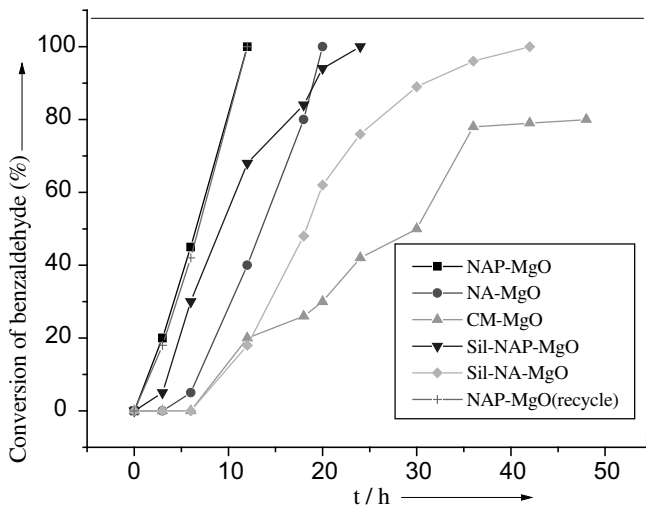
Figure 5.6. Claisen–Schmidt condensation of benzaldehyde with acetophenone using different crystallites of magnesium oxide at 110 °C. (Reproduced with permission from Ref. 16, American Chemical Society, Washington DC.)

In the studies regarding the influence of various oxidants, chiral auxiliaries, solvents, and temperatures on enantioselectivity in the AE reaction, the use of *tert*-butyl hydroperoxide (TBHP), DET, and toluene at −20 °C gave the optimum results. However, in the bifunctional single-pot CSC followed by AE reaction (Table 5.14, Method B), the ee's and conversions are lower than in the independent AE reactions. This is due to the poisoning effect of water adsorbed on to the catalyst, which is formed in situ in the CSC reaction. When the catalyst was dried under a nitrogen flow for 1 h at 250 °C immediately after the CSC, similar enantioselectivity in the AE reaction was obtained, supporting the above theory.

5.7.3. Reaction Mechanism

As expected, NAP-MgO displayed the highest activity compared to NA-MgO and CM-MgO. The CSC and epoxidation of deactivated olefins are driven by base catalysts and accordingly the surface –OH and O^{2-} sites of these oxide crystals are expected to trigger these reactions. To examine the role of –OH groups in the catalytic process, silylated Sil-NA-MgO and Sil-NAP-MgO,[47] devoid of free –OH are prepared and tested in CSC and epoxidation reactions It was found that the silylated MgO samples required longer reaction times than the corresponding MgO samples in the CSC and essentially no epoxidation took place. These results indicate that Brønsted hydroxyls are the sole contributors for the epoxidation reaction, while they aid the CSC, which is largely driven by Lewis basic O^{2-} sites. When protected hydroxyls of DET, (+)-diethyl-2, 3-*O*-isopropyledene-*R*, *R*-tartrate, were used in place of DET in the AE reaction, no ee was observed, which establishes that the hydrogen bond interactions between the –OH groups of DET and MgO are essential
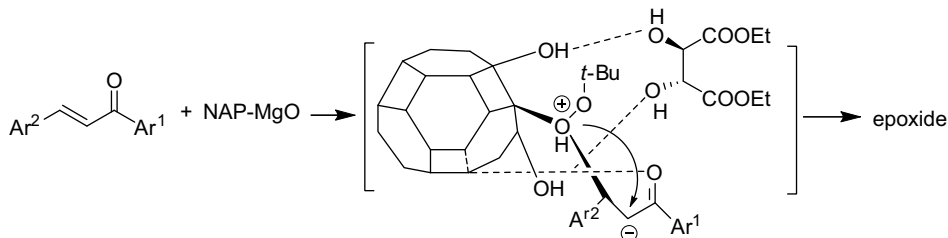
Scheme 5.6. Proposed mechanism for asymmetric epoxidation of unsaturated ketones using TBHP as an oxidant. (Reproduced with permission from Ref.16, American Chemical Society, Washington DC.)

for high enantioselectivity. Although both NAP-MgO and NA-MgO possess defined shapes and the same average concentrations of surface –OH groups, a possible rationale for the display of higher ee by the NAP-MgO is that the –OH groups present on edge and corner sites on the NAP-MgO are more isolated and accessible to the DET, whereas in NA-MgO, relatively large portions of the –OH groups are situated on flat planes in close proximity with each other and are hindered.[10] CM-MgO, which showed no ee, has assorted crystals.

The XPS spectrum of the TBHP-treated NAP-MgO for the O 1s peak exhibits two lines at 530.3 and 532.0 eV, which can be attributed to lattice oxygen in MgO and dioxygen of magnesium peroxide,[105] respectively. This provides evidence that peroxide is formed on interaction of the TBHP with the Mg^+ Lewis acid. An endotherm at 310 °C in the DTA-TGA-MS of the TBHP treated NAP-MgO gives off a fragment ($m/z = 89$ amu) corresponding to *tert*-butyl peroxide, further evidence for the formation of surface *tert*-butyl peroxide. When the TBHP treated NA-MgO and CM-MgO were subjected to DTA-TGA-MS analysis, no such endotherm corresponding to magnesium peroxide was observed. This is due to the presence of higher concentrations of Mg^+ ion (20%) in NAP-MgO. This also reinforces the argument in favor of higher activity of NAP-MgO.

In the AE, the Mg ion of MgO reacts with TBHP to produce magnesium peroxide (MgOOR) and may also interact with the oxygen atom of the carbonyl functionality. The DET bound to the hydroxyls of NAP-MgO directs the delivery of nucleophilic oxygen of the peroxide[106] stereoselectively to give the chiral epoxy ketones (Scheme 5.6). The presence of electron-withdrawing groups on either of the two aromatic rings of the chalcone facilitate the formation of a resonance stabilized oxyanion, which might account for the higher ee's.

5.8. ASYMMETRIC EPOXIDATION OF TERMINAL OLEFINS BY Mn(III) COMPLEXES STABILIZED ON NANOCRYSTALLINE MAGNESIUM OXIDE

Asymmetric epoxidation (AE) of unfunctionalized olefins is an important organic transformation, since the resulting epoxides are important building blocks for the

synthesis of biologically active molecules.[107, 108] Srinivasan et al.[109] first reported Mn(II)–salen complexes are reactive catalysts for the epoxidation of olefins. Later, Jacobsen and co-workers[110, 111] and Katsuki[112] reported chiral Mn(II)–salen complexes for the AE of unfunctionalized olefins. The high enantiomeric excess values achieved are attributed to the directed path of the prochiral olefin to the metal center, while other possible paths are blocked by the introduction of bulky substituents on the salen ligands.

AE have also been achieved by using a chiral Mn–salen complex immobilized on mesoporous materials,[113–117] polymer supports,[118, 119] layered double hydroxides,[120] clays,[121] and zeolites.[122]

Recently, Choudary et al.[123] reported the asymmetric epoxidation of unfunctionalized olefins to epoxides using manganese acetylacetonate stabilized on nanocrystalline magnesium oxide in the presence of (1R, 2R)-(−)-diaminocyclohexane (DAC) as a chiral ligand in good yields and up to 91% enantiomeric excess (Scheme 5.7).[124]

5.8.1. Catalyst Optimization

The different magnesium oxide crystals[1, 16, 41–47] CM-MgO, NA-MgO, and NAP-MgO were evaluated as catalysts in the epoxidation styrene but were found to have no activity (Table 5.15, entry 1). Treatment of the MgO samples with Mn (acac)$_3$ gave samples of Mn(acac)$_n$-MgO, which were also tested as catalyst in the epoxidation reaction (Table 5.15, entries 3–5). Mn(acac)$_n$-MgO gave good yields of epoxidation products, although enantioselectivity was poor; the Mn treated CM-MgO and NAP-MgO showed little or no activity.

5.8.2. Scope of the Reaction

The ion exchange capability of NAP-MgO is well established in the literature.[30, 125] The incorporation of manganese into NAP-MgO is much greater than that of NA-MgO and CM-MgO and is attributed to the presence of an increased number of large surface ionic charges. Various MgO samples (Table 5.15) and oxidants were used for optimization studies of the asymmetric epoxidation reactions. Among the MgO samples screened, Mn(acac)$_n$-NAP-MgO using TBHP as oxidant was found to be superior to NA-MgO and CM-MgO in terms of both yields and ee's. The ee's of the AE product, styrene oxide, were 42%, 0%, and 0% using the Mn(acac)$_n$-NAP-MgO,
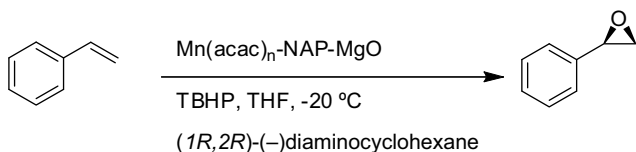
Scheme 5.7. Asymmetric epoxidation of olefins using Mn(acac)$_n$-NAP-MgO in the presence of chiral ligand.

TABLE 5.15. Asymmetric Epoxidation of Styrene Using Different Catalysts at $-20\,°C$

Entry	Catalyst	Time (h)	Yield (%)	ee (%)[a]
1	NAP-MgO	24	0, 0,[b] 0[c]	0
2	Mn(acac)$_3$	24	10	0
3	Mn(acac)$_3$ – DAC	24	10	0
4	Mn(acac)$_n$ – NAP-MgO	24	70, 20,[d] 0[e]	42, 0[c]
5	MnO$_2$-NAP-MgO	24	0	0

[a] Absolute configuration was found to be (R).
[b] NA-MgO.
[c] CM-MgO.
[d] Mn(acac)$_n$-NA-MgO.
[e] Mn(acac)$_n$-CM-MgO.

Mn(acac)$_n$-NA-MgO, and assorted crystals of Mn(acac)$_n$-CM-MgO, respectively (Table 5.15). The AE reactions are conducted in THF and chiral epoxides are obtained in good yields and ee's (Table 5.16). Using 6-cyanochromene, indene, styrene, and 4-methyl styrene, chiral epoxides in good yields and ee's were obtained (Table 5.16).

5.8.3. Reusability Studies

After reusing the catalyst for three cycles, a significant decrease in the yield was observed. This decrease is a result of Mn leaching into solution from the support during the reacton (Table 5.17) as confirmed by AAS. The catalyst was recovered by filtration and the chiral ligand by column chromatography. When the reaction was conducted with the filtrate, no product formation was observed. This indicates that any Mn leached into solution is inactive in the reaction and that the Mn complex bound to MgO is the only active species in the reaction.

5.8.4. Mechanistic Studies

Mechanistic studies have also been reported based on the experimental evidence in the AE using NAP-MgO. NAP-MgO has a three-dimensional polyhedral structure,

TABLE 5.16. Asymmetric Epoxidation of Unfunctionalized Alkenes with Mn(acac)$_n$-NAP–MgO at $-20\,°C$

Entry	Substrate	Time (h)	Yield (%)[a]	ee (%)[b]
1	Styrene	24	70, 55[c]	42, 41[c]
2	4-Methylstyrene	24	78	40
3	*trans*-Stilbene	24	66	24
4	6-Cyanochromene	18	90	91
5	Indene	18	85	84

[a] Yields based on ^{1}H NMR.
[b] ee was determined by HPLC.
[c] Third cycle.

TABLE 5.17. Reusability of Mn(acac)$_n$-MgO Catalyst in the Asymmetric Epoxidation[a] **of Styrene at −20 °C**

Entry	Cycle	Mn Content in the Catalyst (mmol/g)[b]	Yield (%)[c]	ee (%)[d]
1	1	0.369	70	42
2	2	0.332	66	42
3	3	0.258	55	41

[a] Reaction conditions: styrene (1.0 mmol), dry THF (3.0 mL), TBHP (1.0 mL, 3.5 mmol), catalyst (0.100 g), chiral ligand (DAC) (0.025 g).
[b] Mn content determined by AAS analysis.
[c] Yields based on ^{1}H NMR.
[d] ee was determined by HPLC.

with high surface concentrations of edge/corner and various exposed crystal planes (such as 002, 001, 111), leading to an inherently high surface ionic charge per unit area. The presence of corner and edge sites on the surface of NAP-MgO could approach 20%, while on NA-MgO they amount to less than 0.5% and on CM-MgO essentially 0%. For example, an edge or corner O$^-$ anion is coordinatively unsaturated and is seeking Lewis acids to help stabilize and delocalize its charge. Conversely, an Mg^{2+} ion on an edge or corner is seeking Lewis bases (acac$^-$) to stabilize and delocalize its positive charge (Scheme 5.8).

Therefore, these coordinatively unsaturated O$^-$ and Mg^{2+} ions readily accept incoming Lewis acids and Lewis bases, respectively. Thus, Mn(acac)$_n$-NAP-MgO displayed the highest catalytic activity compared to manganese-doped NA-MgO and CM-MgO. MnO$_2$-NAP-MgO formed on calcination of Mn(acac)$_n$-NAP-MgO is inactive for the epoxidation reaction. This may be due to disturbance of the molecular chemistry.

In the proposed mechanism for the epoxidation of olefins such as styrene, the Mn(III) on nano magnesium oxide is complexed with a chiral ligand and subsequently oxidized by t-BuOOH to form a metal-oxo [Mn(IV) = O] (B) (Scheme 5.9), as indicated by XPS analysis.[123] Mn(IV) is indeed found as an active species in Jacobsen–Katsuki catalytic epoxidations.[126, 127] Interaction of the olefin and (B),
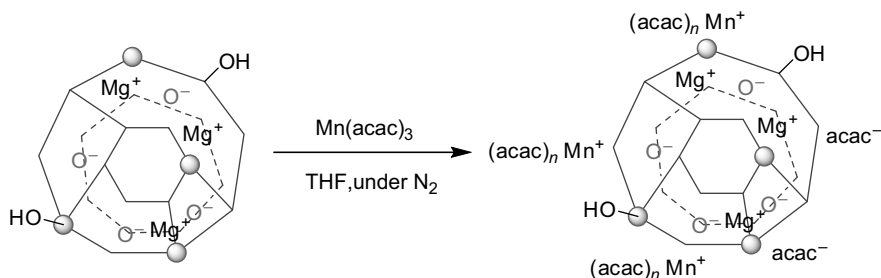
Scheme 5.8. Preparation of Mn(acac)$_n$-NAP-MgO catalyst. (Reproduced with permission from Ref. 123, Wiley-VCH Verlag GmbH.)
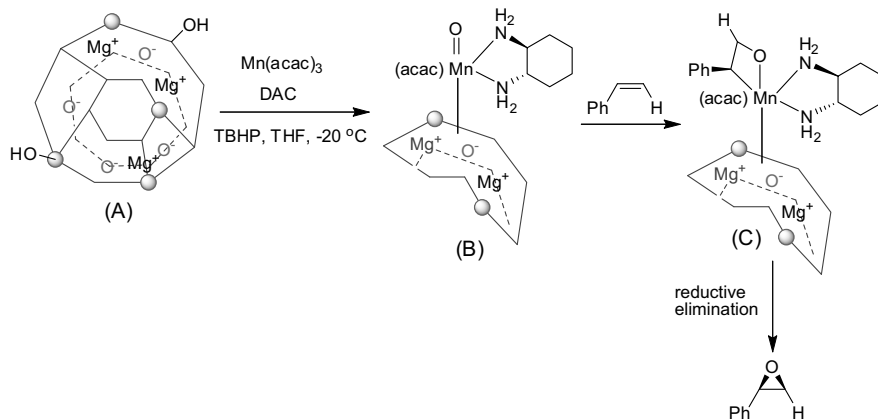
Scheme 5.9. Proposed mechanism for the Mn(acac)$_n$-NAP-MgO catalyzed asymmetric epoxidation of olefins. (Reproduced with permission from Ref. 123, Wiley-VCH Verlag GmbH.)

followed by the oxygen transfer gives an intermediate (C), which on reductive elimination affords the chiral epoxide. High facial selectivity of the complex is due to its surface chemical properties.[10]

5.8.5. Preparation of Mn(acac)$_n$-NAP-MgO

The MgO samples were heated under vacuum to 500 °C before use. Mn(acac)$_n$-NAP-MgO was prepared by treating vacuum dried NAP-MgO (1.0 g) with Mn(acac)$_3$ (0.20 g) in THF (8.0 mL) under a nitrogen atmosphere at room temperature and stirring for 24 h by a method similar to that reported by Klabunde and co-workers.[10] The slurry was filtered off, washed with THF, and vacuum dried to give Mn(acac)$_n$-NAP-MgO (1.105 g, brownish color). The I R spectrum shows evidence for the incorporation of the Mn(acac)$_n$ moiety. The Mn content in Mn(acac)$_n$-NAP-MgO was determined to be 0.369 mmol g^{-1} by atomic absorption spectroscopy (AAS).

5.9. BIFUNCTIONAL CATALYSTS STABILIZED ON NANOCRYSTALLINE MgO FOR THE ONE-POT SYNTHESIS OF CHIRAL DIOLS

Performing a multistep synthesis in one pot, prevalent in biosystems, is an attractive strategy to improve the efficiency of organic processes in terms of conservation of energy, reducing the processing time and inventory of equipment and minimizing the use of chemicals and production of waste.[128, 129] Significant progress using a combination of two catalysts for effecting tandem reactions has been achieved.[130–134] The recent design of a single matrix bifunctional catalyst comprising

a BINOL–BINOP copolymer for the tandem asymmetric diethylzinc addition and hydrogenation of acetyl benzaldehydes marks a new era in bifunctional catalysis.[135]

The Sharpless catalytic asymmetric dihydroxylation (AD) of olefins using an osmium-based catalyst, an inspiring process, provides the most elegant method for the preparation of chiral vicinal diols.[136] Chiral vicinal diol units are often observed as key structures of natural products and also used in the synthesis of chloramphenical (broad spectrum antibiotic), diltiazem hydrochloride (calcium channel blocker), taxol side chain, macrocyclic antitumor drugs, and β-lactams. Although the AD reaction offers a number of processes that could be applied to the synthesis of pharmaceuticals, fine chemicals, and so on, the high cost, toxicity, and possible contamination of osmium catalysts in the products restrict its use in industry. Heterogenization of OsO_4 via microencapsulation,[137–139] ion-exchange techniques,[140–142] and covalent anchoring[143] are employed to address the issue of complete recovery of osmium from the reaction medium.

Bäckvall and co-workers reported highly economical process by using H_2O_2, a stoichiometric oxidant, and NMM in catalytic amounts to continuously generate NMO in situ via oxidation using biomimic flavin[144, 145] or vanadyl acetylacetonate[146] as the electron-transfer mediator in the multicomponent catalytic system for AD reactions of olefins. Choudary et al.[30] demonstrated the reoxidation of NMM to facilitate continuous in situ production of NMO to sustain the Os(VI)/Os (VIII) catalytic cycle induced by a bifunctional heterogeneous catalyst composed of osmium and tungsten oxides on a single matrix using H_2O_2 as the terminal oxidant. Recently, Choudary et al.[30] immobilized osmium tetroxide on nanocrystalline MgO by the counterionic stabilization technique for achiral dihydroxylation.

5.9.1. Preparation of NAP-MgO Supported Bifunctional Catalysts

Choudary et al.[125] reported a new bifunctional catalyst composed of Pd/Os and Os/W systems on the nanocrystalline MgO reactions for the Heck-AD and N-oxidation reactions using H_2O_2 as the terminal oxidant. In an effort to obtain counterionic stabilization of $PdCl_4^{2-}$, OsO_4^{2-}, and WO_4^{2-} with Mg^{2+} of the MgO, commercially available CM-MgO conventionally prepared NA-MgO and aerogel prepared NAP-MgO were treated with Na_2PdCl_4, K_2OsO_4, and Na_2WO_4 to afford the samples of Mg-OsO_4, Mg-PdCl_4-OsO_4 (Mg-PdOs), and Mg-OsO_4-WO_4 (Mg-OsW), respectively. In the reaction with NAP-MgO, the entire amount of Na_2PdCl_4, K_2OsO_4, and Na_2WO_4 used was consumed. On the other hand, a small amount (<0.3%) of palladate, osmate, and tungstate were detected in the treated samples of CM-MgO and NA-MgO. During the preparation of the catalyst, which involves the reaction with Na_2PdCl_4, K_2OsO_4, and Na_2WO_4, the Na^+ and K^+ ions will interact with the O^{x-} sites/anionic vacancies. Similarly, the $PdCl_4^{2-}$, OsO_4^{2-}, and WO_4^{2-} anions interact with the Mg^{2+} sites/cationic vacancies present on corners or edges of nanocrystalline NAP-MgO to form bifunctional catalysts (Scheme 5.10) as described for the one-pot synthesis of chiral diols (see Section 5.9.4).
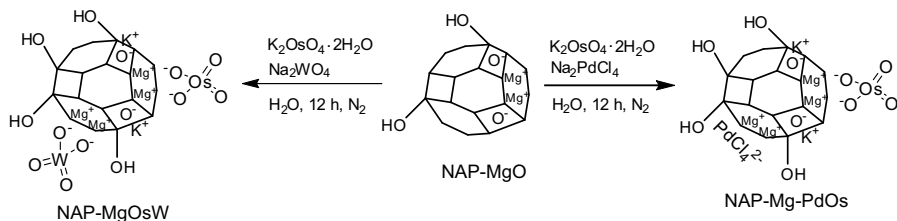
Scheme 5.10. Preparation of NAP-MgO supported bifunctional catalysts. (Reproduced with permission from Ref. 125, Wiley-VCH Verlag GmbH.)

5.9.2. Characterization of Nanocrystalline MgO Supported Catalysts

All the catalysts developed are fully characterized by FTIR, SEM-EDAX, and XPS. In the FTIR spectra of these counterionic stabilized catalysts, broad absorption bands appear in the region 815–860 cm^{-1}, which are assigned to the vibrational asymmetric O=M=O (M = Os and/or W) stretching, significantly different from the sharp bands observed at 819 cm^{-1} for potassium osmate and 831 and 857 cm^{-1} for sodium tungstate. The observation of broad bands in the same region for the catalysts suggests that the osmate and tungstate ions are unaffected upon counterion stabilization onto the support, while experiencing very weak interactions with the support. During the preparation of these catalysts, the surface of NAP-MgO was hydroxylated as indicated by non-H-bonded OH groups at 3715 cm^{-1} in the IR spectra. This is consistent with the reactive profile of NAP-MgO with water.[147] The surface of the nano-MgO is hydroxylated to $Mg(OH)_n$ and requires a longer time and heating to transform the bulk nano-MgO. The XRD patterns of the NAP-Mg-OsO$_4$, NAP-Mg-PdOs, and NAP-Mg-OsW samples also indicate formation of $Mg(OH)_n$ during the preparation.[11] The SEM–EDX (scanning electron microscopy–energy dispersive X-ray analysis) of NAP-Mg-OsO$_4$, NAP-Mg-PdOs, and NAP-Mg-OsW shows the presence of metals 8.96%(Os), 3.98%(Pd), 7.15%(Os) and 7.04%(Os), and 6.81%(W) in the respective samples. The XPS results of fresh and used bifunctional NAP-Mg-PdOs and NAP-Mg-OsW catalysts show almost identical binding energies for Pd,[148–150] Os,[151–153] and W[154–156] (Table 5.18). This confirms that the oxidation states of the respective metals remain static during the counterionic stabilization process and at the end of the reaction.

All these results rule out the formation of bimetallic species and indicate retention of the coordination geometries of the specific divalent anions anchored to nano-MgO in their monomeric form upon counterionic stabilization and use.

5.9.3. Asymmetric Dihydroxylation of Olefins

In 2004, Choudary et al.[30] reported the synthesis and application of NAP-Mg-OsO$_4$ in the achiral dihydroxylation of olefins. Later, AD of *trans*-stilbene was performed using NAP-Mg-OsO$_4$ in the presence of a chiral ligand.[125] A mixture of NAP-Mg-OsO$_4$, NMO, and 1 mol% 1,4-bis(9-O-dihydroquinidinyl)phthalazine [(DHQD)$_2$PHAL] ligand was added to a round bottom flask containing

TABLE 5.18. XPS Binding Energies (eV) for NAP-MgO Supported Catalysts

Catalyst	Pd		Os		W	
	$3d_{5/2}$	$3d_{3/2}$	$4f_{7/2}$	$4f_{5/2}$	$4f_{7/2}$	$4f_{5/2}$
NAP-Mg-OsO$_4$			54.0	56.5		
NAP-Mg-PdOs[a]	336.9	342.3	54.6	57.0		
NAP-Mg-PdOs[b]	337.0	341.9	54.2	56.8		
NAP-Mg-OsW[a]	—	—	54.5	57.0	35.5	37.5
NAP-Mg-OsW[b]	—	—	54.4	57.0	35.0	37.2

[a] Fresh catalyst.
[b] Used catalyst.

t-BuOH-H$_2$O (5:1, 6 mL). *trans*-Stilbene was slowly added to the reaction mixture at room temperature over a period of 12 h and stirred further for a further 3 h to afford the corresponding chiral diol in 85% yield with 99% ee.

NAP-Mg-OsO$_4$ was further subjected to AD of various olefins and the results are summarized in Table 5.19. Slow addition of olefin to the reaction mixture is warranted to keep the availability of the olefin at a bare minimum level in order to achieve higher ee's. The olefins ranging from mono to trisubstituted, activated to simple, are subjected to dihydroxylations. In most cases, the desired diols were formed in higher yields, albeit with reduced ee's, when compared with results obtained in the homogeneous system.

The scope of NAP-Mg-OsO$_4$ catalyst was extended successfully to the hydroxylation of the relatively large substrates stilbene (Table 5.19, entry 1) and methyl cinnamate (Table 5.19, entry 4). It is well documented in the literature that bases, or less often acids, are used in the dihydroxylation reactions for the hydrolysis of osmate esters. Additives such as Et$_4$NOH, Et$_4$NOAc, Et$_4$NF, C$_6$H$_5$PO$_3$(Et$_4$N)$_2$, (Et$_4$N)$_2$CO$_3$, HCl, HI, and tetraethylammonium salts of chelating diacids such as *o*-phthalic,

TABLE 5.19. Asymmetric Dihydroxylation of Olefins with NAP-Mg-OsO$_4$[a]

Entry	Olefin	Isolated Yields (%)	ee (%)	Absolute Configuration (%)
1	Ph⟍═⟋Ph	85	99	*RR*
2	Ph⟍═	91	77	*R*
3	Ph	90	80	*R*
4	Ph⟍═⟋COOMe	96	94	*2S,3R*
5	⬡—Ph	87	58[b]	*1R,2R*

[a] See Ref. 125.
[b] 2 equivalents of TEAA were added.

TABLE 5.20. Influence of Additive and Slow Addition of Methyl Cinnamate on the ee in the Asymmetric Dihydroxylation Reaction of Methyl Cinnamate[a]

Entry	Catalyst	Additive	Slow Addition (h)	ee (%)
1	$K_2OsO_4 \cdot 2H_2O$	—	—	88
2	NAP-Mg-OsO$_4$	—	—	45
3	NAP-Mg-OsO$_4$	—	12	94
4	NAP-Mg-OsO$_4$	Et$_3$N·HI	12	95

[a] See Ref. 125.

camphoric and *cis*-1,2-cyclohexane dicarboxylic acid are effectively used to accelerate the hydrolysis of osmium monoglycolate esters and thus prevent the formation of bisglycolate esters (second cycle) to achieve higher ee.[157, 158] Introduction of additives and/or slow addition of olefin to the reaction mixture to allow the hydrolysis of the formed osmium monoglycolate were also used to obtain higher ee. The effect of the catalyst and Et$_3$N·HI on the enantioselectivity of the AD reaction of methyl cinnamate was also investigated (Table 5.20).

In the AD of methyl cinnamate under homogeneous conditions using the $K_2OsO_4 \cdot 2H_2O$ as catalyst and NMO as oxidant in H_2O-*t*-BuOH, 88% ee was obtained without the slow addition of the olefin under similar reaction conditions, while using NAP-Mg-OsO$_4$ as catalyst gave an ee value of 45%. In the AD of methyl cinnamate catalyzed by NAP-Mg-OsO$_4$ using NMO as the oxidant with slow addition, 94% ee is obtained and in the presence of Et$_3$N·HI as an additive in *t*-BuOH-H_2O, 95% ee was obtained. The Et$_3$N·HI salt can accelerate the hydrolysis of the osmium monoglycolate complex to subdue the second cycle as was done by tetraethylammonium acetate, which is known for the faster rates and higher ee.[159] The higher ee achieved in this case is attributed to Et$_3$N·HI, which is responsible for the acceleration of the hydrolysis of the osmium monoglycolate ester.

5.9.4. One-Pot Synthesis of Chiral Diols

Palladium-Osmium Catalytic System. In order to generate the prochiral olefins in situ for AD reaction, the NAP-Mg-PdOs was first tested in a tandem Heck–AD reaction, which involved stirring iodobenzene, styrene, and Et$_3$N at 70 °C in acetonitrile for 12 h in the presence of 3 mol% of catalyst to give *trans*-stilbene. After completion of the reaction, as judged by TLC, heating was stopped and a mixture of (DHQD)$_2$PHAL (1 mol%) and NMO in *t*-BuOH-H_2O (5:1, 6 mL) was introduced and stirred at room temperature for 12 h, giving the desired diol in 80% yield with 85% ee (Scheme 5.11). The methodology described here uses bulk chemicals such as styrene and acrylates as starting materials to prepare prochiral substrates, stilbenes, and cinnamates in situ and, upon dihydroxylation, give chiral diols in a single pot. This protocol was extended to other substrates (Table 5.21). The NAP-Mg-PdOs catalyst exhibits good performance for a number of cycles with NMO cooxidant. After completion of the reaction, the catalyst was recovered by simple filtration.
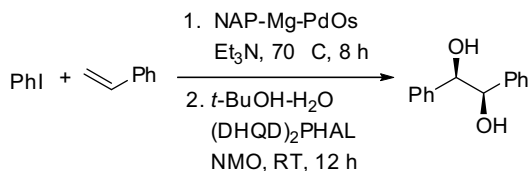
Scheme 5.11. Tandem Heck–asymmetric dihydroxylation catalyzed by NAP-Mg-PdOs bifunctional catalyst.

Osmium–Tungsten Catalytic System. The heterogeneous bifunctional catalyst NAP-Mg-OsW was employed for the simultaneous AD of *trans*-stilbene and N-oxidation of NMM in the presence of H_2O_2 and (DHQD)$_2$PHAL ligand. To a mixture of 3 mol% of NAP-Mg-OsW, 3 mol% of (DHQD)$_2$PHAL ligand, *trans*-stilbene, and NMM in *t*-BuOH-H_2O (5:1, 6 mL), H_2O_2 was slowly added over a period of 12 h to afford the desired diol (Scheme 5.12). Various olefins, including

TABLE 5.21. Synthesis of Chiral Diols Using a Heterogeneous Bifunctional NAP-Mg-PdOs Catalyst[a]

Entry	Aryl Hallide	Olefin	Product	Yield (%)	ee (%)[b]
1				80	85
2				75	67
3				70	82
4				85	73
5				82	78

[a] Nano MgO-PdOs (3 mol%), aryl halide (1 mmol), olefin (1 mmol), and Et$_3$N (1.3 mmol) in CH$_3$CN (2.0 mL) were stirred at 70 °C for 12–16 h. After completion of the Heck coupling, the heating was stopped and NMO (1.3 mmol), (DHQD)$_2$ PHAL (7.8 mg, 0.01 mmol) in *t*-BuOH-H$_2$O (5:1, 6.0 mL) was added under stirring.
[b] ee was determined by HPLC analysis.
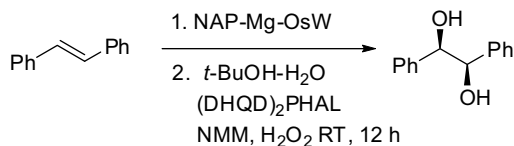
Scheme 5.12. Asymmetric dihydroxylation of *trans*-stilbene using NAP-Mg-OsW.

mono and disubstituted, activated, and simple, were subjected to AD and the results are presented in Table 5.22.

Higher ee's are obtained for the monofunctional osmium catalyst than with the bifunctional catalyst. The slow addition of olefins is an important factor for obtaining high enantioselectivity.

5.9.5. Reaction Pathway

A plausible mechanism for the triple catalytic H_2O_2 oxidation with osmium–tungsten oxides is depicted in Scheme 5.13. The peroxo species generated from tungstate and H_2O_2 rapidly recycles the NMM to NMO, which in turn reoxidizes Os(VI) to Os(VIII).

The bifunctional catalysts NAP-Mg-PdOs and NAP-Mg-OsW were separated subjected to tandem Heck–AD and AD–N-oxidation reactions in a single pot to obtain chiral diols, as shown in Scheme 5.14.

5.9.6. Reusability Studies

The NAP-Mg-PdOs and NAP-Mg-OsW catalysts were recovered quantitatively by simple filtration. The recovered catalysts were reused and showed consistent activity

TABLE 5.22. Synthesis of Chiral Diols Using a Heterogeneous Bifunctional NAP-Mg-OsW Catalyst[a]

Entry	Olefin	Yield (%)	ee (%)
1	Ph / Ph	70	80
2	Ph	75	70
3	COOMe / Ph	80	75

[a] Olefin (1 mmol), NAP-Mg-OsW (3 mol%), (DHQD)$_2$PHAL (1 mol%), NMM (50 mol%), *t*-BuOH-H$_2$O (6.0 mL), H$_2$O$_2$ (slow addition), 12 h.
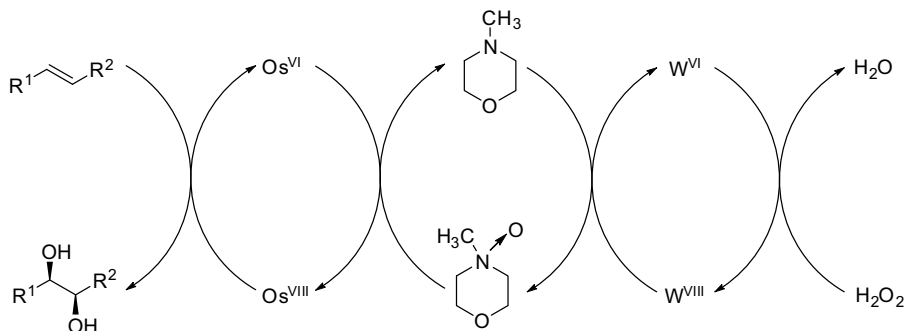
Scheme 5.13. Os and W catalyzed synthesis of diols using H_2O_2 as the terminal oxidant.

and enantioselectivity, even after the fifth cycle (Figure 5.7). When reaction was conducted using the filtrate obtained after the dihydroxylation reaction, no product formation was observed, suggesting no leaching of metal ions takes place. Moreover, the absence of osmium in the filterate as determined by iodometry and SEM-EDAX confirms the osmium leaching does not occur and unambiguously provides evidence for heterogeneity throughout the reaction.

It is interesting to note that NAP-MgO coordinates both the $OsO_4{}^{2-}$ and the Os(VIII) species, possibly through electrostatic interactions. Alternatively, the reduction of Os(VIII) to Os(VI) is too fast to detach neutral OsO_4 from the support. However, when NAP-Mg-OsO$_4$ is treated with the oxidant in the absence of an olefin, osmium is found to leach from the support, suggesting that the NAP-Mg-OsO$_4$ catalyst is not stable in the oxidative environment.
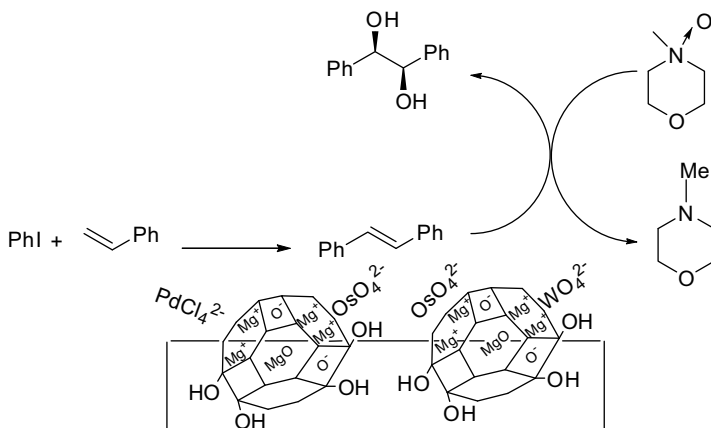
Scheme 5.14. Schematic representation of NAP-Mg-PdOs and NAP-Mg-OsW catalyzed synthesis of chiral diols. (Reproduced with permission from Ref. 125, Wiley-VCH Verlag GmbH.)
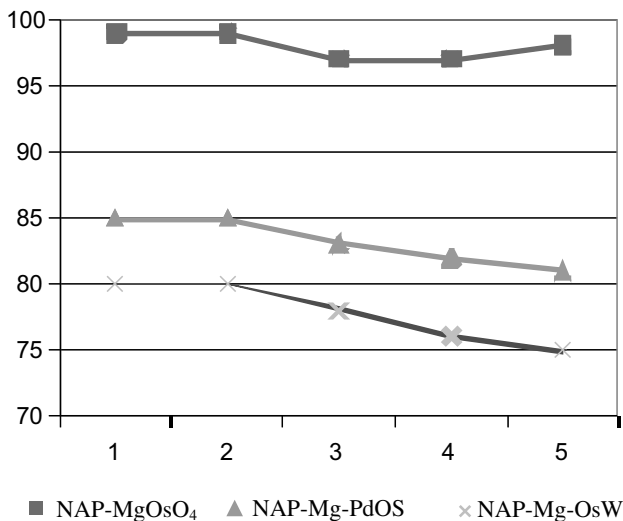
Figure 5.7. Enantioselectivities obtained from multiple uses of NAP-Mg-OsO$_4$, NAP-Mg-PdOs, and NAP-Mg-OsW in the AD of *trans*-stilbene. (Reproduced with permission from Ref. 125, Wiley-VCH Verlag GmbH.)

The bifunctional catalysts comprising Pd, Os, and W for the Heck coupling, N-oxidation, and AD reactions exhibit consistent activity without loss of structural integrity. These results substantiate the retention of coordination geometries of metal complexes in their monomeric form as supported by infrared (IR) spectral analysis and rule out the formation of biheterometallic species during the stabilization process and dihydroxylation reaction. The large positive electric potential of the exchanged catalyst surface induces an enrichment of cooxidant close to the surface. Similarly, the olefin and the aryl halide also build up their concentrations close to the surface as it has a high adsorption coefficient on the support surface. In addition to this, spatial organization and electrical shielding[160] are responsible for the excellent performance of the ion-exchanged catalysts.

5.9.7. Preparation of NAP-MgO Supported Catalysts

(i) NAP-Mg-OsO$_4$:NAP-MgO (1.0 g) was treated with K$_2$OsO$_4$ (0.184 g, 0.5 mmol) dissolved in decarbonated water and stirred for 12 h under a nitrogen atmosphere. The catalyst was filtered off and washed with deionized water and acetone and then dried. The SEM-EDX of the NAP-Mg-OsO$_4$ shows the presence of 8.96% osmium.

(ii) NAP-Mg-PdOs:Na$_2$PdCl$_4$ (0.147 g, 0.5 mmol) and K$_2$OsO$_4$ (0.184 g, 0.5 mmol) were dissolved in decarbonated water. NAP-MgO (1.0 g) was added and the mixture was stirred for 12 h under a nitrogen atmosphere. The catalyst was filtered off and washed with deionized water and acetone, and dried to obtain 1.235 g of NAP-Mg-PdOs (0.375 mmol g^{-1} each of Pd and Os).

(iii) NAP-Mg-OsW:K$_2$OsO$_4$ (0.184 g and 0.5 mmol) and Na$_2$WO$_4$ (0.165 g, 0.5 mmol) were dissolved in decarbonated water and NAP-MgO (1.0 g) was added. The mixture was stirred for 12 h under a nitrogen atmosphere. The catalyst was filtered and washed with deionized water and acetone, and dried to obtain 1.345 g of Mg-OsW (0.370 mmol g^{-1} each of Os and W).

5.10. CONCLUSION

Nanocrystalline magnesium oxide (NAP-MgO) exhibits unusual surface morphologies and possesses more reactive surfaces than the commercial MgO due to the presence of high concentrations of edge/corner sites and other defects, imparting it with unique surface chemistry.

Nanocrystalline magnesium oxide is a recyclable heterogeneous catalyst for the asymmetric Henry (AH) reaction, affording chiral nitro alcohols in excellent yields and impressive enantioselectivities (ee's). Brønsted hydroxyls are the sole contributors for the high ee and increase to the activity of the catalyst in the AH reaction, which is largely driven by Lewis basic O^{2-} and O^{-} sites. It is also proposed that hydrogen bond interactions between the –OH groups of (S)-(−)-binol and the –OH groups of the catalyst are essential for enantioselectivity. Similarly, the asymmetric Michael reaction with nanocrystalline MgO was carried out and ee's were obtained that were comparable to those obtained from homogeneous systems.

NAP-MgO acts as a bifunctional heterogeneous catalyst for the Claisen–Schmidt condensation (CSC) of benzaldehydes with acetophenones to yield chalcones, followed by asymmetric epoxidation (AE) to afford chiral epoxy ketones in moderate to good yields and impressive enantioselectivities (ee's). NAP-MgO, in combination with the chiral auxiliary (1R,2R)-(+)-1,2-diphenyl-1,2-ethylenediamine (DPED), catalyzed the asymmetric Michael addition of malonates to cyclic and acyclic enones.

It is also possible to load metals into the nanocrystalline magnesium oxide, such that very high dispersions are possible, which serve as an unusual catalyst support. The asymmetric epoxidation (AE) of unfunctionalized olefins to epoxides using manganese acetylacetonate stabilized on NAP-MgO has been described.

The single-pot synthesis of chiral diols, mediated by bifunctional solid catalysts consisting of active palladium, osmium, and tungsten species embedded on a matrix of nano-MgO, is described. The desired prochiral olefins and N-methylmorpholine N-oxide, key intermediates for asymmetric dihydroxylation (AD), are generated in situ in the most economical way by Heck coupling and N-oxidation of N-methylmorpholine, respectively. Dispensing with the usual protocol of isolation and purification of intermediates, the bifunctional catalysts trigger the reaction to obtain the chiral diols with minimum waste and conservation of energy. The oxidant, H$_2$O$_2$, employed here in place of NMO is environmentally acceptable, as the only by-product is water. More interestingly, even the water produced from H$_2$O$_2$, during the N-oxidation, is consumed in the AD reaction to mark the highest atom economy in the production of chiral diols.

Some of the impressive features drawn from this research are (i) a simplified procedure, (ii) mild reaction conditions, (iii) good to excellent yields, (iv) easy separation of products, and, most importantly, (v) reusability of the catalyst.
The mechanisms discussed in this chapter will provide some insights into the reaction pathways. More detailed investigations are warranted in order to determine the role of the surface, crystal shape, size, and corner/edge positions of nanocrystalline magnesium oxide. Most importantly, the effective role of the acidic and basic sites of nanocrystalline magnesium oxide in catalysis remains to be determined. The work presented in this chapter hopefully opens a new dimension in the area of heterogeneous asymmetric catalysis and for the synthesis of chiral products.

GLOSSARY

AAS	Atomic absorption spectroscopy
AD	Asymmetric dihydroxylation
AE	Asymmetric epoxidation
AH	Asymmetric Henry
AM	Asymmetric Michael
ASA	Specific surface area
CSC	Claisen–Schmidt condensation
DAC	(1R,2R)-(−)-diaminocyclohexane
(DET)	(+)-Diethyl tartrate
(DHQ)$_2$PHAL	Bis(dihydroquinine)-1,4-phthalazine diether
DMM	Dimethylmalonate
DPED	(1R,2R)-(+)-1,2-diphenyl-1,2-ethylenediamine
DTA	Differential thermal analysis
ED	Electron donating
EW	Electron withdrawing
HPLC	High performance liquid chromatography
IR	Infrared
MS	Mass spectroscopy
NMM	N-methyl morpholine
NMO	N-methyl morpholine N-oxide
SEM–EDX	Scanning electron microscopy-energy dispersive X-ray analysis
TBHP	tert-Butyl hydroperoxide
TGA	Thermogravimetric analysis
XPS	X-ray photoelectron spectroscopy
XRD	Powder X-ray diffraction

ACKNOWLEDGMENTS

for his support in materializing this research program on nanomaterials. We would like to extend our sincere gratitude to all the researchers whose work is described in this chapter for their valuable contributions. We also thank Dr. Steven Priver (School of Applied Sciences, RMIT University, Australia) for helpful discussions and proofreading of the manuscript for this chapter.

REFERENCES

1. Klabunde, K. J.; Mulukutla, R. S. *Nanoscale Materials in Chemistry*. Wiley Interscience, Hoboken, NJ, 2001, Chapters 4 and 7; pp. 85, 108, 223, 225.

2. Hadjipanayis, G. C.; Siegel, R. W.; Eds. *Nanophase Materials: Synthesis, Properties, Applications*. Kluwer; London, 1994.

3. Bell, A. T. *Science*, **2003**, *299*, 1688.

4. Schlogl, R.; Abd Hamid, S. B. *Angew. Chem. Int. Ed.*, **2004**, *43*, 1628.

5. Steigerwald, M. L.; Brus, L. E. *Acc. Chem. Res.*, **1990**, *23*, 183.

6. Henglein, A. *Chem. Rev.*, **1989**, *89*, 1861.

7. Fecht, H. J. In: *Nanomaterials: Synthesis, Properties, and Applications*. Edlestein, A. S.; Cammarata, R. C.; Eds. Institute of Physics, Philadelphia, 1996; p. 105.

8. Martin, T. P.; Naher, U.; Schaber, H.; Zimmerman, U. *J. Chem. Phys.*, **1994**, *100*, 2322.

9. Goldstein, A. N.; Euther, C. M.; Alivasatos, A. P. *Science*, **1992**, *256*, 1425.

10. Klabunde, K. J.; Stark, J. V.; Koper, O.; Mohs, C.; Park, D. G.; Decker, S.; Jiang, Y.; Lagadic, I.; Zhang, D. *J. Phys. Chem.*, **1996**, *100*, 12142.

11. Utamapanya, S.; Klabunde, K. J.; Schlup, J. R. *Chem. Mater.*, **1991**, *3*, 175.

12. Richards, R.; Li, W.; Decker, S.; Davidson, C.; Koper, O.; Zaikovski, V.; Voldin, A.; Reiker, T.; Klabunde, K. J. *J. Am. Chem. Soc.*, **2000**, *122*, 4921.

13. Lucas, E.; Decker, S.; Khaleel, A.; Seitz, A.; Fultz, S.; Ponce, A.; Li, W.; Carnes, C.; Klabunde, K. J. *Chem. Eur. J.*, **2001**, *7*, 2505.

14. Pak, C.; Bell, A. T.; Tilley, T. D. *J. Catal.*, **2002**, *23*, 51.

15. Kakkar, R.; Kapoor, P. N.; Klabunde, K. J. *J. Phys. Chem. B.*, **2006**, *110*, 25941.

16. Choudary, B. M.; Kantam, M. L.; Ranganath, K. V. S.; Mahendar, K.; Sreedhar, B. *J. Am. Chem. Soc.*, **2004**, *126*, 3396.

17. Kantam, M. L.; Mahendar, K.; Sreedhar, B; Kumar, K. V.; Choudary, B. M. *Synth. Commun.*, **2008**, *38*, 3919.

18. Kantam, M. L.; Chakrapani, L.; Choudary, B. M. *Synlett*, **2008** 1946.

19. Kantam, M. L.; Mahendar, K.; Sreedhar, B.; Choudary, B. M. *Tetrahedron*, **2008**, *64*, 3351.

20. Choudary, B. M.; Mahendar, K; Kantam, M. L.; Ranganath, K. V. S.; Athar, T. *Adv. Synth. Catal.*, **2006**, *348*, 1977.

21. Kantam, M. L.; Pal, Ujjwal; Sreedhar, B.; Choudary, B. M. *Adv. Synth. Catal.*, **2007**, *349*, 1671.

22. Kantam, M. L.; Chakrapani, L.; Ramani, T. *Tetrahedron Lett.*, **2007**, *48*, 6121.

23. Choudary, B. M.; Ranganath, K. V. S.; Yadav, J.; Kantam, M. L. *Tetrahedron Lett.*, **2005**, *46*, 1369.

24. Kantam, M. L.; Chakravarti, R; Chintareddy, V. R.; Sreedhar, B.; Bhargava, S. *Adv. Synth. Catal.*, **2008**, *350*, 2544.

25. Kantam, M. L.; Pal, U.; Sreedhar, B.; Bhargava, S.; Iwasawa, Y.; Tada, M.; Choudary, B. M. *Adv. Synth. Catal.*, **2008**, *350*, 1225.

26. Kantam, M. L.; Chakravarti, R.; Pal, U.; Sreedhar, B.; Bhargava, S. *Adv. Synth. Catal.*, **2008**, *350*, 822.

27. Kantam, M. L.; Roy, S.; Roy, M.; Subhas, M. S.; Likhar, P. R.; Sreedhar, B.; Choudary, B. M. *Synlett*, **2006** 2747.

28. Kantam, M. L.; Yadav, J.; Laha, S.; Sreedhar, B.; Bhargava, S. *Adv. Synth. Catal.*, **2008**, *350*, 2575.

29. Kantam, M. L.; Reddy, R. S.; Pal, U.; Sreedhar, B.; Bhargava, S. *Adv. Synth. Catal.*, **2008**, *350*, 2231.

30. Choudary, B. M.; Jyothi, K.; Kantam, M. L.; Sreedhar, B. *Adv. Synth. Catal.*, **2004**, *346*, 45.

31. Montero, J. M.; Gai, P.; Wilson, K.; Lee, A. F. *Green Chem.*, **2009**, *11*, 265.

32. Wang, L.; Yang, J. *Fuel*, **2007**, *86*, 328.

33. Kumar, D.; Reddy, V. B.; Mishra, B. G.; Rana, R. K.; Nadagouda, M. N.; Varma, R. S. *Tetrahedron*, **2007**, *63*, 3093.

34. Duan, G.; Yang, X.; Chen, J.; Huang G.; Lu, L.; Wang, X. *Powder Technol.*, **2007**, *172*, 27.

35. Zhu, K.; Hu, J.; Kubel, C.; Richards, R. *Angew. Chem. Int. Ed.*, **2006**, *45*, 7277.

36. Nagappa, B.; Chandrappa, G. T. *Mesopor. Micropor. Mat.*, **2007**, *106*, 212.

37. Melgunov, M. S.; Fenelonov, V. B.; Melgunova, E. A.; Bedilo, A. F.; Klabunde, K. J. *J. Phys. Chem. B*, **2003**, *107*, 2427.

38. Utiyama, M.; Hattori, H.; Tanabe, K. *J. Catal.*, **1978**, *53*, 237.

39. Pelmenschikov, A.; Morosi, G.; Gamba, A.; Coluccia, S. *J. Phys. Chem.*, **1995**, *99*, 15018.

40. Mishakov, I. V.; Bedilo, A. F.; Richards, R. M.; Chesnokov, V. V.; Volodin, A. M.; Zaikovskii, V. I.; Buyanov, R. A.; Klabunde, K. J. *J. Catal.*, **2002**, *206*, 40.

41. Carnes, C. L.; Klabunde, K. J. *Langmuir*, **2000**, *16*, 3764;

42. Sun, N.; Klabunde, K. J. *J. Am. Chem. Soc.* **1999**, *121*, 5587.

43. Mishakov, I. V.; Heroux, D. S.; Chesnokov, V. V.; Koscheev, S. G.; Mel'gunov, M. S.; Bedilo, A. F.; Buyanov, R. A.; Klabunde, K. J. *J. Catal.*, **2005**, *229*, 344.

44. Jeevanandam, P.; Klabunde, K. J. *Langmuir*, **2002**, *18*, 5309.

45. Chesnokov, V. V.; Bedilo, A. F.; Heroux, D. S.; Mishakov, I. V.; Klabunde, K. J. *J. Catal.*, **2003**, *218*, 438.

46. Gupta, P. P.; Hohn, K. L.; Erickson, L. E.; Klabunde, K. J.; Bedilo, A. F. *AIChE J.*, **2004**, *50*, 3195.

47. Choudary, B. M.; Mulukutla, R. S.; Klabunde, K. J. *J. Am. Chem. Soc.*, **2003**, *125*, 2020 and references cited therein.

48. Rosini, G. In: *Comprehensive Organic Synthesis*, Vol. *2* Trost, B. M.; Ed., Pergamon, Oxford, UK, 1996, 321.

49. Ooi, T.; Doda, K.; Maruoka, K. *J. Am. Chem. Soc.*, **2003**, *125*, 2054.

50. Yamaguchi, M.; Shiraishi, T.; Hirama, M. *J. Org. Chem.*, **1996**, *61*, 3520.

51. Kirby, A. J. *Angew. Chem. Int. Ed. Engl.*, **1996**, *35*, 707.

52. Trost, B. M.; Yeh, V. S. C. *Angew. Chem. Int. Ed.*, **2002**, *41*, 861.

53. Evans, D. A.; Seidel, D.; Rueping, M., Lam, H. W.; Shaw, J. T.; Downey, C. W. *J. Am. Chem. Soc.*, **2003**, *125*, 12692.

54. Notz, W.; Tanaka, F.; Barbas, C. F. III, *Acc. Chem. Res.*, **2004**, *37*, 580.

55. Narasimhan, S.; Velmathi, S.; Balakumar, R.; Radhakrishnan, V. *Tetrahedron Lett.*, **2001**, *42*, 719.

56. Sundararajan, G.; Prabakaran, N. *Org. Lett.*, **2001**, *3*, 389.

57. Arai, T.; Sekiguti, T.; Iizuka, Y.; Takizawa, S.; Sakamoto, S.; Sasai, H. *Tetrahedron: Asymm.*, **2002**, *13*, 2083.

58. Arai, T.; Sasai, H.; Aoe, K.; Okamura, K.; Date, T.; Shibasaki, M. *Angew. Chem. Int. Ed.*, **1996**, *35*, 104.

59. Arai, T.; Yamada, Y. M. A.; Yamamoto, N.; Sasai, H.; Shibasaki, M. *Chem. Eur. J.*, **1996**, *2*, 1368.

60. Kim, Y. S.; Matsunaga, S.; Das, J.; Sekine, A.; Ohshima, T.; Shibasaki, M. *J. Am. Chem. Soc.*, **2000**, *122*, 6506.

61. Matsunaga, S.; Ohshima, T.; Shibasaki, M. *Tetrahedron Lett.*, **2000**, *41*, 8473.

62. Sasai, H.; Suzuki, T.; Arai, S.; Arai, T.; Shibasaki, M. *J. Am. Chem. Soc.*, **1992**, *114*, 4418.

63. Sasai, H.; Tokunaga, T.; Watanabe, S.; Suzuki, T.; Itoh. N.; Shibasaki, M. *J. Org. Chem.*, **1995**, *60*, 7388.

64. Choudary, B. M.; Ranganath, K. V.S., Pal, U.; Kantam, M. L.; Sreedhar, B. *J. Am. Chem. Soc.*, **2005**, *127*, 13167 and references cited therein.

65. Wong, P. C.; Li, Y. S.; Mitchell, K. A. R. *Appl. Sur. Sci.*, **1995**, *84*, 245.

66. Marciniak, G., Delgado, A.; Velly, J.; Leclerc, G.; Decker, N.; Schwartz, J. *J. Med. Chem.*, **1989**, *32*, 1402.

67. Enders, D.; Muller, S.; Demir, A. S. *Tetrahedron Lett.*, **1988**, *29*, 6437.

68. Yoshikawa, N.; Yamada, Y. M. A.; Das, J.; Sasai, H.; Shibasaki, M. *J. Am. Chem. Soc.*, **1999**, *121*, 4168.

69. Trost, B. M. *Science*, **1991**, *254*, 1471.

70. Trost, B. M. *Angew. Chem. Int. Ed. Engl.*, **1995**, *34*, 259.

71. Palomo, C.; Oiarbide, M.; Garcia, J. *Chem. Soc. Rev.*, **2004**, *33*, 65.

72. Machajewski, T. D.; Wong, C.-H. *Angew. Chem. Int. Ed.*, **2000**, *39*, 1352.

73. Yoshikawa, N.; Yamada, Y. M. A.; Das, J.; Sasai, H.; Shibasaki, M. *Angew. Chem. Int. Ed. Engl.*, **1997**, *36*, 1871.

74. Trost, B. M.; Ito, H. *J. Am. Chem. Soc.*, **2000**, *122*, 12003.

75. Trost, B. M.; Ito, H.; Silcoff, E. R. *J. Am. Chem. Soc.*, **2001**, *123*, 3367.

76. Evans, D. A.; Downey, C. W.; Hubbs, J. L. *J. Am. Chem. Soc.*, **2003**, *125*, 8706.

77. Kandasamy, S.; Wolfgang, N.; Tommy, B.; Barbas, C. F. III., *J. Am. Chem. Soc.*, **2001**, *123*, 5260 and references cited therein.

78. List, B. *Acc. Chem. Res.*, **2004**, *37*, 548.

79. Notz, W.; Tanaka, F.; Barbas, C. F. III., *Acc. Chem. Res.*, **2004**, *37*, 580.

80. Hartikka, A.; Arvidsson, P. I. *Tetrahedron: Asymm.*, **2004**, *15*, 1831.

81. Torii, H.; Nakadai, M.; Ishihara, K.; Saito, S.; Yamamoto, H. *Angew. Chem. Int. Ed.*, **2004**, *43*, 1983.

82. Andreae, M. R. M.; Davis, A. P. *Tetrahedron Asymm.*, **2005**, *16*, 2487.

83. Loh, T.-P.; Feng, L.-C.; Yang, H.-Y.; Yang, J.-Y. *Tetrahedron Lett.*, **2002**, *43*, 8741.

84. Chandrasekhar, S.; Narsimhulu, Ch.; Ramakrishna, N.; Sultana, S. *Tetrahedron Lett.*, **2004**, *45*, 4581.

85. Gruttadauria, M.; Riela, S.; Meo, P. L.; D'Anna, F.; Noto, R. *Tetrahedron. Lett.*, **2004**, *45*, 6113.

86. Choudary, B. M.; Chakrapani, L.; Ramani, T.; Vijay Kumar, K.; Kantam, M. L. *Tetrahedron*, **2006**, *62*, 9571.

87. Kawara, A.; Taguchi, T. *Tetrahedron Lett.*, **1994**, *35*, 8805.

88. Kim, D. Y.; Huh, S. C.; Kim, S. M. *Tetrahedron Lett.*, **2001**, *42*, 6299.

89. Ooi, T.; Ohara, D.; Fukumoto, K.; Muruoka, K. *Org. Lett.*, **2005**, *7*, 3195.

90. Kantam, M. L.; Ranganath, K. V. S.; Mahendar, K.; Chakrapani, L.; Choudary, B. M. *Tetrahedron Lett.*, **2007**, *48*, 7646.

91. Ballini, R.; Bosica, G.; Fiorini, D; Palmieri, A; Petrini, M. *Chem. Rev.*, **2005**, *105*, 933.

92. Johnson, R. A.; Sharpless, K. B. In: *Catalytic Asymmetric Synthesis*. Ojima, I.; Ed. VCH, New York, 1993.

93. Pu, L. *Tetrahedron: Asymm.*, **1998**, *9*, 1457 and, references cited therein.

94. Bougauchi, M.; Watanabe, S.; Arai, T.; Sasaki, H.; Shibasaki, M. *J. Am. Chem. Soc.*, **1997**, *119*, 2329.

95. Chen, R.; Qian, C.; Devries, J. G. *Tetrahedron Lett.*, **2001**, *57*, 9837.

96. Elston, C. L.; Jackson, R. F. W.; MacDonald, S. J. F.; Murray, P. J. *Angew. Chem. Int. Ed.*, **1997**, *36*, 410.

97. Jacques, O.; Richards S. J.; Jackson R. F. W. *Chem. Commun.*, **2001**, 2712.

98. Enders, D.; Zhu, J.; Raabe, G. *Angew. Chem. Int. Ed.*, **1996**, *35*, 1725.

99. Itsuno, S.; Sakakura, M.; Ito, K. *J. Org. Chem.*, **1990**, *55*, 6047.

100. Lasterra-Sanchez, M. E.; Felfer, U.; Mayon, P.; Roberts, S. M.; Thornton, S. R.; Todd, C. J. *J. Chem. Soc. Perkin Trans.*, **1996**, *1*, 343.

101. Climent, M. J.; Corma, A.; Iborra, S.; Primo, J. *J. Catal.*, **1995**, *151*, 60 and references cited therein.

102. Kloetstra, K. R.; van Bekkum, H. *Chem. Commun.*, **1995**, 1005.

103. Guida, A.; Lhouty, M. H.; Tichit, D.; Figueras, F.; Geneste, P. *Appl. Catal. A: Gen.*, **1997**, *164*, 251.

104. Sebti, S.; Saber, A.; Rhihil, A.; Nazih, R.; Tahir, R. *Appl. Catal. A: Gen.*, **2001**, *206*, 217.

105. Corneille, J. S.; He, J-W.; Goodman, D.W. *Surf. Sci.*, **1994**, *306*, 269.

106. Yamaguchi, K.; Mori, K.; Mizugaki, T.; Ebitani, K.; Kaneda, K. *J. Org. Chem.*, **2000**, *65*, 6897.

107. Katsuki, T. In: *Catalytic Asymmetric Synthesis* 2nd ed. Oijima, I.; Ed. VCH, New York, 2000, p. 287.

108. Jacobsen, E. N.; Wu. M. H. In: *Comprehensive Asymmetric Catalysis*, Vol. II. Jacobsen, E. N.; Pfaltz, A.; Yamamoto, H.; Eds. Springer, Berlin, 1999, p. 649.

109. Srinivasan, K.; Michaud, P.; Kochi, J. K. *J. Am. Chem. Soc.*, **1986**, *108*, 2309.

110. Zhang, W.; Loebach, J. L.; Wilson, S. R.; Jacobsen E. N. *J. Am. Chem. Soc.*, **1990**, *112*, 2801.

111. Larrow, J. F.; Jacobsen, E. N. *Top. Organomet. Chem.*, **2004**, *6*, 123.

112. Katsuki, T. *Coord. Chem. Rev.*, **1995**, *140*, 189.

113. Choudary, B. M.; Chowdari, N. S.; Kantam, M. L.; Santhi, P. L. *Catal. Lett.*, **2001**, *76*, 213.

114. Pini, D.; Mandoli, A.; Orlandi, S.; Salvadori, P. *Tetrahedron: Asymm.*, **1999**, *10*, 3883.

115. Park, D. W.; Choi, S. J.; Lee, C. Y.; Kim, G. J. *Catal. Lett.*, **2002**, *78*, 145.

116. Xiang, S.; Zhang, Y.; Xin, Q.; Li, C. *Chem. Commun.*, **2002**, 2696.

117. Zhang, X.; Li, C. *Chem. Commun.*, **2005**, 1209.

118. Smith, K.; Liu, C. H. *Chem. Commun.*, **2002**, 886.

119. Clapham, B.; Reger, T. S.; Janda, K. D. *Tetrahedron*, **2001**, *57*, 4637.

120. Bhattacharjee, S.; Anderson, J. A. *Chem. Commun.*, **2004**, 554.

121. Kureshy, R. I.; Khan, N. H.; Abdi, S. H. R.; Sing, A. S.; Jasra, R. V. *J. Catal.*, **2004**, *221*, 234.

122. Ogunwumi, S. B.; Bein, T. *Chem. Commun.*, **1997**, 1285.

123. Choudary, B. M.; Pal, U.; Kantam, M. L.; Ranganath, K. V. S.; Sreedhar, B. *Adv. Synth. Catal.*, **2006**, *348*, 1038.

124. Bulman Page, P. C.; Buckley, B. R.; Heaney, H.; Blacker, A. J. *Org. Lett.*, **2005**, *7*, 375.

125. Choudary, B. M.; Jyothi, K.; Kantam, M. L.; Roy, M.; Sreedhar, B. *Adv. Synth. Catal.*, **2004**, *346*, 1471.

126. Adam, W.; Mock-Knoblauch, C.; Saha-Moller, C. R.; Herderich, M. *J. Am. Chem. Soc.*, **2000**, *122*, 9685.

127. Groves, J. T.; Stern, M. K. *J. Am. Chem. Soc.*, **1988**, *110*, 8628.

128. Domling, A.; Ugi, I. *Angew. Chem. Int. Ed. Engl.*, **1993**, *32*, 563.

129. Kingsbury, J. S.; Garber, S. B.; Giftos, J. M.; Gray, B. L.; Okamoto, M. M.; Farrer, R. A.; Fourkas, J. T.; Hoveyda, A. H. *Angew. Chem. Int. Ed.*, **2001**, *40*, 4251.

130. Jeon, N.; Seo, S. D.; Shin, J. Y. *J. Am. Chem. Soc.*, **2000**, *122*, 10220.

131. Kopecky, D. J.; Rychnovsky, S. D. *J. Am. Chem. Soc.*, **2001**, *123*, 8420.

132. Guindon, Y.; Houde, K.; Prevost, M.; Cardinal-David, B.; Landry, S. K.; Daoust, B.; Bencheqroun, M.; Guerin, B. *J. Am. Chem. Soc.*, **2001**, *123*, 8496.

133. Yamasaki, S.; Kanai, M.; Shibasaki, M. *J. Am. Chem. Soc.*, **2001**, *123*, 1256.

134. Annunziata, R.; Benaglia, M.; Cinquini, M.; Cozzi, F. *Eur. J. Org. Chem.*, **2001**, 1045.

135. Yu, H.-B.; Hu, Q.-S.; Pu, L. *J. Am. Chem. Soc.*, **2000**, *122*, 6500.

136. Kolbe, H. C.; VanNieuwenhze, M. S.; Sharpless, K. B. *Chem. Rev.*, **1994**, *94*, 2483.

137. Kobayashi, S.; Endo, M.; Nagayama, S. *J. Am. Chem. Soc.*, **1999**, *121*, 11229.

138. Kobayashi, S.; Ishida, T.; Akiyama, R. *Org. Lett.*, **2001**, *3*, 2649.

139. Ishida, T.; Akiyama, R.; Kobayashi, *S. Adv. Synth. Catal.*, **2003**, *345*, 576.

140. Choudary, B. M.; Chowdari, N. S.; Jyothi, K.; Kantam, M. L. *J. Am. Chem. Soc.*, **2002**, *124*, 5341.

141. Choudary, B. M.; Chowdari, N. S.; Kantam, M. L.; Raghavan, K. V. *J. Am. Chem. Soc.*, **2001**, *123*, 9220.

142. Choudary, B. M.; Chowdari, N. S.; Madhi, S.; Kantam, M. L. *Angew. Chem. Int. Ed.*, **2001**, *40*, 4620.

143. Severeyns, A.; de Vos, D. E.; Fiermans, L.; Verpoort, F.; Grobet, P. J.; Jacobs, P. A. *Angew. Chem. Int. Ed.*, **2001**, *40*, 586.

144. Bergstad, K.; Jonsson, S. Y.; Bäckvall, J.-E. *J. Am. Chem. Soc.*, **1999**, *121*, 10424.

145. Jonsson, S. Y.; Farnegardh, K.; Bäckvall, J.-E. *J. Am. Chem. Soc.*, **2001**, *123*, 1365.

146. Jonsson, S. Y.; Adolfsson, H.; Bäckvall, J.-E. *Org. Lett.*, **2001**, *3*, 3463.

147. Narske, R. M.; Klabunde, K. J.; Fultz, S. *Langmuir*, **2002**, *18*, 4819.

148. Kumar, G.; Blackburn, J. R.; Albridge, R. G.; Moddeman W. E.; Jones, M. M. *Inorg. Chem.*, **1972**, *11*, 296.

149. Kili, K.; Hilaire, L.; Normand, F. L. *Phys. Chem. Chem. Phys.*, **1999**, *1*, 1623.

150. Verduraz, F. B.; Omar, A.; Escard, J.; Pontvianne, B. *J. Catal.*, **1978**, *53*, 126.

151. White, D. L.; Andrews, S. B.; Faller, J. W.; Barrnett R. J. *Biochim. Biophys. Acta*, **1976**, *436*, 577.

152. Burroughs, P.; Evans, S.; Hamnett, A.; Orchard, A. F.; Richardson, N. V. *J. Chem. Soc. Faraday Trans.*, **1974**, *12*, 1895.

153. Moulder, J. F.; Stickle, W. F.; Sobol, P. E.; Bomden, K. D. *Handbook of X-ray Photoelectron Spectroscopy*. Perkin-Elmer Corp., Waltham, MA, 1992.

154. Sohn, J. R.; Park M. Y. *Langmuir*, **1998**, *14*, 6140.

155. Dong, L.; Hu, Y.; Xu, F.; Lu, D.; Xu, B.; Hu, Z.; Chen, Y. *J. Phys. Chem. B*, **2000**, *104*, 78.

156. Peng, Y.; Meng, Z.; Zhong, C.; Lu, J.; Yang, Z.; Qian, Y. *Chem. Lett.*, **2001**, *1*, 64.

157. Michaelson, R. C.; Austin, R. G.; White, D. A. US Patent 4,413,151 1983.

158. Sharpless, K. B. Amberg; W. K. US Patent 5,227,543 1993.

159. Cainelli, G.; Contento, M.; Manescalchi, F.; Plessi, L. *Synthesis*, **1989**, 45.

160. Vote, D.; Vote, J. G. *Biochemistry*, 2nd ed. Wiley, Hoboken, NJ, 1995, Chapter 14.

Boron-Based Hybrid Nanostructures: Novel Applications of Modern Materials

ZHU YINGHUAI and KOH CHENG YAN

Institute of Chemical and Engineering Sciences, Jurong Island, Singapore

JOHN A. MAGUIRE

Department of Chemistry, Southern Methodist University, Dallas, Texas, USA

NARAYAN S. HOSMANE

Department of Chemistry and Biochemistry, Northern Illinois University, DeKalb, Illinois, USA

This chapter reviews some of the recent developments in the use of nanoparticles as adjuncts to boron containing compounds in boron neutron capture therapy (BNCT) or, in the cases of boron nanotubes (BNTs) and boron nitride nanotubes (BNNTs), the boron agent itself. BNCT is a bimodal therapy in which boron-10 is preferentially localized in a cancer cell and then irradiated with low energy (thermal) neutrons. The ^{10}B absorbs the neutron giving an excited ^{11}B, which immediately undergoes a fission reaction yielding a high energy alpha (α) particle and recoil ^{7}Li particle, plus a low energy gamma (γ) ray. The therapeutic advantage of this method is that the two charged particles deposit their energy through a distance of $\sim$9 µm, which is of the order of a cell dimension. Therefore, damage will be confined to the cell in which fission reaction occurs, sparing neighboring cells that are free of boron. The chemical challenge in BNCT is constructing molecules or delivery agents that preferentially target neoplastic cells. Although this requirement is common to all chemotherapy, the required amount of ^{10}B needed for effective BNCT (10–35 µg/g tumor cell) is much higher than that required in other forms of chemotherapy.

A number of macromolecular entities and new delivery methods used in BNCT are discussed. They include liposomes, dendrimers, carbon nanotubes (CNTs), BNTs and BNNTs, and magnetic nanoparticles. References are given to some of the latest applications.

6.1. BACKGROUND

Many people consider neutron capture therapy (NCT) a new and innovative approach to the treatment of cancer that is still in its formative stage. However, the basic idea behind this approach has been around for more than 70 years, almost as long as the idea of the existence of the neutron. The basic approach in NCT was outlined in 1936 by Gordon L. Locher[1] when he formulated his binary concept of treating cancer: "In particular, there exist the possibilities of introducing small quantities of strong neutron absorbers into the regions where it is desired to liberate ionization energy (a simple illustration would be the injection of a soluble, non-toxic compound of boron, lithium, gadolinium, or gold into a superficial cancer, followed by bombardment with slow neutrons." Table 6.1 lists some isotopes with large neutron capture cross sections, measured in barns (b $= 10^{-24}$ cm^2). From this table, it is apparent that the probability of a nucleus absorbing a neutron is based on nuclear structure rather than mass number. Three isotopes from Table 6.1, ^{10}B, ^{155}Gd, and ^{157}Gd, are the ones that are most studied in NCT; ^{10}B will be the subject of this chapter.

Boron-10 has a nuclear capture cross section of 3838 b, which is more than three orders of magnitude higher than those of other nuclei commonly found in living tissue. On absorption of a thermal neutron ($E < 0.4$ eV), an excited ^{11}B is formed that almost immediately ($\sim 10^{-12}$ s) undergoes a fission reaction producing two high-energy heavy ions, ^{4}He^{2+} (α-particle) and ^{7}Li^{3+}, and a low energy γ ray (see Eq. (6.1)).

$$94\% \qquad ^4\text{He}^{2+}(1.47\text{ MeV}) + {}^7\text{Li}^{3+}\,(0.84\text{ MeV}) + \gamma\,(0.48\text{ MeV})$$

$$^{10}\text{B} + \text{n}_{\text{th}} \rightarrow [{}^{11}\text{B}]$$

$$6\% \qquad ^4\text{He}^{2+} + {}^7\text{Li}^{3+} + 2.79\text{ MeV}$$
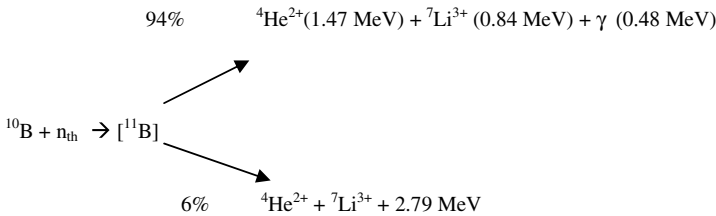
TABLE 6.1. Thermal Neutron Capture Cross Sections and Neutron Capture Reaction Types of Selected Stable and Radioactive Nuclides[a]

Nuclide	Thermal Neutron Capture Cross Section σ_{th}[b] 1 barn $= 10^{-24}$ cm^2	Neutron Capture Reaction	Nuclide	Thermal Neutron Capture Cross Section σ_{th}[b] 1 barn $= 10^{-24}$ cm^2	Neutron Capture Reaction
^{3}He	5333	(n,p)	^{155}Gd	60900	(n,γ)
^{6}Li	941	(n,α)	^{157}Gd	255000	(n,γ)
^{10}B	3838	(n,α)	^{174}Hf	561	(n,γ)
^{113}Cd	20600	(n,γ)	^{199}Hg	2150	(n,γ)
^{135}Xe[b]	2720000	(n,γ)	^{235}U[b]	681	(n,f)
^{147}Sm	40140	(n,γ)	^{241}Pu[b]	1380	(n,f)
^{151}Eu	9200	(n,γ)	^{242}Am[b]	8000	(n,f)

[a] See Refs. 2 and 3.
[b] Radioactive.

The high linear energy transfer (LET) of the emitted alpha and recoiling lithium particles takes place in a very short distance, approximately 4–9 μm in biological tissue, which represents less than a cell diameter. Therefore, if sufficient compounds containing ^{10}B can be preferentially absorbed in a cancer cell, and bombarded with thermal neutrons, cell damage would be confined to that particular cell, sparing neighboring healthy cells. The utility of this elegant protocol depends on certain conditions being satisfied. First, ^{10}B is the isotope that is therapeutically active; this isotope constitutes about 20% of naturally occurring boron. The major isotope, ^{11}B (80%), has very little affinity for neutrons (neutron capture cross section $\sim$5.5 × 10^{-3} b). Therefore, the therapeutic compound must be enriched in ^{10}B. As will be discussed later, there are a number of ways to enrich boron compounds.

Second, a suitable flux of neutrons of the correct energy must be sustained for a reasonable length of time to assure fission events. This will, of course, depend on the concentration of ^{10}B in the tumor cells as well as the location and depth of the tumor. Generally, neutrons can be classified according to their energies as thermal ($0 < E < 0.4$ eV), epithermal $0.4 < E < 10$ keV, and fast neutrons ($E > 10$ keV); it is the thermal neutrons that are therapeutic.[4] It has been estimated that for a concentration of $\sim$$10^9$ boron-10 atoms (10–35 μg/g tumor cell) and a thermal neutron intensity of $\sim$$10^9$ n·cm^{-2}·s^{-1}, the radiation time would be about 30 min, which is thought to be optimal. Under these concentration conditions, about 85% of the radiation dose arises from the ^{10}B capture.[3] However, thermal neutrons do not penetrate tissue to any great extent, it has been estimated that by a depth of 2.5 cm the beam intensity is decreased by 50%.[3] Therefore, unless the tumor is on the surface of the body or has surgically been uncovered, direct radiation with thermal neutrons is ineffective. This was one of the reasons for the failures of the initial BNCT clinical trials. Modern BNCT therapy makes use of higher energy, more penetrating epithermal neutrons as the primary radiation beam. Use of such beams does not require surgical exposure of the tumor. It should be emphasized that no neutron beam is completely uncontaminated. The major contaminates are fast neutrons and gamma rays. Also, even a perfect beam of monochromatic neutrons could lead to radiation damage through the neutron capture of H and N in biological tissue. While these atoms have small neutron capture cross sections (H = 0.333 b; N = 1.83 b), their high tissue content, 10 wt% and 3 wt% for H and N, respectively, make them large contributors to overall radiation dose. In general, radiation doses delivered to both normal and tumor tissues are due to energy contributions from three types of ionizing radiation: (i) low LET γ rays that arise from the capture of thermal neutrons from normal tissue, H(n, γ)^{2}H, and the boron fission reaction itself; (ii) high LET protons from the ^{14}N(n,p)^{14}C reaction; and (iii) high LET particles from the therapeutic ^{10}B(n,α)^{7}Li reaction. In addition, no neutron beam is monochromatic; it is contaminated with fast neutrons and γ rays from the nuclear reactor.[5] At present, nuclear reactors are the only source of nuclear beams of sufficient intensity for NCT use, and there are a limited number of nuclear reactors that produce high quality neutron beams that can be used in medical treatment.[4] Therefore, even under the best of circumstances, NCT will not be a clinically accessible therapy unless accelerator based neutron sources (ABNSs), suitable for

installation in hospitals, are developed. Accelerator based neutron sources are based on neutrons produced when a charged particle, usually a proton, strikes a suitable target.[6, 7] The most studied is the ^{7}Li(p,n)^{7}Be reaction. Although the use of Li targets present practical problems, and a number of other reactions are possible sources for neutrons, the ^{7}Li(p,n)^{7}Be reaction gives high neutron production a low energy spectrum.[7] Until BNCT is proved effective, financial constraints will limit the development of such alternate neutron sources.

All of the above mentioned problems are minor compared to those involved in the development of suitable chemical carriers. Any NCT protocol is based on the preferential accumulation of a therapeutic agent in the tumor cell, while avoiding healthy tissue. For a substance to be an effective boron carrier agent it: (i) must be nontoxic or at least of low toxicity; (ii) should preferably accumulate in tumor cells; and (iii) must persist in tumor cells and rapidly clear the blood and other organs. Calculations show that for effective use, 10^9 ^{10}B atoms/tumor cell, or between 10 and 30 μg ^{10}B/g tumor has to be accumulated and exhibit a T/N ratio of 4–10. The actual amount of boron-10 necessary for effective BNCT depends on where the isotope concentrates in the cell, being less for a compound concentrating in the nucleus than for one concentrating at the cell wall.[9] Therefore, the major approach has been to attach a high boron content molecule to a biomolecule that the tumor cells preferentially absorb. This approach has been used successfully in drug design therapy. However, it is well to point out that the relative effective concentrations for successful BNCT treatment are several orders of magnitude higher than that required in standard drug therapy. This puts an extra heavy burden on boron carriers.

In designing a drug therapy protocol, information must be obtained on the time course of drugs in the blood, normal tissue, and tumor. This is especially critical in BNCT. Since the presence of boron, whether in normal or cancerous cells, will produce a cytotoxic event upon irradiation with neutrons, methods must be developed to minimize toxicity to normal cells. One of the greatest challenges in BNCT is to be able to adequately determine the absorbed dose to a patient and to predict its relative biological effectiveness (RBE). Computational dosimetry is a powerful technique to help in designing effective therapy protocols. A Monte Carlo-based treatment planning system (INEEL), taking into account the complex brain geometries, has been developed for BNCT studies.[25–29] More recently, the successor of the INEEL program, SERA (Simulation Environment for Radiotherapy Applications) has been introduced. This program consists of a succession of interactively cross-launched software modules or command lines designed for the iterative development of BNCT and GdNCT patient treatment plans.[30]

BNCT has been extensively studied as a possible therapy in the treatment of brain tumors, specifically glioblastoma multiforme (GBM). This is one of the most malignant forms of cancer that constitutes about 60,000 cases per year. It is invariably fatal with a mean survival time of 18 months from diagnosis. This cancer infiltrates the brain so aggressively that surgery is rarely able to remove all the cancerous tissue; it must be considered a whole brain disease.[5–10] On the positive side, these types of tumors have little history of metastasizing to other organ sites in the body. Thus, if

tumor eradication could be achieved in the brain, a cure could be attained. Protocols for the treatment of brain tumors are further complicated by the necessity of the drug to pass through the blood–brain barrier (BBB).

The earliest clinical trails, conducted in the mid-1950 s, utilized simple boron compounds such as borax, boric acid, and sodium pentaborate.[11] While these substances were found to be well tolerated by patients, the trails were not successful.[11] The main reasons were that the thermal neutron beam was too weak and the compounds did not preferentially locate in the tumor and that the boron agents were not tumor specific. Since that time, a variety of different carrier molecules have been investigated as possible boron delivery agents to tumor cells.[3] These include carbohydrates,[12] polyamines,[13] nucleosides,[14] antibodies,[15] porphyrins,[16] liposomes,[17] and amino acids.[18] Despite this research activity, there are at present only two boron compounds in clinical trials—sodium borocaptate, $Na_2B_{12}H_{11}SH$ (BSH), and 4-borono-l-phenylalanine (BPA) (see Figure 6.1). The results on these compounds have not been particularly promising, owing to their low tumor-to-blood and tumor-to-brain tissue ^{10}B ratios.[19–22] One of the obstacles to these investigations is the difficulty in moving the different compounds through the different phases toward clinical trails. First, the compound has to be shown not to be cytotoxic; then, it has to be shown to preferentially localize in tumor cells in small animal (rat) studies. If such studies are encouraging, radiation studies might be undertaken; if these are positive, then large animal studies might be initiated. In view of the fact that there are only a few nuclear reactors dedicated to medical uses, such a sequence is quite arduous. Therefore, it is not surprising that most compounds have not progressed beyond looking at the biological distribution of the boron compounds in small animals. In general, there is no shortage of possible candidates for BNCT studies. This chapter will concentrate of studies involving the use of boron carriers based on nanomatrials.[23]
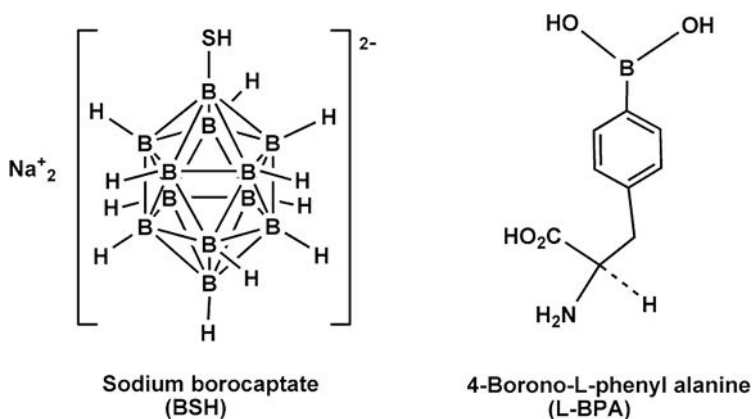
Figure 6.1. Structures of BSH and BPA.

6.2. LIPOSOMES

Liposomes are small, spherical vesicles composed of membranes of phospholipids. The phospholipids are molecules having a hydrophilic head and a hydrophobic tail. Cell membranes are composed of such molecules arranged in two layers. When these membranes are disrupted, they can reassemble as extremely small spheres, usually as bilayers (liposomes). Figure 6.2 shows a cutaway drawing of a bilayer liposome. The membrane thickness is on the order of 4 nm and the vesicle can be composed of one bilayer (unilamellar) or more bilayers (multilamellar). The multilamellar liposomes can be in the range of 500–5000 nm, while the unilamellar liposomes are much smaller. The interior aqueous volume can contain water-soluble drugs for delivery once the liposome enters a cell. In addition, hydrophobic compounds could be stored in the lipid layer.[9, 17, 24] Liposomes have the potential of delivering large amounts of boron to cancer cells.[31] In addition, modification of the liposome surface by PEGylation or attachment of antibodies or receptor groups can enhance the delivery of therapeutic molecules.

Another, similar, vesicle is the low-density lipoprotein (LDL), which is a major carrier of cholesterol. Cancer cells avidly absorb LDL as a source of cholesterol for their rapidly dividing cells. The LDL can be isolated and their cholesterol core replaced by hydrophobic carboranes.[17b, 33] In vitro studies of hamster V-79 cancer cells have shown that such boronated LDLs resulted in intercellular concentrations of ~240 µg ^{10}B/cell, which is about 10× the amount needed for effective BNCT.[33] The use of drug laden vesicles, such as liposomes or LDLs, also take advantage of a general phenomenon of the enhanced permeability and retention (EPR) effect.[32]
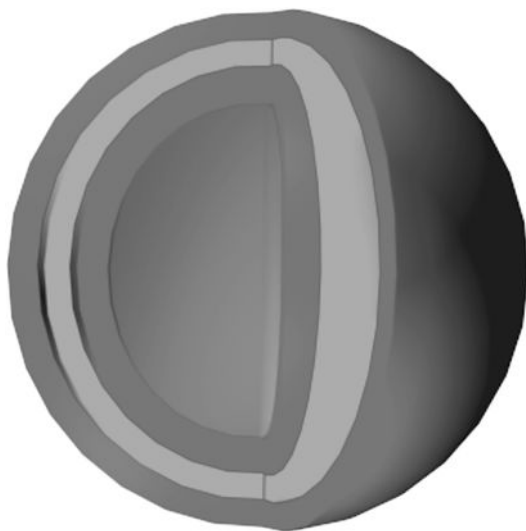
Figure 6.2. Cut-away drawing of a bilayer liposome. Dark shaded area = hydrophilic layer; light shaded area = hydrophobic layer.

Tumor cells have an increased vascular permeability and a decrease in their lymphatic drainage system, which leads to the passive accumulation of macromolecular drugs in these neoplastic cells. The macromolecules may also contain groups that are preferentially taken up by cancer cells. For example, the presence of folate ions on the surface of boron containing liposomes greatly enhances the boron uptake in human KB squamous epithelial cancer cells, which have overexpressed foliate acceptors.[24a] Other examples are the reconstituted LDLs, which still retain their ability to bond to LDL specific sites on the tumor cells. These liposomes and modified LDLs have the ability to deliver massive amounts of ^{10}B to cancer cells and have been termed "supertankers" for boron delivery.[9]

6.3. DENDRIMERS

Dendrimers are highly branched globular macromolecules composed of a central core off of which are repeating branches. These molecules can be constructed systematically with welldefined branching, resulting in defined geometries and molar masses. Different end groups can be attached to the dendrimers, the number of which is controlled by the number of layers (generations) of branching units. Figure 6.3 shows an example of a third-generation dendrimer with amine end groups. These macromolecules have the advantage over polymeric boron carriers, such as polylysine, in that the dendrimers present an ordered array of functional groups. It was found that boronated polylysine, attached to monoclonal antibodies (MoAbs), showed high immunoreactivity in vitro, but lost their in vivo tumor specificity.[34] It was speculated that the large molecular weight distribution of the boronated macromolecules might influence their tumor absorbing properties. In order to obtain a more uniform boron carrier platform, second- and fourth-generation dendrimers, having 12 and 48 terminal amines, respectively, were boronated with $[Na(CH_3)_3NB_{10}H_8NCO]$ and used in place of the polylysines.[35] The boronated starburst dendrimers (BSDs) were then attached to the monoclonal antibody, MoAbIB16-6, which is directed towards murine B-16 melanoma. Biodistribution studies showed that the BSD had a tendency to concentrate in the liver and spleen.[35] Boronated starburst dendrimers were also linked to epidermal growth factors (EGFs) and used as boron delivery agents against epidermal growth factor receptor (EGFR)-positive gliomas $(F98)_{EGFR}$ and wild-type F98 cells $(F98_{WT})$, both with and without additional BPA.[36] The EGFR gene is amplified in human gliobastomas and other primary brain tumors. The results showed that significant amounts of EGF-BSD were retained in the $F98_{EGFR}$ cells, while negligible amounts were found in the brain, blood, liver, kidneys, and spleen. In BNCT experiments on rats implanted with $F98_{EGFR}$ and $F98_{WT}$ cancer cells, it was found that the mean survival time (MST) after irradiation was 45 ± 5 days for $F98_{EGFR}$ bearing animals and 33 ± 2 days for animals bearing $F98_{WT}$ cells. The use of BPA + EFG-BSD did not statistically change the MST.[36] In other studies, the chimeric MoAB cetuximab (IMC-C225), which is directed against (EGFR)-positive gliomas, were used to treat $F98_{EGFR}$ and a mutant form of F98 $(F98_{EGFR-VIII})$ tumors.[37] A heavily boronated generation 5 PAMAM dendrimer $(G-5B_{1100})$ was
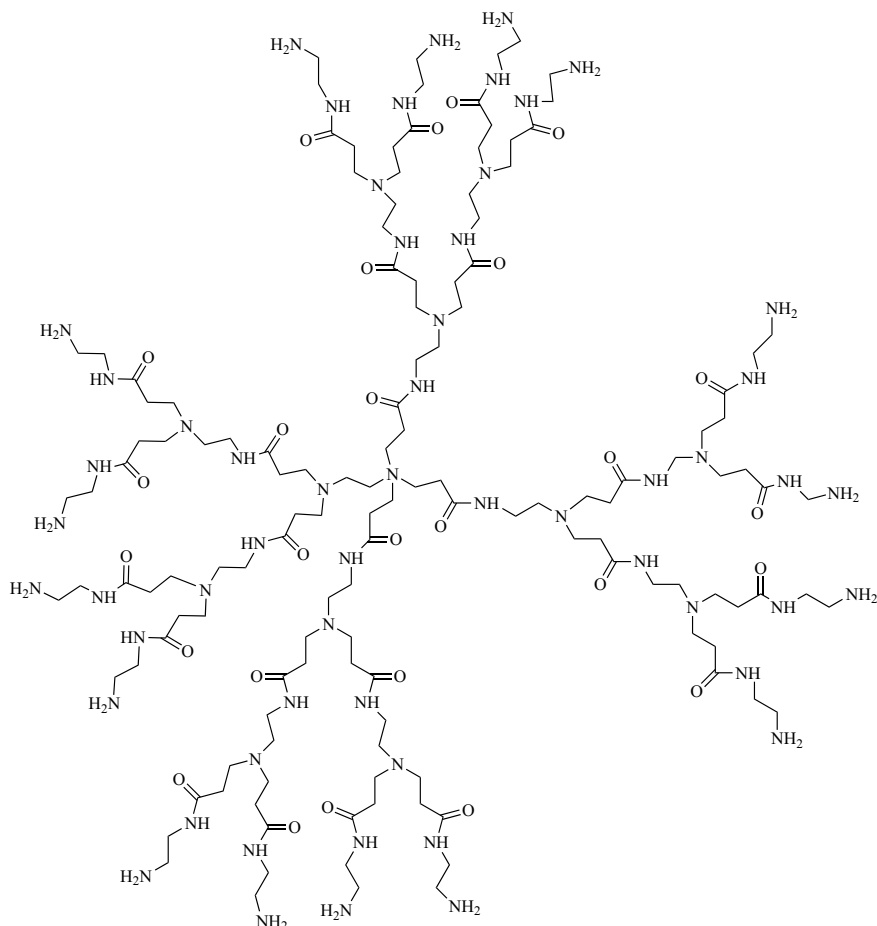
Figure 6.3. Example of a PAMAM dendrimer with amine end groups.

linked to the IMC-C255 to give the bioconjugate, C225-G-5B$_{1100}$, which was tested on rats with F98$_{EGFR}$ and F98$_{WT}$ intracerebral glioma implants. Results showed that 24 h after direct intratumoral injection, $92.3 \pm 23.3\,\mu g\,B/g$ tumor was localized in F98$_{EGFR}$ tumor, $36.5 \pm 18.8\,\mu g\,B/g$ tumor in F98$_{WT}$, and $13.4 \pm 6.1\,\mu g\,B/g$ in normal brain.[37] Based on these encouraging results, BNCT will be conducted on F98$_{EGFR}$ glioma bearing rats.

Fifth-generation polyamidoamine (PAMAM) dendrimers with 128 reactive amino groups were reacted with 105–110 decaborate cages to produce macromolecules having 1050–1100 boron atoms per dendrimer. The boronated dendrimers were attached to vascular endothelial growth factor (VEGF) to give a bioconjugate that was directed against tumor cells having overexpressed VEGF receptors (VEGFR-2). The molecules were tagged with a near IR Cy5 dye, to give a VEGF-BD-Cy5

biomolecule that could be observed, in vitro and in vivo, by near-IR imaging.[38] This approach of attacking the endothelial cells of the tumor vasculature instead of the tumor itself is designed to counter the problems associated with the short circulation times of many antitumor drugs. The growth of primary tumors beyond a few millimeters depends on the development of new blood vessels by angiogenesis, which is regulated by VEGF. Therefore, tumor cells have overexpressed VEGFRs that are targeted by the VEGF-BD-Cy5 biomolecule. Near-IR fluorescence imaging in 4T1 mouse carcinoma showed selective accumulation of VEGF-BD-Cy5, but not BD-Cy5, at the periphery, where angiogenesis is most active.[38]

One of the limitations of using high generations of dendrimers such as PAMAM is that the high amine surface functionality imparts cytotoxicity and liver accumulation. Therefore, water-soluble dendrimers other than the polyamidoamines have been investigated. Adronov and co-workers have reported the synthesis of aliphatic polyester dendrimers containing 4, 8, or 16 *p*-carborane cages in the interior of the dendrimer (see Figure 6.4).[39a] In general, the higher number of hydroxyl groups per carborane, the more water soluble is the dendrimer. For example, 16-[G-5]-OH$_{128}$ (Figure 6.4) was soluble (1 mg/mL) at room temperature but was found to precipitate at a temperature of 63 °C, while 8-[G-5]-OH$_{128}$ was soluble at all temperatures. An alternate approach, described by Zharov and co-workers, was to attach *o*-carboranes to the outside of dendrons based on a 2,2-bis(hydroxymethyl)propanoic acid scaffold. A second-generation dendron containing 40 boron atoms was the highest generation synthetically available, because of severe steric crowding. The attachment of a 10-carbon linker containing a carboxyl group to the carboxyl group at the focal point of the dendron could allow attachment of the boronated dendron to targeting groups for BNCT.[39b]

8-[G-5]-OH$_{128}$ 16-[G-5]-OH$_{128}$
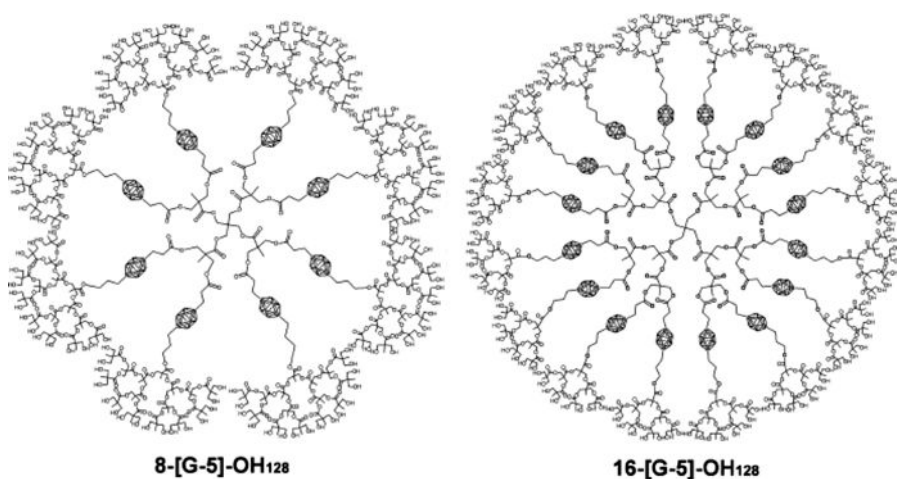
Figure 6.4. Examples of polyester dendrimers having 8 and 16 carborane cages.[39a]

6.4. CARBON NANOTUBES

Carbon nanotubes (CNTs) are forms of carbon in which a sheet of sp^2 hybridized carbon atom are arranged in a cylinder. They can be composed of a single sheet of atoms, single-wall carbon nanotubes (SWCNTs), or several sheets, the so-called multiwall carbon nanotubes (MWCNTs). Carbon nanotubes were first described by Iijma[40] in 1991. Since that time a number of potential medicinal applications of CNTs, mainly as inert carriers for therapeutic compounds, have been proposed.[41] They have been shown to be able to enter various cells without showing cytotoxic behavior at low concentrations. Peptide-functionalized SWCNTs were able to penetrate cell membranes and concentrate in cell nuclei of 3T6 cells, without causing their death or inflicting other damages, at low concentrations.[42] Similar results were obtained in HL60 cells, where it was found that functionalized SWCNTs can help transport large attached groups into cells without themselves exhibiting cell toxicity.[43] The nanotubes, functionalized by boiling in HNO_3 to give –COOH attachment, were found to preferentially enter phagocytic cells and could be detected by their near-IR fluorescence.[44] It was also observed that a number of proteins absorb spontaneously on the side walls of acid oxidized SWCNTs, and the proteins were found to be readily transported inside various mammalian cells.[45] The nanotube–protein conjugates can enter the cytoplasm and perform biological functions.[45] The wide use of SWCNTs as drug delivery agents prompted us to investigate them as possible boron delivery agents in BNCT.[46] We have successfully attached *nido*-carborane units to the side walls of single-wall carbon nanotubes to produce high boron content, water-soluble SWCNTs (Figure 6.5). These were then used to treat mice bearing the EMT6 tumor cells, a mammary carcinoma. A favorable tumor-to-blood ratio of 3.12 and a boron concentration of 21.5 µg/g tumor were obtained after 48 h of administration. In addition, it was observed that retention in tumor tissue was higher than in the blood and other tissues. Although the initial results were good enough for a possibly successful BNCT trial, current research is involved in modifications to improve both the selectivity and boron concentration.

There is general concern regarding the cytotoxicity of carbon nanotubes (CNTs). Because of their insolubility, CNTs are inherently toxic. It has been shown that both SWCNTs and MWCNTs are cytotoxic to certain cell lines at elevated concentrations.[47]

6.5. BORON AND BORON NITRIDE NANOTUBES

Another suggested nanomaterial for use as a BNCT agent is the boron nanotube (BNT).[48] Boron nanotubes are one of a series of boron nanostructures, such as nanoribbons[49] and nanowires,[50] that have recently been synthesized.

The first successful synthesis of a single-wall boron nanotube was achieved by the reaction of BCl_3 and H_2 over an Mg-MCM-41 catalyst.[48] The nanotubes had diameters of ∼3 nm and lengths of ∼16 nm. Unfortunately, the materials were quite sensitive to high-energy electron beams and hence detailed structural characteristics

(a)

(b)
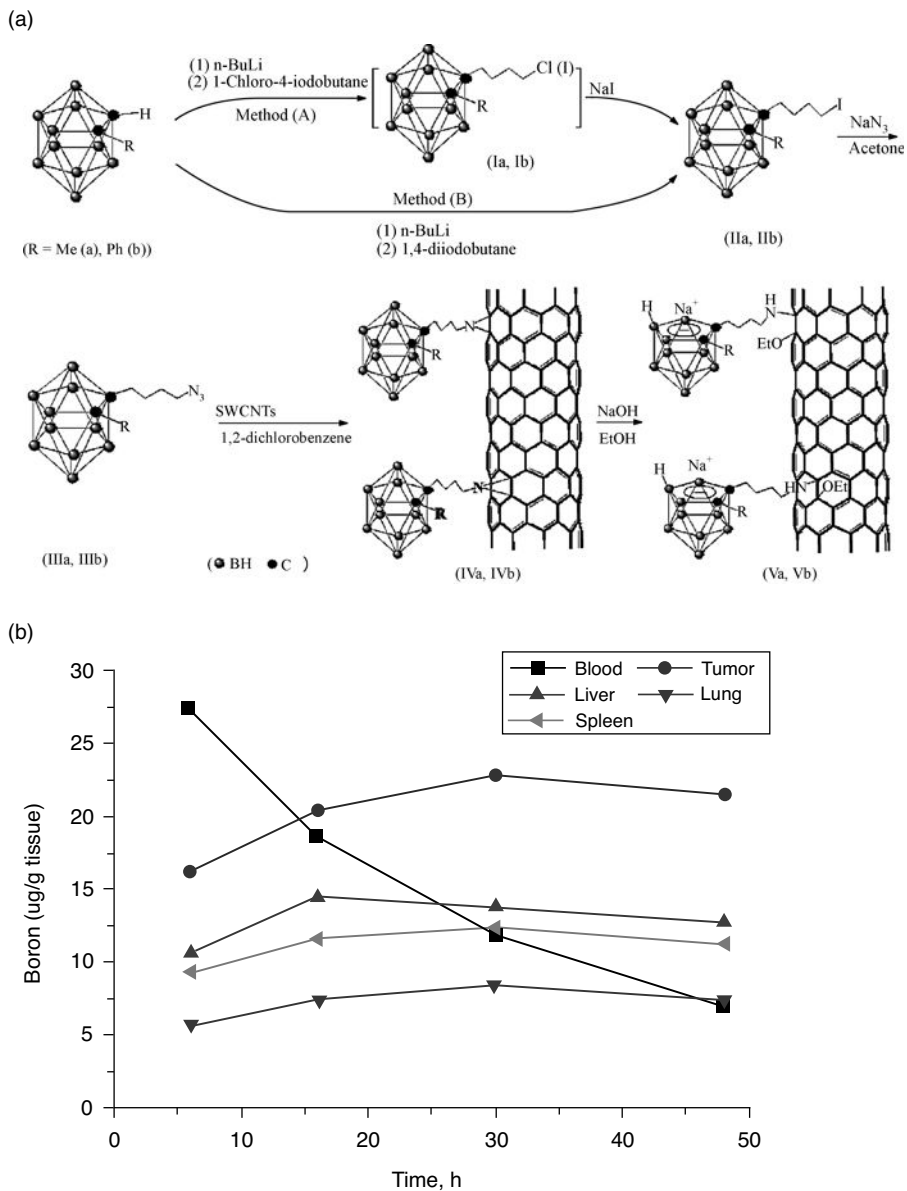
Figure 6.5. (a) Synthesis and (a) biodistribution of carborane functionalized SWCNT.[46]

could not be obtained. However, if the nanotubes could be functionalized to make them water soluble, such structures should prove to be powerful BNCT carriers.

In contrast to boron nanotubes, boron-nitride nanotubes (BNNTs) have been demonstrated to be useful drug delivery agents. Boron-nitride is isoelectronic with carbon; thus, BNNTs are isosteres of CNTs. In comparison to CNTs, BNNTs have

been shown to be nontoxic to HEK293 cells[51] and can be functionalized to promote water solubility. A number of methods of functionalizing BNNTs include interacting them noncovalently with glycodendrimers,[51] coating them with polyethyleneimine (PEI)[52] or poly-l-lysine (PLL),[53] or reacting with substituted quinuclidine bases.[54] The PLL coated BNNT could be further reacted with folic acid to give the foliate conjugated nanomaterial F-PLL-BBNT. In vitro studies showed that the F-PLL-BNNT bioconjugant selectively localized in human glioblastoma multiforme T98G cells.[53] If these encouraging results are found for in vivo studies, then the BNNTs could serve as the boron source in BNCT.

6.6. MAGNETIC NANOPARTICLES

One of the major problems in any type of cancer chemotherapy is that of directing the drug to the tumor and avoiding healthy tissue. Since all chemotherapeutic drugs are by their nature cytotoxic, the localization of these drugs in the vicinity of the tumor could result in the use of lower drug concentrations. As described above this can be done by attaching the drug to a biomolecule that is overused in the malignant cell or to some receptor molecule that is overexpressed in the cancer cells. Another potential way to increase the efficacy of a cancer drug is to physically direct it to the tumor by some external means. This is the basic approach in magnetically targeted therapy (see Figure 6.6). In this approach, the drug of choice is attached to a biocompatible magnetic nanoparticle carrier, usually in the form of a ferrofluid, and is injected into the patient via the circulatory system. When these particles enter the bloodstream, external, high-gradient magnetic fields can be used to concentrate the complex at a specific target site within the body. Once the drug/carrier is correctly concentrated, the drug can be released, either via enzymatic activity or changes in physiological conditions, and be taken up by the tumor cells.[55] The advantage of this methodology is that decreased amounts of cytotoxic drugs would be required, thereby decreasing unwanted side effects.
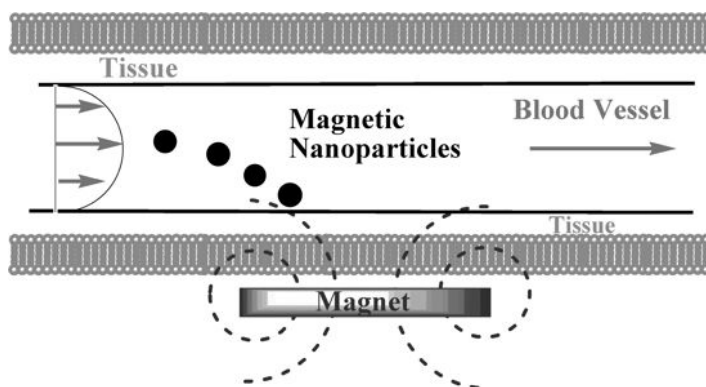
Figure 6.6. Magnetic drug delivery mechanism.
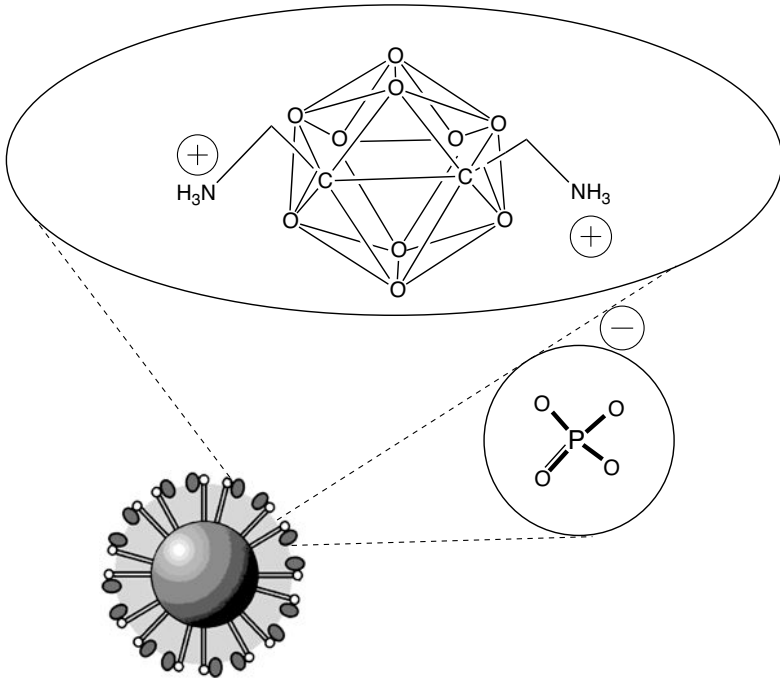
Magnetic nanoparticle   (O = BH)

Figure 6.7. Magnetic nanoparticle–carborane biostructure.

Studies showed that particles as large as 1–2 μm could be concentrated at the site of intracerebral rat glioma-2 (RG-2) tumors; a later study demonstrated that 10–20 nm magnetic particles were even more effective in targeting these tumors in rats.[56, 57] Studies of magnetic targeting in humans demonstrated that the infusion of ferrofluids was well tolerated in most patients, and the ferrofluid could be
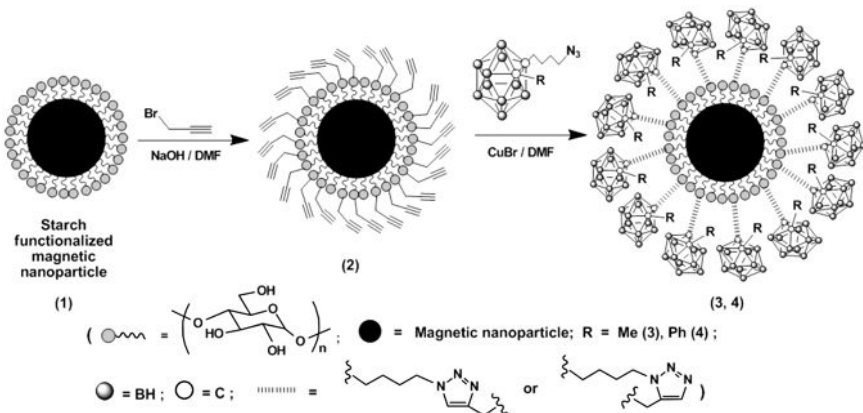
Figure 6.8. Synthesis of encapsulated magnetic nanocomposites.
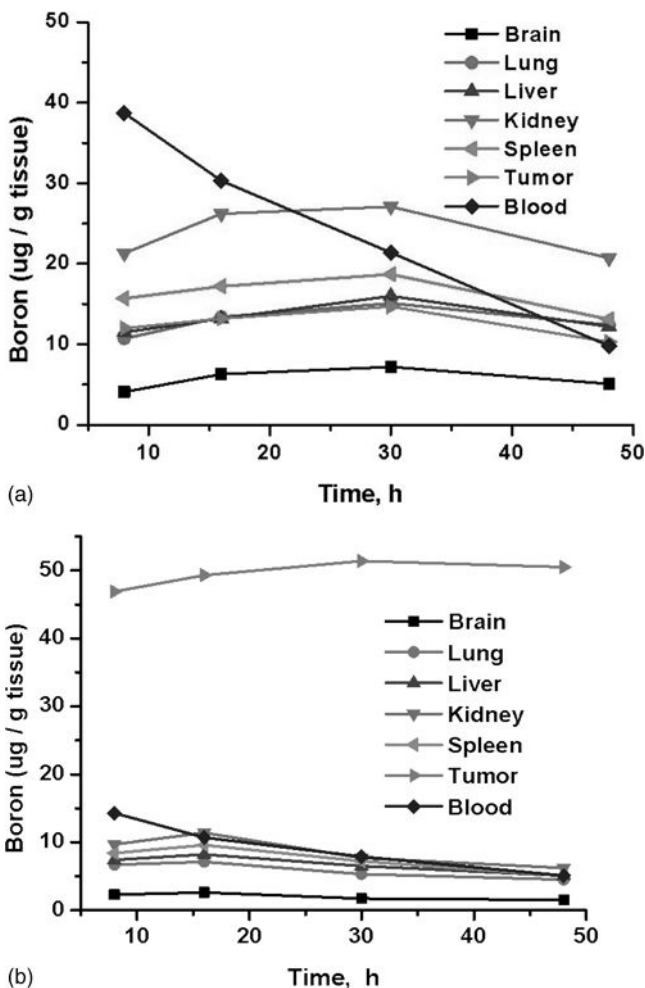
Figure 6.9. Boron tissue distribution of 1-Me-2-butyl-*ortho*-$C_2B_{10}H_{10}$ attached composites, (a) without external magnet and (b) with external magnet.

successfully directed to advanced sarcomas without associated organ toxicity. Recently, FeRx Inc. was granted fast-track status to proceed with multi center Phase I and II clinical trials of their magnetic targeting system for liver tumors. Application of this technique therefore can be considered appropriate vectors for the use of BNCT treatment.

We have successfully immobilized carboranyl dual-chain ammonium salts onto modified magnetic nanoparticles in high loading amounts via the electrostatic interaction between PO_4^- groups on the surface of magnetic nanoparticles and $-NH_3^+$ groups on the carborane cages (Figure 6.7). The use of ionically bound pharmaceuticals allows desorption of the therapeutic agent from the magnetic carrier

so that it can be effective.[55] While this is not necessary in BNCT, it does demonstrate that time release can be advantageous.

Covalent attachment of carborane cages to magnetic nanoparticles has recently been reported.[58] Figure 6.8 shows the sequence by which the cages are attached. Propargyl bromide was reacted with the free hydroxyl groups on a starch coated magnetic nanoparticle to give alkyne enriched nanoparticles. The carborane cages, 1-R-2-butyl-*ortho*-$C_2B_{10}H_{10}$ (R = Me; Ph), could be attached by the reaction of 1-R-2-$(CH_2)_4N_3$-1,2-$C_2B_{10}H_{10}$ to the modified magnetic nanoparticles, as shown on Figure 6.8. Tissue distribution studies of 1-Me-2-butyl-*ortho*-$C_2B_{10}H_{10}$ attached composites were conducted in female BALB/c mice in which breast tumor cells were transplanted into their right flank. Boron concentrations in tumor, blood, lung, liver, spleen, kidney, and brain samples have been measured with and without an external magnetic field. The results are shown in Figure 6.9. As can be seen, no preferential accumulation of boron in the tumor was found in the absence of an external magnetic field. However, in the presence of an external magnet, significant tumor accumulation was found. This is consistent with the fact that magnetic particles under the influence of external magnets localized in the tumors of male Fisher 344 rats bearing RG-2 tumors.[56, 57] It was speculated that the leaky vascular endothelium of the cancer cell allows the entry of the magnetic nanoparticles. This work is only in its initial phases, but it seems that drug attached magnetically directed nanofluids show promise in delivering therapeutic doses to needed areas in an efficient manner.

REFERENCES

1. Locher, G. L. Biological effects and therapeutic possibilities of neutrons. *Am. J. Roentgenol. Radium Ther.*, **1936**, *36*, 1–13.

2. (a) Mughabghab, S. F.; Divadeenam, M.; Holden, N. E. *Thermal Neutron Cross Sections*, Academic Press, New York, 1981. (b) Friedlander, G.; Kennedy, J. W.; Macias, E. S.; Miller, J. M. *Nuclear and Radiochemistry*, 3rd ed. Wiley, Hoboken, NJ, 1981. (c) Leinweber, G.; Barry, D. P.; Trbovich, M. J.; Burke, J. A.; Drindak, N. J.; Knox, H. D.; Ballad, R. V.; Block, R. C.; Danon, Y.; Severnyak L. I. *Nucl. Sci. Eng.*, **2006**, *154*, 261–279.

3. Soloway, A. H.; Tjarks, W.; Barnum, B. A.; Rong, F.-G.; Barth, R. F.; Codogni, I. M.; Wilson, J. G. *Chem. Rev.*, **1998**, *98*, 1515–1562 and references therein.

4. Harling, O. K.; Riley, K. J. *J. Neuro-Oncol.*, **2003**, *62*, 1–17.

5. Barth, R. F.; Coderre, J. A.; Vicente, M. G. H.; Blue, T. *Clin. Cancer Res.*, **2005**, *11*, 3987–4002.

6. Blue, T. E.; Yanch, J. C. *J. Neuro-Oncol.*, **2003**, *62*, 19–31.

7. Kreiner, A. J.; Di Paolo, H.; Burlon, A. A.; Kesque, J. M.; Valda, A. A.; Debray, M. E.; Giboudot, Y.; Levinas, P.; Fraiman, M.; Romeo, V.; Somacal, H. R.; Minsky, D. M. In: *VII, Latin American Symposium on Nuclear Physics and Applications*. Alarcom, R.; Cole, P. L.; Djalali, C.; Umeros, F., Eds. American Institute of Physics, New York, 2007.

8. Hawthorne, M. F.; Lee, M. W. *J. Neuro-Oncol.*, **2003**, *62*, 33–45.

9. Hawthorne, M. F. *Angew. Chem. Int. Ed. Engl.*, **1993**, *32*, 950–984.

10. Laws, E. R.; Shaffrey, M. E. *Int. J. Dev. Neurosci.*, **1999**, *17*, 413–420.

11. Godwin, J. T.; Farr, L. E.; Sweet, W. H.; Robertson, J. S. *Cancer*, **1955**, *8*, 601.

12. (a) Tjarks, W.; Anisuzzaman, A. K. M.; Liu, L.; Soloway, A. H.; Barth, R. F.; Perkins, D. J.; Adams, D. M. *J. Med. Chem.*, **1992**, *35*, 1628–1633. (b) Mauer, J. L.; Serino, A. J.; Hawthorne, M. F. *Organometallics*, **1988**, *7*, 2519–2524.

13. Hariharan, J. R.; Wyzlic, I. M.; Soloway, A. H. *Polyhedron*, **1995**, *14*, 823–829.

14. (a) Anisuzzman, A. K. M.; Alan, F.; Soloway, A. H. *Polyhedron*, **1990**, *9*, 891–892. (b) Goudgaon, N. M.; Kattan, F.-E. G.; Liotta, D. C.; Sxhinazi, R. F. *Nucleosides Nucleotides*, **1994**, *13*, 849. (c) Byun, Y.; Narayanasamy, S.; Johnsamuel, J.; Bandyopadhyaya, A. K.; Tiwari, R.; Al-Madhoun, A. S.; Barth, R. F.; Eriksson, S.; Tjarks, W. *Anti-Cancer Med. Chem.*, **2006**, *6*, 127–144.

15. (a) Kahl, S. B.; Koo, M. S. *J. Chem. Soc. Chem. Commun.* **1990**, *24*, 1769–1771. (b) Chen, C. J.; Kane, R. R.; Primus, F. J.; Szalai, G.; Hawthorne, M. F.; Shively, J. E. *Bioconjug. Chem.*, **1994**, *5*, 557–564.

16. (a) Katan, F. E. G.; Lesnikowski, Z. J.; Yao, S.; Tanious, F.; Wilson, W. D.; Schinazi, R. F., *J. Am. Chem. Soc.*, **1994**, *116*, 7494–7501. (b) Renner, M. W.; Miura, M.; Easson, M. W.; Vicente, M. G. H. *Anti-Cancer Agents Med. Chem.*, **2006**, *6*, 145–157.

17. (a) Shelly, K.; Feakes, D. A.; Hawthorne, M. F.; Schmidt, P. G.; Krisch, T. A.; Bauer, W. F. *Proc. Natl. Acad. Sci. USA*, **1992**, *89*, 9039–9043. (b) Feakes, D. A.; Shelly, K.; Knobler, C. B.; Hawthorne, M. F. *Proc. Natl. Acad. Sci. USA*, **1994**, *91*, 3029–3033.

18. (a) Radel, P. A.; Kahl, S. B. *J. Org. Chem.*, **1996**, *61*, 4582–4588. (b) Kabalka, G. W.; Yao, M. L. *Anti-Cancer Agents Med. Chem.*, **2006**, *6*, 111–125.

19. Coderre, J. A.; Elowitz, E. H.; Chadha M.; Bergland, R.; Capala, J.; Joel, D. D.; Liu, H. B.; Slatkin, D. N.; Chanana, A. D. *J. Neuro-Oncol.*, **1997**, *33*, 141–152.

20. Elowitz, E. H.; Bergland, R. M.; Coderre, J. A.; Joel, D. D.; Chadha, M.; Chanana, A. D. *Neurosurgery*, **1998**, *42*, 463–469.

21. Soloway, A. H.; Hatanaka, H.; Davis, M. A. *J. Med. Chem.*, **1967**, *10*, 714–717.

22. Hatanaka, H.; Nakagawa, Y. *Int. J. Radiat. Oncol. Biol. Phys.*, **1994**, *28*, 1061–1066.

23. Yih, T. C.; Al-Fandi, M. *J. Cell Biochem.*, **2006**, *97*, 1184–1190.

24. (a) Pan, X. Q.; Wang, H.; Shukla, S.; Sekido, M.; Adams, D. M.; Tjarks, W.; Barth, R. F.; Lee, R. J. *Bioconjugate Chem.*, **2002**, *13*, 435–442. (b) Li, T.; Hamdi, J.; Hawthorne, M. F. *Bioconjugate Chem.*, **2006**, *17*, 15–20.

25. Zamenhof, R. G.; Clement, S. D.; Harling, O. K.; Brenner, J. F.; Wazer, D. E.; Madoc-Jones, H.; Yanch, J. C. *Int. J. Radiat. Oncol. Biol. Phys.*, **1989**, *35*, 383–397.

26. Nigg, D. W.; Wheeler, F. J.; Wessol, D. E.; Wemple, C. A.; Babcock, R.; Capala, J. In: *Advances in Neutron Capture Therapy*, Proceedings of the Seventh International Symposium on Neutron Capture Therapy for Cancer, Zürich, Switzerland, Sept. 4–7, 1996; Larsson, B.; Crawford, J.; Weinreich, R.; Eds. Elsevier, Amsterdam, 1997, Volume 1, pp. 91–94.

27. Wheeler, F. J. In: *Advances in Neutron Capture Therapy*, Proceedings of the Seventh International Symposium on Neutron Capture Therapy for Cancer, Zürich, Switzerland, Sept. 4–7, 1996; Larsson, B., Crawford, J., Weinreich, R.; Eds. Elsevier, Amsterdam, 1997; Volume 1, pp. 85–90.

28. Nigg, D. W. *J Neurooncol.*, **2003**, *62*, 75–86.

29. Verbakel, W. F.; Hideghety, K.; Morrissey, J., Sauerwein, W.; Stecher-Rasmussen, F. *Phys. Med. Biol.*, **2002**, *47*, 1059–1072.

30. Wojnecki, C.; Green, S. *Med Phys.*, **2002**, *8*, 1710–1715.

31. Wu G.; Barth R. F., Yang W.; et al. *Anti-Cancer Agents Med. Chem.* **2006**, *6*, 167–184 and references therein.

32. Maeda, H.; Seymour, L. W.; Miyamoto, Y. *Bioconjugate Chem.*, **1992**, *3*, 351–362.

33. Laster, B. H.; Kahl, S. B.; Popenoe, E. A.; Pate, D. W.; Fairchild, R. G. *Can. Res.*, **1991**, *51*, 4588–4593.

34. Barth, R. F.; Mafune, N.; Alam, F.; Adams, D. M.; Soloway, A. H.; Makroglou, G. E.; Oredipe, D. A.; Blue, E.; Steplewski, Z. *Strahlenther. Onkol.*, **1989**, *165*, 142–145.

35. Barth, R. F.; Adams, D. M.; Soloway, A. H.; Alam, A.; Darby, M. V. *Bioconjugate Chem.*, **1994**, *5*, 58–66.

36. Barth, R. F.; Yang, W.; Adams, D. M.; Rotaru, J. H.; Shukla, S.; Sekido, M.; Tjarks, W.; Fenstermaker, R. A.; Ciesielski, M.; Nawrocky, M. M.; Coderre, J. A. *Cancer. Res.*, **2002**, *62*, 3159–3166.

37. Wu, G.; Barth, R. F.; Yang, W.; Chatterjee' M.; Tjarks, W.; Ciesielski, M.; Fenstermaker, R. A. *Bioconjugate Chem.*, **2004**, *15*, 185–194.

38. Backer, M. V.; Gaynutdinov, A. K.; Patel, V.; Bandyopadhyaya, A. K.; Thirumamgel, B. T. S.; Tjarks, W.; Barth, R. F.; Claffey, K.; Backer, J. M. *Mol. Cancer Ther.*, **2005**, *4*, 1423–1429.

39. (a) Parrott, M. C.; Marchington, E. B.; Valliant, J. F.; Adronov, A. *J. Am. Chem. Soc.*, **2005**, *127*, 12081–12089. (b) Galie, K. M.; Mollard, A.; Zharov, I. *Inorg. Chem.*, **2006**, *45*, 7815–7820.

40. Iijma, S. *Nature*, **1991**, *354*, 56–58.

41. Cuenca, A.; Jiang, H.; Hochwald, S.; Delano, M.; Cance, W.; Grobmyer, S. *Cancer*, **2006**, *107*, 459–466.

42. Pantarotto, D.; Briand, J. P.; Prato, M., Bianco, A. *Chem. Commun.*, **2004**, 16–17.

43. Kam, N. W. S.; Jessop, T. C.; Wender, P. A.; Dai, H. *J. Am. Chem. Soc.* **2004**, *126*, 6850–6851.

44. Cherukuri, P.; Bachilo, S. M.; Litovsky, S. H.; Weisman, R. B. *J. Am. Chem. Soc.*, **2004**, *126*, 15638–15639.

45. Kam, N. W. S.; Dai, H. *J. Am. Chem. Soc.*, **2005**, *127*, 6021–6026.

46. Zhu, Y. H.; Ang, T. P.; Carpenter, K.; Maguire, J.; Hosmane, N. S.; Takagaki, M. *J. Am. Chem. Soc.*, **2005**, *127*, 9875–9880.

47. (a) Cui, D. X.; Tain, F. R.; Ozkan, C. S.; Wang, M.; Gao, H. J. *Toxicol. Lett.*, **2005**, *155*, 73–85. (b) Bottini, M.; Bruckner, S.; Nika, K.; Bottini, N.; Bellucci, S.; Magrini, A.; Bergamaschi, A.; Mustelin, T. *Tocicol. Lett.*, **2006**, *160*, 121–126.

48. Ciuparu, D.; Klie, R.; Zhu, Y.; Pfefferle, L. *J. Phys. Chem.*, **2004**, *108*, 3967–3969.

49. Xu, T. T.; Zheng, J. G.; Wu, N.; Nicholls, A. W.; Roth, J. R.; Dikin, D. A.; Ruoff. R. S. *Nano Lett.*, **2004**, *4*, 963–968.

50. Otten, C. J.; Lourie, O. R.; Yu, M.-F.; Cowley, J. M.; Dyer, M. J.; Ruoff, R. S.; Buhro, W. E. *J. Am. Chem. Soc.*, **2002**, *124*, 4564–4565.

51. Chen, X.; Wu, P.; Rousseas, M.; Okawa, D.; Gartner, Z.; Zettl, A.; Bertozzi, C. R. *J. Am. Chem. Soc.*, **2009**, *131*, 890–891.

52. Ciofani, C.; Raffa, V.; Menciassi, A.; Cushieri, A. *Biotechnol. Bioeng.*, **2008**, *101*, 850–858.

53. Ciofani, G.; Raffa, V.; Menciassi, A.; Cushieri, A. *Nanoscale Res. Lett.*, **2009**, *4*, 113–121.

54. Maguer, A.; Leroy, E.; Bresson, L.; Doris, E.; Loiseau, A.; Mioskowski, C. *J. Mater. Chem.*, **2009**, *19*, 1271–1275.

55. Alexiou, C.; Arnold, W.; Klein, R. J.; Parak, F. G.; Hulin, P.; Bergemann, C.; Erhardt, W.; Wagenpfeil, S.; Lübb, A. S. *Cancer Res.*, **2000**, *60*, 6641–6648.

56. Pulfer, S. K.; Ciccotto, S. L.; Gallo, J. M. *J. Neuro-Oncol.*, **1999**, *41*, 99–105.

57. Sincai, M.; Ganga, D.; Ganga, M.; Argherie, D.; Bica, D. *J. Magn. Magn. Mater.*, **2005**, *293*, 438–441.

58. Zhu, Y.; Lin, Y.; Zhu, Y.-Z.; Lu, J.; Maguire, J. A.; Hosmane, N. S., *J. Nanomater.*, **2010**, *2010* (*ID 409320*), 1–8.

The Exploration of Biomedical Multimodality in Small Solid Core Nanoparticles

MARC WALTERS

Department of Chemistry, New York University, New York, New York, USA

7.1. INTRODUCTION

Magnetic resonance imaging (MRI) is a powerful diagnostic tool that provides high-resolution images of differentiated tissues of the body in three dimensions. MRI images derive from differences in the rate of radiofrequency energy absorption (T_1), and decoherence of the transverse nuclear spin magnetization (T_2) by water protons in anatomical structures. The ability of protons to absorb energy is related to the spin density of water protons, and the relaxation rates for the proton spins. Intrinsic MRI images can be acquired because the relaxation rates for water are a function of the environment of the water molecules, that is, soft tissue, mineralized tissue, fat and so on. In clinical applications it is often necessary to distinguish between closely related tissues as when healthy tissue borders embedded tumor lesions. Though different in its cytological characteristics, cancerous tissue is often indistinguishable from adjacent healthy tissue by intrinsic MRI in the absence of an agent to delineate the lesion.

The identification of tumor lesions, atherosclerotic plaque, or myocardial infarction by MRI is achieved with contrast inducing agents that associate preferentially with the diseased tissue. In tumor lesions the localization of a *contrast agent* can be achieved passively by the mechanism of enhanced permeation and retention (EPR). In this process a contrast agent accumulates at the tumor by leaking through the porous blood vessels that result from very rapid angiogenesis at the site of aggressive tumor growth. Radiologists prefer actively targeted agents, however—those that are effective even when the vascular lining is intact (not leaky), as would be found in diseases that do

not perturb the rate of angiogenesis. The nanoparticulate contrast agents presented in this chapter are well suited for multifunctional performance, (multimodality) with the inclusion of targeting agents.

The need for contrast agents was recognized from the very early days of MRI with the pioneering work of Lauterbur and others.[1] Their development for clinical applications derives from the physics of spin relaxation by paramagnetic ions, the study of which was begun by the pioneers of NMR spectroscopy, who described the effects of simple paramagnetic ions on spin relaxation. In the classical approach described by Bloch, we can think of nuclear magnetic dipoles precessing with a characteristic frequency (Larmor frequency) in an external magnetic field along a z-axis to generate a net magnetic dipole that is aligned with the field. This net magnetic dipole is referred to as the *magnetization vector* of the system. When the nuclei are irradiated with energy of the same frequency along a direction that is transverse to the z-axis, energy is absorbed by the precessing nuclei and the magnetization vector is rotated toward the xy-plane. The now excited system relaxes by two pathways. (i) The magnetization vector rotates back toward the z-axis (T_1 relaxation). The time required for this relaxation, T_1, should be short if saturation and signal loss are to be avoided. Higher power of radiation can be absorbed by the system when T_1 is short. In this situation, as the power increases so too does the NMR signal. (ii) Alternatively, the magnetization vector in the xy-plane can lose magnitude by dephasing in the xy-plane. The more quickly this occurs the weaker is the signal. Contrast agents can be selected that promote T_1 or T_2 relaxation. A T_1 agent causes signal intensity increase in its vicinity. The resulting image appears bright relative to the intrinsic MRI image. Conversely, a T_2 agent causes a decrease in signal intensity in its vicinity, which causes an image darkening relative to the intrinsic image. In the discussion that follows frequent mention will be made of *relaxivity* (r_1 or r_2). This term denotes the effectiveness with which a contrast agent reduces the magnitude of T_1 or T_2. For a gadolinium complex the relaxivity is determined as a function of the measured T_1 value for a given concentration of contrast agent (CA), $1/T_1 = r_1[CA]$. Measurements are made at several different CA concentrations and r_1 is determined as a slope. An analogous expression applies in the measurement of r_2.

Radiologists favor T_1 agents because they generate data that are more easily interpreted and are free of image artifacts that occur with T_2 agents. The most prevalent T_1 agents are based on Gd^{3+} which has seven unpaired f electrons, and a correspondingly high magnetic moment. The Mn^{2+} ion, which has five unpaired d electrons and a somewhat lower magnetic moment, is similarly recognized as a useful contrast agent. In fact, manganese(II) in the simple water-soluble form of $MnCl_2$ was the first contrast agent to be considered for MRI image enhancement.[1] Current clinical practice, however, makes the most extensive use of Gd^{3+} containing agents, which were first explored by Carr et al.[2, 3] The most prominent T_2 agents are iron oxide (Fe_3O_4) nanoparticles whose surface chemistry has been richly developed to exploit this class of contrast agent in the clinical environment. In recent years, advances in nanotechnology have enabled the syntheses of superparamagnetic iron oxide (SPIO) particles that are efficient transverse relaxation agents. Typically, the iron oxide particles are surface protected by shrouding them in polymers or materials such as dextran or gold.[4–8] The surface coating material serves a second purpose in providing sites for the attachment of targeting agents, drugs, or stealth promoters such as

polyethylene glycol (PEG). Recent research has taken T$_1$ agents from the molecular scale to the nanoscale in order to achieve multifunctionality (multimodality) and high contrast similar to that which has been observed with SPIO agents.[9]

This chapter discusses the recent developments and future directions in nanoparticulate multimodal T$_1$ contrast agents. Nanoscale T$_1$ agents are featured in this discussion because of the aforementioned preference for molecular T$_1$ agents in clinical applications, and the potential of nanoscience to greatly extend the utility of T$_1$ agents. The iron oxide T$_2$ agents have been extensively reviewed[10, 11] and will not be discussed here. Similarly, micelle-based and pure liposomal agents have been treated elsewhere [12, 13] and their discussion will be eschewed in favor of new species that draw on both materials science and nanoscience to achieve multimodality, and, ultimately, biocompatibility. In the interests of exploring biocompatible agents, this chapter focuses on silica and noble metal based contrast agents, their potential, and challenges en route to clinical applications.

7.2. SILICA T$_1$ CONTRAST AGENTS

The earliest reference to mesoporous silica (MS) as a nanoscale carrier of Gd and other lanthanides for MRI contrast enhancement is by Lin et al.[14] They formed MS from the surfactant cetyltrimethylammonium bromide (CTAB), GdCl$_3$·6H$_2$O, and tetraethylorthosilicate (TEOS) under acidic conditions. The product was then isolated as a precipitate by raising the solution pH to 9 by the addition of NH$_4$OH. This method gave nonspherical particles of dimensions less than 100 nm. Gadolinium loading in the particles was adjustable in the range of 1.3–6.8 wt%. The particles, designated Gd-MS (gadolinium-containing mesoporous silica), were characterized for their relaxivity values by the inversion recovery method to measure T$_1$, and the Carr–Purcell–Meiboom–Gill method to determine T$_2$ in aqueous solution. The relaxivities changed markedly with the extent of Gd loading from r$_1$ = 23.6, r$_2$ = 94.8 s^{-1} mM^{-1} at 1.6% Gd-MS to r$_1$ = 4.4, r$_2$ = 80.4 s^{-1} mM^{-1} at 6.8% Gd-MS. The authors ascribed the decrease in relaxivity to dipole–dipole interactions between the metal ions. Interestingly, X-ray diffraction showed that the two-dimensional (2D) hexagonal pore structure of MS observed at low Gd loading, transformed to worm-like pores at high loading. Additionally, XPS data showed that at a loading level of 6.8% Gd the oxygen 1s peak was broadened and shifted to lower energy, indicative of a replacement of Si by Gd.

Delville and co-workers[15] selected 20 nm SiO$_2$ and 13 nm Al$_2$O$_3$ from commercial sources as particulate substrates for the attachment of aminopropyltrimethoxysilyl (APS) GdDTPA. The derivatized particles were prepared either by amination followed by reaction with DTPA bis(anhydride), or by peptide coupling of the particle surface amines with DTPA. The grafting of APS on silica, as monitored by DRIFTS, resulted in the disappearance of Si–OH bands, and the appearance of the expected CH$_2$ and carbonyl peaks of DTPA. XPS data established that Gd constituted about 4 atom % of silica, and 2 atom % of Al$_2$O$_3$. In this system there are approximately 4 Gd complexes per silica particle as determined by inductively coupled plasma (ICP) mass spectrometry, with an average relaxivity,

r_1, of $42\,s^{-1}\,mM^{-1}$ per Gd at 4.7 T. On a per particle basis r_1 and r_2 were found to be $168\,s^{-1}\,mM^{-1}$ and $589\,s^{-1}\,mM^{-1}$ respectively, at 4.7 T. Uptake by cells in microglia cultures was measured with particles grafted with Gd^{3+} complexes together with tetramethyl rhodamine isothiocyanate (TRITC), a fluorescent marker. Micrographs show that particles were taken up internally in perinuclear sites and also absorbed on cell surfaces. The reported magnetic resonance signal-to-noise ratio for microglia cells increased by a factor of 1.4 after uptake of particles designated as Al_2O_3-APS-DTPAGd. An even larger signal-to-noise increase factor of 3.75 was reported with the uptake of SiO_2-APS-DTPAGd.

Bakalova and co-workers reported the synthesis of a 17 nm nanoparticle with a quantum dot (QD) core and a silica shell.[16] The encapsulation of the QD by silica involved the assembly of a polymerized micelle around the QD followed by the formation of polymerized silane shell around the precursors (Figure 7.1). By avoiding
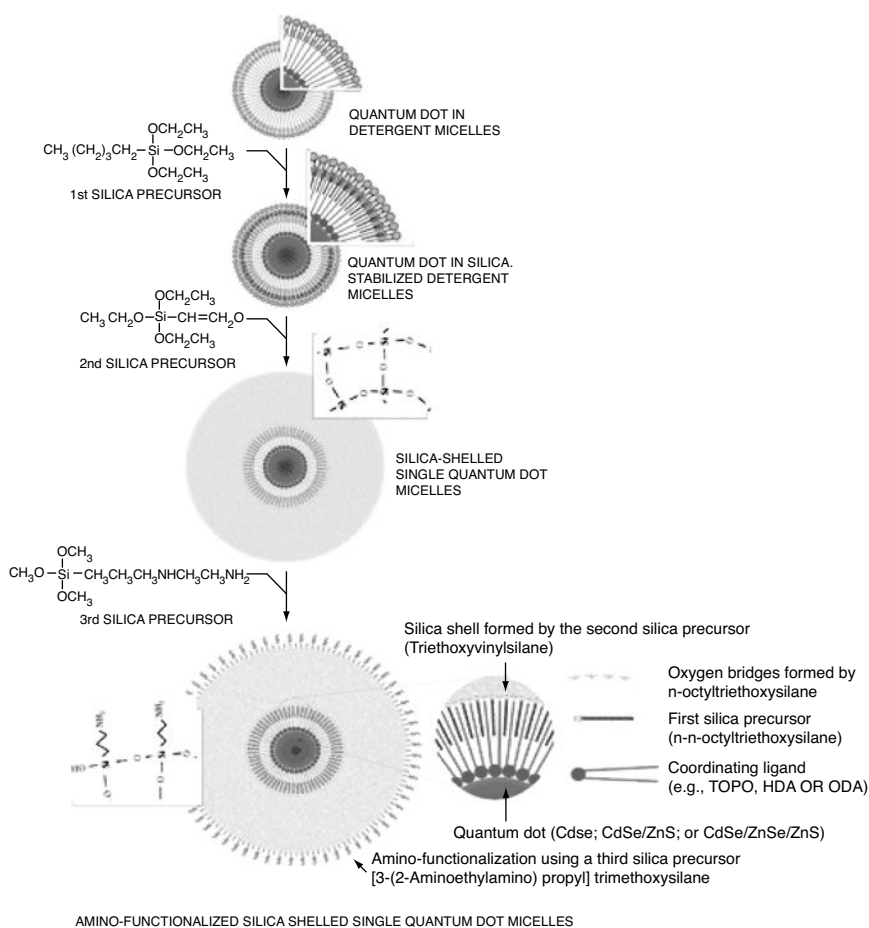
Figure 7.1. Silica shelled single QD micelles.

the incorporation of multiple QDs in their silica particles, they preserved the high quantum yield of the QD luminescence. They employed confocal microscopy to demonstrate the uptake of their particles by HeLa cells that remained viable. The particles containing Resolve Al™-Gd in their interior undergo endocytosis without transfection aids. MRI phantoms of the silica particles containing Resolve Al-Gd, [Gd tris(2,2,6,6-tetramethyl-3,5-heptanedionate)], showed enhancement although the relaxation of the system diminished with prolonged dialysis—an indicator of weak retention of the contrast agent.

In a subsequent publication, the Bakalova group[17] compared particles containing Resolve Al™-Gd in their interior with particles whose silica surface was modified by reaction with [GdDOTA-Bn-NCS]. They found that although both constructs initially retained 25–30% of the initial Gd complex added to the reaction solution, they both experienced a partial loss of Gd during dialyses. Interestingly, T$_1$ and T$_2$ were found to be shorter for the particle containing interior Gd than for the particle bearing surface Gd groups. Again, cells (HeLa, A549, Jurkat, and K562) remained viable following the uptake of these particles. Both types of nanoparticles were found to be nontoxic at a concentration of 500 nM under ultraviolet (UV) and laser irradiation. The particles had an average diameter of 17 nm, too large for rapid renal excretion, which is limited to particles with diameters <5.5 nm.[18]

Fluorescent QDs were combined with Gd complexes on a silica nanoparticle by Yang et al.[19] Their multimodal probe contained a ZnS-passivated CdS : Mn (Cd : Mn/ ZnS/SiO$_2$ core/shell/shell) fluorescent QD. The ∼3 nm QDs were synthesized in AOT reverse-micelles in a water hexane mixture. A 4–7 nm thick silica shell was formed by the polymerization of TEOS in the presence of molecules that occupied the surface of the particle. The surface modifiers included 3-(trihydroxysilyl)propyl methylphosponate (THPMP) and 3-(aminopropyl) triethoxysilane (APTS) to enhance the solubility of the silica nanoparticle. Subsequently n-(trimethoxysilyl- propyl)ethyldiamine triacetic acid trisodium salt (TSPETE), a 5-coordinate ligand, was added along with gadolinium(III) acetate to form a surface bound gadolinium complex. The core–shell particles were 11–17 nm in diameter. Excitation at 345 nm generated a fluorescence peak with a maximum at 590 nm. The relaxivities r$_1$ and r$_2$ per Gd^{3+} of the nanoparticle were determined to be 20.5 and 151 s^{-1} mM^{-1}, respectively, at 4.7 T (200 MHz). The authors suggested that this construct could be applicable for the imaging of cells.

Sharma et al.[20] reported the formation of a gold speckled silica (GSS) nanoparticle that enabled MRI and photoacoustic tomography (PAT) (Figure 7.2). Photoacoustic contrast derives from the absorption of visible light, which generates an acoustic wave due to the thermoelastic expansion of the absorbent.[21] It provides femtomolar sensitivity and high spatial resolution. The multimodality of the GSS particle derives from its capacity for both MRI and PAT imaging. The synthesis of this particle called for the sequential mixing of tetraethylorthosilane with water to form silica particles, followed by a ligand N-(trimethoxysilyl-proplyl)ethyldiaminetriacetic acid (TSPETE), then gadolinium acetate, and lastly gold chloride, which was reduced after absorption to form gold clusters within and on the silica surface. The result was a particle whose surface gold structures were photoacoustically active
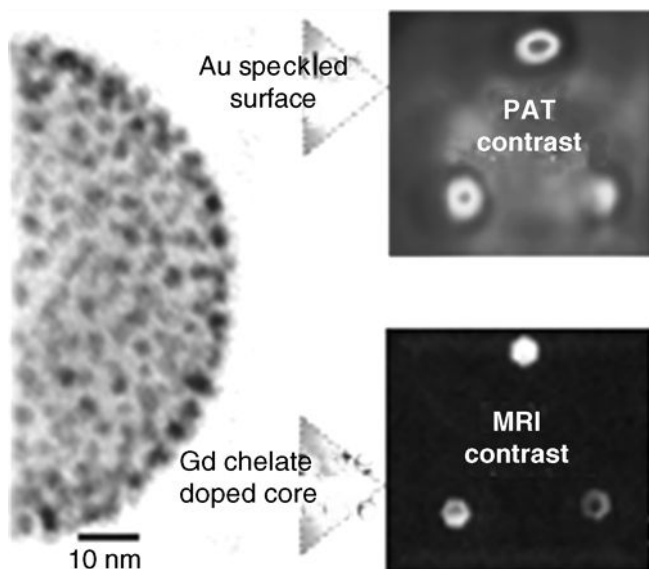
Figure 7.2. Gold speckled silica with PAT and MRI imaging.

for PAT, and supported Gd complexes for MRI contrast enhancement. The gold speckled particle differs greatly from previously reported gold shell particles formed by depositing gold shells on nonconducting silica nanoparticles. The latter were generally large, with diameters in the range of 120–150 nm as compared with the average 50 nm size for GSS nanoparticles as determined by dynamic light scattering and transmission electron microscopy. The elemental composition of the Gd-doped GSS particles was determined by energy-dispersive X-ray spectroscopy (EDS) and inductively coupled plasma (ICP) methods. The resulting MR relaxivities r_1, r_2, and r_2^* were determined to be 13, 110, and 173 s^{-1} mM^{-1} respectively, at a field strength of 4.7 T (200 MHz). The authors pointed out that the dispersal of Gd binding sites on the silica surface could favor the exchange of water to the benefit of r_1, which was larger than for GdDTPA. A similar enhancement of r_1 is expected to result from the attachment of Gd ions to a nanoparticle with an intrinsically large rotational correlation time, τ_R. The presence of 34000 Gd ions on a larger GSS particle of 100 nm diameter constitutes a moderate footprint of 92.4 $\mathring{A}^2$ per Gd binding site, which is smaller than that observed in dendrimers but greater than that of noble metal nanoparticles.

In a series of papers[22, 23] Mou and co-workers described the synthesis of mesoporous silica nanoparticles (MSNs) that contain Gd complexes for cell imaging (Figure 7.3). The silica particles are formed by the hydrolysis of TEOS in the presence of CTAB in aqueous ammonia. In the first such particle, a $100 \times 425 \pm$ 75 nm nanorod (Gd-Dye@MSN-R), formed by reaction with an amidopropyltrimethoxysilane tethered DTPA, GdDTPA was located in pores of 2.2 nm diameter. The particles were rendered bifunctional by the attachment of the
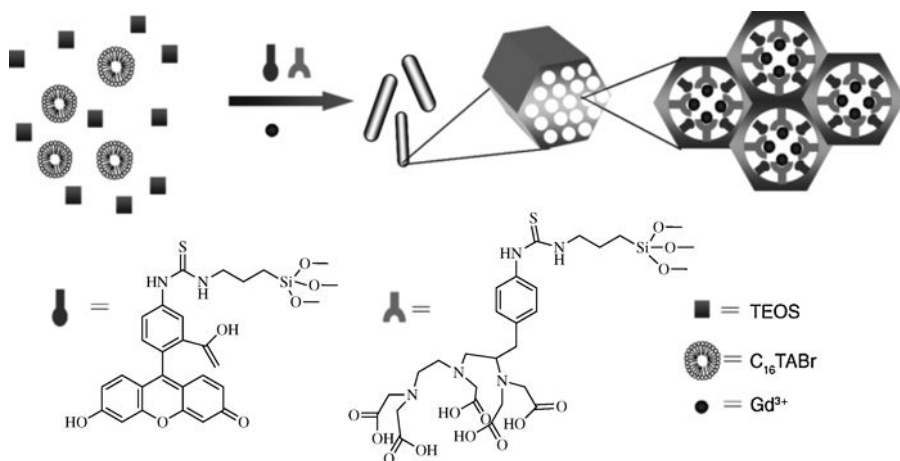
Figure 7.3. Schematic respresentation of the synthesis of mesoporous silica.

fluorophore FITC. Particle morphology was controlled by adjusting the concentration of DTPA to induce rod formation, except for very low concentrations of the ligand, which gave rise to spheres (Gd-Dye@MSN) instead. The particles were found to have a well-ordered 2D hexagonal mesoporous structure. The pore size decreased slightly from 2.31 nm to 2.16 nm with the adsorption of Gd complexes. Rods were reported to incorporate 26637 Gd atoms per rod and have relaxivities of $r_1 = 22$ and $r_2 = 41\,s^{-1}\,mM^{-1}$ at 0.47 T (20 MHz). By contrast the spheres ($\sim$100 nm diameter) exhibited relaxivities of $r_1 = 23$ and $r_2 = 34\,s^{-1}\,mM^{-1}$ at 0.47 T (20 MHz). In both cases the high relaxivities relative to $[Gd(DTPA)]^{2-}$ were ascribed to the slow tumbling rate of the nanoparticles. The $r_2 : r_1$ ratios were 1.86 and 1.48, respectively, which the authors propose is useful for both T$_1$- or T$_2$-weighted imaging.

A solution of Gd-Dye@MSN-R in Dulbecco's Eagle medium was taken up as a cell marker in 3T3-L1 mouse fibroblasts to a level of 3×10^3 particles per cell after a 1 h incubation time in the absence of transfection agents. The nanorods were similarly taken up by monocytes and could generally be expected to label both phagocytic and nonphagocytic cells. MRI at 1.5 T (63 MHz) verified the uptake and image enhancing capability of Gd in MSN-R. Significantly, cell viability and cell function were unaffected by MSN uptake. The particles distributed preferentially to the liver and spleen before excretion through the liver, bile, and intestines, which limits their utility for clinical applications where rapid excretion is required via the kidneys. However, the nanorods proved ideal for the study of cell labeling, trafficking, and metastasis.

Spherical particles were examined for their cellular uptake characteristics by FITC-based flow cytometry and in vitro MRI.[22] In vivo MRI was recorded in a nude mouse model where Gd-Dye@MSN-labeled human mesenchymal stem cells (HMSCs) were implanted into the basal ganglia of the mice and observed over a 14 day period by 1.5 T MRI T$_1$-weighted imaging. The cells remained visible as bright dots for that period with no evidence of cell migration. Furthermore, in related
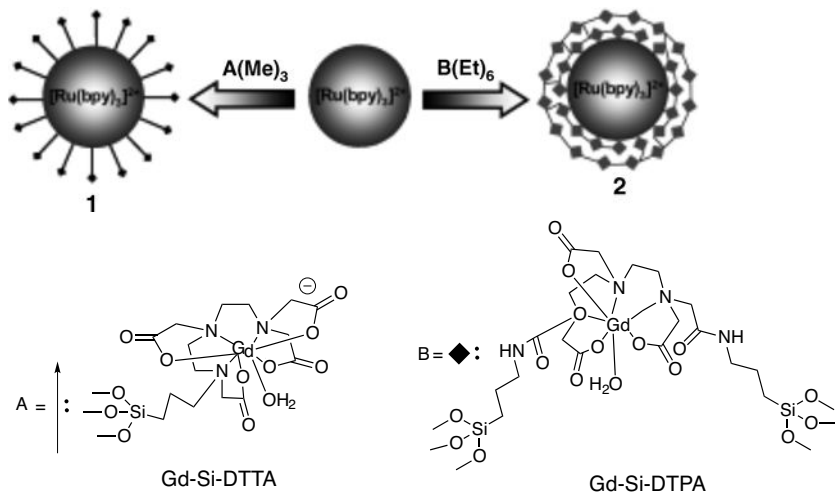
Figure 7.4. Scheme synthesis of hybrid silica nanoparticles 1 and 2.

studies, the authors found no evidence of cytotoxicity even with high loading $(300 \, \text{mg} \, \text{mL}^{-1})$ in the HMSCs.

Lin and co-workers described a multimodal contrast agent formed by the layer-by-layer deposition of Gd complexes and polymers on silica nanoparticles containing $[\text{Ru(bipy)}_3]^{2+}$ ions as luminescence markers[24] (Figure 7.4). The doped silica particle was formed by the hydrolysis of TEOS in the presence of $[\text{Ru(bipy)}_3]^{2+}$. Anionic gadolinium–DTPA complexes were then tethered to the surface with an appended trimethoxy silane chain. A layer-on-layer process followed with the addition of oligomeric cationic Gd(DOTA bis amide) complexes. SEM and TEM data showed silica particles of 37 nm diameter.

The ligand Si-DTTA attaches to the particle surface yielding a product whose longitudinal and transverse relaxivities were $r_1 = 19.7 \, \text{mM}^{-1} \, \text{s}^{-1}$ and $r_2 = 60.0$ $\text{mM}^{-1} \, \text{s}^{-1}$ respectively, with 10200 complexes bound on the particle surface. The attachment of Si-DTPA resulted in particles with lower per Gd relaxivities of $r_1 = 7.8 \, \text{mM}^{-1} \, \text{s}^{-1}$ and $r_2 = 12.3 \, \text{mM}^{-1} \, \text{s}^{-1}$ respectively. The authors attributed these lower relaxivity values to Gd^{3+} ion sites on the particle where water exchange rates are slow. To prove the multimodal properties of the agent particles **1** (Figure 7.4) were taken up in monocytes. The efficient uptake of the particles was revealed by laser scanning confocal fluorescence microscopy (LSCFM) and by T_1- and T_2-weighted MRI images of isolated cells.

In a later study the Lin group[25] treated the silica core to layer-by-layer modification with Gd containing oligomers to achieve a final binding number of $17070 \, \text{Gd}^{3+}$ complexes per particle. The treated particles (**2** in Figure 7.4) showed no improvement $(r_1 = 19.0 \, \text{mM}^{-1} \, \text{s}^{-1}$ and $r_2 = 55.0 \, \text{mM}^{-1} \, \text{s}^{-1})$ in relaxivity relative to particle 1 (in Figure 7.4) containing simply tethered gadolinium DTPA complexes. Particle **2** incorporated RGD to target cancer cells and FITC for LSCFM optical imaging. As above, the particles were tested in vitro on (i) human colon cancer
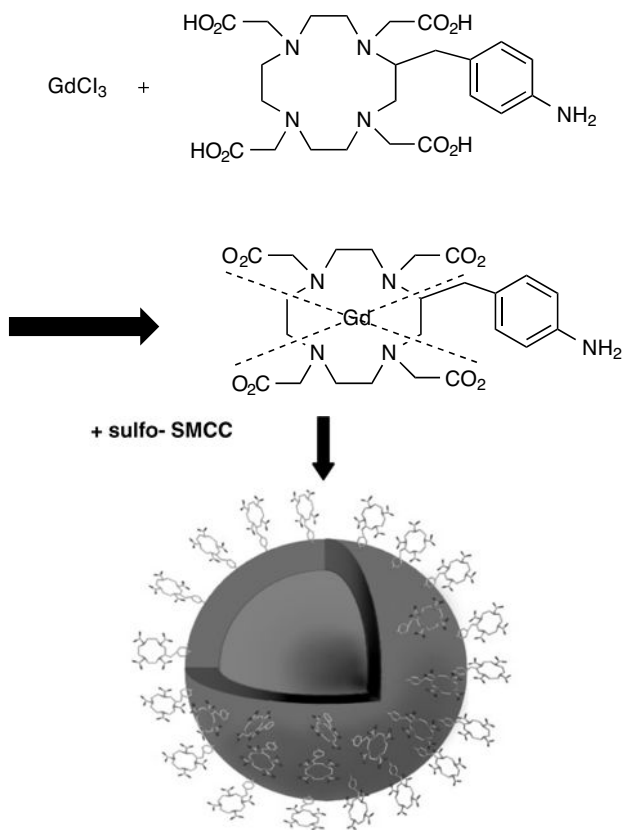
Figure 7.5. Preparation of the paramagnetic probes.

(HT-29) cells and calf pulmonary artery endothelial (CPAE) cells. MR and LSCRM imaging verified the efficient labeling of cells by particles with surface RGD.

A particularly detailed study carried out by Gerion et al.[26] describes the formation and characterization of QD and gold nanoparticles sheathed in a thin layer of silica. Gadolinium complexes were subsequently anchored to the silica surface (Figure 7.5). The resulting particles served as bimodal imaging agents with luminescent properties derived from their core components, and magnetic resonance contrast enhancement induced by appended gadolinium ions.

In the derivatization process CdSe/ZnS QDs were reacted with mercaptopropyl-trimethoxysilane (MPS), which was polymerized in methanol under slightly basic conditions. A second treatment with MPS and PEG silane served to introduce PEG and thiol groups to the silica surface. Similarly, phosphine stabilized gold particles were reacted with MPS in water in a stepwise procedure that yielded a silica coating with terminal PEG and thiol groups. The complex, GdDOTA, with a pendant amino group was then reacted with the crosslinker, sulfo-SMCC, to generate a pendant maleimide group, which then formed a covalent link to sulfur for attachment to the silica surface.

Silica shell formation was confined to a thickness of 2 nm and therefore added approximately 4 nm to an Au particle with a 5 nm diameter. The shell thickness was somewhat greater for larger cores. At 20 MHz the relaxivities for silica coated QDs were remarkably large with r_1 and r_2 values of 43 and 55 $s^{-1} mM^{-1}$ and an excellent r_2/r_1 ratio of 1.28, respectively, per Gd^{3+} ion, compared to values of $r_1 = 3.83$ and $r_2 = 5.85 s^{-1} mM^{-1}$ $r_2/r_1 = 1.53$ at 20 MHz for GdDOTA.[27] Each of the *total* relaxivities of the particle was larger by a multiplicative factor of 45, which is the number of Gd^{3+} ions per particle, as determined by ICP mass spectrometry. Unfortunately, at higher fields r_1 values for the nanoparticles markedly decreased while r_2 values increased.

T_1-weighted imaging in a mouse model showed that the silica coated MRI contrast agents were cleared via the renal system and caused no observable adverse health effects in the animals. The sensitivity of the probes varied as a function of particle size and was 100 nM for 8–10 nm particles and 10 nM for 15 nm particles.

Tillement and co-workers described a Gd_2O_3 nanoparticle that serves as a multimodal theranostic with a capacity for optical, and MR imaging, and neutron capture therapy.[28–30] Gadolinium oxide nanoparticles of 2.2 nm diameter (TEM data) were synthesized using a polyol protocol that involved the hydrolysis of $GdCl_3$ in diethyleneglycol (DEG) by substoichiometric amounts of NaOH (Figure 7.6). A portion of these particles was then employed as seeds for the formation of larger
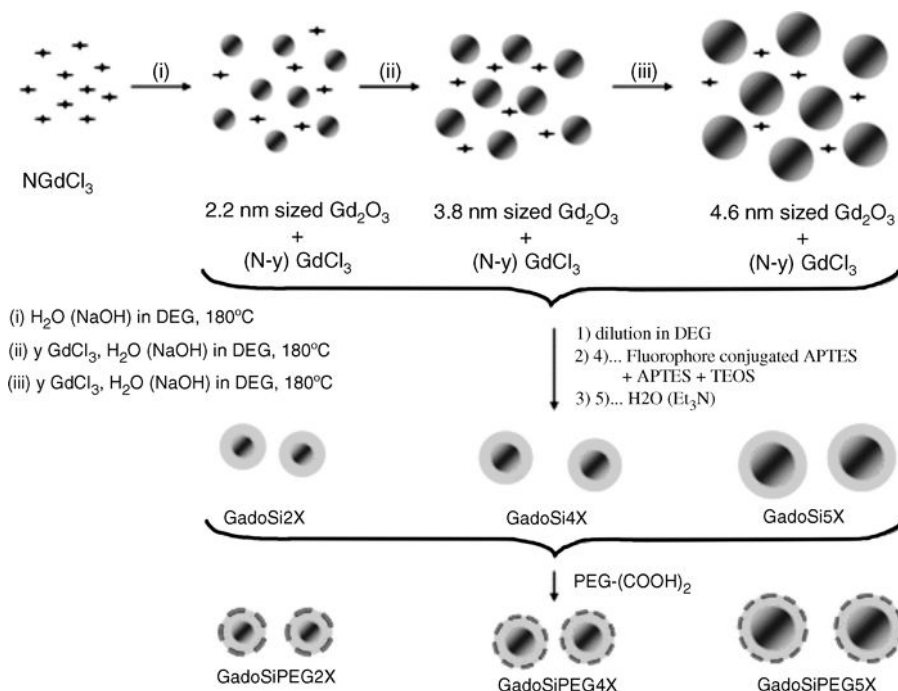
Figure 7.6. Schematic illustration of the synthesis and the surface functionalization fy PEG of gadolinium oxide cores.

particles that grow in the presence of GdCl$_3$ and NaOH. Three sets of particles of 2.2, 3.8, and 4.6 nm were then enveloped in layers of fluorescent silica prepared by standard methods that involved hydrolysis-condensation of a mixture of tetraethylorthosilicate and aminopropyltriethoxysilane and a fluorophore dopant. The silica shell was reported to be about 2 nm thick for the particles. After extensive dialysis to remove excess Gd^{3+} ions, α,ω-dicarboxyPEG was grafted to aminopropyl groups on the surface through the formation of an amide link.

The resultant particles exhibited surprisingly high relaxivities given (i) the lack of an obvious mechanism for water coordination beneath a layer of silica, and (ii) the fraction of gadolinium that is likely inaccessible in the bulk of the Gd$_2$O$_3$ particle. For example, the 2.2 nm diameter Gd$_2$O$_3$ particles had r$_1$ and r$_2$ relaxivities of 8.8 s^{-1} mM^{-1} and 11.4 s^{-1} mM,$^{-1}$ respectively. The authors suggested that the silica layer was sufficiently porous to allow the diffusion of water between bulk water and the gadolinium oxide surface. Further, the authors argue that both surface and bulk Gd^{3+} ions of the Gd$_2$O$_3$ phase accelerate the relaxation of water protons,[31] which would account for the high relaxivity values observed for gadolinium oxide phases.

The efficacy of the nanoparticles for image contrast enhancement was evaluated by fluorescence imaging in nude mice, and by MRI in rats. The agents proved effective in both modalities. Postmortem ICP-MS showed the biodistribution to be essentially limited to the kidneys and the urine of the rat 3 h after injection. The question of long-term release of Gd^{3+} ions from residual particles was not addressed.

In related research gadolinium oxide nanoparticles with the composition Gd$_2$O (CO$_3$)$_2$·H$_2$O were studied by Hu et al.[32] (Figure 7.7). The gadolinium oxide particles were synthesized by the hydrolysis of gadolinium chloride in the presence of urea to form white spheres of ∼441 nm. A silica shell was then deposited on the particle surface by the hydrolysis of TEOS. Amination of the silica was carried out by reaction with 3-aminopropyltriethoxysilane (APTES) and was followed by the
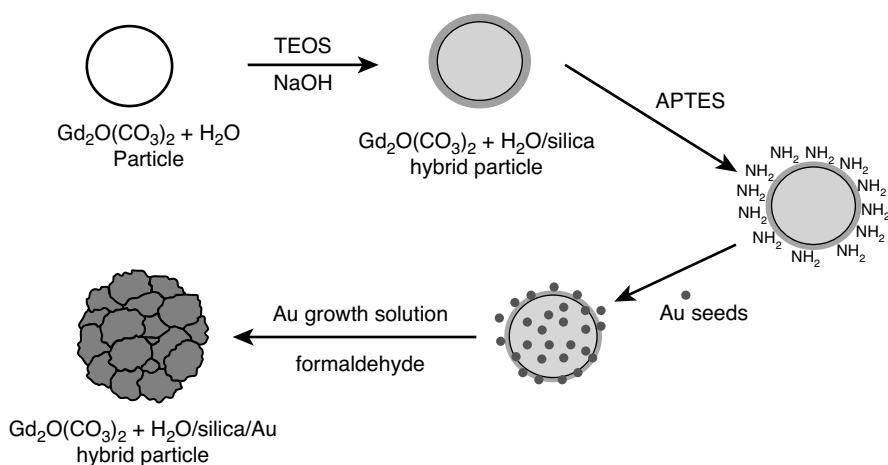
Figure 7.7. Schematic of synthetic steps for the fabrication of gadolinium oxide particle.

formation and surface attachment of gold nanoparticulate seeds. Growth of the seeds generated a gold shell of 63 nm, which resulted in a final particle diameter of 579 nm. Longitudinal relaxivity (r_1), measured at 3 T, varied as a function of gold shell thickness with values of $r_1 = 8.60$ (12 nm), 7.06 (26 nm), and $2.84\,s^{-1}\,mM^{-1}$ (63 nm). The particles were subsequently conjugated with PEG by reaction with PEG disulfide. In this form they were taken up in MBT-2 bladder cancer cells and investigated for their efficacy in photothermal killing. In the absence of light the cells remained viable. Under continuous wave diode laser irradiation at 808 nm, particles with 12 nm thick Au shells proved most effective in killing cells because of their high extinction coefficient for visible and near-IR light.

For most biomedical applications hybrid nanomaterials are derived as stable covalently bonded structures. The constructs of Mulder and co-workers are stable and they incorporate hybrid nanomaterials. However, they assemble in part through noncovalent interactions. The constructs have obvious liposomal characteristics in that they form closed spherical structures with a surfactant bilayer, the external layer of which is lipidic, but with a nonaqueous core and external aqueous environment (Figure 7.8).[33, 34] This construction allows a variety of components to be interspersed among the outer lipids to control the function of the particle. The inner particle is the familiar silica-enveloped QD formed by the standard method of TEOS hydrolysis in the presence of the QD. The lipid coating of silica was formed by heating the hybrid silica particle with octadecanol to anchor hydrophobic chains on the surface of the particle via a condensation reaction. The resulting Q-SiPaLC particles were then dispersed in chloroform/methanol with various lipids to form a multimodal outer lipid layer. Outer lipids were constituted to incorporate GdDTPA, PEG, and maleimide for coupling to thiol containing targeting peptides such as thiol terminated RGD.[33] These particles have a hydrodynamic diameter of 58 nm therefore clearance would likely be relatively slow if PEG adequately shields it from the immune system. Fluorescence studies of the particle with human umbilical vein endothelial cells in vitro show it to be effectively targeted by the $\sim$650 RGD peptides on its surface. The relaxivities r_1 and r_2 were reported to be 14.4 and $23\,mM^{-1}\,s^{-1}$ respectively, with a corresponding r_1 value of $36000\,mM^{-1}\,s^{-1}$ per particle, based on the presence of $2500\,Gd^{3+}$ ions in the surface lipid layer.

In a very recent publication that appeared after this chapter was reviewed, Woods and Sherry describe a nanoconstruct in which cationic polymers, $GdDOTP^{5-}$ and silica nanoparticles are combined to form nanoparticle-assembled capsules (NACs) of 0.2–5.0 μm in diameter.[35] The construct has an interior polymeric region in which $GdDOTP^{5-}$ ions are dispersed. The corona of the particle is comprised of relatively small (13 nm) silica nanoparticles adsorbed on the surface of the polymer core. The maximum relaxivity, $24\,mM^{-1}\,s^{-1}$ (per Gd^{3+}) was observed for a 500 μm NAC containing a polyallyamine core. Lower relaxivity values were observed with increasing capsule diameter, and for particles with a polylysine core. As described in earlier reports, the appreciable magnitude of the relaxivity, r_1, signals a relatively rapid diffusion of water through the silica particle surface.
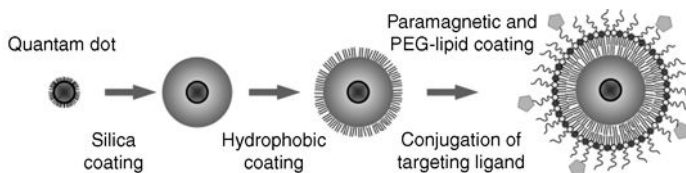
Figure 7.8. Multistep synthesis of Q-SiPaLC particles. (Courtesy of W. Mulder.)

7.3. SILVER AND GOLD T$_1$ CONTRAST AGENTS

More than a decade of research on the attachment of thiols, amines, and other molecular groups to gold surfaces forms the foundation for development of noble metal nanoparticle CAs.[36, 37] The natural biocompatibility of gold[38–40] and its long use as a therapeutic agent favored the choice of gold colloids for the development of multimodal constructs. Tillement and co-workers were the first to describe a CA that incorporates Gd^{3+} in coordination complexes on the surface of a noble metal particle.[41] They prepared gold nanoparticles by the reduction of HAuCl$_4$·3H$_2$O with NaBH$_4$ in the presence of thiols that control particle growth and stability. A dithiolated form of GdDTPA was then assembled on the particle surface. The average particle diameter obtained was 2.4 ± 0.5 nm. XPS, IR, and TGA data suggested that thiol attachment to the Au surface was limited, leaving the remainder in the form of –SS– groups of DTPA oligomeric structures[41] forming flexible loops above the particle surface. GdDTPA coordination complexes were formed by the stoichiometric uptake of approximately 150 Gd^{3+} ions in the DTPA oligomers on the particle surface. At 7 T (300 MHz) the corresponding relaxivity, r$_1$, for the construct was $3.90 \, \text{s}^{-1} \, \text{mM}^{-1}$ per oligomeric Gd^{3+} ion, versus $3.00 \, \text{s}^{-1} \, \text{mM}^{-1}$ for GdDTPA in water.

One challenge that attends the use of colloidal contrast agents is that their solubility is a function of the surface charge or zeta potential. At too low or high a potential, the colloid aggregates, forming a useless precipitate. In a subsequent report,[42] the Tillement group revealed that full incorporation of Gd^{3+} in their gold based particle led to aggregation within a day of formation. To avoid this outcome they incorporated only about 50 Gd^{3+} ions per particle, leaving 2/3 of the DTPA sites as free charged carboxylates to enhance particle surface solvation for higher solubility (Figure 7.9).

The particles were shown to be multimodal in their capacity to provide both CT and MR contrast. Synchrotron radiation computed tomography (SRCT) phantom imaging was obtained at a gold concentration of $1.4 \, \text{mg} \cdot \text{mL}^{-1}$ which is lower than the detection threshold of a conventional CT scanner. In vivo SRCT images of mice and rats were obtained at a concentration of $10 \, \text{mg} \cdot \text{mL}^{-1}$ which corresponds to a 5 mM Gd. MR images were enhanced by the presence of the particles. Postmortem ICP mass spectrometry showed the particles to distribute mostly to the kidneys of the animals, where they were readily cleared in the urine. Interestingly,
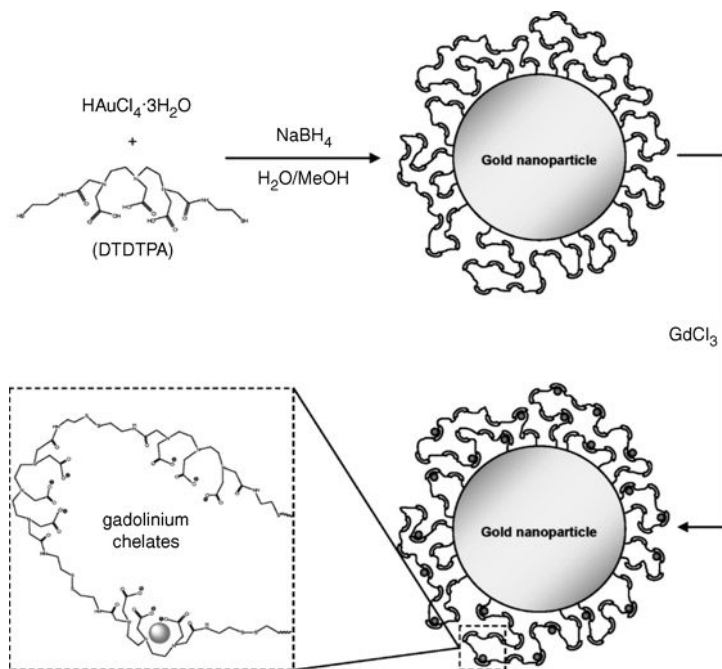
Figure 7.9. Synthesis of Au@DTDTPA-Gd nanoparticles (gray circle = gadolinium ion).

the 2.4 nm sized particles required no modification to shield them from the reticuloendothelial system.

Park and co-workers took a similar tact in attaching GdDTPA-bisglutathione to the surface of 5–7 nm gold nanoparticles.[43] The glutathione was attached to DTPA through amide linkages by reaction of two equivalents of glutathione with DTPA bisanhydride. ICP mass spectrometry results gave 1.36×10^4 Gd^{3+} ions per particle. The relaxivity per Gd^{3+} complex was found to be $10.5 \text{ s}^{-1} \text{ mM}^{-1}$ which is equivalent to $1.87 \times 10^5 \text{ s}^{-1} \text{ mM}^{-1}$ per particle.

Several years ago in exploring the binding of tiopronin to gold nanoparticles as a colloid stabilizer, Murray and co-workers showed that proton relaxation rates were fast enough to broaden into the baseline the ^{1}H-NMR signals of organic groups adjacent to the particle surface.[44] Peak broadening is relatively minor for molecules bound to silver nanoparticles, allowing a full NMR analysis of thiol binding on the surface of the particle. The Walters group took advantage of this circumstance to explore the surface coordination of lanthanide complexes on a silver metal core as the supporting structure.[45] They reacted cysteine with DTPA dianhydride to produce a DTPA diamide with two distal uncoordinated carboxylate groups that lowered the zeta potential to enhance solvation of the nanoparticles. Silver nanoparticles of approximately 10 nm in diameter were formed by the reduction of silver nitrate in water in the presence of DTPA-L-cysteine (DTPA-L-cys). The average particle size was verified by TEM. These workers further exploited the
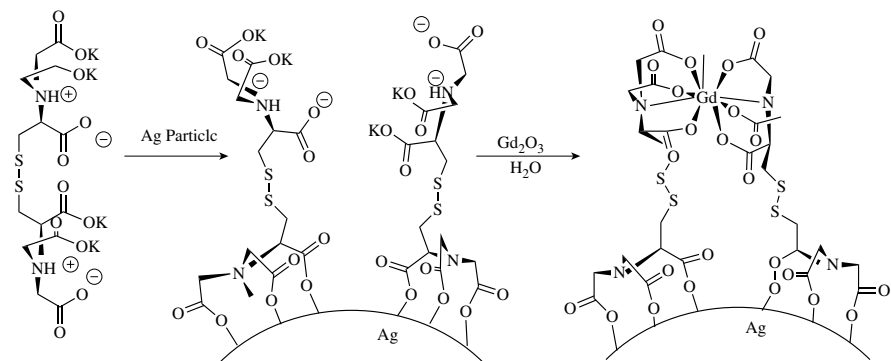
Figure 7.10. Structure of the bifunctional attachment of GdCNTA on a silver nanoparticle.

surface chelate effect[46] by using surface tethered four coordinate cystine-bis-NTA (CNTA) to bind lanthanides in an eight coordinate pocket. ^{13}C-NMR analysis showed that CNTA attaches to silver through one of its carboxylate groups leaving the disulfide group unattached and allowing metal complexation by one of its two NTA groups (Figure 7.10). NMR analysis was carried out on diamagnetic La^{3+} complexes. Isostructural Gd^{3+} complexes were prepared for relaxivity measurements and chemical analyses. TGA data showed that the 10 nm particles accommodate 2600 ligands on their surfaces and, in the case of the DTPA adduct, an equal number of Gd^{3+} ions. The NTA adducts were necessarily only half complexed. Relaxivities (per Gd) at 400 MHz (9.4 T) were, 10.7 and 9.7 s^{-1} mM^{-1} for Gd(DTPA-L-cys) and Gd(CNTA)$_2$, respectively, bound to Ag nanoparticles and 4.6 s^{-1} mM^{-1} for the Gd(DTPA) molecular standard. The corresponding multiplicative relaxivities of the particles were, respectively, 27800 and 12610 s^{-1} mM^{-1}. It may be presumed that the relaxivities are increased due to the large size of the rotational correlation time of the nanoparticles.

Synthetic approaches to the formation of multimodal nanoparticles for MRI have continued to diversify as shown by several recent publications that appeared while this chapter was in review. These will be mentioned briefly.

Nishiyabu et al.[47] describe nanoparticles based on supramolecular networks of nucleotides and lanthanides. Multimodality is achieved in this system by enclosing entities such as dyes, enzymes, and gold nanoparticles. Gold nanoparticles were formed capped with 5′-GMP, and then mixed in buffer with GdCl$_3$ to generate a supramolecular network on the particle surface. The nucleotide/lanthanide nanoparticles were reported to have longitudinal relaxivities (r$_1$) of ∼12.5 s^{-1} mM^{-1}. Much remains to be determined about the utility of these constructs for clinical applications.

Warsi et al.[48] reported a very concise nanoparticulate system in which Gd(DTPA) is tethered to a gold nanoparticle surface through a single linkage that leaves all five carboxylate groups of the ligand available to bind Gd^{3+} and simultaneously avoids oligomerization of DTPA on the particle surface. They reported their construct of be pH stable, making it useful in buffer. However, the construct exhibits a modest

relaxivity that is likely the result of local motions of the complex at the end of the tether. The multimodality of their construct was augmented by the incorporation of biotin, which is useful for targeting.

Marradi et al.[49] have elaborated on a bimodal glyconanoparticle construct that consists of a gold nanoparticle core to which sugars and GdDO3A are tethered with alkane linkers of variable length. They report the longitudinal (r_1) relaxivity range to be $1–25\,mM^{-1}\,s^{-1}$ (per Gd) as a function of the position of Gd^{3+} relative to the surrounding sugar moieties. The authors surmise that proximity of the sugar to GdDO3A favors water exchange, population of the second coordination sphere of the complex, or increases the value of q, the number of water molecules bound to the metal ion.

Two recent publications are particularly far reaching in their goals and results. The first by Moriggi et al.[50] describes a nanoassembly of GdDTTA complexes on a gold nanoparticle core, bound through an N-methyl p-thiophenol to the particle surface. The assembly is structurally characterized with unusual care by analytical and computational (MM3) methods. They reported the formation of a nanoparticulate construct of unusually high relaxivity (r_1) $\sim 60\,mM^{-1}\,s^{-1}$ at 30 MHz, likely arising from a high degree of water binding in the first coordination sphere, $q = 2$. They further reported that the magnetic moment of the Au core is negligible relative to that of Gd^{3+}, which is relevant to the role of Au-based nanoparticles for MRI applications.

The second paper, by Song et al.,[51] describes a gold core assembly on whose surface resides 24-mer poly-dT oligonucleotides bearing the cyanine dye Cy3 as a fluorescent terminal group. The oligomers are each derivatized by click chemistry to bind five GdDOTA groups. The nanoassembly is multimodal by virtue of its suitability for CT, MR, and fluorescence imaging, which are well-known attributes of many of the recent agents as described above. This agent, however, is particularly noteworthy because it is a noncytotoxic, nuclease resistant cell labeling entity that is taken up by endocytosis at micromolar concentration. It persists in vesicles in the perinuclear region of both mother and daughter cells after mitosis and is therefore ideal for cell tracking by CT, fluorescence, and MRI.

7.4. OVERVIEW AND CONCLUSION

The aim of this chapter was to examine recent advances in research on nanoparticles as multimodal MRI contrast agents. The discussion was intentionally focused on particles that incorporate Gd^{3+} as a T_1 or brightening agent because this class of agent is preferred for its radiological characteristics. The nanoparticulate systems discussed above are compositionally complex but generally obtainable in high yield by simple reactions.

The ongoing development of biomedical agents could be frustrated by the toxicity of some of the components. Gadolinium is notoriously toxic as an antagonist to Ca^{2+}. QDs have been amply described both in their merits and their dangers for clinical use. Silver cytotoxicity is an area of active

investigation.[52–59] Each of these potential impediments has yielded or could yield to synthetic approaches involving the use of silica. The toxicity of Gd^{3+} is quenched by the incorporation of the ion in highly stable silica phases as was illustrated earlier. QDs have been coated with silica to yield stable colloids and to provide a shield against toxicity. A similar approach with silver nanoparticles could enable their use as platforms for contrast agents.[60–62] The question of size, however, is entwined with the utilization of silica nanoparticles, which although freely soluble across the pH spectrum and at high ionic strength, have thus far been acquired only in diameters well above the 5.5 nm limit for clearance through the kidneys.[18] The residence time of nanoparticles in the liver, the clearance route that serves larger particles, is in the range of three months, which increases the chance that toxic ions (i.e., Gd^{3+} ions) will escape from a particle surface or the interior of a porous shell.[63] The density of Gd binding sites on a silica shell is much lower than that on metal nanoparticles of the same size. As a result, the sensitivity of silica agents is lower than that of the metal core nanoparticulate agents although some silica agents exhibit high relaxivity per Gd^{3+} ion.

Gold is an attractive substrate because it is nontoxic and provides an excellent surface for the attachment of Gd complexes. Its use is favored by the capacity of the metal for multimodality. However, its hydrophobicity likely accounts for some of the modest relaxivity values reported for $q = 1$ complexes on Au particles. Similar reasoning would explain the modest relaxivities observed for Ag-based nanoparticulate contrast agents. The particle sizes reported for Au are in the range 2.5–10 nm. Therefore, particles of diameter <5.5 nm should easily be accessible and could be envisaged as vehicles that could deposit their cargo of targeted imaging agents and then yield to clearance via the kidneys. The approach to biomedical imaging using the diverse and flexible methods of inorganic chemistry presents twin challenges of high sensitivity and low toxicity that will demand much, but may greatly advance the science of nanochemistry and its utility in the quest for new clinical agents.

GLOSSARY

APS	Aminopropyltrimethoxysilyl
Bn-NCS	4-Isothiocyanatobenzyl
CTAB	Cetyltrimethylammonium bromide
DOTA	1,4,7,10-Tetraazacyclododecane-1,4,7,10-tetraacetate
DRIFTS	Diffuse reflectance infrared Fourier transform spectroscopy
DTPA	Diethylenetriaminepentaacetic acid
FITC	Fluorescein isothiocyanate
DO3A	1,4,7-Tris(carboxymethyl)-1,4,7,10-tetraazacyclododecane
DOTP	1,4,7,10-Tetraazacyclododecane-1,4,7, 10-tetra(methylene-phosphonate)
DTTA	Diethylenetriaminetetraacetate
PEG	Polyethylene glycol

q	Number of water molecules bound to Gd^{3+}
QD	Quantum dot
RGD	Arg-Gly-Asp (RGD) attachment site
sulfo-SMCC	Sulfosuccinimidyl-4-[*N*-maleimidomethyl]cyclohexane-1-carboxylate
TEM	Transmission electron microscopy
TEOS	Tetraethylorthosilicate
TGA	Thermogravimetric analysis

REFERENCES

1. Lauffer, R. B. *Chem. Rev.*, **1987**, *87*, 901.

2. Carr, D. H. *J. Thorac. Imaging*, **1985**, *1*, 74.

3. Carr, D. H.; Brown, J.; Bydder, G. M.; Weinmann, H. J.; Speck, U.; Thomas, D. J.; Young, I. R. *Lancet*, **1984**, *1*, 484.

4. Hasegawa, M.; Kitaguni, H. JP51151320, 1976.

5. Molday, R. S. US Patent 4452773, 1984.

6. Cui, Y.; Hu, D.; Fang, Y.; Ma, J. *Sci. China Ser. B: Chem.*, **2001**, *44*, 404.

7. Cui, Y.; Wang, Y.; Hui, W.; Zhang, Z.; Xin, X.; Chen, C. *Biomed. Microdevices*, **2005**, *7*, 153.

8. Fang, J.; He, J.; Shin, E. Y.; Grimm, D.; O'Connor, C. J.; Jun, M.-J. *Mater. Res. Soc. Symp. Proc.*, **2003**, *774*, 149.

9. Bogdanov, A. A., Jr.; Weissleder, R.; Brady, T. J. *Adv. Drug Delivery Rev.*, **1995**, *16*, 335.

10. Di Marco, M.; Sadun, C.; Port, M.; Guilbert, I.; Couvreur, P.; Dubernet, C. *Int. J. Nanomed.*, **2007**, *2*, 609.

11. Laurent, S.; Forge, D.; Port, M.; Roch, A.; Robic, C.; Vander Elst, L.; Muller, R. N. *Chem. Rev. (Washington, DC, U.S.)*, **2008**, *108*, 2064.

12. Mulder, W. J. M.; Strijkers, G. J.; van Tilborg, G. A. F.; Griffioen, A. W.; Nicolay, K. *NMR Biomed.*, **2006**, *19*, 142.

13. Torchilin, V. P. *Curr. Pharm. Biotechnol.*, **2000**, *1*, 183.

14. Lin, Y. S.; Hung, Y.; Su, J. K.; Lee, R.; Chang, C.; Lin, M. L.; Mou, C. Y. *J. Phys. Chem. B*, **2004**, *108*, 15608.

15. Voisin, P.; Ribot, E. J.; Miraux, S.; Bouzier-Sore, A. K.; Lahitte, J. F.; Bouchaud, V.; Mornet, S.; Thiaudiere, E.; Franconi, J. M.; Raison, L.; Labrugere, C.; Delville, M. H. *Bioconjugate Chem.*, **2007**, *18*, 1053.

16. Bakalova, R.; Zhelev, Z.; Aoki, I.; Ohba, H.; Imai, Y.; Kanno, I. *Anal. Chem.*, **2006**, *78*, 5925.

17. Bakalova, R.; Zhelev, Z.; Aoki, I.; Masamoto, K.; Mileva, M.; Obata, T.; Higuchi, M.; Gadjeva, V.; Kanno, I. *Bioconjugate Chem.*, **2008**, *19*, 1135.

18. Choi, H. S.; Liu, W.; Misra, P.; Tanaka, E.; Zimmer, J. P.; Ipe, B. I.; Bawendi, M. G.; Frangioni, J. V. *Nat. Biotechnol.*, **2007**, *25*, 1165.

19. Yang, H. S.; Santra, S.; Walter, G. A.; Holloway, P. H. *Adv. Mater.*, **2006**, *18*, 2890.

20. Sharma, P.; Brown, S. C.; Bengtsson, N.; Zhang, Q. Z.; Walter, G. A.; Grobmyer, S. R.; Santra, S.; Jiang, H. B.; Scott, E. W.; Moudgil, B. M. *Chem. Mater.*, **2008**, *20*, 6087.

21. Skrabalak, S. E.; Chen, J.; Sun, Y.; Lu, X.; Au, L.; Cobley, C. M.; Xia, Y. *Acc. Chem. Res.*, **2008**, *41*, 1587.

22. Hsiao, J. K.; Tsai, C. P.; Chung, T. H.; Hung, Y.; Yao, M.; Liu, H. M.; Mou, C. Y.; Yang, C. S.; Chen, Y. C.; Huang, D. M. *Small*, **2008**, *4*, 1445.

23. Tsai, C. P.; Hung, Y.; Chou, Y. H.; Huang, D. M.; Hsiao, J. K.; Chang, C.; Chen, Y. C.; Mou, C. Y. *Small*, **2008**, *4*, 186.

24. Rieter, W. J.; Kim, J. S.; Taylor, K. M. L.; An, H. Y.; Lin, W. L.; Tarrant, T.; Lin, W. B. *Angew. Chem. Int. Ed.*, **2007**, *46*, 3680.

25. Kim, J. S.; Rieter, W. J.; Taylor, K. M. L.; An, H.; Lin, W. L.; Lin, W. B. *J. Am. Chem. Soc.*, **2007**, *129*, 8962.

26. Gerion, D.; Herberg, J.; Bok, R.; Gjersing, E.; Ramon, E.; Maxwell, R.; Kurhanewicz, J.; Budinger, T. F.; Gray, J. W.; Shuman, M. A.; Chen, F. F. *J. Phys. Chem. C*, **2007**, *111*, 12542.

27. Bousquet, J. C.; Saini, S.; Stark, D. D.; Hahn, P. F.; Nigam, M.; Wittenberg, J.; Ferrucci, J. T. *Radiology*, **1988**, *166*, 693.

28. Bridot, J. L.; Dayde, D.; Riviere, C.; Mandon, C.; Billotey, C.; Lerondel, S.; Sabattier, R.; Cartron, G.; Le Pape, A.; Blondiaux, G.; Janier, M.; Perriat, P.; Roux, S.; Tillement, O. *J. Mater. Chem.*, **2009**, *19*, 2328.

29. Bridot, J. L.; Faure, A. C.; Laurent, S.; Riviere, C.; Billotey, C.; Hiba, B.; Janier, M.; Josserand, V.; Coll, J. L.; Vander Elst, L.; Muller, R.; Roux, S.; Perriat, P.; Tillement, O. *J. Am. Chem. Soc.*, **2007**, *129*, 5076.

30. Faure, A. C.; Hoffmann, C.; Bazzi, R.; Goubard, F.; Pauthe, E.; Marquette, C. A.; Blum, L. J.; Perriat, P.; Roux, S.; Tillement, O. *Acs Nano*, **2008**, *2*, 2273.

31. Evanics, F.; Diamente, P. R.; van Veggel, F. C. J. M.; Stanisz, G. J.; Prosser, R. S. *Chem. Mater.*, **2006**, *18*, 2499.

32. Hu, K.-W.; Jhang, F.-Y.; Su, C.-H.; Yeh, C.-S. *J. Mater. Chem.*, **2009**, *19*, 2147.

33. Mulder, W. J. M.; Koole, R.; Brandwijk, R. J.; Storm, G.; Chin, P. T. K.; Strijkers, G. J.; Donega, C. D.; Nicolay, K.; Griffioen, A. W. *Nano Lett.*, **2006**, *6*, 1.

34. Koole, R.; van Schooneveld, M. M.; Hilhorst, J.; Castermans, K.; Cormode, D. P.; Strijkers, G. J.; de Mello Donega, C.; Vanmaekelbergh, D.; Griffioen, A. W.; Nicolay, K.; Fayad, Z. A.; Meijerink, A.; Mulder, W. J. M. *Bioconjugate Chem.*, **2008**, *19*, 2471.

35. Plush, S. E.; Woods, M.; Zhou, Y. F.; Kadali, S. B.; Wong, M. S.; Sherry, A. D. *J. Am. Chem. Soc.*, **2009**, *131*, 15918.

36. Whitesides, G. M. *Chimia*, **1990**, *44*, 310.

37. Whitesides, G. M.; Laibinis, P. E. *Langmuir*, **1990**, *6*, 87.

38. Demann, E. T. K.; Stein, P. S.; Haubenrich, J. E. *J. Long-Term Eff. Med. Implants*, **2005**, *15*, 687.

39. Healy, M. A.; Aslam, M. *Pharm. J.*, **1981**, *227*, 634.

40. Tiekink, E. R. T. *Gold Bull. (London, U.K.)*, **2003**, *36*, 117.

41. Debouttière, P. J.; Roux, S.; Vocanson, F.; Billotey, C.; Beuf, O.; Favre-Reguillon, A.; Lin, Y.; Pellet-Rostaing, S.; Lamartine, R.; Perriat, P.; Tillement, O. *Adv. Funct. Mater.*, **2006**, *16*, 2330.

42. Alric, C.; Taleb, J.; Le Duc, G.; Mandon, C.; Billotey, C.; Le Meur-Herland, A.; Brochard, T.; Vocanson, F.; Janier, M.; Perriat, P.; Roux, S.; Tillement, O. *J. Am. Chem. Soc.*, **2008**, *130*, 5908.

43. Park, J.-A.; Reddy, P. A. N.; Kim, H.-K.; Kim, I.-S.; Kim, G.-C.; Chang, Y.; Kim, T.-J. *Bioorg. Med. Chem. Lett.*, **2008**, *18*, 6135.

44. Kohlmann, O.; Steinmetz, W. E.; Mao, X.-A.; Wuelfing, W. P.; Templeton, A. C.; Murray, R. W.; Johnson, C. S., Jr., *J. Phys. Chem. B*, **2001**, *105*, 8801.

45. Siddiqui, T. S.; Jani, A.; Williams, F.; Muller, R. N.; Elst, L.; Laurent, S.; Yao, F.; Wadghiri, Y. Z.; Walters, M. A. *J. Colloid Interface Sci.*, **2009**, *337*, 88.

46. Major, R. C.; Zhu, X. Y. *J. Am. Chem. Soc.*, **2003**, *125*, 8454.

47. Nishiyabu, R.; Hashimoto, N.; Cho, T.; Watanabe, K.; Yasunaga, T.; Endo, A.; Kaneko, K.; Niidome, T.; Murata, M.; Adachi, C.; Katayama, Y.; Hashizume, M.; Kimizuka, N. *J. Am. Chem. Soc.*, **2009**, *131*, 2151.

48. Warsi, M. F.; Adams, R. W.; Duckett, S. B.; Chechik, V. *Chem. Comm. (Cambridge, U.K.)*, **2010**, *46*, 451.

49. Marradi, M.; Alcantara, D.; de la Fuente, J. M.; Garcia-Martin, M. L.; Cerdan, S.; Penades, S. *Chem. Comm.*, **2009**, 3922.

50. Moriggi, L.; Cannizzo, C.; Dumas, E.; Mayer, C. R.; Ulianov, A.; Helm, L. *J. Am. Chem. Soc.*, **2009**, *131*, 10828.

51. Song, Y.; Xu, X. Y.; MacRenaris, K. W.; Zhang, X. Q.; Mirkin, C. A.; Meade, T. J. *Angew. Chem. Int. Ed.*, **2009**, *48*, 9143.

52. Ahamed, M.; Karns, M.; Goodson, M.; Rowe, J.; Hussain, S. M.; Schlager, J. J.; Hong, Y. *Toxicol. Appl. Pharmacol.*, **2008**, *233*, 404.

53. Arora, S.; Jain, J.; Rajwade, J. M.; Paknikar, K. M. *Toxicol. Appl. Pharmacol.*, **2009**, *236*, 310.

54. Babu, K.; Deepa, M. A.; Shankar, S. G.; Rai, S. *Internet J. Nanotechnol.*, **2008**, *2*, no pp given.

55. Hyun, J.-S.; Lee, B. S.; Ryu, H. Y.; Sung, J. H.; Chung, K. H.; Yu, I. J. *Toxicol. Lett.*, **2008**, *182*, 24.

56. Panyala, N. R.; Pena-Mendez, E. M.; Havel, J. *J. Appl. Biomed.*, **2008**, *6*, 117.

57. Tang, J.; Xiong, L.; Wang, S.; Wang, J.; Liu, L.; Li, J.; Wan, Z.; Xi, T. *Appl. Surf. Sci.*, **2008**, *255*, 502.

58. Travan, A.; Pelillo, C.; Donati, I.; Marsich, E.; Benincasa, M.; Scarpa, T.; Semeraro, S.; Turco, G.; Gennaro, R.; Paoletti, S. *Biomacromolecules*, ACS ASAP.

59. Yang, W.; Shen, C.; Ji, Q.; An, H.; Wang, J.; Liu, Q.; Zhang, Z. *Nanotechnology*, **2009**, *20*, 085102/1.

60. Aslan, K.; Wu, M.; Lakowicz, J. R.; Geddes, C. D. *J. Am. Chem. Soc.*, **2007**, *129*, 1524.

61. Xue, C.; Chen, X.; Hurst, S. J.; Mirkin, C. A. *Adv. Mater. (Weinheim, Ger.)*, **2007**, *19*, 4071.

62. Ma, Z. Y.; Dosev, D.; Kennedy, I. M. *Nanotechnology*, **2009**, *20*, 085608/1.

63. Lacava, L. M.; Garcia, V. A. P.; Kuckelhaus, S.; Azevedo, R. B.; Sadeghiani, N.; Buske, N.; Morais, P. C.; Lacava, Z. G. M. *J. Magn. Magn. Mater.*, **2004**, *272–276*, 2434.

A Survey Study of Interactions of Gold Nanoparticles with Common Human Blood Plasma Proteins*

SILVIA H. DE PAOLI LACERDA and JACK F. DOUGLAS

Center for Biologics Evaluation and Research, Food and Drug Administration, Bethesda, Maryland, USA

ALAMGIR KARIM

Department of Polymer Engineering, University of Akron, Akron, Ohio, USA

In order to better understand the physical basis of the biological activity of nanoparticles (NPs) in nanomedicine applications and under conditions of environmental exposure, we performed an array of photophysical measurements to quantify the interaction of model gold NPs having a wide range of NP diameter with common blood proteins. In particular, absorbance, fluorescence quenching, circular dichroism, dynamic light scattering, and electron microscopy measurements were performed on surface-functionalized water-soluble gold NPs having a diameter range from 5 to 100 nm in the presence of common human blood proteins: albumin, fibrinogen, γ-globulin, histone, and insulin. We find that the gold NPs strongly associate with these essential blood proteins, where the binding constant K and the degree of cooperativity of particle–protein binding (Hill constant n) depend on particle size and the native protein structure. We also find tentative evidence that the model proteins undergo conformational change upon association with the NPs and that the thickness of the adsorbed protein layer (bare NP diameter < 50 nm) progressively increases with NP size, effects that have potential general importance for NP aggregation in biological media and the interaction of NPs with biological materials broadly.

8.1. INTRODUCTION

Living systems, such as cells, exploit protein self-assembly to create organized structures that display an amazing array of functions. The promise of the emerging field of nanotechnology revolves around the creation of nanoparticle (NP) synthetic analogs of proteins that exhibit similar efficient self-organization and functionality. Recently, there has been particular interest in using NPs to probe biological processes that are critical for diagnostics and the modulation of cell functions. However, relatively little is known about the potential biological risks from NP therapeutic applications (i.e., NPs as drugs or drug carriers).[1] Tragic experience has educated us about the long time scale (decades) that can separate exposure and pathology, as in the case of nanorods of blue asbestos,[2] and it appears that carbon nanotubes may exhibit a similar carcinogenic potential.[3] Other recent clinical studies have indicated clear adverse health effects of NP exposure in some NP systems such as an essentially immediate increased risk of heart attack in the elderly and associated with NP-induced changes in blood viscosity and blood clotting capacity from NP exposure through respiration.[4] Evidently, NPs can act as a double-edged sword, either as a toxic agent or as a platform for therapy, depending on context. This has led to increasing interest in obtaining an improved understanding of protein–NP interactions and the biological implications of these interactions[5, 6] to aid in the controlled development of these promising materials. Based on this broad biological and medical background relating to using NPs for therapeutic applications and in understanding the toxic response that can result from their environmental exposure, we focus on the adsorption of common plasma proteins on model NPs to better understand the nature of the NP–protein interactions underlying this phenomena.

8.1.1. Background Information About Blood Plasma Proteins

There are a variety of pathways by which NPs enter the bloodstream and their interaction with plasma proteins is inevitable. It is currently unclear whether the NP–blood protein interactions are specific or nonspecific so we included a range of essential proteins in our study. Below, we summarize the proteins considered and summarize briefly some of their essential functions.

The types of biophysical forces (electrostatic, hydrophobic, hydrogen bonding, and van der Waals) involved in the interaction of drugs with protein are likely to be similar to those involved in the interaction of NPs with proteins. The size of NPs and their interactions are frequently similar to those of proteins and viruses, accounting for the significant biological activity of NPs. We can also expect a general tendency of the proteins to bind to the NP and it is the biological response of these "dressed" particles that is of interest from a health standpoint.

A better understanding of the biological effects of NPs most basically requires knowledge of the binding properties of proteins that associate with the particles in biological fluids.[6, 7] As in the case of drugs, NPs can "hitchhike" on carriers or transporters that act on natural endogenous substrates. The types of biophysical forces involved in the interaction of drugs with protein (electrostatic, hydrophobic, hydrogen bonding, and van der Waals) are likely to be similar to those involved in the

interaction of NPs with proteins. Additionally, the size of NPs is comparable to that of proteins and viruses, accounting for the significant biological activity of NPs.

Human blood plasma, like cells, contains many proteins that perform various housekeeping functions. In fact, blood plasma possesses the most complex human-derived proteome: It is estimated that up to 10^4 proteins may be commonly present in serum, most of which are present at very low relative abundances. Plasma proteins participate in molecular transport and are critical for signaling cascades and regulatory events, being also a medically relevant diagnostic tool as biomarkers for diseases and the efficiency of medical treatment.

Table 8.1 shows properties and physiological functions of some essential blood plasma proteins used here to study their interaction with gold NPs decorated with citric acid (the most common surface coating for gold NPs since it assists in their synthesis and promotes NPs' solubility in water).

Human serum albumin (HSA) is a multifunctional transporter molecule and is the most abundant protein in the circulatory system. HSA binds a wide variety of endogenous and exogenous compounds with binding constants in the range of $K < 10^7$ (mol/L)$^{-1}$ to 10^8 (mol/L)$^{-1}$ [18]. There is evidence that HSA may act more specifically by targeting ligands to particular tissues. The association of HSA with NPs may cause conformation modifications of the HSA molecule, which can be expected to lead to transport malfunctions and can be involved in the development of pathology. The diverse HSA function for all transport stages is based on the high conformational flexibility of this protein molecule and its labile binding characteristics. It is likely that, in the presence of NPs, changes occur in HSA binding capacity to metabolites, toxins, and pharmacological drugs.

Fibrinogen is the second most abundant protein in the blood. It can also host NPs, leading to inappropriate biological response. Denaturation of fibrinogen can affect its "polymerization" and therefore affect clotting property. It was demonstrated that NPs increase the risk of heart attack in the elderly by inducing changes in the blood viscosity and clotting capacity.[18]

γ-Globulin is another major blood plasma protein involved in transport and body defenses, as well as control of circulation and biologically active insulin. Nuclear histones are among many other proteins that can interact with NPs traveling in the bloodstream and alter their behavior.

The total protein concentration in bodily fluids can be up to 35% by mass, representing numerous proteins (> 3700) that span a wide range of concentrations.[6] As a result, there is competition between proteins for available NP surface area in a typical biological environment. HSA and fibrinogen may dominate on the particle surface at short exposure times, but these proteins will be subsequently displaced by proteins having a lower abundance but higher affinity at longer exposure times.[19]

8.2. CHARACTERISTIC SCALE OF NP UPTAKE BY CELLS: BIOLOGICAL CONSIDERATIONS

We briefly consider some of the potential implications of our observations. It has been established that cell responses to NPs such as uptake, clearance, and biodistribution

TABLE 8.1. Basic Characteristics of Human Blood Plasma Proteins

	HSA	Fibrinogen	γ-Globulins	Insulin	Histones
Plasma	8.2 g/L	2.68 g/L	25 mg/mL	45 pmol/L	• Higher in patients with lupus and neoplastic diseases
Overall dimension (nm)	11.8 ± 0.1^a (4×14)	28.6 ± 0.2^a $(5 \times 45)^b$	14.6 ± 0.1^a $(11 \text{ to} 13)^b$	10 ± 0.1^a $(2 \times 2.5 \times 3)^b$	46.5 ± 0.2^a -
Isoelectric point	4.7	5.1 to 6.3	6.8 to 6.9	5.3	11.3
M(KDa)	66	340	155–160	5.7	15
Primary physiological function	• Regulates osmotic pressure and pH • Multifunctional transporter • Relevant in biocompatibility and drug delivery	• Blood clotting • Relevant in biocompatibility and drug delivery	• Defense mechanism • Transport	• Hormone with intensive effects on metabolism	• Binding and compaction of DNA in the chromatin. • Gene activation
Chromophore residues	Tryptophan and tyrosine	Tryptophan and tyrosine	Tryptophan and tyrosine	Tyrosine	Tyrosine
References	9	10	11,12	13,14	15–17

[a] Obtained by the average of five individual DLS measurements. Uncertainty is the standard deviation.
[b] See appropriate reference.

after intravenous administration are size dependent.[20, 21] Interestingly, 50 nm often shows up as a characteristic scale in many biological systems. For example, in an uptake study of citrate-coated gold NPs (14 nm to 100 nm) by mammalian cells[22, 23] the fastest and highest uptake by cells occurred with NPs having a diameter of ∼50 nm. Osaki et al.[24] similarly found that 50 nm semiconductor NPs entered cells via receptor-mediated endocytosis more efficiently than smaller NPs. Jiang et al.[25] have also found that 40 nm to 50 nm gold NPs form an upper critical cutoff scale for receptor-mediated internalization. Finally, studies of a range of NPs having a diameter range between 2 nm and 100 nm showed that NPs of ≈50 nm diameter were the most likely to induce cell death.[25] Again, we are confronted with a characteristic nanoscale dimension in the range between 50 nm and 100 nm. What is the biological significance of this scale?

Factors such as NP adsorption on the cell membrane and membrane deformation have been suggested to influence the uptake of NP dependence on size.[22, 26, 27] The rate of cellular uptake should depend on the thermodynamic driving force for the membrane to "wrap" the particle and the rate of membrane receptor diffusion. These competing factors determine how fast and how many NPs are taken up by the cell, and Gao et al.[26] suggest that NPs having a size of about ≈55 nm should exhibit the highest rate of uptake. Experimentally, individual 50 nm citrate-coated gold NPs were observed to enter the cells, while 14 nm diameter NPs required the formation of clusters having at least six NPs before uptake was observed,[22] suggesting that this characteristic length scale is pretty well defined. Interestingly, intercellular vesicles containing 50 nm NPs also tended to exhibit the largest number of included NPs.[22] These observations together suggest that a combination of energetic and kinetic effects associated with NP–membrane binding and the kinetics of NP–membrane receptor binding underlie the optimal uptake of particles having a scale ≈50 nm. It is also notable, however, that the caveolae (invaginations of the plasma membrane that mediate transcellular endocytotic shuttling) have dimensions of 50 nm to 60 nm,[28] so that the size of the caveolae might play a determining role in determining the cutoff scale in the selective uptake of NPs. Evidently, this phenomenon deserves further attention.

Regarding our own measurements, binding constant K values for HSA, fibrinogen, and histone with gold NPs reach their maximum values for NPs having a diameter ≈60 nm. Such an optimal size for particle uptake is probably due to the higher stability receptor–NP binding in receptor-mediated endocytosis. This internalization process is strongly dependent on the time for the membrane to wrap the particle, which depends on the diffusion rate of receptors on the plasma membrane surface. NPs that associate more strongly with protein receptors on the cell surface, resulting in prolonged receptor binding, are more likely to be engulfed by cells if this is geometrically possible. It has been shown that binding of highly extended particles such as carbon nanotubes may be frustrated if these particles become too long for the endocytotic cell machinery to accommodate and the uptake of these NPs is inhibited beyond a critical length.[29] The machinery of NP uptake into the cell is again implicated in the selective size dependence of the NP uptake and response.

In addition to NP size, changes in the NP interactions through protein adsorption onto the NP can also be expected to play a large role, probably on the effectiveness of

NP uptake. Protein adsorption onto negatively charged citrate-coated gold NPs should diminish the electrostatic repulsion between NPs and negatively charged membrane surfaces, leading to an enhanced adsorption of the NP–protein complex onto the membrane, an effect progressively building up as more NP–particle complexes become adsorbed. In this way, the NP becomes more available for cell uptake. Consistent with this argument, we directly observe a strong tendency of the protein-coated NPs to agglomerate on the cell membrane, in emission scanning electron microscopy (FESEM) and fluorescence microscopy imaging (data not shown).

Gold NPs are a natural starting point for understanding NP–protein interactions because of their promise for diverse biomedical applications, including their use as probes in many biodiagnostic systems,[30] photothermal and targeted drug-delivery treatments of cancer.[31, 32] Additionally, gold NPs allow for facile bioconjugation, which makes them useful platforms for multicomponent systems. These attractive properties account for our initial focus on gold NPs as our model particle system. As far as we know, there has been no systematic and comparative study of the binding association of human plasma proteins with gold NP, apart from a study by Brewer et al.[33] on the specific protein bovine serum albumin (BSA) and citrate-coated gold NPs.

A wide range of photophysical techniques such as absorbance, fluorescence quenching, dynamic light scattering, circular dichroism (CD), and electron microscopy (EM) are used in our study to characterize various aspects of the protein–NP interaction and these techniques are briefly described in Section 8.5. These measurement methods allow for the determination of a number of basic properties: the binding (or association) constant of the proteins with gold NPs, changes in protein conformation upon adsorption, NP size, protein–NP aggregation, and thickness of the protein layer on the NP. Specifically, fluorescence quenching measurements give information about the protein–particle binding kinetics and equilibrium and protein conformational change, absorbance and EM give information about the sizes of the bare and coated particles, CD informs about changes in protein structure upon binding, and dynamic light scattering and EM provide information about the formation and size of particle aggregates. The use of these combined methods should provide a general perspective of how NP size affects the nature of protein binding and the extent to which these effects are protein specific.

8.3. RESULTS AND DISCUSSION: PHOTOPHYSICAL MEASUREMENTS RELATING PROTEIN–NANOPARTICLE INTERACTIONS

8.3.1. Fluorescence Quenching of Human Plasma Proteins by Gold NPs of Different Sizes

The application of fluorescence spectroscopy to the study of the structure and conformation of proteins has proved fruitful.[34–45] Specifically, the photoluminesce (PL) quenching technique has been widely applied in biochemical problems owing to its high sensitivity, reproducibility, and convenience. The emission characteristics of

tryptophan, tyrosine, and phenylalanine residues in proteins can provide a convenient handle for investigating binding and conformation changes upon association with small molecules,[36, 46, 47] NPs,[33–35, 48, 49] and membranes.[39, 42] In our studies, we take advantage of the fact that gold metal efficiently quenches the emission of many chromophores.[50] The efficiency of fluorescence quenching ability depends on the distance between the quencher and the chromophore[51] and measurements of PL quenching by proteins reveals information about the relative accessibility of gold NPs to protein chromophore groups.[34, 35, 40, 42, 47, 49, 50]

The effect of gold NPs on the PL intensity of our model blood proteins is illustrated in Figure 8.1, which shows the emission spectra of histone H3 in the control case where the NPs are absent and in the presence of gold NPs. The changes in the histone PL derives solely from the tyrosine residue, and changes in the PL of this residue have previously been used extensively to study the complexing of histone with biological molecules and self-assembled structures.[52] Evidently, gold NPs having a diameter in a range between 5 nm and 100 nm efficiently quench the histone PL, as evidenced by the progressive decrease in the emission maximum intensity with decreasing NP size. This quenching effect indicates a direct interaction with the gold NP chromophore residues of the proteins having an interaction radius of < 10 nm.[53]

The change in the maximum fluorescence emission spectrum intensity I_{max} arises from a change of protein conformation,[33–36, 46, 49] which in the present case is due to protein adsorption onto the NPs, and reflects relative changes in the proximity between the active fluorescence emitters (tyrosine or tryptophan) in the proteins and the quenching agent (the gold NPs). The strong decrease in I_{max} with NP size indicates that the relative fluorescence quenching is increasing progressively with protein concentration, as show in the Figure 8.1f, since the amount of absorbed protein follows this basic trend. Stronger binding of the proteins to the NPs naturally should also give rise to conformational changes of the protein, where more of the amino acids of the bound protein are in proximity with the surface, and to more efficient fluorescence quenching. Particle size, charge, and other thermodynamic factors that affect the strength of protein–NP binding should likewise influence the relative value of the protein–NP binding equilibrium constant K, which quantifies the relative strength of the protein-NP binding. We quantitatively examine the effect of NP size on K below.

The shift of the peak intensity wavelength of the fluorescence emission spectrum intensity in Figure 8.1 also contains significant information about the protein layer adsorbed on the NP. The blue shift of this feature is symptomatic of a shift of the dielectric properties of the medium, or more specifically the polarity of the local environment of the emitter species[20, 34] with the observed blue shift corresponding to a relatively nonpolar environment. Evidently, the local dielectric environment within the fully developed adsorbed protein layers is less polar than the corresponding emitter environment of the protein dispersed in solution. This is another easily understood trend from a qualitative standpoint.

Once the protein associates with the NPs, the tyrosine and tryptophan residues accessible to the metallic surface of the NPs are then quenched. Figure 8.1 shows that this process is accompanied by the appearance of an isobestic point indicating the
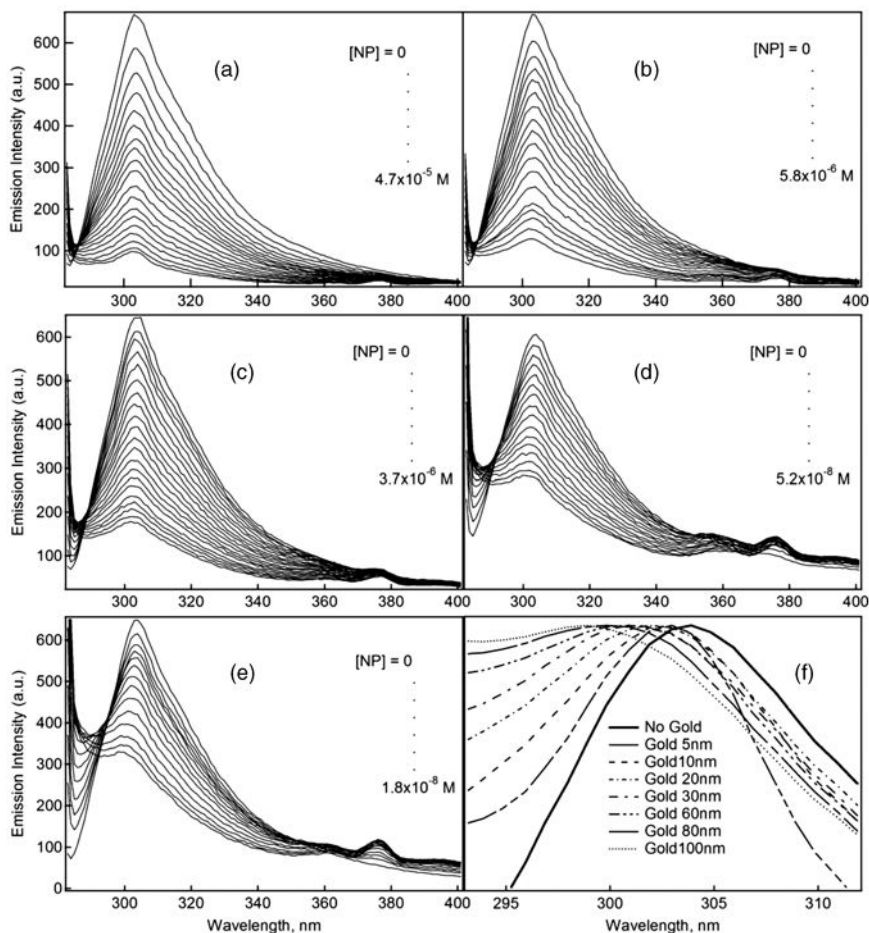
Figure 8.1. Fluorescence quenching of histone (H3) by gold NPs measuring (a) 5 nm; (b) 10 nm, (c) 20 nm, (d) 60 nm, (e) 100 nm, and (f) expanded and normalized emission spectra of histone in the absence and presence of gold NPs showing a shift of the emission peak. The normalization is defined so that the emission peak intensity is divided by I_{max} so that the normalized peak intensity equals 1. The protein concentration was fixed at 0.01 mg/mL and the NP was varied over a range concentration range: (a) 5 nm: (0 to 4) $\times 10^{-5}$ M; (b) 10 nm: (0 to 5.8) $\times 10^{-6}$ M; (c) 20 nm: (0 to 3.7) $\times 10^{-6}$ M; (d) 60 nm: (0 to 5.2) $\times 10^{-8}$ M, and (e) 100 nm: (0 to 1.8) $\times 10^{-8}$ M.

presence of reaction intermediates during conjugation.[54] The presence of the isosbestic point is also indicative of a change of the excited state energy.[54] This feature is found in the histone system as shown in Figure 8.1 and is also found for all the other model blood proteins (HSA, globulins, fibrinogen, and insulin) we consider.

The relative kinetic efficiency of fluorescence quenching can be estimated by fitting the dependence of I^o/I on gold NP concentration (Figure 8.2a) based on a fitting
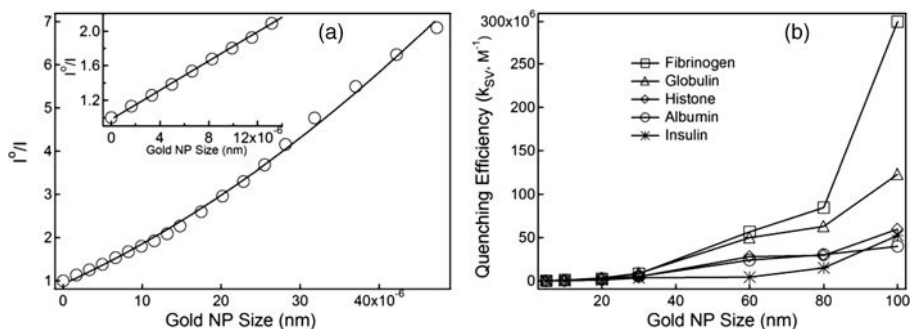
Figure 8.2. Efficiency of fluorescence quenching of plasma proteins. (a) Stern–Volmer plot of HSA fluorescence quenching by gold NPs having a 5 nm diameter. (Inset) Linear regime at the low fluorescence quencher concentration. (b) Effect of NP diameter.

to the Stern–Volmer equation (see Section 8.5).[37] We find that k_{SV} generally increases with NP size, as represented in Figure 8.2b. The larger the gold NP, the stronger the fluorescence quenching becomes. This trend was observed previously by Jiang et al.[25] for Texas Red-labeled herceptin bound to gold NPs, Cy3 dye-labeled RNA adsorbed[55] onto gold NPs, and cationic polymers/oligomers conjugated[50] to gold NPs. The time for the energy transfer and dye's radiative transfer rate were also observed to decrease with increasing NP size.[56] However, since the concentration of gold is the same for these particles, larger particles imply a lower relative particle surface area. The increase in surface area with a progressive decrease in particle size can accommodate a large number of molecules around the gold particles so that smaller particles are more efficient fluorescence quenchers than larger ones. This trend has been observed in NPs in the presence of small fluorescent molecules, such as 1-methylaminopyrene,[57] lissamine,[56] and thionine.[58] Notably, we find the *opposite* trend of fluorescence quenching with NP size in the case of proteins versus biomacromolecule adsorption measurements. The higher surface curvature of the smaller particles reduces the amount of protein that can adsorb onto their surface, and for this reason, the fluorescence quenching is *less efficient* for the smaller NPs.[25] Our measurements of the protein–NP binding equilibrium constant K as a function of particle size also provides insight into the trend toward stronger fluorescence quenching with increasing NP size. Specifically, K increases progressively with NP size so that more of the amino acids of the bound protein on larger NPs are naturally in proximity with the adsorbing gold NP surface and the rate of fluorescence quenching is then higher.

It is known that some proteins bind to the NP surface and retain their native-like structure, while others undergo denaturation of their tertiary structure and even their secondary structure can be disrupted in some cases.[46, 59] Moreover, the protein may be bound in a preferred orientation,[60, 61] and the degree of denaturation depends on NP surface chemistry[62] as well as its NP surface curvature.[63, 64] We utilize circular dichroism or CD to explore in greater detail how the adsorption of proteins on the NPs alters the protein conformation. First, we characterize the strength and cooperativity

of the adsorption of the proteins onto the NP since many of the property changes that we observe directly derive from this adsorption process.

8.3.2. Gold NP–Protein Binding Constant (K) and Protein Binding Cooperativity (n)

Note: We do not expect that the quantum size effect of gold NPs in the studied range affects the protein binding. A surface phenomenon like catalysis by gold NPs (i.e., CO oxidation) presents a quantum size effect for gold NP size of $< 5\,\text{nm}$.[47]

NPs in the diameter range 1 nm to 100 nm display physical properties that can be quite different from those of the bulk metal and are strongly dependent on particle size, interparticle distance, the nature of the protecting organic shell layer about the NP, and NP shape.[65] Several issues must then be addressed in understanding the magnitude of the protein–NP binding interaction. Specifically, we must first consider the geometrical accommodation of the protein onto the NP surface, the chemical interactions between the protein and NP surface. There is also the more subtle matter of the multifunctional nature of the binding interactions of the proteins to the NP, which should affect the cooperative nature of the protein–NP complex formation (i.e., the relative sharpness of the binding transition as the protein concentration or temperature is varied). We quantitatively determine a measure of the binding cooperativity below and explore how NP size affects this basic binding property.

The binding association constants K (see Section 8.5 for its definition and determination) for plasma proteins onto gold NPs were found to be in the range of 10^4 to 10^7 $(\text{mol/L})^{-1}$, the same range as that found previously for the binding of chymotrypsin to amino acid-functionalized gold NPs[66] and bovine serum albumin to 10 nm citrate-coated gold NPs.[33] As shown in Figure 8.3b, the binding association constants for proteins onto gold NPs increase progressively with NP diameter in the range between 5 nm and 60 nm. On the other hand, we find that the binding association constant can become slowly varying for some NPs having a diameter larger than about 80 nm. A comparable crossover scale shows up in diverse nanoscale phenomena,[67, 68] but there has been no generally accepted explanation of its
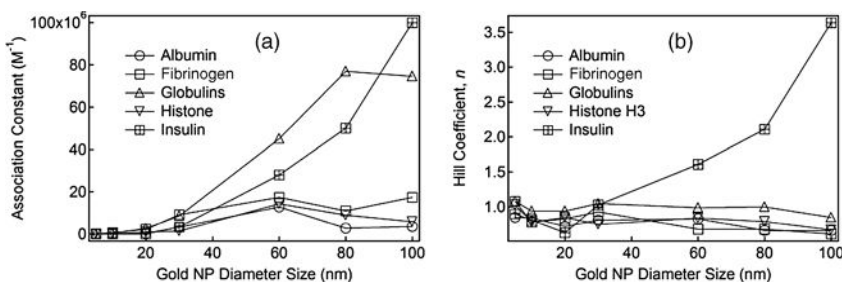
Figure 8.3. Effect of NP size on protein association. (a) Effect of NP size on the binding association constant between gold NP–protein complex. (b) Effect of NP size on the Hill coefficient, n, a quantitative measure of the cooperativity of mutual NP–protein binding.

molecular significance. We briefly discuss the biological significance of this scale with respect to NP uptake by cells.

Apparently, there are competing effects that contribute to the variation of K with NP size and these trends are not universal, despite our observations. For example, Jiang et al.[25] studied the binding of herceptin-coated gold NPs in the range of 2 nm to 70 nm with ErbB2 receptor and found that K tended to increase with increasing NP size. A similar effect was observed on the binding of polyfluorenes to citrate-functionalized gold NPs in a size range between 2 nm and 20 nm.[50] Evidently, the higher protein packing density on the surface of larger NPs leads to a corresponding increase in K. A contrary trend has been established in the chemisorption of oligonucleotide chains to gold NPs, where a less efficient polymer surface packing is observed in larger NPs because of the *enhancement* of the excluded volume interactions within the extended random coil nucleotide chains on the particle surface[69] and proteins in unfolded conformations should exhibit a similar behavior. This comparison emphasizes the potential role of the conformational state of the adsorbed proteins in understanding the nature of protein layers that form on NPs and the associated variation of K with NP size.

We find a clear dependence of the binding and dissociation parameters on protein identity and NP size in our measurements. In real bodily fluids, the total protein concentration can be as large as 35% by volume and there can be several thousand different proteins present whose relative uncertainties span a wide range. Consequently, there must be a competition between these proteins in their adsorption on the NPs dispersed within this complex biological environment. In particular, we expect the two major proteins present in plasma HSA and fibrinogen to generally dominate the interaction with NPs at short times due to their greater availability for adsorption, but over time these species should became displaced by proteins with higher relative affinity, a lower abundance, and slower adsorption kinetics. This general phenomenon has indeed been observed[7–70] but quantification is understandably limited. Although this is an extremely complex phenomenon, measurements on K for individual protein–NP systems should give a rough idea of the *relative* rates in this competitive, many-component adsorption process when particle and protein concentration effects on rates are considered. Measurements exploring the rate at which one species displaces another adsorbed species would also provide more information about this extremely complex and practically important phenomenon, but this will have to await future study. We next turn to quantifying the cooperativity of the protein–NP binding process.

The Hill coefficient n (see Section 8.5 for definition) is a frequently utilized measure of binding cooperativity and Figure 8.4 shows Hill plots associated with our protein–NP binding measurements. Parameters obtained from an analysis of this data and their uncertainties are summarized in Table 8.2. Figure 8.3b shows the relationship between the Hill coefficient n and NP size. For HSA, fibrinogen, histone, and globulin proteins, we observe anticooperative binding ($n < 1$), which indicates within the frame of the Hill model that the association energy per particle progressively decreases with further protein adsorption. Insulin presents an opposite trend and therefore $n > 1$. The trend toward a diminished cooperativity of protein binding to

TABLE 8.2. Gold NP–Protein Binding Parameters Obtained from Fluorescence Quenching Data[a]

	Gold Nanoparticle Diameters						
	5 nm	10 nm	20 nm	30 nm	60 nm	80 nm	100 nm
Histone							
Q_{max}	1.13 ± 0.03[b]	1.42 ± 0.07	1.38 ± 0.03	1.73 ± 0.13	1.35 ± 0.09	1.77 ± 0.29	2.71 ± 1.86
n	1.03 ± 0.03	0.78 ± 0.02	0.85 ± 0.01	0.75 ± 0.02	0.84 ± 0.02	0.79 ± 0.03	0.67 ± 0.062
K_d	$1.00 \times 10^{-5} \pm 9.22 \times 10^{-7}$	$4.10 \times 10^{-6} \pm 5.2 \times 10^{-7}$	$1.04 \times 10^{-6} \pm 5.85 \times 10^{-8}$	$6.76 \times 10^{-7} \pm 1.17 \times 10^{-7}$	$6.95 \times 10^{-8} \pm 1.00 \times 10^{-8}$	$1.11 \times 10^{-7} \pm 3.70 \times 10^{-8}$	$1.69 \times 10^{-7} \pm 1.07 \times 10^{-8}$
K	1×10^5	2.44×10^5	9.62×10^5	1.48×10^6	1.44×10^7	9.01×10^6	5.92×10^6
R^2	0.998	0.999	0.999	0.999	0.999	0.999	0.998
γ-Globulin							
Q_{max}	1.40 ± 0.06	1.26 ± 0.04	1.13 ± 0.04	1.07 ± 0.03	1.03 ± 0.04	0.91 ± 0.11	1.24 ± 0.11
n	1.08 ± 0.03	0.94 ± 0.03	0.94 ± 0.03	1.05 ± 0.04	0.99 ± 0.04	1.00 ± 0.09	0.85 ± 0.04
K_d	$1.00 \times 10^{-5} \pm 1.23 \times 10^{-6}$	$1.92 \times 10^{-6} \pm 1.40 \times 10^{-7}$	$3.71 \times 10^{-7} \pm 3.8 \times 10^{-8}$	$1.15 \times 10^{-7} \pm 7.50 \times 10^{-9}$	$2.22 \times 10^{-8} \pm 2.09 \times 10^{-9}$	$1.30 \times 10^{-8} \pm 3.26 \times 10^{-9}$	$1.34 \times 10^{-8} \pm 2.78 \times 10^{-9}$
K	1×10^5	5.21×10^5	2.70×10^6	8.70×10^6	4.50×10^7	7.69×10^7	7.46×10^7
R^2	0.999	0.999	0.998	0.998	0.998	0.994	0.998

Fibrinogen

Q_{max}	0.99 ± 0.01	1.26 ± 0.06	1.04 ± 0.06	0.92 ± 0.03	1.08 ± 0.37	1.64 ± 0.93	1.20 ± 0.73
n	1.08 ± 0.02	0.78 ± 0.03	0.83 ± 0.04	0.93 ± 0.03	0.68 ± 0.08	0.68 ± 0.07	0.61 ± 0.16
K_d	$3.90 \times 10^{-6} \pm 7.83 \times 10^{-8}$	$1.54 \times 10^{-6} \pm 2.07 \times 10^{-7}$	$4.52 \times 10^{-7} \pm 6.72 \times 10^{-8}$	$1.08 \times 10^{-7} \pm 9.28 \times 10^{-9}$	$5.70 \times 10^{-8} \pm 1.02 \times 10^{-8}$	$9.07 \times 10^{-8} \pm 1.0 \times 10^{-8}$	$5.71 \times 10^{-8} \pm 2.05 \times 10^{-9}$
K	2.56×10^5	6.49×10^5	2.21×10^6	9.26×10^6	1.75×10^7	1.10×10^7	1.75×10^7
R^2	0.999	0.998	0.997	0.999	0.994	0.994	0.987

Insulin

Q_{max}	1.38 ± 0.02	1.72 ± 0.14	4.95 ± 3.44	1.03 ± 0.18	0.72 ± 0.06	0.39 ± 0.06	0.13 ± 0.01
n	0.90 ± 0.01	0.81 ± 0.02	0.63 ± 0.03	1.03 ± 0.09	1.61 ± 0.07	2.11 ± 0.15	3.64 ± 0.55
K_d	$4.00 \times 10^{-5} \pm 1.66 \times 10^{-6}$	$1.00 \times 10^{-5} \pm 2.11 \times 10^{-6}$	$3.00 \times 10^{-5} \pm 4 \times 10^{-6}$	$2.93 \times 10^{-7} \pm 9.55 \times 10^{-8}$	$3.57 \times 10^{-8} \pm 4.01 \times 10^{-9}$	$2.00 \times 10^{-8} \pm 2.91 \times 10^{-9}$	$1.02 \times 10^{-8} \pm 1.28 \times 10^{-9}$
K	2.50×10^5	3.33×10^4	1.00×10^5	3.41×10^6	2.80×10^7	5.00×10^7	9.80×10^7
R^2	0.999	0.999	0.999	0.996	0.999	0.998	0.989

HSA

Q_{max}	1.27 ± 0.31	1.22 ± 0.04	1.94 ± 0.31	1.21 ± 0.08	1.33 ± 0.02	2.91 ± 0.27	2.88 ± 2.22
n	0.85 ± 0.02	0.84 ± 0.02	0.72 ± 0.03	0.81 ± 0.03	0.83 ± 0.04	0.66 ± 0.06	0.66 ± 0.04
K_d	$1.00 \times 10^{-5} \pm 8.83 \times 10^{-7}$	$3.30 \times 10^{-6} \pm 3.15 \times 10^{-7}$	$2.45 \times 10^{-6} \pm 8.99 \times 10^{-7}$	$3.01 \times 10^{-7} \pm 5.08 \times 10^{-8}$	$7.74 \times 10^{-8} \pm 2.08 \times 10^{-8}$	$3.54 \times 10^{-7} \pm 5.29 \times 10^{-8}$	$2.74 \times 10^{-7} \pm 1.24 \times 10^{-8}$
K	1×10^5	3.03×10^5	4.08×10^5	3.32×10^6	1.29×10^7	2.82×10^6	3.65×10^6
R^2	0.999	0.999	0.998	0.999	0.998	0.997	0.999

[a] R^2 is the correlation coefficient from the least squares fit.
[b] Uncertainty intervals represent the maximum from the data point to the fitted curve.

231
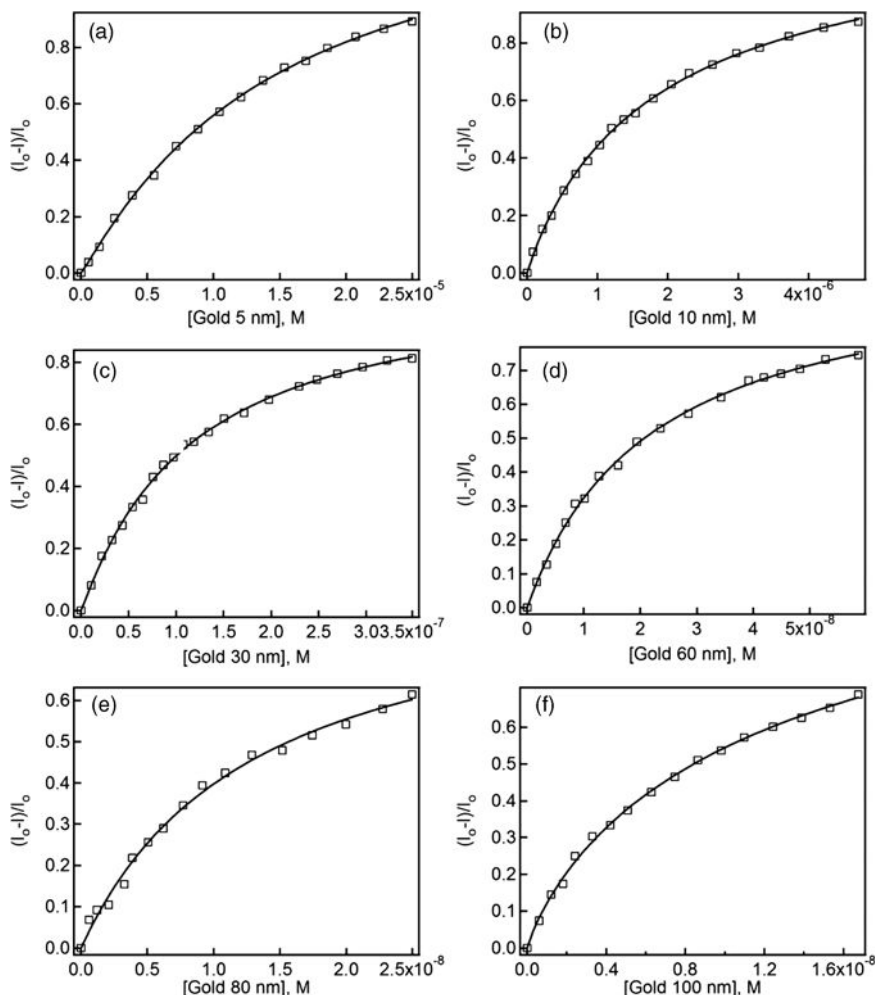
Figure 8.4. Fluorescence quenching properties of γ-globulins by gold NPs of different sizes. Data was fit to Eq. 8.2 (solid line).

larger NPs probably reflects changes in the physicochemical properties of the NP upon progressive protein adsorption. In particular, the adsorption of protein onto the negatively charged citrate-coated gold NPs must reduce the electrostatic binding energy and thus the relative magnitudes of the enthalpy and entropies of protein binding,[71] thus rationalizing the anticooperativity (relatively small value of n) of the protein adsorption on the NP. If the NPs induce the proteins to organize at their boundaries, on the other hand, we may naturally expect an enhancement of the cooperativity of the NP–protein binding transition. (See Table 8.2.)

It appears from Figure 8.5 h that fiber-structures are forming in the insulin/gold particle mixture, suggesting that the gold particles somehow facilitate insulin fiber
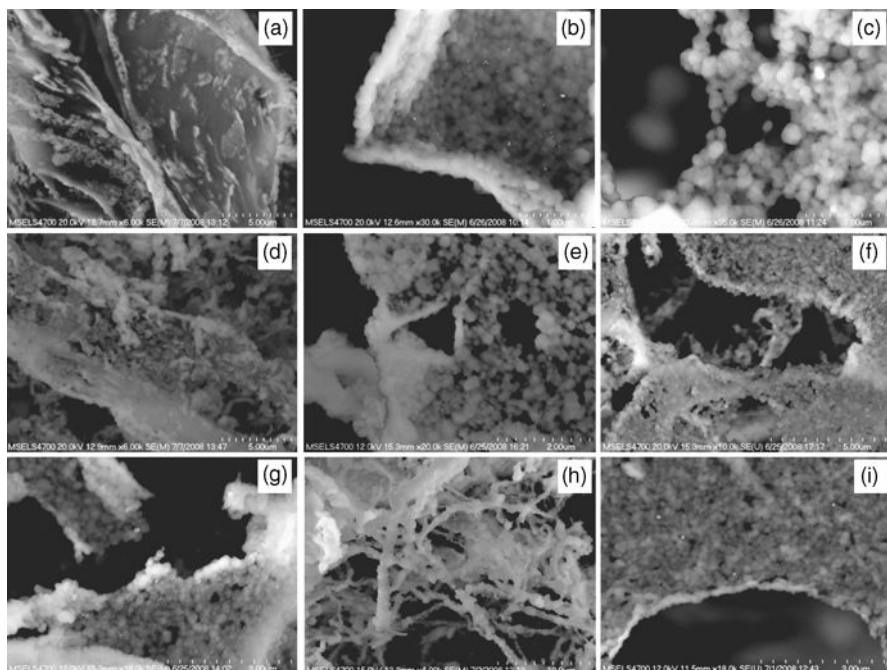
Figure 8.5. Field-emission scanning electron microscopy (FESEM) images of clustered NP states resulting from different NP–protein combinations. (a) HSA; (b) HSA with 20 nm diameter gold NPs; (c) HSA with 80 nm diameter gold NPs; (d) fibrinogen; (e) fibrinogen with 20 nm diameter gold NPs; (f) fibrinogen with 80 nm diameter gold NPs; (g) histone (H3) with 80 nm diameter gold NP; (h) Insulin with 80 nm diameter gold NP; (i) γ-globulin with 80 nm diameter gold NPs. Images presented are representative of at least 20 different regions in each sample.

formation. This NP-induced fiber assembly could well be related to the higher cooperativity of protein binding that we see in this system (see Figure 8.3b). Recently, analytic modeling has demonstrated that a coupling between (protein) adsorption and (fiber growth) self-assembly can alter the sharpness and location of the adsorption transition.[71] From a direct physical standpoint, the protein binding onto the NP surface must alter the charge interaction and dielectric properties of the NPs and the capacity of these "dressed" NPs to induce protein clustering and reorganization upon adsorption. We address the issue of protein reorganization upon NP adsorption below.

8.3.3. Adsorption-Induced Protein Conformational Changes and Circular Dichroism Measurements

It is well established that misfolded proteins, that is, proteins that are not in their functionally relevant "native" conformations, are devoid of normal biological activity. In addition, they often aggregate and/or interact inappropriately with

other cellular components, leading to impairment of cell viability and eventually to cell death.[19] Given these issues, it is crucial to address more specifically the nature of the protein conformational change induced by NP adsorption. We use fluorescence spectroscopy to quantity these changes and we briefly summarize some essential aspects of the physics and chemistry of this type of spectroscopy required to interpret our observations.

As mentioned above, tyrosine and tryptophan fluorescence are players in changes in fluorescence emission induced by changes in local molecular environment. Conformational changes of a protein can in principle be evaluated by the measurement of changes in the peak intensity wavelength λ_{max} in the continuous fluorescence emission intensity spectrum. When multiple tryptophan[45] or tyrosine[43, 72, 73] residues are present, the steady-state fluorescence is the sum of the signals from all the fluorescent residues, located in different parts of the protein. Tryptophan is extremely sensitive to its environment, while this is generally less true for tyrosine, which normally fluoresces with a peak intensity wavelength near ≈ 303 nm, regardless of the polarity of the medium. The λ_{max} shift of tyrosine, on the other hand, is particularly affected by hydrogen bonding between the phenolic hydroxyl groups of tyrosine and other nearby proton acceptors.[54] Histone and insulin contain tyrosine only, and HSA, fibrinogen, globulin, and insulin also contain tryptophan. The amine groups from amino acids forming proteins can bind to the gold surface through a donor–acceptor bond to undercoordinated gold atoms. Cysteine residues bind to gold to form stable protein–gold complexes via coordinate covalent bonding between sulfur and gold. Upon binding, fluorescence of the protein is quenched by gold with substantial blue-shifts of the λ_{max} in their fluorescence spectra, as observed in Figure 8.1f. NPs with greater diameters cause the formation of larger particle–protein interaction surfaces[64] and larger perturbations of the protein conformation as exhibited by Figure 8.1f. Consequently, gold NPs cause bathochromic shifts and peak broadening for all the proteins studied as a result of conformational changes. A blue shift of λ_{max} means that the amino acid residues are buried in a more hydrophobic environment (as discussed above) and are less exposed to the solvent.[43, 72, 74] Figure 8.1f illustrates that the blue shift of λ_{max} induced by the interaction of the gold NPs with proteins increases with NP size. We note that Teichroeb et al.[75] have observed a striking change in the activation energy of protein thermal denaturation with NP size in the adsorption of BSA on gold nanosphere. This effect apparently saturates for some NPs having diameters of ≈ 60 nm, an effect that is likely due to protein conformational change accompanying its adsorption onto NP. This motivates the use of circular dichroism (CD) measurements as a screening test for extensive protein conformational change upon adsorption.

CD is a powerful analytical tool to study the interaction of protein with other molecules and to determine the protein conformation in solution or adsorbed onto other molecules. Here the CD spectra were taken in the wavelength range of 190 nm to 290 nm, and the results are expressed as mean residue ellipticity in millidegrees. Figure 8.6 shows typical CD spectra of HSA, γ-globulin, histone, insulin and fibrinogen in the presence and absence of gold NPs. The ellipticity values in the CD spectra slightly decrease in the presence of gold NPs. This indicates that the
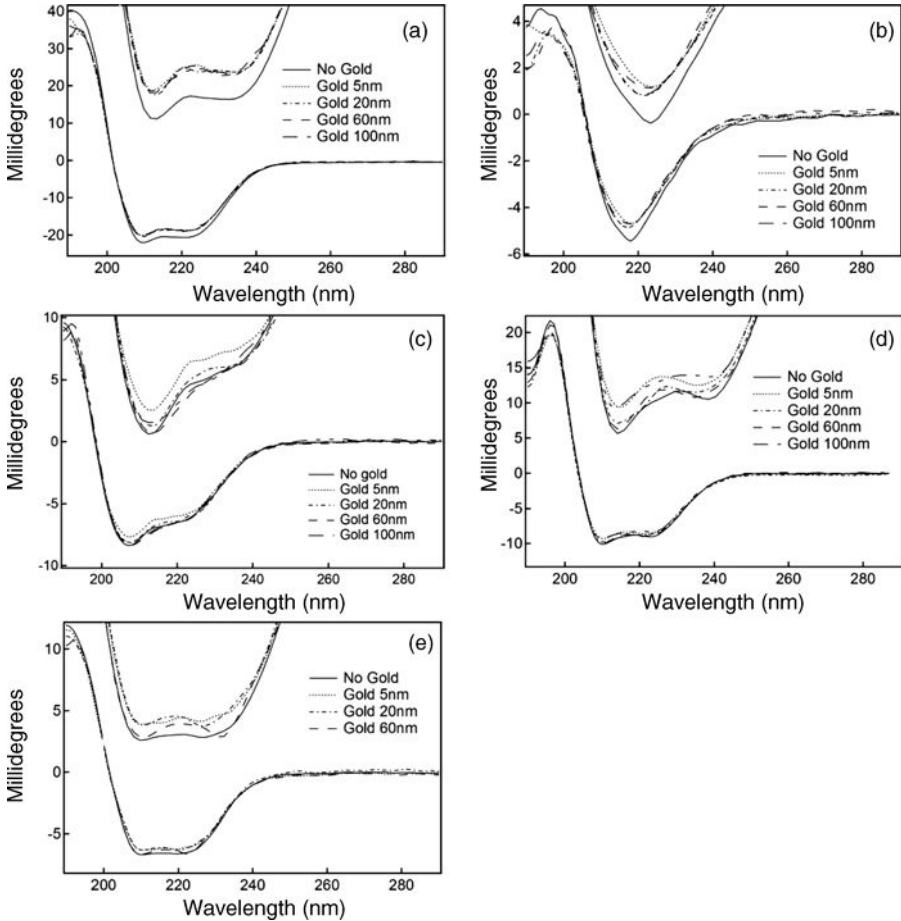
Figure 8.6. Effect of gold NPs on the protein secondary structure. Circular dichroism spectrum: (a) HSA, (b) γ-globulin, (c) histone H3, (d) insulin, and (e) fibrinogen.

conformational change, as indicated also by fluorescence,[76] is limited and occurs only locally; that is, the protein secondary structure (the general three-dimensional form mediated by hydrogen bond) is only slightly disturbed by the NPs.

It has been shown that gold NPs coated with carboxylic groups affect the conformation of protein such as bovine serum albumin (BSA) and anti-BSA antibodies[77] to a much greater degree, indicating that the NP surface coating has an important impact on protein structure where the particle-induced conformational changes should depend on the NP curvature and on protein stability. As demonstrated before, smaller NPs, perhaps owing to the higher surface curvature, seem to better retain native-like protein structure and function in comparison with larger NPs. However, the influence of surface curvature on the structure of adsorbed proteins seems to depend on the particular protein. We conclude that little can generally be said about how NP adsorption induces the extent of protein conformational

rearrangement, even under conditions where the protein binding constants are rather similar. The extent of protein activity probably tracks the extent of adsorption-induced conformational change so that we can expect widely different changes of protein activity after they adsorb onto NPs.

8.3.4. Protein-Mediated NP Aggregation

As in the case of protein adsorption on NPs, the stability of the resulting gold NP complexes against aggregation in biological media is normally highly dependent on the protein concentration and other thermodynamic factors. Indeed, we can expect these phenomena to be strongly linked to each other because the protein adsorption generally changes the NP–NP interactions of the resulting dressed particles, governing the NP association[78] and self-assembly into extended particle clusters, as in the case of protein "nanoparticles." The state of particle aggregation or "dispersion" in turn, is clearly important in NP–cell interactions and in associated NP toxicity resulting from large-scale particle aggregation.[18]

Some basic DLS data for our protein–NP solutions are shown in Table 8.3 resulting from introducing plasma proteins at the same concentration found in the blood to NP solutions. We see that the effective "size" of the NPs increases dramatically as they became coated with the protein and then begin to aggregate due to the presence of this coating. The protein–NP complex formed from this simple mixing process remains stable for 24 h, with the exception of HSA–gold (5 nm) and histone–gold (60 nm) systems, where the apparent hydrodynamic sizes are, respectively, thirteen times and twice as large 24 h after mixing. The NP clustering is also directly apparent in electron microscopy images of gold NP after exposure to the protein solutions (see Figure 8.5).

As expected, the adsorption of the protein onto the NP has a significant impact on the propensity of the NP to aggregate so that the bare surface properties of the particles appear to have little direct relevance for understanding the NP aggregation in biological media.

TABLE 8.3. Dynamic Light Scattering Size Estimates of Gold NP–Protein Complexes[a]

		Diameter of Protein–Gold NP Complex (nm)				
		HSA	Fibrinogen	γ-Globulins	Histone (H3)	Insulin
(5 nm)	0 h	75.8 ± 37.8^b	190.2 ± 24.6	186.7 ± 20.7	209.0 ± 25.5	122.0 ± 23.3
Gold	24 h	186.1	167.2	162.6	297.9	97.8
(60 nm)	0 h	106.82 ± 3.1	95.1 ± 2.7	118.9 ± 3.9	90.7 ± 2.9	53.4 ± 0.5
Gold	24 h	105.2	109.6	89.9	130	50.1
(100 nm)	0 h	122.4 ± 3.6	123.4 ± 3.72	127.2 ± 0.4	119.7 ± 4.7	128.2 ± 13.0
Gold	24 h	109.3	147.3	115.5	151.9	170

[a] Measurements were performed immediately and 24 h after mixing the protein with the gold solutions.
[b] Obtained from average of five separate DLS measurements where the uncertainty represents standard deviation.

These observations are contrasted with the relative stability of gold NPs with negatively charged citrate layers that stabilize the NPs against large-scale aggregation. In this case, the plasmonic optical excitations of gold still reveal information about the aggregation that occurs in these systems. For example, a red shift of a plasmon extinction wavelength maximum in the optical absorption spectrum can be used to quantify the interparticle interaction strength,[79] where a change in the aggregation state of the gold NPs in solution results in a visual color change from red to blue as the particles pass from isolated gold NPs in solution to a clustered state. This effect arises because the assembly-induced plasmon shift depends on the proximity of the NPs and the strength of the interparticle interaction, which regulates the extent of this aggregation. We next apply this technique to gain some quantitative information about the thickness of the adsorbed protein layer, which, along with the NP diameter, governs the average distance between the protein-coated NPs in their clustered state.

Representative plasmonic absorbance measurements of protein-coated gold NPs exhibiting aggregation are shown in Figure 8.7. The concentrations of HSA, fibrinogen, and globulin in each of these measurements are taken to be the same as in blood plasma (Table 8.1) to make our discussion of greater biological significance. We also performed experiments with $10\times$ and $100\times$ dilutions of these protein solutions to assess the effect of protein concentration.
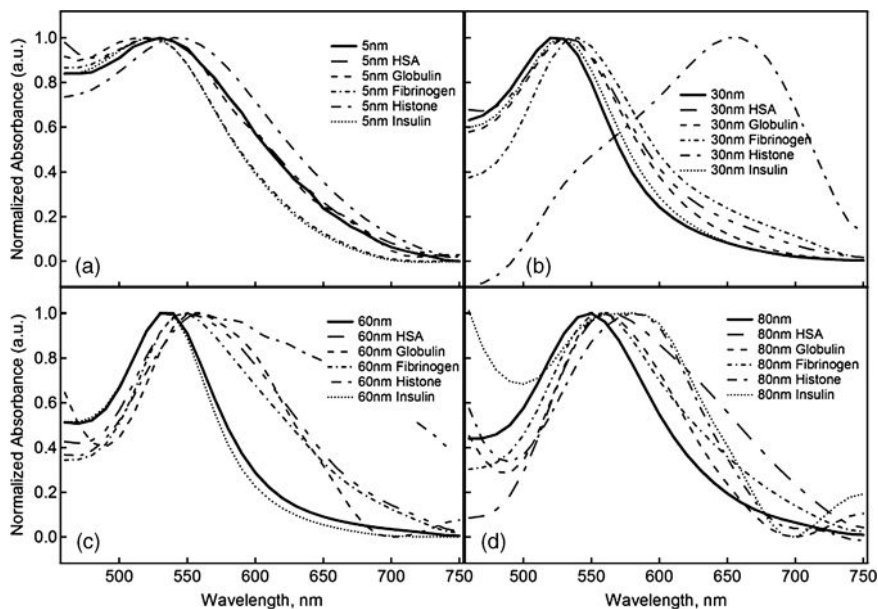
Figure 8.7. Plasmon absorbance of gold NPs in absence and presence of proteins (concentration determination is described in Section 8.5). Measurements were performed immediately after mixing the protein and gold solutions.

As mentioned before, the plasmon shift in gold NPs is normally interpreted as providing a measure of the distance between the particles, either as isolated particles, where that scale is large, or between the particles in aggregates, where the distance is typically comparable to the particle radius (at least for spherical particles). The theoretical dependence of this plasmon shift on interparticle distance is specified. The first thing we notice from Figure 8.8 is that the distance between the particles is deduced to be nearly *independent* of protein dilution. This result is perfectly understandable if the particles are in an aggregated state (see Figure 8.5) and if this state is not sensitive to protein dilution over a large range of concentrations beyond those required to form a saturated protein surface layer on the NP surface. We also observe that the interparticle distance for small NPs (diameter less than 50 nm) increases nearly linearly with the particle radius (insulin is somewhat of an exception). The existence of clustered protein-coated NPs indicates that there is a corresponding near-linear increase in the protein layer with NP size for this class of
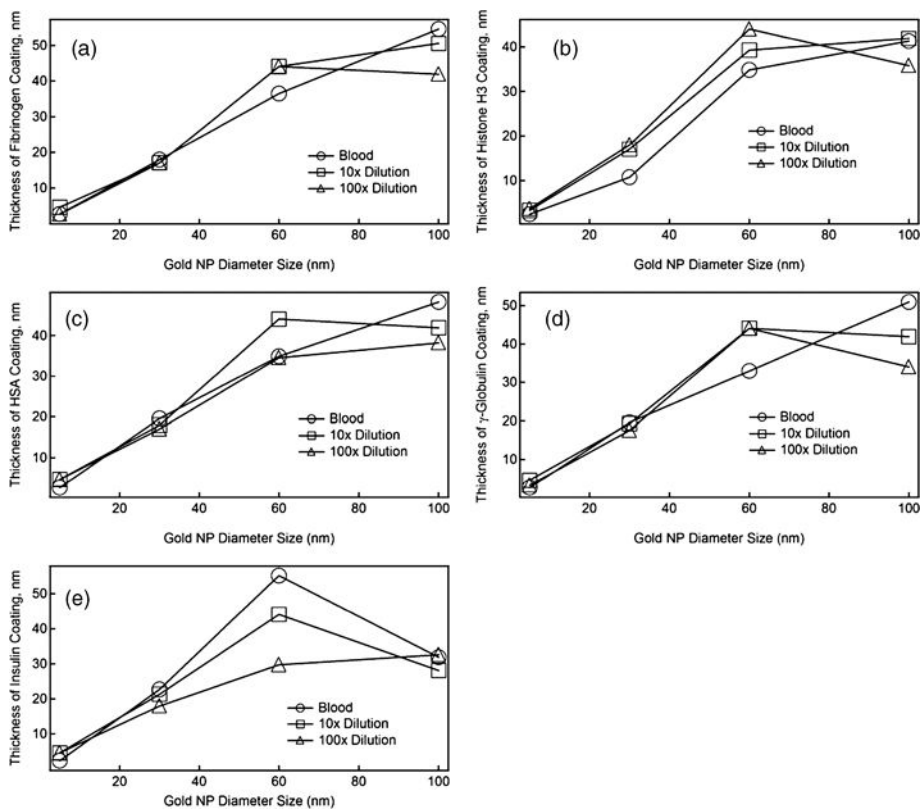
Figure 8.8. Effect of blood protein concentration on the gold interparticle distance: (a) Fibrinogen, (b) histone H3, (c) HSA, (d) γ-globulin, and (e) insulin. Estimates are based on Eq. 8.1.

proteins. Again, we observe changes in this trend near a scale of about 50 nm. We noted before that the strength of the protein–NP binding constant K increases generally with NP size. Apparently, this stronger binding is accompanied by a corresponding increase in the average thickness of the bound protein layer. Ultimately, this progressive increase in the thickness of the adsorbed layer has its limits and at some point the layer must saturate at a value representative of a macroscopic particle. As with so many nanostructures, this type of crossover from molecular to macroscale phenomena occurs on a scale on the order of 50 nm. Since any factor that influences the protein layer thickness has an obvious practical importance for understanding the origins of changes of the effective protein-dressed NP interparticle interaction and the associated NP aggregation, there should be further study of the simple and general trend of increasing protein layer size with NP diameter indicated in Figure 8.8.

8.4. CONCLUSIONS

Concerns about the toxicity and effectiveness of nanoparticles (NPs) introduced into the bloodstream of animals in the course of therapeutic treatment or environmental exposure as air pollutants motivated a survey study of essential blood proteins with model gold NPs that are of particular interest in therapeutic applications. We start with this class of NPs because they have relatively low polydispersity of size and can be synthesized over a wide range of sizes. The capacity to control the surface interaction through surface functionalization also makes this class of particles attractive for an initial survey study on NP–protein interactions that is aimed at understanding general aspects of NP–protein adsorption and the implications of this process having relevance to NP toxicity and the use of these NPs in the developing field of nanomedicine. Although individual NP–protein studies are available to our work, there is no other survey study that systematically explores the impact of NP size, protein, and concentration, and surface interaction on the relative strength of the mutual binding constant quantifying the interaction strength between the protein and the NPs and the relative cooperativity of the protein binding process to them through the determination of the Hill parameter (n) by fluorescence quenching measurements. We also explore how NP and protein type influence the propensity toward protein aggregation through aggregate size measurements using dynamic light scattering and electron microscopy, the thickness of the protein layer about the NPs through light adsorption measurements, and the extent of protein conformational change, as evidenced by circular dichroism measurements. This is the first such comprehensive study of basic NP–protein interactions covering basic blood proteins and, indeed, any important class of proteins.

Under solution conditions approximating physiological conditions, we find that our model gold NPs bind to an array of plasma proteins, leading to an adsorbed protein layer or "corona" that largely defines the biological identity of these particles. We observe a general tendency of the association constant governing the strength of the NP–protein interaction to increase with NP size, while the cooperativity (i.e, the

Hill parameter n characterizing the relative sharpness of the protein–NP binding transition) tends to diminish with NP size for most of the proteins that we have investigated. This effect is attributed to enhanced protein packing in the larger NPs and the more efficient screening of the NP charge interaction as the proteins progressively adsorb onto the NP. We also observe a general tendency of the thickness of the protein layer to increase with NP size, although this trend must saturate at some point and in the present study this seems to correspond to NPs having a scale of about 50 nm, a scale seen for the crossover from the macroscale to the nanoscale physics in many materials science contexts. We also examined conformational transitions of the protein structure upon adsorption onto gold NPs by fluorescence emission spectroscopy, and circular dichroism measurements indicate that factors largely affecting the strength of the protein binding constant (e.g., NP size and concentration) had the evident effect of increasing the fluorescence emission peak intensity, but circular dichroism measurements imply that the actual extent of protein conformational change in these protein layers can be highly variable with protein type. An obvious tendency for the adsorbed protein layers to cause the NPs to aggregate was indicated by dynamic light scattering.

Further study is necessary to understand how the nature of the protein adsorption process changes the protein conformation, and the tendency of the "dressed" particles to aggregate. A better understanding of the properties of these coated particles (specifically, the roles of charge, rigidity effects, hydrophobic, and van der Waals interactions) is also required since the properties of these NP–protein complexes can be central for proper function in biomedical applications[6, 7] and for understanding and controlling the toxicity of these materials. Moreover, an understanding of how NPs having different sizes interact with cells requires the study of the molecular events involved in NP–membrane receptor binding, endocytosis, and subsequent signaling activation. Our study indicates that both general trends and specific features of plasma protein–gold NP complex formation can be quantified. The control of physical, chemical, and biological properties of protein adsorption on NPs in large measure defines the NP fate in living systems.

We finally note that since many nanomedicine applications utilize derivatized PEG gold nanoparticles,[80] it would clearly be of interest to extend our investigation of NP–protein interactions to include this class of NPs since excluded volume interactions in polymer brush layers often lead to diffuse particle interfaces and thus different trends than indicated in the present study might be expected. Moreover, these diffuse interfaces should also swell and contract in response to changes in thermodynamic conditions so that changes in pH, salt, and other thermodynamic variables might also have a significant influence on protein binding in these systems.

8.5. METHODS

8.5.1. Reagents

Human serum albumin (HSA) (A9511), histone H3 (H4380) from calf thymus, human γ-globulins (G5385), human insulin (I9278), and human fibrinogen (F-4883)

were purchased from Sigma Chemical Company.* Citrate-coated gold NP solutions were purchased from Ted Pella. In our experiments, the concentrations of HSA, fibrinogen, and γ-globulin ($10\times$ and $100\times$ dilution of the original plasma protein concentration) are similar to those found in blood plasma (see Table 8.1). A mixture of 10 μL gold NPs and 200 μL protein solutions (plasma concentration) were utilized for our DLS study, as this is a concentration comparable to physiological conditions.

8.5.2. Absorbance Measurements

The effect of proteins on the plasmon excitation wavelength for gold NPs was determined by recording the light absorbance of gold NPs in the absence and presence of protein on the SpectraMax M5 spectrophotometer (Molecular Devices).* Each spectrum is an average of three individual samples recorded twice. The experiments were performed at 25°C.

The magnitude of the particle-clustering-induced plasmon shift on gold NPs is given by Eq. 8.1, which allows an estimation of the strength of the interparticle coupling arising from the proximity of NPs in the clusters. In particular, the plasmon shift of gold NPs in the presence of blood proteins provides a measure of the apparent interparticle distance,[81]

$$\Delta\lambda/\lambda_o \approx 0.18 \exp[-\ (s/D)/0.23] \tag{8.1}$$

where $\Delta\lambda/\lambda_o$ is the fractional plasmon shift, s is the distance between the surfaces of the particles, D is the particle diameter, and 0.23 is the decay constant for the universal trend of plot $\Delta\lambda/\lambda_o$ versus s/D obtained by Jain et al.[81]

8.5.3. Fluorescence Quenching Measurements

Intrinsic tryptophan, tyrosine, and phenylalanine fluorescence quenching induced by gold NPs was recorded on a Cary Eclipse fluorescence spectrophotometer (Varian). Excitation was performed at 280 nm. Fluorescence emission was measured at 25°C in DPBS (without Ca^{2+} and Mg^{2+}) containing various concentrations of gold NPs. The protein concentration was fixed at 0.01 mg/mL. Nanoparticle concentration range was (0 to $4.7) \times 10^{-5}$ M (5 nm), (0 to $5.8) \times 10^{-6}$ M (10 nm), (0 to $3.7) \times 10^{-6}$ M (20 nm), (0 to $4.3) \times 10^{-7}$ M (30 nm), (0 to $5.2) \times 10^{-8}$ M (60 nm), or (0 to $1.8) \times 10^{-8}$ M (100 nm).

As in numerous previous studies of drug binding to proteins (the study of tetradrine binding to albumin provides a representative example[82]), we quantify the fluorescence quenching by the relation

$$Q = (I^0 - I)/I^0 \tag{8.2}$$

*Note: Certain equipment and instruments or materials are identified to adequately specify the experimental details. Such identification does not imply recommendation by the National Institute of Standards and Technology, nor does it imply that the materials are necessarily the best available for the purpose.

where I^0 and I are fluorescence intensities in the absence and presence of gold NPs, respectively.[83, 84] We assume that the binding of proteins to NPs occurs at equilibrium and, correspondingly, we fit our fluorescence quenching data for Q to determine an equilibrium constant k_D describing the gold NP–protein interaction. Since a given protein can be expected to have multiple associative interactions with NPs, we can expect the binding equilibrium to exhibit cooperativity, as in the classic example of binding of multiple O_2 molecules to hemoglobin.[86] Conventionally, this complex phenomenon is taken into account by modeling Q through the Hill equation,[83, 85]

$$Q/Q_{max} = [NP]^n/(k_D^n + [NP]^n) \tag{8.3}$$

where Q_{max} is the saturation value of Q, k_D the protein–NP equilibrium constant, and n is the Hill parameter.[83, 85] Although the modeling on which Eq. 8.3 is based is somewhat idealized, n is generally regarded as a measure of association "cooperativity." For a positively cooperative reaction, $n > 1$, meaning that once one protein molecule is bound to the NP, its affinity for the NP progressively increases in a superlinear fashion. For a negatively cooperative reaction, $n < 1$ and the binding strength of the protein to the NP becomes progressively weaker as further proteins adsorb. For a noncooperative association, where $n = 1$ and where Q formally has the mathematical form of Langmuir adsorption equation,[83, 85] the affinity of the proteins for NPs does not depend on whether other protein molecules are already bound. The "binding constant" K is defined to be the reciprocal of k_D.

At low NP concentrations, fluorescence quenching is dominated by diffusive transport, and a nonequilibrium model for the fluorescence quenching is appropriate. The standard model for this regime is attributed to Stern–Volmer.[37] In particular, the ratio F_0/F at low concentrations is predicted to be linear in concentration of the quenching agent in this theory. Specifically, we then have the relationship

$$I^0/I = 1 + k_{SV}[NP] \tag{8.4}$$

This equation is traditionally used to quantify fluorescence quenching efficiency by additives at low concentrations that bind or otherwise interact with the fluorescent species, where the Stern–Volmer constant (k_{SV}) is conventionally taken as a measure of the quenching efficiency, γ, times the *diffusion*-limited bimolecular rate for the dynamic quenching process.

Fluorescence quenching parameters are estimated as an average of three individual experiments, and the uncertainty is the standard deviation. For the binding constant, the error for each fit was determined by using the standard error analysis method described by the equation $\sigma_i = \sqrt{C_{ii}\chi^2}$, where C_{ii} is the diagonal element of the variance–covariance matrix and χ is the reduced chi value.

8.5.4. Circular Dichroism

Circular dichroism (CD) spectra were recorded on an Olis RSM spectropolarimeter at room temperature, in a 2 mm path cuvette. Ellipticity is expressed in millidegrees.

The gold NPs were added in small aliquots of stock gold solutions to protein solution (1 mg/mL). Each spectrum represents an average of 20 scans. The experiments were performed at 25°C.

8.5.5. Electron Microscopy

Samples for field emission scanning electron microscopy (Hitachi S4700 FE-SEM) were prepared by placing 20 μL of freshly prepared protein–gold solution on aluminum stubs mounted with carbon substrate. The stubs were placed on vials and quickly frozen by exposure to liquid nitrogen followed by lyophilization (200 μL plasma concentration + 10 μL gold).

8.5.6. Dynamic Light Scattering

Dynamic light scattering (DLS) measurements were made with a lab-built setup utilizing a He-Ne laser at 632.8 nm wavelength. A linearly polarized laser beam of 0.7 mm diameter was focused with an $f = 180$ mm achromatic doublet lens in the center of a square quartz sample cell. The diffraction-limited focused light beam waist was 400 μm. The cell had internal dimensions of 10 mm × 2 mm and required just 0.1 mL of sample solution. Light, quasielastically scattered at 90°, was collected by an $f = 8$ mm aspherical lens and coupled to a single-mode fiber with 4.3 μm core size. The fiber was connected to an avalanche photodiode photon counter with 65% detection efficiency at the laser wavelength. Photon counts were registered by a digital correlation board with 10 ns time resolution. The laser incident power of 23 mW was reduced by a set of neutral density filters to keep the photon count below 1 MHz in the detector's linear range. The shortest correlation time was set to 400 ns to avoid the detector after pulsing. The data was initially fit with the quadratic cumulant method and, in cases where the polydispersity values were appreciable, the CONTIN algorithm was used instead. The spatial coherence factor above 0.9 was routinely observed for dilute samples. Data collection time was typically set to 30 s for samples in equilibrium and to 5 s during kinetic series acquisition. The solution (10 μL gold + 200 μL plasma concentration protein) was filtered with PTFE 0.45 μm. Particle size was estimated from an average of five separate measurements and the measurement uncertainty is indicated as standard deviation.

ACKNOWLEDGMENTS

REFERENCES

1. Linse, S.; Cabaleiro-Lago, C.; Xue, W. F.; Lynch, I.; Lindman, S.; Thulin, E.; Radford, S. E.; Dawson, K. A. Nucleation of protein fibrillation by nanoparticles. *Proc. Nat. Acad. Sci. U.S.A.*, **2007**, *104*(21), 8691–8696.

2. Greillier, L.; Astoul, P. Mesothelioma and asbestos-related pleural diseases. *Respiration*, **2008**, *76*(1), 1–15.

3. Poland, C. A.; Duffin, R.; Kinloch, I.; Maynard, A.; Wallace, W. A. H.; Seaton, A.; Stone, V.; Brown, S.; MacNee, W.; Donaldson, K. Carbon nanotubes introduced into the abdominal cavity of mice show asbestos-like pathogenicity in a pilot study. *Nat. Nanotechnol.*, **2008**, *3*(7), 423–428.

4. Holmes, P. *Airborne Particles: Exposure in the Home and Health Effects*. MRC Institute for Environment and Health, Leicester, UK, 2000.

5. Asuri, P.; Bale, S. S.; Karajanagi, S. S.; Kane, R. S. The protein–nanomaterial interface. *Curr. Opin. Biotechnol.*, **2006**, *17*(6), 562–568.

6. Lundqvist, M.; Stigler, J.; Elia, G.; Lynch, I.; Cedervall, T.; Dawson, K. A. Nanoparticle size and surface properties determine the protein corona with possible implications for biological impacts. *Proc. Nat. Acad. Sci. U.S.A.*, **2008**, *105*(38), 14265–14270.

7. Lynch, I.; Cedervall, T.; Lundqvist, M.; Cabaleiro-Lago, C.; Linse, S.; Dawson, K. A. The nanoparticle–protein complex as a biological entity; a complex fluids and surface science challenge for the 21st century. *Adv. Colloid Interface Sci.*, **2007**, *134–135*, 167–174.

8. Paal, K.; Muller, J.; Hegedus, L. High affinity binding of paclitaxel to human serum albumin. *Eur. J. Biochem.*, **2001**, *268*(7), 2187–2191.

9. Weisiger, R.; Gollan, J.; Ockner, R. Receptor for albumin on the liver-cell surface may mediate uptake of fatty-acids and other albumin-bound substances. *Science*, **1981**, *211*(4486), 1048–1050.

10. Hemmerle, J.; Altmann, S. M.; Maaloum, M.; Horber, J. K. H.; Heinrich, L.; Voegel, J. C.; Schaaf, P. Direct observation of the anchoring process during the adsorption of fibrinogen on a solid surface by force-spectroscopy mode atomic force microscopy. *Proc. Nat. Acad. Sci. U.S.A.*, **1999**, *96*(12), 6705–6710.

11. Li, Z. Q.; Perkins, S. J.; Loucheuxlefebvre, M. H. Alpha-1 acid glycoprotein – a small-angle neutron-scattering study of a human-plasma glycoprotein. *Eur. J. Biochem.*, **1983**, *130*(2), 275–279.

12. Kamyshny, A.; Magdassi, S.; Relkin, P. Chemically modified human immunoglobulin G: Hydrophobicity and surface activity at air/solution interface. *J. Colloid Interface Sci.*, **1999**, *212*(1), 74–80.

13. Yu, C. M.; Chin, C. Y.; Franses, E. I.; Wang, N. H. L. In situ probing of insulin aggregation in chromatography effluents with spectroturbidimetry. *J. Colloid Interface Sci.*, **2006**, *299*(2), 733–739.

14. Yagi, N.; Ohta, N.; Lida, T.; Inoue, K. A microbeam X-ray diffraction study of insulin spherulites. *J. Mol. Biol.* **2006**, *362*(2), 327–333.

15. Holdenrieder, S.; Stieber, P. Clinical use of circulating nucleosomes. *Crit. Rev. Clin. Lab. Sci.*, **2009**, *46*(1), 1–24.

16. Deligezer, U.; Akisik, E. E.; Erten, N.; Dalay, N. Sequence-specific histone methylation is detectable on circulating nucleosomes in plasma. *Clin. Chem.*, **2008**, *54*(7), 1125–1131.

17. Watson, K.; Edwards, R. J.; Shaunak, S.; Parmelee, D. C.; Sarraf, C.; Gooderham, N. J.; Davies, D. S. Extra-nuclear location of histones in activated human peripheral-blood lymphocytes and cultured T-cells. *Biochem. Pharmacol.*, **1995**, *50*(3), 299–309.

18. Nel, A.; Xia, T.; Madler, L.; Li, N. Toxic potential of materials at the nanolevel. *Science*, **2006**, *311*(5761), 622–627.

19. Klein, J. Probing the interactions of proteins and nanoparticles. *Proc. Nat. Acad. Sci. U.S.A.*, **2007**, *104*(7), 2029–2030.

20. Jiang, W.; Kim, B. Y. S.; Rutka, J. T.; Chan, W. C. W. Nanoparticle-mediated cellular response is size-dependent. *Nat. Nanotechnol.*, **2008**, *3*(3), 145–150.

21. Choi, H. S.; Liu, W.; Misra, P.; Tanaka, E.; Zimmer, J. P.; Itty Ipe, B.; Bawendi, M. G.; Frangioni, J. V. Renal clearance of quantum dots. *Nat. Biotechnol.*, **2007**, *25*(10), 1165–1170.

22. Chithrani, B. D.; Chan, W. C. W. Elucidating the mechanism of cellular uptake and removal of protein-coated gold nanoparticles of different sizes and shapes. *Nano Lett.*, **2007**, *7*(6), 1542–1550.

23. Chithrani, B. D.; Ghazani, A. A.; Chan, W. C. W. Determining the size and shape dependence of gold nanoparticle uptake into mammalian cells. *Nano Lett.*, **2006**, *6*(4), 662–668.

24. Osaki, F.; Kanamori, T.; Sando, S.; Sera, T.; Aoyama, Y. A quantum dot conjugated sugar ball and its cellular uptake. On the size effects of endocytosis in the subviral region. *J. Am. Chem. Soc.*, **2004**, *126*(21), 6520–6521.

25. Jiang, W.; Kim, B. Y. S.; Rutka, J. T.; Chan, W. C. W. Nanoparticle-mediated cellular response is size-dependent. *Nat. Nanotechnol.*, **2008**, *3*(3), 145–150.

26. Gao, H. J.; Shi, W. D.; Freund, L. B. Mechanics of receptor-mediated endocytosis. *Proc. Nat. Acad. Sci. U.S.A.*, **2005**, *102*(27), 9469–9474.

27. Bao, G.; Bao, X. R. Shedding light on the dynamics of endocytosis and viral budding. *Proc. Nat. Acad. Sci. U.S.A.*, **2005**, *102*(29), 9997–9998.

28. Conner, S. D.; Schmid, S. L. Regulated portals of entry into the cell. *Nature*, **2003**, *422* (6927), 37–44.

29. Becker, M. L.; Fagan, J. A.; Gallant, N. D.; Bauer, B. J.; Bajpai, V.; Hobbie, E. K.; Lacerda, S. H.; Migler, K. B.; Jakupciak, J. P. Length-dependent uptake of DNA-wrapped single-walled carbon nanotubes. *Adv. Mater.*, **2007**, *19*(7), 939.

30. Gobin, A. M.; Lee, M. H.; Halas, N. J.; James, W. D.; Drezek, R. A.; West, J. L. Near-infrared resonant nanoshells for combined optical imaging and photothermal cancer therapy. *Nano Lett.*, **2007**, *7*(7), 1929–1934.

31. Everts, M.; Saini, V.; Leddon, J. L.; Kok, R. J.; Stoff-Khalili, M.; Preuss, M. A.; Millican, C. L.; Perkins, G.; Brown, J. M.; Bagaria, H.; Nikles, D. E.; Johnson, D. T.; Zharov, V. P.; Curiel, D. T. Covalently linked Au nanoparticles to a viral vector: potential for combined photothermal and gene cancer therapy. *Nano Lett.*, **2006**, *6*(4), 587–591.

32. Loo, C.; Lowery, A.; Halas, N.; West, J.; Drezek, R. Immunotargeted nanoshells for integrated cancer imaging and therapy. *Nano Lett.*, **2005**, *5*(4), 709–711.

33. Brewer, S. H.; Glomm, W. R.; Johnson, M. C.; Knag, M. K.; Franzen, S. Probing BSA binding to citrate-coated gold nanoparticles and surfaces. *Langmuir*, **2005**, *21*(20), 9303–9307.

34. Shen, X. C.; Liou, X. Y.; Ye, L. P.; Liang, H.; Wang, Z. Y. Spectroscopic studies on the interaction between human hemoglobin and CdSe quantum dots. *J. Colloid Interface Sci.*, **2007**, *311*(2), 400–406.

35. Gao, D. J.; Tian, Y.; Bi, S. Y.; Chen, Y. H.; Yu, A. M.; Zhang, H. Q. Studies on the interaction of colloidal gold and serum albumins by spectral methods. *Spectrochim. Acta Part A Mol. Biomol. Spectros.*, **2005**, *62*(4–5), 1203–1208.

36. Chadborn, N.; Bryant, J.; Bain, A. J.; O'Shea, P. Ligand-dependent conformational equilibria of serum albumin revealed by tryptophan fluorescence quenching. *Biophys. J.*, **1999**, *76*(4), 2198–2207.

37. Lakowicz, J. R. *Principles of Fluorescence Spectroscopy*. Kluwer Academic/Plenum Press, New York, 1999.

38. Wang, C.; Wu, Q. H.; Li, C. R.; Wang, Z.; Ma, J. J.; Zang, X. H.; Qin, N. X. Interaction of tetrandrine with human serum albumin: a fluorescence quenching study. *Anal. Sci.*, **2007**, *23*(4), 429–433.

39. Clayton, A. H. A.; Sawyer, W. H. Site-specific tryptophan fluorescence spectroscopy as a probe of membrane peptide structure and dynamics. *Eur. Biophys. J. Biophys. Lett.*, **2002**, *31*(1), 9–13.

40. Jang, D. J.; Elsayed, M. A. Tryptophan fluorescence quenching as a monitor for the protein conformation changes occurring during the photocycle of bacteriorhodopsin under different perturbations. *Proc. Nat. Acad. Sci. U.S.A.*, **1989**, *86*(15), 5815–5819.

41. Anbazhagan, V.; Damai, R. S.; Paul, A.; Swamy, M. J. Interaction of the major protein from bovine seminal plasma, PDC-109 with phospholipid membranes and soluble ligands investigated by fluorescence approaches. *Biochim. Biophys. Acta Proteins Proteomics*, **2008**, *1784*(6), 891–899.

42. Lopez, M. M.; Kosk-Kosicka, D. Spectroscopic analysis of halothane binding to the plasma membrane Ca^{2+}-ATPase. *Biophys. J.*, **1998**, *74*(2), 974–980.

43. Zhou, T. Q.; Rosen, B. P. Tryptophan fluorescence reports nucleotide-induced conformational changes in a domain of the ArsA ATPase. *J. Biol. Chem.*, **1997**, *272*(32), 19731–19737.

44. Noronha, M.; Lima, J. C.; Paci, E.; Santos, H.; Macanita, A. L. Tracking local conformational changes of ribonuclease A using picosecond time-resolved fluorescence of the six tyrosine residues. *Biophys. J.*, **2007**, *92*(12), 4401–4414.

45. Gorinstein, S.; Goshev, I.; Moncheva, S.; Zemser, M.; Weisz, M.; Caspi, A.; Libman, I.; Lerner, H. T.; Trakhtenberg, S.; Martin-Belloso, O. Intrinsic tryptophan fluorescence of human serum proteins and related conformational changes. *J. Protein Chem.*, **2000**, *19*(8), 637–642.

46. Roach, P.; Farrar, D.; Perry, C. C. Interpretation of protein adsorption: surface-induced conformational changes. *J. Am. Chem. Soc.*, **2005**, *127*(22), 8168–8173.

47. Cui, F. L.; Wang, J. L.; Cui, Y. R.; Li, J. P. Fluorescent investigation of the interactions between *N*-(*p*-chlorophenyl)-*N'*-(1-naphthyl) thiourea and serum albumin: synchronous fluorescence determination of serum albumin. *Anal. Chim. Acta*, **2006**, *571*(2), 175–183.

48. Jiang, L.; Yang, B. Q.; Ma, Y. D.; Liu, Y. C.; Yang, W. S.; Li, T. J.; Sun, C. C. The binding of phosphorotholate oligonucleotides to CdS nanoparticles. *Chem. Phys. Lett.*, **2003**, *380*(1–2), 29–33.

49. Sandros, M. G.; Gao, D.; Gokdemir, C.; Benson, D. E. General, high-affinity approach for the synthesis of fluorophore appended protein nanoparticle assemblies. *Chem. Commun.*, **2005**, *22*, 2832–2834.

50. Fan, C. H.; Wang, S.; Hong, J. W.; Bazan, G. C.; Plaxco, K. W.; Heeger, A. J. Beyond superquenching: hyper-efficient energy transfer from conjugated polymers to gold nanoparticles. *Proc. Nat. Acad. Sci. U.S.A.*, **2003**, *100*(11), 6297–6301.

51. Zhang, J.; Badugu, R.; Lakowicz, J. R. Fluorescence quenching of CdTe nanocrystals by bound gold nanoparticles in aqueous solution. *Plasmonics*, **2008**, *3*(1), 3–11.

52. Libertini, L. J.; Small, E. W. The intrinsic tyrosine fluorescence of histone-H1—steady-state and fluorescence decay studies reveal heterogeneous emission. *Biophys. J.*, **1985**, *47*(6), 765–772.

53. Jennings, T. L.; Singh, M. P.; Strouse, G. F. Fluorescent lifetime quenching near d = 1.5 nm gold nanoparticles: probing NSET validity. *J. Am. Chem. Soc.*, **2006**, *128*(16), 5462–5467.

54. Roy, S.; Dasgupta, A. K. Controllable self-assembly from fIbrinogen-gold (fibrinogen-Au) and thrombin-silver (thrombin-Ag) nanoparticle interaction. *FEBS Lett.*, **2007**, *581*(28), 5533–5542.

55. Griffin, J.; Ray, P. C. Size- and distance-dependent nanoparticle surface-energy transfer (NSET) method for selective sensing of hepatitis C virus RNA. *Chemistry*, **2008**, *15*(2), 342–351.

56. Dulkeith, E.; Morteani, A. C.; Niedereichholz, T.; Klar, T. A.; Feldmann, J.; Levi, S. A.; van Veggel, F. C. J. M.; Reinhoudt, D. N.; Moller, M.; Gittins, D. I. Fluorescence quenching of dye molecules near gold nanoparticles: radiative and nonradiative effects. *Phys. Rev. Lett.*, **2002**, *89*(20), 203002.

57. Ghosh, S. K.; Pal, A.; Kundu, S.; Nath, S.; Pal, T. Fluorescence quenching of 1-methylaminopyrene near gold nanoparticles: size regime dependence of the small metallic particles. *Chem. Phys. Lett.*, **2004**, *395*(4–6), 366–372.

58. Ding, Y. H.; Chen, Z. Q.; Xie, J.; Guo, R. Comparative studies on adsorption behavior of thionine on gold nanoparticles with different sizes. *J. Colloid Interface Sci.*, **2008**, *327*(1), 243–250.

59. Karlsson, M.; Martensson, L. G.; Jonsson, B. H.; Carlsson, U. Adsorption of human carbonic anhydrase II variants to silica nanoparticles occur stepwise: binding is followed by successive conformational changes to a molten-globule-like state. *Langmuir*, **2000**, *16*(22), 8470–8479.

60. Karlsson, M.; Carlsson, U. Protein adsorption orientation in the light of fluorescent probes: mapping of the interaction between site-directly labeled human carbonic anhydrase II and silica nanoparticles. *Biophys. J.*, **2005**, *88*(5), 3536–3544.

61. Lundqvist, M.; Andresen, C.; Christensson, S.; Johansson, S.; Karlsson, M.; Broo, K.; Jonsson, B. H. Proteolytic cleavage reveals interaction patterns between silica nanoparticles and two variants of human carbonic anhydrase. *Langmuir*, **2005**, *21*(25), 11903–11906.

62. Allen, L. T.; Fox, E. J. P.; Blute, I.; Kelly, Z. D.; Rochev, Y.; Keenan, A. K.; Dawson, K. A.; Gallagher, W. M. Interaction of soft condensed materials with living cells: Phenotype/transcriptome correlations for the hydrophobic effect. *Proc. Nat. Acad. Sci. U.S.A.*, **2003**, *100*(11), 6331–6336.

63. Keselowsky, B. G.; Collard, D. M.; Garcia, A. J. Surface chemistry modulates fibronectin conformation and directs integrin binding and specificity to control cell adhesion. *J. Biomed. Mater. Res. Part A*, **2003**, *66A*(2), 247–259.

64. Lundqvist, M.; Sethson, I.; Jonsson, B. H. Protein adsorption onto silica nanoparticles: conformational changes depend on the particles' curvature and the protein stability. *Langmuir*, **2004**, *20*(24), 10639–10647.

65. Ray, P. C.; Fortner, A.; Griffin, J.; Kim, C. K.; Singh, J. P.; Yu, H. T. Laser-induced fluorescence quenching of tagged oligonucleotide probes by gold nanoparticles. *Chem. Phys. Lett.*, **2005**, *414*(4–6), 259–264.

66. You, C. C.; De, M.; Han, G.; Rotello, V. M. Tunable inhibition and denaturation of alpha-chymotrypsin with amino acid-functionalized gold nanoparticles. *J. Am. Chem. Soc.*, **2005**, *127*(37), 12873–12881.

67. Huang, H. L.; Xu, Y. G.; Low, H. Y. Effects of film thickness on moisture sorption, glass transition temperature and morphology of poly(chloro-*p*-xylylene) film. *Polymer*, **2005**, *46*(16), 5949–5955.

68. Li, L.; Yang, Y. W.; Fang, X. S.; Kong, M. G.; Li, G. H.; Zhang, L. D. Diameter-dependent electrical transport properties of bismuth nanowire arrays. *Solid State Commun.*, **2007**, *141*(9), 492–496.

69. Hurst, S. J.; Lytton-Jean, A. K. R.; Mirkin, C. A. Maximizing DNA loading on a range of gold nanoparticle sizes. *Anal. Chem.*, **2006**, *78*(24), 8313–8318.

70. Lynch, I.; Dawson, K. A. Protein–nanoparticle interactions. *Nano Today*, **2008**, *3*(1–2), 40–47.

71. Douglas, J. F. Theoretical issues relating to thermally reversible gelation by super-molecular fiber formation. *Langmuir*, **2009**, *25*(15), 8386–8391.

72. Lim, B. T.; Kimura, T. Conformation-associated anomalous tyrosine fluorescence of adrenodoxin. *J. Biol. Chem.*, **1980**, *255*(6), 2440–2444.

73. Khrapunov, S. N.; Protas, A. F.; Sivolob, A. V.; Dragan, A. I.; Berdyshev, G. D. Intrinsic fluorescence, difference spectrophotometry and theoretical-studies on tertiary structure of calf thymus histone-H1. *Int. J. Biochem.*, **1985**, *17*(2), 217–222.

74. Zhao, S. Y.; Ragsdale, S. W. A conformational change in the methyltransferase from *Clostridium thermoaceticum* facilitates the methyl transfer from (6S)-methyltetrahydro-folate to the corrinoid iron–sulfur protein in the acetyl-CoA pathway. *Biochemistry*, **1996**, *35*(7), 2476–2481.

75. Teichroeb, J. H.; Forrest, J. A.; Jones, L. W. Size-dependent denaturing kinetics of bovine serum albumin adsorbed onto gold nanospheres. *Eur. Phys. J. Part E. Soft Matter*, **2008**, *26*(4), 411–415.

76. Mandal, A. K.; Bhattacharyya, A.; Bhattacharyya, S.; Bhattacharyya, T.; Roy, S. A cognate tRNA specific conformational change in glutaminyl-tRNA synthetase and its implication for specificity. *Protein Sci.*, **1998**, *7*(4), 1046–1051.

77. Wangoo, N.; Bhasin, K. K.; Mehta, S. K.; Suri, C. R. Synthesis and capping of water-dispersed gold nanoparticles by an amino acid: bioconjugation and binding studies. *J. Colloid Interface Sci.*, **2008**, *323*(2), 247–254.

78. Deroe, C.; Courtoy, P. J.; Baudhuin, P. A model of protein colloidal gold interactions. *J. Histochem. Cytochem.*, **1987**, *35*(11), 1191–1198.

79. Mirkin, C. A. Programming the assembly of two- and three-dimensional architectures with DNA and nanoscale inorganic building blocks. *Inorg. Chem.*, **2000**, *39*(11), 2258–2272.

80. Prencipe, G.; Tabakman, S. M.; Welsher, K.; Liu, Z.; Goodwin, A. P.; Zhang, L.; Henry, J.; Dai, H. PEG branched polymer for functionalization of nanomaterials with ultralong blood circulation. *J. Am. Chem. Soc.*, **2009**, *131*(13), 4783–4787.

81. Jain, P. K.; Huang, W. Y.; El-Sayed, M. A. On the universal scaling behavior of the distance decay of plasmon coupling in metal nanoparticle pairs: a plasmon ruler equation. *Nano Lett.*, **2007**, *7*(7), 2080–2088.

82. Wang, C.; Wu, Q. H.; Li, C. R.; Wang, Z.; Ma, J. J.; Zang, X. H.; Qin, N. X. Interaction of tetrandrine with human serum albumin: a fluorescence quenching study. *Anal. Sci.*, **2007**, *23*(4), 429–433.

83. Ikeda, Y.; Taniguchi, N.; Noguchi, T. Dominant negative role of the glutamic acid residue conserved in the pyruvate kinase M-1 isozyme in the heterotropic allosteric effect involving fructose-1,6-bisphosphate. *J. Biol. Chem.*, **2000**, *275*(13), 9150–9156.

84. De La Cruz, E. M. Cofilin binding to muscle and non-muscle actin filaments: Isoform-dependent cooperative interactions. *J. Mol. Biol.*, **2005**, *346*(2), 557–564.

85. Hill, A. V. The combinations of haemoglobin with oxygen and carbon monoxide, and the effects of acid and carbon dioxide. *Biochem. J.*, **1921**, *15*(5), 577–586.

Genetically Modified Collagen-like Triple Helix Peptide as Biomimetic Template

PRERNA KAUR,* HANYING BAI,* and HIROSHI MATSUI

Department of Chemistry and Biochemistry, City University of New York – Hunter College, New York, New York, USA

9.1. INTRODUCTION

In recent times, various metal and semiconductor nanowires have been developed as building blocks for electronics, optics, and sensors. Nanowires grown on biomolecular templates received attention since the recognition functions of these biomolecules with specific ligands can be tuned to wire molecular electronic devices with desired geometries.[1–3] Most of the biomolecular-nanowire templates from DNAs or peptides need to be fabricated for them to function in a suitable electric device, and there is an extensive effort to coat them with metals and semiconductors.[4–11] While these biomolecular-nanowire templates appear to be promising building blocks for nanodevices, it is essential to have size monodispersity, rigidness, and product yield to impact the real world. For example, biomolecular templates self-assembled from peptidic monomers yield polydisperse materials with heterogeneous diameters and uncontrolled length through the self-assembly process. The tobacco mosaic virus (TMV), a rod-shaped biomolecular template, has been applied for various metal coatings, however, to achieve accurate control of the length with low dispersity is not an easy task.[12–14] The other type—DNA biomolecular templates—have defined lengths determined by the number of nucleic acids, but they lack conformational rigidity. The tendency of supertwisting of the double-helix DNA structure makes it difficult to obtain rigid and linear nanowires.[4] Their production cost and time may not be suitable for large-scale synthesis.

---

*These authors equally contribute to this article.

In this chapter, we discuss collagen and the genetically engineered triple helix peptide nanowire for its applications in nanotechnology and materials. Collagen has been studied for medical reasons. For example, the stability of the triple helix, a building block for collagen fibrils, can be related to diseases when the peptide sequence is mutated. This triple helix also has attractive features for hybrid nanomaterials. The length of the peptide nanowire is uniform as determined by the number of amino acids. By varying the number and the sequence of amino acid residues, the stability of the nanowire can be tuned for device application under harsh environment.

Genetic engineering is more advantageous than chemical synthesis for the functionalization/derivitization of peptide nanowires because the specific position of the peptide can be functionalized by the genetic approach, whereas chemical synthesis requires blocking the undesired position due to the lack of specificity of the chemical reactions and limitation of the length of the peptide that can be synthesized. This approach is becoming even more practical since genetic engineering has advanced for engineering proteins that incorporate nonnatural amino acids. The efficiency of introducing these novel residues in a residue-specific or site-specific manner introduces the flexibility for added functionality. The residue-specific incorporation in which particular amino acids are replaced with nonnatural peptide analogs modifies the physical and chemical properties of proteins.[15] Therefore, this expression system provides us with a perfect platform to investigate and insert any sequence-specific residues based on applicability.

We mainly discuss the peptide nanowires derived from collagen peptide motifs. We recently identified that this triple helix peptide from type I collagen can overcome limitations of other biomolecular templates. The collagen-like triple helix is the genetically engineered polypeptide assembly with a sequence from natural collagen. By using recombinant technology, one can design and amplify a collagen-like triple helix that is monodisperse, easily mineralized with metal ions, and can thus be applied as a rigid biomolecular template for metal/semiconductor nanowire fabrications.[4, 16]

9.2. GENETIC ENGINEERING OF PROTEINS: A PATH FOR NEW FUNCTIONALITY AND PHYSICAL PROPERTY

Fabricating hybrid nanomaterials using a biomimetic approach has tremendous impact not only in medicine and diagnostics but also in biomaterials science with growing interest in using the toolbox of genetic engineering in an exquisite manner.[17] The incorporation of nonnatural amino acids into recombinant proteins emerges as an alternative strategy for the synthesis of artificial proteins that possess diverse chemical, physical, and biological properties.

Recombinant DNA technology in protein engineering can tether the functionality of the protein. Figure 9.1 summarizes the process of protein synthesis via recombinant technology. After construction of the gene library, an individual gene is incorporated into the circular plasmid DNA vector, which can be used to transform an
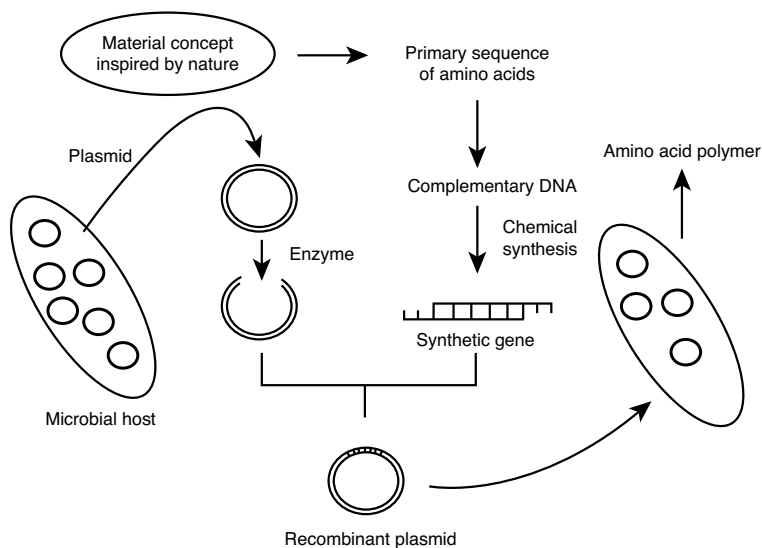
Figure 9.1. The process of genetic engineering for protein synthesis. (From J.C.M. van Hest, D.A. Tirrell, Chem. Commun., **2001**, 1897. Reproduced by permission of The Royal Society of Chemistry.)

appropriate bacterial host. This circular plasmid DNA vector also contains the antibiotic resistant gene for the isolation of the gene of interest after the replication step (see below). The selection of the specific type of vector depends on the copy number of the plasmid, the size of the gene of interest to be ligated in the vector, and, importantly, the host system where the plasmid can replicate using the protein machinery system of the host. The bacterial host *Escherichia coli* is most commonly used because of the simplicity and the efficiency of *E.coli* to grow *under a* wide range of conditions. The plasmids are replicated during every division of the bacterial cells. The plasmids of individual bacterial colonies can be screened primarily on the basis of the presence of the antibiotic resistant gene in the plasmid. To isolate the specific artificial genes, cells are cultured in a medium containing antibiotics. This plasmid will encode the DNA sequence for the desired fusion protein. The selected artificial gene is first analyzed to verify its DNA sequence. This plasmid expresses and produces fusion proteins that contain a promoter site for the recognition by mRNA polymerase, which regulates transcription of the gene (Figure 9.1). This expression plasmid is reintroduced into the bacterial host, and the host cells can be grown to high cell density. During this process, the plasmid switch is turned off in order to prevent the protein production from the gene of interest because premature proteins could be detrimental to the cell growth. After sufficient cell density is reached, the switch is turned on (a process called induction) and the expression of the desired protein begins. Often the synthesis of other cellular proteins is slowed dramatically after induction.

9.3. COLLAGEN

Collagen is abundant in animal tissues in the form of long fibrils with a characteristic periodic structure in the axial direction.[18–20] The collagen fibrils provide the major biomechanical scaffold for cell attachment and anchorage of macromolecules, allowing the form of tissues to be defined and maintained.[21–23] Collagen fibril formation is basically a self-assembly process,[24, 25] which is the intrinsic properties of the peptides, but it is also sensitive to cell-mediated regulation, particularly in young or healing tissues.[26–28] To date, over 27 types of collagen composed of specific d-chains encoded by over 40 different genes have been identified.[22, 25, 29] The most important groups are the fibrillar collagen types I, II, III, IV, and V, which largely contribute to maintaining the structural integrity of organs and tissues by forming supramolecular architectures. Type I is the most abundant collagen type and it forms the largest and strongest fibrillar component that provides tensile strength to bones, skin, tendons, and ligaments.[21, 30–32] Type II collagen is unique to articular cartilage and fibrocartilage, the vitreous body of the eye, and certain other organs.[33] Type III collagen is similar to the structure of type I but less abundant.[10, 34] Type IV is a major component of all membranes as a scaffold and type V is found in some veins and arteries. Other types of collagens are also incorporated into the ECM.[35] Collagens are not only structural components, providing the mechanical strength to tissues, but also offer various specific functions through their interactions with other matrix components (proteoglycans, fibronectin, laminin), secreted soluble factors (interleukin 2, von Willebrand factor, pigment epithelium-derived factor), and cell surface receptors (integrins, discoidin domain receptors, glycoprotein IV).[10]

The fibril-forming collagen molecules consist of an uninterrupted triple helix of approximately 300 nm in length and 1.5 nm in diameter flanked by short extra helical telopeptides.[36–39] The assembly of collagen molecules into fibrils is an entropy driven process, similar to that occurring in other protein self-assembly systems, such as microtubules.[20, 23, 24, 40, 41] These processes are driven by the loss of solvent molecules from the surface of protein molecules and result in assemblies with a circular cross section, which minimizes the surface area/volume ratio of the final assembly. Although the broad principles of collagen fibril self-assembly are generally accepted, less is known about the molecular mechanisms of the assembly process. Fibril-forming collagens are assembled from soluble procollagens,[21] and this assembly is triggered by specific enzymatic cleavage of terminal propeptides with the procollagen metalloproteinases (Figure 9.2). With these proteinases, collagen fibrils are assembled as shown in Figure 9.2.

Triple helix peptide nanowires of interest for material applications are based on the motif of type I collagen. In type I collagen, the triple helix molecule is a heterotrimer comprised of two identical α1 chains and one α2 chain. The α1 and α2 chains are very similar with over 95% identity on amino acid sequence. Each α-chain contains over 1000 amino acids and has a molecular weight of approximately 95,000 Da. These molecules of type I collagen have a length of slightly less than 300 nm and diameter of about 1.4 nm (Figure 9.2).[42]
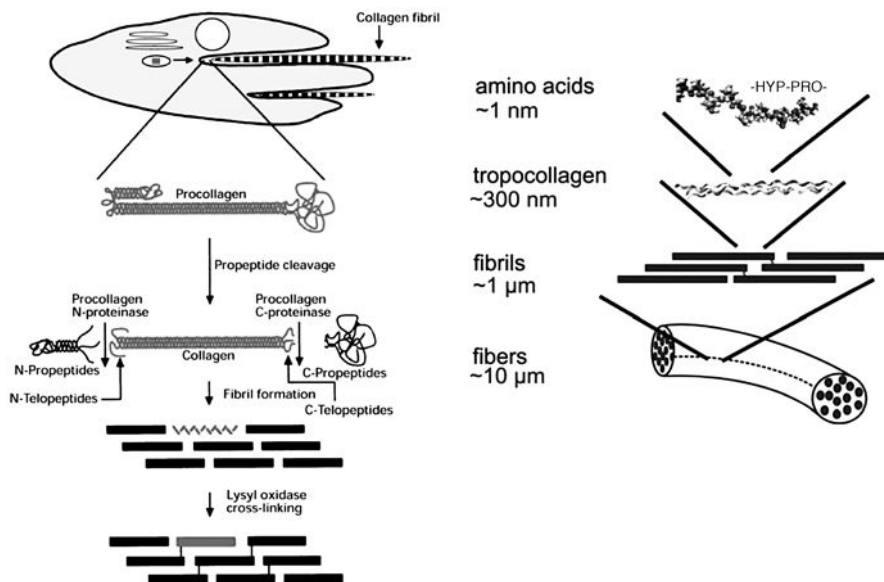
Figure 9.2. Hierarchical structural organization of collagen with amino acid sequence at nano scale up to the scale of collagen fibers in microns. (From K. E. Kadler, D. F. Holmes, J. A. Trotter, J. A. Chapman, *Biochem. J.*, **1996**, *316*, 1. Reproduced by permission of Portland Press. M. J. Buehler, *Curr. Appl. Phys.* **2008**, *8*, 440. Reproduced with permission from Elsevier.)

9.4. CONFORMATION OF TRIPLE HELIX PEPTIDES FROM COLLAGEN

All types of collagen have a unique tertiary structure of triple helix and their conformation is important to assemble stable helical trimers for the application of rigid nanowire building blocks. The basic conformation consists of three polypeptide strands (called α peptides); each forms left-handed polyproline II-like helices with all peptide bonds in a *trans* conformation.[18, 43] These three left-handed helices, staggered by one residue relative to each other, are twisted together along a common axis into a right-handed cooperative coiled coil structure to form a triple helix, which is stabilized by numerous hydrogen bonds.[43] The triple helical regions of collagens are comprised of tandem repeats of Gly-Xaa-Yaa tripeptide units. Isolated polyproline-II helices are not stable if the polypeptide chains also incorporate residues other than proline and hydroxyproline,[31, 44–47] and therefore these hydrogen bonds have a major contribution to the stability of triple helix peptides. It should be noted that the right-handed α-helices with left-handed polyproline-II helices are relatively rare structural elements in proteins with the striking exception of collagens.[26] About one-third of X and Y positions are occupied with proline and post-translationally modified 4-hydroxyproline residues (Hyp), respectively. Such high content of imino acid residues enhances the thermal stability of the triple helix.[35, 48]

9.5. STABILITY OF TRIPLE HELIX PEPTIDES

The stability of triple helix peptide is especially important for material applications because wild-type collagens are not stable enough to be incorporated as building blocks that could be used in a harsh environment. Their mechanical property also needs to be enhanced to develop metal and semiconductor coatings so that they are stable enough to resist under extreme chemical conditions. To develop a strategy to improve the stability, we first need to understand how chemical interactions between these peptides nucleate and assemble collagen triple helix peptides.

Hydrogen bonding is a critical interaction for the triple helix stabilization.[49] The triple helix has the hydrogen-bonding network on the repetitive backbone, but the repeating tripeptide unit consisting of three nonequivalent peptide groups differs from β-sheets or α-helices and all backbone peptide groups do not participate in the hydrogen bonding.[46] All crystal structures show hydrogen bonds between the NH of Gly in one chain and the C=O of the residue at the X position of the neighboring chain.[16, 50, 51] When the Y position is occupied by an amino acid rather than an imino acid, it is hydrated by water molecules and directed into the solvent, which reduces the helix stability.[19, 24] In addition, peptides with the sequence where the X position is occupied by a residue other than Pro show second interchain hydrogen bonds

TABLE 9.1. Predicted and Experimentally Observed[a] T_m Values (°C) for All Possible Gly-X-Y Tripeptide Units[b]

X\Y	O	R	M	I	Q	A	V	E	T	C	K	H	S	D	G	L	N	Y	F	W
P	47	47	43	42	41	41	40	40	40	38	37	36	35	34	33	32	30	30	28	26
E	43	40	38	37	38	35	35	35	36	33	35	31	31	30	29	28	30	26	24	22
A	42	38	37	36	36	33	34	34	34	32	31	30	33	33	27	28	26	25	22	21
K	42	39	37	36	39	35	34	35	34	32	31	30	29	36	27	27	32	24	23	20
R	41	41	36	35	35	34	33	34	33	31	30	29	31	35	26	26	25	24	22	19
Q	40	40	36	35	34	34	33	33	33	31	33	29	28	27	26	26	25	23	22	19
D	40	37	35	34	34	32	33	33	33	31	31	29	28	27	26	26	25	23	21	19
L	39	39	34	33	36	31	32	31	31	29	31	27	27	26	25	27	23	22	20	18
V	39	39	34	33	33	33	32	31	31	29	33	27	27	26	25	24	23	22	20	18
M	39	39	34	33	33	32	31	31	31	29	32	27	26	25	24	24	23	22	20	17
I	38	38	34	33	32	34	31	31	31	29	28	27	26	25	24	24	23	21	20	17
N	38	38	34	33	32	32	31	31	31	29	28	27	26	25	24	24	23	21	19	17
S	38	38	33	32	32	32	31	30	30	28	28	26	26	25	24	23	22	21	19	17
H	37	36	32	31	31	30	29	29	29	27	26	25	24	23	22	22	21	19	18	15
T	36	36	32	30	30	30	29	29	29	27	26	25	24	23	22	22	21	19	17	15
C	36	36	31	30	30	30	29	29	29	27	26	25	24	23	22	22	21	19	17	15
Y	34	34	30	29	28	28	27	27	27	25	24	23	22	21	20	20	19	17	15	13
F	34	33	29	28	28	24	26	26	26	24	23	22	21	20	19	19	18	16	15	12
G	33	33	29	27	27	26	26	26	26	24	27	22	21	20	19	25	18	16	20	12
W	32	32	27	26	26	26	25	24	24	22	21	20	20	19	18	17	16	15	13	11

[a] In bold.
[b] See Ref. 18.

between the X positions and the C=O of the Gly residue, which is mediated by one water molecule. It should be noted that the collagen triple helix has tightly bound water around it and the highly ordered hydration network contributes to the high density molecular packing in fibrils.[48, 52] This water network with respect to molecular stability has biological and physical significances.[18, 53–55]

Amino acid sequences can also be optimized to enhance the stability of triple helix peptides. Variations of the residues in the X and Y positions determine the global thermal stability and modulate the local stability and energetics that are required for self-association, recognition, and binding.[56, 57] For example, the sequence of Gly-Pro-Hyp confers the maximal stability to the collagen triple helix. In general, the most stabilizing residues for the X position are Pro, Glu, Ala, Lys, Arg, Gln, and Asp, while the most stabilizing residues for the Y position are Hyp, Arg, Met, Ile, Gln, and Ala.[27, 58–60] The least stabilizing residues for both positions are the aromatic residues and Gly. The thermal stability of the 400 possible Gly-X-Y sequences as compared to the Gly-Pro-Hyp sequence are presented in Table 9.1.[18] In this table, there is a significant variation in thermal stability between the Gly-Pro-Hyp ($T_m = 47\ °C$) and the Gly-Gly-Phe ($T_m = 20\ °C$).[18, 61, 62] This information is an important asset in designing peptides that will form stable triple helices, as explained in the above paragraphs.

9.6. INTRODUCTION TO GENETICALLY MODIFIED TRIPLE HELIX F877 PEPTIDE

Recently, we developed genetically modified collagen-based triple helix peptides as templates for practical nanowires in various applications. In this peptide, the complete sequence of the recombinant collagen fragment F877 with the 63-residue region of the α1(I) (residues 877–939) is designed to mimic the robust assembly of collagens, as shown in Figure 9.3a. To further increase the stability of the triple helix, repeating sequences of the tripeptide Gly-Pro-Pro with high triple helix propensity were added at both the C and N termini.[16] Altogether, the recombinant triple helix domain consists of 93 amino acid residues, corresponding to 40 nm in length. The C-terminal foldon domain from bacteriophage T4 fibritin functions as the nucleation domain to facilitate the folding of the triple helix with two Cys residues (Gly-Pro-Cys-Cys-Gly) between the triple helix domain and the foldon domain.[16, 63, 64] When oxidized in folded triple helix conformation, the Cys residues form a set of interchain disulfide bonds, also known as the Cys knot, further increasing the stability of the triple helix.[16, 65] Based on this engineering, F877 collagen-like triple helix peptide was modified to become a rigid, rod-shaped structure that is suitable for applications in building blocks of nanodevices.

The presence of foldon and Cys knot is the key to nucleate the triple helix peptide. The C-terminal domain of T4 fibritin (foldon) is obligatory for the formation of the fibritin trimer structure and can be used as an artificial trimerization domain.[63] The C-terminal part of the T4 fibritin trimer is formed from the trimeric coiled-coil domain, which is terminated by a C-terminal trimeric β-sheet propeller consisting of
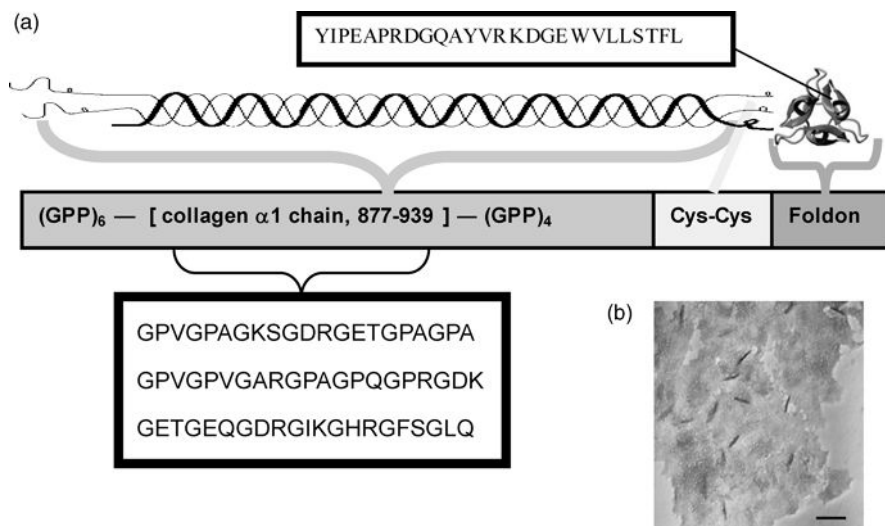
Figure 9.3. (a) Construction of a recombinant protein fragment that models 63 amino acids sequence, residues 877–939, of type I collagen. (b) TEM image of these triple helix peptide nanowires is shown in the bottom right.

monomeric β-hairpin segments.[65] This β-propeller is necessary for the correct folding of the holoprotein and this foldon forms the β-propeller-like structure with a hydrophobic interior. The extensive hydrophobic interactions originate from the small β-sheets formed by threefold-related β-hairpins.[63, 64, 66] In genetically modified triple helix peptide, the C-terminal foldon domain from bacteriophage T4 fibritin can be explored as the nucleation domain to facilitate the formation of the triple helix.[36] Three disulfide bonds are formed between the three chains by covalently oxidizing the cysteine residues into a disulfide knot. This method allows one to covalently link collagen-like peptides with the specific stereochemistry that occurs in nature.[56, 65]

Recombinant collagen protein of F877 can be generated by the following procedure. The DNA sequence and encoded amino acid sequence of expression range in our reconstructed pET32a (+) plasmid is depicted in Figure 9.4. Bam HI restriction enzyme can cut the part of the plasmid where we need to insert a gene, and then the synthetic gene that encodes the F877 fragment is inserted and ligated at that position. T7 RNA polymerase recognizes the specific T7 promoter DNA sequence at the N terminus and initializes the transcription. LacI inhibitor, which blocks the transcription, is bound with the downstream Lac operator in the DNA sequence (Figure 9.5). IPTG binds LacI inhibitor and prevents it from binding the Lac operator, thereby inducing the transcription and the translation of our recombinant protein.

The recombinant collagen proteins are induced, expressed, and purified by the following methodology (Figure 9.6). The gene product of the expression plasmid is a fusion protein including His-tagged thioredoxin at the N-terminal end (Figure 9.3). The exact molecular weight of the recombinant collagen protein was confirmed by

```
        ┌────── T7 promoter ──────┐  ┌──────────Lac operator ──────────┐
001 TAATAC GACTCA CTATAG GGGA AT TGTGAG CGGATA ACAATT

        Xba I
043 CCCCTC TAGAAA TAATTT TGTTTA ACTTTA AGAAGG AGATAT

                      ┌────────His tag────────┐
085 ACC ATG GGT CAT CAC CAT CAC CAT CAC GGT TCT GGT ATG AGC
        Met* Gly [His His His His His His] Gly Ser  Gly [Met Ser
        ┌──────────────Trx tag──────────────┐           ┌──Thrombin
421 AAA GAG TTC CTC GAC GCT AAC CTG GCC GGT TCT GGT TTC GGC
        ··············· 313 bp ···············  Leu Ala] Gly  Ser  Gly  Ser  Gly
    cutting site──────────┐  ┌BamHI
463 CTG GTT CCG CGT GGA TCC GGT CCT CCT GGA CCA CCT GGG CCG
    Leu Ala Pro Arg Gly Ser Gly Pro Pro  Gly Pro Pro  Gly Pro

    Cleavage site ▲
505 CCG GGT CCG CCA GGT CCT CCG GGT CCA CCG GGT CCT GTG GGC
    Pro  Gly Pro Pro  Gly Pro Pro  Gly Pro Pro  Gly Pro Val Gly

547 CCT GCC GGT AAG TCA GGC GAC CGA GGT GAA ACA GGA CCA GCG
    Pro Ala Gly Lys Ser Gly Asp Arg Gly Glu Thr Gly Pro Ala

589 GGT CCG GCC GGT CCG GTA GGT CCA GTT GGC GCG CGT GGT CCC
    Gly Pro Ala Gly Pro Val Gly Pro Val Gly Ala Arg Gly Pro
                            (Gly -> Ser GGT->AGT 901 mutation)
631 GCT GGT CCG CAG GGT CCT CGC GGT GAT AAG GGC GAA ACG GGC
    Ala Gly Pro Gln Gly Pro Arg Gly Asp Lys Gly Glu Thr Gly
        (Gly -> Ser GGT->AGT 913 mutation)  └··········┘ Salt Bridge
673 GAA CAG GGT GAT CGT GGG ATT AAA GGG CAT CGT GGT TTC TCA
    Glu Gln Gly Asp Arg Gly Ile Lys Gly His Arg Gly Phe Ser

715 GGT TTA CAA GGT CCA CCG GGC CCG CCA GGC CCG CCT GGT CCT
    Gly Leu Gln Gly Pro Pro Gly Pro Pro  Gly Pro Pro Gly Pro
                                             ┌BamHI
757 CCA GGT CCG TGC TGT GGC GGA TCC GGT TAC ATC CCG GAA GCT
    Pro Gly Pro Cys Cys Gly    Gly Tyr Ile Pro Glu Ala

799 CCG CGT GAC GGT CAG GCT TAC GTT CGT AAA GAC GGT GAA TGG
             Folden Domain
                                 ┌Eco RI
841 GTT CTG CTG TCT ACC TTC CTG TAA TAA GAA TTC TAA GAT CCG
                                 Stop

883 GCT GCT AAC AAA GCC CGA AAG GAA GCT GAG TTG GCT
    GCTGCCACCGCTGAGCAATAACTAGCATAACCCCTTGGGGCCTCTAAACGGGTC
    TTGAGGGGTTTTTTG (T7 terminal)
```

Figure 9.4. The DNA sequence and the encoded amino acid sequence of the recombinant collagen protein expression range in reconstructed pET32a (+) plasmid.

mass spectrometry. The comparison between the transformed cell sample (Lanes 2 and 3) and nontransformed sample (Lane 1) in gel electrophoresis (SDS-PAGE) can evaluate the degree of the expressed recombinant protein. After purification by affinity chromatography, both trimer and monomer recombinant proteins showed up in Lane 5. After thrombin cleavage of the sample of Lane 5, thioredoxin and 6 X His-tag are cleaved away and the molecular weights of monomer and trimer shift accordingly in Lane 6. Lanes 7 and 8 are purified recombinant protein samples with and without reducing agent DTT, respectively. Here, the reduction breaks Cys knots of trimers, and therefore the reduced sample should lose the band for the trimer if the triple helix is indeed assembled by Cys knots. The different fractions of trimer and monomer proteins in Lanes 7 and 8 demonstrate that oxidized disulfide bonds are formed by the Cys knot at the C terminal of the protein.
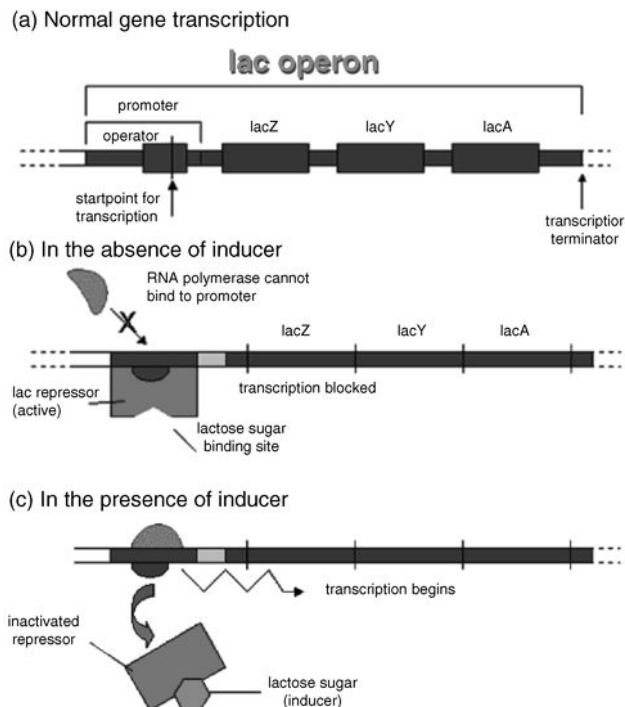
Figure 9.5. (a) Transcription of the gene by mRNA polymerase starts at the operator site in promoter. (b) Lac repressor binds the operator site and prevents the transcription. (c) In the presence of an inducer like IPTG, the inducer binds the repressor and prevents it from binding to the operator. The operator site is now free and mRNA polymerase can start the transcription.

In order to test the feasibility of application of a collagen-like triple helix as a nanowire template, thermal stabilities of two recombinant triple helix molecules were studied (Figure 9.7): one was the F877 triple helix peptide described above and the other is the G901S F877 triple helix peptide where one amino acid mutated with the Gly $\rightarrow$ Ser substitution at position Gly-901. Replacing the obligatory Gly residue at every third position by any other amino acid residue with bulkier side chains is known to weaken the stability of the triple helix conformation, and such mutations have been implicated in connective tissue diseases. From the CD (circular dichroism) spectra with temperature programming, the denaturation temperatures (T_m) that represent the thermal stability of peptides were determined respectively. T_m for F877 is 42 °C while T_m for G901S is 30 °C at 225 nm (inset of Figure 9.7). The small positive peak at ~225 nm and the deep negative peak at ~197 nm are typical of that of a collagen triple helix. The Gly $\rightarrow$ Ser substitution at aa-901 decreases the thermal stability of F877 and reduces the T_m by ~10 °C, while the overall unfolding profile remains similar.[4] This experiment demonstrates that the complete repeat of Gly-Xaa-Yaa structure sustains the stability and rigidity of the entire triple helix peptide.
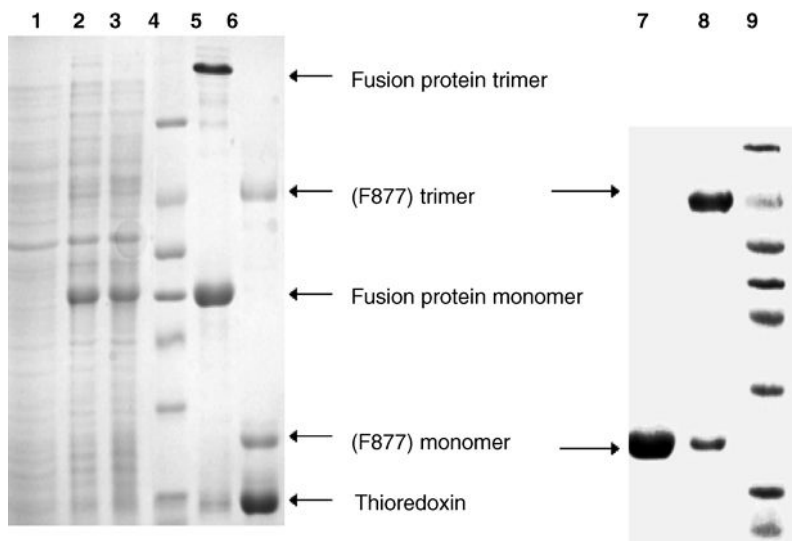
Figure 9.6. SDS-PAGE analysis of the expression of F877 fusion protein. Lane 1: Extracted protein sample from nontransformed host cell (JM109) Lane 2: Extracted protein sample from transformed and noninduced cell. Lane 3: Extracted protein sample from transformed and induced cell with 0.1 mM IPTG. Lanes 4 and 9: Protein molecular weight marker (66, 45, 36, 29, 24, 20, 14.2 kDa). Lane 5: Purified protein by Co^+ – His affinity column Lane 6: Purified protein from Lane 5 with thrombin cleavage. Lane 7: F877 protein with 20 mM DTT. Lane 8 : F877 protein without DTT.
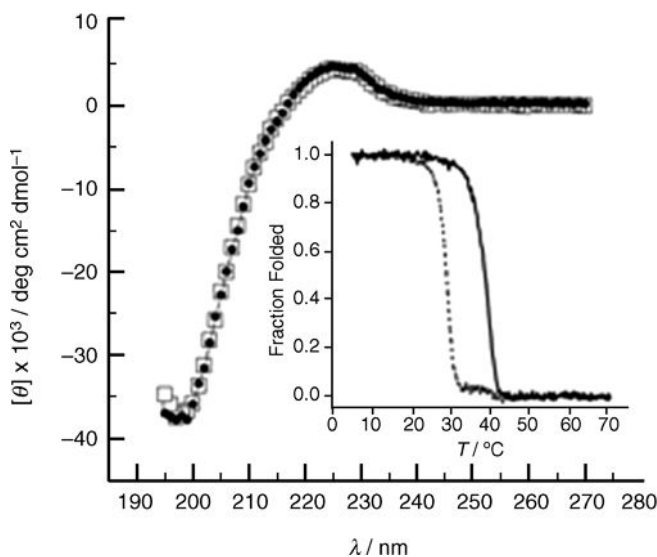
Figure 9.7. Circular dichroism spectra of F877 (●) and G901S (□) at 4 °C. Inset shows denaturation temperatures of F877 (——) and G901S (......).

From the TEM (transmission electron microscopy) image (Figure 9.3b), the triple helix peptide F877 formed monodisperse, linear nanowires with an average length of 40 nm with no bending, which indicated a rather rigid conformation. The length of the triple helix observed under TEM agrees well with the value of approximately 35 nm end-to-end distance of a single triple helix consisting of 93 amino acids and a foldon domain estimated from the triple helix crystal structure. The observed diameter of 4 nm appears to be larger than the 1–2 nm predicted from the crystal structure. This slightly larger diameter in the TEM image could be caused by swelling through hydration.

9.7. FUNCTIONALIZATION OF THE TRIPLE HELIX FOR CREATING COMPLEX HYBRID NANOMATERIALS

The collagen-like triple helix can also be modified at both the N and C termini to create robust materials. This can be achieved in two ways: one is through genetic engineering by incorporating the DNA sequence of the desired peptide and allowing *E. coli* to express it as a fusion protein. The advantage of this method is that all collagen proteins released out of the cells will have the desired fusion protein. On the other hand, the chemical-based method enables one to bind the two proteins or peptides with chemical reactions. One established method is to use EDAC or NHS linkers to form a peptide bond between COOH and NH2 groups of peptides. Hydrogen bonding or charge–charge interaction can also be used to attach peptides noncovalently, and the degree of these interactions can be controlled by pH. These methods are more feasible for the conjugation of short peptides that have few or no free amino groups to prevent nonspecific interactions, but it is not applicable for the conjugation of high molecular weight proteins.

The type of modification that is frequently exploited in protein chemistry is the conjugation of ligands that have strong affinity to their complementary molecules such as biotin–streptavidin, antigen–antibody, and glutathione tags. For example, by genetically linking a particular sequence of peptide with the biotin at the N terminus and/or the C terminus of the collagen-like triple helix, the fusion protein can be expressed with biotin tags at either end. Then, the peptides or nanomaterials conjugated with streptavidin can be bound to the biotinylated peptides. The similar binding scheme can be used by using antibody-toantigen- tagged protein/nanomaterials. These bindings are specific and strong and induces robust assembly. The modified hybrid materials can be studied by techniques like TEM, SEM, and AFM. Recently, there has been progress in using AFM to investigate the type I collagens at the single molecule level to understand their fundamental mechanical behavior.[17]

9.8. METAL COATING ON COLLAGEN-LIKE TRIPLE HELIX PEPTIDE

In the previous section, we introduced a genetically modified collagen-like triple helix peptide F877 by recombinant technology as a rigid and monodispersed
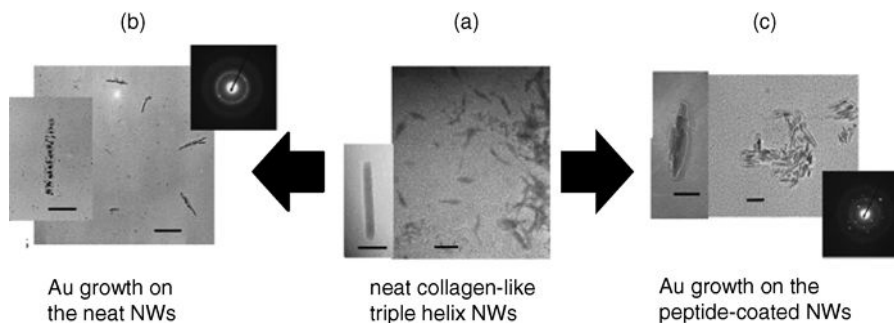
Figure 9.8. TEM images of (a) F877 triple helices, (b) Au growth on F877 triple helices, and (c) Au growth on the mineralization peptide-coated triple helices. Scale bar $= 40\,nm$. Insets are their HRTEM images. Scale bar $= 15\,nm$.

biotemplate.[4, 16] In this section, we introduce an example to metallize this peptide nanowire by coating with Au, targeting it to apply as a conductive nanowire building block for microelectronics. This biomineralization method enables one to grow metal on this rigidity-improved biotemplate.

When the F877 triple helix peptide (Figure 9.8a) was incubated with organic Au salt, trimethylphosphinegold chloride ($AuPMe_3Cl$), for 4 days and then reduced by hydrazine hydrate for 1 day at $4\,°C$, Au crystals were grown on the helix as shown in Figure 9.8b. This TEM image shows that the Au nanocrystal growth was localized on the helix surface. To grow Au on the triple helix more uniformly, the triple helix can be precoated with an Au-mineralizing peptide, Ala-His-His-Ala-His-His-Ala-Ala-Asp (HRE), which has a high affinity for organic Au salts.[8, 67, 68] The subsequent reduction process on these HRE-bound triple helix peptides yields a uniform Au nanocrystal coating (Figure 9.8c).[8] The HRE peptide coating helps increase dispersity of the triple helix nanowires, presumably because the coating of the HRE peptide creates positive charges on the surface, which reduces the potential attractive interaction between the triple helices. In summary, monodisperse Au nanowires with defined dimension of $4\,nm \times 40\,nm$ were obtained by templating recombinant collagen-like triple helices from an *E. coli* expression system. The length of the nanowires can easily be controlled by the number of amino acid residues, and the production of triple helix can be scaled up by means of the cell multiplication. Thus, the unique structural and mechanical properties of collagen-like triple helix combined with the versatility of the recombinant technology offer a promising system to create biomolecular nanowires by design.

9.9. SEMICONDUCTOR COATING ON COLLAGEN-LIKE TRIPLE HELIX PEPTIDE

In this section, we introduce another example of this triple helix peptide coating with oxide semiconductors.[69] This biotemplating method can address both needs for

practical semiconductor nanowires: low temperature synthesis and monodispersity in size for the resulting semiconductor nanowires.

First, we describe the significance of ZnO nanowire fabrication. ZnO has a wide bandgap (3.37 eV) and possesses unique optical, acoustic, catalytic, and electronic properties, which makes ZnO one of the most widely studied semiconductors in the application of solar cells, sensors, ultraviolet nanolasers, catalyst, transparent conductor, piezoelectric materials, and short-wavelength light-emitting devices.[70–73] It requires the fabrication of morphologically and functionally distinct ZnO nanostructures. While recently various methods have been published to grow ZnO in various shapes at near room temperature, there have been no reports on controlling the size and monodispersity of ZnO nanowires at temperatures lower than room temperature.[74–76]

High pH growth media were required to favor condensation and dehydration of the intermediate zinc hydroxide to produce ZnO at low temperature.[77–79] Regular wild-type collagen triple helix peptide is not suitable for the crystallization of ZnO because the wild-type collagen triple helix peptide was not rigid enough to survive in this environment even though the wild-type collagen triple helix is made of three polypeptide chains tightly twisted and bundled together to form a rigid, rod-shaped molecule. Therefore, genetically modified F877 triple helix, whose rigidity was improved by modifying the sequence genetically, was necessary to grow the crystalline ZnO on the surface of triple helix.[4, 69]

Using the same strategy as in the case of the Au coating, a synthetic peptide, ZnO-1 (Glu-Ala-His-Val-Met-His-Lys-Val-Ala-Pro-Arg-Pro-Gly-Gly-Gly-Ser-Cys), which has a high affinity for ZnO crystals and catalyzes ZnO growth at low temperature, was attached to the F877 template via hydrogen bonding.[69, 72] This ZnO-1 peptide-coated F877 triple helix was used for the ZnO nanowire growth. When zinc acetate was hydrolyzed on the ZnO-1 peptide-coated triple helix at pH 10.0 at 4 °C for 9 days, ZnO nanowires were obtained from the supernatant of the growth solution via centrifugation, as shown in Figure 9.9a. The size of the resulting ZnO nanowire is monodisperse (5 × 40 nm), a similar dimension to that of the F877 triple helix, while the coated ZnO nanowire has a rice-like shape and the middle part
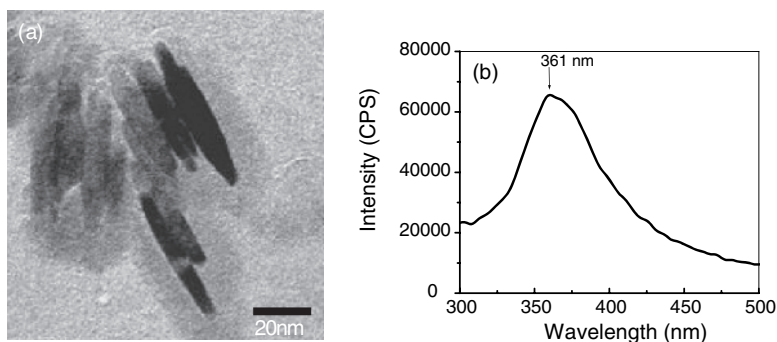
Figure 9.9. (a) TEM images of ZnO growth on mineralization peptide-coated F877 triple helices. (b) Photoluminescence spectrum of (a).

of the wire has a thicker ZnO coating, which was also observed previously when the triple helix was coated by Au. The characteristic bandgap of ZnO at 361 nm was also confirmed by its photoluminescence spectrum (Figure 9.9b). Since the regular wild-type collagen disappeared under the same growth conditions, this result demonstrates that the recombinant collagen-like triple helix enhances its structural stability sufficiently to survive under the extreme base growth conditions.

It should be noted that the same growth conditions at pH 8.6 produced ZnO nanowires but the yield was only 50% and no ZnO nanowires were observed when the solution pH was reduced to less than pH 8.6. Zinc ions form the intermediates $Zn(OH)_x(OH2)_{6-x}$ under extremely high pH conditions, and the condensation of these complexes with elimination of water yields ZnO crystals.[80] The growth and crystallinity of ZnO is dependent on how these intermediates are effectively precipitated and condense to undergo the dehydration reaction.[77] The room-temperature growth of ZnO on triple helix peptide nanowires at high pH follows the same growth mechanism. Crystalline ZnO could not be grown on the triple helix at high pH without ZnO-1 peptide, and it indicates that the ZnO-1 peptide catalyzes the growth of single crystalline ZnO under these extreme conditions. Previously, Umetsu et al.[72] reported that cysteine in the GGGSC tag of the ZnO-1 peptide was required to grow flower-like ZnO microparticles at room temperature, and the combination of this GGGSC tail and the rest of the amino acid residues, EAHVMHKVAPRP, is likely to be important in the growth of single crystalline ZnO nanowires at low temperature and pH 10.0; at pH 10.0, cysteine is negatively charged and this negative charge recruits positive zinc ions onto the template nanowires efficiently. Then, the basic amino-acid-dominant EAHVMHKVAPRP part could produce local pH and charge distributions at the molecular level that favor the condensation of the intermediates and catalyze the dehydration to produce ZnO. Cysteine in the tail could have an additional role in hydrolyzing hexaqua zinc into the intermediate $Zn(OH)_x(OH2)_{6-x}$ effectively and slowing the condensation reaction, which favors single crystal formation on the F877 nanowire.

ACKNOWLEDGMENT

REFERENCES

1. X. Gao, H. M. *Adv. Mater.*, **2005**, *17*, 2037.
2. Whaley, S. R.; English, D. S.; Hu, E. L.; Barbara, P. F.; Belcher, A. M. *Nature*, **2000**, *405*, 665.
3. Braun, E.; Eichen, Y.; Sivan, U.; Ben-Yoseph, G. *Nature*, **1998**, *391*, 775.

4. Bai, H.; Xu, K.; Xu, Y.; Matsui, H. *Angew. Chem. Int. Ed.* **2007**, *46*, 3319.

5. Chung, S. W.; Ginger, D. S.; Morales, M. W.; Zhang, Z. F.; Chandrasekhar, V; Ratner, M. A.; Mirkin, C. A. *Small*, **2005**, *1*, 64.

6. Banerjee, I. A.; Yu, L.; Matsui, H. *J. Am. Chem. Soc.*, **2005**, *127*, 16002.

7. Deng, Z.; Tian, Y.; Lee, S. H.; Ribbe, A. E.; Mao, C. D. *Angew. Chem. Int. Ed.*, **2005**, *44*, 3582.

8. Djalali, R.; Chen, Y.-F.; Matsui, H. *J. Am. Chem. Soc.*, **2003**, *125*, 5873.

9. Mao, C. B.; Solis, D. J.; Reiss, B. D.; Kottmann, S. T.; Sweeney, R. Y.; Hayhurst, A.; Georgiou, G.; Iverson, B.; Belcher, A. M. *Science*, **2004**, *303*, 213.

10. Reches, M.; Gazit, E. *Science*, **2003**, *300*, 62.

11. Sharma, J.; Chhabra, R.; Liu, Y.; Ke, Y. G.; Yan, H. *Angew. Chem. Int. Ed.*, **2006**, *45*, 730.

12. Endo, M.; Wang, H. X.; Fujitsuka, M.; Majima, T. *Chem. Eur. J.*, **2006**, *12*, 3735.

13. Yi, H. M.; Nisar, S.; Lee, S. Y.; Powers, M. A.; Bentley, W. E.; Payne, F.; Rubloff, G. W.; Harris, M. T.; Culver, J. N. *Nano Lett.*, **2005**, *5*, 1931.

14. Tseng, R. J.; Tsai, C.; Ma, L.; Ouyang, J.; Ozkan, C. S.; Yang, Y. *Nature*, **2006**, *1*, 72.

15. Van Hest, J. C. M.; Tirrell, D. A. *Chem. Commun.*, **2001**, *19*, 1897.

16. Xu, K.; Nowak, I.; Kirchner, M.; Xu, Y. *J. Biol. Chem.*, **2008**, *283*, 34337.

17. Langer, R.; Tirell, D. A. *Nature*, **2004**, *428*, 487.

18. Brodsky, B.; Persikov, A. V. *Adv. Protein Chem.*, **2005**, *70*, 301.

19. J. Bella; Eaton, M; Brodsky, B; Berman, H. M. *Science*, **1994**, *266*, 75.

20. Knight, C. G.; Morton, L. F.; Peachey, A. R.; Tuckwell, D. S.; Farndale, R. W.; Barnes, M. J. *J. Biol. Chem.*, **2000**, *275*, 35.

21. Kadler, K. E.; Holmes, D. F.; Trotter, J. A.; Chapman, J. A. *Biochem. J.*, **1996**, *316*, 1.

22. Kielty, C. M.; Grant, M. E. The collagen family: structure assembly and organization in the extracellular matrix. In: *Connective Tissue and its Heritable Disorders*. Royce, P. M.; Steinmann, B. Eds. Wiley-Liss, Hoboken, NJ, 2002; p. 159.

23. Jenkins, C. L.; Raines, R. T. *Nat. Prod. Rep.*, **2002**, *19*, 49.

24. Hulmes, D. J. *J. Struct. Biol.*, **2002**, *137*(1–2), 2.

25. Perumal, S.; Antipova, O.; Orgel, J. P. *Proc. Natl. Acad. Sci. U. S. A.*, **2008**, *105*(8), 2824.

26. Kramer, R. Z.; Bella, J.; Brodsky, B.; Berman, H. M. *J. Mol. Biol.*, **2001**, *311*, 131.

27. Persikov, A. V.; Ramshaw, J. A.; Kirkpatrick, A.; Brodsky, B. *Biochemistry*, **2000**, *39*, 14960.

28. LulloDagger, G. A. D.; Sweeney, S. M.; Körkkö, J.; Ala-Kokko, L.; Antonio, J. D. S. *J. Biol. Chem.*, **2002**, *277*(6), 4223.

29. http://en.wikipedia.org/wiki/Collagen.

30. Ramachandran, G. N.; Kartha, G. *Nature*, **1954**, *174*, 269.

31. Ramachandran, G. N.; Kartha, G. *Nature*, **1955**, *176*, 593.

32. Wess, T. J. *J. Mol. Biol.*, **1998**, *275*(2), 255.

33. Kramer, R. Z.; Venugopal, M. G.; Bella, J.; Mayville, P.; Brodsky, B.; Berman, H. M. *J. Mol. Biol.*, **2000**, *301*, 1191.

34. Bachinger, H. P.; Bruckner, P.; Timpl, R.; Prockop, D. J.; Engel, J. *Eur. J. Biochem.*, **1980**, *106*, 619.

35. Koide, T. *Connective Tissue Res.*, **2005**, *46*, 131.

36. Boudko, S.; Frank, S.; Kammerer, R. A.; Stetefeld, J.; Schulthess, T.; Landwehr, R.; Lustig, A.; Bachinger HP.; Engel, J. *J. Mol. Biol.*, **2002**, *317*, 459.

37. Orgel, J. P. *Proc. Natl. Acad. Sci.*, **2006**, *103*(24), 9001.

38. Fraser, R. D. B.; MacRae, T. P.; Miller, A.; Suzuki, E. *J. Mol. Biol.*, **1983**, *167*, 497.

39. Fraser, R. D.; MacRae, T. P.; Miller, A. *J. Mol. Biol.* **1987**, *193*(1), 115.

40. Koide, T.; Nagata, K. *Top Curr. Chem.*, **2005**, *247*, 85.

41. Okuyama, K.; Arnott, S.; Takayanagi, M.; Kakudo, M. *J. Mol. Biol.*, **1981**, *152*, 427.

42. Buehler, M. J. *Curr. Appl. Phys.*, **2008**, *8*, 440–442.

43. Engel, J.; Bächinger, H. P. *Top Curr. Chem.*, **2005**, *247*, 7.

44. Beck, K.; Brodsky, B. *J. Struct. Biol.*, **1998**, *122*, 17.

45. Birk, D. E.; Bruckner, P. *Top Curr. Chem.*, **2005**, *247*, 185.

46. Ramachandran, G., *Structure of Collagen at the Molecular Level*. Academic Press, New York, 1967.

47. Ramachandran, G. N.; Chandrasekharan, R. *Biopolymers*, **1968**, *6*, 1649.

48. Suzuki, E.; Fraser, R. D. B.; MacRae, T. P. *Int. J. Biol. Macromol.*, **1980**, *2*, 54.

49. Privalov, P. L. *Adv. Protein Chem.*, **1982**, *35*, 1.

50. Xu, Y.; Hyde, T.; Wang, X.; Bhate, M.; Brodsky, B. *Biochemistry*, **2003**, *42*, 8696.

51. Bella, J.; Berman, H. M. *J. Mol. Biol.*, **1996**, *264*, 734.

52. Traub, W.; Piez, K. A. *Adv. Protein Chem.*, **1971**, *25*, 243.

53. Leikin, S.; Parsegian, V. A.; Yang, W.-H.; Walrafen, G. E. *Proc. Natl. Acad. Sci. U. S. A.*, **1997**, *94*, 11312.

54. Leikin, S.; Rau, D. C.; Parsegian, V. A. *Proc. Natl. Acad. Sci. U. S. A.*, **1994**, *91*, 276.

55. Leikin, S.; Rau, D. C.; Parsegian, V. A. *Nat. Struct. Biol.*, **1995**, *2*, 205.

56. Stetefeld, J.; Frank, S.; Jenny, M.; Schulthess, T.; Kammerer, R. A.; Boudko, S.; Landwehr, R.; Okuyama, K.; Engel, J. *Structure*, **2003**, *11*, 339.

57. Bruckner, P.; Eikenberry, E. F.; Prockop, D. J. *Eur. J. Biochem.*, **1981**, *118*, 607.

58. Bachinger, H. P.; Bruckner, P.; Timpl, R.; Engel J. *Eur. J. Biochem.*, **1978**, *90*, 605.

59. Bachinger, H. P.; Davis, J. M. *Int. J. Biol. Macromol.*, **1991**, *13*, 152.

60. Persikov, A. V.; Ramshaw, J. A. M.; Kirkpatrick, A.; Brodsky, B. *Biochemistry*, **2005**, *44*, 1414.

61. Persikov, A. V.; Ramshaw, J. A. M.; Brodsky, B. *J. Biol. Chem.*, **2005**, *280*, 19343.

62. Bann, J. G.; Bachinger, H. P. *J. Biol. Chem.*, **2000**, *275*, 24466.

63. Meier, S.; Güthe, S.; Kiefhaber, T.; Grzesiek, S. *J. Mol. Biol.*, **2004**, *344*, 1051.

64. Güthe, S.; Kapinos, L.; Möglich, A.; Meier, S.; Grzesiek, S.; Kiefhaber, T. *J. Mol. Biol.*, **2004**, *337*, 905.

65. Mechling, D. E.; Bächinger, H. P. *J. Mol. Biol.*, **2000**, *275* (May 12), 14532.

66. Tao, Y.; Strelkov, S. V.; Mesyanzhinov, V. V.; Rossmann, M. G. *Structure*, **1997**, *5*, 789.

67. M. Slocik, J.; T. Moore, J.; Wright, D. W. *Nano Lett.*, **2002**, *2*, 170.

68. Slocik, J. M.; Naik, R. R.; Stone, M. O.; Wright, D. W. *J. Mater. Chem.* **2005**, *15*, 749.

69. Bai, H.; Xu, F.; Anjia, L.; Matsui, H. *Soft Matter*, **2009**, *5*, 966.

70. Greene, L. E.; Yuhas, B. D.; Yang, P. D. *Inorg. Chem.*, **2006**, *45*, 7535.

71. Tian, Z. R.; Voigt, J. A.; Liu, J.; Konishi, H.; Xu, H. *Nat. Mater.*, **2003**, *2*, 821.

72. Umetsu, M.; Mizuta, M.; Tsumoto, K.; Ohara, S.; Takami, S.; Watanabe, H.; Kumagai, I.; Adschiri, T. *Adv. Mater.*, **2005**, *17*, 2571.

73. Yin, M.; Gu, Y.; Kuskovsky, I. L.; Andelman, T.; Zhu, Y.; Neumark, G. F.; O'Brien, S. *J. Am. Chem. Soc.*, **2004**, *126*, 6206.

74. Liu, B.; Zeng, H. C. *Langmuir*, **2004**, *20*, 4196.

75. Li, F.; Ding, Y.; Gao, P. X. X.; Xin, X. Q.; Wang, Z. L. *Angew. Chem. Int. Ed.*, **2004**, *43*, 5238.

76. Greene, L. E.; Law, M.; Goldberger, J.; Kim, F.; Johnson, J. C.; Zhang, Y. F.; Saykally, R. J.; Yang, P. D. *Angew. Chem. Int. Ed.*, **2003**, *42*, 3031.

77. Kisailus, D.; Schwenzer, B.; Gomm, J.; Weaver, J. C.; Morse, D. E. *J. Am. Chem. Soc.*, **2006**, *128*, 10276.

78. Jung, S. H.; Oh, E.; Lee, K. H.; Yang, Y.; Park, C. G.; Park, W. J.; Jeong, S. H. *Cryst. Growth Des.*, **2008**, *8*, 265.

79. Oliveira, A. P. A.; Hochepied, J. F.; Grillon, F.; Berger, M. H. *Chem. Mater.* **2003**, *15*, 3202.

80. Yu, Q. J.; Yu, C. L.; Yang, H. B.; Fu, W. Y.; Chang, L. X.; Xu, J.; Wei, R. H.; Li, H. D.; Zhu, H. Y.; Li, M. H.; Zou, G. T.; Wang, G. R.; Shao, C. L.; Liu, Y. C. *Inorg. Chem.*, **2007**, *46*, 6204.

Polydiacetylene-Containing Liposomes as Sensory Materials

MANAS K. HALDAR, MICHAEL D. SCOTT, and SANKU MALLIK

Department of Pharmaceutical Sciences, North Dakota State University, Fargo, North Dakota, USA

Conjugated dialkynes undergo topotactic polymerization upon irradiation with ultraviolet light. Liposomes incorporating the conjugated dialkynes in the lipid bilayers have been efficiently photopolymerized below the phase transition temperature. The resultant ene-yne backbone of the polymerized liposomes has been extensively investigated as sensors for viruses, bacteria spores, toxins, proteins, and metal ions and for *in vivo* imaging of angiogenesis. Antibodies, ligands, inhibitors, and other small molecules have been used for selective recognition of the analytes by these liposomes. Upon binding, the ene-yne backbone of the polymerized liposomes is perturbed, inducing changes in the color and fluorescent emission spectra. These color or fluorescence spectral changes are usually monitored to detect the presence of the analyte of interest. The ene-yne moiety has been demonstrated to be efficiently sensitive to the emission from liposome-incorporated lanthanide ions. Changes in the sensitized emission of lanthanide ions have been used as an alternative method to detect proteins employing time-resolved luminescence spectroscopy. The excited-state lifetimes of the polymerized liposome-incorporated lanthanide ions have the potential to distinguish between the isozymes of an enzyme family.

10.1. INTRODUCTION

10.1.1. Liposomes

Liposome is a term derived from two Greek words: *lipos*, meaning fat, and *soma*, meaning body. Liposomes are spherically enclosed lipid bilayers with an aqueous

interior and exterior. They can be prepared from naturally occurring or synthetic amphiphilic molecules. Liposomes can encapsulate hydrophilic and hydrophobic molecules in the aqueous interior and in the lipid bilayers, respectively. Currently, liposomes are finding applications in industrial, pharmaceutical, and diagnostic applications and there are several liposomal drug formulations approved by the FDA for human use.[1–16]

10.1.2. Polymerized Liposomes

Liposomes are vulnerable to various degradation factors during preparation, storage, and usage. During preparation, the process of sonication or homogenization may increase the decomposition rate. Stability can also be negatively influenced by pH during the storage of liposomes. The hydrophobic moieties of the lipids are prone to oxidative degradation or lipid peroxidation. Liposomal stability can be increased with suitable structural modifications. By incorporating cholesterol or sphingomyelin, liposomal decomposition rates can be reduced. Liposomal stability can also be increased by extending the length of the hydrophobic moiety of the lipid molecules.

In pursuit of enhanced liposomal stability, Ringsdorf,[17, 18] Regen,[19] Chapman,[20] and O'Brien[21] pioneered the use of polymerized liposomes. These liposomes were prepared from polymerizable lipid molecules. Polymerized liposomes demonstrated uniform size distribution and are considerably more stable compared to their unpolymerized counterparts. Various polymerizable groups (e.g., butadiene,[22] diacetylene,[22] vinyl,[23] or methacryloyl[19]) have been used to achieve the polymerization of the lipid bilayers. These reactive groups on the lipid may be in the head group region, the hydrocarbon core, or at the hydrocarbon termini.

10.1.3. Polydiacetylene-Containing Liposomes

The 1,4 addition of diacetylenic monomers, initiated by UV irradiation, creates polydiacetylene (PDA) polymers. PDA was first prepared in 1969 by Wegner[24] and since then it has been an area of extensive research. Ringsdorf was the first to prepare PDA vesicles and study its absorption and emission properties in response to environmental changes.[18, 25, 26] Charych and her co-workers pioneered the application of PDA materials for biosensing by detecting influenza virus.[27]

Once diacetylene molecules are properly aligned, they undergo 1,4-photopolymerization to form the conjugated ene-yne backbone (Scheme 10.1). The
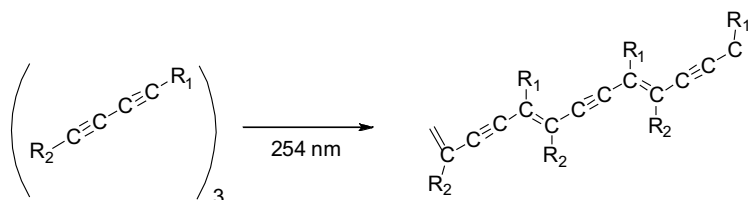
Scheme 10.1. The formation of polydiacetylene polymer from the diacetylenic monomers using 1,4 addition via UV irradiation at wavelength 254 nm. For clarity, only three monomers are shown.

polymerization of the self-assembled monomers leads to physical stabilization of the structure. The increased physical stabilization gives PDA an increased mechanical strength and thermal stability.[28] The resulting PDA polymer may be colored blue, red, or yellow. ^{13}C NMR,[29–31] Raman spectroscopy,[32, 33] and X-ray diffraction studies[34, 35] suggest that the backbone has a primarily ene-yne character, or alternating double and triple bonds (Scheme 10.1).

The stability, color, and extent of polymerization are influenced by distance of the head group to the diacetylene moiety. When they are in close proximity, better packing of amphiphiles leads to increased degree of polymerization and enhanced stability.[36–38] If the distance between the head group and the diacetylene is increased it will cause a reduction in the extent of polymerization and increase the probability that the polymer will be colored yellow.[38]

PDA liposomes usually have lipids with two alkyl chains; but liposomes can be formulated with a single or multiple alkyl chains in the lipids. The length and number of the lipid tails controls the self-assembly process of the amphiphiles in addition to the transition temperature from "crystalline" to "liquid" chain packing. It has also been observed that an increase in the size of the chains results in a red color upon polymerization.[39] PDA polymers that have nonequivalent tails are 6500-fold less efficient at polymerization than those of the corresponding equivalent two-tailed monomers.[40] The increase in efficiency of two-tailed monomers is likely the result of better alignment for more optimal geometry.

10.1.4. Color Changes in Polydiacetylene Liposomes

Usually the PDA polymer has a deep blue color but it may also be red or yellow. The color of PDA is a result of the energy of electronic excitations. This energy is affected by the state of the monomers packing and the polymer's exposure to environmental variables, for example, heat (thermochormism),[32, 41–53] mechanical stress (mechanochromism),[54–59] or solvent (solvatochromism).[30, 43, 60, 61] Under extended exposure to UV light, it has been observed that PDA can undergo depolymerization and chain scission, leading to a hypsochromic shift in the absorption.[62, 63] In a few cases, the absorbance wavelength of PDA can shift toward longer wavelength also.[36]

The color transition from blue to red has been associated with PDA's backbone undergoing a conformational change from planar to nonplanar. The change from planar to nonplanar is associated with changes in the positions of the PDA's side chains.[64–66] When the side chains undergo a near hexagonal packing, it increases the order of the packing. This increase of packing order will result in an increase in the red color observed in PDA.[67] When the PDA is a part of the bilayers of liposomes, the same photophysical properties are also observed.

10.2. APPLICATIONS OF POLYDIACETYLENE LIPOSOMES

Polydiacetylene liposomes have been used for detection and analyses of metal ions,[68–70] cyclodextrins,[71] nucleic acids,[72] proteins,[73–82] bacteria,[64, 68, 83–85] viruses,[27, 86–88] and so on (Figure 10.1). Some of these applications are discussed
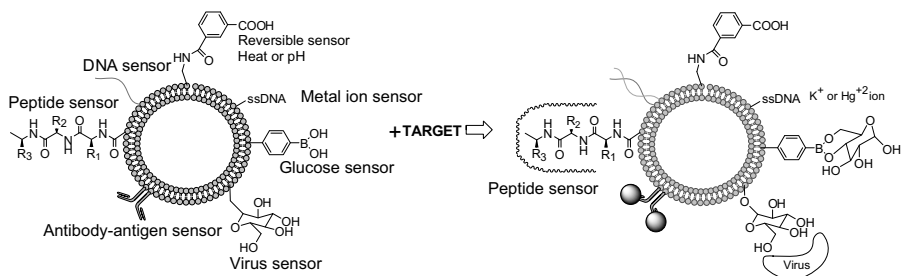
Figure 10.1. General scheme for detection of analytes by PDA liposomes. Binding of the analyte to the receptor on the liposome surface induces structural perturbations in the PDA structure, leading to changes in color.

below. For these applications, a recognition moiety is attached to the diacetylene liposomes and then the liposomes are photopolymerized to produce an intense blue color. Recognition of the target perturbs the ene-yne backbone and induces color change from blue to red (and from nonfluorescent to fluorescent), similar to that observed for PDA polymers in response.[42, 89, 90] The change can be monitored visually or by employing a spectrophotometer. Color change induced by ligand receptor interaction is known as biochromism.

10.2.1. Detection of Viruses and Bacteria

The recognition of influenza virus by sialic acid containing polydiacetylene lipid films and liposomes with concurrent change in color laid the foundation of detection of microorganisms by PDA vesicles.[27, 86] Jalinek[64, 83] and co-workers reported a bacteria detection method with polydiacetylene vesicles embedded in agar. DMPC and 10,12-tricosadiynoic acid (2:3 molar ratio) were used for preparing the liposomes. These vesicles did not contain any active recognition elements. After probe sonication at 70 °C, the liposomes were mixed with agar, allowed to cool, and polymerized. Incubation with three types of bacteria (gram positive, gram negative, and representative common pathogenic bacteria) showed the color change from blue to red for all the cases. The color change was found to be dependent on the number of bacteria and incubation time. It was proposed that by properly adjusting the incubation time, a single bacterium could be detected using this method. In agar medium, the bacteria proliferate and the detection becomes easier. The peptides, toxins, and other molecules secreted by the bacterial cells also bind to the polymerized liposomes, causing the color change. This method was used successfully to detect bacteria in contaminated foods. However, the main disadvantage is the nonspecificity of detection and any agent that binds to the liposomes and induces perturbation of the ene-yne backbone gives the color changes.

A traceless detection of *Escherichia coli* has been reported by Ahn and co-workers (Figure 10.2).[84] Two polymerizable lipids (one containing biotin, Figure 10.2) and DMPC were used to form the liposomes. The liposomes were spotted on streptavidin
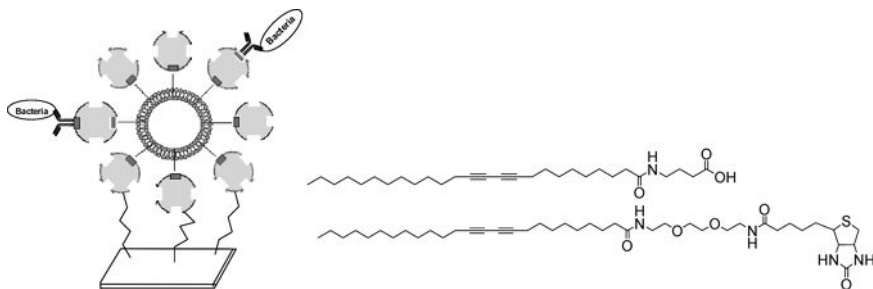
Figure 10.2. Schematic representation of the traceless detection of *E. coli* developed by Ahn and co-workers. The structures of the polymerizable lipids used in this study are also shown.

coated glass slides and polymerized with UV light. These polymerized vesicles were then hybridized for 2 hours in buffer solution containing streptavidin. The glass slides were treated with biotin conjugated to a primary antibody for *E. coli*. Fluorescence changes from the polymerized liposomes were observed in the presence of *E. coli* and not with *Salmonella typimurium*.

Reppy and co-workers reported the detection of microorganisms based on antibody functionalized polydiacetylene vesicles prepared from 10,12-pentacosa-diynoic acid.[85] The polymerized liposomes were deposited on polylysine treated membranes. Out of PDVF, MCE, CN, Nylon, and PC, only MCE and PC membranes were found suitable for storing the liposome-coated membranes for extended periods of time (up to 13 months). The coated membranes act as sieves and were used to detect the presence of *E. coli*. Filtration of the solution increases *E. coli* concentration at the membrane and enhanced the color changes.

Li and co-workers employed mannose for a recognition element to detect *E. coli*.[68] A mannose containing saturated lipid (Figure 10.3) along with 10,12-pen-tacosadiynoic acid was used for liposome formation. Upon binding of *E. coli* to the resultant polymerized liposomes, the color changed from blue to red. The effects of alkaline earth (Ca^{2+}, Mg^{2+}, and Ba^{2+}) and transition metal ions (Cd^{2+}, Ag^+, Cu^{2+}, Fe^{3+}, Zn^{2+}, and Ni^{2+}) on this detection methodology were also studied. It was observed that the ions Cd^{2+}, Ag^+, Ca^{2+}, Mg^{2+}, and Ba^{2+} favored the chromic transition of the polymerized liposomes in the presence of *E. coli*. The ions Cu^{2+}, Zn^{2+}, Ni^{2+}, and Fe^{3+} inhibited the transition. It is hypothesized that the later group of metal ions bind strongly to the carboxylic acid head groups, making the ene-yne backbone of the polymerized liposomes more rigid for conformational changes.
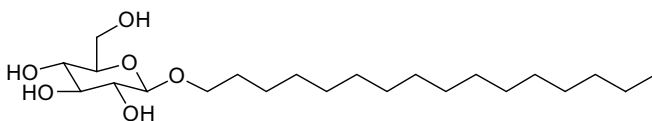
Figure 10.3. The structure of mannose containing saturated lipid used by Li and co-workers as the recognition element for *E. coli* is shown.
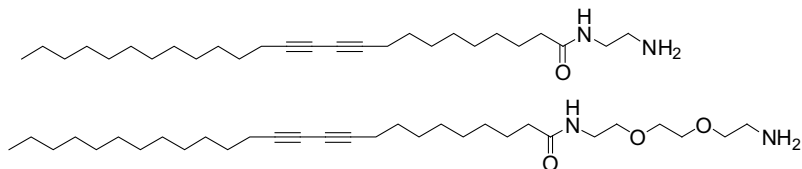
Figure 10.4. Polymerizable lipids used for the detection of oligosaccharides (with primary amine as the head groups) are shown.

10.2.2. Detection of α-Cyclodextrin from Mixtures of Oligosaccharides

Application of PDA vesicles for microarray-based sensing was first demonstrated by Ahn and co-workers.[71] Polymerizable lipid with primary amine as the head group (Figure 10.4) was employed for vesicle formation. The vesicles were incubated on an aldehyde modified glass slide. The glass slide was partially covered with a photomask and irradiated with UV light to polymerize the liposomes. Generation of patterned red fluorescent PDA confirmed the success of PDA vesicle immobilization on glass slides. The polymerized array of liposomes was exposed to solutions of different oligosaccharides (α-cyclodextrin, γ-cyclodextrin, meltoheptaose, etc.) and poly-acrylic acid. Changes in color and fluorescence emission properties of the vesicles were observed in the presence of α-cyclodextrin and polyacrylic acid.

10.2.3. Detection of Metal Ions

Detection of metal ions employing PDA liposomes is reported by Kim and co-workers (Figure 10.5).[69] Liposomes were formed from a polymerizable epoxy lipid and 10,12-tricosadiynoic acid. The liposomes were immobilized on an amine-functionalized glass surface. The remaining epoxy groups on the liposome surface were used to link a thymine rich DNA aptamer, selective for the Hg^{2+} ions. The grafted liposomes were subsequently photopolymerized to generate the blue color. In the presence of added Hg^{2+} ions, the liposomes changed from blue to red, with a detection limit of $5 \mu M$. The method was selective for the Hg^{2+} ions compared to Cd^{2+}, Zn^{2+}, Sn^{2+}, K^+, Na^+, Ir^{3+}, and Cu^{2+}. The same protocol has been used to detect K^+ ions (detection limit: $100 \mu M$) by employing an aptamer selective for this metal ion.[70] The system was capable of detecting the K^+ ions in the presence of Na^+ ions.[70]

10.2.4. Detection of Nucleic Acids

Jung and co-workers has used PDA liposomes for the detection of nucleic acids "amplified" by the polymerase chain reaction (PCR).[72] These liposomes incorpo-rated polymerizable lipids containing primary amines and quarternary ammonium groups (Figure 10.6). The binding of the negatively charged nucleic acids to the cationic polymerized liposomes leads to the changes in color and fluorescence emission spectra. The polymerized liposomes containing the primary amine groups were found to be better compared to the liposomes containing the tertiary amine
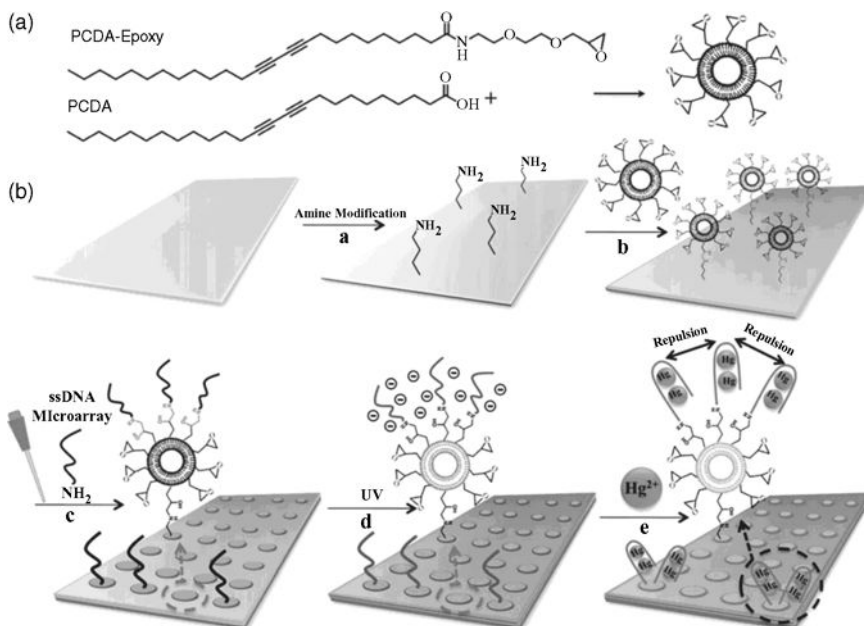
Figure 10.5. The scheme for the detection of Hg^{2+} employing polymerized liposomes is shown. (Reproduced with permission from Ref. 69. Copyright Wiley-VCH Verlag GmbH & Co. KGaA.)

functionality. However, the method did not demonstrate any sequence selectivity for the nucleic acids and the PCR buffer also caused considerable color changes for the PDA liposomes.

10.2.5. Detection of Toxins

Pan and Charych, after their pioneering work for virus detection by PDA platform, extended its application for detection of cholera toxins.[87] Initially, they employed sphingolipid gangliosides (Figure 10.7) along with 5,7-dicosadiynoic acid for film
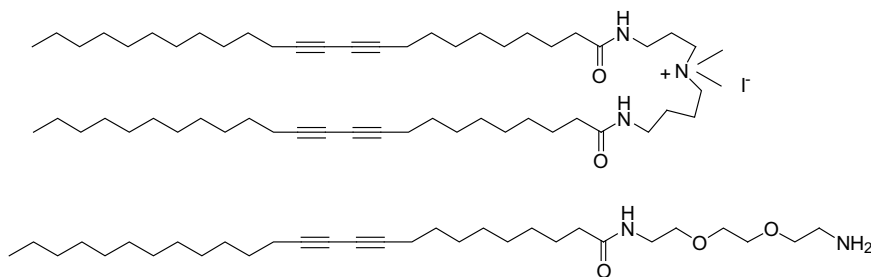
Figure 10.6. Chemical structures of the lipids with quaternary and primary amine as head groups are shown.
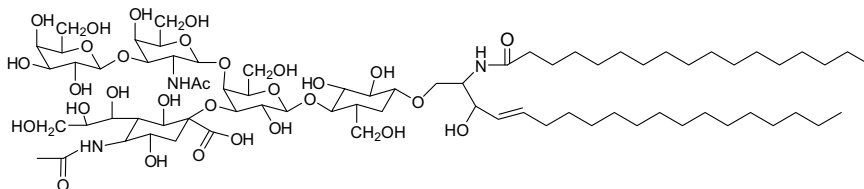
Figure 10.7. The structure of the sphingolipid ganglioside GM1 used for detecting cholera toxin is shown.

formation and the polymerized film was used for detecting cholera toxin.[88] The ganglioside head group of these lipids acts as the selective recognition element for the cholera toxin. Subsequently, polymerized liposomes were prepared from the same lipids and detection of cholera toxins was studied. Addition of cholera toxin changed the blue color of the polymerized liposomes to red. A calibration curve was constructed and used for the detection of the toxin (limit: $100\,\mu g/mL$).

Ma and Cheng have reported a PDA based sensor for colorimetric detection of bacterial pore forming toxin, streptolysin O (SLO).[91] A polymerizable phosphatidyl choline, cholesterol, and another polymerizable lipid (Figure 10.8) were used to form the liposomes. The blue color of the polymerized liposomes changed to fluorescent red upon addition of SLO from *Streptococcus pyrogenes.* The amount of cholesterol in the liposomes and the polymerization conditions were found to play important roles in the overall efficiency of the detection process. High amounts of cholesterol (>30%) or prolonged polymerization time decreased the membrane fluidity and reduced the chromatic changes upon addition of SLO. Using the optimized conditions, a very low limit of detection was observed (100 pM).

10.2.6. Detection of Interactions with Cell Membranes

Jelinek and co-workers demonstrated that the changes in fluorescence of PDA can be used to detect the interactions of drug molecules with the membranes of live cells.[92, 93] Diacetylene patches containing 10,12-tricosadiynoic acid were transferred from diacetylene vesicles to the membranes of leukemia cells and were polymerized with UV radiation. This fusion efficiency was found to depend on the lipid composition of the liposomes and the presence of cholesterol on the plasma membrane. The interactions of these cells with lidocaine (a local anesthetic), polymixin-B (an antibiotic), and oleic acid were studied by confocal fluorescence microscopy. The PDA patch on the live cells showed bright red fluorescence when the cell membranes were perturbed. The blue to red color change in the presence of oleic acid was apparent when the cells were sedimented by centrifugation.
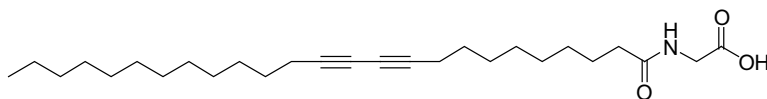
Figure 10.8. Lipid used by Ma and Cheng to detect bacterial toxins.

The same PDA fusion methodology was also used to study attachment, perturbation of the membrane, and entry of vaccinia virus to the cell membrane.[94] The PDA patch was introduced on epithelial cell membranes and polymerized. Attachment of viral particle to the membranes induced changes in color (blue to red) and emission spectra. It was observed that the lipid composition of the membrane had a profound effect for the interactions of the PDA labeled cells with the virus particles. Membrane domains or lipid rafts rich in cholesterol and sphingomylein favored the interactions with the vaccinia virus.

10.2.7. Detection of Proteins

The lanthanide ions offer several advantages compared to organic fluorophores. The ions have large Stokes' shifts; the long excited state lifetime allows gated detection with minimal interference from the emission of organic fluorophores present.[73–77] As the absorption of the lanthanide ions originates from the ^5D to ^7F transition, the intensity is low, but the possibility of oxygen quenching is also less. The intensity can be considerably enhanced by employing a sensitizer (antenna) to transfer energy to the lanthanide ions. Roy and co-workers have shown that when a polymerizable lipid capable of chelating lanthanide ions is used, the ene-yne backbone of polymerized liposomes act as a sensitizer for the emission of the chelated lanthanide ions.[78, 79]

The number of Lewis bases chelating the lanthanide ions also plays an important role in determining the solution stability of the polymerized liposomes. Thus, polymerized liposomes from the EDTA lipid (Figure 10.9) were stable and efficiently sensitized the chelated Tb^{3+} ions.[78] On the other hand, polymerized liposomes containing Tb^{3+} ions chelated with chelidamic acid (Figure 10.9) were found to aggregate in solution.[79]

The efficiency of energy transfer from the liposomes to the chelated lanthanide ions can be further enhanced by incorporating the aminosalicylic acids in the structure of the polymerizable lipids (Figure 10.10).[80, 81] Mallik and co-workers
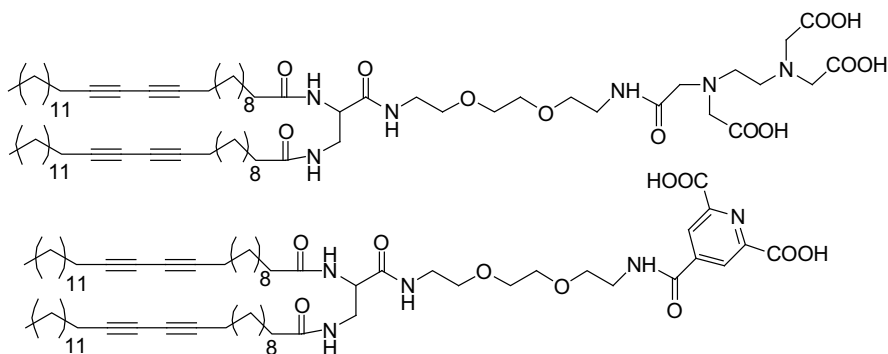
Figure 10.9. Structures of the polymerizable diacetylene containing lipid with lanthanide chelating head groups (EDTA or chelimadic acid) used by Roy and co-workers for Tb^{3+} sensitization are shown.

$R = CH_3 (CH_2)_{11}$———≡≡———$(CH_2)_8$
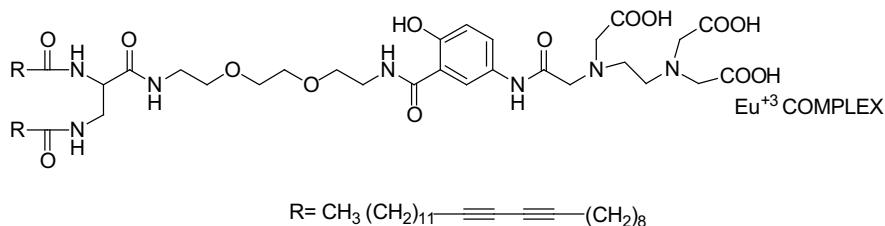
Figure 10.10. The structure of the lanthanide chelating lipid used for detecting proteins employing polymerized liposomes is shown.

prepared polymerized liposomes incorporating the Eu^{3+} complex of the lipid shown in Figure 10.10. The time-resolved luminescence emission intensity of the Eu^{3+} ions was found to increase linearly with the concentration of added proteins. The generated calibration curve was used to detect low levels of proteins: bovine carbonic anhydrase, bovine serum albumin, γ-globulin, and thermolysin (limit: 0.9–1.8 µg/mL). The excited-state lifetimes of the chelated Eu^{3+} ions in the presence of these proteins were used to distinguish between these proteins.[80, 81]

Differentiating isozymes of an enzyme's family is a challenging problem due to the similarity of the active site structures. Isozymes are evolutionarily designed to catalyze the same reaction, and hence, their active sites are very similar. However, the surface patterns of amino acid residues of isozymes are not completely conserved during evolution. Based on these differences, biological antibodies efficiently distinguish between the isozymes. Mallik and co-workers have demonstrated that the same structural differences can also be employed to differentiate isozymes of carbonic anhydrases by using suitably constructed polymerized liposomes.[82] In these liposomes, in addition to a polymerizable phosphatidylcholine, three additional polymerizable lipids were incorporated (Figure 10.11). The inhibitor lipid, which contains the benzenesulfonamide group, acts as the initial anchoring site for the

$R = CH_3 (CH_2)_{11}$———≡≡———$(CH_2)_8$
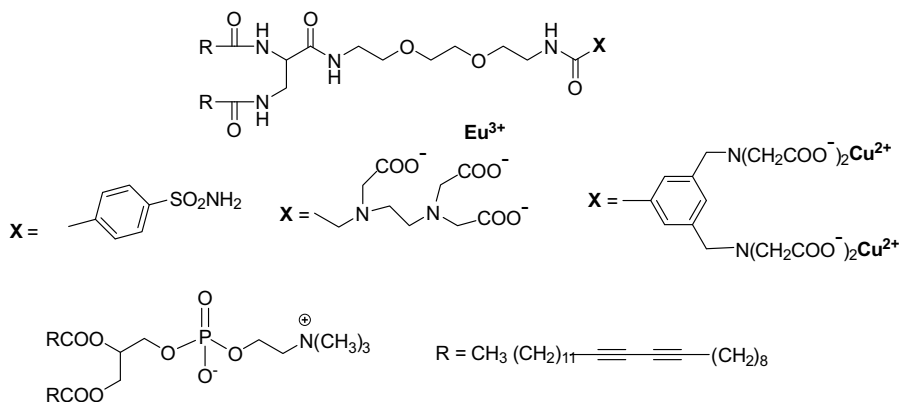
Figure 10.11. The structures of the polymerizable lipids used in the liposomes for detection of carbonic anhydrase isozymes.

TABLE 10.1. Excited-State Lifetimes of Eu^{3+} Ions (τ_1 and τ_2) in the Presence of Carbonic Anhydrase (CA) Isozymes and the Limits of Detection for These Isozymes

Enzyme	τ_1 (μs)	τ_2 (μs)	Limit of Detection (μg/mL)
No enzyme	57	158	—
CA I	93	399	4.3
CA II	94	455	0.22
CA VII	55	301	1.2
CA XII	85	426	4.4
Bovine CA	83	232	1.1

carbonic anhydrases. The affinity of the polymerized liposomes for the enzymes is further enhanced by the coordination of the chelated Cu^{2+} ions to the surface exposed histidine residues. Since the surface patterns of histidines are different for the isozymes, the affinities of the polymerized liposomes were expected to be different for the isozymes tested. The time-resolved luminescence emission intensities of the Eu^{3+} ions in the presence of carbonic anhydrase isozymes were used to determine the limits of detection (Table 10.1). The excited-state lifetimes of Eu^{3+} ions in the presence of four different isozymes were found to be sufficiently different (Table 10.1).

10.2.8. In Vivo Detection of Angiogenesis

Detection of angiogenesis in the periphery of solid tumors is a new method of monitoring cancer progression. Integrin is expressed on the surface of the neovascular cells but is absent in the mature normal cells. Thus, integrin $\alpha_v\beta_3$ is an attractive target for mapping cancer growth and metastasis. Danthi and co-workers used polymerized liposomes as probes for in vivo detection and imaging of cancer cells expressing this integrin.[95] They performed extensive optimization studies to prepare a potent ligand for the integrin $\alpha_v\beta_3$. This ligand was conjugated to diacetylene containing lipids to generate the targeting moiety (Figure 10.12). The polymerized liposomes incorporating this lipid were used for in vivo imaging of cells expressing the integrin $\alpha_v\beta_3$ on the surface. The liposomes also demonstrated enhanced accumulation inside these integrin expressing cells.

R = CH$_3$(CH$_2$)$_{11}$———≡≡———(CH$_2$)$_8$
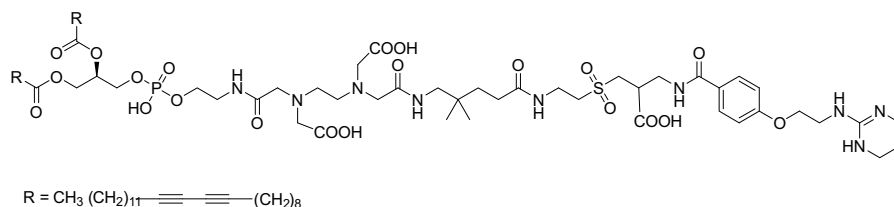
Figure 10.12. Structure of the polydiacetylene lipid used as a probe for integrin $\alpha_v\beta_3$ expressing cancer cells.

10.3. CONCLUSIONS

Polymerized liposomes containing the ene-yne backbone have been tested extensively as sensors for viruses, bacterial spores, toxins, and proteins, and for *in vivo* imaging of angiogenesis. Antibodies, ligands, inhibitors, and other small molecules have been used for selective binding of the analytes to these liposomes. In most of these studies, the color and fluorescence emission changes induced upon binding have been monitored to determine the presence of the analyte of interest. Time-resolved luminescence spectroscopy of lanthanide ions incorporated into the polymerized liposomes has been used to distinguish between proteins and isozymes. The lipid composition and the polymerization conditions play important roles in determining the efficiency of the chromatic transitions. One of the obstacles to be solved in this detection system is the nonreversible nature of the chromatic changes of the polymerized liposomes. Detection based on fluorescence resonance energy transfer employing these polymerized liposomes may provide a solution to this potential problem.[96, 97]

ACKNOWLEDGMENTS

REFERENCES

1. Ostro, M. J. *Liposomes: From Biophysics to Therapeutics,* Marcel Dekker, New York, 1987.
2. Litzinger, D. C.; Huang, L. *Biochim. Biophys. Acta.*, **1992**, *1113*, 201.
3. Gao, X.; Huang, X. L. *Gene Therapy*, **1995**, *2*, 710.
4. Lasic, D. D.; Needham, D. *Chem. Rev.*, **1995**, *95*, 2601.
5. Lasic, D. D.; Papahadijopoulos, D. *Curr. Opin. Solid State Mater. Sci.*, **1996**, *1*, 392.
6. Rosoff, M. *Vesicles from the Surfactant Science Series 62.* Marcel Dekker, New York, 1996.
7. Lasic, D. D.; Strey, H.; Stuart, M. C. A.; Podgornik, R.; Frederik, P. M. *J. Am. Chem. Soc.*, **1997**, *119*, 832.
8. Maurer, N.; Fenske, D. B.; Cullis, P. R. *Expert Opin. Biol. Therapy*, **2001**, *1*, 923–947.
9. Ranade, V. V.; Hollinger, M. A. *Drug Delivery Systems*, 2nd ed. CRC Press, Boca Raton, FL, 2004; p. 464.
10. Diaz-Gonzalez, M.; Gonzalez-Garcia, M. B.; Costa-Garcia, A. *Electroanalysis*, **2005**, *17*, 1901–1918.
11. Gregoriadis, G. *Liposome Technology Vol. 1*, Informa Healthcare USA, New York, NY, 2007.
12. Torchilin, V. P. *Adv. Drug Deliv. Rev.*, **2006**, *58*, 1532–1555.

13. Michaeli, D.; Grimes, S.; Barenholz, Y.; Even-Chen, S. Liposomal Vaccine. USPTO Application 20070082043 (White & Case LLP Patent Department, New York, NY, USA), April 12, 2007.

14. Eckstein, F. *Expert Opin. Biol. Therapy.*, **2007**, *7*, 1021–1034.

15. Mozafari, M. R.; Johnson, C.; Hatziantoniou, S.; Demetzos, C. *J. Liposome Res.*, **2008**, *18*, 309–327.

16. Meure, L. A.; Knott, R.; Foster, N. R.; Dehghani, F. *Langmuir*, **2009**, *25*, 326–337.

17. Akimoto, A.; Dorn, K.; Gros, L.; Ringsdorf, H.; Schupp, H. *Angew. Chem. Int. Ed. Engl.*, **1981**, *20*, 90–91.

18. Ringsdorf, H.; Schlarb, B.; Venzmer, J. *Angew. Chem. Int. Ed.*, **1988**, *27*, 113–158.

19. Regen, S. L.; Czech, B.; Singh, A. *J. Am. Chem. Soc.*, **1980**, *102*, 6638.

20. Johnston, D. S.; Sanghera, S.; Pons, M.; Chapman, D. *Biochim. Biophys. Acta*, **1980**, *602*, 57.

21. O'Brien, D. F.; Whitesides, T. H.; Klingbiel, R. T. *J. Polym. Sci. Polym. Lett. Ed.*, **1981**, *19*, 95.

22. Hub, H.; Hupfer, B.; Koch, H.; Ringsdorf, H. *Angew. Chem.*, **1980**, *92*, 962.

23. Naegele, D.; Ringsdorf, H. *Polym. Sci. Polym. Chem. Ed.*, **1977**, *15*, 2821.

24. Wegner, G. *Makromol. Chem.*, **1971**, *154*, 35–48.

25. Day, D.; Ringsdorf, H. *J. Polym. Sci. Polym. Lett. Ed.*, **1978**, *16*, 205–210.

26. Bader, H.; Ringsdorf, H. *Angew. Chem. Int. Ed. Engl.*, **1981**, *20*, 91–92.

27. Charych, D. H.; Nagy, J. O.; Spevak, W.; Bednarski, M. D. *Science*, **1993**, *261*, 585–588.

28. Sheth, S. R.; Leckband, D. E. *Langmuir*, **1997**, *13*, 5652–5662.

29. Plachetta, C.; Schulz, R. C. *Makromol. Chem. Rapid Commun.*, **1982**, *3*, 815–819.

30. Nava, A. D.; Thakur, M.; Tonelli, A. E. *Macromolecules*, **1990**, *23*, 3055–3063.

31. Lee, D.; Sahoo, S. K.; Cholli, A. L.; Sandman, D. J. *Macromolecules*, **2002**, *35*, 4347–4355.

32. Exarhos, G. J.; Risen, W. M.; Baughman, R. H. *J. Am. Chem. Soc.*, **1976**, *98*, 481–487.

33. Campbell, A. J.; Davies, C. K. L.; Batchelder, D. N. *Macromol. Chem. Phys.*, **1998**, *199*, 109–122.

34. Enklemann, V.; Lando, J. B. *Acta Crystallogr. Sect. B*, **1978**, *34*, 2352–2353.

35. Fischetti, R. F.; Filipkowski, M.; Garito, A. F.; Blasie, J. K. *Phys. Rev. B*, **1988**, *37*, 4714–4726.

36. Tieke, B.; Lieser, G. *J. Colloid Interface Sci.*, **1982**, *88*, 471–486.

37. Menzel, H.; Mower, M. D.; Cai, M.; Evans, C. E. *J. Phys. Chem. B*, **1998**, *102*, 9550–9556.

38. Tachibana, H.; Yamanaka, Y.; Sakai, H.; Abe, M. Matsumoto, M. *Macromolecules*, **1999**, *32*, 8306–8309.

39. Huo, Q.; Russell, K. C.; Leblanc, R. M. *Langmuir*, **1999**, *15*, 3972–3980.

40. Lopez, E.; O'Brien, D. F.; Whitesides, T. H. *J. Am. Chem. Soc.*, **1982**, *104*, 305–307.

41. Chance, R. R.; Baughman, R. H.; Muller, H.; Eckhardt, C. J. *J. Chem. Phys.*, **1977**, *67*, 3616–3618.

42. Chance, R. R.; Patel, G. N.; Witt, J. D. *J. Chem. Phys.*, **1979**, *71*, 206.

43. Chance, R. R. *Macromolecules*, **1980**, *13*, 386.

44. Singh, A.; Thompson, R. B.; Schnur, J. M. *J. Am. Chem. Soc.*, **1986**, *108*, 2785.

45. Tanaka, H.; Thakur, M.; Gomez, M. A.; Tonelli, A. E. *Macromolecules*, **1987**, *20*, 3094.

46. Batchelder, D. *Contemp. Phys.*, **1988**, *29*, 3.

47. Tanaka, H.; Gomez, M. A.; Tonelli, A. E.; Thakur, M. *Macromolecules*, **1989**, *22*, 1208.

48. Wenzel, M.; Atkinson, G. H. *J. Am. Chem. Soc.*, **1989**, *111*, 6123.

49. Mino, N.; Tamura, H.; Ogawa, K. *Langmuir*, **1991**, *7*, 2336–2341.

50. Hankin, S. H. W.; Downey, M. J.; Sandman, D. J. *Polymer*, **1992**, *33*, 5098.

51. Beckham, H. W.; Rubner, M. F. *Macromolecules*, **1993**, *26*, 5198.

52. Deckert, A. A.; Horne, J. C.; Valentine, B.; Kiernan, L.; Fallon, L. *Langmuir*, **1995**, *11*, 643–649.

53. Kuriyama, K.; Kikuchi, H.; Kajiyama, T. *Chem. Lett.*, **1995**, *12*, 1071.

54. Mitra, V. K.; Risen, W. M.; Jr., Baughman, R. H. *J. Chem. Phys.*, **1977**, *66*, 2731.

55. Batchelder, D. N.; Bloor, D. *J. Polym. Sci: Polym. Phys. Ed.*, **1979**, *17*, 569.

56. Galiotis, C.; Young, R. J.; Batchelder, D. N. *J. Polym. Sci. Polym. Phys.* Ed., **1983**, *21*, 2483.

57. Rubner, M. *Macromolecules*, **1986**, *19*, 2129.

58. Tomioka, Y.; Tanaka, N.; Imazeki, S. *Thin Solid Films*, **1989**, *179*, 27.

59. Hammond, P. T.; Nallicheri, R. A.; Rubner, M. F. *Mater. Sci. Eng.*, **1990**, *A126*, 281.

60. Patel, G. N.; Khanna, Y. P. *J. Polym. Sci. Polym. Phys. Ed.*, **1982**, *20*, 1029.

61. Batchelder, D. N. *Contemp. Phys.*, **1988**, *29*, 3.

62. Morgan, J.; Rumbles, G.; Crystall, B.; Smith, T. A.; Bloor, D. *Chem. Phys. Lett.*, **1992**, *196*, 455–461.

63. Bloor, D.; Worboys, M. R. *J. Mater. Chem.*, **1998**, *8*, 903–912.

64. Reppy, M. A.; Pinzola, B. A. *Chem. Commun.*, **2007**, *42*, 4317–4338.

65. Mallouk, T.; Harrison, D. J. *Interfacial Design and Chemical Sensing*. American Chemical Society, Washington, DC, 1993; p. 561.

66. Okada, S.; Peng, S.; Spevak, W.; Charych, D. *Acc. Chem. Res.*, **1998**, *31*, 229–239.

67. Lio, A.; Reichert, A.; Ahn, D. J.; Nagy, J. O.; Salmeron, M.; Charych, D. H. *Langmuir*, **1997**, *13*, 6524.

68. Sun, C.; Zhang, Y.; Fan, Y.; Li, Y.; Li, J. *J. Inorg. Biochem.*, **2004**, *98*, 925–930.

69. Lee, J.; Jun, H.; Kim, J. *Adv. Mater.*, **2009**, *21*, 3674–3677.

70. Lee, J.; Kim, H.-J.; Kim, J. *J. Am. Chem. Soc.*, **2008**, *130*, 5010.

71. Kim, J.-M.; Lee, Y. B.; Yang, D. H.; Lee, J.-S.; Lee, G. S.; Ahn, D. J. *J. Am. Chem. Soc.*, **2005**, *127*, 17580–17581.

72. Jung, Y. K.; Kim, T. W.; Kim, J.; Kim, J.-M.; Park, H. G. *Adv. Funct. Mater.*, **2008**, *18*, 701–708.

73. Mazor, O.; Hillairet de Boisferon, M.; Lombet, A.; Gruaz-Guyon, A.; Gayer, B.; Shrzydelski, D.; Kohen, F.; Forgez, P.; Scherz, A.; Rostere, W.; Solomon, Y. *Anal. Biochem.*, **2002**, *1*, 75–81.

74. Lundin, K.; Blomberg, K.; Nordstorm, T.; Lindquist, C. *Anal. Biochem.*, **2001**, *1*, 92–97.

75. Lim, M. J.; Patton, W. F.; Lopez, M. F.; Spofford, K. H.; Shojaee, S. N.; Shepro, D. *Anal. Biochem.*, **1997**, *2*, 184–195.

76. Gudgin-Dickson, E. F.; Pollak, A.; Diamandis, E. P. *J. Photochem. Photobiol. B: Biology*, **1995**, *1*, 3–19.

77. Roy, B. C.; Fazal, M. A.; Arruda, A.; Mallik, S.; Campiglia, A. D. *Org. Lett.*, **2000**, *2*, 3067.

78. Roy, B. C.; Santos, M.; Mallik, S.; Campiglia, A. D. *J. Org. Chem.*, **2003**, *68*, 3999–4007.

79. Okabayashi, Y.; Ikenchi, I. *Analyst*, **1998**, *6*, 1329–1332.

80. Harrocks, W. D. Jr.; Sudnick, D. R. *Acc. Chem. Res.*, **1981**, *14*, 384.

81. Santos, M.; Roy, B. C.; Goicoechea, H.; Campiglia, A. D.; Mallik, S. *J. Am. Chem. Soc.*, **2004**, *126*, 10738.

82. Elegbede, A. I.; Haldar, M. K.; Manokaran, S.; Mallik, S.; Srivastava, D. K. *Chem. Commun.*, **2007**, 4495.

83. Silbert, L.; Ben Shlush, I.; Israel, E.; Porgador, A.; Kolusheva, S.; Jelinek, R. *Appl. Environ. Microbiol.*, **2006**, *72*, 7339.

84. Kim, K. W.; Hoi, H. C.; Lee, G. S.; Ahn, D. J.; Oh, M. K. *Collioids Surf. B: Biointerfaces*, **2008**, *66*, 213–217.

85. Pinzola, B. A.; Nguyen, A. T.; Reppy, M. A. *Chem. Commun.*, **2006**, *8*, 906–908.

86. Reichert, A.; Nagy, J. O.; Spevak, W.; Charych, D. *J. Am. Chem. Soc.*, **1995**, *117*, 829.

87. Pan, J. J.; Charych, D. *Langmuir*, **1997**, *13*, 1365.

88. Charych, D. R.; Cheng, J.; Reichert, A.; Kuziemko, G.; Strogh, M.; Nagy, J. O.; Spevak, W.; Stevens, R. C. *Chem Biol.*, **1996**, *3*, 113.

89. Mino, N.; Tamura, H.; Ogawa, K. *Langmuir*, **1992**, *8*, 594.

90. Nallicheri, R. A.; Rubner, M. F. *Macromolecules*, **1991**, *24*, 517.

91. Ma, G.; Cheng, Q. *Langmuir*, **2005**, *14*, 6123–6126.

92. Orynbayeva, Z.; Kolusheva, S.; Livneh, E.; Lichtenshtein, A.; Nathan, I.; and Jelinek, R. *Angew. Chem. Int. Ed.*, **2005**, *44*, 1092–1096.

93. Groysman, N.; Orynbayeva, Z.; Katz, M.; Kolusheva, S.; Khanin, M.; Danilenko, M.; Jelinek, R. *Biochim. Biophys. Acta*, **2008**, *5*, 1335–1343.

94. Orynbayeva, Z.; Kolusheva, S.; Groysman, N.; Gavrielov, N.; Lobel, L.; Jelinek, R. *J. Virol.*, **2007**, *3*, 1140–1147.

95. Xie, J.; Shen, Z.; Li, K. C. P.; Danthi, N. *Int. J. Nanomed.*, **2007**, *2*, 479–485.

96. Ma, G.; Cheng, Q. *Langmuir*, **2006**, *22*, 6743–6745.

97. Li, X.; Matthews, S.; Kohli, P. *J. Phys. Chem. B*, **2008**, *112*, 13263–13272.

Block-Copolymer-Templated Synthesis of Ordered Silicas with Closed Mesopores

MICHAL KRUK

Center for Engineered Polymeric Materials, Department of Chemistry, College of Staten Island, City University of New York, Staten Island, New York, USA and Graduate Center, City University of New York, New York, USA

CHIN MING HUI

Center for Engineered Polymeric Materials, Department of Chemistry, College of Staten Island, City University of New York, Staten Island, New York, USA

The current quest for the increase in processing power of the integrated circuits requires a decrease in the separation between their structural elements. This structural change is difficult to realize without the development of better on-chip insulating media, which are required to exhibit low dielectric constant.[1–4] The desired low-dielectric-constant (low-k) materials must also have a number of other properties, such as sufficiently high thermal and chemical stability to sustain plasma etching involved in the electronic chips manufacture, as well as the long-term stability of the low-k properties. The materials currently used for on-chip insulations in the electronics industry often have a dielectric constant of about 4. A significantly lower dielectric constant (down to ~2) can be achieved by a proper selection of the composition of the insulating media. Another way to reduce the dielectric constant is to introduce void spaces (pores) in the material, because the air has a dielectric constant close to 1. Silica (hydroxylated silicon dioxide, $SiO_{2-x/2}(OH)_x$) is an attractive choice of chemical composition for on-chip insulating media, but without internal nanoporosity, its dielectric constant is too high. It is easy to introduce nanoporosity in silica materials, and indeed desired low dielectric constants can readily be achieved this way.[5] However, porous silica easily adsorbs moisture from

the air, resulting in an unacceptable increase in the dielectric constant. This problem can be overcome through the attachment of hydrophobic organic groups to the silica-based framework,[3, 6, 7] or the substitution of some of the Si–O–Si linkages in the silica structure by Si–R–Si linkages, where R is a hydrophobic organic group.[8] Both of these approaches result in the introduction of hydrophobic groups on the silica surface, which hinders the adsorption of water molecules and helps in maintaining low-k properties over extended periods of time. The drawback of the organic groups is their potential susceptibility to damage during the manufacture of the integrated circuits. Another approach to prevent the degradation of low-k properties is to generate closed (inaccessible) nanopores instead of open (accessible) ones, so that water vapor would not have a physical access to the pores and thus could not compromise the properties of the material.[3, 9, 10]

It was shown in the early 1990s that nanoscale porosity of silicas can conveniently be generated in a predictable way using surfactant micelles as templates.[11–13] This approach can be used to form cylindrical pores (diameter 2–30 nm),[11, 12, 14, 15] spherical pores (diameter $\sim$3–27 nm),[16–19] and other periodic porous structures.[11, 12, 20] Surfactants that are suitable as micellar templates include alkylammonium surfactants,[11, 12] oligomeric alkyl-poly(ethylene oxide) surfactants,[18] and block copolymers with poly(ethylene oxide) block(s).[14, 18] The micelle-templating approach has been extended to some other compositions relevant for the manufacture of on-chip insulations,[21, 22] including polymethylsilsesquioxane (formula unit: $SiO_{1.5-x/2}(CH_3)(OH)_x$)[3, 6, 7] and bridged silsesquioxanes (formula unit: $SiO_{1.5-x/2}R_{0.5}(OH)_x$, where R is an organic group that connects—that is, bridges—two silicon atoms).[23–27] These families of materials inherently have quite low dielectric constants, which can be further lowered by the introduction of porosity. Moreover, the surfaces of these materials tend to be hydrophobic, thus preventing the undesirable adsorption of water vapor.

Micelle-templated porous silicas and organosilicas typically exhibit well-accessible porous structures with a high specific surface area and large pore volume.[12, 14, 23–25, 28, 29] A micelle-templated formation of ordered mesoporous materials with closed (inaccessible) spherical pores has been reported only in several studies,[3, 30–34] while the literature on micelle-templated materials with accessible porosity consists of at least several thousand contributions. The formation of closed-pore materials (silicas and organosilicas) was first reported in the case of the use of poly(ethylene oxide)–polystyrene (PEO-PS) micellar templates,[3, 30–32] which are not commercially available. The pore closure was postulated to be related to properties of poly(ethylene oxide)–polystyrene templates.[3] The difficulty in forming closed-pore structures through the micelle templating stems from the need to remove the template to make the pore space available, which cannot be realized without pore connectivity. So the closed void spaces can be created only if the template is removed prior to pore closure. If the pores close prior to complete removal of the template, its residue is trapped in the pores. In particular, Deng et al.[32] reported the formation of silicas with closed mesopores, which contained a certain amount of carbon nanoparticles.

An alternative way to create closed porosity in micelle-templated silicas and organosilicas is to remove the template and then close the passages between the pores through the surface grafting of monofunctional organosilanes (organosilanes having

one group reactive with respect to the silica surface, e.g., organomonochlorosilanes or organomonoalkoxysilanes).[35–38] To achieve this goal, one needs to choose a material with cage-like mesopores, such as spherical mesopores with narrow entrances[35–37] or cylindrical mesopores with major constrictions (plugs; materials with such pores were originally reported by Van der Voort et al.[39]),[38] and one needs to ensure a high grafting density of the organic groups bonded to the surface. The grafting reaction introduces a uniform layer of organosilyl groups on the surface of the material, and when the length of the extended organosilyl group is comparable to the radius of the entrances to the pores, the entrances become blocked and the internal pore space is effectively inaccessible.[35]

Our recent work[33, 34] showed that the formation of closed-pore silicas through the micelle templating can be achieved using a commercially available surfactant, Pluronic F127 poly(ethylene oxide)–poly(propylene oxide)–poly(ethylene oxide) block copolymer with formula $EO_{106}PO_{70}EO_{106}$ (where EO stands for an $-OCH_2CH_2-$ unit and PO stands for an $-OCH(CH_3)CH_2-$ unit). We have demonstrated the formation of silicas with face-centered cubic (fcc; Fm3m symmetry) and body-centered cubic (bcc; Im3m symmetry) arrangements of closed spherical mesopores. The pores are open up to certain threshold temperatures (somewhere between about 500 and 900°C for materials that were studied so far), and become closed (inaccessible) above the threshold temperature. Shown in Figure 11.1 are the results that we reported earlier[33] for SBA-16 silica with body-centered cubic structure, which is the most commonly studied block-copolymer-templated silica with spherical mesopores.[18, 40] SAXS patterns showed that the bcc structure was thermally stable up to at least 950°C, when heated under air for 5 hours, because the intensity of the scattering patterns was largely independent of the calcination temperature. The degree of shrinkage upon calcination gradually increased as the calcination temperature increased. When compared to an as-synthesized (copolymer-containing) sample, the unit-cell parameter was reduced by 10% after calcination at
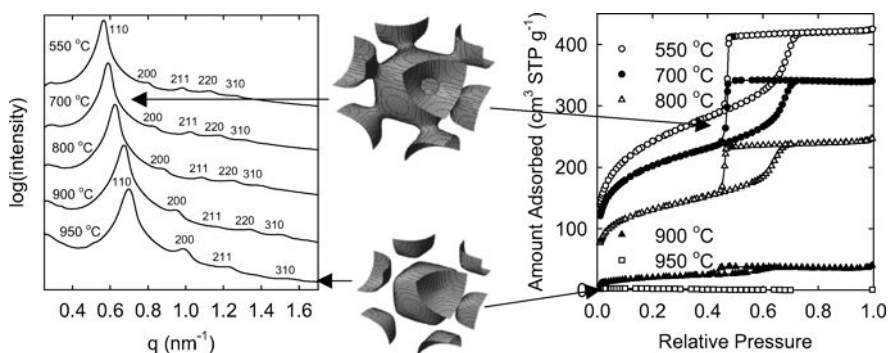
Figure 11.1. (a) Small-angle X-ray scattering patterns and (b) nitrogen adsorption isotherms for SBA-16 silica with body-centered cubic structure (Im3m) calcined at different temperatures. The structures in the middle illustrate the pore structure symmetry and the pore connectivity. The figure is adapted from our earlier publication.[33]

550°C, while the calcination at 950°C brought about the shrinkage of 27%. The accessibility of the pores to the nitrogen gas (the adsorbate typically used in the pore structure characterization) was greatly reduced after heating at 900°C and essentially fully suppressed after heating at 950°C, as seen from a negligible uptake of nitrogen by this material (see Figure 11.1). Clearly, the diameter of the pore entrances decreased as the calcination temperature increased, reaching at temperatures of 900–950°C the dimensions close to or smaller than the size of the nitrogen molecule. The pore closure is likely to involve a gradual reduction of the pore entrance diameter, most likely facilitated by the local condensation of silanols on the pore walls. Eventually, the pore entrance is so narrow that it is no longer penetrable by gas molecules, such as nitrogen. At this point, the proximity of the silanol groups on the opposite sides of the pore entrance wall may eventually lead to the complete fusion of the entrance through the condensation of silanols with the formation of siloxanes.

As the calcination temperature increased from 550 to 800°C, a gradual decrease in the pore cage diameter from 7.7 to 6.8 nm was observed for the samples with fully accessible mesopores (see Figure 11.2). For the sample calcined at 900°C, the diameter of accessible mesopores was ∼6 nm, but most likely only a fraction of the mesopores were actually accessible, while the pore size distribution did not reflect the closed (inaccessible) mesopores, which cannot be probed using the gas adsorption method. Therefore, the pore cage diameters for the sample with a fraction of closed mesopores (calcined at 900°C) and the sample with closed mesopores (calcined at 950°C) were assessed through the extrapolation of pore diameter data for the materials with accessible mesopores. The extrapolation was based on an
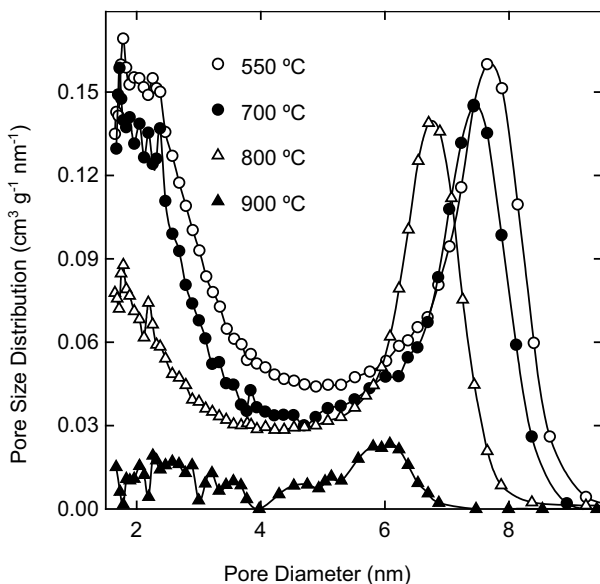
Figure 11.2. Pore size distributions calculated from gas adsorption data for SBA-16 silicas calcined at different temperatures.
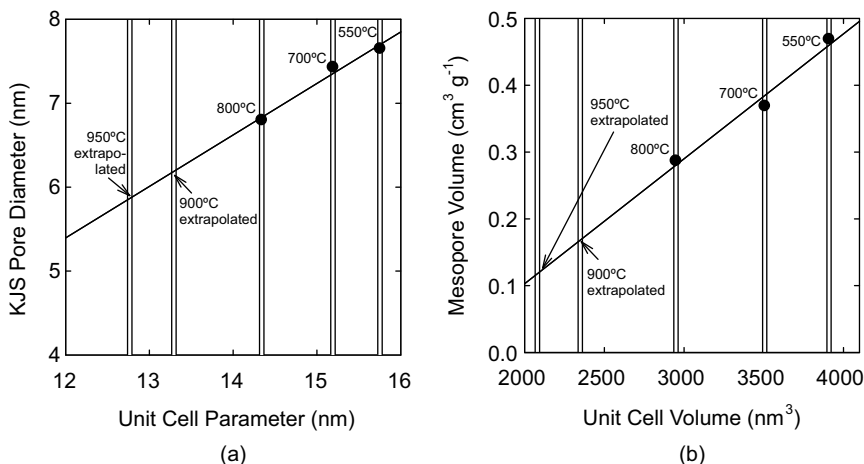
Figure 11.3. (a) The measured and estimated pore diameter of SBA-16 as a function of the unit-cell parameter at different calcination temperatures. (b) The measured and estimated primary mesopore volume of SBA-16 as a function of the unit-cell volume at different calcination temperatures.

approximately linear relation between the pore diameter and the unit-cell parameter (see Figure 11.3) and it indicated a pore diameter of ∼6.1 nm for the sample calcined at 900°C, and ∼5.9 nm for the sample calcined at 950°C, the former value being consistent with the diameter of residual accessible mesopores in the considered sample (see Figure 11.2). It should be noted that the diameters of open mesopores were calculated from nitrogen adsorption data using the Kruk–Jaroniec–Sayari (KJS) method calibrated for cylindrical pores of diameter 2–6.5 nm.[41] This procedure is known to underestimate the diameter of spherical mesopores (which are character-istic of SBA-16) by ∼2 nm in the pore size range similar to that considered here.[42] Therefore, all pore diameter values discussed above (whether directly calculated or extrapolated) are likely to be underestimated by ∼2 nm.

Figure 11.3 also shows the primary (ordered) mesopore volume as a function of the unit cell volume, which was assessed as a cube of the unit-cell parameter. The values for the samples whose pores were closed (fully or in part) can be estimated by extrap-olating the data for open-pore samples. The estimated volumes of the mesopores in the samples calcined at 900 and 950°C were ∼0.15 and ∼0.10 cm^3 g^{-1} respectively. Given that the volumes of accessible pores were ∼0.06 and ∼0.00 cm^3 g^{-1} for the samples calcined at 900 and 950°C, respectively, the volume of closed mesopores was ∼0.10 cm^3 g^{-1} in both cases. This mesopore volume is rather low and the development of silicas with higher volume of closed mesopores would be desirable.

A thermally induced pore closure process was also observed[33, 34] for Fm3m structure of large-pore FDU-12 (LP-FDU-12) silica[19] synthesized without an acid treatment,[43] but in this case, closed-pore silicas were obtained at much lower temperatures (550–640°C). For the LP-FDU-12 silica calcined at temperatures from 450 to 640°C, SAXS patterns featured several peaks whose relative positions
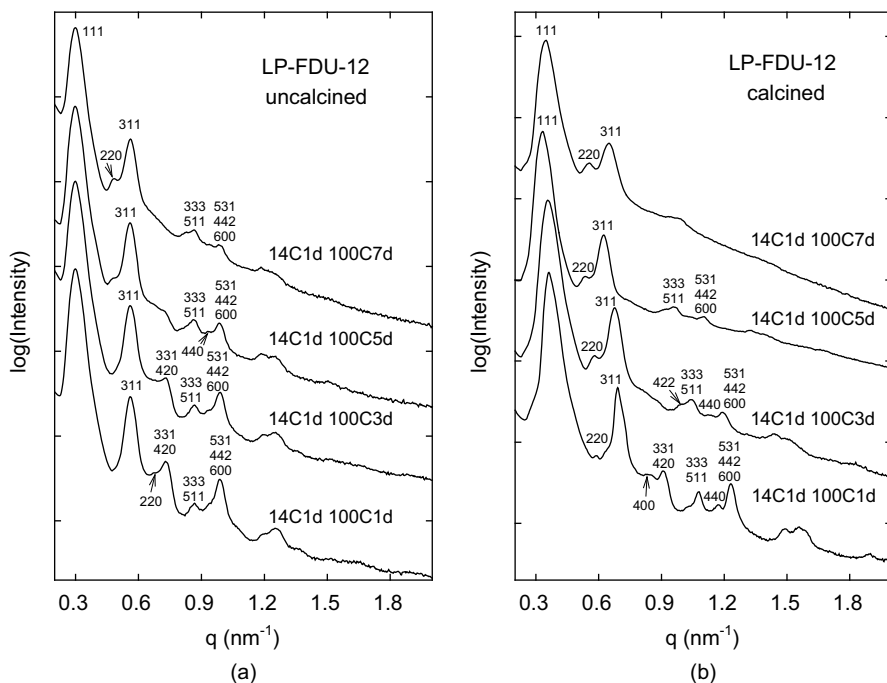
Figure 11.4. Small-angle scattering patterns for (a) as-synthesized (uncalcined) and (b) calcined LP-FDU-12 silicas synthesized at an initial temperature of 14 °C and hydrothermally treated in the synthesis mixture at 100 °C for periods of time from 1 to 7 days.

were characteristic of the face-centered cubic structure (Fm3m) (similar to SAXS patterns shown in Figure 11.4 for samples calcined at 550°C that are discussed hereafter).[33, 34] The unit-cell parameters were in the range from 30 to 36 nm. The calcination led to a significant shrinkage, which was highly temperature dependent. The decrease in the unit-cell parameter was 13–14%, 17–18%, and 20–22% after calcination at 450, 550, and 640°C, respectively. Adsorption isotherms for samples calcined at 450 and 550°C exhibited pronounced capillary condensation steps at relative pressures of ∼0.85 (see isotherm for one of the samples calcined at 450°C shown in Figure 11.5), indicating the presence of large, uniform mesopores. LP-FDU-12 samples calcined at 450°C exhibited an appreciable adsorption capacity, while the increase in the calcination temperature to 550°C led to a significant decrease in the uptake of nitrogen. Finally, the calcination at 640°C reduced the uptake to essentially zero, which indicates the lack of pores accessible to nitrogen molecules.

The entrance diameter (in the narrowest point) for one of the LP-FDU-12 samples calcined at 450°C was estimated[33] to be ∼2 nm on the basis of the pore accessibility after the surface modification with triorganomonochlorosilanes of gradually increasing size.[35, 36] As can be seen in Figure 11.5, the introduction of trimethylsilyl (TMS) groups on the surface of LP-FDU-12 resulted in a slight decrease in uptake of
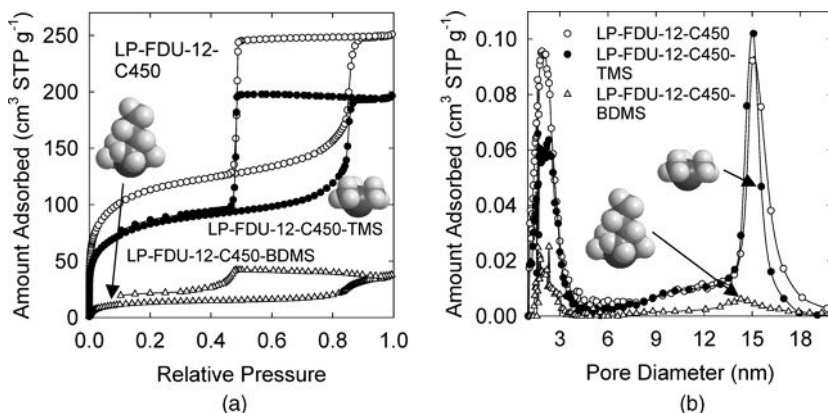
Figure 11.5. (a) Nitrogen adsorption isotherms and (b) pore size distributions of LP-FDU-12 silica (calcined at 450 °C) before and after surface modification with trimethylsilyl (TMS) and butyldimethylsilyl (BDMS) groups. The pictures of models of the TMS and BDMS groups are included to illustrate the relative size of these two kinds of surface groups. The adsorption data for unmodified LP-FDU-12 were taken from our earlier publication.[33]

nitrogen paralleled by a decrease in the BET specific surface area from 405 to 301 $m^2 g^{-1}$, while the introduction of butyldimethylsilyl (BDMS) groups resulted in a major decrease in uptake, drop in the BET specific surface area to 50 $m^2 g^{-1}$ and development of a pronounced low-pressure hysteresis.[44] The difference between pore accessibility is seen more clearly from pore size distributions (Figure 11.5b), where BDMS-modified LP-FDU-12 showed a very weak peak, unlike the unmodified sample and TMS-modified sample. Clearly, the access to the mesopores was greatly suppressed by the modification with BDMS. Given that monolayers of TMS and BDMS groups can block access of nitrogen molecules to pores of diameter up to 1.2 nm and 1.9 nm, respectively,[35] one can conclude that the considered LP-FDU-12 sample calcined at 450°C exhibited pore entrance sizes primarily below ~1.9 nm.

On the basis of the unit-cell size and pore diameter, one can estimate that the distance between adjacent spherical mesopores of the LP-FDU-12 sample calcined at 450°C was ~6 nm.[33] This distance is likely to correspond to the pore entrance length. Given that the pore entrance diameter (in the narrowest point) was ~2 nm, the pore entrance length-to-diameter ratio was 3 : 1, and thus one can readily envision that the reduction of the pore entrance diameter through the thermal treatment would eventually lead to the closure of the entrance. The obtained ordered closed-pore silicas were white powders.[33, 34] It is clear that the block copolymer template was removed without the formation of the carbon residue, which was observed in an ordered closed-pore silica templated by PEO-PS copolymer.[32] Pluronic (PEO-PPO-PEO) copolymers usually decompose at relatively low temperatures,[18] so they may be inherently more convenient than PEO-PS copolymers, whose PS block has an appreciable tendency to carbonize.

As suggested elsewhere,[33] the propensity to the pore closing depends on the extent of shrinkage during calcination, which in turn is dependent on the synthesis

conditions for a particular ordered mesoporous silica material. The procedure originally proposed[19] for the synthesis of LP-FDU-12 involved the initial low-temperature step (~15°C), after which the fcc structure is already formed,[33] followed by the heating of the synthesis mixture at 100°C for 1 day and subsequent hydrothermal treatment of as-synthesized, dried sample in 2 M HCl solution at 100–140°C for several days. LP-FDU-12 silicas synthesized in the above three-step procedure exhibited significant pore volumes after calcination at 550°C,[43] thus showing that such materials were not prone to pore closing. This appears to be related to a shrinkage of 10% or less during the calcination at 550°C. On the other hand, the shrinkage upon calcination at 550°C was 16–18% in cases where the acid treatment was not employed,[43] which commonly resulted in a low pore volume due to the closing of part (or all) of the mesopores.

Shown in Figure 11.4 are SAXS patterns of as-synthesized and calcined LP-FDU-12 silicas synthesized with different durations of the second step of the synthesis (which is the hydrothermal treatment of the synthesis mixture) and without the acid treatment (which is the third step of the synthesis). All patterns were characteristic of the fcc structure, although the relative intensity of particular peaks varied to some extent as the time of the hydrothermal treatment was prolonged. One day and 3 day treatments afforded materials whose unit-cell parameter decreased 16–17% after calcination at 550°C and uptakes of nitrogen gas were very small (the corresponding BET specific surface areas were ~10 m^2 g^{-1} or less), thus revealing the closed-pore nature of the silicas. On the other hand, longer hydrothermal treatments (5 and 7 days) reduced the shrinkage to 10–14%, and afforded silicas with accessible mesopores (see Figure 11.6) and appreciable BET specific surface areas (591 and 270 m^2 g^{-1} for the samples prepared with 5 and 7 day treatments, respectively). However, even in
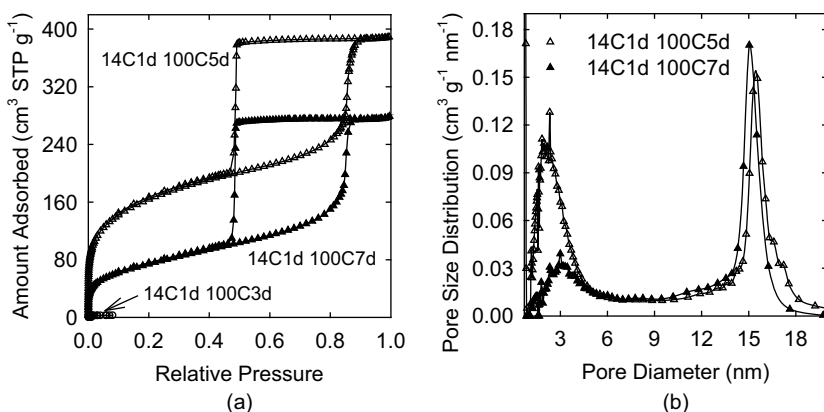
Figure 11.6. (a) Nitrogen adsorption isotherms and (b) pore size distributions for LP-FDU-12 samples synthesized without the acid treatment. Note that uptake for the 14C1d 100C3d sample was so small that the measurement was discontinued, while uptake for the 14C1d 100C1d sample was even lower (essentially no uptake). Consequently, it was not possible to calculate pore size distributions for the above two samples.

this case, the shrinkage was higher for the sample heated for 7 days in comparison to the sample heated for 5 days, which appears to be anomalous. It is clear that even for long times of heating of the synthesis mixture, there is a tendency to substantial shrinkage. Therefore, the hydrothermal treatment in acid is advisable if one wants to obtain LP-FDU-12 with fully accessible mesopores. On the other hand, if one is interested in preparing closed-pore silicas at low temperature, acid treatments and longer hydrothermal treatment times should be avoided.

Our studies[33] also demonstrated the thermally induced pore closure for ordered organosilicas with organic groups in the framework (which are referred to as periodic mesoporous organosilicas, PMOs[23–27, 45]). PMOs are particularly interesting as low-k materials, because the organosilica framework inherently has a lower dielectric constant than that of the silica framework,[8, 46] and additionally, the surfaces of organosilicas are fairly hydrophobic, thus reducing the uptake of moisture from the air. PMOs used by us to prepare closed-pore materials were templated by Pluronic F127 block copolymer. The uniform mesopores of these PMOs remained accessible up to 500°C and were completely closed at 600°C, while SAXS data still indicated the retention of the original periodic structure. The aforementioned study employed PMOs with methylene groups, because their frameworks are quite thermally stable,[47, 48] thus giving better prospects for the pore closure without the degradation of the organic groups. Since we did not find any prior report on the synthesis of polymer-templated methylene PMOs with cage-like mesopores, elaboration of their synthesis was needed.[33] For the obtained PMOs, the pore closure with retention of the original periodic structure was clearly documented.[33] However, the temperature of 600°C and the use of air atmosphere that were required to close the pores of methylene PMOs most likely led to the conversion of Si–CH$_2$–Si moiety of the methylene PMO to Si–CH$_3$ groups, or even to complete elimination of the organic groups with the formation of siloxane bonds.[47, 48] So PMO with closed mesopores was not obtained in the aforementioned study.

The suggested mechanism of the thermally induced pore closure process is illustrated in Scheme 11.1. The starting point of the synthesis is the formation of an ordered silica–copolymer (or organosilica–copolymer) composite, in which the copolymer "micelles" are embedded in the silica (or organosilica) framework. More specifically, the hydrophilic blocks (i.e., poly(ethylene oxide), PEO, blocks) of the copolymer are occluded in the silica (or organosilica) framework, while the hydrophobic blocks (i.e., poly(propylene oxide), PPO, blocks) form separate domains. Such a structure of silica/copolymer composites emerged from NMR studies[49, 50] and provided the basis of the explanation of the pore connectivity in the structure of SBA-15 silica.[51, 52] The PEO blocks belonging to adjacent "micelles" apparently are in contact with one another, which results in the occurrence of passages in the silica framework, which connect the adjacent ordered mesopore spaces (filled with PPO blocks) in the silica structure. The calcination at a lower temperature (e.g., 450°C) results in a removal of the block copolymer and is accompanied by some degree of shrinkage of the silica framework. It leaves behind a silica (or organosilica) structure with accessible ordered mesopores connected by smaller pores (micropores or mesopores) that correspond to spaces where once the PEO blocks were located
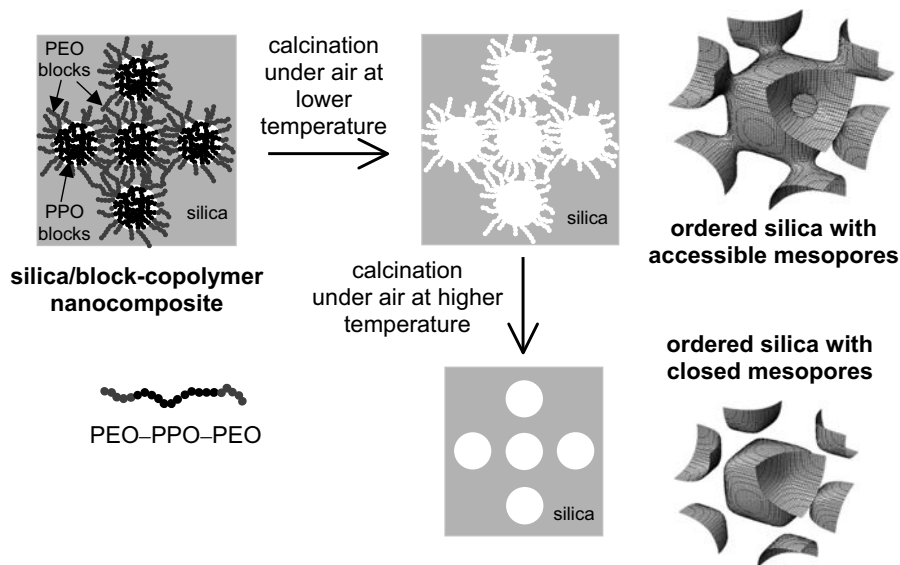
Scheme 11.1. Proposed mechanism of the temperature-induced pore closing in surfactant-templated mesoporous silicas.

(see Scheme 11.1). If the connections between the mesopores are sufficiently narrow and the wall thickness is sufficiently large, the calcination at higher temperature (e.g., 550–950°C) may induce further shrinkage that can result in the reduction in size or fusion of the connections between the pores, thus affording a material with effectively closed (isolated) mesopores. It should be noted that in the case of PMOs, the organic groups in the framework are stable up to certain temperatures, depending on the nature of the groups and on the atmosphere used during calcination. Thus, excessively high temperature would result in the loss of organic groups (or the conversion of the bridging organic groups to pendent groups in some cases in certain temperature ranges) and thus to the conversion of an organosilica framework to the silica framework.

The onset of the pore closure depends on the synthesis conditions for the formation of micelle-templated materials and on their framework type. The main factors that were identified as important for the successful pore-closing process include:[33]

- Cage-like pore structure, such as a spherical pore with entrances
- Pore entrance diameter much smaller than the pore cage diameter
- Appreciable pore entrance length in comparison to the pore entrance diameter
- Large degree of shrinkage of the structure upon thermal treatment.

It can be concluded that the formation of surfactant-templated ordered closed-pore silicas can readily be achieved through an appropriate selection of starting silica–surfactant composites with the help of the criteria outlined above. The

temperature at which the thermally induced pore closure takes place depends on the particular material and the synthesis conditions, being in the 550–950°C range for materials studied so far. While PMOs undergo the pore closure process, the challenge of preserving the integrity of bridging groups during the thermal treatment remains.

ACKNOWLEDGMENTS

REFERENCES

1. Hermans, T. M.; Choi, J.; Lohmeijer, B. G. G.; Dubois, G.; Pratt, R. C.; Kim, H.-C.; Waymouth, R. M.; Hedrick, J. L. *Angew. Chem. Int. Ed.*, **2006**, *45*, 6648–6652.

2. Davis, M. E. *Nature*, **2002**, *417*, 813–821.

3. Yu, K.; Smarsly, B.; Brinker, C. J. *Adv. Funct. Mater.*, **2003**, *13*, 47–52.

4. Jain, A.; Rogojevic, S.; Ponoth, S.; Agarwal, N.; Matthew, I.; Gill, W. N.; Persans, P.; Tomozawa, M.; Plawsky, J. L.; Simonyi, E. *Thin Solid Films*, **2001**, *398–399*, 513–522.

5. Zhao, D. Y.; Yang, P. D.; Melosh, N.; Feng, Y. L.; Chmelka, B. F.; Stucky, G. *Adv. Mater.*, **1998**, *10*, 1380–1385.

6. Balkenende, A. R.; de Theije, F. K.; Kriege, J. C. K. *Adv. Mater.*, **2003**, *15*, 139–143.

7. de Theije, F. K.; Balkenende, A. R.; Verheijen, M. A.; Baklanov, M. R.; Mogilnikov, K. P.; Furukawa, Y. *J. Phys. Chem. B*, **2003**, *107*, 4280–4289.

8. Lu, Y.; Fan, H.; Doke, N.; Loy, D. A.; Assink, R. A.; LaVan, D. A.; Brinker, C. J. *J. Am. Chem. Soc.*, **2000**, *122*, 5258–5261.

9. Ree, M.; Yoon, J.; Heo, K. *J. Mater. Chem.*, **2006**, *16*, 685–697.

10. Lee, B.; Park, Y.-H.; Hwang, Y.-T.; Oh, W.; Yoon, J.; Ree, M. *Nature Mater.*, **2005**, *4*, 147–150.

11. Kresge, C. T.; Leonowicz, M. E.; Roth, W. J.; Vartuli, J. C.; Beck, J. S. *Nature*, **1992**, *359*, 710–712.

12. Beck, J. S.; Vartuli, J. C.; Roth, W. J.; Leonowicz, M. E.; Kresge, C. T.; Schmitt, K. D.; Chu, C. T. W.; Olson, D. H.; Sheppard, E. W.; McCullen, S. B.; Higgins, J. B.; Schlenker, J. L. *J. Am. Chem. Soc.*, **1992**, *114*, 10834–10843.

13. Yanagisawa, T.; Shimizu, T.; Kuroda, K.; Kato, C. *Bull. Chem. Soc. Jpn.*, **1990**, *63*, 988–992.

14. Zhao, D.; Feng, J.; Huo, Q.; Melosh, N.; Frederickson, G. H.; Chmelka, B. F.; Stucky, G. D. *Science*, **1998**, *279*, 548–552.

15. Cao, L.; Man, T.; Kruk, M. *Chem. Mater.*, **2009**, *21*, 1144–1153.

16. Huo, Q.; Margolese, D. I.; Ciesla, U.; Feng, P.; Gier, T. E.; Sieger, P.; Leon, R.; Petroff, P. M.; Schueth, F.; Stucky, G. D. *Nature*, **1994**, *368*, 317–321.

17. Huo, Q.; Leon, R.; Petroff, P. M.; Stucky, G. D. *Science*, **1995**, *268*, 1324–1327.

18. Zhao, D.; Huo, Q.; Feng, J.; Chmelka, B. F.; Stucky, G. D. *J. Am. Chem. Soc.*, **1998**, *120*, 6024–6036.

19. Fan, J.; Yu, C.; Lei, J.; Zhang, Q.; Li, T.; Tu, B.; Zhou, W.; Zhao, D. *J. Am. Chem. Soc.*, **2005**, *127*, 10794–10795.

20. Kleitz, F.; Choi, S. H.; Ryoo, R. *Chem. Commun.*, **2003**, 2136–2137.

21. Burkett, S. L.; Sims, S. D.; Mann, S. *Chem. Commun.*, **1996**, 1367–1368.

22. Macquarrie, D. J. *Chem. Commun.*, **1996**, 1961–1962.

23. Inagaki, S.; Guan, S.; Fukushima, Y.; Ohsuna, T.; Terasaki, O. *J. Am. Chem. Soc.*, **1999**, *121*, 9611–9614.

24. Melde, B. J.; Holland, B. T.; Blanford, C. F.; Stein, A. *Chem. Mater.*, **1999**, *11*, 3302–3308.

25. Asefa, T.; MacLachlan, M. J.; Coombs, N.; Ozin, G. A. *Nature*, **1999**, *402*, 867–871.

26. Guan, S.; Inagaki, S.; Ohsuna, T.; Terasaki, O. *J. Am. Chem. Soc.*, **2000**, *122*, 5660–5661.

27. Inagaki, S.; Guan, S.; Ohsuna, T.; Terasaki, O. *Nature*, **2002**, *416*, 304–307.

28. Corriu, R. J. P.; Embert, F.; Guari, Y.; Mehdi, A.; Reye, C. *Chem. Commun.*, **2000**, 1116–1117.

29. Corriu, R. J. P.; Hoarau, C.; Mehdi, A.; Reye, C. *Chem. Commun.*, **2000**, 71–72.

30. Yu, K.; Hurd, A. J.; Eisenberg, A.; Brinker, C. J. *Langmuir*, **2001**, *17*, 7961–7965.

31. Yu, K.; Wu, X.; Brinker, C. J.; Ripmeester, J. *Langmuir*, **2003**, *19*, 7282–7288.

32. Deng, Y.; Yu, T.; Wan, Y.; Shi, S.; Meng, Y.; Gu, D.; Zhang, L.; Huang, Y.; Liu, C.; Wu, X.; Zhao, D. *J. Am. Chem. Soc.*, **2007**, *129*, 1690–1697.

33. Kruk, M.; Hui, C. M. *J. Am. Chem. Soc.*, **2008**, *130*, 1528–1529.

34. Kruk, M.; Hui, C. M. *Polym. Prep.*, **2008**, *49*(2), 855–856.

35. Kruk, M.; Antochshuk, V.; Matos, J. R.; Mercuri, L. P.; Jaroniec, M. *J. Am. Chem. Soc.*, **2002**, *124*, 768–769.

36. Kim, T. W.; Ryoo, R.; Kruk, M.; Gierszal, K. P.; Jaroniec, M.; Kamiya, S.; Terasaki, O. *J. Phys. Chem. B*, **2004**, *108*, 11480–11489.

37. Antochshuk, V.; Kruk, M.; Jaroniec, M. *J. Phys. Chem. B*, **2003**, *107*, 11900–11906.

38. Celer, E. B.; Kruk, M.; Zuzek, Y.; Jaroniec, M. *J. Mater. Chem.*, **2006**, *16*, 2824–2833.

39. Van Der Voort, P.; Ravikovitch, P. I.; De Jong, K. P.; Benjelloun, M.; Van Bavel, E.; Janssen, A. H.; Neimark, A. V.; Weckhuysen, B. M.; Vansant, E. F. *J. Phys. Chem. B*, **2002**, *106*, 5873–5877.

40. Sakamoto, Y.; Kaneda, M.; Terasaki, O.; Zhao, D. Y.; Kim, J. M.; Stucky, G.; Shin, H. J.; Ryoo, R. *Nature*, **2000**, *408*, 449–453.

41. Kruk, M.; Jaroniec, M.; Sayari, A. *Langmuir*, **1997**, *13*, 6267–6273.

42. Matos, J. R.; Kruk, M.; Mercuri, L. P.; Jaroniec, M.; Zhao, L.; Kamiyama, T.; Terasaki, O.; Pinnavaia, T. J.; Liu, Y. *J. Am. Chem. Soc.*, **2003**, *125*, 821–829.

43. Kruk, M.; Hui, C. M. *Microporous Mesoporous Mater.*, **2008**, *114*, 64–73.

44. Kruk, M.; Jaroniec, M. *Chem. Mater.*, **2001**, *13*, 3169–3183.

45. Matos, J. R.; Kruk, M.; Mercuri, L. P.; Jaroniec, M.; Asefa, T.; Coombs, N.; Ozin, G. A.; Kamiyama, T.; Terasaki, O. *Chem. Mater.*, **2002**, *14*, 1903–1905.

46. Hatton, B. D.; Landskron, K.; Whitnall, W.; Perovic, D. D.; Ozin, G. A. *Adv. Funct. Mater.*, **2005**, *15*, 823–829.

47. Asefa, T.; MacLachlan, M. J.; Grondey, H.; Coombs, N.; Ozin, G. A. *Angew. Chem. Int. Ed.*, **2000**, *39*, 1808–1811.

48. Asefa, T.; Kruk, M.; Coombs, N.; Grondey, H.; MacLachlan, M. J.; Jaroniec, M.; Ozin, G. A. *J. Am. Chem. Soc.*, **2003**, *125*, 11662–11673.

49. Melosh, N. A.; Lipic, P.; Bates, F. S.; Wudl, F.; Stucky, G. D.; Fredrickson, G. H.; Chmelka, B. F. *Macromolecules*, **1999**, *32*, 4332–4342.

50. de Paul, S. M.; Zwanziger, J. W.; Ulrich, R.; Wiesner, U.; Spiess, H. W. *J. Am. Chem. Soc.*, **1999**, *121*, 5727–5736.

51. Ryoo, R.; Ko, C. H.; Kruk, M.; Antochshuk, V.; Jaroniec, M. *J. Phys. Chem. B*, **2000**, *104*, 11465–11471.

52. Kruk, M.; Jaroniec, M.; Ko, C. H.; Ryoo, R. *Chem. Mater.*, **2000**, *12*, 1961–1968.

Organic–Inorganic Hybrid Nanomaterials: Organization, Functionalization, and Potential Applications in Environmental Domain

AHMAD MEHDI

Institut Charles Gerhardt Montpellier, UMR 5253 CNRS, Chimie Moléculaire et Organisation du Solide, Université Montpellier II, Montpellier, France

This chapter treats the organization and functionalization of hybrid organic–inorganic materials. We attempt to show the best ways to organize materials in terms of properties at the nanometric scale. For the purpose of constructing such materials, we describe two families of organized materials. The first is the mesoporous hybrid organic–inorganic materials, which are prepared in the presence of structure-directing agents. We describe the functionalization of the channel pores of ordered mesoporous silica, the silica framework, and the functionalization of both simultaneously. This approach requires a mastery of the preparation chemistry for the appropriate precursors as well as of the structure. This family is currently the best support for exploring polyfunctional materials, which can provide a route to interactive materials. The second family is the lamellar hybrid organic–inorganic materials, which are a new class of nanostructured materials. These materials are obtained by self-assembly (van der Waals interactions) of bridged organosilica precursors containing long alkylene chains during the sol-gel process without any structure-directing agent. This methodology has been extended to functional materials, which can also be obtained from monosilylated precursors.

12.1. INTRODUCTION

One of the main challenges in nanomaterials science is the discovery of the ways to organize the matter in terms of properties: chemical, physical, and so on. As far as the molecular chemistry is concerned, this organization will start from the nanometric scale. For that purpose, the sol-gel route, which could be called inorganic polymerization, is probably one of the best experimental approaches.[1] Indeed, this way for material synthesis exhibits two very important characteristics. (i) We have absolute compatibility with all the different aspects of chemistry, molecular chemistry (organic, inorganic) polymer chemistry, coordination chemistry, and biochemical and even biological chemistry as well.[2] All these different aspects of chemistry are compatible with the sol-gel process. That means that very wide possibilities exist for this chemical approach. (ii) Indeed, by changing the nature of the organic moiety, it is possible to obtain materials presenting a large variety of properties. These materials are generally considered amorphous and control of their structure during the sol-gel process remains a challenge and an exciting area of research in nanosciences and nanotechnology.

In this chapter, two families of organized and functionalized materials will be developed. The first one concerns the ordered mesoporous organosilicas, which are obtained by direct synthesis, that is, cocondensation of tetraethylorthosilicate (TEOS) and an organotrialkoxysilane R'-Si(OR)$_3$ or (OR)$_3$Si-R'-Si(OR)$_3$ in the presence of a structure-directing agent (SDA). In these materials, the functional groups (R') are accessible, regularly distributed, and located on the pores' surface or in the framework. The second family is the self-organized lamellar hybrid organic–inorganic materials. These materials are obtained by hydrolysis and polycondensation of bridged organosilica precursors containing at least two hydrolyzable –Si(OR)$_3$ without any SDA. Some examples for potential applications (i.e., chelating properties of these materials toward transition metals and lanthanides ions) will be given.

12.2. MESOPOROUS FUNCTIONALIZED MATERIALS PREPARED IN THE PRESENCE OF STRUCTURE-DIRECTING AGENT

The use of surfactant as a SDA for the synthesis of mesostructured silica has constituted one of the major discoveries of materials science in the past decades.[3] These materials are obtained by a sol-gel type polycondensation performed in the presence of surfactant micellar aggregates, which act as templates (Scheme 12.1). After elimination of the surfactant, the materials are characterized by long-range order and exhibit high surface area with a narrow pore size distribution, the pore size being controlled by the surfactant. Indeed, numerous scientists have focused their interest on the modification of the inner pores surfaces of mesoporous materials in order to render them suitable for applications,[4, 5] including catalysis,[6] separation,[7] metal removal,[8] molecular sieves,[9] and immobilization of biomolecules[10] by the incorporation of specific organofunctional groups in accordance with the desired application requirements.
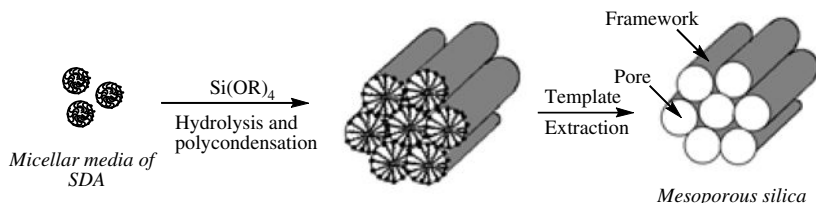
Scheme 12.1. Preparation of mesoporous silica.

12.2.1. Functionalization of the Channel Pores

The functionalization of the inner pore surface of the mesoporous materials can be achieved according to two main approaches. The first is the postsynthetic grafting of an organotrialkoxysilane $R'Si(OR)_3$ or organotrichlorosilanes ($R'SiCl_3$) onto the pore surface of a mesoporous ordered silica.[11] This method, which has been used very often, is very general and allows the introduction of a large variety of functional groups thanks to the reactive surface silanols. However, it permits neither control of the loading nor distribution of the organic functional groups, which depend on several parameters, such as the number of the surface silanol (SiOH) residual groups and the diffusion of reagents through the pore channels as well as steric factors.[12] A one-step alternative approach overcoming the main restrictions of the postsynthesis method consists of the copolymerization of tetraethylorthosilicate (TEOS) and an organotrialkoxysilane $R'Si(OR)_3$ in the presence of a structure-directing agent (Scheme 12.2).[13,14] This method allows control of the loading as well as regular distribution inside the pores channels.[15] However, it also presents some restrictions. Indeed, the precursor must be chosen carefully, that is, to be sufficiently hydrophobic to enter the core of the micelle and not too bulky to avoid its perturbation. These materials were at first prepared in the presence of cationic surfactant.[13a] Shortly after, the nonionic assembly route was investigated by using primary alkylamine[13b] as SDA and more recently the triblock copolymer as $EO_{20}PO_{70}EO_{20}$ [poly(ethylene oxide)–poly(propylene oxide)–poly(ethylene oxide)] called pluronic P123 was used.[16] This last surfactant proved to be very convenient under acidic conditions for the preparation of functionalized silica with hexagonal structure. The resulting materials have large uniform pore sizes, high surface areas, and high thermal and hydrothermal stabilities. They exhibit a good stability, which is very important for the expected applications.

By using the direct synthesis approach, a large variety of organic groups were introduced with regular distribution on the surface of the channel pores. We can cite
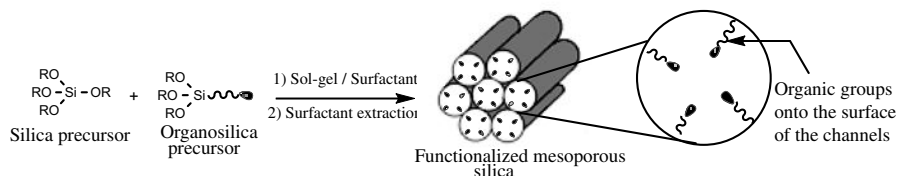
Scheme 12.2. Direct synthesis of functionalized mesoporous silica.
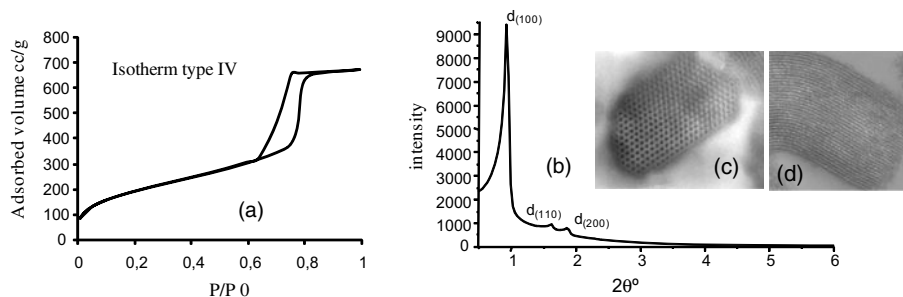
Figure 12.1. N_2 adsorption–desorption isotherm (a), XRD pattern (b), and TEM images (perpendicular (c) and parallel (d) of the channels) for mesoporous material containing CN groups.

as examples mercaptopropyl,[17] cyanopropyl,[18] chloropropyl,[19] diethylphosphona-topropyl,[20] and propylimidazol[21] groups, which have been introduced with high content. N_2 adsorption–desorption measurements of these different materials revealed type IV isotherms (see an example in Figure 12.1a), characteristic of mesoporous materials with a narrow pore size distribution and high surface areas $(600–1000 \, m^2 \, g^{-1})$. In addition, their hexagonal structure was show by powder X-ray diffraction (XRD) patterns (see an example in Figure 12.1b) and transmission electron microscopy (TEM) images (see examples in Figure 12.1c and 12.1d). The characteristics are very similar to those of SBA-15 silica type.[16]

An important characteristic of materials functionalized onto the pore surfaces is that the organic groups are easily accessible and can undergo further chemical transformations quantitatively and without disrupting the ordered structure. We have selected some examples, which have been subsequently chemically modified (Table 12.1); this is an important point, as it corresponds to an extension of the range of hybrid materials originating from direct synthesis (i.e., materials with organic groups regularly distributed inside the channel pores with control of the loading).

It is worth noting that, in the materials containing chloropropyl groups, a long reaction time is necessary to obtain a total nucleophilic substitution. Thus, the iodopropyl pendant group could be a particularly useful candidate for subsequent modification since it is a very good leaving group in nucleophilic displacement and a much better one than the chloro group. We reported recently on an original synthesis of mesoporous materials containing iodopropyl.[22] The key step in the synthetic procedure was to use HI instead of HCl as catalyst. Indeed, when HCl was used, the

TABLE 12.1. Some Examples of Chemical Modifications in the Pores

	X	Cl	CN	PO(OEt)$_2$	SH
	Y	(tetraazacyclotetradecane structure)	COOH	PO(OH)$_2$	SO$_3$H
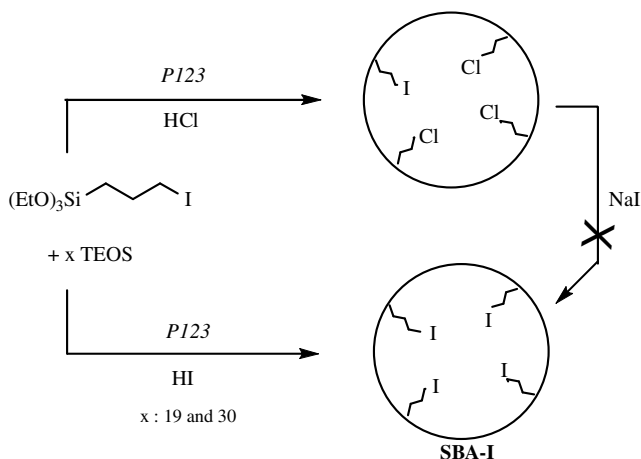
Scheme 12.3. Direct synthesis of iodopropyl-functionalized material.

cocondensation of 3-iodopropyltriethoxysilane and TEOS in the presence of P123 gave rise to ordered mesoporous silica containing mostly chloropropyl groups (70%) in addition to iodopropyl groups. Furthermore, it is worth noting that no exchange reaction occurred when ordered mesoporous silica containing chloropropyl groups was treated with NaI in excess (Scheme 12.3).

The usefulness of this material for the immobilization of various species was shown and compared to that of the ordered mesoporous silicas containing chloropropyl groups.

The chemical transformations within the channel pores of SBA-I material permit introduction of a wide variety of chemical functions, considerably enlarging their potentialities (Table 12.2). It was observed that several functional groups can easily be introduced into ordered mesoporous silica thanks to the iodopropyl group and with a much better yield than from the chloropropyl linker. As an example, introduction of cyclam (attachment by one bond) was achieved by treating the material SBA-I with 1.4 equiv. of cyclam in acetonitrile at reflux. Ninety-five percent of the mono substitution was obtained after 1 hour at reflux, whereas 32 h under the same experimental conditions were necessary to obtain 90% of chloro substitution included within the material SBA-Cl.

Mesoporous pore's functionalized materials have been considered as ideal nanoreactors for the deposition or growth of various guest molecules. Among them, the introduction of metallic nanoparticles constitutes a judicious choice for preparing nanocomposite materials able to display catalytic properties[23] that can find application as catalytic filters (Scheme 12.4).[24]

Thus, the formation of Mn_3O_4 nanoparticles[18b] was obtained by thermolysis of the magnetic cluster $[Mn_{12}O_{12}(C_2H_5COO)_{16}, (H_2O)_3]$ anchored to mesoporous silica functionalized with $-CO_2H$ groups; control of the growth of monodispersed indium (Figure 12.2) and indium oxide nanoparticles or nanorods was also possible thanks to phosphonate groups contained within ordered mesoporous silicas.[25]

TABLE 12.2. Chemical Transformations Within the Channel Pores of SBA-I Material

Reagents	SBA-I Yields (%)	SBA-Cl and Time (h)
Cyclam	95 (1)	90 (32)
Ephedrine	91 (24)	62 (48)
Diamine	100 (8)	—
Triamine	100 (4)	100 (48)
Triethylphosphite	100 (4)	20 (72)
Phosphine	58 (24)	8 (48)

Scheme 12.4. Growing of metal nanoparticles in the pores.
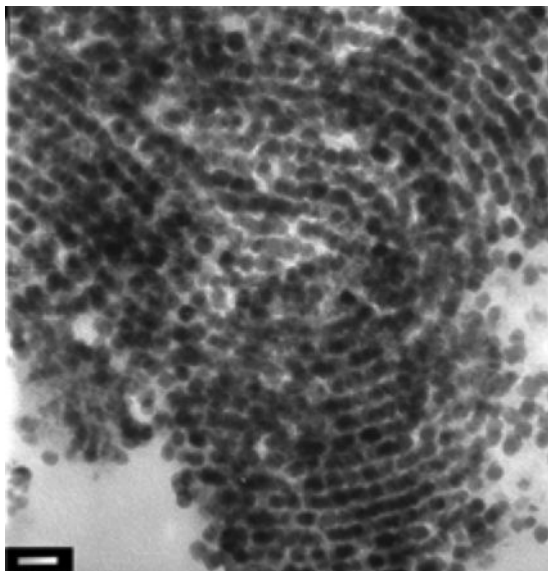
Figure 12.2. TEM image of material containing indium nanoparticles. Scale bar = 20 nm.

Acetylacetonatopropyl groups, introduced into the pore channels of silica by direct synthesis, allowed the growing and organization of Fe_3O_4 nanoparticles, giving rise to magnetic silica.[26] It was shown that the functionalization of the silica played a crucial role in the synthesis of Fe_3O_4-containing nanocomposites. Mercaptopropyl-functionalized mesoporous silica is very convenient for heavy metal ion (Hg^{2+}) adsorption;[8,27] they were also used in the field of catalysis[28] after transformation of SH groups in sulfonic acid groups. In addition to these applications, we have demonstrated that the hexagonal channels of mercaptopropyl-functionalized porous silica were effective hosts for the stabilization of gold(0) nanoparticles with a narrow size distribution directly correlated to the pore size distribution.[17b]

12.2.2. Bifunctionalization of the Channel Pores

Introduction of two distinct organic groups into the channel pores of mesoporous materials was also considered but gave rise to a number of much more limited studies.

Mann and co-workers[29] were the first to prove that the method of template directed cocondensation could be extended to synthesis of MCM-41 structures containing two distinct types of covalently linked organic functionalities. Then, several authors prepared bifunctional materials with the view to improve the catalytic performance of the materials by the introduction of hydrophobic groups in addition to the functional groups.[30–32] Some authors combined direct synthesis (cocondensation reaction) and postsynthesis reaction (grafting) to efficiently prepare bifunctional ordered meso-porous materials.[33,34] Other recent reports have dealt with the role of bifunctional materials as catalysts superior to the conventional monofunctionalized mesoporous silicas.[35] Finally, bifunctional materials were prepared in a two-step grafting process to test their potentiality as one-pot bifunctionnal catalysts.[36] All these reports pointed out the great interest of bifunctional mesoporous materials as compared to the conventional monofunctionalized one. However, the question of the distribution of two distinct organic groups located in the channel pores and introduced by direct synthesis has only been evoked and remains unsolved.

Recently, we studied the distribution (regular or irregular distribution or segregation) of two distinct organic groups located within the channel pores of mesoporous hybrid materials.[37] First, various ordered monofunctional mesoporous organosilicas were prepared by cocondensation of tetraethylorthosilicate (TEOS) and an organotriethoxysilane Σ–$(CH_2)_3$–$Si(OEt)_3$ (with Σ = acetylacetonate (acac), CN, SH, Cl, NH_2, and H). We have chosen two probes, both of them depending on the proximity of two organic groups. One was based on the chelating property toward $EuCl_3$ of acetyl acetonate groups (acac) and carboxylate groups. The other concerns the ion-exchange capability of the sulfonic acid moieties, which varies with the proximity of the acid groups. Thanks to the probes, we first showed that all the organic groups (SH, CN, acac) are accessible and regularly distributed within the channel pores of monofunctional mesoporous materials. Second, several ordered mesoporous materials SBA–Σ,Σ' containing two distinct functional groups including at least one probe were prepared in one step by co-condensation of TEOS and two organotriethoxysilanes Σ–$(CH_2)_3$–$Si(OEt)_3$ and Σ'–$(CH_2)_3$–$Si(OEt)_3$, under the same experimental conditions as previously. Taking into account the results obtained with the monofunctional materials as references, the distribution of two distinct functional groups located on the pores surfaces of mesoporous materials was determined. It appeared that the distribution of two distinct organic groups within the channel pores of mesoporous materials highly depends on the nature of the organic groups. We have shown that three different types of distribution for a pair of organic groups can occur (Scheme 12.5): regular distribution (**A**), irregular distribution (**B**), or segregation (**C**). It is worth noting that the distribution of organic groups depends on their solubility within the hydrophobe core of the micelle. The main factors explaining the repartition are probably polarity, lipophilicity, and bulkiness. We found a regular mixture for the pair's acac,SH, NH_2,SH, and SH,Cl. In these cases, the polarity of both organic groups is rather weak. Therefore, they should behave in the same way within the micelle. At the opposite extreme, the segregation of both distinct organic groups was observed for three different pairs: SH,H, SH,CN, and CN,H. In these cases, the difference in polarity between the two groups could explain the
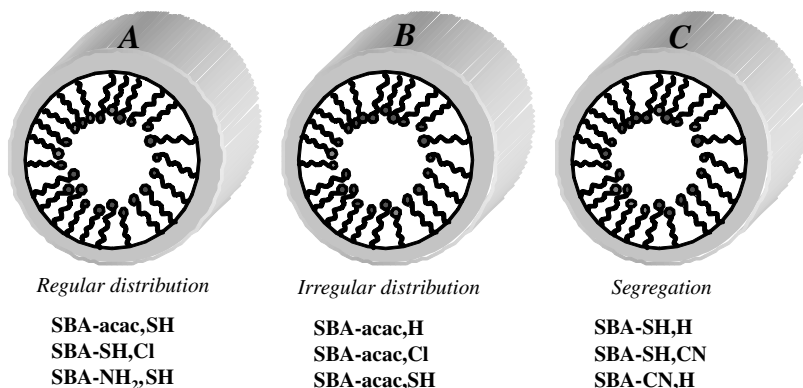
Scheme 12.5. Types of distribution of organic units in the bifunctional materials in SBA-Σ,Σ'.

segregation. The irregular distribution observed for the pairs acac,H, acac,Cl, and acac,CN corresponds to the situation just in between the other two. The presence of the rather bulky acac groups seems to involve a perturbation in the distribution except for the pair acac,SH. In this last case, hydrogen bond formation between both groups could explain the regular distribution.

We have established the distribution of different pairs of organic groups within the channel pores of mesoporous materials and pointed out the importance of some parameters, which probably play a role in the distribution of a pair of organic groups. However, this study does not permit one to predict the distribution of any pair of organic groups.

12.2.3. Functionalization of the Framework

The discovery in 1999 of periodic mesoporous organosilicas (PMOs) constituted a real advance in materials science.[38] Indeed, the hydrolytic polycondensation of bridged organosilica precursors of general formula $[(RO)_3Si]_mR'$ ($m \geq 2$) in the presence of a structure-directing agent allows the integration of organic groups into the walls of mesoporous silica through covalent Si–C bonds. The first examples of PMOs mainly concerned the introduction of small and relatively inert organic spacers originating from commercially available precursors. These studies were focused on the formation of highly ordered PMOs. Shortly after, efforts were made to introduce in the framework bridging groups able to induce chemical or physical (optical, electronic, magnetic) properties. Framework functionalization remains a challenge. Indeed, the main limitation to the formation of PMOs (even obtained by cocondensation with tetraethylorthosilicate (TEOS)) results from the fact that all the precursors of general formula $[(RO)_3Si]_mR'$ ($m \geq 2$) do not give rise to periodic mesoporous materials or give rise to ordered materials, but the organic fragments are not in all cases in the framework. That could be due either to the lack of rigidity of some organic precursors or/and to their poor hydrophilic character.[39,40] Several papers concerning materials obtained by cocondensation of at least a bis-silylated
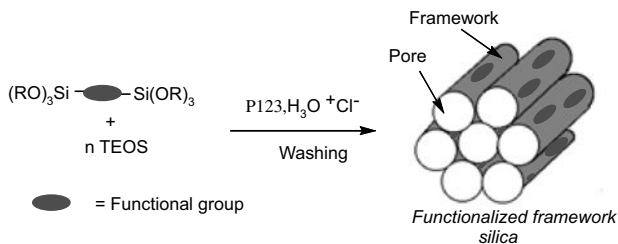
Scheme 12.6. Preparation of functionalized framework mesoporous.

organosilane with TEOS were reported due to the great interest of the functionalization of the framework to tailor the properties of mesoporous silica (Scheme 12.6).[41,42]

Mesoporous thiophene-bridged organosilicas with large pores were prepared for the first time starting from bis-silylated thiophene precursor (Scheme 12.7a) under acidic conditions using P123 as SDA.[43] Indeed, thiophene-bridged PMOs could be of great interest for electrochemical applications or for certain sensor applications. Bipyridinium units (Scheme 12.7b), which are known for their electron acceptor ability and their photo and thermochromic responses, were also incorporated within the pore walls.[44] Chiral organic moieties in the pore walls are an exciting target, which might permit new types of asymmetric syntheses and chiral separations. With a view to this, a chiral periodic mesostructured organosilica was prepared by co-hydrolysis and polycondensation of TEOS and a chiral vanadyl salen complex bearing two terminal trimethoxysilyl groups attached to the ligand (Scheme 12.7c).[45] This material induces a 30% enantioselectivity in the cyanosilylation of benzaldehyde and proved to be an extremely stable catalyst. PMOs with chiral binaphthyl and
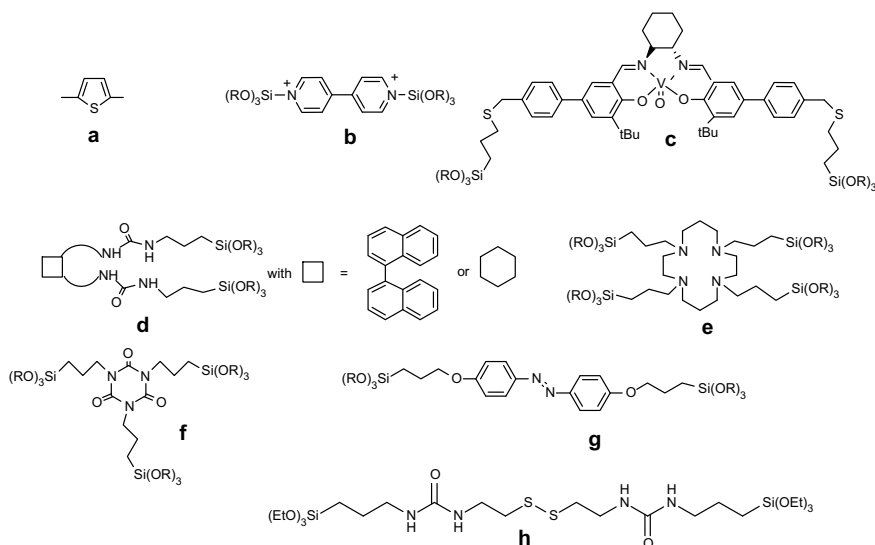
Scheme 12.7. A selection of bridged silylated precursors.

cyclohexyl units in the framework were also reported (Scheme 12.7d).[46] Hybrid materials able to strongly chelate cations are of interest, as such systems can give rise to materials presenting physical properties (e.g., optic, electric, or magnetic), depending on the nature of the salt. Thus, transition metal ions and lanthanides can provide these physical properties. As cyclam (1,4,8,11-tetraazacyclodecane) was well known for its remarkable binding ability toward transition metal ions,[47] we prepared cyclam-containing hybrid materials, in the presence of a structure-directing agent, with the aim of locating the cyclam moieties inside the framework. We determined the experimental conditions leading to the incorporation of cyclam units within the silica framework by cohydrolysis and polycondensation of TEOS and the tetrasilylated cyclam derivative (Scheme 12.7e).[48] Olkhovyk and Jaroniec described the preparation of PMOs with large heterocyclic bridging groups.[49] These materials were obtained by cohydrolysis and polycondensation of tris[3-(trimethoxysilyl) propyl]isocyanurate (Scheme 12.7f) and TEOS in the presence of P123 under acidic conditions. In spite of the flexibility of this organic moiety, the authors determined the experimental conditions that lead to a hexagonal structure of P6mm symmetry with an organic group loading of up to 30 mol%. The introduction of these chelating groups into the silica framework renders these materials attractive adsorbents for heavy metal ions, which was evidenced for mercury ions. The immobilization of photochromic azobenzene moieties into the pore walls of silica is of interest, as these materials could give rise to applications such as optical switches or optical data storage devices. This was achieved by cohydrolysis and polycondensation of 4,4′-[(triisopropoxysilyl) propyloxy]azobenzene (Scheme 12.7g) and TEOS in a aqueous solution at pH = 1.5 containing a high concentration of P123.[50] Thanks to the direct liquid crystal templating (LCT) approach, a material containing 20 wt% of the azobenzene group with a worm-like structure was obtained. Furthermore, we showed that there is a partial and reversible trans–cis isomerization of bridged azobenzene moieties located in the framework of the mesoporous material in spite of their attachment at both ends to the silica matrix. This process does not occur in the corresponding material prepared in the absence of surfactant. This striking result points out that the surfactant templating approach induces a regular dilution of the azobenzene moieties in the material.

Isocyanurate-containing silsesquioxane-bridged periodic mesoporous organosilicas (ICS–PMOs) modified by an alkyl-bridged organosilane ($-CH_2CH_2-$) were synthesized by Zhang et al.[51] These materials were used to chemically adsorb H_2PtCl_6, and Pt nanoparticles were subsequently prepared within the mesopores of ICS–PMO by $NaBH_4$ reduction.

Recently, we described a methodology allowing the confinement of monodisperse gold nanoparticles (Au NPs) of small size (~2 nm) in the framework of 2D hexagonal mesoporous organosilica containing SH groups (Scheme 12.8). For that purpose, a hydrophilic bis-silylated precursor containing a disulfide unit (Scheme 12.7h) was prepared. Materials with S_2 functionalized framework were obtained in one step by the "direct synthesis" method, which consists of a cohydrolysis and polycondensation of this bridged organosilica precursor with tetraethylorthosilicate (TEOS) in the presence of a nonionic triblock copolymer (P123) as structure-directing agent.
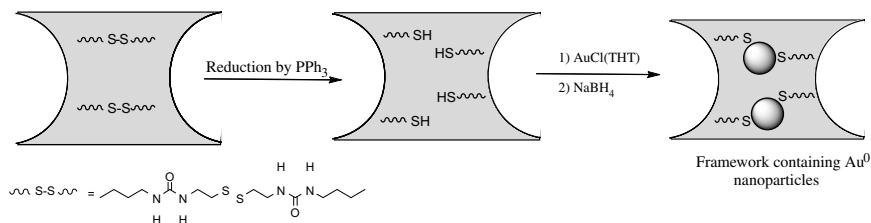
Scheme 12.8. Growing of Au nanoparticles in the framework.

Reduction of –SS– groups leads quantitatively to SH functional groups within the framework of 2D hexagonal mesoporous silicas. The subsequent growth of mono-disperse gold nanoparticles (Au NPs) of small size ($\sim$2 nm) within the walls of mesoporous materials was acheived.[52]

The generalization of the method to other NPs is expected on the condition of adapting the functionalization of the walls to the NPs chosen. This methodology could open the way to materials containing two kinds of NPs perfectly located at the nanometric scale: one in the channel pores and the other in the framework. That should involve, in the future, the design of novel materials presenting properties unsuspected until then.

12.2.4. Functionalization of the Channel Pores and the Framework

One of the major interests of the location of organic groups in the framework is the possibility for functionalization of the channel pores, leading to bifunctional hybrid materials. Indeed, the concept of including two different organic groups into a mesoporous material, where one is terminally attached in the channel pores and the other integrated to the framework, is of great interest because it opens the route to interactive materials; that is, materials coupling two properties one of which is located in the channel pores and the other in the framework, and at a nanometric range to each other. The first examples of bifunctional PMOs were reported shortly after the discovery of this new class of materials. They constituted a real advance in functionalized materials as they gave proof that the concept of including two different organic groups into a mesoporous material, where one is terminally attached in the channel pores and the other integrated into the framework, was realizable. Thus, Ozin and co-workers described the first examples of organic–inorganic hybrid periodic mesoporous materials prepared by direct synthesis and containing both bridging ethylene groups in the framework and terminal vinyl groups into the channel pores.[53] At the same time, Markowitz and co-workers described a variety of PMOs containing functional groups in the channel pores and bridged-ethane groups in the framework.[54] Inagaki and co-workers described the synthesis of highly bifunctional organic–inorganic hybrid mesoporous materials containing bridged phenylene groups in the framework and mercaptopropyl groups in the channel pores.[55] The oxidation of SH groups into sulfonic acid groups was further achieved in order to provide catalytic active sites. Jaroniec and co-workers reported mesoporous materials with large heterocyclic bridging groups and mercaptopropyl ligands.[56]
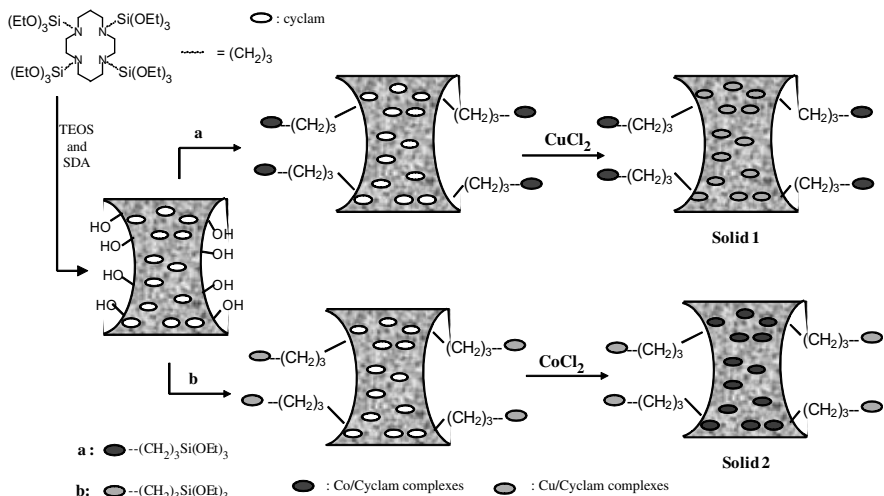
Scheme 12.9. Mesoporous hybrid materials containing two different chelated transition metal ions, one in the channel pores and the other in the framework. **Solid 1**: Co^{2+} in the channel pores and Cu^{2+} in the framework; **Solid 2**: Cu^{2+} in the channel pores and Co^{2+} in the framework.

We described the preparation of mesoporous hybrid materials containing bridged metal (Cu^{II}, Co^{II}, Eu^{III}, Gd^{III}) cyclam complexes inside the silica framework.[57] Grafting of a metal–N-triethoxysilylpropylcyclam complex inside the channel pores of these materials gave rise to a hybrid material containing two chelated transition metal salts (Cu^{II}-Co^{II} or Cu^{II}-Eu^{III} as examples)—one located inside the framework, the other in the channel pores and vice versa without any ion exchange (Scheme 12.9).

We investigated also the one-pot synthesis of bifunctional organosilica and three examples will be given. The first one is the direct synthesis of bifunctional organosilica containing chelating groups in the framework and reactive functional groups in the channel pores. These materials were obtained by direct synthesis using cocondensation of a bridged organosilica with chelating properties, tetraethylorthosilicate (TEOS) and an organotrialkoxysilane $ZSi(OR)_3$ with $Z =$ cyanopropyl, mercaptopropyl, and chloropropyl in the presence of a nonionic triblock copolymer (P123) as SDA. We investigated the influence of different parameters on the textural and structural characteristics of materials (concentration of the triblock copolymer P123, cosurfactant, and hydrothermal treatment) and the ability of chelating groups for complexation–decomplexation reactions (Scheme 12.10).[58]

The second example concerns a material containing a rather large NLO chromophore in the framework (bridged azobenzene phosphonium salt) and mercaptopropyl groups able to stabilize gold(0) nanoparticles in the channel pores of mesoporous silica (Scheme 12.11).[59] Indeed, the presence of gold nanoparticles in a material containing an NLO chromophore is expected to exalt the NLO response.[60] The bifunctionalized material was achieved in one step by using the
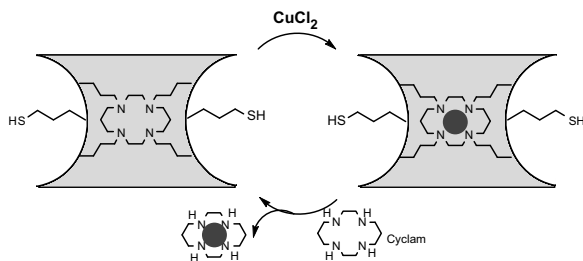
Scheme 12.10. An example of bifunctional mesoporous material.
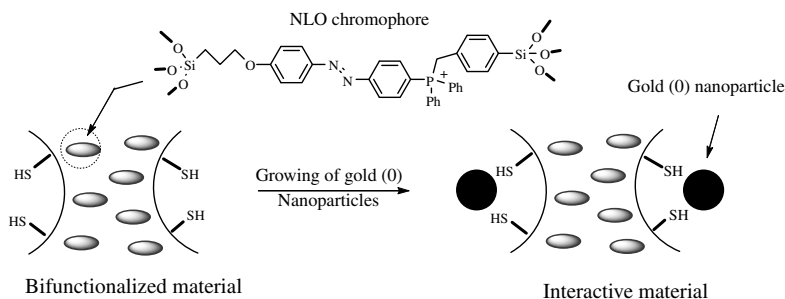
Scheme 12.11. Material with NLO groups in the framework and Au NPs in the pores.

direct LCT approach. Thanks to the high concentration of the nonionic triblock copolymers P123, we obtained a mesoporous silica containing the large bridged azobenzene phosphonium salt in the framework (8 wt%) and mercaptopropyl groups (16 wt%) in the channel pores with a wormhole framework. Gold nanoparticles were subsequently prepared according to a procedure described previously. The TEM image (Figure 12.3) shows that the nanoparticles size distribution was in agreement with the pore size of the host material. Thus, the LCT methodology could be a general route for materials coupling two properties, which could interact.
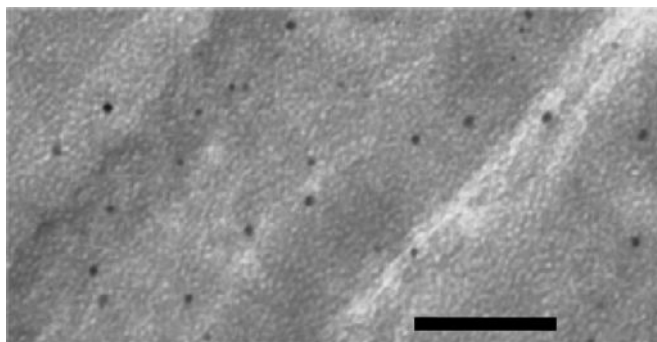
Figure 12.3. TEM image for material with NLO groups in the framework and Au NPs in the pores. Scale bar = 100 nm.
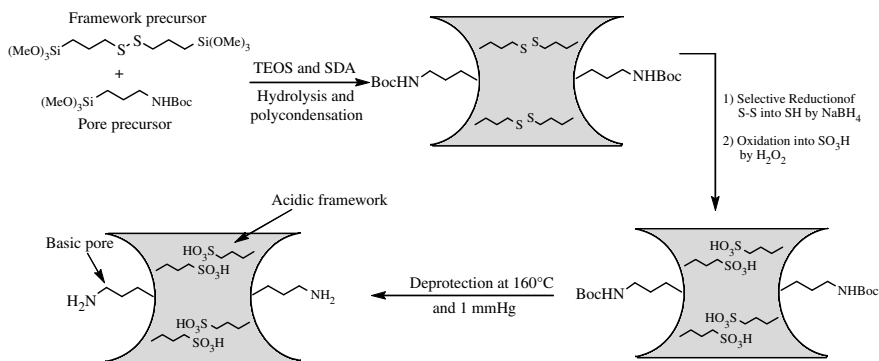
Scheme 12.12. Preparation of acido-basic bifunctionalized material.

The last example of bifunctionalized material that we have selected shows clearly how we can find the synthetic routes leading to material containing two antagonist functionalities located at the nanometric scale in a successful cohabitation and avoiding their mutual destruction. Recently, we reported the first synthesis of bifunctional mesoporous material containing two antagonist functions—an acidic group in the framework and a basic one in the channel pore. This novel material was synthesized by cocondensation of a ternary mixture of α,ω-bis-trimethoxysilyl-4,5-dithiooctane $(MeO)_3Si–(CH_2)_3–S–S–(CH_2)_3–Si(OMe)_3$, tetraethylorthosilicate (TEOS), and 3-t-butyloxycarbonyl aminopropyltriethoxysilane $(MeO)_3Si–(CH_2)_3–NHBoc$, in the presence of P123 as template under low acidic medium (Scheme 12.12).[61]

The bifunctional material having an acidic framework and basic pores was obtained by appropriate chemical transformations of the resulting material, that is, reduction of disulfide units into SH groups followed by their oxidation into SO_3H groups and deprotection of amino groups by thermal treatment under vacuum.

The self-assembly synthesis of mesoporous organosilicas with framework and surface groups is a promising method toward obtaining nanostructures with two opposing properties that coexist peacefully.

12.3. SYNTHESIS OF LAMELLAR FUNCTIONAL MATERIALS BY SELF-ASSEMBLY

Nanostructured organic–inorganic hybrid materials have attracted much attention as they constitute a unique class of materials combining the properties of the organic moieties and the inorganic matrix. Starting from bis-silylated precursors of the general formula $[(RO)_3Si]_mR'$ ($m \geq 2$), it is possible to obtain hybrid materials called bridged polysilsesquioxanes with a large variety of spacers R' including functionalized organic groups.[62] These materials are generally considered as amorphous. However, it was shown that the organic moieties (R') induce a self-organization during the polycondensation. XRD patterns obtained from bulk samples show broad

peaks consistent with some nanometer scale ordering.[63] The rigidity of the organic groups seemed to be crucial; the organic groups with rigid cores lead to birefringent materials. In contrast, flexible organic groups such as alkylene-bridging groups $(CH_2)_n$ gave rise to nonbirefringent systems.[64] In all cases, the polycondensation was achieved in organic solvent (THF or MeOH) in the presence of a stoichiometric amount of water and ammonium fluoride as catalyst.

The control of the structure of hybrid materials is a great challenge, as the organic moieties are susceptible to having physical or chemical properties directly or after chemical modification. Up to now, few examples of polysilsesquioxanes with long-range structure were reported: Moreau co-workers[65] described for the first time hybrid silica with lamellar structure, followed by Liu co-workers,[66] both using hydrogen-bonding interactions for inducing the order.

Kuroda and co-workers prepared layered silica-organic nanostructured materials by hydrolysis and polycondensation of alkoxytrichlorosilanes ($C_nH_{2n+1}OSiCl_3$, $n = 12$, 14, 16, and 20).[67] Shimojima and Kuroda showed also self-assembly of siloxane oligomers with long alkyl chains $C_nH_{2n+1}Si(OSi(OMe)_3)_3$ ($n = 10$ or 16) during their hydrolysis and polycondensation, the mesostructure (hexagonal or lamellar) being controlled by the alkyl chain length.[68] Furthermore, some of us observed that the level of periodicity starting from bis-silane triols is higher than that obtained starting from the corresponding bis(trimethoxysilyl) precursor, suggesting that the hydrophilic head $Si(OH)_3$ forces the hydrophobic core to assemble.[69]

These results prompted us to consider again the hydrolytic polycondensation of bridged organosilica precursors with long alkylene chains $(MeO)_3Si–(CH_2)_n–Si(OMe)_3$ ($n = 10$, 12, 18, and 30). We observed a drastic difference in the organization of the hybrid materials $O_{1.5}Si–(CH_2)_n–SiO_{1.5}$ by using H_2O as the solvent at pH 1.5 instead of an organic solvent (THF) and in water; the structure of the materials was found to be highly dependent also on the alkylene chain lengths.[70]

When the number n of CH_2 units is lower than 10, there is no self-assembly. The polycondensation provides a material without long-range order. When the length of the chains is between 10 and 18 CH_2 units, there is formation of very well ordered lamellar materials confirmed by powder X-ray diffraction and TEM measurements (Figure 12.4).

We observed that, in the case of the longest chains ($n = 30$), the lipophilicity controls the organization and the organic precursor behaves as a surfactant. The obtained material has a hexagonal structure. A mechanism of self-assembly was proposed (Scheme 12.13). The long hydrophobic alkylene chains should assemble together in water, which involves the close proximity of silanols groups formed at pH 1.5 and their polycondensation as a consequence. Thus, self-assembly should be due to weak hydrophobic van der Waals interactions between the long alkylene chains in water. For the alkylene chains in C_{12} and C_{18}, the likely alignment of alkylene chains[71] controls the lamellar structure. In contrast, the longest chains in C_{30} should be bent and they should assemble together to form micellar rods with a hydrophobic core and a hydrophilic surface.[72]

We then showed that this strategy could be extended to the formation of lamellar functional materials starting from bridged organosilica precursors with long alkylene
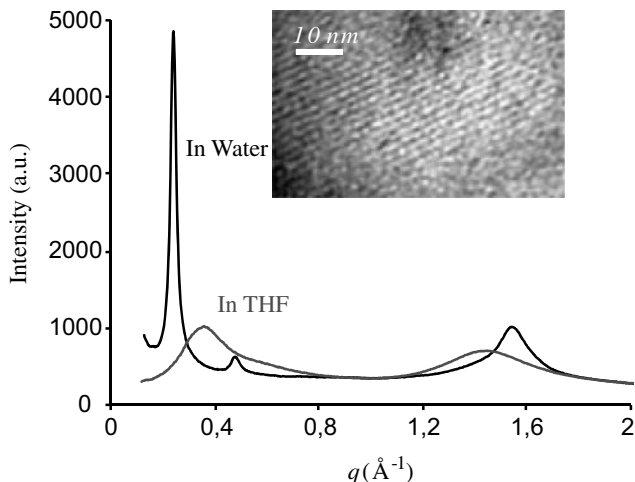
Figure 12.4. XRD patterns of materials ($n = 18$) obtained in water and in THF. The inset shows the TEM image of material obtained in water.

chains comprising a functionalized core that could be chemically modified in a further step.

Lamellar materials with –SH groups have been obtained by introducing –S–S– bridges in the core of the alkylene chains (Scheme 12.14).[73] Cleavage of S–S bonds into SH bonds was achieved by a mild oxidoreduction reaction giving rise to materials with a high content in thiol groups (Scheme 12.14). Finally, SH groups were converted into SO$_3$H groups by treatment of the materials with H$_2$O$_2$ solution followed by acidification with diluted H$_2$SO$_4$ solution. Interestingly, the well-defined layer structure of the obtained materials was maintained after the chemical transformation.

The next example concerns the preparation of lamellar materials containing amino groups. In order to prepare such materials, we used CO$_2$ gas as an assembly agent.
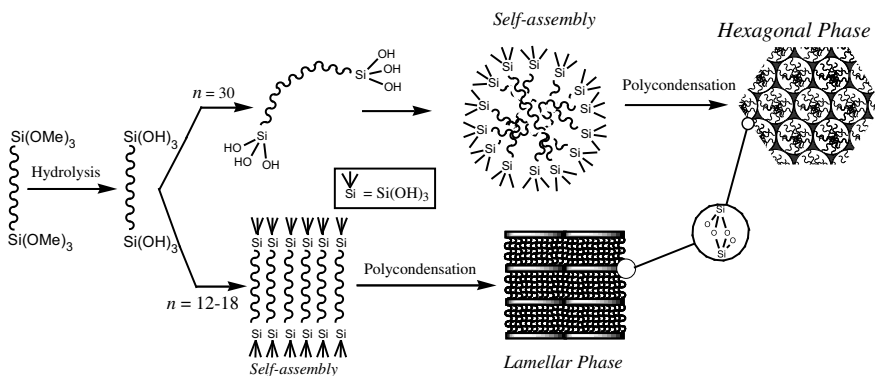
Scheme 12.13. Self-assembly of alkylene chains thanks to hydrophobic interactions.

Scheme 12.14. Self-organization of bridged organosilica with disulfide units and subsequent chemical transformation.

Indeed, CO_2 reacts with primary and secondary amines at ordinary temperature and pressure to give ammonium carbamate salts, which are thermally unstable and release CO_2 upon heating (Scheme 12.15).[74]

This "old chemistry" has been used successfully recently by some others.[75] Thus, reactions between CO_2 and immobilized amines have been employed for gas sensing. Rudkevich and Xu used CO_2 gas to construct novel types of supramolecular polymers by employing both hydrogen bonding and dynamic thermally reversible carbamate bonds, which lead to switchable materials.[76]

We developed a novel method allowing the preparation of highly structured and functionalized materials with amino functions by introducing transformable cores based on ionic interactions (ammonium carbamate salts) and van der Waals inter-actions.[77] The CO_2 uptake on the commercially available *N*-(6-aminohexyl)-3-

R = alkyl and R' = alkyl or H

Scheme 12.15. Reversible reaction between CO_2 and amines.

Figure 12.5. XRD patterns of materials with ammonium carbamate groups and the corresponding material with amino groups.

aminopropyltrimethoxysilane was used to afford a supramolecular network of bis-silylated ammonium carbamate salts, the hydrolytic polycondensation of which gave rise to structured hybrid materials (Scheme 12.16A). Subsequent loss of CO_2 was achieved upon heating, giving rise to materials containing free amino groups (Scheme 12.16B) in which the structure was maintained as evidence by X-ray diffraction measurements (Figure 12.5).

It is very important to note that these materials cannot be obtained directly from the precursors containing free amino groups without CO_2. In our approach, CO_2 acted as bridging groups to obtain a bis-silylated species.

Recently, we described a new approach to obtain ordered and highly functionalized silicas containing carboxylic[78] and phosphonic[79] acid groups starting from monosilylated precursors. This method is based on the in situ formation of acid dimers followed by the polycondensation of silanols groups. In addition, we evidenced that long-range order was promoted by the force and the number of the acid groups and also by the van der Waals interactions between the long alkylene chains. Furthermore, these materials were proved to be able to chelate very high contents in lanthanide ions.

These materials were obtained by hydrolysis and polycondensation of monosilylated precursors cyanoalkyltrialkoxysilane ($NC–(CH_2)_nSi(OR)_3$) and diethylphosphonatoalkyltriethoxysilane ($(EtO)_2(O)P–(CH_2)_nSi(OEt)_3$) with $n = 3$, 5, and 11 in acidic media without any structure-directing agent. The hydrolysis of –CN and –$P(O)(OEt)_2$ groups into –COOH and –$P(O)(OH)_2$ involves the in situ formation of dimers by strong hydrogen bonds, which is the crucial step to obtain a solid (Scheme 12.17).

It is worth noting that under the same experimental conditions the hydrolysis of chloropropyltriethoxysilane does not allow the formation of a material due to the absence of formation of bis-silylated derivatives by dimerization. This result
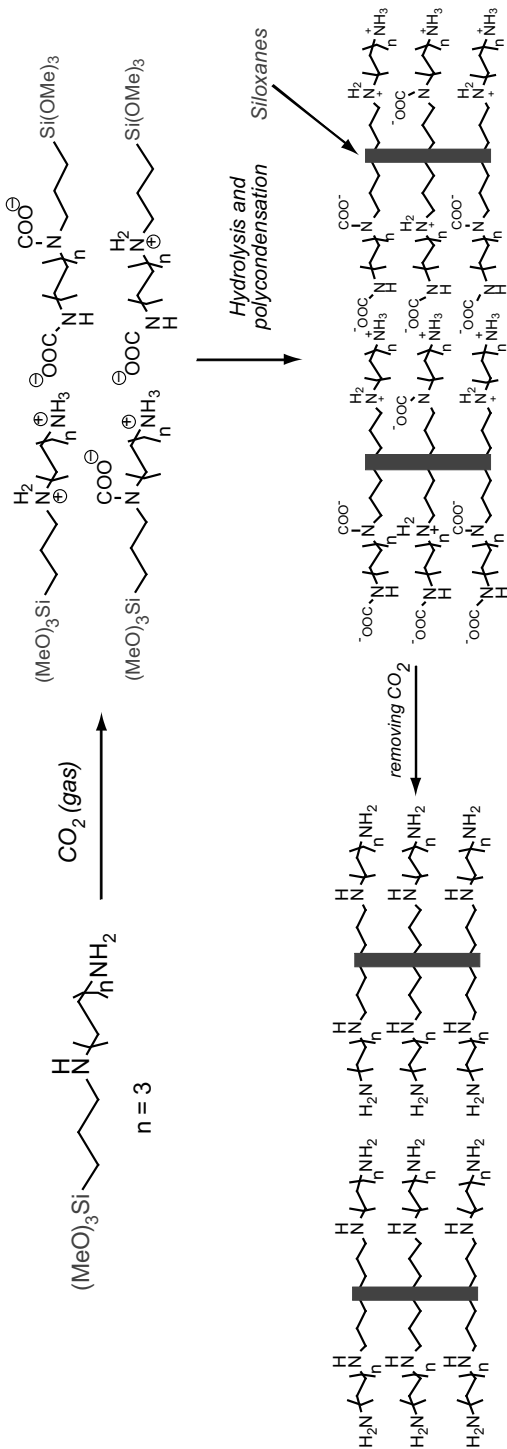
Scheme 12.16. Preparation of amino functionalized lamellar hybrid materials by self-assembly.

Scheme 12.17. Material formation thanks to the hydrogen bond interactions between monomeric species.

demonstrates that the crucial step to get a solid starting from cyanoalkyltrialkoxysilanes is the in situ formation of dimers between the carboxylic acid units by hydrogen bondings.

In addition, the better self-assembly of material (with $n = 11$) in comparison to materials with $n = 3$ and 5 shows the involvement of hydrophobic interactions between the long alkylene chains to get lamellar structure. That is in agreement with long-range order formed during the hydrolytic polycondensation of bridged organosilica with long alkylene chains described above. These materials with high content of H^+/g could be also good candidates for high proton conductivity, which is particularly useful in the fuel cell domain.

Finally, we reported last year an easy preparation of a bis-zwitterionic lamellar material containing ammonium carboxylate groups by a sol-gel process using ethylenediamine as bridging groups.[80] This material was prepared in one step by a sol-gel process from only 3-aminopropyltriethoxysilane (APTES), succinic anhydride, and ethylene diamine (Scheme 12.18).

The in situ formation of ammonium carboxylate groups playing as bridging groups was proved by ^{13}C NMR and FT-IR spectroscopies. This material was proved to be very convenient for solid/liquid extraction of trivalent lanthanide ions (La, Eu, Gd, and Yb) by exchange reaction (see Section 12.4).[81] Furthermore, this study

Scheme 12.18. Preparation of the bis-zwitterionic lamellar hybrid material.

highlights the great potential offered by the hybrid materials prepared from molecular precursors by the sol-gel process.

12.4. POTENTIAL APPLICATIONS

As we mentioned earlier, hybrid organic–inorganic materials, combining the properties of organic moieties and inorganic matrix, are a very interesting class of materials that offer a large domain of potential applications. Indeed, by changing the nature of the organic moiety, it is possible to obtain materials presenting a wide range of possibilities in terms of chemical or physical properties.

In order to point out some potential applications, several examples concerning the chemical properties of hybrid materials described above will be given.

The growing of monodispersed RuO_2 nanoparticles was achieved thanks to phosphonate groups contained within ordered mesoporous silicas.[82] The use of mesoporous nanomaterials containing RuO_2 nanoparticles ($RuO_2@SiO_2$ nanomaterials) as catalytic filters for gas sensors, as well as after deposition as "on-chip"
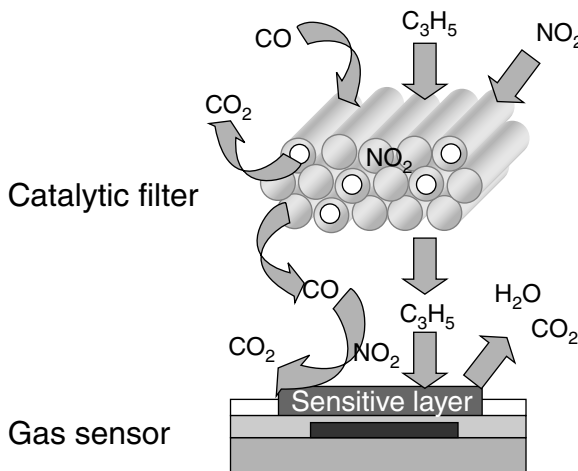
Scheme 12.19. Nanomaterials containing RuO_2 NPs as catalytic filters for gas sensors.

filters or as external filters, revealed their very interesting catalytic behavior for the preferential detection of propane in a gas mixture of propane/carbon monoxide/ nitrogen dioxide in air (Scheme 12.19). The efficiency of the propane discrimination was dependent on the metal content of the nanocomposite materials: a higher Ru/Si weight ratio induced higher SC_3H_8/SCO ratios. The $RuO_2@SiO_2$ nanomaterials partially removed CO from the gas mixture by selectively oxidizing it to CO_2, leaving the hydrocarbon content unaltered. The catalytic behavior of these nanomaterials was greatly enhanced in comparison with another hybrid nanomaterial similarly prepared from unfunctionalized commercial silica for which nanoparticles that were not well dispersed in the silica grains were observed.

This synthetic method was a simple and reproducible way to produce well-controlled composite metal- or metal-oxide-containing silica nanomaterials displaying interesting catalytic properties for gas-sensing applications. This study demonstrated that a single approach, deposition of a catalyst suspended in a liquid, may allow the sensitivity of gas sensors to be modulated; it also showed that the nature of the material employed was critical for obtaining reproducible results.

In the context of sustainable development, efforts have to be made to produce goods, raw materials, and chemicals by taking into account environmental constraints. Particularly, catalysis has an important role to play, because it enables one to achieve reactions with higher rates and higher selectivity in the desired products. In this context, the metathesis of functionalized olefins, mainly with Ru-based catalysts, has become a key reaction in organic synthesis, because it is atom economical (no or little by-products, reduction of the number of steps) and environmentally friendly (low temperatures of reaction, etc.). In fact, it represents a good example of a "green reaction." From the industrial point of view, this reaction is already very important in petrochemical processes, for example, propene production by cross-metathesis of ethene and 2-butene, and there is a large research effort in industry to incorporate this reaction to produce bulk and fine chemicals. However, until now, there is no key

industrial process relying on the metathesis of functionalized olefins, and this originates from the following two major reasons. (i) The existing highly active homogeneous catalysts based on ruthenium are very expensive and deactivate rapidly (needs high loading). Moreover, contamination of the reaction products by metals and the difficulty to remove traces of metals in organic products are also key problems for the drug industry. (ii) The classical heterogeneous or homogeneous supported catalysts, developed so far, display very poor performances and do not present any advantage compared to the best homogeneous catalysts (need high loading, no regeneration, etc.).

Thus, we developed successfully a stable well-defined catalytic hybrid nanomaterial that is highly active in the metathesis reaction of functionalized olefins.[83] This material was achieved by generating well-defined ruthenium–N-heterocyclic carbene ligands (Ru–NHC) supported systems perfectly dispersed in a mesoporous hybrid material and further stabilized by surface ligands (Scheme 12.20).

These catalytic nanomaterials display high activity (TOF) and stability (TON vs. time, recycling, and leaching). Furthermore, from the overall catalytic performances and stereochemical studies, we demonstrated that the active "single site" corresponds to a Ru–NHC species. Finally, the versatility of such a synthetic methodology and its transfer to various metals and ligands (including sensitive ones) is a very promising approach toward a wide range of tailor-made well-defined heterogeneous catalysts.

The chelating capability of the lamellar nanomaterials containing different organic groups (SH, NH_2, COOH, etc.) has been tested for transition metal and lanthanide ions.

Materials with SH groups were treated with an aqueous solution of $HgCl_2$ at room temperature. It was observed that the ratio of metal ions per thiol moieties was found to be around 1/3, confirming the high mercury adsorption capacity (2.3 mmol of Hg^{2+} per gram). These values are high in comparison with most of those obtained for thiol-modified mesoporous silica described in the literature.[84]

This high adsorption affinity toward mercury ions renders these materials promising for removal of other heavy metal ions from aqueous solutions (i.e., environmental remediation).

Amino-functionalized materials are probably the most widely studied organic–inorganic materials due to their numerous potential applications such as catalysis and metal sorbents.[85] Amine-containing materials were also often prepared as sorbents for gas removal, in particular, CO_2.[86]

The accessibility of the amine groups in the lamellar nanomaterials as well as their chelating ability toward transition metal or lanthanide anhydrous salts was
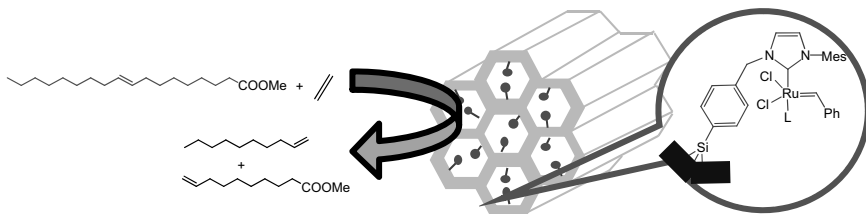
Scheme 12.20. Catalytic hybrid nanomaterials for alkenes metathesis.

investigated. For that purpose, the materials were treated with an ethanolic solution of $CuCl_2$, $Eu(NO_3)_3$, or $Gd(NO_3)_3$. The N/Cu molar ratio was found to be around 2. That means that two amino groups are necessary on average for chelating one Cu^{2+}, which is very low. Indeed, in solution, the complexation of Cu^{2+} requires generally four nitrogen atoms. Thus, it appears that all the amino groups are operative as ligands and that, in this case, long-range order does not improve considerably the chelating properties of the materials.

In the case of complexation of europium salts, the N/Eu molar ratio was found to be 6.5 and 4.8 for materials obtained from 3-aminopropyltrimethoxysilane and N-(6-aminohexyl)-3-aminopropyltrimethoxysilane, respectively.[77]

It is worth noting that complexation of $CuCl_2$ and $EuCl_3$ was also investigated within amine-free materials containing only long alkylene chains. In all cases, a salt uptake less than 1% was obtained, showing that the salt uptake was due to a complexation reaction and not adsorption. This result renders these materials as good candidates for ion separation, including actinides.

Similar study was done on materials containig carboxylic acid groups. For that purpose, the carboxylic acid groups were transformed into potassium carboxylate salts by treating M1($n = 3$), M2 ($n = 5$), and M3 ($n = 11$), with either a t-BuOK solution in t-BuOH at 25°C or potassium acetylacetonate (K(acac)) in ethanol, giving rise to materials named M1K–M3K (Scheme 12.21).

The exchange reactions were confirmed by elemental analyses. The K/Si molar ratio was found to be 0.90, 0.99, and 0.93 for M1K, M2K, and M3K respectively. These values are very close to the theoretical values (1), indicating that the overall
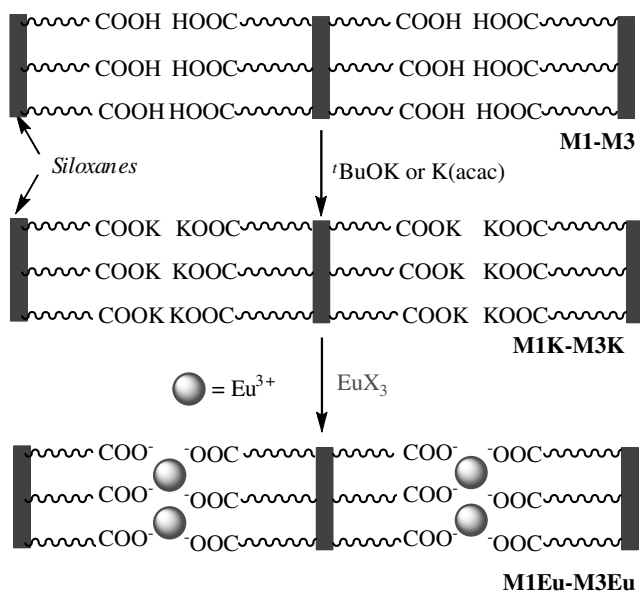
Scheme 12.21. Chelating ability of M1K–M3K toward europium salts.

–COOH groups were accessible. Finally, the chelating ability of M1K–M3K toward europium salts was tested.[79] The solids were treated with an ethanolic solution of $EuCl_3$ at room temperature. The resulting solids were copiously washed with ethanol to eliminate any noncomplexed salts and named M1Eu, M2Eu, and M3Eu, respectively (Scheme 12.21). The titration by EDTA of the whole filtrate containing the noncomplexed salt was done and revealed the incorporation of one Eu^{III} per three carboxylate units for M1K and M2K on average. Interestingly, the Eu^{III} uptake within M3K was found to be one Eu^{III} per two carboxylate units. Elemental analyses of Si and Eu in M1Eu–M3Eu confirmed the content in europium obtained by titration. Furthermore, it is worth noting that the content in potassium in M1Eu–M3Eu was found to be very low (<50 ppm) showing that all the carboxylate groups were operative. The Eu^{III} uptake within M3K requiring only two carboxylate units instead of three within M1K and M2K was explained as the consequence of a more regular packing arrangement of the carboxylate groups. It is worth noting that there is no Eu^{III} uptake directly from M1–M3.

These last results motivate us to the bis-zwitterionic lamellar material containing ammonium carboxylate groups for solid/liquid extraction of trivalent lanthanide ions (La, Eu, Gd, and Yb) by exchange reaction. In ethanol, the exchange ethylenediammonium versus Ln(III) was proved to be total by complexometry measurements and elemental analyses, one Cl^- ion per one Ln(III) remaining as expected for charge balance. In contrast, in aqueous solution, the material was found to be selective toward lanthanide; the cation uptake depends on the nature of the salt, the difference between two lanthanides reaching up to 20% in some cases (Figure 12.6). This suggests that this material could be very convenient for storage and separation of lanthanides and actinides. Finally, thanks to the Fe^{3+} containing material, which presents the same high-angle diffraction peaks as the lanthanide-containing materials, a structural model was proposed (Figure 12.7).
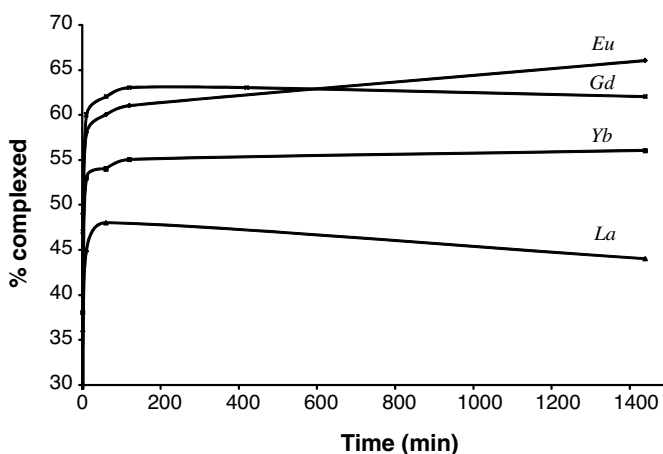
Figure 12.6. Kinetic measurements of ion-exchange reactions from zwitterionic materials toward Ln(III) in water.
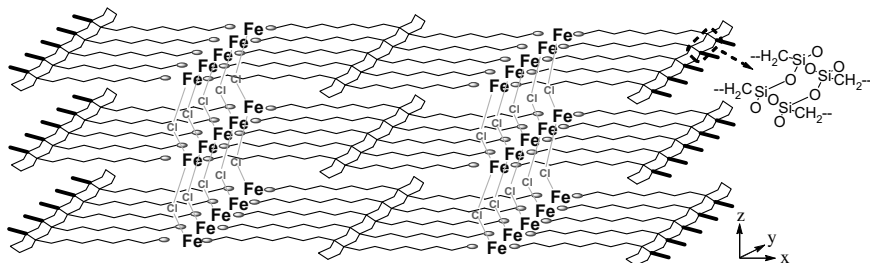
Figure 12.7. Three-dimensional representation of zwitterionic material containing Fe^{III} ions.

12.5. CONCLUSION

This chapter attempts to show the potential uses offered by hybrid organic–inorganic nanomaterials. The ordered mesoporous hybrid materials family appear to permit location control of the functional groups in the solids. Thus, this family opens the route to interactive materials, that is, materials in which several functions susceptible to present physical properties can interact at the nanometric scale. We have shown also that it is possible to obtain long-range ordered bridged silsesquioxanes by changing the experimental conditions only. The organization was found to be highly dependent on the alkylene chain lengths. This methodology was extended to the formation of functional hybrid organic–inorganic materials from bridged organo-silica precursors with long alkylene chains having a functionalized and chemically transformable core. By playing on the nature of the functional core, it was possible to obtain lamellar materials containing a high content in SH groups, amino groups, and carboxylic acid groups. The unexpected chelating properties of these materials toward transition metal and lanthanide ions were found to be high and in relation with the local organization of the material. This suggests that this material could be a good candidate for storage and separation of lanthanides and actinides. Furthermore, this study highlights the great potential offered by the hybrid materials prepared from molecular precursors by the sol-gel process. Finally, a large number of new hybrid nanomaterials offering various properties will be synthesized in the near future thanks to the creative force of the chemical synthesis and the imagination of the chemists.

REFERENCES

1. Brinker, C. J.; Scherrer, G. W. *Sol-Gel Science: The Physics and Chemistry of Sol-Gel Processing.* Academic Press, San Diego, CA, 1990.
2. Dave, B. C.; Miller, J. M.; Dunn, B.; Valentine, J. S.; Zink, J. I. *J. Sol-Gel Sci. Technol.*, **1997**, *18*, 629. Nassif, N.; Coiffier, A.; Coradin, T.; Roux, C.; Livage, J. *J. Sol-Gel Sci. Technol.*, **2003**, *26*, 1141. Zhou, J. C.; Chuang, M. H.; Lan, E. H.; Dunn, B.; Gillman, B. P. L.; Smith, S. M. *J. Mater. Chem.*, **2004**, *14*, 2311.

3. Kresge, C. T.; Leonowicz, M. E.; Roth, W. J.; Vartuli, J. C.; Beck, J. S. *Nature*, **1992**, *359*, 710. Beck, J. S.; Vartuli, J. C.; Roth, W. J.; Leonowicz, M. E.; Kresge, C. T.; Schmitt, K. D.; Chu, T.-W.; Olson, D. H.; Sheppard, E. W.; McCullen, S. B.; Higgins, J. B.; Schlenker, J. L. *J. Am. Chem. Soc.*, **1992**, *114*, 10834. Tanev, P. T.; Pinnavaia, T. J. *Science*, **1995**, *267*, 865. Prouzet, E.; Pinnavaia, T. J. *Angew. Chem. Int. Ed. Engl.*, **1997**, *36*, 516. Zhao, D.; Huo, Q.; Feng, J.; Chmelka, B. F.; Stucky, G. D. *J. Am. Chem. Soc.*, **1998**, *120*, 6024.

4. Sanchez, C.; Julian, B.; Belleville, P.; Popall, M. *J. Mater. Chem.*, **2005**, *15*, 3559.

5. Vinu, A.; Hossain, K. Z.; Ariga, K. *J. Nanosci. Nanotechnol.*, **2005**, *5*, 347.

6. Maschmeyer, T.; Rey, F.; Sankar, G.; Thomas, J. M. *Nature*, **1995**, *378*, 159. Shyu, S.-G. Cheng, S.-W. Tzou, D.-L. *Chem. Commun.*, **1999**, 2337. Jin Bæ, S.; Kim, S.-W.; Hyeon, T.; Moon Kim, B. *Chem. Commun.*, **2000**, 31. Luts, T.; Frank, R.; Suprun, W.; Fritzsche, S.; Hey-Hawkins, E.; Papp, H. *J. Mol. Catal A*, **2007**, *273*, 250.

7. Salesch, T.; Bachmann, S.; Brugger, S.; Rabelo-Schaefer, R.; Albert, K.; Steinbrecher, S.; Plies, E.; Mehdi, A.; Reyé, C.; Corriu, R. J. P.; Lindner, E. *Adv. Funct. Mater.*, **2002**, *2*, 134.

8. Mercier, L.; Pinnavaia, T. J. *Adv. Mater.*, **1997**, *9*, 500. Feng, X.; Fryxxell, G. E.; Wang, L. Q.; Kim, A. Y.; Liu, J.; Kemner, K. M. *Science*, **1997**, *276*, 923.

9. Zhang, W.; Wang, J.; Tanev, P. T.; Pinnavaia, T. J. *Chem. Commun.*, **1996**, 979.

10. Moelans, D.; Cool, P.; Baeyens, J.; Vansant, E. F. *Catalysis Commun.*, **2005**, *6*, 591. Galarneau, A.; Renard, G.; Mureseanu, M.; Tourrette, A.; Biolley, C.; Choi, M.; Ryoo, R.; Di Renzo, F.; Fajula, F. *Microporous. Mesoporous. Mater.*, **2007**, *104*, 103.

11. Zhang, W.; Froba, M.; Wang, J.; Tanev, P. T.; Wong, J.; Pinnavaia, T. J. *J. Am. Chem. Soc.*, **1996**, *118*, 9167. Cauvel, A.; Renard, G.; Brunel, D. *J. Org. Chem.*, **1997**, *62*, 749. Macquarrie, D. J.; Jackson, D. B.; Mdoe, J. E. J.; Clark, J. H. *New J. Chem.*, **1999**, *23*, 539.

12. Walcarius, A.; Delacôte, C. *Chem. Mater.*, **2003**, *15*, 4181.

13. (a) Burkett, S. L.; Sims, S. D.; Mann, S. *Chem. Commun.*, **1996**, 1367. (b) Macquarrie, D. J. *Chem. Commun.*, **1996**, 1961. Macquarrie, D. J.; Jackson, D. B.; Tailland, S.; Utting, K. A. *J. Mater. Chem.*, **2001**, *11*, 1843. (c) Mori, Y.; Pinnavaia, T. J. *Chem. Mater.*, **2001**, *13*, 2173. (d) Corriu, R. J. P.; Hoarau, C.; Mehdi, A.; Reyé, C. *Chem. Commun.*, **2000**, 71.

14. Corriu, R. J. P.; Embert, F.; Guari, Y.; Mehdi, A.; Reyé, C. *Chem. Commun.*, **2001**, 1116.

15. Mouawia, R.; Mehdi, A.; Reyé, C.; Corriu, R. J. P. *New J. Chem.*, **2006**, *1*, 1077.

16. Yang, P. D.; Zhao, D. Y.; Chmelka, B. F.; Stucky, G. D. *Chem. Mater.*, **1998**, *10*, 2033.

17. (a) Margolese, D.; Melero, J. A.; Christiansen, S. C.; Chmelka, B. F.; Stucky, G. D.; *Chem. Mater.*, **2000**, *12*, 2448. (b) Guari, Y.; Thieuleux, C.; Mehdi, A.; Reyé, C.; Corriu, R. J. P.; Gomez-Gallardo, S.; Philippot, K.; Chaudret, B. *Chem. Mater.*, **2003**, *15*, 2017.

18. (a) Yang, C. M.; Zibrowius, B.; Schüth, F.; *Chem. Commun.*, **2003**, 1772. (b) Folch, B.; Larianova, J.; Guari, Y.; Guerin, C.; Mehdi, A.; Reyé, C. *J. Mater. Chem.*, **2004**, *14*, 2703.

19. Corriu, R. J. P.; Mehdi, A.; Reyé, C.; Thieuleux, C. *Chem. Mater.*, **2004**, *16*, 159.

20. Corriu, R. J. P.; Datas, L.; Guari, Y.; Mehdi, A.; Reyé, C.; Thieuleux, C. *Chem. Commun.*, **2001**, 763.

21. Corriu, R. J. P.; Lancelle, E.; Mehdi, A.; Reyé, C.; Brandes, S.; Guilard, R. *J. Mater. Chem.*, **2002**, *12*, 1355.

22. Alauzun, J.; Mehdi, A.; Reyé, C.; Corriu, R. J. P. *New J. Chem.*, **2007**, *31*, 911.

23. Taguchi, T.; Schüth, F. *Microporous Mesoporous Mater.*, **2005**, *77*, 1.

24. Cabot, A.; Arbiol, J.; Cornet, A.; Morante, J. R.; Chen, F.; Liu, M. *Thin Solid Films*, **2003**, *436*, 64. Arbiol, J.; Cabot, A.; Morante, J. R.; Chen, F.; Liu, M. *Appl. Phys. Lett.*, **2002**, *81*, 3449.

25. Guari, Y.; Soulantica, K.; Philippot, K.; Thieuleux, C.; Mehdi, A.; Reyé, C.; Chaudret, B.; Corriu, R. J. P. *New J. Chem.*, **2003**, *7*, 1029.

26. Matsura, V.; Guari, Y.; Larionova, J.; Guerin, C.; Caneschi, A.; Sangregorio, C.; Lancelle-Beltran, E.; Mehdi, A.; Corriu, R. J. P. *J. Mater. Chem.*, **2004**, *14*, 3026.

27. Lim, M. H.; Blanford, C. F.; Stein, A. *Chem. Mater.*, **1998**, *10*, 467. Mercier, L.; Pinnavaia, T. J. *Environ. Sci. Technol.*, **1998**, *32*, 2749. Brown, J.; Mercier, L.; Pinnavaia, T. J. *Chem. Commun.*, **1999**, 69. Brown, J.; Richer, R.; Mercier, L. *Microporous Mesoporous Mater.*, **2000**, *37*, 41.

28. Van Rhijn, W. M.; De Vos, D. E.; Sels, D. E.; Bossaert, W. D.; Jacobs, P. A. *Chem. Commun.*, **1998**, 37. Bossaert, W. D.; De Vos, D. E.; Van Rhijn, W. M.; Bullen, J.; Grobet, P. J.; Jacobs, P. A. *J. Catal.*, **1999**, *182*, 156. Diaz, I.; Mohino, F.; Pérez-Pariente, J.; Sastre, E. *Appl. Catal. A*, **2001**, *205*, 19.

29. Hall, S. R.; Fowler, C. E.; Lebeau, B.; Mann, S. *Chem. Commun.*, **1999**, 201.

30. Macquarrie, D. J. *Green Chemistry*, **1999**, 195.

31. Margolese, D.; Melero, J. A.; Christiansen, S. C.; Chmelka, B. F.; Stucky, G. D. *Chem. Mater.*, **2000**, *12*, 2448.

32. Cano-Serrano, E.; Blanco-Brieva, G.; Campos-Martin, J. M.; Fieorro, J. L. G. *Langmuir*, **2003**, *19*, 7621.

33. Zhang, W.-H. Lu, X.-B. Xiu, J.-H. Hua, Z.-L. Zhang, L.-X. Robertson, M.; Shi, J.-L. Yan, D.-S. Holmes, J. D. *Adv. Funct. Mater.*, **2004**, *14*, 544.

34. Mbaraka, I. K.; Shanks, B. H. *J. Catal.*, **2005**, *229*, 365.

35. Huh, S.; Chen, H.-T.; Wiench, J. W.; Pruski, M.; Lin, V. S.-Y. *Angew. Chem. Int. Ed.*, **2005**, *44*, 1826.

36. Goettmann, F.; Grosso, D.; Mercier, F.; Mathey, F.; Sanchez, C. *Chem. Commun.*, **2005**, 1240.

37. Mouawia, R.; Mehdi, A.; Reyé, C.; Corriu, R. J. P. *J. Mater. Chem.*, **2008**, *18*, 4193.

38. Inagaki, S.; Guan, S.; Fukushima, Y.; Ohsuna, T.; Terasaki, O. *J. Am. Chem. Soc.*, **1999**, *121*, 9611; Melde, B. J.; Holland, B. T.; Blanford, C. F.; Stein, A. *Chem. Mater.*, **1999**, *11*, 3302; Asefa, T.; MacLachlan, M. J.; Coombs, N.; Ozin, G. A. *Nature*, **1999**, *402*, 867; Yoshina-Ishii, C.; Asefa, T.; Coombs, N.; MacLachlan, M. J.; Ozin, G. A. *Chem. Commun.*, **1999**, 2539.

39. Burleigh, M. C.; Markowitz, M. A.; Spector, M. S.; Gaber, B. P. *Chem. Mater.*, **2001**, *13*, 4760.

40. Benitez, M.; Das, D.; Ferreira, R.; Pischel, U.; Garcia, H. *Chem. Mater.*, **2006**, *18*, 5597.

41. Kuroki, M.; Asefa, T.; Whitnal, W.; Kruk, M.; Yoshina-Ishii, C.; Jaroniec, M.; Ozin, G. A. *J. Am. Chem. Soc.*, **2002**, *124*, 13886.

42. (a) Vinu, A.; Hossain, K. Z.; Ariga, K. *J. Nanosci. Nanotechnol.*, **2005**, *5*, 347. (b) Hoffmann, F.; Cornelius, M.; Morell, J.; Fröba, M. *J. Nanosci. Nanotechnol.*, **2006**, *6*, 265. (c) Hoffmann, F.; Cornelius, M.; Morell, J.; Fröba, M. *Angew. Chem. Int. Ed.*, **2006**, *45*, 3216.

43. Morell, J.; Wolter, G.; Fröba, M. *Chem. Mater.*, **2005**, *17*, 804.

44. Alvaro, M.; Ferrer, B.; Fornés, V.; Garcia, H. *Chem. Commun.*, **2001**, 2546.

45. Baleizao, C.; Gigante, B.; Das, D.; Alvaro, M.; Garcia, H.; Corma, A. *Chem. Commun.*, **2003**, 1860.

46. Alvaro, M.; Benitez, M.; Das, D.; Ferrer, B.; Garcia, H. *Chem. Mater.*, **2004**, *16*, 2222.

47. Bernhardt, P. V.; Lawrance, G. A. *Coord. Chem. Rev.*, **1990**, *104*, 297.

48. Corriu, R. J. P.; Mehdi, A.; Reyé, C.; Thieuleux, C. *Chem. Commun.*, **2002**, 1382.

49. Olkhovyk, O.; Jaroniec, M. *J. Am. Chem. Soc.*, **2005**, *127*, 60.

50. Besson, E.; Mehdi, A.; Lerner, D. A.; Reyé, C.; Corriu, R. J. P. *J. Mater. Chem.*, **2005**, *15*, 803.

51. Zhang, W. H.; Zhang, X.; Hua, Z.; Harish, P.; Schroeder, F.; Hermes, S.; Cadenbach, T.; Shi, J.; Fischer, R. A. *Chem. Mater.*, **2007**, *19*, 2663.

52. Besson, E.; Mehdi, A.; Reyé, C.; Corriu, R. J. P. *J. Mater. Chem.*, **2009** *19*, 4746.

53. Asefa, T.; Kruk, M.; MacLachlan, M. J.; Coombs, N.; Grondey, H.; Jaroniec, M.; Ozin, G. A. *J. Am. Chem. Soc.*, **2001**, *123*, 8520.

54. Burleigh, M. C.; Markowitz, M. A.; Spector, M. S.; Gaber, B. P. *Chem. Mater.*, **2001**, *13*, 4760. Burleigh, M. C.; Markowitz, M. A.; Spector, M. S.; Gaber, B. P. *J. Phys. Chem. B*, **2001**, *105*, 9935.

55. Yang, Q.; Kapoor, M. P.; Inagaki, S. *J. Am. Chem. Soc.*, **2002**, *124*, 9694.

56. Olkhovyk, O.; Pikus, S.; Jaroniec, M. *J. Mater. Chem.*, **2005**, *15*, 4285.

57. Corriu, R. J. P.; Mehdi, A.; Reyé, C.; Thieuleux, C. *New J. Chem.*, **2003**, *27*, 905. Corriu, R. J. P.; Mehdi, A.; Reyé, C.; Thieuleux, C. *Chem. Commun.*, **2003**, 1564.

58. Alauzun, J.; Mehdi, A.; Reyé, C.; Corriu, R. J. P. *J. Mater. Chem.*, **2007**, *17*, 349.

59. Besson, E.; Mehdi, A.; Matsura, V.; Guari, Y.; Reyé, C.; Corriu, R. J. P. *Chem. Commun.*, **2005**, 1775.

60. Anceau, C.; Brasselet, S.; Zyss, J.; Gadenne, P. *Opt. Lett.*, **2003**, *28*, 713.

61. Alauzun, J.; Mehdi, A.; Reyé, C.; Corriu, R. J. P. *J. Am. Chem. Soc.*, **2006**, *128*, 8719.

62. Shea, K. J.; Loy, D. A. *Chem. Mater.*, **2001**, *13*, 3306. Corriu, R. J. P. *Angew. Chem. Int. Ed. Engl.*, **1996**, *35*, 4001.

63. Boury, B.; Corriu, R. J. P. *Chem. Commun.*, **2002**, 795. Boury, B.; Corriu, R. J. P. *Chem. Rec.*, **2003**, *3*, 120.

64. Vergnes, A.; Nobili, M.; Delord, P.; Cipelleti, L.; Boury, B.; Corriu, R. J. P. *J. Sol-Gel Sci. Technol.*, **2003**, *26*, 621.

65. Moreau, J. J. E.; Vellutini, L.; Wong Chi Man, M.; Bied, C. *J. Am. Chem. Soc.*, **2001**, *123*, 1509. Moreau, J. J. E.; Vellutini, L.; Wong Chi Man, M.; Bied, C.; Bantignies, J-L. Dieudonné, P.; Sauvajol, J.-L. *J. Am. Chem. Soc.*, **2001**, *123*, 7957.

66. Liu, N.; Yu, K.; Smarsly, B.; Dunphy, D. R.; Jiang, Y. B.; Brinker, C. J. *J. Am. Chem. Soc.*, **2002**, *124*, 14540.

67. Fujimoto, Y.; Shimojima, A.; Kuroda, K. *Chem. Mater.*, **2003**, *15*, 4768.

68. Shimojima, A.; Kuroda, K. *Angew. Chem. Int. Ed.*, **2003**, *42*, 4057.

69. Cerveau, G.; Chappellet, S.; Corriu, R. J. P. *J. Mater. Chem.*, **2003**, *13*, 2888.

70. Alauzun, J.; Mehdi, A.; Reyé, C.; Corriu, R. J. P. *J. Mater. Chem.*, **2005**, *15*, 841.

71. Kaneko, Y.; Matsumoto, N. T.; Fujii, K.; Kurashima, K.; Fujita, T. *J. Mater. Chem.*, **2003**, *13*, 2058.

72. Duchet, J.; Chapel, J.-P. Chabert, B.; Gerard, J.-F. *Macromolecules*, **1998**, *31*, 8264.

73. Alauzun, J.; Mehdi, A.; Reyé, C.; Corriu, R. J. P. *Chem. Commun.*, **2006**, 347.

74. Hoerr, C. W.; Harwood, H. J.; Ralston, A. W. *J. Org. Chem.*, **1944**, *9*, 201.

75. Rudkevich, D. M.; Xu, H. *Chem. Commun.*, **2005**, 2651.

76. Rudkevich, D. M.; Xu, H. *Chem. Eur. J.*, **2004**, *10*, 5432.

77. Alauzun, J.; Mehdi, A.; Reyé, C.; Corriu, R. J. P. *J. Am. Chem. Soc.*, **2005**, *127*, 11205. Alauzun, J.; Besson, E.; Mehdi, A.; Reyé, C.; Corriu, R. J. P. *Chem. mater.*, **2008**, *20*, 503.

78. Mouawia, R.; Mehdi, A.; Reyé, C.; Corriu, R. J. P. *J. Mater. Chem.*, **2007**, *17*, 616.

79. Mouawia, R.; Mehdi, A.; Reyé, C.; Corriu, R. J. P. *J. Mater. Chem.*, **2008**, *18*, 2028.

80. Besson, E.; Mehdi, A.; Chollet, H.; Reyé, C.; Guilard, R.; Corriu, R. J. P. *J. Mater. Chem.*, **2008**, *18*, 1193.

81. Besson, E.; Mehdi, A.; Van der Lee, A.; Chollet, H.; Reyé, C.; Guilard, R.; Corriu, R. J. P. *Chem. Eur. J.*, **2010**, *16*, 10226.

82. Jansat, S.; Pelzer, K.; Garcia Anton, J.; Raucoules, R.; Philippot, K.; Maisonnat, A.; Chaudret, B.; Guari, Y.; Mehdi, A.; Reyé, C.; Corriu, R. J. P. *Adv. Funct. Mater.*, **2007**, *17*, 3339.

83. Maishal, T. K.; Alauzun, J.; Basset, J. -M. Copéret, C.; Corriu, R. J. P.; Jeanneau, E.; Mehdi, A.; Reyé, C.; Veyre, L.; Thieuleux, C. *Angew. Chem. Int. Ed.*, **2008**, *47*, 8654. Karamé, I.; Alauzun, J.; Basset, J.-M. Boualleg, M.; Camus, J.-M. Copéret, C.; Corriu, R. J. P.; Jeanneau, E.; Maishal, T. K.; Mehdi, A.; Reyé, C.; Veyre, L.; Thieuleux, C. *Chem. Eur. J.*, **2009**, *15* 11820.

84. Brown, J.; Richer, R.; Mercier, L. *Microporous Mesoporous Mater.*, **2000**, *37*, 41.

85. Hicks, J. C.; Dabestani, R.; Buchanan, A. C.; Jones, C. W. *Chem. Mater.*, **2006**, *18*, 5022. Wang, X.; Lin, K. S. K.; Chan, J. C. C.; Cheng, S. *J. Phys. Chem. B*, **2005**, *109*, 1763. Chujo, T.; Gonda, Y.; Oumi, Y.; Sano, T.; Yoshitake, H. *J. Mater. Chem.*, **2007**, *17*, 1372. Yokoi, T.; Yoshitake, H.; Yamada, T.; Kubota, Y.; Tatsumi, T. *J. Mater. Chem.*, **2006**, *16*, 1125. Walcarius, A.; Etienne, M.; Bessiere, J. *Chem. Mater.*, **2002**, *14*, 2757.

86. Khatri, R. A.; Chuang, S. S. C.; Soong, Y.; Gray, McM. *Energy and Fuels*, **2006**, *20*, 1514.

INDEX

Achiral, 140, 144, 145, 150, 152, 165, 166
Acyclic enones, 146, 154, 173
Aerobic, 10, 18, 30, 35, 140
Agglomeration, 2, 25
Alcoholysis, 81–83, 85, 87, 88, 91, 93
Alloy particles, 10, 12
Alkoxysilane, 104, 125
Alumina, 158
Amino substituted polysiloxane, 85
Antibodies, 152, 185–187, 235, 269
Arrhenius plot, 17, 19
Atherosclerotic plaque, 199
Autoclave, 143

Bacterial cells, 253
Bactericides, 66
Bandgaps, 139, 140
Bidentate, 146, 148, 153
Biodegradable, 68, 69
Biomedical applications, 210
Biotemplate, 263
Biotin, 214, 262, 272, 273
Block copolymer, 2, 25, 28, 98, 101, 102, 286, 287, 291, 293, 294
Blood plasma proteins, 219–222
Boron carrier, 184, 185, 187
Boron nanotubes, 181, 190, 191
Boron neutron capture therapy, 181
Boron nitride nanotubes, 181, 190, 191
β-sheet, 257
Brownian motion, 107

Calcination, 163, 287–294
Carbanion pump, 101, 102
Carbon nanotubes, 25, 44, 59, 181, 190, 220, 223, 244, 245
Carborane cages, 189, 194, 195
Catalysis, 1, 2, 3, 5, 9, 11, 14, 20, 21, 23, 26, 34, 35, 37, 42, 43, 53, 55–57, 61, 68, 72, 73, 74, 81–83, 87, 88, 139, 140, 141, 144, 156, 165, 174, 178, 228, 300, 305, 321, 322, 326
Catalytic filters, 303, 320, 321
Cation exchange resin, 26, 27, 29–31, 43, 45–51, 53
Ceramic, 24
Chalk–Harrod-like mechanism, 81
Chalcones, 146, 150, 157, 173
Chelate resin, 35
Chiral auxiliary, 145, 146, 149, 153, 155–157, 173
Chiral separations, 308
Cholesterol, 186, 270, 276, 277
Claisen–Schmidt condensation, 141, 157, 159, 173, 174
Circular dichroism, 219, 224, 227, 233–235, 239, 240, 242, 260, 261
Closed-pore materials, 286, 293
Coagulation, 10, 11
Collagen, 251, 254–260, 263, 264, 265
Collagen fibril self-assembly, 254
Composite, 1, 3–6, 11, 14, 16–20, 25, 26, 32, 36, 37, 42, 43, 45–47, 51, 80, 91, 193–195, 293, 294, 303, 305, 321